JCTC Journal of Chemical Theory and Computation

Perspective on Diabatic Models of Chemical Reactivity as Illustrated by the Gas-Phase S_N2 Reaction of Acetate Ion with 1,2-Dichloroethane

Rosendo Valero, Lingchun Song, Jiali Gao,* and Donald G. Truhlar*

Department of Chemistry and Supercomputing Institute University of Minnesota, Minneapolis, Minnesota 55455-0431

Received August 4, 2008

1. Introduction

A useful starting point for elucidating the factors that determine the activation barrier in many condensed-phase and enzyme-catalyzed reactions is an understanding of the intrinsic reactivity of the uncatalyzed reaction in the gas phase. Subsequently, the effect of solvation and/or catalysis can be considered. For example, a computation of the change of a reaction's activation barrier from aqueous solution to an enzyme can be very informative, although it is not sufficient to generate a complete picture of enzyme catalysis[1] nor adequate to validate the potential energy surface and computational techniques.[1,2] Valence bond (VB) theory provides a fundamental framework for this purpose because of its direct connection to concepts such as chemical bonding, reactivity, and electronic resonance.[3] When ab initio self-consistent-field valence bond (VBSCF) theory is represented in terms of a two-state model,[4] describing the interactions between the reactant and the product diabatic states, the intuitive nature of such a simple model is particularly useful both for understanding and for computation. However, when such a multiconfigurational VB wave function is reduced to a two-state representation, the construction of these two states is not unique, as we illustrate in this article, and this can lead to different interpretations of chemical reactivity and the origin of solvent effects. Consequently, it is essential to carefully examine the nature of a specific two-state VB model before it is applied to chemical reactions in solution and in enzymes. In this article, we aim to provide a perspective on different ways of constructing diabatic states, and we discuss some limitations on their usefulness for describing the potential energy surface of the adiabatic ground state.

Consider, for a more specific example, the haloalkane dehalogenase catalytic cycle. The haloalkane dehalogenase enzyme catalyzes the hydrolytic cleavage of carbon-halogen bonds in a broad range of halogenated alkanes to yield the corresponding alcohol with concomitant release of the halide anion.[5−11] The efficiency of the enzymatic conversion is maximal with 1,2-dichloroethane (DCE) as the substrate.[8] The catalytic action of haloalkane dehalogenase has been shown to consist of two chemical reaction steps. The first step involves a nucleophilic substitution (S_N2) reaction in which the carboxylate group of Asp124 attacks the halogenated hydrocarbon, displacing the halide anion and forming an enzyme-ester covalent intermediate.[5] The second step is the hydrolysis of the intermediate by an activated water molecule, assisted by His289 and Asp260 residues of the enzyme, to yield the alcohol and to return the enzyme to its native form for the next catalytic cycle.[6] The factors that affect the catalytic efficiency of the enzyme have been the focus of many theoretical studies.[12−32] The reactions of several nucleophiles (hydroxide, formate, and acetate) with substrates such as methyl chloride, chloroethane, and DCE have been used to mimic the attack of the Asp124 residue of haloalkane dehalogenase on a haloalkane.[13,14,20,22,23] Many theoretical studies of S_N2 reactions in the gas phase and in solution, including those just cited, have made use of ab initio or semiempirical molecular orbital or post-Hartree-Fock electronic structure calculations.[33−49] Nucleophilic substitution reactions have also been investigated by density functional theory.[41,48,50−53] The use of valence-bond (VB) theory to study these reactions quantitatively is less common because of the higher computational cost and slow convergence (with respect to adding configurations) of VB calculations, but VB theory has the advantage of providing unique insight into the electronic structure.[54−59] Examples of nucleophilic substitution reactions studied using VB methodology include the identity $X^- + RX' \rightarrow XR + X'^-$ reactions (R = alkyl; X, X′ = F, Cl, Br, I);[54−57,60−68] nonidentity versions of these reactions (X not the same as

* Corresponding author e-mail: jgao@umn.edu (J.G.), truhlar@umn.edu (D.G.T.).

10.1021/ct800318h CCC: $40.75 © 2009 American Chemical Society
Published on Web 12/04/2008

X′);[54−57] the $Cl^- + CH_3SH_2^+ \rightarrow ClCH_3 + SH_2$ and $H_3N + CH_3SH_2^+ \rightarrow H_3NCH_3^+ + SH_2$ reactions;[61] the particular case $CH_3Cl + NH_3 \rightarrow Cl^- + CH_3NH_3^+$ of the general Menshutkin reaction;[55,58,69−72] reactions of esters and ketyl radical anions;[56,73] reactions at peptide bonds;[74] and reaction at phosphorus.[75]

A challenging question in condensed-phase reaction dynamics is the definition of the ***reaction coordinate***. Arguably, the choices that have been made may be divided into two categories: (1) the use of a set of solute geometrical variables or a combination of approximate functions of relevant bond orders that vary systematically from the reactants to the products and (2) the use of a generalized solvent coordinate such as, in the Marcus theory of electron transfer reactions, the ***energy gap*** between the reactant and product diabatic states. In the first case, two common choices are (i) an analytic function of internal coordinates, such as the breaking and forming bond distances, or the distance between the reactants and (ii) the distance along a union of the steepest descent paths in mass-scaled coordinates from the saddle point to reactants and products. Choice (i)[76−80] is usually called a distinguished reaction coordinate, and choice (ii)[80−86] is called a minimum-energy-path (MEP) coordinate or an intrinsic reaction coordinate.

Sometimes one considers an ensemble of reaction paths and hence of reaction coordinates, as in ensemble-averaged variational transition state theory[87,88] and in the transition path sampling method,[89] but we shall not need to consider such theories for the present perspective article.

In category (2), the energy gap is typically defined as the difference in energy between two ***diabatic states*** of the reagents (also called "solute" or "primary subsystem"), one representing the reactants and the other representing the products, with both including their interactions with their surroundings (also called "solvent" or "bath" or "secondary subsystem"). For example, for an outer-sphere electron transfer reaction, the product state differs from the reactant state by the rearrangement of one electron, and the energy difference between these states is a function of the coordinates and polarization state of the solvent. Thus a diabatic energy gap can be considered to be a collective solvent coordinate. Such a diabatic gap was originally invoked by Marcus[90,91] in weak-overlap electron transfer theory and has subsequently been used more broadly to describe other charge transfer processes in the condensed phase.[61,62,92−107] Other collective solvent coordinates have also been used.[108−116] In addition, diabatic states and diabatic potential energy surfaces (sometimes called quasiadiabatic states and distortion potentials in this context) have sometimes been used for dynamical treatments by using separate coordinate systems for reactants and products.[117−121]

Although diabatic energy functions for condensed-phase reactions were originally defined in terms of classical models, for example, the nonequilibrium electronic polarization energy of a dielectric medium interacting with a spherical ion,[122] progress in the treatment of complex reactions can be achieved by using quantum mechanical electronic structure theory to define the diabatic states and calculate their energies. The present article is primarily concerned with such quantum mechanical calculations. When one uses electronic structure theory to treat the Born-Oppenheimer dynamics of complex systems, the nuclear coordinates are parameters in the electronic Hamiltonian and electronic wave functions. The electronic Hamiltonian (which is defined, as usual, to include the nuclear repulsion) is diagonalized, and the eigenvalues as functions of nuclear coordinates are the (adiabatic) potential energy surfaces for nuclear motion. That is called the adiabatic representation. Here we employ an analogous treatment for a two-state diabatic representation. In this representation, the electronic Hamiltonian (which in general is Hermitean and here is assumed real symmetric, so there is only one unique off-diagonal element) is not diagonal. The diagonal matrix elements are the ***diabatic potential energy surfaces***, and the off-diagonal Hamiltonian matrix element is the ***diabatic coupling*** which decreases the energy as compared to the diabatic crossing energy, thereby stabilizing the transition state of the adiabatic ground state.[123−126]

In previous work, the diabatic potential energy surfaces have often been modeled without explicit calculations of electronic wave functions—for example by molecular mechanics such as in the Warshel-Weiss empirical valence bond formalism[92−103] (we shall abbreviate this specific formalism as EVB; other VB treatments—both older and newer—with empirical elements are called semiempirical VB to distinguish them from EVB), by solvent dielectric continuum theory,[122] by linear response theory,[127] or by phenomenological fitting of reaction rates.[62,128,129] The EVB model treats the diabatic coupling as a parametrized function—typically, as for example in the case considered here,[21] as a constant. Further, a fundamental assumption of the EVB model is that the overlap integral between the diabatic states is zero. However, this model has been found to be insufficient to reproduce the vibrational frequencies at the transition state.[130,131] As a result, the EVB model is not well suited for computing detailed rate quantities such as kinetic isotope effects that require an accurate treatment of the potential energy surface, the zero-point energy (ZPE), and quantum mechanical tunneling.[2] In other semiempirical VB models, the overlap-dependence of the diabatic coupling is treated implicitly by parametrizing the off-diagonal element to fit the entire adiabatic potential surface. Methods in the latter category include molecular mechanics with valence bond (MMVB),[132] multiconfigurational molecular mechanics (MCMM),[116,133,134] multistate empirical valence bond (MS-EVB),[135] and the generalized Gaussian algorithm of Chang and Miller[130] and Schlegel and Sonnenberg.[131]

In contrast, the fourfold way and mixed molecular orbital and valence bond (MOVB) methods that we describe in this article use electronic structure theory to derive the diabatic states; the ability of electronic structure theory to predict details of potential energy surfaces (such as vibrational frequencies) is one motivation for using quantum mechanical electronic structure theory in the diabatic formalism.

In comparing theories of diabatic states, it is important to keep in mind that diabatic electronic states are not uniquely defined,[4,59,105,136−141] and a number of definitions have proved useful in various contexts. Many of these, whether

or not quantum mechanics is explicitly employed, are most easily understood in terms of VB theory.[4,59,136,141−149] In VB theory, an electronic configuration state function (CSF) with a definite bonding pattern and set of formal atomic charges is called a VB structure. Note that, depending on the state, a VB structure may be a single Slater determinant or a linear combination of determinants. A resonance structure may be expressed in terms of one or more VB structures. For example, in VB theory, the wave function for the resonance structure of the HCl molecule can be written as a linear combination of a covalent (Heitler-London) VB structure which is described by two Slater determinants for the spin pairing between the two electrons that form the single bond, and two ionic VB structures ($[H^+ Cl^-]$ and $[H^- Cl^+]$), each of which is represented by a single Slater determinant. In discussion, it is important to distinguish between VB structures (single CSFs) and VB resonance wave functions (linear combinations of CSFs); the latter will usually be called configuration interaction wave functions. Although the electronic wave function for a given VB structure changes when the coordinates of the nuclei change, it varies gradually, and it retains a recognizable bonding pattern even globally; Hartree-Fock (HF) wave functions may change suddenly, and they may also change the bonding pattern. Furthermore, HF orbitals, unlike VB orbitals, do not have a definite atomic parentage. In the original VB theory of Heitler, London, Slater, and Pauling, a VB structure changes only because the fixed atomic orbitals in terms of which it is defined move with the nuclei; in modern VB theory, such as generalized valence bond[150] (GVB) or valence bond self-consistent field[151] (VBSCF), the defining orbitals also breathe and polarize and may even delocalize across a bond.[152]

One approximation used in the EVB formalism[92−103] is that the partial atomic charges of the EVB states are assumed to be independent of the reaction coordinate and are based on reactant and product molecular mechanics parameters. In VB theory, this is equivalent to assuming that the ionic character of a VB structure is invariant to changes in geometry and external field, which is a severe approximation.[62,63] Among other consequences, it implies that the partial charges on VB structures are the same in the gas phase, in solution, or in enzymes. Although in principle, it is possible to make the atomic partial charges in EVB-type models dependent on molecular structure, it is rarely done, and such a procedure is laborious for chemical reactions.[68,75] Overcoming this kind of limitation of molecular mechanics-based treatments is another motivation for calculating diabatic potentials by using quantum mechanical electronic structure theory.

The first wave function approach considered in this article is the mixed molecular orbital and valence bond (MOVB) method.[60,141] The MOVB method constructs VB-like diabatic states by a block localization procedure applied to molecular orbital calculations.[153−160] Two MOVB schemes are considered:[4] in one, called the variational diabatic configuration (VDC) scheme, the energies of the diabatic states are each variationally optimized and in another, called consistent diabatic configuration (CDC) scheme, the energy of the adiabatic ground state is variationally minimized.

The other approach that we will use to define diabatic states is called the fourfold way;[161−163] it is based on the use a threefold density criterion and possibly one or more reference orbitals to construct diabatic molecular orbitals (DMOs), the use of these orbitals to define diabatic CSFs, and the determination of diabatic states in terms of the diabatic CSFs by configurational uniformity. This method has its roots in the theory of photochemical reactions, and it uses the concepts of DMOs[161−164] and configurational uniformity[161−163,165,166] to determine diabatic states as smoothly varying linear combinations of adiabatic CSFs; since the diabatic states are smooth functions of geometry, they resemble, to some extent, VB states.[142] A key feature of this method is that the diabatic states span exactly the same space as the same number N (two in the example considered here) of adiabatic states, which may be chosen as the ground state and the (N–1) lowest-energy adiabatic states or—as in the example considered here—as the ground state and an excited adiabatic state with the charge character of the product, so that the diabatic energy gap can serve as a reaction coordinate. A second key feature is that one can base the method on correlated wave functions, which are more accurate than HF ones.

In the present work, we illustrate the diabatization methods by applying them all to the same example. The example chosen is the S_N2 reaction of acetate ion with DCE in the gas phase

$$CH_3CO_2^- + ClCH_2CH_2Cl \rightarrow CH_3CO_2 - CH_2CH_2Cl + Cl^- \quad (1)$$

which is motivated by the haloalkane dehalogenase reaction discussed in the second paragraph. Although the main focus is on the definition of diabatic states for the gas-phase reaction, we also consider the reaction in water to compare the free energies of solvation and activation obtained with the EVB PES with those reported in the literature.[21,28] In addition to serving as a model S_N2 reaction, reaction 1 is of interest for developing bioremediation strategies. The production of halogenated hydrocarbons for use as herbicides, pesticides, refrigerants, or solvents has given rise to environmental concerns due to their toxicity and possible role as carcinogenic agents.[167] A possible route for bioremediation of contaminated soils and waters[168−170] involves the action of the haloalkane dehalogenase enzyme[5−11,171−173] present in, for instance, the bacterium *Xanthobacter autotrophicus* GJ10.

The remainder of the article is organized as follows. Section 2.1 reviews the general valence bond framework for the treatment of S_N2 reactions. In section 2.2 the electronic structure methods used to determine the adiabatic and diabatic electronic states are introduced. The fourfold way with configuration uniformity algorithm for diabatization is explained in section 2.3, and the details of its application to the acetate + DCE reaction are given in the Appendix. The MOVB method is explained in section 2.4. The definition of diabatic coupling for nonorthogonal and orthogonal MOVB wave functions is detailed in section 2.5. The main features of the EVB theory are sketched in section 2.6. The method used to calculate free energies of solvation and

activation in water is presented in section 2.7. Sections 2.8 presents the basis sets employed. The main results of the present study are presented in section 3. Section 3.1 contains the definition of reaction coordinate and reaction path for the acetate + DCE reaction. The adiabatic energy profiles obtained along the reaction path are presented and discussed in section 3.2, where the accuracy of the adiabatic reaction energy and barrier height is assessed by comparing them to high-level calculations. Section 3.3 present a detailed comparison of the diabatic energies and couplings obtained with the different methods. Section 3.4 is concerned with the solvation and activation free energies of the reaction in water. Finally, the conclusions are presented in section 4.

2. Theory and Methods

2.1. Valence-Bond Treatment of S_N2 Reactions. The general scheme for the treatment of S_N2 reactions using VB theory has been developed in a number of previous works.[4,55,56,64,66,174,175] The reaction $:X^- + R\text{-}Y \rightarrow X\text{-}R + :Y^-$, where $:X^-$ and $:Y^-$ are the nucleophile and the leaving group, respectively, and R is an alkyl group, can be used to illustrate the general case. Four electrons participate directly in the nucleophilic displacement, i.e., two from the reactant nucleophile $:X^-$ and two from the R-Y bond. If these electrons are distributed among the three frontier orbitals of the three fragments (X, R, and Y), a total of six VB structures can be generated,[64] which are depicted below:

$$\begin{array}{ccc} X{:}^-R-Y & X-R:Y^- & X{:}^-R^+:Y^- \\ \mathbf{1} & \mathbf{2} & \mathbf{3} \\ X{:}^-:R^-Y^+ & X^\bullet:R^-{}^\bullet Y & X^+:R^-:Y^- \\ \mathbf{4} & \mathbf{5} & \mathbf{6} \end{array} \qquad (2)$$

The VB many-electron wave function is expressed as a linear combination of the CSFs that correspond to the six VB structures in eq 2. Structures **1** and **2** represent Heitler-London covalent configurations, each of which consists of two Slater determinants, and have the largest weights, corresponding to the reactant and the product state, respectively. They are the dominant configurations, and a minimal description of the diabatic states must always include them.[4,56,174,175] Structure **3** is the triple-ion configuration that is most stable and has the greatest resemblance to the transition state. The VB configuration correlation diagram[56] of these resonance structures for the acetate + DCE reaction is shown in Figure 1. The VB picture of an S_N2 reaction is that the VB configurations corresponding to structures **1** and **2**, "dressed" by the proper ionic configurations,[56] experience an avoided crossing along the reaction coordinate, and their interaction gives rise to two adiabatic states.[56,174,175] The excited adiabatic state assumed in this scheme has in fact been detected in photoexcitation experiments.[176,177] The ground state has a reaction barrier, and the excited state has a local minimum at approximately the same geometric location, corresponding to the crossing point of the diabatic states (Figure 1). The VB studies performed on S_N2 reactions in the gas phase and in solution have found that the use of structures **1**, **2**, and **3** is sufficient to obtain quantitative results because in structures **4**, **5**, and **6** a negative charge is placed on a less electronegative atom, resulting in high energies and relatively small configuration weights in the VB wave function.[60,61,64–66] Nevertheless, structures **4** and **6** can play significant roles in the definition and understanding of diabatic states. Note that structure **5** represents a spin paired interaction between two electrons, each localized on one of the nonbonded atoms, in the presence of a doubly occupied orbital. It corresponds to a charge-transfer excited state that does not contribute to the nominal configuration interaction wave function either for the reactant state or for the product state. Nevertheless, structure **5** can mix with other VB structures to stabilize the adiabatic ground state, and it has the largest contribution at the transition state where the molecular geometry is the most compact. We have found that the effect of structure **5** in lowering the reaction barrier is very small, less than 1 kcal/mol for a typical S_N2 reaction.[4] Thus, it is not essential to include structure **5** in defining the diabatic and adiabatic states.

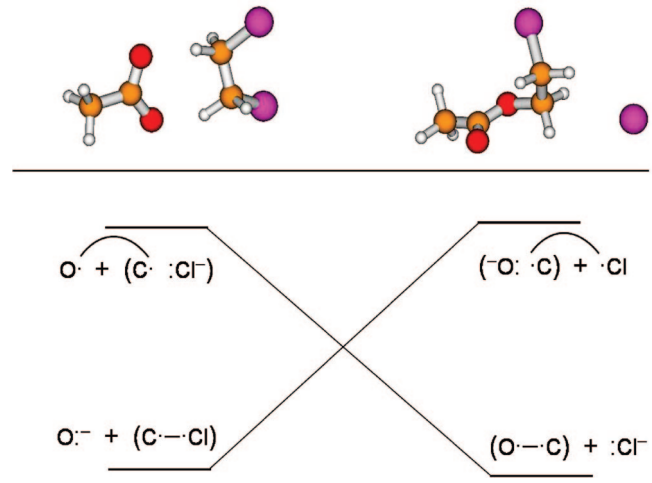

Figure 1. Reactant and product VB structures and schematic correlation diagram for the acetate + DCE S_N2 reaction.

2.2. Electronic Structure Methods. The fourfold way[161–163] and the MOVB[60,141] scheme are based on different approaches to the construction of diabatic states.

In the ***fourfold way*** with configuration uniformity, adiabatic states are generated first, and they are subsequently transformed to an equivalent set of diabatic states; the transformation also yields the diabatic energies and couplings. In the general cases, to obtain good reaction energies and barrier heights without empirical parameters, dynamic electron correlation effects need to be included in the wave function. In the present implementation, the state-averaged CASSCF, or SA-CASSCF,[178,179] method (in the state average, the ground state is weighted 75% and the excited state 25%) has been chosen to define configuration interaction (CI) coefficients and MOs that are then used as the basis for multiconfigurational quasidegenerate perturbation theory at second order (MC-QDPT)[180–182] to include dynamic correlation. (Note that MC-QDPT is very similar to another well known method called multistate complete-active-space second-order perturbation theory[183] (MS-CASPT2)). The CASSCF active space has been selected in analogy to the discussion of section 2.1. Thus, the active space is formed by four electrons in three active MOs. The four active electrons correspond to two electrons from one of the attacking oxygen

atoms in the acetate ion and the two electrons in the C−Cl bond of DCE. The three active MOs are the oxygen lone pair centered on the attacking oxygen of $CH_3CO_2^-$, one of the *p* orbitals of Cl^- in the products, and the σ^*_{C-Cl} orbital delocalized over the three atoms that participate directly in the forming and breaking bonds.

It is important to note that the excited electronic state used in the fourfold way analysis is the first excited state of the acetate + DCE system in the CASSCF calculations within the active space chosen, but it is not the first excited state of the system. The spectroscopic first singlet excited electronic state in fact is the one that derives from an $n\rightarrow\pi^*$ transition of the acetate ion. However, that electronic state is not directly relevant to the nucleophilic substitution reaction and is excluded in the present treatment. Here we formulate the problem in terms of only the two crossing diabatic states that correspond to the different bonding patterns (charge arrangements) of the reactant and product. For this reason, the active space chosen must be considered as a "model space".

The MC-QDPT calculations use a modified 6-31+G(d)[184−187] basis set called 6-31&G(d), which is explained in the Appendix, which contains extra computational details not germane to our focus.

The diabatic states in the ***MOVB method*** are generated by following a different strategy. In MOVB, we first construct VB states in terms of block-localized MOs for each fragment in the corresponding VB structure. In the original formulation of the MOVB method, the VB matrix elements are determined analytically using nonorthogonal determinant wave functions.[60,141] In the limit of a single fragment in which the MOs are fully delocalized, the MOVB state reduces precisely to the HF limit. (The HF method is accurate enough for the present S_N2 example; in cases where electron correlation effects must be included, the method can be applied at the Kohn-Sham level rather than with HF.)

In order to obtain ***reference values*** for the relative energies of the acetate + DCE ground-state potential energy surface (PES), we have followed the strategy of choosing an accurate yet computationally affordable method to carry out the stationary point geometry optimizations and then using these geometries to calculate refined relative energies using high-level wave function methods. Thus, the geometry optimizations were performed using the M06-2X[188] density functional with the MG3S[189] basis set. The M06-2X functional has been shown[188] to provide accurate main-group thermochemistry, kinetics, noncovalent interactions, and electronic excitation energies to valence and Rydberg states. The MG3S basis set is a multiply polarized basis of triple-ζ quality that contains diffuse functions centered in all heavy atoms and that was designed to provide accurate relative energies in density functional theory. Three high-level methods were used to perform single-point calculations on the M06-2X/MG3S stationary point geometries, namely, Gaussian-3X with scaled energies (G3SX),[190−192] its MP3 version with a reduced order of perturbation theory (G3SX(MP3)),[192] and the BMC-CCSD[193] multicoefficient correlation method.[194] These high-level calculations will be denoted G3SX//M06-2X, G3SX(MP3)//M06-2X, and BMC-CCSD//M06-2X, respectively.

The M06-2X density functional was also employed to obtain ***reaction path*** geometries on the ground-state PES that were then used to compute the MC-QDPT adiabatic and diabatic reaction profiles. The ground-state reaction path was also calculated with the B3LYP[195−198] functional for comparison with the other methods. For the MOVB method, diabatic energies were calculated at the optimized ground-state adiabatic reaction path geometries obtained at the HF level.

Note that in this work we are only concerned with the segment of the reaction path that connects the reactant ion-molecule complex and the product ion-molecule complex of the gas-phase S_N2 reaction, by analogy with the structures relevant to the S_N2 step of the haloalkane dehalogenase catalytic cycle.[12−32] Thus, infinitely separated reactants and products are not considered in the present study.

2.3. Fourfold Way Algorithm for Diabatization. The fourfold way[161−163] is a direct diabatization method that has been applied successfully in our group to determining the first two singlet diabatic electronic states of the Li + FH → LiF + H[162] and the HNCO → HN + CO, H + NCO[163] reactions, to the construction of global diabatic PESs for the ground and first singlet excited electronic states of NH_3,[199,200] and to the calculation of the six lowest singlet diabatic states of the photodissociation reactions of $BrCH_2C(O)Cl$[201] and $BrCH_2Cl$[202] along the C−Br and C−Cl dissociative reaction coordinates. The key principles of fourfold way with configurational uniformity[161−163] are the construction of suitable DMOs and their use to construct diabatic configuration state functions (DCSFs) that are employed to enforce configurational uniformity on the multiconfiguration wave function of the CASSCF or MC-QDPT step; here we use the latter. The DMOs and the DCSFs must have three properties: (1) they must be uniquely defined at each nuclear configuration, (2) they must be smooth along continuous nuclear-coordinate paths, and (3) when the multiconfigurational wave functions are expressed in terms of DMOs, each state must be dominated by at most a few DCSFs in regions where the electronic states are weakly interacting. To construct DMOs, the one-electron density matrices and transition density matrices are used to define the functional

$$D_3(\alpha_N, \alpha_R, \alpha_T) = \alpha_N D^{NO} + \alpha_R D^{NO} + \alpha_T D^{TD} \qquad (3)$$

where α_N, α_R, and α_T are parameters usually set to the values 2, 1, and 0.5 (we use the standard values in the present work), D^{NO} is a natural orbital density matrix, D^{ON} is an occupation number density matrix, and D^{TD} is a transition density matrix. The criterion for constructing DMOs based on maximization of the D_3 functional is called the threefold density criterion. For some systems (including the present one), one needs additional constraints on MO uniformity. This is done by introducing a set of λ reference MOs and defining a new term, called the reference overlap term, which contains an overlap-like quantity between the MOs at the current geometry and the reference MOs. Use of eq 3 without reference orbitals is called the threefold way; when one or more reference MO is included, the method is called the

fourfold way, since it depends on the three functionals in eq 3 and on the set of reference MOs.

The DMOs are used to construct orthonormal DCSFs that are distributed into groups, with each group spanning a characteristic subspace that defines a diabatic state. The basic requirement is that the group list be the same for all nuclear geometries. The adiabatic many-electron wave functions are finally expressed in the basis of the DCSFs, and their CI coefficients are used to define the adiabatic-to-diabatic transformation matrix which is then used to generate the diabatic energy matrix. Diagonalization of the diabatic matrix gives back the adiabatic energy matrix.

The fourfold way yields two VB-like configurations that correspond to the covalent VB structures of eq 2 (i.e., structures **1** and **2**, each mixed with structure **3** proportionally); these configurations may be called resonance[60,203,204] structures. The bonding patterns of these resonance configurations in the reactant and product regions of the acetate + DCE system are shown in Figure 1.

The role of the reference MOs for the acetate + DCE reaction is somewhat different than for most reactions studied previously[199−202] with the fourfold way, but it is analogous to that in the two-arrangement reaction Li + FH → LiF + H.[162] In most cases[199−202] studied so far, the reference MOs are introduced to fix the orientation of the DMOs that are localized on a given atom but that become degenerate with other orbitals at either reactants or products, and whose coefficients would otherwise mix with the other degenerate orbitals along the reaction coordinate making it impossible to define consistent groups of DCSFs. In the case of acetate + DCE, the reference MOs also play this role, as they help to discriminate between the two degenerate lone pairs on oxygen in the reactant and between the three degenerate orbitals of chloride in the product. However, in this case as well as in the case of the LiFH[162] two-arrangement system, there is a complication with the deformation of the DMOs obtained by the threefold way along the reaction path. Applying the threefold way, a DMO that is localized on a given atom in reactants can become delocalized along the path and can transform into a DMO localized on a different atom in products. For the acetate + DCE reaction, reference MOs are essential for obtaining diabatic states that are VB-like states, because they effectively project the delocalized MOs obtained by CASSCF or MC-QDPT onto localized MOs centered on the atoms, and they consequently generate VB-like configurations once the wave function is re-expressed in terms of the fourfold way DMOs. What is required is to obtain two crossing VB-like diabatic states analogous to those in VB theory.

Note that the adiabatic energies obtained by the MC-QDPT fourfold way are different from the energies obtained without applying the fourfold way. The two different sets of energies are denoted MC-QDPT(4) and MC-QDPT, respectively, or when indicating that they are calculated at stationary points or along reaction paths optimized with the M06-2X density functional, they are denoted MC-QDPT(4)//M06-2X or MC-QDPT//M06-2X. That the MC-QDPT and MC-QDPT(4) energies are different can be understood considering the way the MC-QDPT adiabatic energies are calculated. When the fourfold way is not applied, the MC-QDPT wave function is based on the CASSCF canonical MOs,[180] whereas when the fourfold way is applied, the MC-QDPT wave function is based on the CASSCF DMOs for the active space and on the canonical MOs for the inactive and virtual subspaces. This causes the adiabatic energies to differ between these two cases, because whereas the CASSCF adiabatic energies are strictly invariant with respect to rotations of active orbitals, this is not true for MC-QDPT.[162] In the calculations reported here, only the MC-QDPT(4)//M06-2X adiabatic energies are computed along the reaction path, for consistency with the diabatic energies obtained at the same level.

2.4. Diabatic States from the Molecular Orbital-Valence Bond (MOVB) Method. The MOVB method[60,141] is based on a block-localized wave function (BLW) approach.[153−160] The BLW method has been applied to a variety of problems including interaction energy decomposition and conjugation delocalization effects.[205−208]

For each given VB structure, the molecular system is divided into a number of polyatomic fragments, for which MOs are formed by using only basis functions on that fragment; the number of electrons and total charges of each fragment are fully determined by the VB structure. Therefore, for the present S_N2 reaction between acetate ion and dichloroethane, the wave functions for the reactant (Ψ^R_{MOVB}) and product (Ψ^P_{MOVB}) states are given by

Reactant

$$[CH_3CO_2^-][Cl-CH_2CH_2Cl];\Psi^R_{MOVB}=\hat{A}\{\varphi_{Ac^-}\varphi_{Cl-CH_2CH_2Cl}\} \quad (4a)$$

Product

$$[CH_3CO_2-H_2CH_2Cl][Cl^-];\Psi^P_{MOVB}=\hat{A}\{\varphi_{AcCH_2CH_2Cl}\varphi_{Cl^-}\} \quad (4b)$$

where $\hat{A}$ is an antisymmetrizing operator, and $\phi_{\mathbf{F}}$ specifies a product of molecular orbitals that are expressed as linear combinations of atomic orbitals in fragment **F**. The Lewis structures for different fragments in the reactant and product diabatic states as well as their associated total charges are defined by square brackets. The MOs within each fragment in eqs 4a and 4b are restricted to be orthogonal as in HF theory, but the MOs of different fragments are not orthogonal—a key feature of conventional valence bond theory, for which the fragments are atoms.

The wave function of each VB structure is defined by a single Slater determinant (eqs 4a and 4b), and the MOs of the MOVB treatment are fragment localized, that is, they are delocalized within each fragment, but by construction they are localized on one or another fragment. Each VB wave function obtained by the BLW method represents a diabatic electronic state. We have shown that the reactant state wave function defined by eq 4a in MOVB corresponds to an ab initio VB wave function containing covalent configuration **1** and ionic configurations **3** and **4** for the C−Cl bond that is cleaved, and the nucleophile $CH_3CO_2^-$ ion acts as a "spectator" ion that interacts and polarizes the C−Cl bond structure.[4] In the same vein, the product state wave function defined by eq 4b consists of contributions from covalent

structure **2** and ionic structures **3** and **6**.[4] We note that the outer spin-pairing structure **5** does not contribute to the Lewis bond configuration interaction wave function of either the reactant or the product state; thus, it is not included in the MOVB wave function; however, comparison of the results from ab initio VBSCF calculations, with and without inclusion of structure **5**, shows that it only affects the reaction barrier by about 1 kcal/mol.[4] The total MOVB wave function is then written as a linear combination of the diabatic states obtained with BLW

$$\Phi_{\mathrm{MOVB}} = a^{\mathrm{R}}\Phi^{\mathrm{R}}_{\mathrm{MOVB}} + a^{\mathrm{P}}\Phi^{\mathrm{P}}_{\mathrm{MOVB}} \tag{4c}$$

where a^{R} and a^{P} are MOVB configuration coefficients for the reactant and product states, respectively. The adiabatic energies are obtained by solving the generalized eigenvalue problem[61] in the nonorthogonal MOVB basis of the two diabatic states.

Two different variational schemes are employed to optimize the VB wave functions.[4] In the first scheme, the optimal fragment localized MOs at each molecular geometry are obtained so as to minimize the expectation value of the Hamiltonian for each individual VB structure (Ψ^{R}_{MOVB} and Ψ^{P}_{MOVB}). In other words, the energy for each VB structure is separately optimized. The resulting VB states are called variational diabatic configurations (VDC). An alternative procedure, called consistent diabatic configuration (CDC) theory, is to simultaneously optimize both VB structures and configurational coefficients, as in the multiconfiguration self-consistent field (MCSCF) method, to minimize the ground-state adiabatic energy. The resulting VB states are called consistent diabatic configurations since they are consistently obtained with respect to the variational energy of the adiabatic ground state.

In either scheme we may work in the nonorthogonal or orthogonal representation. In the former case the secular equation is the generalized eigenvalue problem[4]

$$\begin{vmatrix} H^{\mathrm{n}}_{11} - V & H^{\mathrm{n}}_{12} - S_{12}V \\ H^{\mathrm{n}}_{12} - S_{12}V & H^{\mathrm{n}}_{22} - V \end{vmatrix} = 0 \tag{5}$$

where H^{n}_{11} and H^{n}_{22} are the energies of the nonorthogonal VB states, H^{n}_{12} is the nonorthogonal off-diagonal Hamiltonian matrix element, S_{12} is the overlap integral, and the resonance energy (defined as the stabilization energy at the diabatic state crossing) is the difference between V and the lower of H^{n}_{11} and H^{n}_{22} (Note that $S_{21} = S_{12}$, and $H^{\mathrm{n}}_{21} = H^{\mathrm{n}}_{12}$.). Alternatively, the nonorthogonal diabatic states may be orthogonalized, in which case the off-diagonal Hamiltonian matrix element is the resonance energy itself. Hence there are four combinations, namely orthogonal and nonorthogonal CDC and VDC states.

The MOVB method is more efficient than other self-consistent field valence bond (VBSCF) methods[58,66,150,151,209−213] for obtaining the adiabatic ground-state potential energy surface of a reactive system, but the trade-off is lower accuracy since each VB structure is approximated by a single Slater determinant of block-localized MOs. There are at least three ways that the accuracy of the MOVB method can be improved. The first is to use multiconfigurational methods such as generalized valence bond (GVB) theory[209] to construct the individual diabatic states; this could provide a better treatment of electron correlation within each fragment. In the limit of this approach in which orbitals are block-localized on individual atoms, MOVB is equivalent to ab initio VBSCF, which is comparable to the familiar CASSCF method with an appropriate choice of active space.[214−217] Secondly, computational accuracy can be improved by forming an effective Hamiltonian, in which the off-diagonal Hamiltonian matrix element (H_{12}) is required to reproduce high-level ab initio calculations or experimental data. Thirdly, one can use Kohn-Sham or generalized Kohn-Sham density functional theory instead of HF theory, but this requires additional assumptions to approximate the diabatic coupling. These approaches are not employed in the present examples.

2.5. Diabatic Couplings from MOVB Wave Functions. The calculations described in section 2.4 originally yield H_{11}, H_{22}, and H_{12} in a nonorthogonal representation.[4,60,127] For dynamics calculations it is often necessary to consider orthogonal states. For example, the usual rate of electron transfer rearrangement in the nonadiabatic limit is derived by Fermi's Golden rule;[218,219] if one used nonorthogonal initial and final states in a Golden Rule calculation, a constant coupling operator would cause a finite rate of charge transfer. If one treats the dynamics to infinite order, i.e., exactly, one can obtain correct results with either orthogonal or nonorthogonal representations, if used consistently. However, much of the literature of charge rearrangements is based on the Golden Rule or other perturbation treatments, and difficulties with formulating such treatments in terms of nonorthogonal representations are well known.[220,221]

The preferred way to transform to orthogonal states is by the symmetric orthogonalization method of Löwdin[222] because, of all possible orthogonalizations, this yields states with the most resemblance to the original nonorthogonal ones. The resulting transformed 2×2 Hamiltonian matrix in the symmetrically orthogonalized representation is[61,142]

$$\mathbf{H}^{\mathrm{s}} = \mathbf{S}^{-1/2T}\mathbf{H}^{\mathrm{n}}\mathbf{S}^{-1/2} \tag{6}$$

where S_{11} and S_{22} are unity because the nonorthogonal states are normalized, S_{12} ($= S_{21}$) is the overlap between the diabatic states, T denotes a transpose, and $\mathbf{H}^{\mathrm{n}}$ is the Hamiltonian in the nonorthogonal representation.

It is useful to compare the eigenvalue problem for the ground-state adiabatic potential energy surface V, in the two representations. In the symmetrically orthogonal representation it is the standard eigenvalue problem

$$\begin{vmatrix} H^{\mathrm{s}}_{11} - V & H^{\mathrm{s}}_{12} \\ H^{\mathrm{s}}_{12} & H^{\mathrm{s}}_{22} - V \end{vmatrix} = 0 \tag{7}$$

whereas in the nonorthogonal representation it is given by eq 5. Comparing eqs 5 and 7 shows that the off-diagonal element of the Hamiltonian enters the theory in a different way in the orthogonal and nonorthogonal representations. It would be meaningless to specify H^{n}_{12} without also specifying S_{12} .

Interestingly, if one defines (as done above) the resonance energy, B, as the stabilization energy at the diabatic state

crossing, it is clear that in the orthogonal diabatic state representation

$$B = |H_{12}^{s}| \tag{8}$$

On the other hand, in the nonorthogonal diabatic state representation, solving eq 5 analytically shows that the resonance energy is

$$B = \frac{|\theta|}{1 - S_{12}sign(\theta)} \tag{9a}$$

where

$$\theta \equiv H_{12}^{n} - S_{12}H_{11}^{n} \tag{9b}$$

Equation 9a, combined with the definition of B, can also be rearranged to

$$B = |H_{12}^{n} - S_{12}V| \tag{10}$$

that is, the resonance energy is the absolute value of the difference between the nonorthogonal off-diagonal Hamiltonian matrix element and the adiabatic ground-state energy scaled by the overlap integral. If one treats B as a parameter in an effective two-state VB Hamiltonian approach, B is implicitly dependent on the overlap.[4,126] (Notice that if one changes the sign of both diabatic wave functions, none of the matrix elements changes sign; whereas if one changes the sign of only one diabatic wave function, then H_{12}^{n} and S_{12} change sign, but B computed by eq 9a or 10 is invariant to such a sign change.)

2.6. Diabatic Energies from the Empirical Valence Bond (EVB) Method. The EVB method[92−103] of Warshel and Weiss has as its main features[223] (a) using molecular mechanics to model chemical reactions in the context of VB theory; (b) assuming orthogonality of diabatic states to eliminate unknown overlap integrals; (c) calibrating the energy of the molecular fragments to try to make the method suitable for the study of reactions in solution and large molecules such as enzymes; (d) including solvation effects in the diagonal Hamiltonian matrix elements; and (e) assuming the off-diagonal Hamiltonian matrix elements are independent of environment, for example, the same in solution as in an enzyme. Note that (b) and (c) are mutually incompatible because if the diabatic states are assumed orthogonal or transformed to be so, they contain orthorgonalization tails from other fragments. If molecular fragments are used to calibrate such orthogonal diabatic states, this treatment of overlap contributes an additional source of error over and above the assumption that the fragments are not internally polarized (distorted by valence interactions and noncovalent effects) when incorporated into the whole system. (Similar errors due to distortion and neglect of overlap have been discussed carefully in the context of diatomics-in-molecules theory,[224] which is another semiempirical valence bond method.) If real molecular fragments are used to model the potential energy surfaces of the orthogonalized diabatic states, the neglect of the overlap can be a severe error if electronic structure methods are used as we see below. Furthermore, due to the neglect of internal polarization, if the diabatic coupling is only fitted to reproduce the barrier height of the adiabatic ground state, severe errors may arise in other regions of the potential energy surface.[130,131] In step (d), the off-diagonal matrix elements are determined empirically by comparison with experimental kinetics data and are assumed to have generally simple functional forms or are taken as constant. In step (e), they are assumed to be unaffected by the surroundings. These features of the nondiagonal matrix elements are drawbacks of EVB theory.

In this work we characterize the ground-state adiabatic potential energy surface derived from EVB for the acetate + DCE reaction, taking the molecular mechanics parameters for the diabatic states to be the same as those used in ref 21 (see the Appendix).

2.7. Free Energies of Solvation and Activation in Water. The standard-state free energy of activation in water at a temperature T in the separable equilibrium solvation (SES) approximation can be calculated from the geometries of the gas-phase reactants and the TS as follows[225]

$$\Delta G_{w}^{0,\ddagger}(T) = \Delta V_{g}^{\ddagger} + \Delta G_{RVE}^{\ddagger}(T) + \Delta\Delta G_{S}^{0,\ddagger}(T) \tag{11}$$

where T is the temperature; $\Delta V_{g}^{\ddagger}$ is the potential energy barrier in the gas phase; $\Delta G_{RVE}^{\ddagger}$ is the difference between the internal gas-phase free energies of the TS and reactants, with RVE standing for rotational, vibrational, and electronic degrees of freedom; and $\Delta\Delta G_{S}^{0,\ddagger}$ is the difference in standard-state free energies of solvation of the TS and reactants. (Note that we include zero point vibrational energies in the $\Delta G_{RVE}^{\ddagger}$ term, whereas some workers include it in $\Delta V_{g}^{\ddagger}$.) We neglect the $\triangle G_{RVE}^{\ddagger}$ term in the calculations, as this term is not our focus here and does not affect our discussion. All the calculations presented here are for a temperature of 298.15 K.

We calculate $\Delta\Delta G_{S}^{0,\ddagger}(T)$ by using the SM8 universal continuum solvation model[226] in combination with CM4M,[227] which is the parametrization of Charge Model 4[228] (CM4) that is specifically designed to be used with the M06 suite (M) of density functionals. The M06-2X functional with the 6-31G(d) basis set has been chosen for the calculations. The SM8/M06-2X/CM4M model has been shown to reproduce free energies of solvation for a set of 120 ions in water with a mean unsigned error of 3.4 kcal/mol.[226]

2.8. Basis Sets. All B3LYP, HF, MC-QDPT, and M06-2X/SM8 calculations in this article use the 6-31+G(d,p), 6-31+G(d,p), 6-31&G(d), and 6-31G(d) basis sets, respectively. The 6-31&G(d) basis is defined in the Appendix for gas-phase M06-2X calculations, MG3S is used for stationary points, and 6-31G(d) has been used for the construction of contour plots.

3. Results

We first define the reaction coordinate used for the plots, and we explain how the reaction path and energies along the reaction path were obtained for each of the methods employed. Then, relative adiabatic ground-state potential energy values at stationary points are presented to evaluate the quality of results at different levels of theory. The free energies of solvation and activation in water are calculated

Table 1. Value of Key Bond Distances (in Å) and Angles (in degrees) Obtained for the Stationary Points of the Acetate + DCE Reaction with the HF, B3LYP, M06-2X, and EVB Methods[a]

	HF			B3LYP			M06-2X			EVB			
	RS	TS	PS	RS	TS	PS	RS	TS	PS	RS	TS1	TS2	PS
C−O(d_1)	3.19	2.12	1.44	3.12	2.09	1.46	3.09	2.01	1.44	2.37	1.86	1.95	1.70
Cl−C(d_2)	1.82	2.36	3.49	1.84	2.35	3.44	1.81	2.28	3.23	2.40	2.90	3.34	4.89
O−C−Cl (a_1)	126	164	166	126	164	169	129	166	165	170	124	169	98
O−C−C (a_2)	86	91	113	91	96	114	72	95	113	95	107	100	118

[a] The geometric parameters are defined in Figure 2. 'RS', 'TS', and 'PS' stand for the reactant ion-molecule complex, the transition state, and the product ion-molecule complex, respectively.

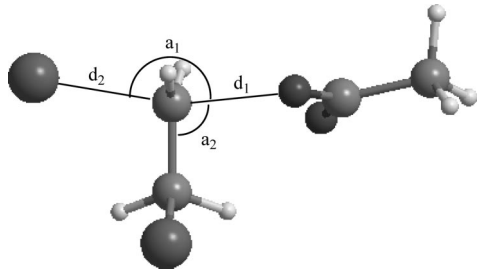

Figure 2. Geometric variables for the acetate + DCE reaction showing the formation of the O−C bond and the breaking of the C−Cl bond.

and compared with the dynamical results based on the EVB potential surface reported in the literature. Then, we describe the diabatic states. Finally, we discuss the diabatic state coupling along the reaction path.

3.1. Reaction Coordinate and Reaction Path. The reaction coordinate for reaction 1 is defined as the difference between the bond distances of the breaking bond (C−Cl) and the forming bond (O−C)

$$z = R(\mathrm{C-Cl}) - R(\mathrm{O-C}) \tag{12}$$

As mentioned in section 1, such a reaction coordinate is sometimes called a distinguished reaction coordinate. The reaction paths were constructed by fixing the value of this distinguished reaction coordinate and optimizing the rest of geometrical variables on the ground-state adiabatic PES. The values of some of the key geometric parameters for the stationary points obtained using the HF, B3LYP, M06-2X, and the EVB computational methods are presented in Table 1. The definition of these variables is illustrated in Figure 2. Tables containing the Cartesian coordinates of all the points calculated along the reaction paths with these four methods are presented in Tables S2−S5 of the Supporting Information. Overall, the optimized M06-2X geometrical parameters are in good agreement with those obtained at the HF and B3LYP levels. The average of the root-mean-square deviations in the O−C and C−Cl bond distances for the HF and B3LYP results at the reactant ion-molecule complex and the transition state, as compared with the more reliable M06-2X results, are 0.12 and 0.08 Å, respectively.

The first point along the reaction path is the reactant ion-molecule complex with the DCE molecule in a gauche conformation, because this conformation is preferred for the nucleophilic attack of the acetate ion. The O−C distance at this geometry calculated at the M06-2X level is 3.09 Å, which is slightly shorter than the O−C distance optimized at the other two levels. The O−C distance at the optimized M06-2X transition state is 2.01 Å, which is also shorter than that optimized at the HF and B3LYP levels. The product ion-molecule complex has R(O−C) = 1.44 Å. The C−Cl distances obtained at the M06-2X level are also shorter than those obtained at the HF and B3LYP levels at the three stationary points.

As can be observed in Table 1, the bond distances and angles obtained with EVB are quite different from those obtained with the other methods. As also shown in Table 1, two different transition states (each confirmed by frequency analysis to have only a single imaginary frequency) are found on the ground-state adiabatic potential energy surface instead of the single transition state obtained with HF and with density functional methods. The data presented in Table 1 also show that the EVB stationary point geometries are shifted towards the region of products, as shown most clearly by the O−C and C−Cl bond distances: the EVB reactant complex has distances comparable to those of the TS obtained with the other methods, and the EVB transition states have distances roughly comparable to that of the HF and density functional product complex. The shape of the EVB ground potential surface is therefore quite different to that of the potential surfaces obtained with electronic structure methods. This will be more clearly seen in the next section, where we compare contour plots obtained with density functionals to those obtained with EVB.

3.2. Adiabatic Ground-State Energy. Shown in Figure 3(a) are the ground-state adiabatic potential energies as functions of the reaction coordinate obtained at the B3LYP, M06-2X, CDC-MOVB, and fourfold way (MC-QDPT(4)// M06-2X) levels of theory. In Figure 3(b) we present analogous results obtained with EVB theory; these are given separately because they span a larger range of the reaction coordinate.

The energies of the stationary points along the gas-phase reaction path are sketched in Figure 4, where ΔV_g represents a difference in gas-phase potential energy. The two key electronic energy differences are defined in this scheme, namely, the reaction energy from the reactant complex to the product complex (ΔV_g), and the reaction barrier with respect to the reactant complex ($\Delta V_g^{\ddagger}$). Table 2 summarizes the values obtained in the present work for these quantities. To our knowledge, the product complex has not been reported in the literature, and there are no data to which to compare.

The barrier heights and reaction energies obtained with the three high-level wave function methods used as a reference (presented in Table 2) agree reasonably well with

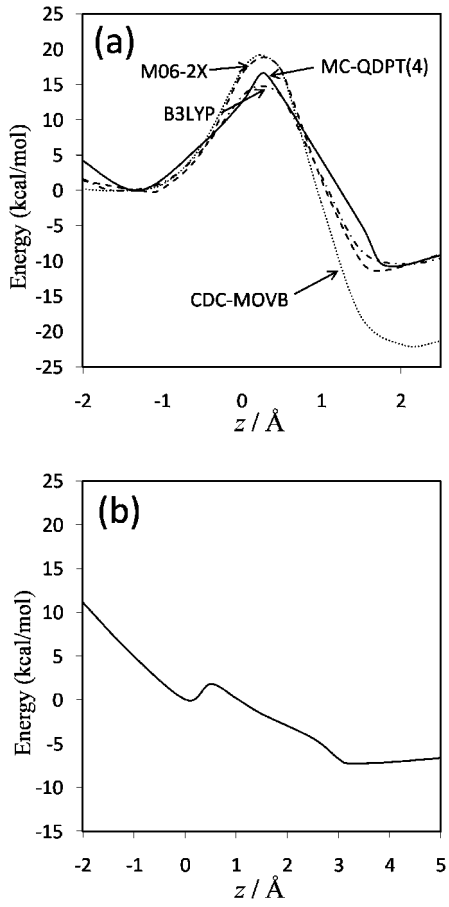

Figure 3. Ground-state adiabatic potential energy profiles along the reaction coordinate computed with (a) MC-QDPT(4)// M06-2X (full line), M06-2X (dashed line), CDC-MOVB (dotted line), and B3LYP (dashed-dotted line) and (b) EVB. For each method, the zero of energy is taken as the ground-state adiabatic energy of the ion-molecule reactant complex. Note the change in the scale of the abscissa between parts (a) and (b).

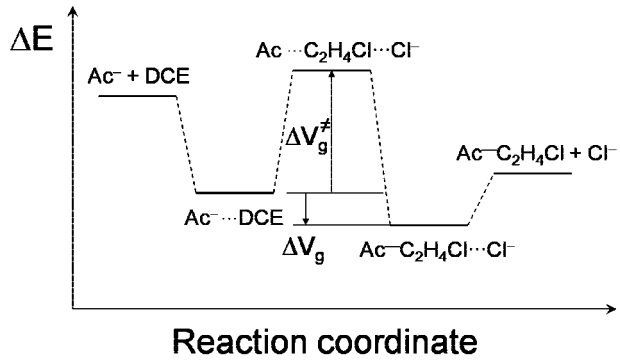

Figure 4. Definition of reaction energy and reaction barrier on the ground-state PES used in the present study.

each other. The presumably most accurate method, G3SX// M06-2X, gives a barrier height of 16.9 kcal/mol. The MC-QDPT(4)//M06-2X barrier height is in good agreement with this high-level value, whereas density functional theory at the B3LYP level gives too low a barrier and the M06-2X barrier is slightly too large (Table 2 and Figure 3). The energy of reaction predicted by the high-level methods is between about −10.0 and −11.0 kcal/mol, in good agreement

Table 2. Reaction Energy and Barrier Height (in kcal/mol) of the Acetate + DCE Reaction in the Gas Phase

method	ΔV_g	$\Delta V_g^{\ddagger}$
M06-2X	−11.3	18.9
BMC-CCSD//M06-2X	−9.9	18.0
G3SX(MP3)//M06-2X	−10.5	17.2
G3SX//M06-2X	−10.7	16.9
MC-QDPT//M06-2X	−15.1	13.2
MC-QDPT(4)//M06-2X	−10.6	16.7
B3LYP	−10.3	14.9
HF	−18.4	18.3
MOVB (scheme VDC)	−21.7	23.8
MOVB (scheme CDC)	−22.0	19.2
EVB	−7	22.9,2.3[a]

[a] The first value corresponds to TS1, and the second value corresponds to TS2 (see Table 1 for the geometries of TS1 and TS2).

with the density functional and MC-QDPT(4)//M06-2X results. The EVB reaction energy of −7.0 kcal/mol is in reasonable agreement with the high-level results. The higher of the two barriers obtained by EVB (22.9 kcal/mol) is about 6 kcal/mol higher than our best estimate, and, as mentioned before, the geometry of the saddle point disagrees with all four other calculations. Of particular relevance is the presence of the second EVB saddle point with a barrier of only 2.3 kcal/mol. Following the path of steepest descent from either transition state leads in one direction to the reactant complex and in the other to the product complex. (Thus, the path of steepest descent from the higher saddle point does not lead to the lower one.) This implies that there is an alternative, lower-energy path for the reaction to proceed, avoiding the higher barrier. This is most likely an artifact of the fitting of the EVB method to empirical data for its use to study the reaction in water and in the haloalkane dehalogenase enzyme. The relevance of such a low barrier for dynamical studies of the reaction in water and in the haloalkane dehalogenase enzyme will be considered below.

To further examine the shape of the ground-state adiabatic PES, we have constructed 2-D contour plots for the reaction at the B3LYP and M06-2X levels and have compared them to those calculated at the EVB level. To make these plots, a grid of points was defined spanning a range of values of the O−C and C−Cl distances. The ground-state adiabatic energies that are plotted were obtained by fixing the values of these two distances and optimizing the rest of geometric parameters. The contour plots obtained using B3LYP are presented in Figure 5(a), those obtained using M06-2X are shown in Figure 5(b), and the ones obtained from EVB are presented in Figure 5(c). In Figure 5(a),(b), the reactant ion-molecule complex is located in the lower right-hand corner, with an energy which is zero by definition. The system then evolves towards the transition state, which is located at an energy of 14.9 kcal/mol for B3LYP (Table 2) and at an energy of 16.5 kcal/mol for M06-2X, and it reaches the product ion-molecule complex in the upper left-hand corner of the figures. The EVB contour plot presented in Figure 5(c) is substantially different; the most notable features are the shift of the reactant complex toward the region of the B3LYP TS and the "shelf" located between the contours of 1.0 and 4.0 kcal/mol containing the lower transition state. Note that the TS with the higher barrier is not reflected in

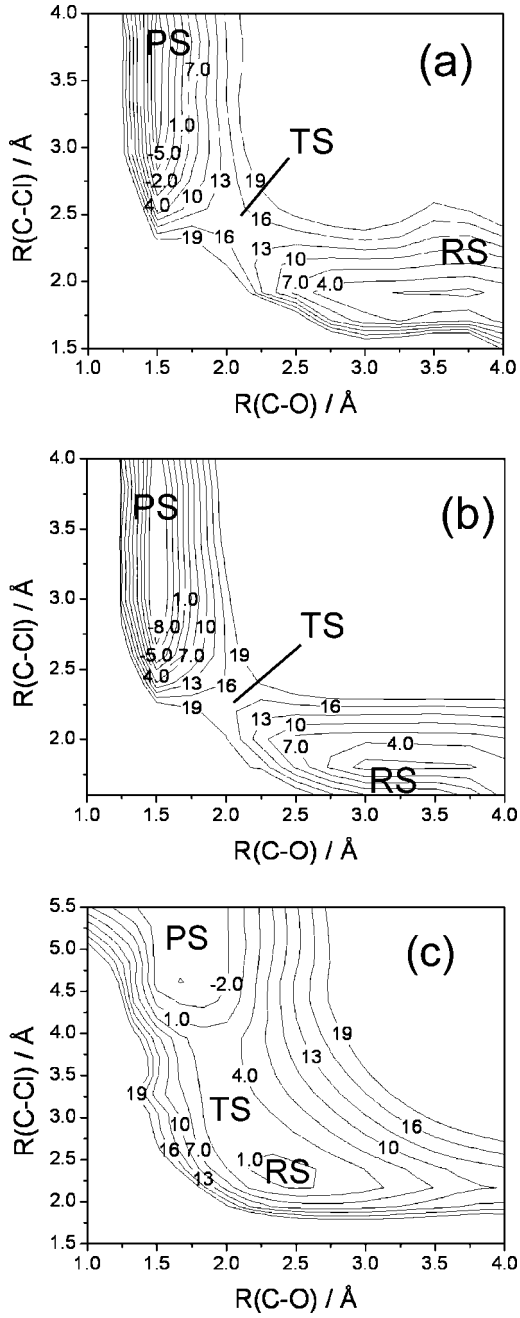

Figure 5. Contour plots of the ground-state adiabatic potential surface in the plane of the O−C and C−Cl distances. The levels of calculation used to construct the plots are (a) B3LYP, (b) M06-2X, and (c) EVB. "RS", "TS", and "PS" stand for the reactant ion-molecule complex, the transition state, and the product ion-molecule complex, respectively. Note the different ordinate between parts (a) and (b). The energy units used are kcal/mol.

the plot, as the optimizations fixing the values of the O−C and C−Cl distances close to those of the TS with the higher barrier always lead to the lower energies observed in the figure. We conclude that the features of the EVB ground-state PES for acetate + DCE reaction in the gas phase do not reflect those obtained with high-level electronic structure theory.

3.3. Diabatic States. The diabatic potential energy curves (and the ground-state adiabatic potential curves) obtained using the nonorthogonal and orthogonal representations for

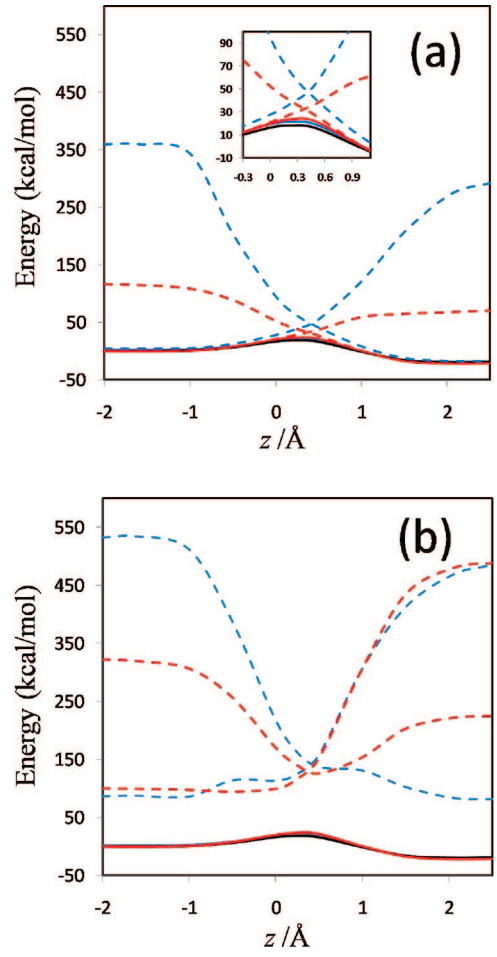

Figure 6. Comparison of adiabatic and diabatic potential profiles. (a) Adiabatic HF profile (black line) and adiabatic and diabatic MOVB potential energy profiles obtained by nonorthogonal VDC (red lines) and nonorthogonal CDC (blue lines) schemes. The panel in the center is a blowup of the central region of the larger panel. (b) Same as part (a) except MOVB results are in the orthogonal representation. In both (a) and (b) the zero of energy is chosen as the ground-state HF adiabatic energy of the ion-molecule reactant complex.

MOVB with VDC and CDC methods are presented in Figure 6; the diabatic curves and the ground- and first-excited adiabats obtained with the fourfold way are shown in Figure 7; and the analogous curves obtained with the EVB method are presented in Figure 8. In comparing these curves, one should keep in mind that the fourfold way diabatic states span the same space as the ground and selected excited adiabatic states, whereas the MOVB states involve no reference or excited adiabatic states, and the EVB curves involve no electronic structure information at all. The corresponding diabatic couplings for the MOVB method in the nonorthogonal and orthogonal representations and for the fourfold way (MC-QDPT(4)//M06-2X) and EVB calculations are depicted in Figure 9.

We emphasize that there is no unique way of defining the diabatic states corresponding to the reactant state and the product state, in part because diabatic states are intrinsically nonunique[4,59,105,136−141] and in part because it is necessary to apportion the contributions from additional VB structures (such as, in the present example, the key ionic configuration

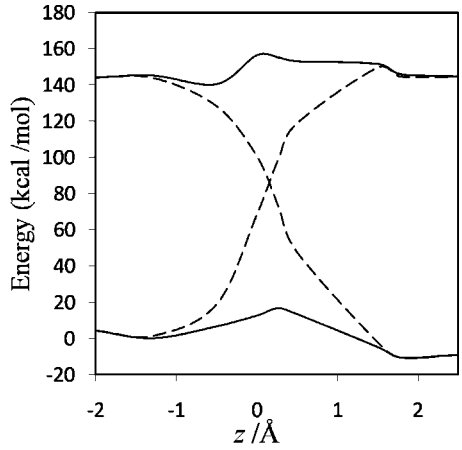

Figure 7. Fourfold way (MC-QDTP(4)//M06-2X) adiabatic and diabatic energies along the reaction coordinate. The zero of energy is chosen as the ground-state adiabatic energy of the ion-molecule reactant complex.

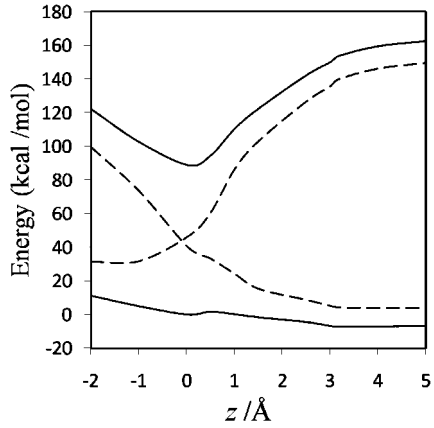

Figure 8. EVB adiabatic and diabatic energies along the reaction coordinate. The zero of energy is chosen as the ground-state adiabatic energy of the ion-molecule reactant complex.

3 as well as the high-energy covalent configuration **6** in eq 2) into two explicit states along the entire reaction coordinate.

The MOVB reactant and product diabatic energy profiles in VDC and CDC models and in the nonorthogonal and orthogonal representations are presented in Figure 6. Figure 6(a) shows that in the nonorthogonal representation, the diabatic energy increases by about 70 and 290 kcal/mol for VDC and CDC states, respectively, in going from the equilibrium reactant ion-dipole geometry to the equilibrium product state geometry. Similarly, for the reverse reaction, the product state energy increases by 115 and 360 kcal/mol for VDC and CDC schemes, respectively, at the reactant geometry. Thus, optimizing each of the MOVB structures separately affords much smaller energies at geometries far from their respective regions of minimal energy than does optimizing the ground-state energy. The fourfold way values for these quantities are approximately 140 kcal/mol both for the reactant and product diabatic states (Figure 7). The orthogonal representation for MOVB yields results very different to those from the nonorthogonal representation, as can be seen in Figure 6(b). The energies of the orthogonal MOVB states are significantly higher than for the nonor-

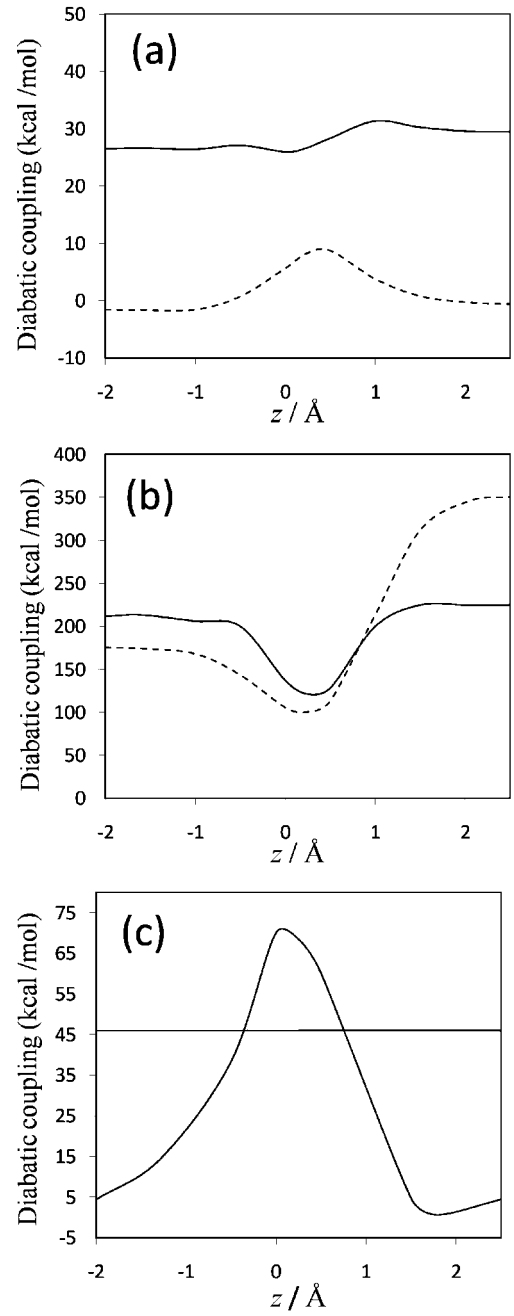

Figure 9. Diabatic coupling matrix elements as a function of the reaction coordinate. (a) Nonorthogonalized MOVB resonance energy of eq 9a or the equivalent eq 10 (full line for the CDC method, and dashed line for the VDC method), (b) orthogonalized MOVB H^{a}_{12} (CDC is given as a full line, and VDC is shown by a dashed line), and (c) diabatic coupling according to the orthogonal fourfold way (MC-QDTP(4)//M06-2X) (curve with a peak) and EVB (straight line).

thogonal representation, and the curves do not join the adiabatic ground-state curve in the reactant and product regions. Thus, the energy variations in the fourfold way reactant and product diabatic states are larger than the MOVB results in the VDC method but smaller than those in the CDC optimization (either nonorthogonal or orthogonal). The maximum energy changes in the reactant and product states of EVB theory are about 140 and 100 kcal/mol, respectively.

Orthogonalization of the MOVB states involves the overlap between the MOVB structures. The overlaps for the

Table 3. Computed Overlap Integrals Using the MOVB Wave Functions at the Reactant Complex (RS), Transition State (TS), and Product Complex (PS) Geometries Optimized at the HF Level

z	VDC-MOVB	CDC-MOVB
RS	0.853	0.605
TS	0.910	0.770
PS	0.938	0.659

reactant complex, the transition state, and the product complex are presented in Table 3, and overlaps at other locations along the reaction path are presented in Table S6 of the Supporting Information. As observed in Table 3, the overlaps are always quite large, especially in VDC states where they go up to 0.94 in the product region. The overlap integrals from the CDC wave functions are significantly smaller than the VDC values (Table 3). Apparently, optimizing the MOVB structures separately causes the fragment orbitals to delocalize more than optimizing the ground-state energy (CDC theory), thereby causing a stronger overlap between the structures. This may also be recognized as increased ionic character in the VDC reactant diabatic state at the product state geometry, which has greater resemblance with the product diabatic state near its minimum.[4] Also, the overlaps in VDC states increase continuously along the reaction path, whereas the CDC overlaps are maximal in the transition state region. The values obtained for the overlaps can be compared, for instance, with those obtained in a breathing-orbital VB study of the $X^- + CH_3X$ (X = F, Cl, Br, I) identity reactions,[64] where for the TS geometry, smaller values oscillating between 0.47 for F and 0.33 for I were obtained for the VB wave function overlap. In yet another study, ab initio VBSCF/6-31+G(d,p) calculations on the ammonia exchange reaction of NH_3 and $CH_3NH_3^+$ show overlap integrals varying from 0.6 to 0.7 from the ion-dipole complex minimum to the transition state.[4] Thus, a more conventional VB approach yields smaller, but still significant, overlaps than MOVB, because the VB orbitals are more constrained in the former case and are not allowed to delocalize as extensively as in the MOVB method. Overlap is simply not negligible in VB theory.

The energy difference between the product and reactant diabatic states at the reactant geometry is called the reorganization energy in condensed-phase reactions, and it plays a key role in Marcus theory. In other contexts, this energy difference is called promotion energy, for example by Shaik.[56] Figures 6−8 show that the reorganization energy varies from 115 to 440 kcal/mol for the four MOVB schemes and is 140 kcal/mol in both the fourfold way and the EVB model. The close agreement of the reorganization energy from the nonorthogonal VDC-MOVB scheme with that of the fourfold-way is not straightforward to interpret because the orthogonal fourfold way and EVB schemes should strictly be compared only to the orthogonal MOVB results.

Note that the fourfold way states are obtained by following a strategy in which both the ground and the first excited state surfaces are used in the definition of the two diabatic states, whereas in the MOVB schemes no excited adiabatic state plays any role. Nevertheless, both the fourfold way and the MOVB method share the characteristic that the definition of the diabatic states is based on electronic structure considerations. In contrast the EVB diabatic states are based on the value of molecular mechanics analytical energy expressions used in regions far away from equilibrium conformation—where they are not valid and were not designed to be used. The EVB diabatic energy profiles shown in Figure 8 do not agree qualitatively with either the MOVB or the fourfold-way ones in that the region of the transition state does not correspond to the crossing of the diabatic curves although it is typically described in this way. In the present S_N2 reaction (chosen to model the haloalkane dehalogenase reaction), the transition state is located at a larger value of the reaction coordinate (about 1.3 Å). As already mentioned, the EVB barrier on the ground-state adiabatic PES is much lower than that obtained with the other methods.

The diabatic couplings obtained by all six schemes are shown in Figure 9. First one notes that some features of the diabatic couplings obtained by the MOVB method, the fourfold way, and the EVB calculations are qualitatively different. Focusing first on the nonorthogonal MOVB method (Figure 9(a)), the diabatic coupling obtained with the CDC scheme, in which it represents the stabilization energy of the transition state at the diabatic energy crossing and is dependent on the overlap integral according to eqs 9a and 10, has a rather different shape from that obtained with the VDC model. The CDC resonance energy remains relatively constant along the reaction path, as in EVB theory, and is nonzero at the reactant and product regions. Interestingly, the quantitative result of about 30 kcal/mol is also close to the EVB constant value of ∼45 kcal/mol (Figure 9(c)). On the other hand, the VDC resonance energy curve in Figure 9(a) has very similar shape but smaller diabatic coupling, in comparison with the fourfold way method. This reflects the more ionic character in the VDC states in which the stabilization energy due to diabatic coupling is partially included in the diabatic energies, and this is mirrored by greater overlap integrals than those between the CDC states. However, when the nonorthogonal CDC and VDC diabatic states are orthogonalized by Löwdin transformation, the $H^{\S}_{12}$ couplings, shown in Figure 9(b), have a much larger magnitude than those of B in nonorthogonal representation shown in Figure 9(a), and the former couplings present a minimum around the transition state geometry. The different behavior of $H^{\S}_{12}$ as compared with B is probably a consequence of the large overlap between the nonorthogonal MOVB structures, which should cause the nonorthogonal and orthogonal wave functions to differ considerably. Interestingly, while the symmetric transformation enforces orthogonality between diabatic states, the "penalty" of distorting the wave functions is transferred to enhanced diabatic coupling to yield the same ground-state energy. In the fourfold way (Figure 9(c)), the diabatic states are orthogonal by construction and—also by construction—are zero at reactants and products, and the diabatic state coupling is most dominant in the strong interaction region where the two VB states become degenerate and have the greatest overlap. This is qualitatively in agreement with the nonor-

Table 4. Free Energies of Solvation and Activation in Water (in kcal/mol) and Energies of Activation in the Gas Phase, for the Acetate + DCE Reaction Obtained from EVB and from M06-2X Geometries[a]

method	$\Delta X_g^{\ddagger}$	ΔG_S^{RS}	ΔG_S^{TS}	$\Delta G_w^{\ddagger}$
optimized geometries at SM8	16.9[b]	−58.1	−53.4	21.6
molecular dynamics on EVB PES[21,28]	2.0[c]	−77.8[d]	−54.9[d]	24.9[e]
SM8 on stationary point EVB geometries	2.3[f]	−58.0	−73.7	−13.4
SM8 on sampled EVB geometries[g]	−6.2[f]	−64.8	−58.3	0.3

[a] "RS" and "TS" stand for the reactant ion-molecule complex and the transition state, respectively. The experimental free energy of activation in water is 28.2 kcal/mol.[24,27,230] [b] $\Delta V_g^{\ddagger}$ calculated at the G3SX//M06-2X level. [c] $\Delta G_g^{\ddagger}$ derived from columns 3, 4, and 5 and eq 11. [d] Taken from ref 28. [e] Taken from ref 21. [f] $\Delta V_g^{\ddagger}$ calculated from the ground-state EVB PES. [g] Representative geometries of the molecular dynamics trajectory sampling presented in Figure 1(a) of ref 21.

thogonal VDC-MOVB method. The maximum values of the fourfold-way and EVB H_{12} curves are much smaller than the magnitude of the MOVB couplings in the orthogonal representation but larger than those in the nonorthogonal representation. The fourfold way coupling decays rather rapidly but not at the same rate in the directions towards the reactant state and the product state. This uneven rate of decrease in the diabatic coupling strength is usually not considered in EVB, where either a single exponential function or a constant diabatic coupling are assumed.

3.4. SM8 Free Energies of Solvation and Free Energies of Activation. We have applied the SM8 solvation model to the reactant ion-molecule complex and the TS, and we have calculated free energies of activation by adding the gas-phase reaction barrier to the difference of the free energies of solvation. The results are presented in Table 4. The second row gives the results of molecular dynamics simulations of the free energy of activation in water from ref 21 and the corresponding free energies of solvation from ref 28. Comparing the values of these quantities shows that the gas-phase free energy of activation (that is, the sum of the first two terms on the right-hand side of eq 11) is only 2 kcal/mol. This value is substantially smaller than expected from the electronic structure calculations presented in this work, which indicate that the value of the electronic gas-phase barrier is about 17 kcal/mol. However, the result would be consistent with the lower electronic barrier of 2.3 kcal/mol found for EVB (see Figure 5(c)), which was pointed out in refs 1 and 27, and with the general shape of the EVB ground-state PES. Note that the final result, namely, the free energy of activation, is in good agreement with experiment.

The results presented in the first row of Table 4 have been obtained by optimizing the geometries of the reactant ion-molecule complex and of the TS in the presence of the solvent by SM8. The gas-phase geometries of reactants and of the TS taken as the reference for the calculation of free energies of solvation are those obtained by M06-2X. The value of the electronic gas-phase potential energy barrier has been assumed to be that of the best level of calculation used in the present study, namely, G3SX//M06-2X. Regarding the free energies of solvation, as shown in the table, it is interesting that the values obtained for reactants and for the TS are rather similar, in contrast to other S_N2 reactions (for example, the prototype $Cl^- + CH_3Cl$ reaction[66,229]) where reactants are preferentially solvated by a large amount over the TS. This is probably due to the delocalized nature of the charge in the acetate anion. The overall free energy of activation is 21.6 kcal/mol, smaller than the experimental value of 28.2 kcal/mol.[24,27,230] at 373 K. Note that solute-solvent charge transfer is not taken into account by the present treatment. For the acetate anion in a microsolvated environment, a charge transfer to water of +0.18 was obtained with the SM8 model also employed here.[231] Consideration of this and other factors affecting the solvation free energies could lead to a better agreement with experiment.

The results shown in the third and fourth row of Table 4 employ the EVB PES. In this case, pointwise calculations of free energies of solvation have been performed at the SM8 level at EVB geometries. In the third row, which has been obtained from EVB reactant and TS geometries, one observes that the energy of activation obtained is negative, in strong disagreement with the value obtained from molecular dynamics simulations.[21,28] It is noteworthy that the solvation energy for the TS is considerably larger than that for reactants, which is the opposite of that found from the simulations[28] and contrary to what is expected for S_N2 reactions. This is caused by the already mentioned shift of the EVB reactant and TS geometries with respect to those obtained by electronic structure calculations (see Table 1): the TS has an extended C−Cl distance and the Cl^- anion has a large free energy of solvation. The large discrepancy obtained for the free energy of activation is due at least in part to the fact that the geometries chosen are not quite representative of the geometries actually sampled in the liquid-phase molecular dynamics simulations, such as those shown in Figure 1(a) of ref 21. To address this point, we have chosen two geometries, one with an O−C distance of 3.2 Å and a Cl−C−O angle of 150.0° as representative of the reactants region, and another one with an O−C distance of 2.2 Å and a Cl−C−O angle of 165.0° as representative of the TS region. These two parameters were fixed while the rest of the geometrical parameters were optimized, and pointwise SM8 calculations were again performed on the optimal structures. The results, presented in the fourth row of Table 4, show a free energy of activation close to zero and a larger solvation energy for the reactant state, as expected for the acetate + DCE S_N2 reaction. Note also the negative reaction barrier in the gas phase using these structures (Table 4). Olsson at al. argued in footnote 68 of ref 28 that TS structures are similar in the gas phase and in aqueous solution, but the structures of the reactant states are different, the elongated ion-dipole structure in water is 13 kcal/mol higher, and the compressed ion-dipole complex in the enzyme is 6 kcal/mol higher in energy than that at the gas-phase minimum.[28] According to this analysis[28] a negative reaction barrier of about −11 kcal/mol would be obtained in water, in close agreement with the value in the fourth row of Table 4. It is possible that an average over many molecular configurations such as that shown in Figure 1(a) of ref 21 could reconcile this result with the gas-phase

activation barrier of 2.0 kcal/mol obtained in the first row of the table. However, Olsson et al.[28] stated that a gas-phase activation barrier deduced from their "thermodynamic cycle is in excellent agreement with ab initio estimates of this barrier (about 17 kcal/mol)". The free energy of activation obtained is actually in disagreement with that from molecular dynamics simulations by more than 20 kcal/mol.

Therefore, none of the calculations presented using the EVB PES has been able to reasonably reproduce the results presented in refs 21 and 28. We believe that it is mainly the qualitatively wrong shape of the EVB PES in the gas phase which causes the inconsistencies in the computation of free energies of solvation and activation in water. In our opinion, a careful study of the EVB gas-phase reactions should be undertaken prior to reparametrizing the PES for use in studies in condensed phase or in the active center of an enzyme.

3.5. Other Methods. It is interesting to compare the present treatments to Voter and Goddard's generalized resonating valence bond (GRVB) method.[232] As compared to MOVB, we note that GRVB uses a multiconfiguration wave function, whereas the MOVB method uses a single Slater determinant. As compared to the fourfold way, we note that GRVB is an approximate way to calculate the ground electronic state, whereas the fourfold way starts with arbitrarily accurate calculations that approximate the ground and excited states and then finds diabatic states that span the same space as the two lowest-energy adiabats.

To construct an accurate and efficient VB-based model for modeling chemical and enzymatic reactions, an effective Hamiltonian MOVB (EH-MOVB) approach has been developed;[233] this method can be parameterized similarly as the EVB model, but the molecular structures can be optimized to obtain good agreement with ab initio MO or VBSCF results. The EH-MOVB method can be carried out at either the semiempirical or ab initio level of theory, using either Hartree-Fock or density functional theory. Accuracy is improved by introducing a scaling factor on the diabatic coupling ($H_{12}^{\mathrm{EH-MOVB}} = \beta H_{12}^{\mathrm{MOVB}}$) to yield the correct barrier height and a diabatic energy shift constant ($H_{22}^{\mathrm{EH-MOVB}} = H_{22}^{\mathrm{MOVB}} + \Delta\varepsilon$) to reproduce the experimental energy of reaction. The EH-MOVB theory is based on ab initio valence bond theory with a multiconfiguration reduction to generate the diabatic states.[4] The level of theory to describe the diabatic states can be systematically improved, and the diabatic coupling is dependent on all *3N* degrees of freedom where *N* is the number of atoms in the system. The method has been illustrated for the S_N2 reaction between hydrosulfide and chloromethane at the EH-MOVB/6-31+G(d,p) level, and excellent agreement has been obtained with ab initio VBSCF or other high-level results for optimized structures and the potential energy surface.[233]

4. Concluding Remarks

We hope that the perspective presented here is useful for elucidating the importance of consistently defining diabatic states when using them to discuss condensed-phase properties such as reaction rates of enzymatic reactions. The construction of diabatic states for the gas-phase reaction is often a useful first step for applications where liquid-phase diabatic states are desired for interpretative purposes, but there is no unique method for defining diabatic states in either phase. The main focus of the present study is a comparison between three methods, namely, the molecular orbital valence bond (MOVB) method, the fourfold way, and empirical valence bond (EVB) calculations, of generating diabatic, VB-like states, as illustrated by application to the acetate + DCE system in the gas phase. For the MOVB case, we consider two schemes, called variational diabatic configurations (VDC) and consistent diabatic configurations (CDC). Furthermore, whereas the fourfold way and EVB are defined only in an orthogonal representation, MOVB is directly defined in a nonorthogonal representation, which can be transformed to an orthogonal representation by Löwdin symmetric orthogonalization method.

There are many different motivations for working with diabatic states, and in the case of the EVB calculations presented here the goal of the original workers was to predict the free energy profile in an enzyme reaction for use with a collective reaction coordinate based on an energy gap. It is recognized by all practitioners that all the approaches used here are approximate ones, and when one applies these same methods to other problems, the quality of the results will depend on the quality of the parameterization, the basis set, and various problem-specific details. For parameterized methods, one must keep in mind the nature of the parameterization. If one calibrates an analytic potential energy surface, especially one with an analytic form restricted for computational efficiency, to produce one or two properties one cannot necessarily expect the potential energy surface to be accurate along any coordinate chosen. Thus, one might argue that an EVB surface should be used only for calculating the potential energy surface along the same collective energy-gap coordinate for which it was designed and created. That is one possible way to proceed, but our goal here was to examine the underlying diabatic potential surfaces because they are often interpreted in a physical way as providing information about reorganization energy, promotion energy, and enzyme mechanisms and for understanding the origin of rate acceleration in enzyme catalysis. Thus, in the present paper, we are examining the EVB diabatic curves in a different context using a geometrical reaction coordinate different than that (an energy-gap coordinate) for which they were originally parameterized along. Our justification for this is that we believe that—for many purposes—dynamical methods based on a collective reaction coordinate and dynamical methods based on a valence-coordinate reaction path should both utilize an atomically qualitatively correct description of the potential energy surface as a function of all relevant atomic coordinates, and our goal was to compare—in this context—three classes of methods employing the concept of diabatic states in various ways. By calculating not only the transition state theory rate constant but also the transmission coefficient, one can unify treatments based on different choices of the reaction coordinate.[1,2,105] It has been shown that the transmission coefficients are close to unity for the present S_N2 reaction in water and in haloalkane dehalogenase enzyme when making use of the

asymmetric stretch reaction coordinate,[27] so this choice of reaction coordinate is a very relevant one.

The diabatic potential energy profiles along the asymmetric stretch reaction coordinate obtained with the fourfold way agree qualitatively but not quantitatively with the nonorthogonal MOVB method with the VDC model; this is very interesting since the underlying electronic structure methods employed in this work for MOVB (ab initio HF) and the fourfold way (ab initio MC-QDPT) are very different and since the fourfold way yields an orthogonal representation. The results obtained with EVB, which is based on a parameterization of MM diabatic states to reproduce free energies in condensed phase, are quite different from those obtained with MOVB and the fourfold way, which are based on electronic structure calculations, but are closer in general magnitude to the fourfold-way results. However, the EVB gas-phase adiabatic reaction path shows a systematic shift towards product geometries with, e. g., the EVB ion-molecule reactant minimum resembling the TS geometry obtained with electronic structure methods. Also EVB has two different reaction paths, one bearing a barrier of 22.9 kcal/mol, in qualitative agreement to the barrier obtained by MOVB and the fourfold way, and a second reaction path of much lower energy, with a barrier of only 2.3 kcal/mol. This second reaction path is an artifact of the EVB parameterization. A calculation of free energies of solvation and activation in water based on the EVB PES has been unable to reproduce the free energy of activation obtained by molecular dynamics simulations (24.9 kcal/mol). These findings cast doubts on the reported EVB results and suggest that a careful parameterization of the gas-phase reaction might have been useful in order to obtain more meaningful results for the condensed-phase reaction by the EVB method.

The energy variations predicted by the two electronic structure methods (MOVB and the fourfold way) for the reactant and product states at the product and reactant equilibrium geometries, respectively, are large. The MOVB values for these quantities depend to a large extent on the representation (nonorthogonal or orthogonal) and on the optimization strategy adopted for the wave functions. An interesting question for future consideration is whether any of the electronic-structure reorganization energies calculated by the methods used here should be used as the solute contribution to the reorganization energies[106,107] for the condensed-phase reaction.

The diabatic couplings obtained with the fourfold way decrease steeply from the region of the transition state towards reactants and products, where they are close to zero. In contrast, the couplings obtained with the MOVB method have a much larger magnitude, are either relatively constant along the reaction coordinate or present a minimum in the transition state region, and are nonzero in the reactant and product regions. An exception is the nonorthogonal VDC-MOVB model, which has qualitatively similar features to those found by the fourfold way. These differences reflect the fact that the diabatic coupling absorbs the nonuniqueness in the definition of the diabatic states. No functional form is assumed for the diabatic coupling in MOVB or in the fourfold way since the diabatic coupling (off-diagonal element of the Hamiltonian matrix) is determined by using electronic structure methods; however, the values of the diabatic coupling that are obtained are intimately determined by the specific definition of the diabatic state wave function. This is quite different from the situation in the EVB method, where either an exponential dependence on the distance between the nucleophile and the leaving group involved in an S_N2 reaction or a constant coupling as for the acetate + DCE reaction is assumed.

The reaction energies obtained by density functional theory and by the fourfold way agree well with those obtained by the three high-level methods (G3SX, G3SX(MP3), and BMC-CCSD), which predict values ranging from −10 and −11 kcal/mol. The results for the diabatic states are especially significant because in the fourfold way, changes in the exponent of the diffuse basis functions of chlorine and in the weight of the two adiabatic states involved in the underlying SA-CASSCF wave function were carried out to obtain simultaneously a barrier height and reaction energy (on the *adiabatic* potential energy surface) in good agreement with the high-level ab initio results. The resulting fourfold way barrier (16.7 kcal/mol) agrees very well with the barriers predicted by the high-level methods, especially with the most reliable one, which is the G3SX//M06-2X value, and is somewhat higher than the B3LYP value but lower than the M06-2X value.

Although this perspective has been quantitatively illustrated only with gas-phase diabatic states, most of the considerations are equally valid for condensed-phase reactions, for which a number of valence-bond electronic structure approaches are now available.[61,63,65,67,68,72,101,141] In previous work on aqueous S_N2 reactions, the MOVB method based on VDC diabatic states led to solute-solvent interaction energies that vary weakly with the reaction coordinate, in contrast to previous studies of other S_N2 reactions using the EVB method.[94] Further work on the analogy between S_N2[234] and other types of reactions (such as hydride, proton, or hydrogen atom transfer reactions in enzymes[106] or electron-transfer reactions[90,91,93,235−241]) and on the reorganization energies defined in terms of CDC diabatic states would be useful.

In light of the large quantitative differences between diabatic states obtained by employing different defining equations, algorithms, or representations, we recommend that justification needs to be made for employing specific definitions in specific contexts in cases where the quantitative values are important. For qualitative discussion purposes, one can have more leeway in the definition employed. In applications to enzymatic reactions, it is useful, if possible, to first investigate the corresponding model reaction in the gas phase to justify the definition of diabatic states and to validate the entire potential energy surface and structures of the adiabatic ground state. Then, a valence-bond-based potential can be used to model the reaction in aqueous solution to validate or even to calibrate the interactions between solute and solvent. Finally, after validation of the potential energy surface in the gas phase and solute-solvent interactions in water, the method can be applied to the enzyme reaction to understand catalysis.

5. Summary

Diabatic models are widely employed for studying chemical reactivity in condensed phases and enzymes, but there has been little discussion of the pros and cons of various diabatic representations for this purpose. Here we discuss and contrast six different schemes for computing diabatic potentials for a charge rearrangement reaction. They include (i) the variational diabatic configurations (VDC) constructed by variationally optimizing individual valence bond structures and (ii) the consistent diabatic configurations (CDC) obtained by variationally optimizing the ground-state adiabatic energy, both in the nonorthogonal molecular orbital valence bond (MOVB) method, along with the orthogonalized (iii) VDC-MOVB and (iv) CDC-MOVB models. In addition, we consider (v) the fourfold way (based on diabatic molecular orbitals and configuration uniformity), and (vi) empirical valence bond (EVB) theory. To make the considerations concrete, we calculate diabatic electronic states and diabatic potential energies along the reaction path that connects the reactant and the product ion−molecule complexes of the gas-phase bimolecular nucleophilic substitution (S_N2) reacton of 1,2-dichloethane (DCE) with acetate ion, which is a model reaction corresponding to the reaction catalyzed by haloalkane dehalogenase. We utilize ab initio block-localized molecular orbital theory to construct the MOVB diabatic states and ab initio multiconfiguration quasidegenerate perturbation theory to construct the fourfold-way diabatic states; the latter are calculated at reaction path geometries obtained with the M06-2X density functional. The EVB diabatic states are computed with parameters taken from the literature. The MOVB and fourfold-way adiabatic and diabatic potential energy profiles along the reaction path are in qualitative but not quantitative agreement with each other. In order to validate that these wave-function-based diabatic states are qualitatively correct, we show that the reaction energy and barrier for the adiabatic ground state, obtained with these methods, agree reasonably well with the results of high-level calculations using the composite G3SX and G3SX(MP3) methods and the BMC-CCSD multicoefficient correlation method. However, a comparison of the EVB gas-phase adabatic ground-state reaction path with those obtained from MOVB and with the fourfold way reveals that the EVB reaction path geometries show a systematic shift towards the products region and that the EVB lowest-energy path has a much lower barrier. The free energies of solvation and activation energy in water reported from dynamical calculations based on EVB also imply a low activation barrier in the gas phase. In addition, calculations of the free energy of solvation using the recently proposed SM8 continuum solvation model with CM4M partial atomic charges lead to an activation barrier in reasonable agreement with experiment only when the geometries and the gas-phase barrier are those obtained from electronic structure calculations, i.e., methods i−v. These comparisons show the danger of basing the diabatic states on molecular mechanics without the explicit calculation of electronic wave functions. Furthermore, comparison of schemes i−v with one another shows that significantly different quantitative results can be obtained by using different methods for extracting diabatic states from wave function calculations, and it is important for each user to justify the choice of diabatization method in the context of its intended use.

Acknowledgment. The authors are grateful to R. A. Marcus, Yousung Jung, Oksana Tishchenko, and Jonathan Young for stimulating discussions and to Avital Shurki for correspondence about EVB parameters. This work was supported in part by the National Science Foundation under grant No. CHE07-04974 (D.G.T.) and by the National Institutes of Health under grant no. GM46736 (J.G.).

Appendix: Computational Details

In the MC-QDPT calculations, the intruder-state avoidance (ISA)[242] method has been used to avoid artifacts due to intruder states in the MC-QDPT wave function. The level shift parameter[242] b of the ISA method was set to $0.02E_h^2$ (1 $E_h \equiv 1$ hartree).

Initially, the MC-QDPT calculations used the 6-31+G(d)[184−187] basis set. However, the resulting MC-QDPT reaction profiles had artifacts in either the reactant or the product region, depending on the weights of the electronic states in the CASSCF step. This problem is caused by the diffuse functions, especially those on the carbon and oxygen atoms, because the character of the excited state in the reactant and product regions is that of a resonance embedded in the continuum, as has been explained elsewhere.[144] This problem was eliminated by omitting diffuse functions on all atoms except on the two chlorine atoms of DCE. Furthermore, the exponents of the diffuse functions of chlorine were increased from the standard value of 0.483 to 0.09 to obtain a good reaction energy and barrier. The resulting basis set will be denoted as 6−31&G(d).

Several SA-CASSCF(4,3) calculations were performed in which the weight of the two electronic states in the state average was varied in the range 50:50 to 90:10. Other combinations of weights in which the excited state has a higher weight than the ground state yielded an unbalanced description of the adiabatic states and were discarded. The best state weightings were ascertained by comparison to the high-level calculations and were found to be those with 75:25 weights, and these are used in the rest of this article.

The first step in the application of the fourfold way to the acetate + DCE system is to establish a standard orientation so that the Cartesian coordinates of the atoms are uniquely and continuously defined at all nuclear configurations. In the standard orientation, the molecule is situated as follows. The attacking oxygen of $CH_3CO_2^-$ is placed at the origin, the carbon atom of $ClCH_2CH_2Cl$ that is attacked by that oxygen is on the positive Z axis, and the chlorine atom that is bound to that carbon atom in reactants, acetate + DCE, is on the first quadrant of the XZ axis. The remaining atoms do not have a particular orientation since they do not participate directly in the nucleophilic displacement reaction. Two reference MOs were introduced as follows. The first one is the oxygen lone pair of the attacking oxygen atom of acetate, and it is obtained at the reactant ion-molecule configuration by the threefold way. The second reference MO is obtained by the threefold way at the product ion-molecule configuration as the p orbital of the chloride ion

which derives from the cleaved C−Cl bond. In order to keep the character of the DMO centered on the chlorine atom fixed it becomes necessary to define a specific molecular orientation (denoted by primed coordinates), and for a general molecular geometry the reference MO must be transformed to the standard orientation (unprimed). The reference MO centered on the oxygen does not need a specific orientation since the oxygen atom is always located at the coordinate origin. The specific orientation is defined in the same way as the standard orientation, except that the chlorine atom is placed along the positive Z' axis of the specific orientation. The reference MO centered on the chlorine atom is transformed from the specific to the standard orientation at each point along the reaction coordinate by means of a rotation matrix that depends on the angle between the C−Cl bond and the Z axis.

It is necessary to have a one-to-one correspondence of the fourfold-way DMOs at consecutive geometries. For this, two reference geometries have to be chosen in regions where diabatic states are equal to adiabatic states to a good approximation. The fourfold way is then carried out at each of the reference geometries. The procedure is advanced by taking several consecutive geometries separated by small steps along the minimum energy path that connects reactants and products. This procedure ensures that the DMOs of products are ordered in the same way along the whole reaction path so that they can produce consistent groups of DCSFs.

The matrix elements of the MOVB Hamiltonian are evaluated using methods for nonorthogonal determinants, and the computational details can be found in refs 60 and 141. In the VDC method, the MOs are obtained using a reorthogonalization technique,[154] although an iterative sequence of Jacobi rotations approach is also possible.[155]

The EVB parameters used in this work are presented in Table S1 of the Supporting Information. The corrections with respect to the way that the parameters are presented in ref 21 are (1) the bond angle force constants have been transformed from (kcal/mol)·rad^{-2} to (kcal/mol)·deg^{-2}; (2) the C···O nonbonded van der Waals term is only included in the reactant configurations, and the C...Cl term is only included in the product configuration, and (3) for these terms, the exponents have been changed to $\alpha = 3.90$ for the reactant configuration, and to $\alpha = 4.00$ for the product configuration to match the values used in the published[21] work. These corrections enable us to generate the EVB potential corresponding to the treatment of ref 21.

Software. The fourfold way calculations were carried out with HONDOPLUS, version 5.1;[243] the BLW calculations were performed using the Xiamen VB (XMVB) program;[244] the Minnesota Gaussian Functional Module (MN-GFM),[245,246] version 3.0 was used for the M06-2X calculations; the G3SX, G3SX(MP3), and BCM-CCSD calculations were carried out with MLGAUSS, version 2.0;[246,247] and the SM8 solvation free energy calculations were performed with the Minnesota Gaussian Solvation Module (MN-GSM).[248]

Supporting Information Available: EVB parameters, Cartesian coordinates of all the points calculated on the ground-state adiabatic reaction paths, and MOVB overlaps. This material is available free of charge via the Internet at http://pubs.acs.org.

References

(1) Gao, J.; Ma, S.; Major, D. T.; Nam, K.; Pu, J.; Truhlar, D. G. *Chem. Rev.* **2006**, *106*, 3188.

(2) Pu, J.; Gao, J.; Truhlar, D. G. *Chem. Rev.* **2006**, *106*, 3140.

(3) Hiberty, P. C.; Shaik, S. *J. Comput. Chem.* **2007**, *28*, 137.

(4) Song, L.; Gao, J. J. Phys. Chem. A **2008**, ASAP.

(5) Pries, F.; Kingma, J.; Pentenga, M.; van Pouderoyen, G.; Jeronimus-Stratingh, C. M.; Bruins, A. P.; Janssen, D. B. *Biochemistry* **1994**, *33*, 1242.

(6) Pries, F.; Kingma, J.; Krooshof, G. H.; Jeronimus-Stratingh, C. M.; Bruins, A. P.; Janssen, D. B. *J. Biol. Chem.* **1995**, *270*, 10405.

(7) Schanstra, J. P.; Janssen, D. B. *Biochemistry* **1996**, *35*, 5624.

(8) Schanstra, J. P.; Kingma, J.; Janssen, D. B. *J. Biol. Chem.* **1996**, *271*, 14747.

(9) Krooshof, G. H.; Ridder, I. S.; Tepper, A. W. J. W.; Bos, G. J.; Rozeboom, H. J.; Kalk, K. H.; Dijkstra, B. W.; Janssen, D. B. *Biochemistry* **1998**, *37*, 15013.

(10) Schindler, J. F.; Naranjo, P. A.; Honaberger, D. A.; Chang, C.-H.; Brainard, J. R.; Vanderberg, L. A.; Unkefer, C. J. *Biochemistry* **1999**, *38*, 5772.

(11) Lewandowicz, A.; Rudzinski, J.; Tronstad, L.; Widersten, M.; Ryberg, P.; Matsson, O.; Paneth, P. *J. Am. Chem. Soc.* **2001**, *123*, 4550.

(12) Damborsky, J.; Kuty, M.; Nemec, M.; Koca, J. *J. Chem. Inf. Comput. Sci.* **1997**, *37*, 562.

(13) Maulitz, A. H; Lightstone, F. C.; Zheng, Y.-J.; Bruice, T. C *Proc. Natl. Acad. Sci. U.S.A.* **1997**, *94*, 6591.

(14) Lightstone, F. C.; Zheng, Y.-J.; Maulitz, A. H.; Bruice, T. C *Proc. Natl. Acad. Sci. U.S.A.* **1997**, *94*, 8417.

(15) Damborsky, J.; Bohac, M.; Prokop, M.; Kuty, M.; Koca, J. *Prot. Eng.* **1998**, *11*, 901.

(16) Kuty, M.; Damborsky, J.; Prokop, M.; Koca, J. *J. Chem. Inf. Comput. Sci.* **1998**, *38*, 736.

(17) Lightstone, F. C.; Zheng, Y.; Bruice, T. C. *Bioorg. Chem.* **1998**, *26*, 169.

(18) Lightstone, F. C.; Zheng, Y.; Bruice, T. C. *J. Am. Chem. Soc.* **1998**, *120*, 5611.

(19) Damborsky, J.; Koca, J. *Prot. Eng.* **1999**, *12*, 989.

(20) Lau, E. Y.; Kahn, K.; Bash, P. A.; Bruice, T. C *Proc. Natl. Acad. Sci. U.S.A.* **2000**, *97*, 9937.

(21) Shurki, A.; Strajbl, M.; Villà, J.; Warshel, A. *J. Am. Chem. Soc.* **2002**, *124*, 4097.

(22) Kahn, K.; Bruice, T. C. *J. Phys. Chem. B* **2003**, *107*, 6876.

(23) Hur, S.; Kahn, K.; Bruice, T. C *Proc. Natl. Acad. Sci. U.S.A.* **2003**, *100*, 2215.

(24) Devi-Kesavan, L. S.; Gao, J. *J. Am. Chem. Soc.* **2003**, *125*, 1532.

(25) Soriano, A.; Silla, E.; Tuñón, I. *J. Phys. Chem B.* **2003**, *107*, 6234.

(26) Kmunicek, J.; Bohac, M.; Luengo, S.; Gago, F.; Wade, R. C.; Damborsky, J. *J. Comput.-Aided Mol. Des.* **2003**, *17*, 299.

(27) Nam, K. N.; Prat-Resina, X.; García-Viloca, M.; Devi-Kesavan, L. S.; Gao, J. *J. Am. Chem. Soc.* **2004**, *126*, 1369.

(28) Olsson, M. H. M.; Warshel, A. *J. Am. Chem. Soc.* **2004**, *126*, 15167.

(29) Soriano, A.; Silla, E.; Tuñón, I.; Ruiz-López, M. F. *J. Am. Chem. Soc.* **2005**, *127*, 1946.

(30) Rosta, E.; Klähn, M.; Warshel, A. *J. Phys. Chem. B* **2006**, *110*, 2934.

(31) Silberstein, M.; Damborsky, J.; Vajda, S. *Biochemistry* **2007**, *46*, 9239.

(32) Otyepka, M.; Banas, P.; Magistrato, A.; Carloni, P.; Damborsky, J. *Proteins: Struct., Funct., Bioinf.* **2008**, *70*, 707.

(33) Jorgensen, W. L.; Buckner, J. K. *J. Phys. Chem.* **1986**, *90*, 4651.

(34) Shi, Z.; Boyd, R. J. *J. Am. Chem. Soc.* **1989**, *111*, 1575.

(35) Tucker, S. C.; Truhlar, D. G. *J. Phys. Chem.* **1989**, *93*, 8138.

(36) Deng, L.; Branchadell, V.; Ziegler, T. *J. Am. Chem. Soc.* **1994**, *116*, 10645.

(37) Hu, W.-P.; Truhlar, D. G. *J. Am. Chem. Soc.* **1995**, *117*, 10726.

(38) Glukhovtsev, M. N.; Pross, A.; Radom, L. *J. Am. Chem. Soc.* **1995**, *117*, 2024.

(39) Hu, W.-P.; Truhlar, D. G. *J. Am. Chem. Soc.* **1996**, *118*, 860.

(40) Glukhovtsev, M. N.; Pross, A.; Schlegel, H. B.; Bach, R. D.; Radom, L. *J. Am. Chem. Soc.* **1996**, *118*, 11258.

(41) Strajbl, M.; Florián, J.; Warshel, A. *J. Am. Chem. Soc.* **2000**, *122*, 5354.

(42) Schmatz, S.; Botschwina, P.; Stoll, H. *Int. J. Mass Spectrom* **2000**, *201*, 277.

(43) Gonzalez, J. M.; Cox, R. S., III; Brown, S. T.; Allen, W. D.; Schaefer, H. F., III *J. Phys. Chem. A* **2001**, *105*, 11327.

(44) Gonzalez, J. M.; Pak, C.; Sidney Cox, R.; Allen, W. D.; Schaefer, H. F., III; Császár, A. G.; Tarczay, G. *Chem. Eur. J.* **2003**, *9*, 2173.

(45) Uggerud, E. *Chem. Eur. J.* **2006**, *12*, 1127.

(46) Laerdahl, J. K.; Civcir, P. U.; Bache-Andreasson, L.; Uggerud, E. *Org. Biomol. Chem.* **2006**, *4*, 135.

(47) Ocrhran, R. A.; Uggerud, E *Int. J. Mass Spectrom.* **2007**, *265*, 169.

(48) Zheng, J.; Zhao, Y.; Truhlar, D. G. *J. Chem. Theory Comput.* **2007**, *3*, 569.

(49) Pliego, J. R., Jr.; Piló-Veloso, D. *Phys. Chem. Chem. Phys* **2008**, *10*, 1118.

(50) Bickelhaupt, F. M. *J. Comput. Chem.* **1999**, *20*, 114.

(51) Zhao, Y.; Gonzalez-Garcia, N.; Truhlar, D. G. *J. Phys. Chem. A* **2005**, *109*, 2012.

(52) Bento, A. P.; Sola, M.; Bickelhaupt, F. M. *J. Comput. Chem.* **2005**, *26*, 1497.

(53) Van Bochove, M. A.; Bickelhaupt, F. M. *Eur. J. Org. Chem.* **2008**, 649.

(54) Shaik, S. *J. Am. Chem. Soc.* **1983**, *105*, 4359.

(55) Shaik, S.; Reddy, A. C. *J. Chem. Soc., Faraday Trans.* **1994**, *90*, 1631.

(56) Shaik, S.; Shurki, A. *Angew. Chem., Int. Ed.* **1999**, *38*, 586.

(57) Hiberty, P. C.; Shaik, S. *Theor. Chem. Acc.* **2002**, *108*, 255.

(58) Amovilli, C. In *Valence Bond Theory*; Cooper, D. L., Ed.; Theor. Comp. Chem. Series 10; Elsevier: Amsterdam, 2002; pp 415−445.

(59) Truhlar, D. G. *J. Comput. Chem.* **2007**, *28*, 73.

(60) Mo, Y.; Gao, J. *J. Comput. Chem.* **2000**, *21*, 1458.

(61) Gao, J.; García-Viloca, M.; Poulsen, T. D.; Mo, Y. *Adv. Phys. Org. Chem.* **2003**, *38*, 161.

(62) Blavins, J. J.; Cooper, D. L.; Karadakov, P. B. *J. Phys. Chem. A* **2004**, *108*, 914.

(63) Song, L.; Wu, W.; Zhang, Q.; Shaik, S. *J. Phys. Chem.* **2004**, *108*, 6017.

(64) Song, L.; Wu, W.; Hiberty, P. C.; Shaik, S. *Chem. Eur. J.* **2006**, *12*, 7458.

(65) Hong, G.; Rosta, E.; Warshel, A. *J. Phys. Chem. B* **2006**, *110*, 19570.

(66) Su, P.; Wu, W.; Kelly, C. P.; Cramer, C. J.; Truhlar, D. G. J. Phys. Chem A, published online at DOI:10.1021/jp711655k.

(67) Sharir-Ivry, A.; Crown, H. A.; Wu, W.; Shurki, A. *J. Phys. Chem. A* **2008**, *112*, 2489.

(68) Sharir-Ivry, A.; Shurki, A. J. Phys. Chem. A, published online at DOI:10.1021/jp801722e.

(69) Gao, J. *J. Am. Chem. Soc.* **1991**, *113*, 7796.

(70) Gao, J.; Xia, X. *J. Am. Chem. Soc.* **1993**, *115*, 9667.

(71) Amovilli, C.; Mennucci, B.; Floris, F. M. *J. Phys. Chem. B* **1998**, *102*, 3023.

(72) Su, P.; Ying, F.; Wu, W.; Hiberty, P. C.; Shaik, S. *ChemPhysChem* **2007**, *8*, 2603.

(73) Grochowski, P; Lesyng, B.; Bala, P.; McCammon, J. A *Int. J. Quantum Chem.* **1996**, *60*, 1143.

(74) Trylska, J.; Grochowski, P.; Geller, M. *Int. J. Quantum Chem.* **2001**, *82*, 86.

(75) Kolmodin, K.; Hansson, T.; Danielsson, J.; Åqvist, J. In *Transition State Modeling for Catalysis*; Truhlar, D. G., Morokuma, K., Eds.;ACS Symposium Series 721; American Chemical Society: Washington, DC, 1999; p 370.

(76) Rothman, M. J.; Lohr, L. L., Jr.; Ewig, C. S.; Van Wazer, J. R. In *Potential Energy Surfaces and Dynamics Calculations*; Truhlar, D. G., Ed.; Plenum: New York, 1979; p 653.

(77) Chandrasekhar, J.; Smith, S. F.; Jorgensen, W. L. *J. Am. Chem. Soc.* **1984**, *106*, 3049.

(78) Kottalam, J.; Case, D. A. *J. Am. Chem. Soc.* **1988**, *110*, 7690.

(79) Steckler, R.; Truhlar, D. G. *J. Chem. Phys.* **1990**, *93*, 6570.

(80) Heidrich, D. In *The Reaction Path in Chemistry: Current Approaches and Perspectives*; Heidrich, D., Ed.; Kluwer: Dordrecht, 1995; p 1.

(81) Shavitt, I. Theoretical Chemistry Laboratory Technical Report No. WIS-AEC-23; University of Wisconsin: Madison, 1959.

(82) Marcus, R. A. *J. Chem. Phys.* **1966**, *45*, 4493.

(83) Truhlar, D. G.; Kuppermann, A. *J. Am. Chem. Soc.* **1971**, *93*, 1840.

(84) Fukui, K. In *The World of Quantum Chemistry*; Daudel, R., Pullman, B., Eds.; Reidel: Dordrecht, 1974; p 113.

(85) Natanson, G. A.; Garrett, B. C.; Truong, T. N.; Joseph, T.; Truhlar, D. G. *J. Chem. Phys.* **1991**, *94*, 7875.

(86) Alhambra, C.; Gao, J.; Corchado, J. C.; Villà, J.; Truhlar, D. G. *J. Am. Chem. Soc.* **1999**, *121*, 2253.

(87) Truhlar, D. G.; Gao, J.; Alhambra, C.; Garcia-Viloca, M.; Corchado, J. C.; Sánchez, M. L.; Villà, J. *Acc. Chem. Res.* **2002**, *35*, 341.

(88) Truhlar, D. G.; Gao, J.; Garcia-Viloca, M; Alhambra, C.; Corchado, J. C.; Sánchez, M. L.; Poulsen, T. D *Int. J. Quantum Chem* **2004**, *100*, 1136.

(89) Bolhuis, P. G.; Dellago, C.; Chandler, D. *Faraday Discuss.* **1998**, *110*, 421.

(90) Marcus, R. A. *Discuss. Faraday Soc.* **1960**, *29*, 21.

(91) Marcus, R. A. *Rev. Mod. Phys.* **1993**, *65*, 599.

(92) Warshel, A.; Weiss, R. M. *J. Am. Chem. Soc.* **1980**, *102*, 6218.

(93) Warshel, A. *J. Phys. Chem.* **1982**, *86*, 2218.

(94) Hwang, J. K.; King, G.; Creighton, S.; Warshel, A. *J. Am. Chem. Soc.* **1988**, *110*, 5297.

(95) Warshel, A.; Chu, Z. T. *J. Chem. Phys.* **1990**, *93*, 4003.

(96) Yadav, A.; Jackson, R. M.; Holbrook, J. J.; Warshel, A. *J. Am. Chem. Soc.* **1991**, *113*, 4800.

(97) Warshel, A. *Computer Modeling of Chemical Reactions in Enzymes and Solutions*; Wiley: New York, 1991.

(98) Aqvist, J.; Warshel, A. *Chem. Rev.* **1993**, *93*, 2523.

(99) Kong, Y. S.; Warshel, A. *J. Am. Chem. Soc.* **1995**, *117*, 6234.

(100) Muller, R. P.; Warshel, A. *J. Phys. Chem.* **1995**, *99*, 17516.

(101) Wesolowski, T.; Muller, R. P.; Warshel, A. *J. Phys. Chem.* **1996**, *100*, 15444.

(102) Kuznetsov, A. In *Electron and Ion Transfer in Condensed Media*; Kornyshev, A. A., Tosi, M. P., Ulstrup, J., Eds.; World Scientific: Singapore, 1997: p 165.

(103) Warshel, A.; Bentzien, J. In *Transition State Modeling for Catalysis*; Truhlar, D. G., Morokuma, K., Eds.; ACS Symposium Series 721; American Chemical Society: Washington, DC, 1999; p 489.

(104) Billeter, S. R.; Webb, S. P.; Agarwal, P. K.; Iordanov, T.; Hammes-Schiffer, S. *J. Am. Chem. Soc.* **2001**, *123*, 11262.

(105) Schenter, G. K.; Garrett, B. C.; Truhlar, D. G. *J. Phys. Chem. B* **2001**, *105*, 9672.

(106) Marcus, R. A. *J. Chem. Phys.* **2006**, *125*, 194504.

(107) Marcus, R. A. *J. Phys. Chem. B* **2007**, *111*, 6643.

(108) Lee, S.; Hynes, J. T. *J. Chem. Phys.* **1988**, *88*, 6853.

(109) Kim, H. J.; Hynes, J. T. *J. Am. Chem. Soc.* **1992**, *114*, 10528.

(110) Schenter, G. K.; McRae, R. P.; Garrett, B. C. *J. Chem. Phys.* **1992**, *97*, 9116.

(111) Truhlar, D. G.; Schenter, G. K.; Garrett, B. C. *J. Chem. Phys.* **1993**, *98*, 5756.

(112) Basilevsky, M. V.; Chudinov, G. E.; Napolov, D. V. *J. Phys. Chem.* **1993**, *97*, 3270.

(113) Garrett, B. C.; Schenter, G. K. In *Structure and Reactivity in Aqueous Solution*; Cramer, C. J., Truhlar, D. G., Eds.; ACS Symposium Series 568; American Chemical Society: Washington, DC, 1994; p 122.

(114) Mathis, J. R.; Hynes, J. T. *J. Phys. Chem.* **1994**, *98*, 5445.

(115) Ruiz-López, M. F.; Rinaldi, D.; Bertrán, J. *J. Chem. Phys.* **1995**, *103*, 9249.

(116) Chuang, Y.-Y.; Truhlar, D. G. *J. Am. Chem. Soc.* **1999**, *121*, 10157.

(117) Schatz, G. C.; Ross, J. *J. Chem. Phys.* **1977**, *66*, 2943.

(118) Engler, C.; Rabe, E.; Schultz, H.; Lorenz, W. *Theor. Chim. Acta* **1989**, *75*, 67.

(119) Halvick, P.; Zhao, M.; Truhlar, D. G.; Schwenke, D. W.; Kouri, D. J. *J. Chem. Soc., Faraday Trans.* **1990**, *86*, 1705.

(120) Caratzoulas, S.; Jackson, B. *J. Chem. Phys.* **1996**, *105*, 8639.

(121) Shin, C.; Shin, S. *J. Chem. Phys.* **2000**, *113*, 6528.

(122) Marcus, R. A. *J. Chem. Phys.* **1956**, *24*, 979.

(123) London, F. *Z. Elektrochem.* **1929**, *35*, 552.

(124) Porter, R. N.; Karplus, M. *J. Chem. Phys.* **1964**, *40*, 1105.

(125) Shaik, S. S. *J. Am. Chem. Soc.* **1981**, *103*, 3692.

(126) Shaik, S. S.; Hiberty, P. C. *A Chemist's Guide to Valence Bond Theory*; John Wiley & Sons, Inc.: Hoboken, New Jersey, 2007.

(127) Marcus, R. A. *J. Chem. Phys.* **1965**, *43*, 679.

(128) Kreevoy, M. M.; Lee, I.-S. H. *J. Am. Chem. Soc.* **1984**, *106*, 2550.

(129) Lee, I.-S. H.; Ji, Y. R.; Jeoung, E. H. *J. Phys. Chem. A* **2006**, *110*, 3875.

(130) Chang, Y. T.; Miller, W. H. *J. Phys. Chem.* **1990**, *94*, 5884.

(131) Schlegel, H. B.; Sonnenberg, J. L. *J. Chem. Theory Comput.* **2006**, *2*, 905.

(132) Bernardi, F.; Olivucci, M.; Robb, M. A. *J. Am. Chem. Soc.* **1992**, *114*, 1606.

(133) Tishchenko, O.; Truhlar, D. G. *J. Phys. Chem. A* **2006**, *110*, 13530.

(134) Higashi, M.; Truhlar, D. G. *J. Chem. Theory Comput.* **2008**, *4*, 790.

(135) Minichino, C.; Voth, G. A. *J. Phys. Chem. B* **1997**, *101*, 4544.

(136) Garrett, B. C.; Truhlar, D. G. In *Theory of Scattering: Papers in Honor of Henry Eyring*; Henderson, D., Ed.; Theor. Chem. Advances Perspectives Series 6A; Academic: New York, 1981; p 215.

(137) Delos, J. B. *Rev. Mod. Phys.* **1981**, *53*, 287.

(138) Mead, C. A.; Truhlar, D. G. *J. Chem. Phys.* **1982**, *77*, 6090.

(139) Pacher, T.; Cederbaum, L. S.; Köppel, H. *J. Chem. Phys.* **1988**, *89*, 7367.

(140) Sidis, V. *Adv. Chem. Phys.* **1992**, *82*, 73.

(141) Mo, Y.; Gao, J. *J. Phys. Chem. A* **2000**, *104*, 3012.

(142) Numrich, R. W.; Truhlar, D. G. *J. Phys. Chem.* **1975**, *79*, 2745.

(143) Kubach, C.; Sidis, V. *Phys. Rev. A* **1976**, *14*, 152.

(144) Kabbaj, O. K.; Lepetit, M. B.; Malrieu, J. P.; Sini, G.; Hiberty, P. C. *J. Am. Chem. Soc.* **1991**, *113*, 5619.

(145) Bianco, R.; Hynes, J. T. *J. Chem. Phys.* **1995**, *102*, 7864.

(146) Dobrovsky, I.; Levine, R. D. *Chem. Phys. Lett.* **1998**, *286*, 155.

(147) Shurki, A.; Crown, H. A. *J. Phys. Chem. B* **2005**, *109*, 23638.

(148) Shurki, A. *Theor. Chem. Acc.* **2006**, *116*, 253.

(149) Mo, Y.; Song, L.; Lin, Y. *J. Phys. Chem. A* **2007**, *111*, 8291.

(150) Goddard, W. A., III; Dunning, T. H., Jr.; Hunt, W. J.; Hay, P. J. *Acc. Chem. Res.* **1973**, *6*, 368.

(151) van Lenthe, J. H.; Balint-Kurti, G. G. *J. Chem. Phys.* **1983**, *78*, 5699.

(152) Hiberty, P. C.; Flament, J. P.; Noizet, E. *Chem. Phys. Lett.* **1992**, *189*, 259.

(153) Raimondi, M.; Gianinetti, E. *J. Phys. Chem.* **1988**, *92*, 899.

(154) Gianinetti, E.; Raimondi, M.; Tornagui, E, *Int. J.Quantum Chem* **1996**, *60*, 157.

(155) Mo, Y.; Peyerimhoff, S. D. *J. Chem. Phys.* **1998**, *109*, 1687.

(156) Gianinetti, E.; Vandoni, I.; Famulari, A.; Raimondi, M. *Adv. Quantum Chem.* **1998**, *31*, 251.

(157) Mo, Y.; Zhang, Y.; Gao, J. *J. Am. Chem. Soc.* **1999**, *121*, 5737.

(158) Mo, Y.; Gao, J.; Peyerimhoff, S. D. *J. Chem. Phys.* **2000**, *112*, 5530.

(159) Khaliullin, R. Z.; Head-Gordon, M.; Bell, A. T. *J. Chem. Phys.* **2006**, *124*, 204105.

(160) Khaliullin, R. Z.; Cobar, E. A.; Lochan, R. C.; Bell, A. T.; Head-Gordon, M. *J. Phys. Chem. A.* **2007**, *111*, 8753.

(161) Nakamura, H.; Truhlar, D. G. *J. Chem. Phys.* **2001**, *115*, 10353.

(162) Nakamura, H.; Truhlar, D. G. *J. Chem. Phys.* **2002**, *117*, 5576.

(163) Nakamura, H.; Truhlar, D. G. *J. Chem. Phys.* **2003**, *118*, 6816.

(164) Garcia, V. M.; Reguero, M.; Caballol, R.; Malrieu, J. P. *Chem. Phys. Lett.* **1997**, *281*, 161.

(165) Ruedenberg, K.; Atchity, G. A. *J. Chem. Phys.* **1993**, *99*, 3799.

(166) Atchity, G. A.; Ruedenberg, K. *Theor. Chem. Acc.* **1997**, *97*, 47.

(167) *National Institute for Occupational Safety and Health 1978 Current Intelligence Bulletin # 25, Publication No. 79-146*; pp 91−100.

(168) Fetzner, S.; Lingens, F. *Microbiol. Rev.* **1994**, *58*, 641.

(169) Janssen, D. B.; van der Ploeg, J. R.; Pries, F. *Environ. Health Perspect.* **1995**, *103*, 29.

(170) Leisinger, T. *Curr. Opin. Biotechnol.* **1996**, *7*, 295.

(171) Keuning, S.; Janssen, D. B.; Witholt, B. *J. Bacteriol.* **1985**, *163*, 635.

(172) Wischnak, C.; Muller, R. *Biotechnology, 2nd ed.* **2000**, *11b* (241), 241–271.

(173) Ridder, I. S.; Dijkstra, B. W. *Cattech* **2000**, *3*, 126.

(174) Shaik, S. S.; Pross, A. *J. Am. Chem. Soc.* **1982**, *104*, 2708.

(175) Shaik, S.; Schlegel, H. B.; Wolfe, S. *Theoretical Aspects of Physical Organic Chemistry: The S_N2 Mechanism;* Wiley: New York, 1992.

(176) Cyr, D. M.; Bailey, C. G.; Serxner, D.; Scarton, M. G.; Johnson, M. A. *J. Chem. Phys.* **1994**, *101*, 10507.

(177) Dessent, C. E. H.; Johnson, M. A. *J. Am. Chem. Soc.* **1997**, *119*, 5067.

(178) Ruedenberg, K.; Sundberg, R. In *Quantum Science*; Calais, J.-L., Goscinski, O., Lindenberg, J., Öhrn, Y., Eds.; Plenum: New York, 1976; p 505.

(179) Roos, B. O. *Adv. Chem. Phys.* **1987**, *68*, 399.

(180) Nakano, H. *J. Chem. Phys.* **1993**, *99*, 7983.

(181) Nakano, H. *Chem. Phys. Lett.* **1993**, *207*, 372.

(182) Nakano, H.; Nakajima, T.; Tsuneda, T.; Hirao, K. *J. Mol. Struct.* **2001**, *573*, 91.

(183) Finley, J.; Malmqvist, P.-ÅA; Roos, B.O.; Serrano-Andrés, L .*Chem. Phys. Lett* **1998**, *288*, 299.

(184) Hariharan, P. C.; Pople, J. A. *Theor. Chim. Acta* **1973**, *28*, 213.

(185) Francl, M. M.; Petro, J. J.; Hehre, W. J.; Binkley, J. S.; Gordon, M. S.; DeFrees, D. J.; Pople, J. A. *J. Chem. Phys.* **1982**, *77*, 3564.

(186) Clark, T.; Chandrasekar, J.; Spitznagel, G. W.; Schleyer, P. v. R. *J. Comput. Chem.* **1983**, *4*, 294.

(187) Gill, P. M. W.; Johnson, B. G.; Pople, J. A.; Frisch, M. J. *Chem. Phys. Lett.* **1992**, *197*, 499.

(188) Zhao, Y.; Truhlar, D. G. *Theor. Chem. Acc.* **2008**, *120*, 215.

(189) Lynch, B. J.; Zhao, Y.; Truhlar, D. G. *J. Phys. Chem. A* **2003**, *107*, 1384.

(190) Curtiss, L. A.; Raghavachari, K.; Redfern, P. C.; Rassolov, V.; Pople, J. A. *J. Chem. Phys.* **1998**, *109*, 7764.

(191) Curtiss, L. A.; Raghavachari, K.; Redfern, P. C.; Pople, J. A. *J. Chem. Phys.* **2000**, *112*, 1125.

(192) Curtiss, L. A.; Redfern, P. C.; Raghavachari, K.; Pople, J. A. *J. Chem. Phys.* **2001**, *114*, 108.

(193) Lynch, B. J.; Zhao, Y.; Truhlar, D. G. *J. Phys. Chem. A* **2005**, *109*, 1643.

(194) Fast, P. L.; Corchado, J. C.; Sánchez, M. L.; Truhlar, D. G. *J. Phys. Chem. A* **1999**, *103*, 5129.

(195) Becke, A. D. *Phys. Rev. A* **1988**, *38*, 3098.

(196) Lee, C.; Yang, W.; Parr, R. G. *Phys. Rev. B* **1988**, *37*, 785.

(197) Becke, A. D. *J. Chem. Phys.* **1993**, *98*, 5648.

(198) Stephens, P. J.; Devlin, F. J.; Chabalowski, C. F.; Frisch, M. J. *J. Phys. Chem.* **1994**, *98*, 11623.

(199) Nangia, S.; Truhlar, D. G. *J. Chem. Phys.* **2006**, *124*, 124309.

(200) Li, Z. H.; Valero, R.; Truhlar, D. G. *Theor. Chem. Acc.* **2007**, *118*, 9.

(201) Valero, R.; Truhlar, D. G. *J. Chem. Phys.* **2006**, *125*, 194305.

(202) Valero, R.; Truhlar, D. G. *J. Phys. Chem. A* **2007**, *111*, 8536.

(203) Pauling, L. The Nature of the Chemical Bond; Cornell University Press: Ithaca, 1939.

(204) Wheland, G. W. *The Theory of Resonance and Its Applications to Organic Chemistry;* Wiley: New York, 1955.

(205) Mo, Y.; Gao, J. *J. Phys. Chem. A* **2001**, *105*, 6530.

(206) Mo, Y.; Subramanian, G.; Gao, J.; Ferguson, D. M. *J. Am. Chem. Soc.* **2002**, *124*, 4832.

(207) Mo, Y.; Wu, W.; Song, L.; Lin, M.; Zhang, Q.; Gao, J. *Angew. Chem., Int. Ed.* **2004**, *43*, 1986.

(208) Mo, Y.; Gao, J. *Acc. Chem. Res.* **2007**, *40*, 113.

(209) Hunt, W. J.; Hay, P. J.; Goddard, W. A., III *J. Chem. Phys.* **1972**, *57*, 738.

(210) Nakano, H. ; Sorakubo, K.; Nakayama, K.; Hirao, K. In *Valence Bond Theory*; Cooper, D. L., Ed.; Theor. Comp. Chem. Series 10; Elsevier: Amsterdam, 2002; p 55.

(211) Garrett, J.; Cooper, D. L.; Raimondi, M. In *Valence Bond Theory*; Cooper, D. L., Ed.; Theor. Comp. Chem. Series 10; Elsevier: Amsterdam, 2002; p 55.

(212) Li, J.; McWeeny, R. *Int. J. Quantum Chem* **2002**, *89*, 208.

(213) Hiberty, P. C.; Shaik, S. S. *Theor. Chem. Acc.* **2002**, *108*, 235.

(214) Hunt, W. J.; Hay, P. J.; Goddard, W. A. *J. Chem. Phys.* **1972**, *57*, 738.

(215) Siegbahn, P. E. M.; Almlöf, J.; Heiberg, A.; Roos, B. O. *J. Chem. Phys.* **1981**, *74*, 2384.

(216) Hiberty, P. C. *Theochem* **1998**, *451*, 237.

(217) Tishchenko, O.; Zheng, J.; Truhlar, D. G. *J. Chem. Theory Comput.* **2008**, *4*, 1208.

(218) Marcus, R. A. *J. Chem. Phys.* **1984**, *81*, 4494.

(219) May, V.; Kühn, O. *Charge and Energy Transfer Dynamics in Molecular Systems*; Wiley-VCH: Berlin, 2000; p 284.

(220) Mittleman, M. H. *Phys. Rev.* **1961**, *122*, 1930.

(221) Truhlar, D. G.; Cartwright, D. C.; Kuppermann, A. *Phys. Rev.* **1968**, *175*, 113.

(222) Löwdin, P. O. *Adv. Quantum Chem.* **1970**, *5*, 185.

(223) Truhlar, D. G. *J. Phys. Chem. A* **2002**, *106*, 5048.

(224) Tully, J. C. In *Semiempirical Methods of Electronic Structure Theory, Part A Techniques*; Segal, G. A., Ed.; Modern Theoretical Chemistry Series Vol. 7; Plenum: New York, 1977; p 173.

(225) See for instance Chuang, Y.-Y.; Radhakrishnan, M. L.; Fast, P. L.; Cramer, C. J.; Truhlar, D. G. *J. Phys. Chem. A* **1999**, *103*, 4893.

(226) Marenich, A. V.; Olson, R. M.; Kelly, C. P.; Cramer, C. J.; Truhlar, D. G. *J. Chem. Theor. Comput.* **2007**, *3*, 2011.

(227) Olson, R. M.; Marenich, A. V.; Cramer, C. J.; Truhlar, D. G. *J. Chem. Theory Comput.* **2007**, *3*, 2046.

(228) Kelly, C. P.; Cramer, C. J.; Truhlar, D. G. *J. Chem. Theory Comput.* **2005**, *1*, 1133.

(229) Chandrasekhar, J.; Smith, S. E.; Jorgensen, W. L. *J. Am. Chem. Soc.* **1985**, *107*, 154.

(230) Okamoto, K.; Kita, T.; Araki, K.; Shingu, H. *Bull. Chem. Soc. Jpn.* **1967**, *40*, 1912.

(231) Marenich, A. V.; Olson, R. M.; Chamberlin, A. C.; Cramer, C. J.; Truhlar, D. G. *J. Chem. Theory Comput.* **2007**, *3*, 2055.

(232) Voter, A. F.; Goddard, W. A., III *J. Am. Chem. Soc.* **1986**, *108*, 2830.

(233) Song, L.; Mo, Y.; Gao, J. J. Chem. Theory Comput., in press.

(234) Marcus, R. A. *J. Phys. Chem. A* **1997**, *101*, 4072.

(235) Marcus, R. A.; Sutin, N. *Biochim. Biophys. Acta* **1985**, *811*, 265.

(236) Kuharski, R. A.; Bader, J. S.; Chandler, D.; Sprik, M.; Klein, M. L.; Impey, R. W. *J. Chem. Phys.* **1988**, *89*, 3248.

(237) Chandler, D.; Kuharski, R. A. *Faraday Discuss. Chem. Soc.* **1988**, *85*, 329.

(238) King, G.; Warshel, A. *J. Chem. Phys.* **1990**, *93*, 8682.

(239) Ichiye, T. *J. Chem. Phys.* **1996**, *104*, 7561.

(240) Ungar, L. W.; Newton, M. D.; Voth, G. A. *J. Phys. Chem. B* **1999**, *103*, 7367.

(241) Blumberger, J.; Tavernelli, I.; Klein, M. L.; Sprik, M. *J. Chem. Phys.* **2006**, *124*, 64507.

(242) Witek, H. A.; Choe, Y.-K.; Finley, J. P.; Hirao, K. *J. Comput. Chem.* **2002**, *10*, 957.

(243) (a) Nakamura, H.; Xidos, J. D.; Chamberlin, A. C.; Kelly, K. C.; Valero, R.; Thompson, J. D.; Li, J.; Hawkins, G. D.; Zhu, T.; Lynch, B. J.; Volobuev, Y.; Rinaldi, D.; Liotard, D. A.; Cramer, C. J.; Truhlar, D. G. HONDOPLUS, version 5.1, based on HONDO, version 99.6; University of Minnesota: Minneapolis, MN, 2007. (b) Dupuis, M.; Marquez, A.; Davidson, E. R. *HONDO, version 99.6, based on HONDO, version 95.3*; Quantum Chemistry Program Exchange, Indiana University: Bloomington, IN, 1999.

(244) (a) Song, L.; Wu, W.; Mo, Y.; Zhang, Q. XMVB: An Ab Initio Nonorthogonal Valence Bond Program; Xiamen University: Xiamen, 1999. (b) Song, L.; Mo, Y.; Zhang, Q.; Wu, W. *J. Comput. Chem.* **2005**, *26*, 514.

(245) Zhao, Y.; Truhlar, D. G. MN-GFM 3.0; University of Minnesota: Minneapolis, 2006.

(246) Frisch, M. J.; Trucks, G. W.; Schlegel, H. B.; Scuseria, G. E.; Robb, M. A.; Cheeseman, J. R.; Montgomery, J. A., Jr.; Vreven, T.; Kudin, K. N.; Burant, J. C.; Millam, J. M.; Iyengar, S. S.; Tomasi, J.; Barone, V.; Mennucci, B.; Cossi, M.; Scalmani, G.; Rega, N.; Petersson, G. A.; Nakatsuji, H.; Hada, M.; Ehara, M.; Toyota, K.; Fukuda, R.; Hasegawa, J.; Ishida, M.; Nakajima, T.; Honda, Y.; Kitao, O.; Nakai, H.; Klene, M.; Li, X.; Knox, J. E.; Hratchian, H. P.; Cross, J. B.; Bakken, V.; Adamo, C.; Jaramillo, J.; Gomperts, R.; Stratmann, R. E.; Yazyev, O. ; Austin, A. J.; Cammi, R.; Pomelli, C.; Ochterski, J. W.; Ayala, P. Y.; Morokuma, K.; Voth, G. A.; Salvador, P.; Dannenberg, J. J.; Zakrzewski, V. G.; Dapprich, S.; Daniels, A. D.; Strain, M. C.; Farkas, O.; Malick, D. K.; Rabuck, A. D.; Raghavachari, K.; Foresman, J. B.; Ortiz, J. V.; Cui, Q.; Baboul, A. G.; Clifford, S.; Cioslowski, J.; Stefanov, B. B.; Liu, G.; Liashenko, A.; Piskorz, P.; Komaromi, I.; Martin, R. L.; Fox, D. J.; Keith, T.; Al-Laham, M. A.; Peng, C. Y.; Nanayakkara, A.; Challacombe, M.; Gill, P. M. W.; Johnson, B.; Chen, W.; Wong, M. W.; Gonzalez, C.; Pople, J. A. *Gaussian 03, revision D.01*; Gaussian, Inc.: Wallingford, CT, 2004.

(247) Zhao, Y.; Truhlar, D. G. MLGAUSS-version 2.0; University of Minnesota: Minneapolis, 2005.

(248) Olson, R. M.; Marenich, A. V.; Chamberlin, A. C.; Kelly, C. P.; Thompson, J. D.; Xidos, J. D. ; Li, J.; Hawkins, G. D.; Winget, P.; Zhu, T.; Rinaldi, D.; Liotard, D. A; Cramer, C. J.; Truhlar, D. G.; Frisch, M. J. *MN-GSM, version 2007-beta*; University of Minnesota: Minneapolis, 2007.

CT800318H

JCTC Journal of Chemical Theory and Computation

Accurate DFT Descriptions for Weak Interactions of Molecules Containing Sulfur

Philippe C. Aeberhard,[†] J. Samuel Arey,[‡] I-Chun Lin,[§] and Ursula Rothlisberger*,[||]

Inorganic Chemistry Laboratory, University of Oxford, South Parks Road, Oxford OX1 3QR, U.K., Environmental Chemistry Modeling Laboratory and Laboratory of Computational Chemistry and Biochemistry, Ecole Polytechnique Fédérale de Lausanne, 1015 Lausanne, Switzerland, and Department of Chemical System Engineering, School of Engineering, University of Tokyo, Tokyo 113-8656, Japan

Received July 26, 2008

Abstract: Dispersion corrected atom centered potentials (DCACPs) have been shown to significantly improve the density functional theory (DFT) description of weak interactions. In this work, we have calibrated a DCACP for sulfur in combination with the widely used Generalized Gradient Approximation (GGA) BLYP, thereby augmenting the existing library of DCACPs for the first- and second-row elements H, C, N, O, and rare gases. Three weakly bound complexes as well as elemental (orthorhombic) sulfur are used as test cases to evaluate the transferability of the DCACP to different chemical environments. It is found that the sulfur DCACP systematically improves the agreement of DFT-calculated weak interactions with respect to MP2 and CCSD(T) level results.

I. Introduction

Dispersion corrected atom centered potentials (DCACPs) were introduced[1] to address the inadequate treatment of dispersion forces in Kohn−Sham density functional theory (DFT) when used in conjunction with approximated local or semilocal exchange-correlation functionals. The widely used generalized gradient approximation (GGA) and local density approximation (LDA) functionals are intrinsically unable to correctly reproduce dispersion forces, since dispersion forces are, by their nature, a nonlocal effect, whereas these functionals only depend on local quantities (density or density gradient). The procedure reported in the recent literature[1,2] constructs an analytic atom-centered correction term calibrated such that the treated DFT method correctly reproduces the MP2 or CCSD(T) level binding energy for a dispersion-dominated interaction. Existing work demonstrates that DCACPs can significantly improve the DFT description of dispersion interactions of rare gases (He, Ne, Ar, Kr) and molecules involving elements C, H, N, and O for a wide variety of chemical environments.[2−6] In a similar approach aimed at mixed quantum mechanical/molecular mechanical calculations, DiLabio[7] also makes use of adjustable atom centered potentials (termed Quantum Capping Potentials) of carbon atoms to successfully describe dispersion forces between hydrocarbon molecules in DFT calculations. A number of other methods to recover the dispersion forces in DFT exist; attempts have been made to directly include dispersion forces in the DFT formalism[8,9] promising a more rigorous treatment, but these approaches are currently too time-consuming for any practical applications or are otherwise limited. Other authors use a purely empirical van der Waals correction,[10] similar to the approach taken with DCACPs.

In this work, a DCACP was calibrated for sulfur using CCSD(T)/aug-cc-pVTZ calculations of the weakly interacting CS_2 dimer as a reference. The resulting DCACP is hypothesized to be generally valid for weak interactions arising from other chemical environments, i.e. to exhibit good transferability. To assess the transferability of the DCACP to chemical environments differing significantly from the calibration system, the DCACP was applied to four test systems (Figure 1): solid elemental sulfur; the SO_2 dimer; a hydrogen bonded $CH_3OH-S(CH_3)_2$ complex; and to the internal rotation of 2′,3′-dideoxytiazofurin. For all systems, results from DFT with DCACPs were compared to uncorrected DFT and to high-level benchmark (MP2 or CCSD(T)) calculations or experimental data. DFT results for the test systems are reported using the BLYP functional, which has been found previously to perform well in conjunction with DCACPs compared with other functionals (PBE, BP).[2] BLYP usually shows the most repulsive van der Waals interactions among GGA functionals, hence the DCACP for BLYP is

* Corresponding author e-mail: ursula.roethlisberger@epfl.ch; url: http://lcbcpc21.epfl.ch.

[†] University of Oxford.

[‡] Environmental Chemistry Modeling Laboratory, Ecole Polytechnique Fédérale de Lausanne.

[§] University of Tokyo.

[||] Laboratory of Computational Chemistry and Biochemistry, Ecole Polytechnique Fédérale de Lausanne.

10.1021/ct800299y CCC: $40.75 © 2009 American Chemical Society
Published on Web 12/22/2008

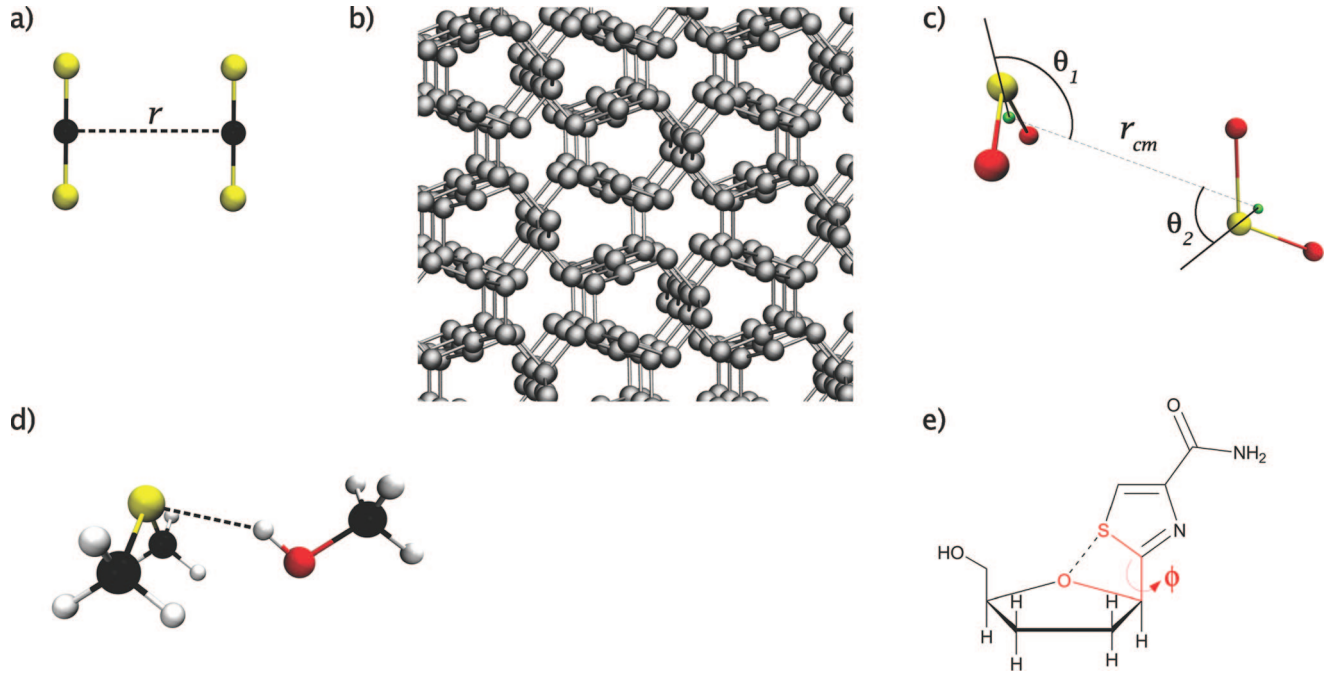

Figure 1. Molecular structures of the systems that were assessed. (a) CS_2 dimer: all 6 atoms lie in one plane, the two linear CS_2 molecules are parallel. (b) Crystalline cyclic octasulfur: the unit cell (orthorhombic, $a = 10.38$ Å, $b = 12.75$ Å, $c = 24.41$ Å, space group no. 70, *Fddd*) contains 16 S_8 molecules. Experimentally determined structure.[20] (c) SO_2 dimer: C_s symmetry, r_{cm} is the distance between the centers of mass, θ_1 or θ_2 is the angle formed by the two centers of mass and the sulfur atom of the respective SO_2 molecule. (d) Methanol dimethylsulfide complex: C_s symmetry. (e) 2′,3′-Dideoxytiazofurin, experimentally determined crystal structure.[30]

consistently attractive[2] and therefore most likely to meaningfully represent dispersion forces.

II. Method

A. Construction, Calibration, and Testing of the DCACP for S. The dispersion correction consists of an atom-centered term which is applied to every atom in the system. The DCACP for sulfur has the mathematical form of the nonlocal f-channel of Goedecker type[11] pseudopotentials

$$v_{f,\mathbf{R_I}}^{\mathrm{DCACP}}(\mathbf{r},\mathbf{r}') = \sum_{m=-3}^{+3} Y_f^m(\hat{\mathbf{r}}) p_f(r;\sigma_2)\sigma_1 p_f(r';\sigma_2) Y_f^{m*}(\hat{r}') \quad (1)$$

where $r = |\mathbf{r} - \mathbf{R_I}|$ is the distance from sulfur nucleus I, $\hat{\mathbf{r}}$ is the unit vector in the direction of $\mathbf{r} - \mathbf{R_I}$, and Y_f^m denotes spherical harmonics of angular momentum $l = 3$. Each atom at position $\mathbf{R_I}$ in the system adds a $v_{\mathbf{R_I}}^{\mathrm{DCACP}}(\mathbf{r},\mathbf{r}')$ term to the external potential $v_{\mathrm{ext}}(\mathbf{r},\mathbf{r}')$ of the system, such that the total external potential is $v'_{\mathrm{ext}}(\mathbf{r},\mathbf{r}') = v_{\mathrm{ext}}(\mathbf{r},\mathbf{r}') + \sum_I v_{\mathbf{R_I}}^{\mathrm{DCACP}}(\mathbf{r},\mathbf{r}')$. The DCACP for each atom is completely specified by two parameters that are determined by the calibration procedure: σ_1, which determines the amplitude of the potential, and σ_2, which describes the width of the radial projector operator p_f. These parameters must be calibrated specifically for each element and exchange-correlation functional. In this work, the DCACP parameters were determined for the GGA functional BLYP with respect to sulfur.

The calibration follows a recently established method[2] and proceeds by minimizing a penalty functional

$$\mathscr{P}(\sigma_1,\sigma_2) = |E_{\mathrm{minpoint}}^{\mathrm{Benchmark}} - E^{\mathrm{DCACP}}(r_{\mathrm{min}})|^2 + |E_{\mathrm{midpoint}}^{\mathrm{Benchmark}} - E^{\mathrm{DCACP}}(r_{\mathrm{mid}})|^2 + \sum_I w_I F_I^2 \quad (2)$$

where r_{min} and r_{mid} are the equilibrium and midpoint distance of the intermolecular interaction energy curves of the CS_2 dimer given by benchmark calculations; the midpoint is the distance where the interaction energy is half the equilibrium energy. F_I is the force on nucleus I of the complex at the benchmark equilibrium distance, r_{min}. The weighting factor w_I determines the relative importances of the ionic force term and energy terms in the penalty functional and has units of distance. It was chosen as $w_I = 100$ atomic units for all sulfur atoms and zero for the carbon atoms, analogous to previous calibrations of the other elements; details on the determination of the weighting factor can be found elsewhere.[2]

B. Computational Methods. The performances of the DFT and dispersion corrected-DFT methods were evaluated based on predictions for geometries and energies of weak interactions. Intermolecular dissociation energies were reported in terms of D_e in the notation of Herzberg,[12] i.e. zero point vibrational and thermal contributions were excluded. DFT energies were computed using the plane-wave code CPMD[13] with the pseudopotentials of either Goedecker et al.[11] (using a plane-wave cutoff of 170 Ry) or Troullier and Martins[14] (using a plane-wave cutoff of 70 Ry). The nuclear geometries for DFT calculations were fully relaxed using the same level of theory as the DFT computed energies, except where noted otherwise. Therefore, for most cases, the DFT energies were assessed using geometries that were different than the benchmark geometries. The ability to correctly predict theoretical or experimental benchmark geometries was itself part of the DFT performance evaluation. Benchmark geometries were taken either from theory or experiment, as explained in the Results. In cases where benchmark geometries were computed, we used MP2/aug-cc-

pVTZ or higher wave function theory methods. Benchmark energies were computed at a level of wave function theory that was considered appropriate and reasonably computationally affordable for each case, ranging from MP2/aug-cc-pVDZ (for 2′,3′-dideoxytiazofurin) to CBS-QB3 (for the $CH_3OH-S(CH_3)_2$ complex). For example, a recent assessment found that MP2/6−31+G(d,p) and CCSD(T)/6−311+G(d,p) gave reasonable results for dispersion-dominated interactions, but a complete basis set extrapolation (CBS-QB3) was needed for accurate treatment of hydrogen bond energies.[15] All benchmark energies were computed using either the MOLPRO 2006.1[16] or Gaussian03[17] software packages.

III. Results

A. Calibration. Ideally, DCACPs are calibrated using molecular complexes which are (a) primarily bound by dispersion forces; (b) closed shell systems with a well defined ground state; and (c) small enough to be treated with high-level (MPn, CCSD(T)) methods. To develop a DCACP for sulfur, we chose the CS_2 dimer in its parallel conformation as a reference system (symmetry D_{2h}, Figure 1(a)). The parallel conformation cancels quadrupole moment electrostatic contributions to the intermolecular interaction. CS_2 is analogous to CO_2, which had previously been used to calibrate the DCACP for oxygen.[2] Compared to CO_2, CS_2 is highly polarizable and exhibits very weak electrostatic interactions with the environment.[18] This suggests that the CS_2 dimer will interact primarily via dispersion and exchange forces, making it an ideal candidate for calibration of the sulfur DCACP.

The benchmark method (CCSD(T)/aug-cc-pVTZ with counterpoise correction)[19] predicted a significant dispersion interaction for the CS_2 dimer. We found an interaction energy minimum of −5.9 kJ/mol at an intermolecular separation distance of $r =$ 4.10 Å (Figure 2). In the range of $r =$ 3.5 to 5.5 Å, the benchmark interaction energy was consistent with a fitted Lennard-Jones type 12−6 potential at the 1% significance level (χ^2 test). By comparison, BLYP predicted a purely repulsive interaction at all intermolecular distances.

The sulfur DCACP was calibrated using the existing carbon DCACP[2] for the two carbon atoms in the CS_2 dimer, and the sulfur DCACP parameters σ_1 and σ_2 were determined by minimizing the penalty functional given by eq 2. Table 1 shows the sulfur DCACP parameters found for the DFT functional, BLYP. When applied to a large range of CS_2 dimer intermolecular distances, the calibrated sulfur DCACP gave good agreement with the CCSD(T) benchmark (Figure 2).

B. Transferability. To evaluate the transferability of the sulfur DCACP to chemical environments other than that of the calibration system, four systems were evaluated (geometries shown in Figure 1). In all cases, calculations using the existing suite of DCACPs for H, C, N, and O,[2] together with the newly calibrated sulfur DCACP, were compared to both uncorrected DFT and high level benchmark calculations, where possible.

Crystalline Orthorhombic Sulfur. Crystalline orthorhombic sulfur (also known as cyclic octasulfur), having a unit cell that consists of 16 S_8 molecules, has been well characterized at a temperature of 100 K by X-ray diffraction.[20] In a simple qualitative assessment of DFT predictions for this crystal,

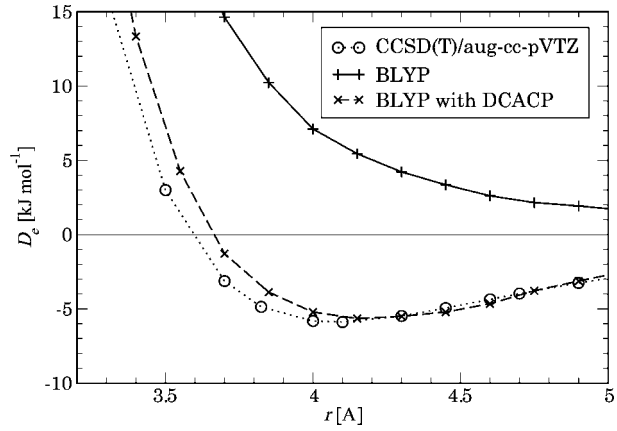

Figure 2. The calculated CS_2 dimer interaction energy versus intermolecular distance (r) using three methods. In all cases (BLYP, BLYP with DCACP, and CCSD(T)), the C−S bond lengths were kept fixed at 1.558 Å (based on a B3LYP/6−311+G(2d) geometry optimization of the monomer[34] and in agreement with the experimental value),[35] and r was the only internal coordinate varied. When BLYP is used with the calibrated DCACP, an interaction energy minimum of −5.6 kJ/mol is found at a separation distance of $r =$ 4.15 Å, in agreement with the benchmark method (CCSD(T)/aug-cc-pVTZ with counterpoise correction).[19] By contrast, uncorrected BLYP predicts a purely repulsive interaction.

Table 1. Sulfur DCACP Calibration Results

functional	σ_1 [Hartree]	σ_2 [Bohr]	E_{min} [Hartree]	E_{mid} [Hartree]
BLYP	$-1.393\cdot10^{-3}$	3.273	$-2.242\cdot10^{-3}$	$-1.004\cdot10^{-3}$
benchmark[a]	-	-	$-2.244\cdot10^{-3}$	$-1.001\cdot10^{-3}$

[a] CCSD(T)/aug-cc-pVTZ with counterpoise correction.[19]

the DFT methods were used to fully relax the geometry of the crystal in orthorhombic periodic boundary conditions; the experimental crystal structure geometry was used as an initial guess, and the experimentally observed lattice parameters were imposed. At the relaxed geometry, the association energy of the crystal was determined, defined as the total energy of the crystal structure divided by 16, minus the energy of the S_8 monomer.[36] In this qualitative test, BLYP wrongly predicted a pure repulsive, positive association energy (87 kJ/mol), indicating that the crystal structure should not exist. By comparison, BLYP with the sulfur DCACP predicted a negative association energy (−82 kJ/mol), suggesting that crystal structure formation is favorable with respect to the gas phase S_8 monomer.

In a more sophisticated test, the crystal structure lattice vector lengths a, b, c were allowed to vary isotropically (with the lattice angles kept fixed). At each lattice volume, the crystal structure geometry was completely relaxed, with the aim of finding the lattice volume that would correspond to a global energy minimum.[37] Within a computationally feasible interval around the experimental value (Figure 3), BLYP never predicted a favorable association energy. By contrast, BLYP with sulfur DCACP found a minimum of the association energy with lattice vectors that are only 3.4% longer than the experimentally observed lengths. In summary, conventional BLYP does not even qualitatively correctly predict the existence of orthorhombic elemental sulfur. However, when

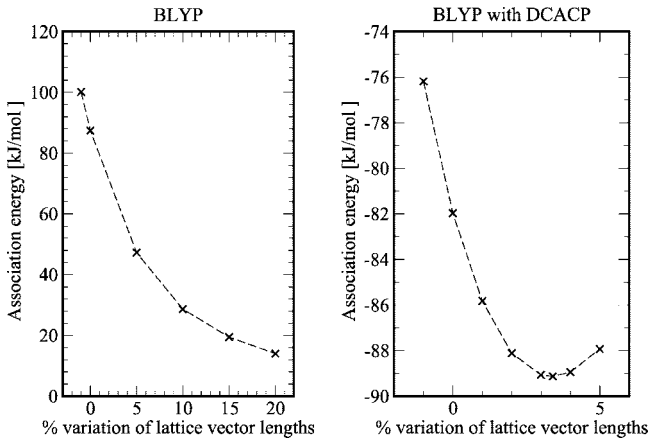

Figure 3. The crystal association energy was evaluated at several different cell parameters for orthorhombic sulfur, using both conventional BYLP (left) and BLYP with DCACP (right). The crystal geometry was fully relaxed at each cell size. The horizontal axis shows the amount by which the cell parameters *a*, *b*, *c* were isotropically varied from the experimentally observed lengths. The suggested energetic minimum for BLYP with DCACP, at lattice length variation of 3.4%, was interpolated from the other points.

the sulfur DCACP is applied, BLYP predicts favorable crystal structure formation, having an energetic minimum at lattice vectors that are close to those observed experimentally.

To further evaluate the sulfur crystal calculations, we compared predicted and experimental enthalpy of deposition (i.e., the negative of the enthalpy of sublimation) at 0 K. The computed deposition enthalpy was given by the calculated association energy of the relaxed structure at the optimized crystal lattice lengths (−89.1 kJ/mol), plus the estimated change in zero point energy (ZPE) in going from the gas phase to solid phase (−0.3 kJ/mol).[38] We obtain a value of −89.4 kJ/mol, which can be interpreted as the energy of forming orthorhombic sulfur from gaseous S_8 at a temperature of 0 K. By comparison, the experimental deposition enthalpy, extrapolated to 0 K, is −105.7 kJ/mol.[39] This shows that the DCACP correction not only corrects the qualitative DFT prediction of a stable crystal structure but also estimates the quantitative stability of the crystal with reasonable accuracy.

The SO_2 Dimer. The SO_2 interaction is important in atmospheric chemistry, where the photooxidation of 2 SO_2 to SO_3 + SO is believed to proceed mainly via a weakly bound gas phase SO_2 dimer.[23] Based on the theoretical and experimental data by Bone et al.,[24] the minimum energy configuration of the SO_2 dimer has C_s symmetry, as shown in Figure 1(c). In this conformation, BLYP incorrectly predicted a very weak binding energy of only −2.2 kJ/mol (Table 2). By contrast, BLYP with DCACPs predicted a −11.2 kJ/mol interaction energy, in close agreement with the benchmark result of −11.5 kJ/mol (CCSD(T)/aug-cc-pVTZ with counterpoise correction).[19] Notably, BLYP with sulfur and oxygen DCACPs predicted significantly stronger SO_2 dimer binding energy than BLYP with the DCACP corrections for oxygen only. Both electrostatics and dispersion forces control the interaction between SO_2 molecules, which are strongly polar (SO_2 experimental dipole moment = 1.633 Debye, i.e. comparable to that of water). Hence, although the sulfur DCACP was calibrated using a dispersion-dominated system (the CS_2 dimer), its applicability extends to this system, where electrostatics are also important.

Table 2. Binding Energies of the SO_2 Dimer[a]

method	D_e [kJ/mol]	r_{cm} [Å]	θ_1	θ_2
benchmark[b]	−11.5	3.78	119.5	58.0
BLYP	−2.2	4.00	132	64
BLYP with oxygen DCACP only	−6.2	3.94	130	68
BLYP with oxygen and sulfur DCACPs	−11.2	3.93	133	65
experimental[32]	N/A	3.822(1)	127.0(20)	60.5(6)

[a] DFT geometries were fully optimized at the indicated levels. See Figure 1(c) for the meaning of geometrical parameters r_{cm}, θ_1, and θ_2. [b] MP4(SDQ)/aug-cc-pVTZ geometry and CCSD(T)/aug-cc-pVTZ energy with counterpoise correction.[19]

Table 3. Hydrogen Bond Binding Energies and Equilibrium Geometry Parameters of the $CH_3OH-S(CH_3)_2$ Complex[a]

method	D_e [kJ/mol]	S···H distance [Å]
benchmark[b]	−22.6	2.33
BLYP	−14.3	2.44
BLYP with DCACPs for C, H, O	−24.0	2.35
BLYP with DCACPs for C, H, O, S	−26.2	2.33

[a] DFT geometries were fully optimized at the indicated levels. [b] MP2/aug-cc-pVTZ geometry and CBS-QB3 energy[33] evaluated at the MP2 geometry.

The Hydrogen Bonded $CH_3OH-S(CH_3)_2$ Complex. Hydrogen bonding to sulfur may be relevant in biological systems, where ligands could interact with methionine or cysteine groups, hence modeling efforts may require accurate treatment of this contact. BLYP significantly underestimated the hydrogen-bond binding energy (−14.3 kJ/mol) and overestimated the hydrogen-bond distance (2.44 Å), when compared to the CBS-QB3 benchmark energy and MP2/aug-cc-pVTZ geometry (−25.3 kJ/mol and 2.33 Å; Table 3). By comparison, BLYP with DCACPs improved both the equilibrium distance (2.33 Å) and binding energy (−26.2 kJ/mol) of the $CH_3OH-S(CH_3)_2$ hydrogen bond. The sulfur DCACP makes a small but significant contribution (ca. 2 kJ/mol) to the total binding energy, in comparison to the other DCACPs. It is worth noting that dispersion forces may contribute significantly to hydrogen bonding,[25−27] which may partly explain why BLYP sometimes poorly estimates this interaction.[28]

The Intramolecular Rotation of 2′,3′-Dideoxytiazofurin. The molecule 2′,3′-dideoxytiazofurin [2-(2′,3′-dideoxy-β-D-glycero-pentafuranosyl)thiazole-4-carboxamide, Figure 1] is a biologically active compound which has been shown to have clinically effective antitumor activity.[29] The molecule features an unusually close distance (2.83 Å) between the sulfur atom in the thiazole ring and the oxygen atom O1′ in the furanose ring in its crystal structure;[30] several thiazole nucleoside analogs exhibit the same close contact in their crystal structures,[31] which suggests that it is not due to a crystal packing effect but to an attracting force between these two atoms. This attraction was quantified by calculating the total energy at varying O−C−C−S dihedral angles, ϕ (Figure 1). Figure 4 shows the variation of the total energy as a function of ϕ. BLYP predicted correctly the qualitative behavior of the energy profile but was systematically biased low by 2−3 kJ/mol. This reflects the strong electrostatic component of the S−O interaction that is usually reasonably accounted for by GGAs. By comparison, BLYP with DCACPs exhibited very good agreement with the benchmark data, having a root mean squared error of 0.73 kJ/mol with respect to benchmark results (MP2/aug-cc-pVDZ counterpoise

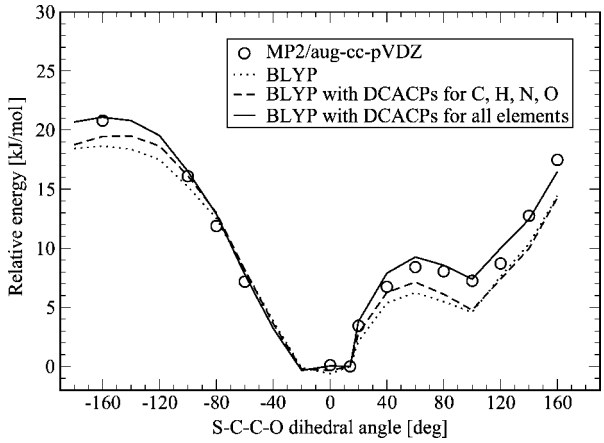

Figure 4. The relative energy of 2′,3′-dideoxytiazofurin as a function of the S−C−C−O dihedral angle. For each level of theory, the zero of the energy scale is set to the calculated total energy for the experimentally observed crystal geometry (S−C−C−O dihedral angle of 14.1). In the remaining calculations, only the S−C−C−O dihedral angle was varied, while the other internal coordinates were kept fixed.

correction).[19] Additional computations using only DCACPs for the elements C, N, O, and H showed that the marginal contribution of the sulfur DCACP is significant, relative to the other DCACPs (Figure 4).

IV. Conclusion

The library of dispersion corrected atom centered potentials for the GGA functional BLYP[2] has been augmented by a third-row element, sulfur. The very good results from four simple sulfur-containing test systems show that the sulfur DCACP is highly transferable to chemical environments other than the calibration system. These tests show that, although the DCACP was calibrated in a simple, almost purely dispersion controlled system (the CS_2 dimer), significant improvements to the calculation of binding energies are also achieved in weakly bound systems having strong electrostatic interactions. Moreover, our results demonstrate that, in several chemical environments, the sulfur DCACP makes an important contribution to the weak interaction beyond that of the DCACPs for other elements. With the sulfur atom DCACP now at hand, there is now a full set of DCACPs available for modeling a standard protein in DFT. A library of DCACPs applicable to BLYP, PBE, and BP for sulfur and other elements is available online at our Web site [see http://lcbcpc21.epfl.ch/dcacp/dcacp.html].

References

(1) von Lilienfeld, O. A.; Tavernelli, I.; Rothlisberger, U.; Sebastiani, D. *Phys. Rev. Lett.* **2004**, *93*, 153004.

(2) Lin, I-C.; Coutinho-Neto, M. D.; Felsenheimer, C.; von Lilienfeld, O. A.; Tavernelli, I.; Rothlisberger, U. *Phys. Rev. B* **2007**, *75*, 205131.

(3) von Lilienfeld, O. A.; Tavernelli, I.; Rothlisberger, U.; Sebastiani, D. *Phys. Rev. B* **2005**, *71*, 195119.

(4) Tapavicza, E.; Lin, I-C.; von Lilienfeld, O. A.; Tavernelli, I.; Coutinho-Neto, M. D.; Rothlisberger, U. *J. Chem. Theory Comput.* **2007**, *3*, 1673.

(5) Lin, I-C.; von Lilienfeld, O. A.; Coutinho-Neto, M. D.; Tavernelli, I.; Rothlisberger, U. *J. Phys. Chem. B* **2007**, *111*, 14346.

(6) Lin, I-C.; Rothlisberger, U. *Phys. Chem. Chem. Phys.* **2008**, *10*, 2730.

(7) DiLabio, G. A. *Chem. Phys. Lett.* **2008**, *455*, 348.

(8) Rapcewiez, K.; Ashcroft, N. W. *Phys. Rev. B* **1991**, *44*, 4032.

(9) Andersson, Y.; Langreth, D. C.; Lundqvist, B. *Phys. Rev. Lett.* **1996**, *76*, 102.

(10) Neumann, M. A.; Perrin, M.-A. *J. Phys. Chem. B* **2005**, *109*, 15531.

(11) Goedecker, S.; Teter, M.; Hutter, J. *Phys. Rev. B* **1996**, *54*, 1703.

(12) Herzberg, G. *Molecular Spectra and Molecular Structure. I. Spectra of Diatomic Molecules*, 2nd ed.; Van Nostrand: New York, NY, 1950.

(13) *CPMD, version 3.11*; IBM Corp and MPI Stuttgart: Stuttgart, Germany, 2006.

(14) Troullier, N.; Martins, J. L. *Solid State Commun.* **1990**, *74*, 613.

(15) Zhao, Y.; Truhlar, D. G. *J. Chem. Theory Comput.* **2006**, *2*, 1009.

(16) Werner, H.-J.; Knowles, P. J.; Lindh, R.; Manby, F. R.; Schütz, M.; Celani, P.; Korona, T.; Rauhut, G.; Amos, R. D.; Bernhardsson, A.; Berning, A.; Cooper, D. L.; Deegan, M. J. O.; Dobbyn, A. J.; Eckert, F.; Hampel, C.; Hetzer, G.; Lloyd, A. W.; McNicholas, S. J.; Meyer, W.; Mura, M. E.; Nicklass, A.; Palmieri, P.; Pitzer, R.; Schumann, U.; Stoll, H.; Stone, A. J.; Tarroni, R.; Thorsteinsson, T. *Molpro, version 2006.1*; University College Cardiff Consultants Limited: Cardiff, U.K., 2006.

(17) Frisch, M. J.; Trucks, G. W.; Schlegel, H. B.; Scuseria, G. E.; Robb, M. A.; Cheeseman, J. R.; Montgomery, J. A., Jr.; Vreven, T.; Kudin, K. N.; Burant, J. C.; Millam, J. M.; Iyengar, S. S.; Tomasi, J.; Barone, V.; Mennucci, B.; Cossi, M.; Scalmani, G.; Rega, N.; Petersson, G. A.; Nakatsuji, H.; Hada, M.; Ehara, M.; Toyota, K.; Fukuda, R.; Hasegawa, J.; Ishida, M.; Nakajima, T.; Honda, Y.; Kitao, O.; Nakai, H.; Klene, M.; Li, X.; Knox, J. E.; Hratchian, H. P.; Cross, J. B.; Bakken, V.; Adamo, C.; Jaramillo, J.; Gomperts, R.; Stratmann, R. E.; Yazyev, O.; Austin, A. J.; Cammi, R.; Pomelli, C.; Ochterski, J. W.; Ayala, P. Y.; Morokuma, K.; Voth, G. A.; Salvador, P.; Dannenberg, J. J.; Zakrzewski, V. G.; Dapprich, S.; Daniels, A. D.; Strain, M. C.; Farkas, O.; Malick, D. K.; Rabuck, A. D.; Raghavachari, K.; Foresman, J. B.; Ortiz, J. V.; Cui, Q.; Baboul, A. G.; Clifford, S.; Cioslowski, J.; Stefanov, B. B.; Liu, G.; Liashenko, A.; Piskorz, P.; Komaromi, I.; Martin, R. L.; Fox, D. J.; Keith, T.; Al-Laham, M. A.; Peng, C. Y.; Nanayakkara, A.; Challacombe, M.; Gill, P. M. W.; Johnson, B.; Chen, W.; Wong, M. W.; Gonzalez, C.; Pople, J. A. *Gaussian 03, Revision C.02*; Gaussian, Inc.: Wallingford, CT, 2004.

(18) Arey, J. S.; Green, W. H.; Gschwend, P. M. *J. Phys. Chem. B* **2005**, *109*, 7564.

(19) Boys, S. F.; Bernardi, F. *Mol. Phys.* **1970**, *19*, 553.

(20) Coppens, P.; Yang, Y. W.; Blessing, R. H.; Cooper, W. F.; Larsen, F. K. *J. Am. Chem. Soc.* **1977**, *99*, 760.

(21) Delley, B. *J. Chem. Phys.* **2000**, *113*, 7756.

(22) Malcolm W. Chase, J. NIST-JANAF Thermochemical Tables. Part II, Cr-Zr. In *Journal of Physical and Chemical Reference Data*, 4th ed.; American Chemical Society: Washington, DC, and American Institute of Physics: New York, NY, 1998; Monograph No. 9.

(23) Green, M.; Lee, E. K. C. *J. Phys. Chem.* **1986**, *90*, 6470.

(24) Bone, R. G. A.; Sueur, C. R. L.; Amos, R. D.; Stone, A. J. *J. Chem. Phys.* **1992**, *96*, 8390.

(25) Cybulski, S. M.; Chalasiński, G.; Moszyński, R. *J. Chem. Phys.* **1990**, *92*, 4357.

(26) Cybulski, S. M.; Scheiner, S. *Chem. Phys. Lett.* **1990**, *166*, 57.

(27) Scheiner, S. *Annu. Rev. Phys. Chem.* **1994**, *45*, 23.

(28) Zhao, Y.; Truhlar, D. G. *J. Chem. Theory Comput.* **2007**, *3*, 289.

(29) Tricot, G. J.; Jayaram, H. N.; Lapis, E.; Natsumeda, Y.; Nichols, C. R.; Kneebone, P.; Heerema, N.; Weber, G.; Hoffman, R. *Cancer Res.* **1989**, *49*, 3696.

(30) Burling, F. T.; Gabrielsen, B.; Goldstein, B. M. *Acta Crystallogr., Sect. C: Cryst. Struct. Commun.* **1991**, *C47*, 1272.

(31) Burling, F. T.; Goldstein, B. M. *J. Am. Chem. Soc.* **1992**, *114*, 2313.

(32) Taleb-Bendiab, A.; Hillig, K. W., II; Kuczkowski, R. L. *J. Chem. Phys.* **1991**, *94*, 6956.

(33) Montgomery, J. A., Jr.; Frisch, M. J.; Ochterski, J. W.; Petersson, G. A *J. Chem. Phys.* **1999**, *110*, 2822.

(34) Dobrogorskaya, Y.; Mascetti, J.; Pàpai, I.; Nemukhin, A.; Hannachi, Y. *J. Phys. Chem. A* **2003**, *107*, 2711.

(35) Suzuki, I. *Bull. Chem. Soc. Jpn.* **1975**, *48*, 1685.

(36) Association energies are reported based on a fixed plane wave energy cutoff of 70 Ry. Additional computations demonstrated that basis set convergence was achieved to within <1 kJ/mol at this energy cutoff. To avoid the introduction of plane wave artifacts, the gas phase S_8 monomer was computed using the same energy cutoff, boundary conditions (orthorhombic, periodic), and unit cell dimensions as the crystal. Additional computations demonstrated that at these specifications, the monomer has negligible self-interaction across the periodic cell boundary; variation of the unit cell dimensions for the monomer contributed negligibly (<0.1 kJ/mol) to the association energy.

(37) Association energies are reported based on a plane wave energy cutoff of 70 Ry. Additional computations demonstrated that basis set convergence was achieved to within <1 kJ/mol at both the largest and smallest lattice parameters applied.

(38) The change in ZPE upon deposition at 0 K was estimated from the computed ZPE of sulfur solid (32.1 kJ/mol) by Delley[21] minus the ZPE value of gas phase S_8 (32.4 kJ/mol) calculated from the measured vibrational frequencies of S_8 reported in NIST-JANAF thermochemical tables.[22]

(39) The deposition enthalpy of S_8 at 0 K was estimated as follows: $\Delta H^{\circ}_{\text{deposition,0K}} = H^{\circ}(\text{crystal, 0 K}) - H^{\circ}(\text{crystal, 298.15 K}) + H^{\circ}(\text{crystal, 298.15 K}) - H^{\circ}(\text{gas, 298.15 K}) + H^{\circ}(\text{gas, 298.15 K}) - H^{\circ}(\text{gas, 0 K})$. The difference terms $H^{\circ}(\text{crystal, 0 K}) - H^{\circ}(\text{crystal, 298.15 K})$ and $H^{\circ}(\text{gas, 298.15 K}) - H^{\circ}(\text{gas, 0 K})$ were directly taken from reference thermochemical tables,[22] and the difference term $H^{\circ}(\text{crystal, 298.15 K}) - H^{\circ}(\text{gas, 298.15 K})$ is given by the experimental negative of the enthalpy of sublimation taken from the same reference tables.[22]

CT800299Y

JCTC Journal of Chemical Theory and Computation

First-Principle Calculations of Large Fullerenes

Patrizia Calaminici,* Gerald Geudtner, and Andreas M. Köster

Departamento de Química, CINVESTAV, Avenida Instituto Politecnico Nacional 2508, A.P. 14-740, Mexico D.F. 07000, Mexico

Received August 21, 2008

Abstract: State of-the-art density functional theory calculations have been performed for the large fullerenes C_{180}, C_{240}, C_{320}, and C_{540} using the linear combination of Gaussian-type orbitals density functional theory (LCGTO-DFT) approach. For the calculations all-electron basis sets were employed. All fullerene structures were fully optimized without symmetry constrains. The analysis of the obtained structures as well as a study on the evolution of the bond lengths and calculated binding energies are presented. The fullerene results are compared to diamond and graphene which were calculated at the same level of theory. This represents the first systematic study on these large fullerenes based on nonsymmetry adapted first-principle calculations, and it demonstrates the capability of DFT calculations for energy and structure computations of large scale structures without any symmetry constraint.

Introduction

Fullerenes are carbon clusters formed by the closing of a graphite sheet with the needed curvature supplied by intersecting, among a given number of graphitic hexagons, of twelve pentagons.[1,2] These carbon aggregates have been experimentally known for more than twenty years,[3] and, consequently, a large number of works, experimental as well as theoretical, focused on this subject (see, for example refs 4−7 and references therein). One main reason for the large interest in the study of fullerenes is certainly to be found in their particularly appealing geometrical form. The best known fullerene is the so-called buckminsterfullerene that contains sixty carbon atoms (C_{60}) and is composed of twelve pentagonal carbon rings located around the vertices of an icosahedron and twenty hexagonal carbon rings at the centers of icosahedral faces.[3] Larger fullerenes that have an icosahedral symmetry can be constructed[8,9] as well. These clusters, known as *giant fullerenes*, can be thought of as cut-out pieces of graphene that are folded into final shape (icosahedron). This kind of procedure generates twelve pentagonal carbon rings situated around vertices of an icosahedron, while all other carbon rings are hexagonal. Giant or large fullerenes have been the subject of different theoretical studies in the last years. For a more detailed overview we address the reader to refs 10−23 and references therein. Most of these studies were focused either to understand if the shape of these clusters is spherical or faceted,[10,11,15−19] to calculate their response properties,[12] or to test new algorithms developed for the investigation of large systems.[13,14] Most previous first-principle type theoretical studies of large fullerenes have been performed either at the Hartree−Fock level of theory using symmetry restrictions and relative small basis sets or employing analytic density-functional theory.[10−23] To the best of our knowledge, no systematic study on large fullerenes based on nonsymmetry adapted first-principle calculations has been performed so far. In this Letter we present the first all-electron density functional theory based study on the large fullerenes C_{180}, C_{240}, C_{320}, and C_{540}. The structures of these clusters were fully optimized without any symmetry constraint. This work provides insight into the structural changes, the evolution of the bond lengths, and binding energies with increasing fullerene size.

Computational Details

All calculations were performed using the density functional theory (DFT) deMon2k program.[24] The exchange-correlation potential was numerically integrated on an adaptive grid.[25] The grid accuracy was set to 10^{-5} in all calculations. The Coulomb energy was calculated by the variational fitting procedure proposed by Dunlap, Connolly, and Sabin.[26,27] The calculation of the exchange correlation energy was performed employing the auxiliary function density.[28] The structure optimizations were performed in the local density approximation (LDA) employing the Dirac exchange functional[29] in combination with the correlation functional from Vosko, Wilk, and Nusair (VWN).[30] DFT optimized double-ζ plus valence polarization (DZVP) all-electron basis sets optimized for local functionals[31] were employed. For the structure optimization a quasi-Newton method in internal redundant coordinates with analytic energy gradients was used.[32] The geometry optimizations were performed using the parallel version of the deMon2k code.[24] The convergence was based on the Cartesian gradient and displacement vectors with a threshold of 10^{-4} and 10^{-3} a.u., respectively. The diamond and graphene calculations were performed in the same

* Corresponding author e-mail: pcalamin@cinvestav.mx.

10.1021/ct800347u CCC: $40.75 © 2009 American Chemical Society
Published on Web 11/26/2008

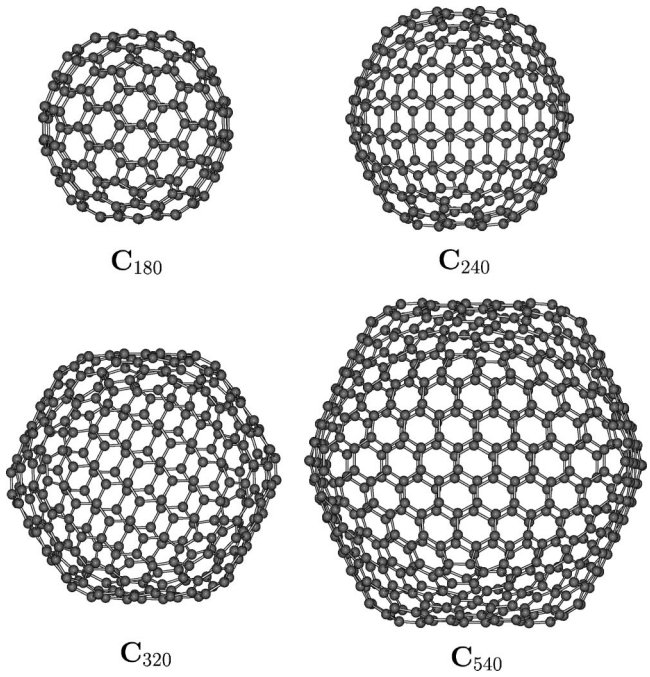

Figure 1. Optimized structure of C_{180}, C_{240}, C_{320}, and C_{540} fullerenes. The calculations have been performed with the VWN functional in combination with DZVP basis sets.

theoretical framework employing the cyclic cluster model (CCM).[33] For this reason the here reported relative energy differences between the fullerene binding energies and the cohesive energies in diamond and graphene should be quite reliable.

Results and Discussion

In Figure 1 the DFT optimized singlet structures of C_{180}, C_{240}, C_{320}, and C_{540} are depicted. These structures have been fully optimized at the all-electron level using DZVP basis sets in combination with the VWN functional. A long standing discussion in the literature addresses the question if giant fullerenes prefer a faceted or a spherical shape. This question was raised by transmission electron microscopy (TEM) images that have shown evidence of possible spheroidal structures in concentric carbon particles.[34−36] Using a divide-and-conquer method for density functional calculations the structure and stability of C_{240} were studied, and the most stable structure was claimed to be highly spherical.[15] However, this result was not confirmed by any successive theoretical work. Instead, all other calculations indicated strong evidence of a faceted shape for this fullerene.[10,11,16−20] It has been clearly explained in the literature that depending on the view axis, simulated TEM of icosahedral fullerenes can provide either images with spherical or with polyhedral shapes.[18] In addition, an explanation of why experimental results showed rounder shapes for large fullerenes was also given.[18] As Figure 1 shows our first-principle based structure optimizations predict that larger fullerenes, C_{240}, C_{320}, and C_{540}, prefer a faceted shape. Moreover, as Figure 1 shows, even for the smallest fullerene studied here, C_{180}, there is clear evidence that the faceted shape is preferred over a spherical shape if first-principle all-electron optimizations without any symmetry restriction are performed. Details about the timing of these calculations are reported in ref 14. We notice that our

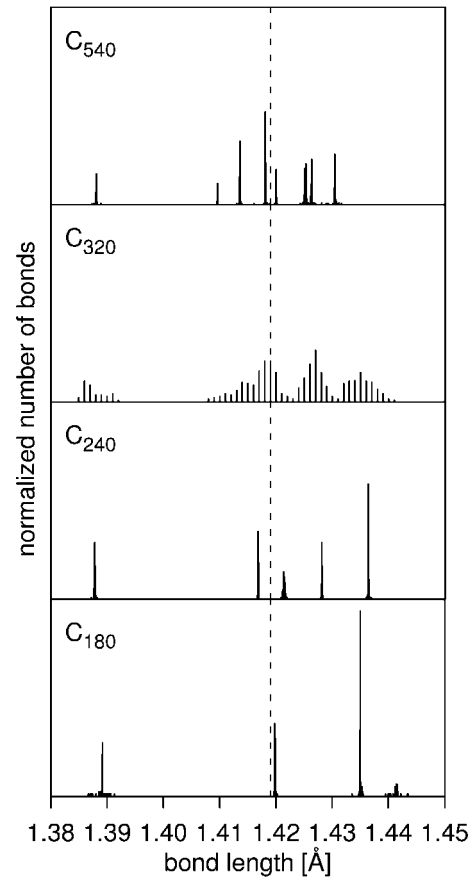

Figure 2. Normalized number of bonds for C_{180}, C_{240} C_{320}, and C_{540} versus the bond lengths (in Å).

results are in agreement with most of the previous reported theoretical studies.[10,11,16−20] In order to gain more insight into the structural changes of these systems as the number of carbon atoms increases we performed a detailed analysis of the bond length evolution. In Figure 2 the normalized number of bonds for C_{180}, C_{240} C_{320}, and C_{540} are plotted versus the bond length. The dashed line at 1.419 Angstrom represents the graphene bond length obtained from the periodic deMon2k calculation.[33] Most obvious from this figure is the difference of C_{320} to all other fullerenes. In fact, whereas usually a discrete distribution of bond lengths is found, in C_{320}, a wide, in some ranges almost continuous, bond length distribution is observed. This clearly indicates a break in the expected high symmetry of the system. Our studies show that the C_{320} fullerene possesses a ground-state potential energy surface (PES) of higher multiplicity, most likely either triplet or quintet. This observation is in agreement with the conclusions given by Fowler.[37] Further test calculations revealed that for this fullerene also in the cases of triplet and quintet PESs the continuous bond length distribution observed for the singlet PES persists. Of course, only nonsymmetry adapted optimizations can lead to such a result. To the best of our knowledge this symmetry breaking in larger fullerenes due to their electronic structure has never been observed in previous calculations. As Figure 1 shows the observed symmetry breaking does not alter the global shape of the giant fullerene. For the other systems, C_{180}, C_{240}, and C_{540}, the expected discrete bond length distribution is obtained, indicating that the symmetry of the electronic structures matches with the expected geometrical symmetry. In these systems the number of different bond lengths

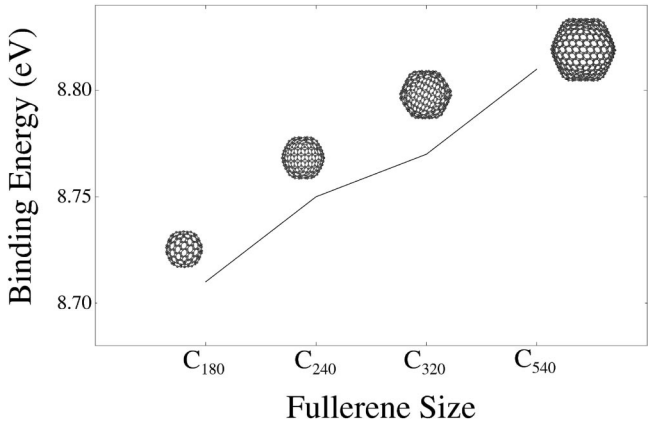

Figure 3. Binding energy (in eV) for C_{180}, C_{240}, C_{320}, and C_{540} fullerenes. The calculations have been performed with the VWN functional in combination with DZVP basis sets.

increases with system size, and an accumulation of bond lengths around the graphene bond length is observed. More surprising is the trend that the longest bond length in the cluster shortens with increasing cluster size. This indicates that delocalization increases with cluster size despite the global building pattern, i.e. the appearance of twelve pentagons. With the aim to guide future desirable experiments on large fullerenes and to gain more information about their stability we have also explored the behavior of the binding energy of the studied fullerenes with increasing fullerene size. The results of the uncorrected binding energy (in eV) per carbon atom obtained with the VWN functional are illustrated in Figure 3. The inclusion of the basis set superposition error (BSSE) decreases the calculated binding energies to 8.64 eV (C_{180}), 8.68 eV (C_{240}), 8.69 eV (C_{320}), and 8.75 eV (C_{540}), respectively. The depicted trend in Figure 3 is not altered by the BSSE correction. In fact the BSSE is in giant fullerenes much smaller than for the equivalent graphene calculation. As can be seen from Figure 3 the binding energy increases monotonically with the number of carbon atoms increases. This indicates that the large fullerenes become more and more stable with increasing size. However, the increase is very moderate. From the comparison of the CCM calculations we find that the binding energy of C_{540} is very close to the cohesive energy of diamond (8.78 eV). This indicates that C_{540} has a similar binding energy to diamond which fuels the hope that such giant fullerenes could indeed be prepared. However, the binding energy of even the largest fullerene, C_{540}, studied here is still far away from the corresponding value in graphene which was calculated to be 8.91 eV.[33] This is in the range of other calculated cohesive energies for graphene.[38,39] Because the fullerenes and graphene calculations are performed within the same theoretical framework, the relative energy differences found here, are reliable.

Conclusions

In conclusion, state of-the-art density functional theory calculations have been performed for the large fullerenes C_{180}, C_{240}, C_{320}, and C_{540} using the linear combination of Gaussian-type orbitals density functional theory. The calculations were of all electron types. All structures have been fully optimized without any symmetry restriction. This work confirms that for all large fullerenes studied here a faceted shape is preferred over the spherical shape. The analysis of the bond length evolution shows for the C_{320} a qualitative different pattern than for the other fullerenes. The most likely explanation for this difference is a symmetry breaking in the electron structure of C_{320}. The shortening of the longest bond length with increasing cluster size indicates that delocalization increases with cluster size. The calculated binding energies are in the range of diamond but considerably below the graphene value. Thus, even giant fullerenes like the ones studied here are only meta-stable.

Acknowledgment. Financial support from the CONACYT projects 48775-U and 60117-U is gratefully acknowledged. The authors would like to thank the referees for their comments.

References

(1) Kadish, K. M.; Ruoff, R. S. In *Fullerenes: Chemistry, Physics, and Technology*; John Wiley & Sons Inc.: New York, 2007.

(2) Andreoni W. In *The Physics of Fullerene-Based and Fullerene-Related Materials;* Kluwer Academic Publishers: Dordrecht, Netherlands, 2007.

(3) Kroto, H. W.; Heath, J. R.; O'Brien, S. C.; Curl, R. F.; Smalley, R. E. C_{60}-Buckminsterfullerene. *Nature (London)* **1985**, *318*, 162–163.

(4) Seifert, G.; Vietze, K.; Schmidt, R. Ionization Energies of fullerenes - Size and charge dependence. *J. Phys. B* **1996**, *29*, 5183–5192.

(5) Boltalina, O. V.; Ioffe, I. N.; Sidorov, L. N.; Seifert, G.; Vietze, K. Ionization energy of fullerenes. *J. Am. Chem. Soc.* **2000**, *122*, 9745–9749.

(6) Cioslowski, J. In *Electronic Structure Calculations on Fullerenes and Their Derivatives;* Oxford University Press: New York, 1995.

(7) Bülh, M.; Hirsch, A. Spherical aromaticity of fullerenes. *Chem. Rev.* **2001**, *101*, 1153–1183.

(8) Kroto, H. W.; McKay, K. The formation of quasi-icosahedral spiral shell carbon particles. *Nature* **1988**, *331*, 328–331.

(9) Itoh, S.; Ordejón, P.; Drabold, D. A.; Martin, R. M. Structure and energetics of giant fullerenes: An order-N molecular dynamics study. *Phys. Rev. B* **1996**, *53*, 2132–2140.

(10) Bakowies, D.; Bülh, M.; Thiel, W. Can large fullerenes be spherical. *J. Am. Chem. Soc.* **1995**, *117*, 10113–10118.

(11) Scuseria, G. E. The equilibrium structures of giant fullerenes - faceted or spherical shape - An ab-initio Hartree-Fock study of icosahedral. C_{240} and C_{540}. *Chem. Phys. Lett.* **1995**, *243*, 193–198.

(12) Zope, R. R.; Baruah, T.; Pederson, M. R.; Dunlap, B. I. Static dielectric response of icosahedral fullerenes from C_{60} to C_{2160} characterized by an all-electron density functional theory. *Phys. Rev. B* **2008**, *77*, 115452.

(13) Dunlap, B. I.; Zope, R. R. Efficient quantum-chemical geometry optimization and the structure of large icosahedral fullerenes. *Chem. Phys. Lett.* **2006**, *422*, 451–454.

(14) Geudtner, G.; Janetzko, F.; Köster, A. M.; Vela, A.; Calaminici, P. Parallelization of the deMon2k code. *J. Comput. Chem.* **2006**, *27*, 483–490.

(15) York, D.; Lu, J. P.; Yang, W. Density-functional calculations of the structure and stability of C_{240}. *Phys. Rev. B* **1994**, *49*, 8526–8528.

(16) Haddon, R. C.; Scuseria, G. E.; Smalley, R. E. C_{240} - The most chemically inert fullerene. *Chem. Phys. Lett.* **1997**, *272*, 38–42.

(17) Bates, K. R.; Scuseria, G. E. Why are buckyonions round. *Theor. Chem. Acc.* **1998**, *99*, 29–33.

(18) Scuseria, G. E. Ab initio calculations of Fullerenes. *Science* **1996**, *271*, 942–945.

(19) Xu, C. H.; Scuseria, G. E. An O(N) tight-binding study of carbon clusters up to C_{8640}: the geometrical shape of the giant icosahedral fullerenes. *Chem. Phys. Lett.* **1996**, *262*, 219–226.

(20) Dunlap, B. I.; Brenner, D. W.; Mintmire, J. W.; Mowrey, R. C.; White, C. T. Local density functional electronic structures of three stable icosahedral fullerenes. *J. Phys. Chem.* **1991**, *95*, 8737–8741.

(21) Heggie, M. I.; Terrones, M.; Eggen, B. R.; Jungnickel, G.; Jones, R.; Latham, C. D.; Briddon, P. R.; Terrones, H. Quantitative density-functional study of nested fullerenes. *Phys. Rev. B* **1998**, *57*, 13339–13342.

(22) Shao, N.; Gao, Y.; Yoo, S.; An, W.; Zeng, X. C. Search for lowest-energy fullerenes: C_{98} to C_{110}. *J. Phys. Chem. A* **2006**, *110*, 7672–7676.

(23) Shao, N.; Gao, Y.; Zeng, X. C. Search for lowest-energy fullerenes 2: C_{38} to C_{80} and C_{112} to C_{120}. *J. Phys. Chem. C* **2007**, *111*, 17671–17677.

(24) Köster A. M.; Calaminici P.; Flores-Moreno P.; Geudtner G.; Goursot A.; Heine T.; Janetzko F.; Patchkovskii S.; Reveles J. U.; Vela A.; Salahub D. R. deMon2k; The deMon developers: 2004.

(25) Köster, A. M.; Flores-Moreno, R.; Reveles, J. U. Efficient and reliable numerical integration of exchange-correlation energies and potentials. *J. Chem. Phys.* **2004**, *121*, 681–690.

(26) Dunlap, B. I.; Connolly, J. W. D.; Sabin, R. J. 1st-row diatomic molecules and local density models. *J. Chem. Phys.* **1979**, *71*, 4993–4999.

(27) Mintmire, W.; Dunlap, B. I. Fitting the Coulomb potential variationally in linear combination of atomic orbitals density functional calculations. *Phys. Rev. A* **1982**, *25*, 88–95.

(28) Köster, A. M.; Reveles, J. U.; M. del Campo, J. Calculations of exchange-correlation potentials with auxiliary function densities. *J. Chem. Phys.* **2004**, *121*, 3417–3424.

(29) Dirac, P. A. M. Note on exchange phenomena in the Thomas atom. *Proc. Cambridge Philos. Soc.* **1930**, *26*, 376–385.

(30) Vosko, S. H.; Wilk, L.; Nusair, M. Accurate spin-depentent electron liquid correlation energies for local spin-density calculations - a critical analysis. *Can. J. Phys.* **1980**, *58*, 1200–1211.

(31) Godbout, N.; Salahub, D. R.; Andzelm, J.; Wimmer, E. Optimization of gaussian-type basis-sets for local spin-density functional calculations. 1. boron through neon, optimization technique and validation. *Can. J. Phys.* **1992**, *70*, 560–571.

(32) Reveles, J. U.; Köster, A. M. Geometry optimization in density functional methods. *J. Comput. Chem.* **2004**, *25*, 1109–1116.

(33) Janetzko, F.; Köster, A. M.; Salahub, D. R. Development of the cyclic cluster model formalism for Kohn-Sham auxiliary density functional theory methods. *J. Chem. Phys.* **2008**, *128*, 024102.

(34) Iijima, S. Direct observation of the tethrahedral bonding in graphitized carbon-black by high-resolution electron-microscopy. *J. Cryst. Growth* **1980**, *50*, 675–683.

(35) Ugarte, D. Curling and closure of graphitic networks under electron-beam irradiation. *Nature* **1992**, *359*, 707–709.

(36) Ugarte, D. Onion-like graphitic particles. *Carbon* **1995**, *33*, 989–993.

(37) Fowler, P. W. How unusual is C_{60}? Magic numbers for carbon clusters. *Chem. Phys. Lett.* **1986**, *131*, 444–450.

(38) Trickey, S. B.; Müller-Plate, F.; Diercksen, G. H. F.; Boettger, J. C. Interplanar binding and lattice relaxation in a graphite dilayer. *Phys. Rev. B* **1992**, *45*, 4460–4468.

(39) Dunlap, B. I.; Boettger, J. C. Local-density-functional study of the fullerenes, graphene and graphite. *J. Phys. B* **1996**, *29*, 4907–4913.

CT800347U

JCTC Journal of Chemical Theory and Computation

A DFT Study of the Kinetic Isotope Effects on the Competing S_N2 and E2 Reactions between Hypochlorite Anion and Ethyl Chloride

Anna Pabis, Piotr Paluch, Joanna Szala, and Piotr Paneth*

Faculty of Chemistry, Technical University of Lodz, Zeromskiego 116, 90-924 Lodz, Poland

Received October 1, 2008

Abstract: Kinetic isotope effects (KIEs) on the two alternative reactions, S_N2 and E2, between hypochlorite anion and ethyl chloride in water have been studied theoretically using B3LYP and M06−2X functionals. It has been found that the latter one yields more correct geometries and energetics. Although, in the qualitative sense, KIEs obtained using both DFT functionals are in agreement, interpretation of some of them, like ^{18}O-KIE in the present case, leads to different mechanistic conclusions.

Introduction

The competition between S_N2 (bimolecular nucleophilic substitution) and E2 (bimolecular elimination) reaction pathways in the gas and condensed phases has been intensively investigated over past few years.[1] Both mechanisms are of significant importance in organic chemistry. In environmental chemistry frequently only analysis of the remaining reactant is possible, and therefore means allowing distinguishing between the two mechanisms received much attention. One of the ways to differentiate these two types of reactions is to evaluate kinetic isotope effects (KIEs); secondary deuterium KIEs are expected at room temperature to be normal (larger than unity) for the E2 mechanism and inverse (smaller than unity) for the S_N2 mechanism.

The above-mentioned competition has been examined both theoretically and experimentally. Available theoretical studies are mostly concerned with reactions occurring in the gas phase, rarely introducing explicit solvent models that allow considering solvation effects. To the best of our knowledge no studies on E2 vs S_N2 competition in condensed phases that involve implicit (continuum) solvent model have been reported. Experimental studies of the gas-phase reactions, on the other hand, remain rather involved due to the instrumentation requirements and the fact that both reactions lead to the same ionic product, which makes the analysis quite troublesome.

In recent work, Hu and Truhlar[2] have evaluated the reaction rate constants and deuterium kinetic isotope effects on the reaction between ClO^- and C_2H_5Cl for both S_N2 (eq 1) and E2 (eq 2) pathways in the gas phase, using dual−level generalized transition state theory and statistical calculations based on high-level, correlated electronic calculations. They have used MP2 theory level and modified aug-cc-pVDZ basis set.

$$ClO^- + C_2H_5Cl \rightarrow C_2H_5OCl + Cl^- \quad (1)$$

$$ClO^- + C_2H_5Cl \rightarrow ClOH + C_2H_4 + Cl^- \quad (2)$$

Villano et al.[3] have recently shown that experimental results differ substantially from the theoretical predictions. This discrepancy prompted us to extend studies of these model reactions. Because of the shortage of the theoretical studies in the condensed phase we have elected to model reactions in solution by using implicit model of water. There are two additional reasons for undertaking these studies. The first one is computational; DFT methods proved very efficient in predicting mechanisms of chemical reactions and are used nowadays routinely. In organic chemistry the B3LYP functional is being considered the most robust and versatile. However, in recent years a plethora of new functionals has been developed with a promise of much better performance. One of the most recent of these is the family of M0*x* functionals introduced by Truhlar and co-workers.[4] In this contribution we compare results obtained with B3LYP and a number of M0*x* functionals. Second, hypochloride is an important species in chemical, biochemical, and atmospheric studies, but its reactivity is yet not fully understood. It is used as a bleaching agent[5] and as a disinfectant.[6] It is also a postulated intermediate in many enzymatic halogenation/dehalogenation processes,[7] yet its isotopic fate remains puzzling.[8] Thus it is of great interest to fully characterize main mechanisms that involve this reactant.

Methods and Results

Calculations were carried out at the DFT level of theory using the standard 6−31+G(d,p) basis set.[9] The polarizable continuum solvent model[10] (PCM) with parameters for water was used. UFF[11] radii of all atoms, including hydrogen atoms, were used in the cavity building. 1 molar concentration was assumed as the standard state. The following functionals were employed: B3LYP,[12] M05,[13] M05−2X,[13] M06,[14] and M06−2X.[14] In the reference calculations the MP2[15] level with the aug-cc-pVDZ basis set[16] was used. The *Gaussian03* electronic structure

* Corresponding author e-mail: paneth@p.lodz.pl.

10.1021/ct800412h CCC: $40.75 © 2009 American Chemical Society
Published on Web 12/18/2008

Table 1. Comparison of the Selected Geometrical Parameters of the S_N2 Transition State

	gas						water					
	MP2	B3LYP	M05	M05−2X	M06	M06−2X	MP2	B3LYP	M05	M05−2X	M06	M06−2X
Cl_9-O	1.707	1.726	1.676	1.689	1.696	1.691	1.710	1.729	1.680	1.691	1.699	1.692
$O-C_5$	2.097	2.198	2.138	2.118	2.149	2.101	2.105	2.216	2.704	2.134	2.186	2.115
C−C	1.510	1.501	1.491	1.503	1.491	1.504	1.508	1.497	1.486	1.499	1.487	1.501
C_5-Cl_{10}	2.168	2.235	2.278	2.205	2.227	2.198	2.197	2.256	2.282	2.229	2.242	2.219
C_5-O-Cl_9	108.1	114.3	115.0	109.8	111.1	109.6	106.3	111.8	111.8	108.1	108.3	108.6
$H_2-C_1-H_4$	108.1	108.3	108.3	108.3	108.0	108.1	108.9	109.2	109.3	109.2	108.9	109.0
$O-C_5-C_1$	89.0	88.3	89.6	89.7	89.2	89.5	91.4	91.3	92.4	92.2	92.3	91.6
$C_5-C_1-H_3$	109.1	108.3	89.6	108.3	108.7	108.6	109.1	108.4	108.2	108.4	108.8	108.6
$Cl_{10}-C_5-C_1$	99.0	100.8	99.6	99.0	99.3	98.9	99.2	101.2	100.8	99.4	100.1	99.3
$H_7-C_5-H_6$	117.4	117.0	117.3	117.4	116.7	117.3	117.6	117.2	117.2	117.7	116.8	117.6
rms(bonds)	-	0.055	0.055	0.021	0.037	0.016	-	0.057	0.27	0.021	0.043	0.014
rms(angles)	-	2.7	8.5	0.82	1.3	0.68	-	2.4	2.4	0.87	1.0	0.97

Table 2. Comparison of the Selected Geometrical Parameters of the E2 Transition State

	gas						water					
	MP2	B3LYP	M05	M05−2X	M06	M06−2X	MP2	B3LYP	M05	M05−2X	M06	M06−2X
Cl_9-O	1.713	1.725	1.681	1.689	1.696	1.691	1.713	1.721	1.673	1.688	1.687	1.690
$O-C_1$	2.636	2.627	2.619	2.631	2.625	2.627	2.638	2.655	2.671	2.636	2.661	2.626
$O-H_3$	1.226	1.281	1.209	1.237	1.246	1.217	1.299	1.376	1.426	1.310	1.408	1.286
H_3-C_1	1.412	1.353	1.416	1.395	1.379	1.411	1.341	1.281	1.245	1.326	1.254	1.341
H_2-C_1	1.099	1.093	1.092	1.089	1.095	1.092	1.097	1.092	1.090	1.088	1.092	1.091
C−C	1.436	1.425	1.426	1.425	1.429	1.433	1.424	1.415	1.407	1.414	1.407	1.419
C_5-Cl_{10}	2.108	2.212	2.115	2.146	2.104	2.094	2.197	2.350	2.426	2.250	2.406	2.201
C_1-H_3-O	175.6	171.9	171.8	176.9	177.9	177.1	176.8	174.8	179.1	177.5	177.4	177.4
H_3-O-Cl_9	102.9	106.4	108.0	103.8	103.5	104.3	101.2	103.3	101.4	102.2	98.9	103.3
$H_2-C_1-H_4$	112.6	111.9	111.9	112.6	111.4	111.8	113.8	113.2	113.9	113.8	113.5	113.3
$C_5-C_1-H_3$	102.8	105.3	105.9	103.3	105.2	104.1	99.9	102.2	100.5	100.3	101.2	101.2
$Cl_{10}-C_5-C_1$	116.0	115.7	116.4	115.2	115.4	115.8	113.8	113.0	112.0	112.9	110.9	113.4
$H_6-C_5-H_7$	112.6	113.4	112.3	113.2	112.1	112.3	114.2	115.0	115.6	114.8	115.3	114.1
rms(bonds)	-	0.050	0.016	0.020	0.017	0.011	-	0.069	0.11	0.024	0.096	0.011
rms(angles)	-	2.4	2.9	0.79	1.5	1.1	-	1.6	1.3	0.69	1.7	1.1

program[17] alone or with the MN-GSM module[18] was used. All stationary points were fully optimized using default convergence criteria. Vibrational analysis was performed for each stationary point. All minima and transition states (TSs) were confirmed to have zero and exactly one imaginary frequency, respectively, and Hessians from these calculations were used in calculations of KIEs by the conventional transition state theory using the Isoeff program.[19]

Selected geometric parameters of the optimized transition states are collected in Tables 1 and 2 for the S_N2 and E2 mechanisms, respectively. Complete transition state structures (together with Gibbs free energies and imaginary frequencies) optimized in the reaction field of the implicit solvent are collected in the Supporting Information. Atom numbering is presented in the left panel of Figure 1, which illustrates the transition state for the gas-phase S_N2 reaction. The right panel illustrates the structure of the corresponding transition state of the E2 reaction. Table 3 summarizes nongeometrical results obtained for these theory levels; energetics, Mulliken partial atomic charges, dipole moments, imaginary frequencies, and KIEs are collected.

Discussion

Previously reported results have been compared to MP2 calculations in which the aug-cc-pVDZ basis set has been modified.[2] Since not all geometric features of these structures are available, we have repeated MP2 calculations using the full aug-cc-pVDZ basis set. These results are collected in Tables 1 and 2 under the MP2 heading and are used in the following discussion as the reference level for the DFT calculations in which the standard 6−31+G(d,p) basis set has been used. The last two lines in these tables list the root-mean-square deviation of the listed bond lengths and valence angles from those obtained at the reference level. As can be seen generally M0*x* functionals, and especially the M0*x*-2X functionals, yield much better geometric results than those obtained using B3LYP. We note that the overall best performance is obtained with the M06−2X functional, and therefore we have used it in the following calculations.

From the mechanistic point of view results listed in Tables 1 and 2 indicate that the presence of the solvent leads to the looser transition state of reaction (1); both $O-C_5$ and C_5-Cl_{10} bond lengths are longer than in the gas phase calculations. These bond lengths are significantly shorter in M06−2X calculations than in B3LYP suggesting that this latter theory level overestimates bond lengths at transition states. The large value of the C_5-Cl_{10} bond indicated a late transition state. In the case of the E2 mechanism inclusion of the solvent results in elongation of the $O-H_3$ bond and shortening of the H_3-C_1 bond indicating that the transition state in the gas phase is later than in the aqueous solution. Again this change is exaggerated in B3LYP calculations.

In agreement with literature reports,[20] B3LYP underestimates the height of the activation barrier. This is corrected in M06−2X calculations. The cost of calculations using this latter functional is about 30% higher than when B3LYP is used both in energy

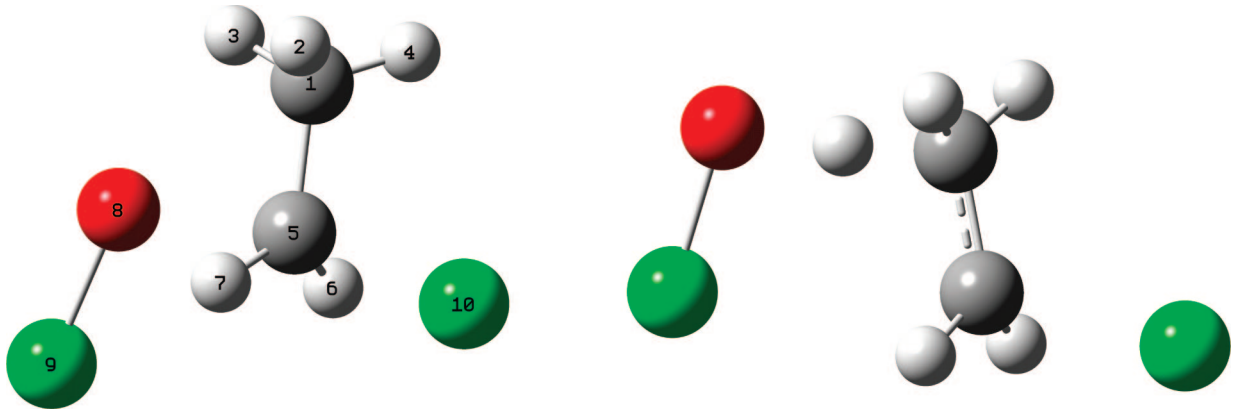

Figure 1. Gas-phase structures of the S_N2 (left) and E2 (right) transition states for reactions between hypochlorite and ethyl chloride at 300 K.

Table 3. Calculated KIEs, Partial Atomic charges (q), Dipole Moments (μ), Imaginary Frequencies (ν), and Gibbs Free Energies for the Reactions between Hypochlorite and Ethyl Chloride in Water at 300 K

	S_N2		E2	
	M06−2X	B3LYP	M06−2X	B3LYP
Cl_9	0.9989	0.9998	0.9983	0.9988
Cl_{10}	1.0071	1.0066	1.0055	1.0059
O	0.992	0.998	0.978	0.987
CD_3	0.97	1.00	5.71	5.13
CD_2	1.03	1.01	1.16	1.19
C_5	1.0563	1.0455	1.0150	1.0126
C_1	0.9996	1.0013	1.0100	1.0059
qCl_9	−0.06	−0.08	−0.05	−0.09
qCl_{10}	−0.60	−0.60	−0.43	−0.48
qO	−0.71	−0.70	−0.56	−0.55
qH_3	0.20	0.19	0.34	0.33
μ [D]	1.49	1.54	1.71	1.85
νi [cm^{-1}]	577.4	426.3	1245.3	856.2
$\Delta G^{\ddagger}$ [kcal/mol]	11.0	9.2	17.9	15.5
ΔG_r [kcal/mol]	−31.6	−29.8	−7.9	−10.3

and Hessian calculations, the price worth being paid since both energetics and geometries obtained from M06−2X calculations are closer to values obtained experimentally and at the theoretical reference level. Mulliken partial atomic charges[21] are very close for both these functionals. Harmonic frequencies, on the other hand, show some differences. Most importantly, the imaginary vibrations differ quite significantly, especially in the case of the transition state for the E2 pathway. The high value of this frequency in M06−2X calculations indicates the dominating contribution of the proton movement in the reaction coordinate and implies that nonclassical effects, in particular tunneling, should be considered in the case of this mechanism.

Our focus in this contribution is on the consequences of using B3LYP in calculations of isotope effects because this functional has been used widely for many years in their calculations. It is thus encouraging to note that in general values of KIEs obtained for both mechanisms with B3LYP and M06−2X are not too far apart, and qualitative conclusions drawn on the basis of calculations at both considered theory levels should be quite similar. Among heavy-atom KIEs two values deserve closer inspection. ^{13}C-KIE on the central carbon atom (C_5) in the S_N2 mechanism is underestimated by about 1% in B3LYP calculations. The absolute values of these KIEs correctly indicate a primary isotope effect, but the position of the transition state on the reaction coordinate may be assigned differently on the basis of the value obtained with the B3LYP functional. The other isotope effect is ^{18}O-KIE in the E2 mechanism. It is inverse KIE, i.e., it is smaller than unity. Inverse KIEs are obtained for the incoming group nucleophiles since the number of bonds increases on transition from reactants to the transition state. B3LYP underestimates this isotope effect which may lead to a conclusion that the reaction is stepwise and the intrinsic KIE is partially masked by a commitment, i.e., that an isotope-insensitive step is partly rate-determining.[22] Furthermore, if the observed value was close to 0.99, a different mechanism would be suggested on the basis of the B3LYP calculations. It is worth noticing that this ^{18}O-KIE is a good indicator of the mechanism since in E2 its value is closer to unity by 1% than when the S_N2 mechanism operates.

We are particularly interested in values of chlorine KIEs as they can potentially be used for analysis of dehalogenation pathways in environmental processes.[8,23] The role of the hypochlorite anion and its isotopic fractionation in enzymatic halogenation/dehalogenation processes remains unclear.[7] Disappointingly, present results indicate that chlorine KIEs do not provide any appreciable insight into the mechanism of the studied reactions. The incoming group chlorine KIE is slightly inverse for both mechanisms. The leaving group chlorine KIE is slightly larger for the S_N2 mechanism than for the E2 mechanism, but the difference is too small to be a diagnostic of the mechanisms.

Acknowledgment. This work was supported by grant 1344/T09/2005/29 from the Ministry of Science and Higher Education, Poland. Access to supercomputing facilities at ICM, PCCS, and Cyfronet (Poland) and MSI (U.S.A.) is gratefully acknowledged.

Supporting Information Available: Structures, imaginary frequencies, and Gibbs free energies of the transition state structures optimized using continuum solvent model. This material is available free of charge via the Internet at http://pubs.acs.org.

References

(1) (a) Gronert, S. *Acc. Chem. Res.* **2003**, *36*, 848. (b) Bickelhaupt, F. M.; Baerends, E. J.; Nibbering, N. M. M. *Chem. Eur. J.* **1996**, *2*, 196.

(2) Hu, W.-P.; Truhlar, D. G. *J. Am. Chem. Soc.* **1996**, *118*, 860.

(3) Villano, S. M.; Kato, S.; Bierbaum, V. M. *J. Am. Chem. Soc.* **2006**, *128*, 736.

(4) Zhao, Y.; Truhlar, D. G. *Theor. Chem. Acc.* **2008**, *120*, 215.

(5) Goffin, V.; Piérard, G. E.; Henry, F.; Legawe, C.; Maibach, H. I. *Ecotoxicol. Environ. Saf.* **1997**, *37*, 199.

(6) Weinberg, H. S.; Delcomyn, C. A.; Unnam, V. *Environ. Sci. Technol.* **2003**, *37*, 3104.

(7) Yeh, E.; Blasiak, L. C.; Koglin, A.; Drennan, C. L.; Walsh, C. T. *Biochemistry* **2007**, *46*, 1284.

(8) Paneth, P. Chlorine Isotope Effects in Biological Systems. In *Isotope Effects in Chemistry and Biology*, 1st ed.; Kohen, A., Limbach, H. H., Eds.; CRC Press, Inc.: Baton Rouge, LA, 2006; pp 875−891.

(9) (a) Becke, A. D. *Phys. Rev. A* **1988**, *38*, 3098. (b) Becke, A. D. *J. Chem. Phys.* **1993**, *98*, 5648. (c) Lee, C.; Yang, W.; Parr, R. G. *Phys. Rev. B* **1988**, *37*, 785.

(10) Miertus, S.; Scrocco, E.; Tomasi, J. *J. Chem. Phys.* **1981**, *55*, 117.

(11) Rappe, A. K.; Casewit, C.; Colwell, K.; Goddard, W. A., III; Skiff, W. M. *J. Am. Chem. Soc.* **1992**, *114*, 10024.

(12) (a) Hariharan, P. C.; Pople, J. A. *Theor. Chim. Acta* **1973**, *28*, 213. (b) Francl, M. M.; Pietro, W. J.; Hehre, W. J.; Binkley, J. S.; Gordon, M. S.; DeFrees, D. J.; Pople, J. A. *J. Chem. Phys.* **1982**, *77*, 3654.

(13) Zhao, Y.; Schultz, N. E.; Truhlar, D. G. *J. Chem. Phys.* **2005**, *123*, 161103.

(14) (a) Zhao, Y.; Schultz, N. E.; Truhlar, D. G. *J. Chem. Theory Comput* **2006**, *2*, 364. (b) Zhao, Y.; Truhlar, D. G. *Theor. Chem. Acc.* **2008**, *120*, 215. Erratum: *Theor. Chem. Acc.* **2008**, *119*, 525.

(15) Müller, C.; Plesset, M. S. *Phys. Rev.* **1934**, *46*, 618.

(16) Woon, D. E.; Dunning, T. H., Jr. *J. Chem. Phys.* **1993**, *98*, 1358.

(17) Frisch, M. J.; Trucks, G. W.; Schlegel, H. B.; Scuseria, G. E.; Robb, M. A.; Cheeseman, J. R.; Montgomery, J. A., Jr.; Vreven, T.; Kudin, K. N.; Burant, J. C.; Millam, J. M.; Iyengar, S. S.; Tomasi, J.; Barone, V.; Mennucci, B.; Cossi, M.; Scalmani, G.; Rega, N.; Petersson, G. A.; Nakatsuji, H.; Hada, M.; Ehara, M.; Toyota, K.; Fukuda, R.; Hasegawa, J.; Ishida, M.; Nakajima, T.; Honda, Y.; Kitao, O.; Nakai, H.; Klene, M.; Li, X.; Knox, J. E.; Hratchian, H. P.; Cross, J. B.; Bakken, V.; Adamo, C.; Jaramillo, J.; Gomperts, R.; Stratmann, R. E.; Yazyev, O.; Austin, A. J.; Cammi, R.; Pomelli, C.; Ochterski, J. W.; Ayala, P. Y.; Morokuma, K.; Voth, G. A.; Salvador, P.; Dannenberg, J. J.; Zakrzewski, V. G.; Dapprich, S.; Daniels, A. D.; Strain, M. C.; Farkas, O.; Malick, D. K.; Rabuck, A. D.; Raghavachari, K.; Foresman, J. B.; Ortiz, J. V.; Cui, Q.; Baboul, A. G.; Clifford, S.; Cioslowski, J.; Stefanov, B. B.; Liu, G.; Liashenko, A.; Piskorz, P.; Komaromi, I.; Martin, R. L.; Fox, D. J.; Keith, T.; Al-Laham, M. A.; Peng, C. Y.; Nanayakkara, A.; Challacombe, M.; Gill, P. M. W.; Johnson, B.; Chen, W.; Wong, M. W.; Gonzalez, C.; Pople, J. A. *Gaussian 03; Revision E.01 ed.*; Gaussian, Inc.: Wallingford, CT, 2008.

(18) (a) Xidos, J. D.; Li, J.; Hawkins, G. D.; Winget, P.; Zhu, T.; Rinaldi, D.; Liotard, D. A.; Cramer, C. J.; Truhlar, D. G.; Frisch, M. J. *MN-GSM-version 99.8*; University of Minnesota: Minneapolis, 2001. (b) Olson, R. M.; Marenich, A. V.; Chamberlin, A. C.; Kelly, C. P.; Thompson, J. D.; Xidos, J. D.; Li, J.; Hawkins, G. D.; Winget, P.; Zhu, T.; Rinaldi, D.; Liotard, D. A.; Cramer, C. J.; Truhlar, D. G.; Frisch, M. J. *MN-GSM-2008*; University of Minnesota: Minneapolis, 2008.

(19) Anisimov, V.; Paneth, P. *J. Math. Chem.* **1999**, *26*, 75.

(20) (a) Lingwood, M.; Hammond, J. R.; Hrovat, D. A.; Mayer, J. M.; Thatcher Borden, W. *J. Chem. Theory Comput.* **2006**, *2*, 740. (b) Lynch, B.; Truhlar, D. G. *J. Phys. Chem. A* **2001**, *105*, 2936. (c) Ignatyev, I. S.; Sundius, T. *Chem. Phys. Lett.* **2006**, *326*, 101. (d) Baptisto, L.; Bauerfeldt, G. F.; ArbillaG.; Silva, E. C. *J. Mol. Struct. THEOCHEM* **2006**, *761*, 73. (e) Bento, A. P.; Sola, M.; Bickelhaupt, F. M. *J. Chem. Theory Comput.* **2008**, *4*, 929.

(21) Mulliken, R. S. *J. Chem. Phys.* **1955**, *23*, 1833.

(22) Dybala-Defratyka, A.; Szatkowski, L.; Kaminski, R.; Wujec, M.; Siwek, A.; Paneth, P. *Environ. Sci. Technol.* **2008**, *42*, 7744.

(23) Paneth, P. *Acc. Chem. Res.* **2003**, *36*, 120.

CT800412H

JCTC Journal of Chemical Theory and Computation

A Multiscale Treatment of Angeli's Salt Decomposition

Juan Torras,[†] Gustavo de M. Seabra,[‡] and Adrian E. Roitberg[‡]

Departament d'Enginyeria Química, EUETII, Universitat Politècnica de Catalunya, Pça. Rei 15, 08700-Igualada, Spain, and Quantum Theory Project, Departments of Physics and of Chemistry, University of Florida, Gainesville, Florida 32611-8435

Received June 20, 2008

Abstract: Sodium trioxodinitrate's ($Na_2N_2O_3$, Angeli's salt) unique cardiovascular effects have been associated with its ability to yield HNO upon dissociation under physiological conditions. Due to its potential applications in new therapies for heart failure, the dissociation of Angeli's salt has recently received increased attention. The decomposition mechanism has been previously studied by quantum mechanical methods using a continuum approximation (PCM) for the solvent effects. In this work we use our recently developed interface of the Amber and Gaussian packages via the PUPIL package to study Angeli's salt dissociation in a hybrid QM/MM scheme where the water solvent molecules are treated explicitly with classical mechanics while the solute is treated with full quantum mechanics (UB3LYP/6−31+G(d) and UMP2/6−31+G(d)) level. Multiple steered molecular dynamics was used with the Jarzynski relationship to extract the free energy profile for the process. We obtain 4.8 kcal mol^{-1} and 6.4 kcal mol^{-1} free energy barriers for the N−N bond breaking for UB3LYP and UMP2, respectively. The geometries and Mulliken charges for reactant, transition state, and products have been characterized through a number of hybrid QM/MM molecular dynamics runs with the N−N distance restrained to representative values of each species. The results highlight the role of individual solvent molecules for the reaction energetics and provide a comparison point against implicit solvation methods.

Introduction

In aqueous solution and in biological media, Angeli's salt, $Na_2N_2O_3$ (AS, compound **1**, Scheme 1),[3,4] spontaneously decomposes to yield the critical bioregulatory species nitroxyl (HNO/NO^-) and has been widely used in studies of nitroxyl's pharmacological properties.[3−10] Similarities in structures and decomposition rates of Angeli's salt and NO donors such as diethylamine-NO ($Na[Et_2NN(O)NO]$, DEA/NO) have allowed comparison between the properties of NO and HNO, revealing that, although some of pharmacological HNO properties are similar to that of NO,[5,6] the cardiovascular effects elicited by HNO are often distinct.[7,8]

The suggested mechanism for the decomposition of Angeli's salt at physiological pH is believed to involve the protonation of the dianion $N_2O_3^{2-}$ on the NO oxygen to form **(2)**, followed by tautomerization into **(3)** and heterolytic cleavage of the N−N bond releasing HNO **(4)** and NO_2^- **(5)**, as depicted in Scheme 1 [the numbering in (**3**) shows the convention adopted here].

The dissociation of Angeli's salt in anaerobic medium was recently the subject of a thorough quantum mechanical study at the B3LYP/6−311+G(d) level of theory by Houk et al.,[1] where the aqueous solvation energies were estimated by single point calculations with implicit water, represented by the Polarizable Continuum Model (PCM),[9−12] on the vacuum-optimized B3LYP/6−311+G(d) structures and applied to the gas-phase energies. Some key structures were also reoptimized with PCM and the same basis set. The results of that breakthrough work support the mechanism depicted in Scheme 1 at physiological pH. The free energy barrier for the N−N bond cleavage step was computed as 6.0 kcal/mol in vacuum, changing to 7.8 kcal/mol when the structures are reoptimized with PCM.[1] A later experimental and theoretical study of AS decomposition in aerobic conditions concluded

* Corresponding author e-mail: roitberg@ufl.edu.
[†] Universitat Politècnica de Catalunya.
[‡] University of Florida.

10.1021/ct800236d CCC: $40.75 © 2009 American Chemical Society
Published on Web 12/12/2008

Scheme 1. Proposed Mechanism for Angeli's Salt Decomposition Pathway in Anaerobic Media

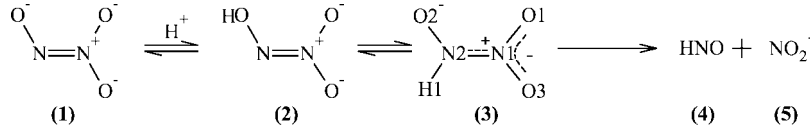

that interaction with O_2 is likely to occur only after the N−N bond breakage.[7]

In the previous work, the free energies were obtained by performing a standard vibrational frequency and thermochemistry analysis, which yields the thermal energy corrections to enthalpies and free energies. Thermochemical quantities are calculated from the partition function using the equations for noninteracting particles (ideal gas) in the canonical ensemble, such as described in statistical thermodynamics textbooks.[13] The solvent effects were included by using the Polarizable Continuum solvent Model (PCM) which has the advantage of greatly reducing the size of the system by approximating the bulk solvent by a homogeneous dielectric continuum polarizable by the solute, which is placed in a molecular-shaped cavity.[9−12] The computational speedup however comes at the price of neglecting the atomistic nature of the solvent, and the solvent configurational sampling is assumed to be implicit, ignoring local anisotropies around the solute. The basic assumption of continuum models is the notion that the implicit part of the system (solvent) is well described by the bulk dielectric constant. This also assumes that the structure and dynamics of individual solvent molecules can be neglected. This assumption obviously fails for the first solvation shells and especially in the case of ionic compounds. Evidently the choice of the system to be treated as the solute is then critical, and recent studies indicate that, in some cases, inclusion of explicit solvent molecules treated at the same level of theory as the solute of interest may be required.[14,15]

Other alternatives for the inclusion of solvent effects that explicitly take into consideration the structure of the solvent include the use of molecular mechanics (MM) methods for configurational sampling, followed by full QM calculations on snapshots taken from the MM trajectories, with the solvent molecules included as point charges. An example of this strategy are the MD/QM[16,17] and MC/QM[18−22] methods which use classical force fields and Molecular Dynamics (MD) or Monte Carlo (MC) for configurational sampling, respectively. Implicit in those methods, however, is the assumption of reasonable overlap between the conformational space sampled by the QM and MM potential energy surfaces.

Another possibility, which is the method of choice in the present study, is the use of hybrid QM/MM simulations, where a sampling method such as MD[23,24] or MC[25,26] is used as before, but the energy is calculated by dividing the system into two parts: a small section containing the portion of interest (solute) and treated by quantum mechanics, plus the remainder of the system (e.g., solvent) treated using classical force fields. The MD or MC equations are then propagated on this hybrid QM/MM surface.

Since a QM calculation is required at every MD or MC step, most implementations of QM/MM use semiempirical quantum Hamiltonians, such as the native QM/MM support present in the latest version of the MD program AMBER (Amber 9).[27−29] (With the exception of fully quantum methods such as Car−Parrinello[30] or Born−Oppenheimer Molecular Dynamics,[31,32] the complexity of those methods, however, limits the size of the system that can be accurately treated.) These semiempirical methods have the shortcoming of yielding unpredictable results if the system differs significantly from the molecules present in the parametrization set. For more unusual molecules a full QM method may be necessary, and interfaces have been designed between MM and QM programs for that purpose, such as ChemShell,[33] QoMMMa,[34] and, more recently our own, the PUPIL package,[2,35] developed initially in the Materials Science field for the integration of arbitrary molecular dynamics and quantum mechanics programs.[36,37]

We have recently reported[2] interfaces of the PUPIL package with the widely used programs Gaussian[38] (for quantum mechanics) and Amber[27,39] (Molecular Dynamics). The advantage of the PUPIL implementation lies in the fact that the software packages communicate directly and exclusively with the PUPIL interface: Whenever forces are needed for the QM atoms during the MD calculation, AMBER requests those from PUPIL, which then uses the QM program of choice (Gaussian03 in the present case) to calculate those forces and communicate them back to AMBER. Since each package is an independent unit, it is possible to use any method available in either package.

In the present work we report the application of the Gaussian/PUPIL/Amber interface for the study of the Angeli's salt dissociation (Scheme 1) in explicit water, avoiding the shortcomings of implicit solvation models. The N-protonated Angeli's salt (**3**) is treated quantum mechanically and immersed in a box of classical TIP3P[40] water molecules. The Free Energy Profile for the N−N bond cleavage is calculated by Multiple Steering Molecular Dynamics,[41,42] which is implemented in AMBER. The present results are compared to previous calculations[1] to show the relevance of explicit consideration of solvent molecules.

Theory

QM/MM. In the hybrid QM/MM scheme[23,24] used here the system is partitioned in two regions: a quantum mechanical (QM) region comprising a small number of atoms relevant to the specific problem being treated and a classical mechanics (MM) region with all the remaining atoms. The final Hamiltonian for such system can be written as

$$\hat{H} = \hat{H}^{QM} + \hat{H}^{MM} + \hat{H}^{QM/MM} \quad (1)$$

where $\hat{H}^{QM}$ is the Hamiltonian for the QM part, calculated using the QM program and method of choice, and $\hat{H}^{MM}$ is the Hamiltonian for the MM part, calculated by the MM program using the usual force field equations. The remaining

term, $\hat{H}^{QM/MM}$, describes the interaction between the QM and MM parts and typically contains terms for electrostatic, van der Waals, and bonded interactions across the region boundaries:

$$\hat{H}^{QM/MM} = \hat{H}^{QM/MM}_{vdW} + \hat{H}^{QM/MM}_{elect} + \hat{H}^{QM/MM}_{bonded} \quad (2)$$

In PUPIL's QM/MM implementation, the $\hat{H}^{QM/MM}_{vdW}$ term is calculated as usual by the MM program, using the standard 12−6 Lennard-Jones in eq 3, and parameters derived from the force field in use for both the QM and MM atoms. It has been shown that the use of the MM parameters in this interaction does not introduce significant errors in the calculation.[43]

$$E^{QM/MM}_{vdW} = \sum_{\alpha}^{QM}\sum_{A}^{MM}\left[\frac{A_{\alpha A}}{R^{12}_{\alpha A}} - \frac{B_{\alpha A}}{R^{6}_{\alpha A}}\right] \quad (3)$$

The electrostatic interaction between the QM and MM regions can be divided in two parts. First, the influence of the MM atoms on the QM zone is taken into account by electronic embedding: The MM atoms are passed to the QM program as point charges fixed at their respective positions, using the charge values from the force field parameters. Second, the force contribution from the quantum atoms to the total force acting upon each classical atom (F^{QM}_i) is needed. Gaussian03 uses a fast multipole method to evaluate the effect of the external charges onto the QM system, allowing for a very fast calculation. However, this formalism does not allow us to compute the forces from the QM region onto the MM charges. In the present implementation these forces are obtained after the QM calculation by projecting the obtained electronic density into a grid (a Gaussian Cube file) and calculating the interaction of the MM charge with each point in the grid as in

$$F^{QM}_i = \sum_{j}^{N_{cube}} \mathbf{r_{ij}} \frac{q_{PC_i} dq_j}{|r_{ij}|^3} \quad (4)$$

where q_{PC_i} is the MM point charge, N_{cube} is the total number of electron density points, and

$$dq_j = \rho_j dx dy dz \quad (5)$$

defines an individual volume element on the electron density grid.

If covalent bonds cross the boundaries of the QM/MM system PUPIL can use a link atom approach,[44] where a new quantum particle (link atom) is introduced along the bond between the QM and MM region at a specific distance, usually around 1 Å, in order to satisfy valence requirements. The approach used by PUPIL has been described in more detail elsewhere.[2]

Free Energies via Multiple Steering Molecular Dynamics. The accurate calculation of the free-energy change along the chemical reaction path remains a challenge, and different methods have been developed to deal with this issue.[24,42,45−68] The multiple steering molecular dynamics (MSMD) method relates a system's nonequilibrium dynamics to its equilibrium properties and has been described in more detail elsewhere,[41,42,59,69−72] so only a short summary is presented here.

Consider a system subject to an external time-dependent perturbation [$\lambda=\lambda(t)$] and described by the Hamiltonian $H(\mathbf{r},\lambda)$. Writing $\Delta G(\lambda)$ as the free energy change and $W(\lambda)$ as the external work performed on the system as it evolves from an initial to a final state ($\lambda_0 \rightarrow \lambda$), the free energy and work are connected by the Jarzynski relationship[42]

$$e^{-\beta\Delta G(\lambda)} = \langle e^{-\beta W(\lambda)} \rangle \quad (6)$$

where the brackets represent an average taken over an ensemble of molecular dynamics trajectories starting at different snapshots extracted from an equilibrated ensemble at the initial distance. It is important to note that eq 6 assumes a converged average, which is formally true only with an infinite number of process realizations. In practical applications standard deviations up to a few kT are considered acceptable (see, for example, ref 61), and the error in ΔG can be estimated by

$$\Delta G \approx \langle W \rangle - \frac{\beta}{2}\sigma^2_W \quad (7)$$

which is just the result of a cumulant expansion of eq 6[42] and is the same as the fluctuation−dissipation relation obtained earlier by Hermans.[73]

Also, the equilibrium average of a state function can similarly be extracted from the nonequilibrium ensemble by[69,70]

$$\langle F(\lambda) \rangle_{eq} = \frac{\langle F(\lambda) e^{-\beta W(\lambda)} \rangle_{non-eq}}{\langle e^{-\beta W(\lambda)} \rangle_{non-eq}} \quad (8)$$

The time-dependent Hamiltonian $H(\mathbf{r},\lambda)$ can be written as the sum of the time-independent Hamiltonian for the unperturbed system, $H_0(\mathbf{r})$, and a time-dependent external perturbation, which here is chosen as a harmonic potential whose minimum moves at a constant velocity, v. Representing the chosen reaction path as $\lambda(\mathbf{r})$, one can write

$$H(\mathbf{r},\lambda) = H_0(\mathbf{r}) + \frac{1}{2}k[\lambda(\mathbf{r}) - \lambda_0 - vt]^2 \quad (9)$$

The free energy of a process along the chosen reaction coordinate can then be calculated by performing a large number of simulations, each being one independent realization of the process and starting from a different snapshot extracted from an ensemble initially equilibrated at $\lambda=\lambda_0$ and then properly averaging the resulting work values as described in eq 6.

Computational Methods. Due to the computational demands of the QM methods applied here, a scheme was devised to avoid long equilibrations at the QM level, which involved the equilibration of the system in a sequence of steps of increasing complexity. According to this scheme, the system was first equilibrated and brought to 300 K by fully classical molecular dynamics and then relaxed at the approximated density functional SCC-DFTB[74] level. Finally, the initial structures chosen for the pulling simulations were further relaxed at the final UB3LYP/6−311G(d,p)and UMP2/6−311G(d,p) levels.

Parameters for the Angeli's Salt. Even though the Angeli's salt is to be treated quantum mechanically classical parameters are still needed since in the PUPIL system the

MD program has no knowledge of the quantum system and the parameter arrays still need to be correctly filled, and also because classical MD simulations are performed in the initial relaxation. Those parameters are not used for the final analysis, where the solute is treated with full quantum mechanics.

Starting from the published coordinates from Dutton et al.[1] (a07, supplemental information), the Antechamber[27] program was used in conjunction with DIVCON[75−77] to generate General Amber Force Field (GAFF)[78] parameters for the Angeli's salt, using AM1-BCC[79,80] charges. All those programs are part of the standard Amber distribution.[27]

System Preparation. The system was comprised of one molecule of the N-protonated Angeli's salt **(3)**, one Na^+ ion added to neutralize the system, and a total of 2388 water molecules (TIP3P),[40] under periodic boundary conditions. This system was first subjected to 10,000 minimization steps, using the MM Hamiltonian to remove any clashes, and then heated to 300 K during 100 ps at constant volume. A time step of 1.0 fs and using a Langevin thermostat with a 2.0 ps^{-1} collision frequency were used. Finally, the system was allowed to relax for an additional 100 ps at constant pressure (1 atm) with a pressure relaxation time of 1 ps, still using a fully MM Hamiltonian. All of these steps used the SHAKE algorithm to restrain bonds containing hydrogen.[81] Next, the solute (**3**) was made quantum, to be treated with the approximated Self-Consistent-Charge Density-Functional Tight-Binding SCC-DFTB method,[74,82] which we recently implemented in the Amber package,[28] and the remainder of the system (water molecules plus Na^+ ion) was treated classically. The system was then relaxed again (using Amber's native QM/MM implementation[28,29]) for another 50 ps with constant volume, then 500 ps constant pressure, and the same parameters as for the fully classical steps. At this point, the system was considered to be sufficiently equilibrated, and another 2 ns run at constant volume was used to extract the average N−N distance, r_{eq} (1.29 Å).

Generation of an Equilibrated Initial Ensemble (Forward Reaction). The Jarzynski equality assumes that all pulling processes start from structures belonging to the same initial equilibrated ensemble. To generate the initial structures, the N−N distance was restrained to a number slightly smaller than r_{eq} by applying a harmonic potential centered at 1.27 Å with a large force constant (2500 kcal mol^{-1} $Å^{-2}$) and run a 3 ns QM/MM simulation using the SCC-DFTB Hamiltonian for the solute, extracting 20 structures from the last 2 ns. Finally, we run another 1000 steps of MD using the Amber/PUPIL/Gaussian interface to treat the Angeli's salt as quantum at a much more computationally expensive level, the unrestricted form of Becke's 3-parameter hybrid functional[83] (UB3LYP) with the 6−311+G(d)[84,85] basis set, as implemented in Gaussian, while the rest of the system is treated by MM, so that the starting structures are consistent with this level of theory.

Multiple Steered Molecular Dynamics (MSMD). Forward Reaction. With the structures properly equilibrated at the initial distance, the N−N bond in each structure was broken using the Amber/PUPIL/Gaussian interface by running independent simulations starting from each of the 20 structures obtained as described above, treating the solute (**3**) at the UB3LYP/6−311+G(d) level. In each simulation, a harmonic potential with a large force constant (5000 mol^{-1} $Å^{-2}$) is applied, and the center of the potential is moved from 1.27 to 4.0 Å at a 0.5 Å/ps or 5460 MD steps of 1.0 fs.

Table 1. Bond Distances and Free Energies Obtained from Multiple Steered Molecular Dynamics (MSMD) UB3LYP/6-311+G(d) for the Cleavage of the N−N Bond[a]

species	pulling direction	N−N distance (Å)	ΔG (kcal/mol)
reactant	forward	1.332	0.0
	reverse	1.343	0.0
	average	1.338	0.0
	Dutton et al.[1]	1.311	0.0
transition state	forward	1.676	4.77
	reverse	1.696	4.86
	average	1.686	4.81
	Dutton et al.[1]	1.768	7.8
products	forward	4.0	−3.78

[a] The maximum standard deviation is 2.94 kcal/mol for the reaction and 1.3 kcal/mol at the transition state.

Reverse Reaction. From the 20 final structures obtained in the pulling from reactants to products, one structure was chosen. The system is then restrained at the final distance (4.0 Å) and re-equilibrated for 3 ns using SCC-DFTB for the solute from which 20 new structures were extracted from the final 2 ns to generate an equilibrated ensemble at the final N−N separation. These 20 structures were again thermalized using the full DFT method for 1000 steps (2 ps) and then pulled in the direction of the reverse reaction, i.e., to reform the N−N bond, following the same procedure as described above.

Radial Distribution Functions. The N−N distances of 1.34 Å, 1.69 Å, and 4.00 Å were chosen as representatives of the reactants, transition state, and products (see Table 1). For those geometries, better statistics were obtained by choosing one snapshot at the desired N−N distance from each of the ten runs described for the forward reaction, and this was used as the starting configuration for a 10 ps MD run with the solute treated at the UB3LYP/6−311+G(d) level, with the N−N distance restrained to the respective value by a force constant of 5000 kcal mol^{-1} $Å^{-2}$. After the runs, the various trajectory files corresponding to each distance were combined to yield a total of 100 ps MD trajectory for the calculation of the Radial Distribution Functions (RDFs), averaged geometries, and atomic Mullkien charges.

Results and Discussion

As detailed in the previous section, the equilibrium N−N distance at the SCC-DFTB/TIP3P level was determined during equilibration to be around 1.29 Å. In order to obtain a clear minimum in Free Energy, the pulling started at a slightly smaller distance (1.27 Å) and was stopped at an N−N distance of 4.0 Å. The set of 20 pulling realizations yielded the distribution of work values shown in Figure 1 (**a**: forward, **b**: reverse reaction.) The work is set to zero at the initial simulation distance. There is a large spread in work values toward the end of the process, which is due to the finite pulling speed: at the limit of infinitely small pulling

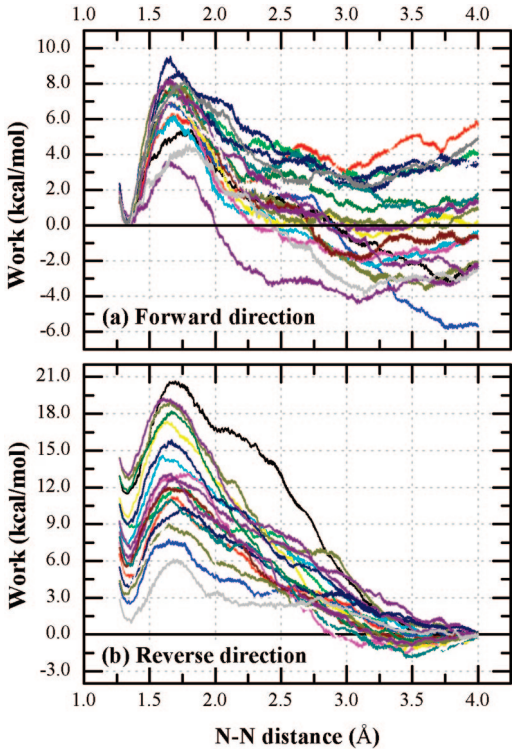

Figure 1. Work values (kcal/mol) obtained from the various realizations of the forward (a) and reverse (b) processes. The position of the zero was chosen as the reactants minimum in (a) and the products in (b).

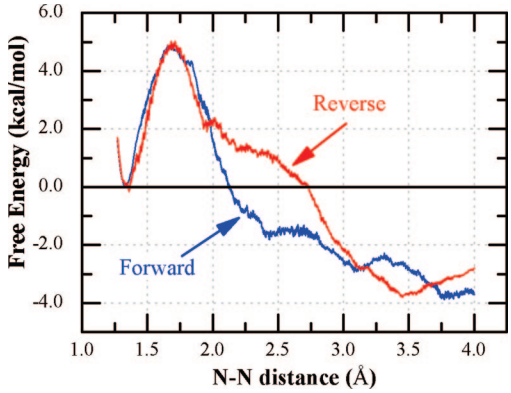

Figure 2. Free energy changes (in kcal/mol) for the breaking of the N−N bond (forward process, blue) and forming the N−N bond (reverse process, red), obtained with the Angeli's salt treated at the UB3LYP/6−311+G(d) level. Each curve is the average of 20 process realizations according to eq 6.

speeds all work curves should be congruent. The maximum standard deviation occurs close to the end points of the simulations, being around 2.94 kcal/mol for the reaction (∼4.9*RT*) and just ∼1.3 kcal/mol (∼2.18*RT*) at the transition state.

The work values were averaged according to eq 6 to yield the Free Energy change as a function of N−N distance depicted in Figure 2. The free energy profiles for the forward and reverse reactions agree extremely well for N−N distances from 1.23 Å to around 1.8 Å, yielding basically the same geometries for transition state and reactant and the same activation energy. At larger distances some hysteresis can be noted between the forward and backward pulling

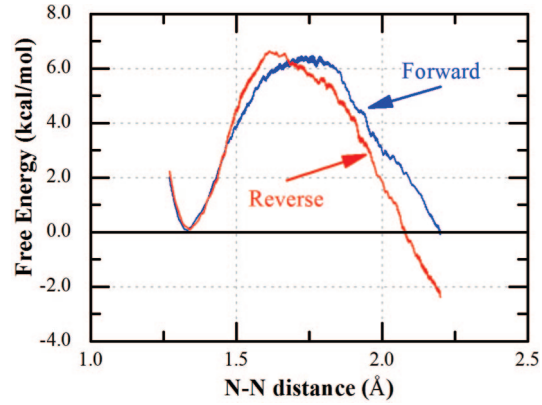

Figure 3. Free energy changes(in kcal/mol) for the breaking of the N−N bond(forward process, blue) and forming the N−N bond(reverse process, red), obtained with the Angeli's salt treated at the UMP2/6−311+G(d) level. Each curve is the average of 10 process realizations according to eq 6.

curves which can be attributed to a high pulling velocity for a charged system in an explicit water study, where the water molecules need larger relaxation times to adjust to the changing AS geometries, especially when the N−N bond is almost broken.[86] However, the free energy at the final pulling distance (∼4.0 Å) is essentially the same. The energetic data are shown in Table 1, together with results from previous calculations by Dutton et al.[1] using PCM (implicit) solvation. The distances extracted from the multiple steered molecular dynamics (MSMD) calculations are very close to the ones obtained from implicit solvation. The interaction with explicit water molecules slightly weakens the N−N bond as compared to the PCM solvation, as indicated by the facts that the N−N distance at the reactant is slightly larger (+0.03 Å) and that the transition state is reached at a smaller N−N separation (−0.1 Å) in the explicit solvent case. The difference in energies is more notable, and the presence of the explicit solvent molecules stabilizes the transition state by ∼3 kcal/mol (about 38%) compared to the PCM results. (It is important to notice that the referred PCM results include zero point energy and thermal corrections to 298 K which lower the reaction barrier by 1.80 kcal/mol. Such corrections are not explicitly included in our calculations. One can argue that while an MD derived potential of mean force includes at least part of the thermal component to the free energy, it is clear that this does not include quantized vibrations.)

Those calculations were also repeated using second order Møller−Plesset perturbation theory (MP2)[87] for the quantum region but with only 10 realizations of the process in each direction (Figure 3). The results indicate a slightly larger barrier than predicted with UB3LYP (∼6.5 kcal/mol) but still lower than the PCM results. Previous studies have shown that B3LYP generally underestimates reaction barriers by about 4 kcal/mol, while MP2 calculations can *over*estimate the same barrier by up to 6 kcal/mol.[88−90] To the best of our knowledge, there is no experimental barrier height estimate for this particular reaction. Although these barrier height errors can in principle be reduced by the use of a larger basis set, one of the previous studies has shown that, already with the 6−31+(G) basis set, the B3LYP functional can provide results with accuracy similar to the one obtained with the aug-cc-pVTZ basis set,[89] which

Table 2. Bond Distances in Å and Angles in Degrees (± Standard Deviation) for the Different Species from AS Dissociation[a]

	reactant			transition state			products	
coordinate	This work	(a)	(b)	This work	(a)	(b)	This work	(c)
O1−N1	1.252 ± 0.026	1.247	1.260	1.227 ± 0.026	1.223	1.223	1.260 ± 0.029	1.265
O3−N1	1.282 ± 0.029	1.278	1.280	1.234 ± 0.026	1.244	1.233	1.260 ± 0.029	1.265
N1−N2	1.338 ± 0.010	1.344	1.311	1.686 ± 0.009	1.637	1.768	4.000 ± 0.008	-
O2−N2	1.312 ± 0.031	1.299	1.303	1.294 ± 0.032	1.283	1.279	1.209 ± 0.019	1.200
H1−N2	1.023 ± 0.026	1.022	1.032	1.043 ± 0.029	1.042	1.049	1.060 ± 0.030	1.066
O1−N1−O3	123.9 ± 2.8	124.9	123.3	124.5 ± 3.1	124.6	123.9	116.2 ± 2.6	116.0
O1−N1−N2	119.5 ± 3.0	119.5	119.5	117.1 ± 3.9	117.9	117.1	-	-
O2−N2−N1	124.3 ± 3.6	126.0	124.3	113.6 ± 4.0	115.7	111.6	-	-
O2−N2−H1	120.8 ± 4.3	123.0	122.0	111.2 ± 3.8	112.9	110.8	109.3 ± 3.3	108.6
O1N1N2O2	−0.2 ± 13.2	12.1	−0.2	17.2 ± 14.7	25.2	17.0	-	-
O1N1N2H1	180.4 ± 14.4	171.2	179.9	132.2 ± 17.7	143.0	130.1	-	-
O1N1N2O3	−179.9 ± 7.3	−176.1	−180.0	−166.8 ± 8.6	−164.7	−165.2	-	-

[a] This work: average values and standard deviation from 100 ps MD trajectory using PUPIL/Amber, with the N−N distance restrained to the value shown. Columns marked with (a), (b), or (c) were obtained from the B3LYP/6-311+G(d) optimized structures reported in the supplemental information from Dutton et al.:[1] (a) structures optimized in vacuum; (b) structures optimized in PCM water; and (c) from the nitrite and nitroxyl structures optimized in vacuum.

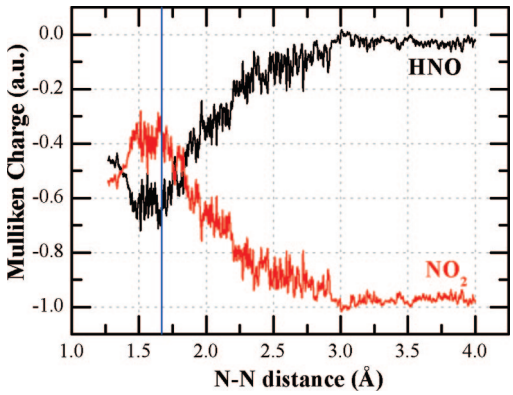

Figure 4. Average charges on the HNO and NO_2 fragments.

indicates that any error in the current calculations is more likely to be intrinsic to the B3LYP method instead of arising from basis set incompleteness issues.

To gain more insight on the nature of the species involved, additional molecular dynamics calculations were performed with the N−N distance restrained to 1.34 Å, 1.69 Å, and 4.00 Å, corresponding respectively to reactant, transition state, and product, and Table 2 compares the geometrical properties of the different species. The values obtained by Dutton et al.[1] are also included as a reference. In general, the values obtained in this work agree well with previous calculations. In most cases, the reoptimization of the vacuum structures in PCM generally brings the distances closer to the ones obtained in explicit water.[1] The largest discrepancies are noted in the N−N distances: the distance for the reactant in explicit water is very similar to the result obtained in vacuum (Δd=0.006 Å) and addition of PCM considerably shortens this distance (Δd=−0.027 Å), while the opposite effect is seen at the transition state where Δd=−0.049 Å is obtained from gas phase calculation and a larger difference (Δd=0.082 Å) under PCM calculations.

Figure 4 shows the Mulliken charge in each fragment (NO_2 in red and HNO in black) as a function of reaction coordinate, averaged from all the forward pullings using eq 8. The blue vertical line marks the N−N distance at the transition state (∼1.67 Å, as determined from the forward reaction). The averaged Mulliken charges for the 100 ps MD trajectory over each atom and moiety are shown in Table 3.

Table 3. Mulliken Charges and Standard Deviation for Different Species from AS Dissociation, Obtained from 100 ps MD Trajectory Using PUPIL/Amber[a]

atom	reactant	transition state	products
O1	−0.27 ± 0.07	−0.19 ± 0.06	−0.33 ± 0.07
N1	0.12 ± 0.08	−0.02 ± 0.00	−0.30 ± 0.07
O3	−0.37 ± 0.07	−0.20 ± 0.06	−0.34 ± 0.07
total	−0.52	−0.41	−0.97
O2	−0.48 ± 0.06	−0.43 ± 0.07	−0.07 ± 0.04
N2	−0.41 ± 0.07	−0.49 ± 0.07	−0.33 ± 0.04
H1	0.41 ± 0.07	0.34 ± 0.04	0.38 ± 0.04
total	−0.48	−0.58	−0.02

[a] The N−N distance has been restrained to 1.338, 1.686, and 4.000 Å for reactant, TS, and products, respectively.

At the N−N equilibrium distance the charge for each moiety is about the same (∼−0.5 au). As the N−N distance increases there's initially a slight polarization in the HNO direction, due to a charge transfer mainly from the NO_2 oxygens to the nitrogens involved in the N−N bond, as seen by the decrease in the (negative) charge from the oxygens and corresponding increase on the nitrogens. After the transition state most of the excess charge in the HNO moiety is transferred to the NO_2 side, and after ∼3 Å the charges at each fragment are stabilized and the bond can be considered broken.

Figure 5 shows the radial distribution functions of water molecules around the solute for the reactant, transition state, and products. It is important to notice that, at an N−N distance of 4.0 Å, the two fragments are still interacting and the HNO hydrogen (H1) tends to form a hydrogen bond to the NO_2 oxygens as shown in Figure 6, in detriment of the H-bond between it and water molecules, which explains the absence of a H-bond structure around H1 in the products (Figure 5a). The H-bond structure also disappears around the HNO oxygen (O2, Figure 5b), due to its reduced charge in the product (Table 3). Since the transition state structure is close to the reactants, one would expect the reactants and TS RDFs

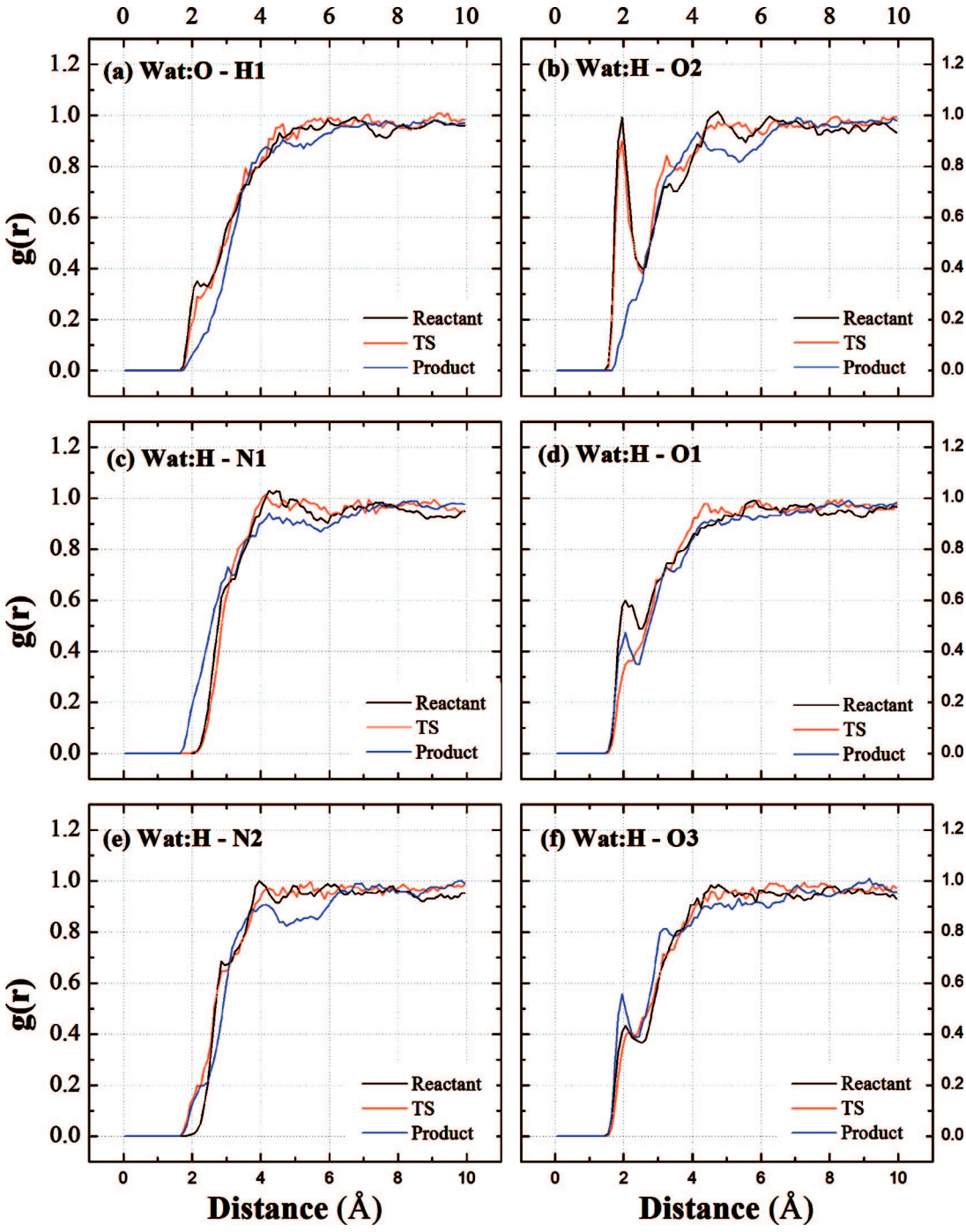

Figure 5. Radial distribution function (RDF) between water and Angeli's salt atoms (AS) for reactants, transition state (TS), and products (HNO,NO_2^-).

to be mostly similar, and this is clearly what happens in most cases. The small change in the RDFs from the reactants to transition states is mainly due to the reduction of charge in those atoms. The most noticeable difference is in Figure 5d. As seen in Table 3, the charge on O1 greatly decreases going from reactants to TS which, together with the fact that the charge in O2 is mostly constant in the same range, explains the absence of the clear H-bond around O1 in the TS. The charge in O1 is then restored in the products, and a new H-bond is formed as shown. A similar hydrogen bond also seems to form with O3 in the product (Figure 5f). Charges over the N1 atom (see Table 3) from NO_2^- product are more negative ($q_{N1}=-0.30$ au) than in the reactant ($q_{N1}=0.12$ au) and from the transition state ($q_{N1}=-0.02$ au). That can easily induce a closer distance between water hydrogen and the N1 atom as it is shown in Figure 5c. The effect of the (negative) charge increase in N2 going from reactant to TS can be noted in Figure 5e, with the water molecules at a slightly shorter distance in the TS.

Conclusions

We have presented a QM/MM study of the Angeli's salt dissociation in explicit water using the recently developed Gaussian/PUPIL/Amber interface, where the Angeli's salt

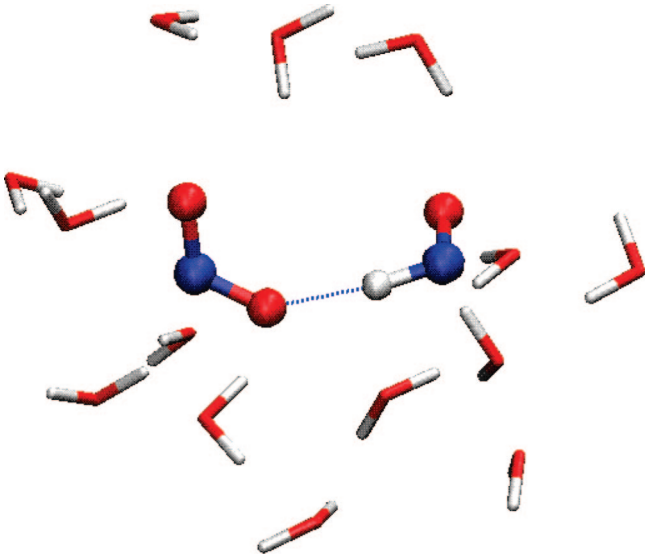

Figure 6. Representative snapshot of the products forming an internal hydrogen bond, extracted from the 100 ps trajectory with the N−N distance restrained to 4.0 Å. For clarity, only the water molecules within 3.5 Å of the solute are shown.

is treated by quantum mechanics at the UB3LYP/6−311+G(d) level and the environment (water and counterion) are treated classically. The multiple steered molecular Dynamics (MSMD) was applied together with the Jarzinsky relationship to determine the free energy change for the reaction. A free energy barrier of 4.81 kcal mol^{-1} is obtained, ∼3 kcal mol^{-1} lower than previously reported by Dutton et al.[1] using an implicit (PCM) representation for the solvent effects, at the same level of quantum calculation. Preliminary calculations using MP2 and the same basis set for the quantum zone show a higher barrier (∼6.5 kcal/mol) but still lower than the previously reported values. The geometries, averaged over the QM/MD trajectory, in general agree with the values reported by Dutton et al.[1]

Acknowledgment. This material is based upon work also supported by the NSF under the following programs: Partnerships for Advanced computational Infrastructure, Distributed Terascale Facility (DFT) and Terascale Extensions: Enhancements to the Extensible Terascale Facility. The authors thank the University of Florida High-Performance Computing Center and Teragrid (Grants TG-MCA05S010 and TG-CHE060072T) for providing computational resources and support. This work was partially funded by grant CHE-0822935 to A.E.R.

References

(1) Dutton, A. S.; Fukuto, J. M.; Houk, K. N. *J. Am. Chem. Soc.* **2004**, *126*, 3795–3800.

(2) Torras, J.; Seabra, G. d. M.; Deumens, E.; Trickey, S. B.; Roitberg, A. E. *J. Comput. Chem.* **2008**, *29*, 1564–1573.

(3) Angeli, A. *Gazz. Chim. Ital.* **1896**, *26*, 17.

(4) Angeli, A. *Gazz. Chim. Ital.* **1903**, *33*, 245–252.

(5) Fitzhugh, A. L.; Keefer, L. K. *Free Radical Biol. Med.* **2000**, *28*, 1463–1469.

(6) Naughton, P.; Foresti, R.; Bains, S. K.; Hoque, M.; Green, C. J.; Motterlini, R. *J. Biol. Chem.* **2002**, *277*, 40666–40674.

(7) Miranda, K. M.; Dutton, A. S.; Ridnour, L. A.; Foreman, C. A.; Ford, E.; Paolocci, N.; Katori, T.; Tocchetti, C. G.; Mancardi, D.; Thomas, D. D.; Espey, M. G.; Houk, K. N.; Fukuto, J. M.; Wink, D. A. *J. Am. Chem. Soc.* **2005**, *127*, 722–731.

(8) Wink, D. A.; Miranda, K. M.; Katori, T.; Mancardi, D.; Thomas, D. D.; Ridnour, L.; Espey, M. G.; Feelisch, M.; Colton, C. A.; Fukuto, J. M.; Pagliaro, P.; Kass, D. A.; Paolocci, N. *Am. J. Physiol. Heart Circ. Physiol.* **2003**, *285*, H2264–2276.

(9) Mierts, S.; Scrocco, E.; Tomasi, J. *J. Chem. Phys.* **1981**, *55*, 117–129.

(10) Tomasi, J.; Persico, M. *Chem. Rev.* **1994**, *94*, 2027–2094.

(11) RCammi, J. T. *J. Comput. Chem.* **1995**, *16*, 1449–1458.

(12) Cossi, M.; Barone, V.; Cammi, R.; Tomasi, J. *Chem. Phys. Lett.* **1996**, *255*, 327–335.

(13) McQuarrie, D. A. *Statistical Thermodynamics*; Harper and Row: New York, 1973.

(14) Kelly, C. P.; Cramer, C. J.; Truhlar, D. G. *J. Phys. Chem. A* **2006**, *110*, 2493–2499.

(15) Kongsted, J.; Mennucci, B. *J. Phys. Chem. A* **2007**, *111*, 9890–9900.

(16) Roitberg, A. E.; Worthington, S. E.; Holden, M. J.; Mayhew, M. P.; Krauss, M. *J. Am. Chem. Soc.* **2000**, *122*, 7312–7316.

(17) Worthington, S. E.; Roitberg, A. E.; Krauss, M. *J. Phys. Chem. B* **2001**, *105*, 7087–7095.

(18) Guedes, R. C.; Coutinho, K.; Costa Cabral, B. J.; Canuto, S. *J. Phys. Chem. B* **2003**, *107*, 4304–4310.

(19) Rocha, W. R.; Martins, V. M.; Coutinho, K.; Canuto, S. *Theor. Chem. Acc.* **2002**, *108*, 31–37.

(20) Rocha, W. R.; Coutinho, K.; de Almeida, W. B.; Canuto, S. *Chem. Phys. Lett.* **2001**, *335*, 127–133.

(21) Coutinho, K.; Saavedra, N.; Serrano, A.; Canuto, S. *THEOCHEM* **2001**, *539*, 171–179.

(22) Rocha, W. R.; De Almeida, K. J.; Coutinho, K.; Canuto, S. *Chem. Phys. Lett.* **2001**, *345*, 171–178.

(23) Field, M. J.; Bash, P. A.; Karplus, M. *J. Comput. Chem.* **1990**, *11*, 700–733.

(24) Warshel, A.; Levitt, M. *J. Mol. Biol.* **1976**, *103*, 227–249.

(25) Gao, J.; Xia, X. *Science* **1992**, *258*, 631–635.

(26) Gao, J. *J. Phys. Chem.* **1992**, *96*, 537–540.

(27) Case, D. A.; Darden, T. A.; Cheatham, T. E., III; Simmerling, C. L.; Wang, J.; Duke, R. E.; Luo, R.; Crowley, M.; Walker, R. C.; Zhang, W.; Merz, K. M.; Wang, B.; Hayik, S.; Roitberg, A.; Seabra, G.; Kolossváry, I.; Wong, K. F.; Paesani, F.; Vanicek, J.; Wu, X.; Brozell, S. R.; Steinbrecher, T.; Gohlke, H.; Yang, L.; Tan, C.; Mongan, J.; Hornak, V.; Cui, G.; Mathews, D. H.; Seetin, M. G.; Sagui, C.; Babin, V.; Kollman, P. A. *AMBER 10*; University of California: San Francisco, 2008.

(28) Seabra, G. M.; Walker, R. C.; Elstner, M.; Case, D. A.; Roitberg, A. E. *J. Phys. Chem. B* **2007**, *111*, 5655–5664.

(29) Walker, R. C.; Crowley, M. F.; Case, D. A. *J. Comput. Chem.* **2008**, *29*, 1019–1031.

(30) Car, R.; Parrinello, M. *Phys. Rev. Lett.* **1985**, *55*, 2471.

(31) Schlegel, H. B.; Millam, J. M.; Iyengar, S. S.; Voth, G. A.; Daniels, A. D.; Scuseria, G. E.; Frisch, M. J. *J. Chem. Phys.* **2001**, *114*, 9758–9763.

(32) Pulay, P.; Fogarasi, G. *Chem. Phys. Lett.* **2004**, *386*, 272–278.

(33) Sherwood, P.; de Vries, A. H.; Guest, M. F.; Schreckenbach, G.; Catlow, C. R. A.; French, S. A.; Sokol, A. A.; Bromley, S. T.; Thiel, W.; Turner, A. J.; Billeter, S.; Terstegen, F.; Thiel, S.; Kendrick, J.; Rogers, S. C.; Casci, J.; Watson, M.; King, F.; Karlsen, E.; Sjovoll, M.; Fahmi, A.; Schafer, A.; Lennartz, C. *THEOCHEM* **2003**, *632*, 1–28.

(34) Harvey, J. N. *Faraday Discuss.* **2004**, *127*, 165–177.

(35) Torras, J.; Deumens, E.; Trickey, S. B.; Cheng, H.-P.; Cao, C.; He, Y.; Muralidharana, K.;Roitberg, A. E.; Seabra, G. M. *University of Florida Quantum Theory Project*; 2008.

(36) Torras, J.; Deumens, E.; Trickey, S. B. *J. Comput.-Aided Mater. Des.* **2006**, *13*, 201–212.

(37) Torras, J.; He, Y.; Cao, C.; Muralidharana, K.; Deumens, E.; Cheng, H.-P.; Trickey, S. B. *Comput. Phys. Commun.* **2007**, *177*, 265–279.

(38) Frisch, M. J.; Trucks, G. W.; Schlegel, H. B.; Scuseria, G. E.; Robb, M. A.; Cheeseman, J. R. Montgomery, J. A., Jr.; Vreven, T.; Kudin, K. N.; Burant, J. C.; Millam, J. M.; Iyengar, S. S.; Tomasi, J.; Barone, V.; Mennucci, B.; Cossi, M.; Scalmani, G.; Rega, N.; Petersson, G. A.;Nakatsuji, H.; Hada, M.; Ehara, M.; Toyota, K.; Fukuda, R.; Hasegawa, J.; Ishida, M.; Nakajima, T.; Honda, Y.; Kitao, O.; Nakai, H.; Klene, M.; Li, X.; Knox, J. E.; Hratchian, H. P.;Cross, J. B.; Bakken, V.; Adamo, C.; Jaramillo, J.; Gomperts, R.; Stratmann, R. E.; Yazyev, O.;Austin, A. J.; Cammi, R.; Pomelli, C.; Ochterski, J. W.; Ayala, P. Y.; Morokuma, K.; Voth, G. A.; Salvador, P.; Dannenberg, J. J.; Zakrzewski, V. G.; Dapprich, S.; Daniels, A. D.; Strain, M. C.; Farkas, O.; Malick, D. K.; Rabuck, A. D.; Raghavachari, K.; Foresman, J. B.; Ortiz, J. V.; Cui, Q.; Baboul, A. G.; Clifford, S.; Cioslowski, J.; Stefanov, B. B.; Liu, G.; Liashenko, A.; Piskorz, P.; Komaromi, I.; Martin, R. L.; Fox, D. J.; Keith, T.; Al-Laham, M. A.; Peng, C. Y.;Nanayakkara, A.; Challacombe, M.; Gill, P. M. W.; Johnson, B.; Chen, W.; Wong, M. W.;Gonzalez, C.; Pople, J. A. Gaussian, Inc.: Wallingford, CT,2004.

(39) Case, D. A.; Cheatham, T. E., III; Darden, T.; Gohlke, H.; Luo, R.; Merz, K. M., Jr.; Onufriev, A.; Simmerling, C.; Wang, B.; Woods, R. J. *J. Comput. Chem.* **2005**, *26*, 1668–1688.

(40) Jorgensen, W. L. *J. Am. Chem. Soc.* **1981**, *103*, 335–340.

(41) Xiong, H.; Crespo, A.; Marti, M.; Estrin, D.; Roitberg, A. *Theor. Chem. Acc.* **2006**, *116*, 338–346.

(42) Jarzynski, C. *Phys. Rev. Lett.* **1997**, *78*, 2690–2693.

(43) Riccardi, D.; Li, G.; Cui, Q. *J. Phys. Chem. B* **2004**, *108*, 6467–6478.

(44) Senn, H. M. ; Thiel, W. In *Atomistic Approaches in Modern Biology*; M. R., Ed.; Springer: Berlin, 2007; Vol. *268*, pp 173−290.

(45) Truhlar, D. G.; Gao, J.; Alhambra, C.; Garcia-Viloca, M.; Corchado, J.; Sanchez, M. L.; Villa, J. *Acc. Chem. Res.* **2002**, *35*, 341–349.

(46) Gao, J.; Truhlar, D. G. *Annu. Rev. Phys. Chem.* **2002**, *53*, 467–505.

(47) Hu, H.; Lu, Z.; Yang, W. *J. Chem. Theory Comput.* **2007**, *3*, 390–406.

(48) Major, D. T.; Gao, J. *J. Chem. Theory Comput.* **2007**, *3*, 949–960.

(49) Gunaydin, H.; Acevedo, O.; Jorgensen, W. L.; Houk, K. N. *J. Chem. Theory Comput.* **2007**, *3*, 1028–1035.

(50) Bowman, A. L.; Ridder, L.; Rietjens, I. M. C. M.; Vervoort, J.; Mulholland, A. J. *Biochemistry (Moscow)* **2007**, *46*, 6353–6363.

(51) Valiev, M.; Garrett, B. C.; Tsai, M.-K.; Kowalski, K.; Kathmann, S. M.; Schenter, G. K.; Dupuis, M. *J. Chem. Phys.* **2007**, *127*, 051102-–4.

(52) Rosta, E.; Klahn, M.; Warshel, A. *J. Phys. Chem. B* **2006**, *110*, 2934–2941.

(53) Christen, M.; Kunz, A.-P. E.; van Gunsteren, W. F. *J. Phys. Chem. B* **2006**, *110*, 8488–8498.

(54) Marsili, S.; Barducci, A.; Chelli, R.; Procacci, P.; Schettino, V. *J. Phys. Chem. B* **2006**, *110*, 14011–14013.

(55) Riccardi, D.; Schaefer, P.; Yang, Y.; Yu, H.; Ghosh, N.; Prat-Resina, X.; Konig, P.; Li, G.; Xu, D.; Guo, H.; Elstner, M.; Cui, Q. *J. Phys. Chem. B* **2006**, *110*, 6458–6469.

(56) Wales, D. J.; Bogdan, T. V. *J. Phys. Chem. B* **2006**, *110*, 20765–20776.

(57) Claeyssens, F.; Harvey, J. N.; Manby, F. R.; Mata, R. A.; Mulholland, A. J.; Ranaghan, K. E.; Schütz, M.; Thiel, S.; Thiel, W.; Werner, H.-J. *Angew. Chem., Int. Ed.* **2006**, *45*, 6856–6859.

(58) Kastner, J.; Thiel, W. *J. Chem. Phys.* **2005**, *123*, 144104–5.

(59) Roitberg, A. E. *Annu. Rep. Comp. Chem.* **2005**, *1*, 103–111.

(60) Li, G. H.; Zhang, X. D.; Cui, Q. *J. Phys. Chem. B* **2003**, *107*, 8643–8653.

(61) Park, S.; Khalili-Araghi, F.; Tajkhorshid, E.; Schulten, K. *J. Chem. Phys.* **2003**, *119*, 3559–3566.

(62) Kumar, S.; Rosenberg, J. M.; Bouzida, D.; Swendsen, R. H.; Kollman, P. A. *J. Comput. Chem.* **1995**, *16*, 1339–1350.

(63) Roux, B. *Comput. Phys. Commun.* **1995**, *91*, 275–282.

(64) Kumar, S.; Rosenberg, J. M.; Bouzida, D.; Swendsen, R. H.; Kollman, P. A. *J. Comput. Chem.* **1992**, *13*, 1011–1021.

(65) Torrie, G. M.; Valleau, J. P. *J. Comput. Phys.* **1977**, *23*, 187–199.

(66) Mulholland, A. J. *Drug Discovery Today* **2005**, *10*, 1393–1402.

(67) Warshel, A. *Computer Modeling of Chemical Reactions in Enzymes and Solution*; Wiley: New York, 1991.

(68) Woods, C. J.; Manby, F. R.; Mulholland, A. J. *J. Chem. Phys.* **2008**, *128*, 014109–8.

(69) Crooks, G. E. *Phys. Rev. E* **2000**, *61*, 2361.

(70) Hummer, G.; Szabo, A. *Proc. Natl. Acad. Sci. U.S.A.* **2001**, *98*, 3658–3661.

(71) Collin, D.; Ritort, F.; Jarzynski, C.; Smith, S. B.; Tinoco, I.; Bustamante, C. *Nature (London)* **2005**, *437*, 231–234.

(72) Cuendet, M. A. *J. Chem. Phys.* **2006**, *125*, 144109–12.

(73) Hermans, J. *J. Phys. Chem.* **1991**, *95*, 9029–9032.

(74) Elstner, M. *Theor. Chem. Acc.* **2006**, *116*, 316–325.

(75) Dixon, S. L.; Merz, J. K. M. *J. Chem. Phys.* **1996**, *104*, 6643–6649.

(76) Yang, W.; Lee, T.-S. *J. Chem. Phys.* **1995**, *103*, 5674–5678.

(77) Dixon, S. L.; Merz, J. K. M. *J. Chem. Phys.* **1997**, *107*, 879–893.

(78) Wang, J.; Wolf, R. M.; Caldwell, J. W.; Kollman, P. A.; Case, D. A. *J. Comput. Chem.* **2004**, *25*, 1157–1174.

(79) Jakalian, A.; Bush, B. L.; Jack, D. B.; Bayly, C. I. *J. Comput. Chem.* **2000**, *21*, 132–146.

(80) Jakalian, A.; Jack, D. B.; Bayly, C. I. *J. Comput. Chem.* **2002**, *23*, 1623–1641.

(81) Ryckaert, J.-P.; Ciccotti, G.; Berendsen, H. J. C. *J. Comput. Phys.* **1977**, *23*, 327–341.

(82) Otte, N.; Scholten, M.; Thiel, W. *J. Phys. Chem. A* **2007**, *111*, 5751–5755.

(83) Becke, A. D. *J. Chem. Phys.* **1993**, *98*, 5648–5652.

(84) Frisch, M. J.; Pople, J. A.; Binkley, J. S. *J. Chem. Phys.* **1984**, *80*, 3265–3269.

(85) Krishnan, R.; Binkley, J. S.; Seeger, R.; Pople, J. A. *J. Chem. Phys.* **1980**, *72*, 650–654.

(86) GonzalezLebrero, M. C.; Estrin, D. A. *J. Chem. Theory Comput.* **2007**, *3*, 1405–1411.

(87) Møller, C.; Plesset, M. S. *Phys. Rev.* **1934**, *46*, 618.

(88) Zhao, Y.; Gonzalez-Garcia, N.; Truhlar, D. G. *J. Phys. Chem. A* **2005**, *109*, 2012–2018.

(89) Riley, K. E.; Op'tHolt, B. T.; Merz, K. M. *J. Chem. Theory Comput.* **2007**, *3*, 407–433.

(90) Sousa, S. F.; Fernandes, P. A.; Ramos, M. J. *J. Phys. Chem. A* **2007**, *111*, 10439–10452.

CT800236D

JCTC Journal of Chemical Theory and Computation

Extracting Kinetic and Stationary Distribution Information from Short MD Trajectories via a Collection of Surrogate Diffusion Models

Christopher P. Calderon*,† and Karunesh Arora‡

Department of Computational and Applied Mathematics and Department of Statistics, Rice University, Houston, Texas 77005-1892, and Department of Chemistry, Biophysics Program, University of Michigan, 930 North University Avenue, Ann Arbor, Michigan 48109

Received July 17, 2008

Abstract: Low-dimensional stochastic models can summarize dynamical information and make long time predictions associated with observables of complex atomistic systems. Maximum likelihood based techniques for estimating low-dimensional surrogate diffusion models from relatively short time series are presented. It is found that a heterogeneous population of slowly evolving conformational degrees of freedom modulates the dynamics. This underlying heterogeneity results in a collection of estimated low-dimensional diffusion models. Numerical techniques for exploiting this finding to approximate skewed histograms associated with the simulation are presented. In addition, statistical tests are used to assess the validity of the models and determine physically relevant sampling information, e.g. the maximum sampling frequency at which one can discretely sample from an atomistic time series and have a surrogate diffusion model pass goodness-of-fit tests. The information extracted from such analyses can possibly be used to assist umbrella sampling computations as well as help in approximating effective diffusion coefficients. The techniques are demonstrated on simulations of adenylate kinase.

1. Introduction

A significant understanding of complex biomolecules like proteins and nucleic acids has been obtained through the use of low-dimensional equations approximating the dynamics of these systems.[1,2] Single-molecule experiments and computer simulations are allowing researchers to better understand the physics governing complex biomolecular systems at small length and time scales.[1−16] Advances in nanotechnology are starting to demand higher accuracy from stochastic dynamical approximations of small biomolecular systems. Fortunately, the time series associated with current experiments and simulations contain a rich amount of information related to molecular motion occurring over a broad range of time scales.[17] However, the presence of a wide range of relevant time scales significantly complicates determining reliable low-dimensional models associated with small scale, but highly complex systems.[18−21] We refer to such approximate models as "surrogate" models; some authors use the term "effective model" in a similar context.[20−22]

In single-molecule experiments, researchers can usually only monitor and/or manipulate a small number of observable quantities that describe the system. This is because simultaneously tracking the position and velocity of many atoms in a system at the same time is very challenging experimentally. Experiments usually do have the luxury of being able to directly measure quantities associated with longer time scales of physical interest, e.g. it is sometimes possible to monitor a protein unfold and refold nearly quasi-statically.[23] On the other hand, atomistic simulations provide detailed descriptions of the dynamics (i.e., monitoring the position and velocity of every particle is possible) but encounter computational limitations. Perhaps the most serious being the small time step size enforced by numerical stability

* Corresponding author e-mail: calderon@rice.edu.
† Rice University.
‡ University of Michigan.

10.1021/ct800282a CCC: $40.75 © 2009 American Chemical Society
Published on Web 11/24/2008

considerations. Current simulations can only reasonably explore $\approx \mathcal{O}(ns) - \mathcal{O}(\mu s)$ length trajectories in all-atom MD simulations of biomolecules[17,24] due to the time step constraint. Rapid advances in experiments and simulations are likely to further facilitate making comparisons between these two information sources and using both to refine/construct surrogate models.[25−28]

We present surrogate models which can approximate both simulation[29,30] and experimental time series,[31,32] but the focus here is exclusively on simulation data. Throughout, we refer to quantities monitored in our time series as "system observables" (SOs). "Pathwise" statistical methods are used to estimate diffusion models from observed time series. We use the term "pathwise" simply to refer to situations where all statistical inference procedures (estimation, hypothesis tests, etc.) are applied to a single time series. We use all-atom MD simulations to generate multiple trajectories (i.e., a batch of time series). We estimate the parameters of a new surrogate model for each observed time series as opposed to aggregating the time series together to estimate the parameters of a single model. We demonstrate surrogate models which can account for state-dependent noise. This has relevance to several systems because it is known that when a high-dimensional system is summarized with a small number of SOs, that the noise magnitude often varies as a function of the SO.[3,18,29,30,33−36] The information in the surrogate diffusion models can also be related to the effective friction experienced by a particular SO in different portions of phase space.[30,32,37−39] The methods presented make heavy use of recent developments in statistical testing and modeling[29,30,34,40−44] to assess the validity of the estimated models and quantitatively learn about the various multiscale noise sources. For example, we analyze histograms of a root-mean-square-displacement (rmsd) type SO and determine how much variability is due to traditional thermal noise and that introduced by conformational heterogeneity. The former is usually associated with fast-scale motions whose details are not of interest and the latter with slow-scale collective motions.

Besides quantifying the contributions of various noise sources to the observed variability of the SO, the collection of estimated models can be also be used to help traditional physical chemistry computations. For example, they can be used to reduce the variance of equilibrium statistics and can also be used to quantify how certain factors influence the dynamics and stationary distributions of SOs. This is relevant because it is known that conformational degrees of freedom often can cause skewed distributions of low-dimensional SOs. Correlating information accessible in the laboratory with that in computer simulations has the potential to help in various computational chemistry tasks.[15,31,45−49]

Our techniques are demonstrated on short (525 ps) constrained umbrella sampling trajectories of the enzyme adenylate kinase.[50,51] It is shown that surrogate models, calibrated from observational data, can be used to predict and/or refine approximations of stationary distributions associated with a selected SO. The particular SO studied is related to known "open" and "closed" crystal structures of the enzyme.[51] We demonstrate that the diffusion coefficient[52] can be approximated using the surrogate models and that confidence bands for this quantity can be constructed using a single short time trajectory. We demonstrate that these estimates can be obtained with much less data than traditional approaches used in MD.[24,52,53] We also show that an experimentally accessible[49] slowly evolving conformational coordinate correlates with the surrogate model parameters. In this system, taking the state-dependence of the noise magnitude into account[29,30,33,35−37] as well as the underlying conformational heterogeneity is shown to be important to faithfully approximate the complex high-dimensional atomistic simulation using low-dimensional surrogate diffusion models. The Supporting Information provides results demonstrating that the same ideas can be applied to approximate the SO associated with longer (10−50 ns length) unconstrained molecular dynamics of the so-callled "Engrailed Homeodomain".[54]

The article is organized as follows: Section 2 provides a theoretical background reviewing our basic motivation and some established results from statistical physics. This background helps in physically interpreting the information contained in the collection of surrogate diffusion models we attempt to fit from observations. This section also presents the statistical methods we employ and contains a discussion illustrating how the information extracted from the methods can help computational physical chemistry. Section 3 provides the MD simulation details. Section 4 presents the numerical results and Section 5 concludes.

2. Theoretical Background

2.1. Data-Driven Multiscale Stochastic Modeling. The basic idea of using "short bursts" of simulation times series to estimate effective dynamical models motivated the types of methods we propose.[20,55,56] We obtain the parameters of surrogate diffusion models[29,30] from observed time series using maximum likelihood type (ML) techniques. The type of modeling we propose would fall under the label of a "data-driven" modeling procedure. Several other researchers are developing data-driven methods for describing various complex systems ranging from molecular dynamics to weather forecasting.[20,29,30,33,56−59] The basic idea behind a data-driven description is to assimilate information contained in empirical observations, either simulation or experiment, coming from a complex high-dimensional system into a surrogate model.

If accurate surrogate models can be calibrated from short time series, then these models can be used for a variety of purposes, e.g. they can be used to simulate sample paths for longer time intervals than those accessible to the MD simulation. Other applications are discussed in Section 4. These basic ideas are not new to chemical physics, and it is well-known that the multiple time scales associated with the underlying complex process significantly complicates these types of tasks.[18,21,60] Our main contributions to this type of endeavor are associated with showing how modern time series analysis tools can be used to help in quantitatively determining some "coarse-graining" parameters and also determine the goodness-of-fit of surrogate models in a

pathwise fasion. We also demonstrate how a *collection* of low-dimensional models can be used to study various all-atom simulations and single-molecule experiments where certain collective degrees of freedom are associated with slow time scales and influence the estimated surrogate models.[30,31,61,62] The motivation for using a collection of simple low-dimensional models as opposed to more complicated high-dimensional models as surrogates is discussed in detail in ref 61 and in the Conclusions.

2.2. Generalized Langevin Equations. The generalized Langevin equation (GLE) has been used to describe the evolution of certain MD trajectories.[21] Although we do not utilize this structure in our models, we introduce it here because several analogies can be drawn to the modeling methods we introduce and can aid in the physical interpretation of our procedure. A generic GLE typically takes the form

$$\dot{\Phi} = F(\Phi) + \int_0^t \mathrm{K}(\Phi(t-s), s)ds + \sqrt{2k_BT}N(t) \qquad (1)$$

where k_BT is Boltzmann's constant multiplied by the system temperature, Φ is the vector of SOs the modeler wishes to dynamically track, a dot above a variable denotes the time derivative, $F(\cdot)$ represents the *Markovian* contribution to the dynamics,[19,21] $N(\cdot)$ represents the "orthogonal noise" coming from degrees of freedom not explicitly resolved in the model,[19] and $K(\cdot,\cdot)$ denotes the so-called "memory kernel". $K(\cdot,\cdot)$ is usually interpreted as a *non-Markovian* contribution to the dynamics. The specific functional form of the memory kernel and the orthogonal noise can, in principle, be determined once the full system dynamics are specified using the Mori-Zwanzig projection operator formalism.[19,21] The orthogonal noise is typically constructed to have a zero mean over ensembles, and its value depends on the initial conditions of all degrees of freedom in the system. For a single realization, the orthogonal dynamics can slowly evolve making the "noise" term appear to be a systematic bias when viewed over short time scales of a single trajectory. Observations of this nature motivated the authors in ref 63 to use a long-memory (fractional Gaussian) process to describe the orthogonal noise observed in experimental data tracking a protein's slow conformational dynamics.

The AdK system studied is also associated with slow conformational dynamics. However, the surrogate models we propose attempt to approximate $F(\Phi) + \int_0^t K(\Phi(t-s), s)ds$ using a Markovian term $\mu(\Phi)$ and use a fairly simple noise process (standard Brownian motion). One of the surrogate models attempts to utilize the so-called "overdamped approximation".[38] The term "overdamped" is meant to refer to the fact that a particle has a position and velocity, but knowledge of the velocity is not needed to accurately approximate the statistical properties of the particle position. This is a temporal coarse-graining procedure commonly used in statistical physics.[18,38] It has been labeled as somewhat *ad hoc* because it requires quantitative knowledge of the time that one needs to wait between adjacent observations for such an approximation to be valid, and this selection is usually based on intuitive physical arguments as opposed to precise mathematical criteria.[21] We demonstrate that down-sampling (or subsampling)[30,60] ideas along with statistical hypothesis tests[42,44,64] can be used to help put a quantitative handle on an overdamped approximation. We refer to fast-scale noise which may induce short time memory as "fast-scale memory" throughout the text. Velocity is one possible source, but others like vibrational motion would contribute to this type of fast-scale memory. The modeling of slow conformational degrees of freedom is more subtle. This article focuses on modeling the output of MD simulations, so producing time series where a long-memory process of the type given in ref 63 can be estimated is somewhat problematic. This is because in simulations it is difficult to sample for a large temporal amount, so the fitted parameters of a long-memory process would likely contain substantial uncertainty. To approximate the variability induced by slowly evolving conformational degrees of freedom in relatively short time series we use a *collection* of surrogate models. We expand on this point throughout the text.

2.3. Time Scale Separation in System Observables. If the $K(\cdot,\cdot)$ in eq 1 is zero everywhere and the noise process is a standard Gaussian white-noise process with "Dirac-delta time correlation", then this is commonly written as a diffusion type stochastic differential equation (SDE).[65] SDEs have a rich history[66] in the physical sciences; early studies focused primarily on analyzing properties of Fokker−Planck type partial differential equation (PDE) associated with the stochastic process as opposed to the SDE. We utilize the SDE view, sometimes called the pathwise view,[21] because we feel it facilitates connecting the physics to the estimated surrogate models.

The data-driven modeling methods we propose assume that the effective dynamics[21] of the underlying high-dimensional atomistic simulations can be accurately captured by a small set of SOs whose dynamics are governed by the following system of SDEs

$$\begin{aligned} d\Phi &= \alpha(\Phi, \mathcal{O})dt + \sqrt{2}\sigma(\Phi, \mathcal{O})dW_t^1 \\ d\mathcal{O} &= \beta(\Phi, \mathcal{O})dt + \sqrt{2}\kappa(\Phi, \mathcal{O})dW_t^2 \end{aligned} \qquad (2)$$

where the W_t^i represent standard Brownian motions,[65] Φ represents a "fast-scale" coordinate, and $\mathcal{O}$ represents a "slow-scale" conformational coordinate. We assume that observations are made on a time scale shorter than Φ's characteristic relaxation time and that the dynamics of $\mathcal{O}$ are associated with much "slower" time scales than those of Φ. The functions $\alpha(\cdot,\cdot)$ and $\beta(\cdot,\cdot)$ are referred to as the drift functions, and $\sigma(\cdot,\cdot)$ and $\kappa(\cdot,\cdot)$ are related to the diffusion matrix.[65]

We do not assume that we have the system of SDEs in eq 2 available in closed-form. We only assume that the stochastic dynamics of the higher-dimensional atomistic system can be accurately approximated by this system of SDEs (i.e., evolution rules are more complicated than eq 2). Recall that the data-driven approach we use attempts to estimate effective dynamical equations from time series. If a scale separation exists, the dimension of the SDE system can often be reduced.[21,22,55,66] This can significantly facilitate estimation of a surrogate model. Traditional SDE model reduction techniques often ignore the details of the "fast" component and focus on describing the details of the "slow" component's evolution.[21,55,67,68] In our notation, the modeler

would treat Φ as a "noise" and focus on stochastic dynamical models that explicitly model $\mathcal{C}$. We do the opposite, namely we estimate a scalar SDE of the form

$$d\Phi = \mu^{\mathcal{C}}(\Phi)dt + \sqrt{2}\sigma^{\mathcal{C}}(\Phi)dW_t^1 \quad (3)$$

to the SO time series. Recall we assume that our time series observations are spaced by a time shorter than the relaxation time of Φ (and hence *much* shorter than that of $\mathcal{C}$). If we additionally assume that the local noise, κ, of the slow coordinate $\mathcal{C}$ is small, then this coordinate will not have time to appreciably change in a short time simulation. $\mathcal{C}$ can be treated as an effective constant that modulates the drift and noise functions observed, e.g. $\mu^{\mathcal{C}}(\cdot) \equiv \mu(\cdot, \mathcal{C})$, $\sigma^{\mathcal{C}}(\cdot) \equiv \sigma(\cdot, \mathcal{C})$.

However, a wide range of $\mathcal{C}$ are explored, albeit slowly, at "thermodynamic" equilibrium (i.e. the stationary distribution). [Note that the underlying system maybe biased, as in umbrella sampling simulations, but we still refer to the stationary state as "thermodynamic" equilibrium.] Ideally, the computational cost associated with a standard long time integration would be moderate so that observing substantial changes in both effective fast and slow components would be possible. In this case, we would attempt to either estimate the system given in eq 2 directly or use more traditional time scale separation techniques.[21,22,55,67] With longer times series, we could also entertain using a single more complicated model[63] attempting to capture slow fluctuations and relate this to a memory kernel. Unfortunately, due to computational limitations, generating long time trajectories is problematic in many complex all-atom systems. We propose methods that estimate a collection of SDEs of the form given in eq 3. The initial conformation of each MD simulation is drawn randomly from an equilibrium ensemble, so each different time series trajectory is associated with a different $\mathcal{C}$ value. We demonstrate how to use this collection to assist in computations commonly encountered in physical chemistry. Note carefully that the system of SDEs approximating the dynamics in eq 3 is usually much smaller in dimension than the full atomistic system. By only modeling one component (Φ), we are applying an additional reduction to the system of SDEs. Reduction of this sort introduces the collection of surrogate model phenomenon we discuss throughout.

Before providing specific details of the assumed surrogate models, we would like to comment on the process we used for assigning "fast" and "slow" variables in AdK. In ref 51, there was interest in generating stationary histograms associated with a coordinate quantifying the difference in rmsd of intermediate conformations with respect to the open and closed enzyme states (in what follows we simply call this distance "rmsd type"). Dynamically monitoring this rmsd type quantity in the laboratory is not currently feasible. There were FRET measurements available providing information about a distance between dye labeled residues Lys145 and Ile52.[49] These particular residues were chosen since they lie in two domains of AdK that undergo the largest conformational change between the open to closed state of AdK and help detect functionally relevant motion.[51] In our simulations we do not directly attempt to manipulate this residue distance despite its physical relevance; it has been shown that this residue distance explores a wide range of values but does so slowly with respect to the time scale of simulations.[51] As a result we used the rmsd type distance as Φ and the distance between the center of mass of residues Lys145 and Ile52 as $\mathcal{C}$. In order to enhance sampling of Φ, a harmonic biasing potential was introduced (see Section 3). The biasing potential also made a linear effective force approximation seem more plausible in a surrogate model (later we quantitatively tested this assumption). This biasing potential altered the effective underlying energy landscape and also made the dynamics associated with Φ "faster" in relation to $\mathcal{C}$. Recall we also assumed that the local fluctuation magnitude associated with $\mathcal{C}$ was small. This assumption was due to the fact that collective conformational degrees of freedom do not typically wildly fluctuate in an enzyme.

The above considerations clearly utilized our physical intuition about the system. In general, measurements of fast Φ type coordinates are difficult to accurately monitor and/or control in the laboratory. However, several slowly evolving conformational degrees of freedom can readily be monitored and/or manipulated by novel single-molecule techniques.[3,5−16] We demonstrate that a measurable correlation exists between the selected SOs. The time scale separation between the correlated SOs is exploited in the methods we report. This is one way in which simulation predictions can be compared to experimental observations.[51]

However, we would like to note that selecting coordinates having a large time scale separation can be difficult if physical intuition alone is used. The problem is even harder if the interest is in analyzing unconstrained simulations. General, data-driven procedures for identifying "good" variables where a significant time scale separation exists is challenging but would be of great help in studying systems where physical intuition is lacking.[69,70] In addition, other more sophisticated types of multiscale approximations can be applied to SDEs like those in eq 2 using less restrictive assumptions about the dynamics.[21,56,68,71]

2.4. Proposed Functional Form of Surrogate SDE Models. For every observed time series, we proposed two model structures to use along with eq 3, namely

$$\text{Model 1}: \mu^{\mathcal{C}}(\Phi) = (A + \mathrm{B}(\Phi - \Phi_0)),\ \sigma^{\mathcal{C}}(\Phi) = C \quad (4)$$

$$\text{Model 2}: \mu^{\mathcal{C}}(\Phi) = \frac{\sigma^{\mathcal{C}}(\Phi)^2}{k_B T}(A + \mathrm{B}(\Phi - \Phi_0)),\ \sigma^{\mathcal{C}}(\Phi) = (C + D(\Phi - \Phi_0)) \quad (5)$$

where Φ_0 corresponds to a user specified point [For example, this could coincide with the constraint point of an US simulation[51] or the mean value of the observed time series. We use the latter in this article.], and $\theta \equiv (A, B, C, D)$ are parameters (D is only used in Model 2). Model 1 is known as the Ornstein-Uhlnebeck (OU) model. The drift function can readily be interpreted as coming from a harmonic potential connected to a heat bath whose fluctuations are independent of the state. Model 2 explicitly utilizes the overdamped (OD) Langevin approximation[18,29,30,38] and also takes the noise magnitude's dependence on the current state into account using a relatively simple model. The estimated parameters can be interpreted as local approximations of the

effective force and effective local diffusion coefficient. [Note that if the dynamics can be approximated by the OD model above and the noise magnitude is truly constant, then the parameters of the two different estimated surrogate models can be directly compared and the difference should only be due to different sampling uncertainty magnitudes associated with the parametrization used.]

2.5. Fitting and Testing the Surrogate Models. For discretely sampled time series, the maximum likelihood estimator attempts to find the parameter vector maximizing the logarithm of the joint density associated with the observations, $\log(p(\Phi_0, \Phi_1,..., \Phi_N; \theta))$, where subscripts denote the time index of the observations. The parameter yielding this maximum is denoted by $\hat{\theta}$. For general SDEs, obtaining $\hat{\theta}$ analytically is problematic because the joint density cannot usually be expressed in closed-form. The OU model is appealing because it does admit a closed-form expression for the ML parameter estimate and also yields some other useful diagnostic information. For example, an asymptotic expression for the parameter covariance can be obtained.[43] For the case where we cannot obtain the ML estimate in closed-form, we appeal to approximate likelihood methods.[40,41] Both ML approximation methods previously cited yielded similar $\hat{\theta}$ values in the cases explored. A url link to MATLAB scripts illustrating how to obtain $\hat{\theta}$ for both the OU and OD models given a time series is provided in the Supporting Information.

The "Q test-statistic" developed in ref 42 is used to check the validity of the assumed surrogate model. This test is designed to check for temporal dependencies which are atypical for an assumed model. We demonstrate that it can be used to detect if fast-scale memory effects are statistically significant. The test is also appealing because it applicable to both stationary and nonstationary signals. This test also provides us with physically relevant coarse-graining information. We demonstrate how we can use this test to determine the appropriate frequency at which data can be discretely sampled from a simulation and provide a diffusion model which is not rejected by a hypothesis test. If one is willing to make a stationarity assumption about the time series, more powerful tests can be used.[44,64] We demonstrate that the "T_3" test statistic of ref 64 is useful in assessing the accuracy of a stationary density predicted using a short simulation burst. This test is shown to have better power than the Q-test.

2.6. Computing the Stationary Density Associated with Scalar SDEs. Under mild regularity conditions, the stationary density, denoted by $p^{EQ}(\Phi; \mathcal{O})$, associated with a scalar diffusion model given in eq 3 can be expressed in closed-form using only information contained in the estimated SDE coefficient functions via the relation[72,73]

$$p^{EQ}(\Phi;\mathcal{O}) = \frac{Z}{(\sigma^{\mathcal{O}}(\Phi))^2}\int_{\Phi_{\mathrm{REF}}}^{\Phi} \exp(\mu^{\mathcal{O}}(\Phi')/(\sigma^{\mathcal{O}}(\Phi'))^2)d\Phi' \quad (6)$$

where Z is a constant used to ensure that the density integrates to unity, and Φ_{REF} is a specified constant used as a "reference point". It is assumed that the diffusion process obtained by the ML estimate admits a well-behaved stationary density. [Technical difficulties can be encountered when evaluating $p^{EQ}(\Phi; \mathcal{O})$ if one allows the diffusion coefficient to take a zero value (especially relevant to the OD model). Careful selection of Φ_{REF} along with using a finite support can help in numerically dealing with this issue. However, one must be careful to ensure that all regions of non-negligible probability are accounted for in the finite support. SDE simulation can be used to assist in this type of task. Alternatively, one can modify $\sigma^{\mathcal{O}}$ to smoothly approach a minimum value >0 and use an infinite support for $p^{EQ}(\Phi; \mathcal{O})$.] Recall that for each time series, we estimate a new set of parameters and hence a new SDE of the form given in eq 3. The different trajectories each have unique conformational state initial conditions (i.e. different $\mathcal{O}$ values) in the underlying detailed atomistic simulations. Each of these estimated models can be used to compute a "stationary" density resulting in a collection of "stationary" densities. Quotes are used in the previous sentence because in each short times series burst the value of $\mathcal{O}$ is effectively fixed and the Φ coordinate fluctuates about a fixed point. $\mathcal{O}$ determines this fixed point as well as the shape of the "stationary" density of Φ. The thermodynamic stationary distribution ($\equiv \Pi^{EQ}$) needs to account for the variability inherent in $\mathcal{O}$. Due to the slow time scale associated with this coordinate, it is difficult to exhaustively sample phase space in a single simulation trajectory. If we somehow had access to a closed-form expression describing the (thermodynamic) probability density of $\mathcal{O}$, denoted by $f(\cdot)$ [We simply assume that this density exists and is statistically independent of the Φ variable. Including dependence on Φ is in principle possible, but the time scale separation is large enough to make this coupling fairly weak in the particular systems studied.], we could integrate this quantity out using

$$\Pi^{EQ}(\Phi) := \int p^{EQ}(\Phi;\mathcal{O})f(\mathcal{O})d\mathcal{O} \approx \frac{1}{N}\sum_{i=1}^{N} p_i^{EQ}(\Phi;\mathcal{O}_i) \quad (7)$$

The right-hand-side of the above represents a Monte Carlo approximation of the continuous integral to the left. N represents the number of time series batches used to calibrate N different surrogate models describing Φ's dynamics. $\mathcal{O}_i$ denotes the temporal average value of $\mathcal{O}$ observed in time series batch i. The subscript i on p_i^{EQ} denotes using the invariant density obtained for Φ associated with $\mathcal{O}_i$ (using eq 6 for each estimated SDE). To more systematically overcome the conformational sampling barrier, one could attempt to generate initial conformations utilizing more sophisticated equilibrium sampling methods.[24,53] We demonstrate such sampling strategies are not necessary to obtain accurate results in the systems studied here but may be useful in other applications.

Effectively we are modeling the more complex distribution $\Pi^{EQ}(\Phi)$ using a mixture of simpler densities. This mixture modeling can also be given a physical interpretation. The thermal noise for a fixed value of $\mathcal{O}$ induces a certain amount of variability in the SO of interest; for each single SDE "i" this can be quantified using $p_i^{EQ}(\Phi; \mathcal{O}_i)$. The variability induced by conformational heterogeneity can be quantified by looking at how disjointed a *collection* of $\{p_i^{EQ}(\Phi; \mathcal{O}_i)\}_{i=1}^{N}$ is relative to the average quantity. [To do so one must have an estimate of the inherent uncertainty associated with a finite length discrete time series used to estimate the parameters.]

2.7. Relation to Computational Chemistry. One interest in this paper is in approximating the global stationary histogram associated with a Φ type coordinate using a small amount of MD time series. Two complications are commonly encountered: (1) Time correlation in MD trajectories can complicate constructing reliable estimates due to statistical dependence,[74] and (2) dynamics induced by "orthogonal coordinates" can induce skewed (non-Gaussian) distributions in the stationary histogram associated with the fast SO of interest. Such skewed distributions are commonly encountered in both experiments and simulations when a low-dimensional SO is modulated by a diverse population of conformational degrees of freedom not explicitly included in the model.[46−48]

Knowledge of the shape of such global stationary distributions is important in a variety of applications, e.g. in umbrella sampling type applications one needs to ensure a high degree of overlap between adjacent sampling windows,[51,74] and knowledge of the skewed histogram shape can help one in refining the grids used in such computations. The non-Gaussian shape of a work histogram is also important in nonequilibrium free energy computations.[30,47] We demonstrate that our modeling procedures, utilizing a collection of SDE models, can help in predicting such shapes and treat the two issues listed in the above paragraph. We also demonstrate that the time scale separation between the fast-time scale coordinate Φ and the slow conformational coordinate $\mathcal{O}$ influences kinetic quantities of interest such as the diffusion coefficient.[33,52]

3. Simulation Details

We assign $\Phi \equiv \Delta D_{rmsd}$ (difference in rmsd of the instantaneous structures from the reference open and closed crystal structure of the enzyme) and $\mathcal{O} \equiv$ the distance between mass centers of residues Ile-52 and Lys-145 characterizing the dynamics of large-scale conformational transitions in AdK (see ref 51 for details). This distance type SO has also been measured in solution using single molecule FRET experiments by Henzler-Wildman et al.[49]

As detailed in ref 51, the initial path between the open and closed conformations of AdK was generated using the Nudged Elastic Band (NEB) method.[75] Subsequently, 81 configurations obtained from NEB path optimization, separated by the interval of 0.2 Å in ΔD_{rmsd} space, were subjected to US simulations. During these US simulations, production dynamics of 525 ps at 300 K was performed from each configuration with a weak restraint of 10 kcal/mol/Å^2 in ΔD_{rmsd} (the specified target SO value in each window is denoted by ΔD^0_{rmsd}). No restraints were applied along the conformational SO, ($\mathcal{O}$). Solvent effects were modeled implicitly using GBMV approximation[76] in CHARMM.[77]

For further statistical analysis, 50−100 restrained trajectories of 525 ps in length each were performed from the seven starting conformations along the path corresponding to the ΔD^0_{rmsd} values of (measured in Å) −5.79, −3.67, −0.01, 1.38, 3.30, 5.34, and 7.02. All trajectories were subjected to similar restraint of 10 kcal/mol/Å^2 along ΔD_{rmsd} but were started with the different initial velocities, assigned randomly. The time series of ΔD_{rmsd} and distance $\mathcal{O}$ were extracted from the trajectories (sampled every 0.15 ps) and used in analysis below.

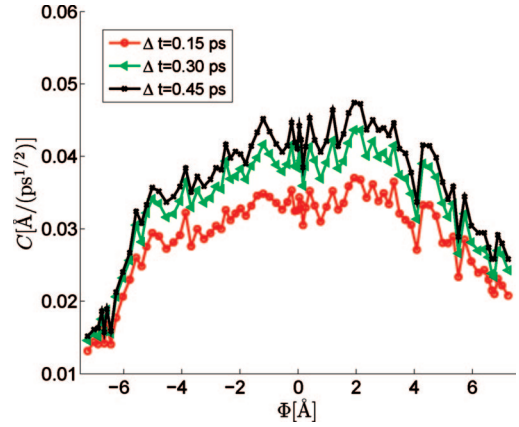

Figure 1. The C parameter of the Ornstein-Uhlenbeck process was estimated using short time series from 81 different (independent) US windows. The values estimated are denoted by symbols, and the purpose of the line connecting the points is only to guide the eye. Each parameter estimate came from a time series containing 350 uniformly spaced entries. Three different ds values were used. The corresponding time Δt between observations is reported in the legend.

4. Results

4.1. Parameter Estimates and Goodness-of-Fit Tests. The ML parameters of the OU model were obtained at each of the 81 different US windows. The measured noise magnitude (C) depends significantly on the value of Φ. This is demonstrated in Figure 1. Parameter estimates were obtained using three different down-sampling (or subsampling) parameters.[60] The down-sampling parameter is an integer represented by "*ds*". Knowledge of this parameter is related to temporal coarse-graining; it determines the amount of time used to "average out" certain fast-scale non-Markovian memory effects.[18,21,34,56,68,71] To get a better physical understanding of this quantity, suppose one is numerically integrating a high-dimensional chaotic deterministic Hamiltonian system using a constant time-step size δt. The output of a discrete error-free integration would be the sequence $\{p_i\}$ where $p_i \equiv -\int_{i\delta t}^{(i+1)\delta t} \nabla_q \mathcal{H}(t)dt$ (using notation from classical mechanics). If we attempted to fit a diffusion approximation directly to the sequence $\{p_i\}$, it would likely fail because the fast-scale chaotic motion has not had sufficient time to "mix" and the noise is not a "white noise process" (i.e., temporal correlations exist in the fast-scale noise[67]). Alternatively, if we used the sequence $\{p_i^{ds}\}$ where, $p_i^{ds} \equiv -\int_{i(ds\times\delta t)}^{(i+1)(ds\times\delta t)} \nabla_q \mathcal{H}(t)dt$, the chaotic motion would have more time to "mix" and would make a diffusion model more plausible. The surrogate models estimated from our MD simulations, although inherently stochastic due to the Langevin thermostat, still exhibit dependence on the down-sampling because systematic forces associated with fast-scale memory still need time to average out.

Next we demonstrate how surrogate models calibrating from short time simulations can be tested for goodness-of-fit. An US point ($\Delta D_{rmsd} = 7.02$) exhibiting significant state

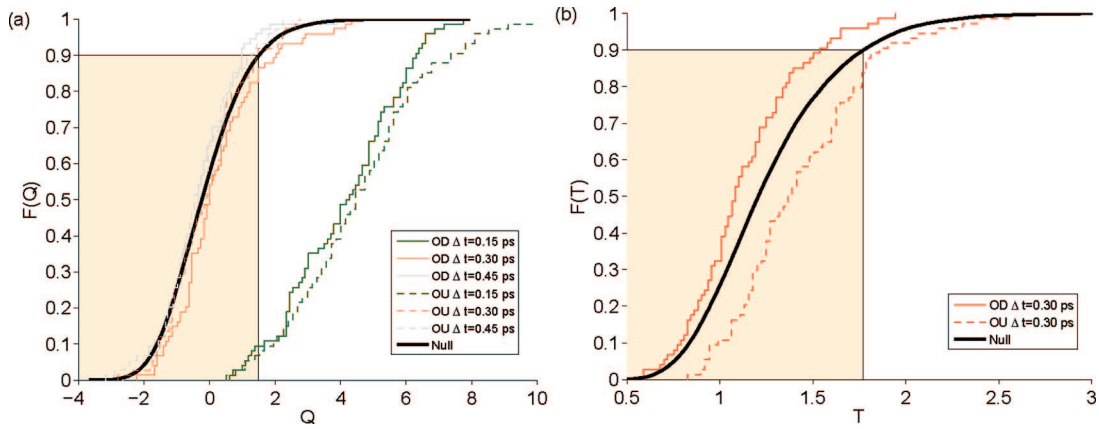

Figure 2. Hypothesis test results. In each panel, the staircase plots correspond to the empirical distribution function (EDF) of the test statistics obtained from batches of 75 time series (each using different *d*s values, the corresponding time between observations, Δt, are reported in the legend), and the solid curve corresponds to the distribution of the null computed for a finite sample size of 350 which was the length of each time series analyzed in this plot. The shaded region is used to show the $\alpha = 0.10$ critical value. The percent of models rejected at this level can be found by noting the point on the *x*-axis where a color change occurs (denote by x_{crit}) and then evaluating 1-EDF(x_{crit}). Panel (a): The Q-test statistic given in ref 42 was applied to determine the time needed to wait between observations before diffusion models can be used to accurately approximate simulation data. The surrogate model parameters were estimated for each path, and then the Q-test statistic was computed using the data and the estimated model. Panel (b): The T_3 test statistic[64] computed using the same estimated parameters and data.

dependence in the noise was analyzed in detail. At this point, 75 MD trajectories were simulated, and Φ was observed every 0.15 *ps* (the interval is much larger than the integration step-size of 1.5 *fs*). For every proposed *ds*, we estimated 75 surrogate model parameter vectors (both OU and OD). A total of three *ds* values were tested ($ds = 1, 2, 3$). The total number of time series observations used to estimate each surrogate parameter vector was fixed to be 350 in each case so the terminal length of the time series depended on *ds*; however, each time series used (regardless of *ds*) started with the same initial observations to maximize the degree of temporal overlap in the Φ time series used in parameter estimation.

We utilized both the "Q-test statistic"[42] and the "T_3 test statistic".[64] It is demonstrated that they both have utility in regards to our applications. Ideal finite sample null distributions associated with a time series size of 350 were obtained using Monte Carlo simulation to generate 1×10^4 samples. This sample size was assumed large enough to obtain accurate continuous cumulative distribution function (CDF) approximation of the null. The relatively small batch size of MD simulation samples led us to treat the distribution associated with the test statistics as empirical distribution functions (EDFs). The reference null distribution and various EDFs are plotted in Figure 2. We shade the plot to highlight the critical region associated with a significance level (α) of 10%. The x-intercept of the shaded region is the critical value associated with this level, and the percentage of rejected models can be obtained by evaluating the EDF at this value and subtracting this result from unity. Although we shade for $\alpha = 10\%$, the plot can be used to to assess any α of interest.

Panel (a) of Figure 2 plots the Q-test results testing both the OD and OU surrogate models using various *ds* parameters. The percentage of test statistics rejected for $ds = 1$, 2, and 3 was roughly 90%, 15%, and 5%, respectively, for the OD model and was 95%, 10%, and 7.5%, respectively, for the OU model. This suggests that when simulation data of the AdK system are discretely observed, the time between adjacent observations should be $\geq$0.30 ps before a "statistically acceptable" diffusion model can be used. Artifacts of fast-scale non-Markovian type effects can readily be detected by the Q-test when one samples more frequently in time than this value using even fairly small time series (here 350 observations per trajectory). The other US windows analyzed (not reported) also indicated that $ds = 2$ was the appropriate coarse-graining parameter to use; this corresponded to 0.30 ps between observations. All subsequent results used this spacing between time series observations. The main utility of such a pathwise goodness-of-fit analysis is that a very small number of short sample paths can be used to determine the time one needs to wait to let fast-scale non-Markovian effects "average out".[21,71] One of the appealing features of the Q-test is that the underlying nature of the signal is not important (stationary or nonstationary cases can be treated), but for this generality one pays a price in regards to statistical power. The Q-test performs similarly for the OD and OU test despite there being fairly large state-dependence at this point. Later we demonstrate that ignoring this dependence causes poor predictions related to stationary histogram estimation. It would be useful if we could apply a more powerful pathwise test in order to see how well the two different models perform. The T_3 statistic[64] makes use of a stationarity assumption. Panel B reports the results associated with applying this test. The T_3 tests more clearly demonstrates the OD model fits the observations better (roughly 5% of the OD models were rejected whereas about 20% of the OU were using $ds = 2$). Results reported in the Supporting Information show that increasing the time series sample size to 700 makes rejection easier in both cases, but the OU is still more strongly rejected at the $\alpha = 10\%$ significance level.

4.2. Diffusion Coefficient Approximation. Approximating the dynamics with a simple process like the OU model is appealing because the ML parameter can be obtained

Table 1. Diffusion Coefficient ($\tilde{D}$) Estimation[a]

	$\Delta t = 0.15$ *ps*	$\Delta t = 0.30$ *ps*	$\Delta t = 0.45$ *ps*
$\tilde{D}$ ($N = 350$)	1.0350×10^{-3}	1.4387×10^{-3}	1.5989×10^{-3}
Emp Std. Dev. $\tilde{D}$	1.1912×10^{-4}	1.6584×10^{-4}	1.7161×10^{-4}
Asymp. Std. Dev.$\tilde{D}$	1.1136×10^{-4}	1.5481×10^{-4}	1.7190×10^{-4}
$\tilde{D}$ ($N = 700$)	1.0237×10^{-3}	1.4012×10^{-3}	1.5564×10^{-3}
Emp Std. Dev. $\tilde{D}$	9.7924×10^{-5}	1.2283×10^{-4}	1.3652×10^{-4}
Asymp. Std. Dev.$\tilde{D}$	7.7736×10^{-5}	1.0632×10^{-4}	1.1810×10^{-4}

[a] The effective diffusion coefficient (in asymptotic mean square diplacement sense) was computed from the MD data at the point $\Delta D^0_{rmsd} = 1{:}38$. The valued obtained was 1.27×10^{-3}Å^2/ps (see text). The diffusion coefficient estimated by the OU models is reported using three different down-sampling rates. Results using a times series of length $N = 350$ and $N = 700$ are reported. In each case, results from analyzing 50 batches of time series are summarized by using the mean and empirically measured standard deviation ("Emp Std. Dev.") of the diffusion coefficient estimated surrogate models (each time series gave one estimate). We also report the large sample uncertainty estimate ("Asymp. Std. Dev.") of the maximum likelihood estimate. Techniques for approximating this quantity are reported in ref 43.

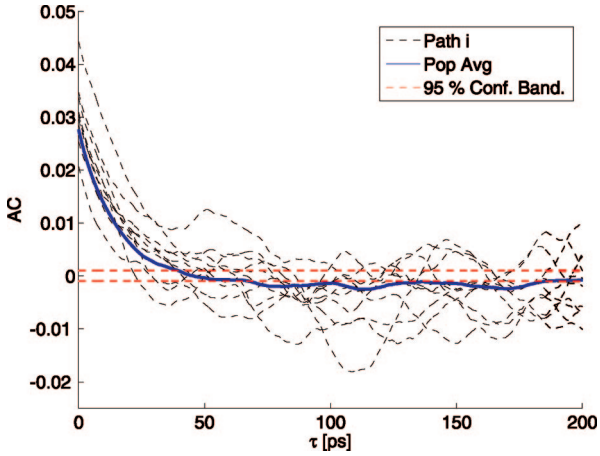

Figure 3. Autocorrelation (AC) measured from MD data taken from US point $\Delta D^0_{rmsd} = 7.03$. The thick line represents the mean AC function obtained using the full 525 time series and estimating the AC for each sample path and then averaging the results. The thin AC labeled as "Path i" are some representative ACs. The thick dotted horizontal lines correspond to the 95% confidence intervals.

directly (a numerical parameter search is not necessary)[43]. In Table 1 we report the mean and standard deviation of C^2 estimated with the OU model. The OD and OU model predictions for this quantity were nearly identical due to the low state-dependence on the noise, so we focus on the latter. [We studied a case where the state-dependence on the noise is mild to facilitate physical interpretation and to compare to established diffusion coefficient methods used in MD simulation analysis.[24,33,35,36]]

Also, if the OU model accurately captures the data, we can exploit several analytical results for statistical inference purposes. For example, the large sample asymptotic standard deviation of C^2 can be computed analytically by exploiting the Gaussian property of this process. Table 1 demonstrates that our surrogate models can approximate such quantities. In the atomistic simulation community, the diffusion coefficient is typically determined by using an empirically measured autocorrelation function to determine the τ where correlations are small, and then C^2 is computed by using ensemble averaging over temporal blocks.[24,33,35,36] The time requires to wait between observations can be fairly large when one uses this approach or variants of it.[52]

Figure 3 plots the autocorrelation (AC) of the detailed MD samples analyzed in Table 1. The AC of each 525 ps MD time series was computed for 50 independent MO simulations. The plot contains some sample ACs as well as the "mean" AC function, i.e. the function obtained by averaging the AC obtained from 50 MO runs. The 95% confidence bands for zero correlation are also plotted for the time series sample size used (dotted lines). The observed autocorrelation was used to find a relaxation time (τ) by fitting the early portion to a single exponential via least-squares (resulting in $\tau \approx 15$ *ps*). The diffusion coefficient was then computed using[33,52] $\langle(\Phi(t + \tau) - \Phi(t))^2\rangle/(2\tau) = 1.27 \times 10^{-3}$, where brackets denote ensemble averaging over nonoverlapping temporal blocks. This number was compared to the effective diffusion coefficient predicted by the OU model for various *ds* values (results reported Table 1). Our models actually exploit the temporal correlation to get better estimates of such quantities and do not necessarily require long time series observations. Recall that a value of $ds = 2$ (corresponding to 0.30 ps between observations) performed fairly well in regards to the Q-test on all of the data we observed for AdK, and coincidentally this parameter also appears to most closely capture the diffusion coefficient computed via traditional ensemble MD methods.[52] We also report the mean, predicted uncertainty, and the measured uncertainty in the estimated C^2 for various *ds* values. [Note that as one waits a longer time, fast-scale non-Markovian effects become less important. However in longer time series, artifacts of the evolution on $\mathcal{C}$ type coordinates can more readily be measured and in this case it appears to increase the effective diffusion coefficient.]

Note how in Figure 3 one initially observes a roughly single-exponential decay. This feature allowed us to approximate the effective diffusion coefficient using a single time series of length ≈100 ps. With this small amount of data, we were even able to compute confidence bands which were fairly accurate. However, closer inspection of the AC signal at longer times reveals it may be more complex than an exponential decay. Complex ACs are common in single-molecule experiments where conformational fluctuations persist for a relatively long-time.[15,16,63] Such artifacts may limit the predictive power of a diffusion coefficient calibrated from a scalar SO observed over fairly short time scales. The diffusion coefficient information reported in Table 1 *does not* attempt to account for complex long time behavior. [A single OU model predicts an AC with a single exponential rate of decay.]

The bottom panel of Figure 4 demonstrates that the estimated noise magnitude (C_i) of surrogate model "*i*"

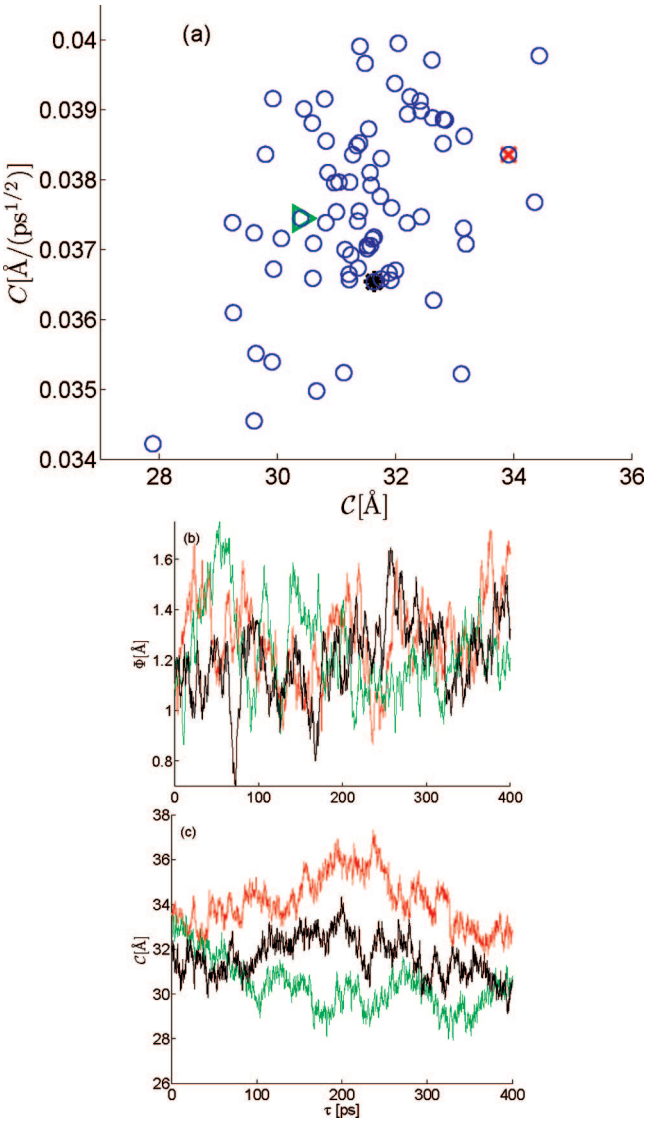

Figure 4. (a) Scatter plot of the estimated *C* of the Ornstein-Uhlenbeck (OU) Model vs $\langle \mathcal{C} \rangle$. The data consist of the estimated OU noise parameter (*C*) obtained using time series consisting of uniformly sampled observations spaced by $\Delta t = 0.30$. The noise parameter was estimated for 50 batches of short time series, and all US runs used simulations corresponding to the US constraint point $\Delta D^0_{rmsd} = 1{:}38$ plotted against the (temporal) average value of $\mathcal{C}$ for the corresponding ΔD_{rmsd} time series used to estimate the OU parameters. The linear correlation (r) between the estimated *C* and $\langle \mathcal{C} \rangle$ was found to be 0.34 and the associated p-value was $1{:}0 \times 10^{-3}$. (b) Representative time series of the "fast" ΔD_{rmsd} coordinate and (c) "slow" $\mathcal{C}$ coordinate. The three color coded trajectories in (b) and (c) correspond to the three color coded symbols in (a).

correlates with $\mathcal{C}_i$. The figure also contains some sample trajectories demonstrating the time scale separation existing between Φ and $\mathcal{C}$. Panel A of Figure 4 uses three distinct (color-coded) symbols to identify the three sample trajectories plotted in panels B and C. The fast Φ SO oscillates about the observed temporal mean associated with path *i*, whereas the slow $\mathcal{C}$ SO exhibits a slow random walk (i.e., not oscillating about a mean). Given that panel A demonstrates that the intensity of effective thermal noise varies with $\mathcal{C}$

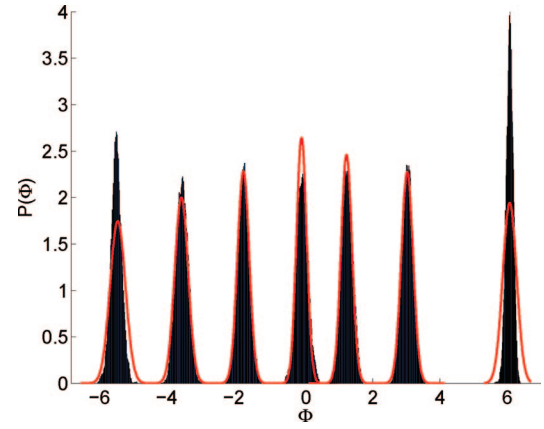

Figure 5. The histogram obtained from running MD simulations using 7 different constraint points are reported. Each data point contains the results from 50 independent simulations run for 105/*ps* (again uniform sampling with $\Delta t = 0.30$/*ps*). The prediction of the simple OU model which accounts for the conformational heterogeneity (see text for details) is shown as a solid line. In most cases this crude approximation is accurate; the largest discrepancy here is in the left and rightmost distributions.

and $\mathcal{C}$ does a random walk through phase space, this influences the distribution of the SO of interest (Φ). This plot provides one fairly simple illustration of how a time scale separation can affect histograms relevant to thermodynamic applications.

The time scale separation can be explored more quantitatively by estimating different stochastic models and analyzing the results. For example, if one estimates the effective force using the OD model for $\mathcal{C}$ and then compares the result of the same model estimated for Φ, the characteristic time scale associated with each effective force is roughly quantified by looking directly at the *B* parameter. In the SDE considered, the parameter *B* corresponds to the linear sensitivity of the effective force. For the data observed, the characteristic time scale associated with $\mathcal{C}$ ranges from $\approx 40-100$ times the length of that associated with Φ if the ratio of the linear sensitivities are used to quantify the time scale gap. [It should also be noted that when a coupled 2-d model was estimated, the eigenvalues of the effective force (of the coupled system) indicated a similar separation in time scales].

4.3. Stationary Histogram Approximation. Finally, we present results illustrating how a collection of simple models can be used to obtain stationary histogram information usually sought in umbrella sampling type applications. We demonstrate that a collection of surrogate models can account for variability associated with the slow $\mathcal{C}$ time scale. Figure 5 reveals that the collection of OU invariant densities seems to accurately capture the general shape of Π^{EQ}. However the cases at the edges of the US simulation points do not approximate the shape of the histograms as well. Using a mixture of OD models remedies the situation in both cases. [Results for the case near $\Phi \approx -6$ are given in the Supporting Information Figure 1.] Figure 6 plots the resulting density prediction (Π^{EQ}) along with the measured Φ histogram obtained directly from the MD data. The inset plots some sample $p^{EQ}(\cdot)$ functions measured from these models

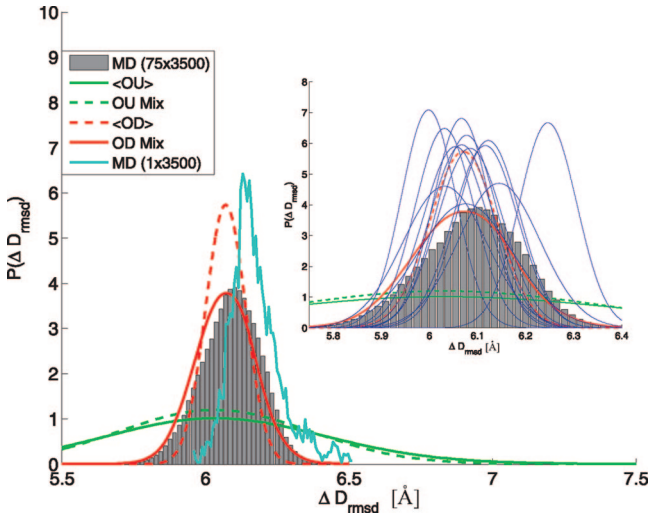

Figure 6. Stationary density estimate focusing on the rightmost density shown in Figure 5 (corresponding to $\Delta D^0_{rmsd} = 7.02$). The result obtained using the Ornstein-Uhlenbeck (OU) surrogate models was poor. A batch of over-damped (OD) models was estimated from the same times series used to fit the Ornstein-Uhlenbeck models in Figure 5. The solid lines denote the invariant density obtained by appealing to eq 7, and the dotted lines represent the invariant density prediction obtained by using $\langle\theta\rangle$ (green corresponds to OU, red, to OD surrogates). The inset displays some representative invariant density predictions (i.e., "p_i^{EQ}" in eq 7) using thin blue lines. The histogram of Φ coming from an ensemble of 75 genuine MD time series of length 525 ps is represented as a bar graph (labeled as MD (75 $\times$ 3500)). The jagged line corresponds to the histrogram obtained from one MD time series of length 525 (labeled as MD (1 $\times$ 3500)).

(these are used to construct Π^{EQ}). The accuracy obtained by this "mixture of density" plots gives further evidence that a diverse ensemble of $\mathcal{C}$ values modulate the dynamics of Φ. For points near the boundaries the correlation between $\mathcal{C}$ and Φ is stronger than that shown in Figure 4 (see the Supporting Information Figure 2), and accounting for this variability is important if one demands high accuracy in the surrogate model density estimates (referring to both $p^{EQ}(\cdot)$ and Π^{EQ}).

Before concluding, we provide a description which hopes to show why a "mixture of densities" can help in approximating the Π^{EQ} of a SO associated with a complex molecule. Accurately approximating Π^{EQ} usually requires one to exhaustively sample phase space, not just a small region explored in single short trajectory. The variability induced by "very fast-degrees" of freedom (e.g., vibrational degrees of freedom and solvent bombardment) is modeled in each single surrogate diffusion using Brownian motion. This along with the drift parameters determines $p^{EQ}(\cdot)_i$ which provides one with quantitative information about how fast-scale fluctuations cause variability in Φ for a relatively frozen value of $\mathcal{C}$. Slow time scale conformational variability (e.g., that introduced by the distribution of $\mathcal{C}$) is accounted for using a collection of surrogate models. In ref 51 it was shown that the free energy profile of $\mathcal{C}$ was effectively flat. It effectively does a random walk in phase space when viewed over long time scales, whereas Φ is constrained with a harmonic potential. The skewed histogram of Φ observed in the single 525 ps run shown in Figure 6 is an artifact of this modulating effect.

5. Conclusions

We have demonstrated that a collection of fairly simple surrogate diffusion models estimated from time series data can accurately capture dynamical features of short constrained AdK simulations. The techniques presented should be thought of as a "postprocessing" analysis in which statistical summaries (such as correlation and the invariant distribution of SOs) are obtained by time series techniques. In most cases, the parameters of the diffusion models were modulated by degrees of freedom associated with large-scale conformational changes. The slow SO monitored in AdK is experimentally accessible in solution via single molecule FRET experiments.[49] We also demonstrated that pathwise statistical inference could be used to obtain efficient parameter estimates from temporally correlated MD observations. Application of goodness-of-fit tests helped identify the time needed to wait (a coarse-graining parameter) before fast-scale non-Markovian artifacts "averaged out".

Information extracted from a collection of surrogate diffusion models can be used to assist free energy computations as well as obtain kinetic information in the form of effective diffusion using a relatively short amount of detailed simulation trajectories in certain situations. Confidence bands and goodness-of-fit tests can be used to check the quality of the approximation without requiring a large number of expensive simulations. This technique shows promise in reducing the computational load needed to obtain kinetic and thermodynamic properties of complex biomolecules and may be used to assist established sampling techniques like WHAM, parallel tempering, or metadynamics[24,74,78] where many histograms need to be approximated. The findings are not isolated to very short constrained simulations; the Supporting Information reports results demonstrating results using longer unconstrained simulations coming from an explicitly solvated protein trajectory obtained from the dynameomics.org library.[26] We also see the statistical analysis tools presented here as being useful in data-mining applications.

The surrogate models we appealed to in this article did not explicitly exploit the structure of any underlying governing equations. The proposed models had a phenomenological motivation. The collection of estimated surrogate models did give dynamic and static information about a Φ type coordinate over a broad range of phase space not typically explored in a single simulation and did so using SDE models which we could efficiently estimate, quantify the uncertainty in our estimates, and readily interpret in terms of established statistical physics. We could also assess the goodness-of-fit of the estimated models in an *a posteriori* fashion. If simplified models coming from mathematical model reduction techniques are available, e.g.,[19,71] the parameters of reduced models could possibly be estimated from observations. One could also consider attempting to model the dynamics of more SOs and/or utilize the structure of a generalized Langevin equation resulting in more complicated surrogate models.

The statistical analysis of such models (estimation and inference) is fairly involved and introduces many new mathematical challenges, but interesting results are being obtained in that direction.[63] Data-driven modeling is particularly attractive because recent advances in single-molecule manipulation methods[1−16] are making a variety of low-dimensional SOs available to dynamically analyze. Synergystically combining data-driven modeling techniques with new and established simulation methods as well as mathematical multiscale analysis shows great promise in providing new insights into complex biological systems.

Acknowledgment. We thank two anonymous referees for helpful comments which improved the quality of the manuscript. In addition C.P.C. was supported by NSF grant nos. DMS 0240058 and ACI-0325081 and NIH grant T90 DK070121-04, partial computational support from the Rice Computational Research Cluster funded by NSF under Grant CNS-0421109, and a partnership between Rice University, AMD, and Cray.

Note Added after ASAP Publication. This article was released ASAP on November 24, 2008, with a minor error in eq 2. The correct version was posted on November 26, 2008.

Supporting Information Available: Information related to Figures 4 and 6 of the main text and a url link to MATLAB scripts demonstrating the parameter estimation procedure. This material is available free of charge via the Internet at http://pubs.acs.org.

References

(1) Bustamante, C.; Bryant, Z.; Smith, S. *Nature* **2003**, *421*, 423.

(2) Carrion-Vazquez, M.; Oberhauser, A.; Fisher, T.; Marszalek, P.; Li, H.; Fernandez, J. *Prog. Biophys. Mol. Bio.* **2000**, *74*, 63.

(3) Stock, G.; Ghosh, K.; Dill, K. *J. Chem. Phys.* **2008**, *128*, 194102.

(4) Collin, D.; Ritort, F.; Jarzynski, C.; Smith, S.; Tinoco, I., Jr.; Bustamante, C. *Nature* **2005**, *437*, 231.

(5) Min, W.; Gopich, I.; English, B.; Kou, S.; Xie, X.; Szabo, A. *J. Phys. Chem. B* **2006**, *110*, 20093.

(6) Smith, S.; Cui, Y.; Bustamante, C. *Science* **1996**, *271*, 795.

(7) Rief, M.; Clausen-Schaumann, H.; Gaub, H. *Nat. Struct. Biol.* **1999**, *6*, 346.

(8) Clausen-Schaumann, H.; Rief, M.; Tolksdorf, C.; Gaub, H. *Biophys. J.* **2000**, *78*, 1997.

(9) Albrecht, C.; Neuert, G.; Lugmaier, R.; Gaub, H. *Biophys. J.* **2008**, *94*, 4766.

(10) Lee, G.; Rabbi, M.; Marszalek, R. C. P. *Small* **2007**, *5*, 809.

(11) Ke, C.; Humeniuk, M.; S-Gracz, H.; Marszalek, P. *Phys. Rev. Lett.* **2007**, *99*, 018302.

(12) Harris, N. C.; Song, Y.; Kiang, C.-H. *Phys. Rev. Lett.* **2007**, *99*, 068101.

(13) Dixit, S.; Singh-Zocchi, M.; Hanne, J.; Zocchi, G. *Phy. Rev. Lett.* **2005**, *94*, 118101.

(14) Vendruscolo, M.; Dobson, C. *Science* **2006**, *313*, 1586.

(15) Liu, S.; Bokinsky, G.; Walter, N.; Zhuang, X. *Proc. Natl. Acad. Sci. U.S.A.* **2007**, *104*, 12634.

(16) Greenleaf, W.; Frieda, K.; Foster, D.; Woodside, M.; Block, S. *Science* **2008**, *319*, 630.

(17) Schlick, T.; Skeel, R. D.; Brunger, A. T.; Kale, L. V.; Board, J. A.; Hermans, J.; Schulten, K. *J. Comput. Phys.* **1999**, *151*, 9.

(18) Zwanzig, R. Brownian motion and Langevin equations. In *Nonequilibrium Statistical Mechanics*, 1st ed.; Oxford University Press: New York, 2001; pp 3, 24, 143.

(19) Chorin, A. J.; Kupferman, A. K. R. *Proc. Natl. Acad. Sci. U.S.A.* **1998**, *95*, 4094.

(20) Kopelevich, D.; Panagiotopoulos, A.; Kevrekidis, I. *J. Chem. Phys.* **2005**, *122*, 044908.

(21) Givon, D.; Kupferman, R.; Stuart, A. *Nonlinearity* **2004**, *17*, R55.

(22) E, W.; Liu, D.; Vanden-Eijnden, E. *Commun. Pur. Appl. Math.* **2005**, *58*, 1544.

(23) Borgia, A.; Williams, P.; Clarke, J. *Annu. Rev. Biochem.* **2008**, *77*, 101.

(24) Schlick, T. Molecular dynamics: Basics. In *Molecular Modeling and Simulation: An Interdisciplinary Guide*, 2nd ed.; Marsden, J., Sirovich, L., Wiggins, S., Antman, S., Eds.; Springer-Verlag: New York, 2002; pp 394−406.

(25) Sotomayor, M.; Schulten, K. *Science* **2007**, *316*, 1144.

(26) Simms, A.; Toofanny, R.; Kehl, C.; Benson, N.; Daggett, V. *Protein. Eng. Des. Sel.* **2008**, *21*, 369.

(27) Maragakis, P.; Lindorff-Larsen, K.; Eastwood, M.; Dror, R.; Klepeis, J.; Arkin, I.; Jensen, M.; Xu, H.; Trbovic, N.; Friesner, R.; Palmer, A.; Shaw, D. *J. Phys. Chem. B* **2008**, *112*, 6155.

(28) Moffitt, J.; Chemla, Y.; Smith, S.; Bustamante, C. *Annu. Rev. Biochem.* **2008**, *77*, 19–1.

(29) Calderon, C. *J. Chem. Phys.* **2007**, *126*, 084106.

(30) Calderon, C.; Chelli, R. *J. Chem. Phys.* **2008**, *128*, 145103.

(31) Calderon, C.; Chen, W.; Harris, N.; Lin, K.; Kiang, C. J. Phys.: Condens. Matter **2008**, in press.

(32) Calderon, C.; Harris, N.; Kiang, C.-H.; Cox, D. J. Phys. Chem. B **2008**, in press.

(33) Hummer, G. *New J. Phys.* **2005**, *7*, 1.

(34) Calderon, C. *Multiscale Model. Simul.* **2007**, *6*, 656.

(35) Chahine, J.; Oliveira, R.; Leite, V.; Wang, J. *Proc. Natl. Acad. Sci. U.S.A.* **2007**, *104*, 14646.

(36) Snow, C.; Rhee, Y.; Pande, V. S. *Biophys. J.* **2006**, *95*, 078102.

(37) Sigg, D.; Qian, H.; Bezanilla, F. *Biophys. J.* **1999**, *76*, 782.

(38) Park, S.; Schulten, K. *J. Chem. Phys.* **2004**, *120*, 5946.

(39) Khatri, B. S.; Byrne, K.; Kawakami, M.; Brockwell, D.; Smith, D.; Radford, S.; McLeish, T. *Faraday Discuss* **2008**, *139*, 35.

(40) Aït-Sahalia, Y. *Econometrica* **2002**, *70*, 223.

(41) Jimenez, J.; Ozaki, T. *J Time Ser. Anal.* **2005**, *27*, 77.

(42) Hong, Y.; Li, H. *Rev. Finance Stud.* **2005**, *18*, 37–84.

(43) Chen, S.; C. Y., T. submitted to *J. Econometrics*. http://www.stat.iastate.edu/preprint/articles/2006-21.pdf (accessed Oct 1, 2008).

(44) Chen, S.; Tang, C. *Ann. Stat.* **2008**, *36*, 167.

(45) Walther, K.; Brujic, J.; Li, H.; Fernandez, J. *Biophys. J.* **2006**, *90*, 3806.

(46) Minh, D.; Bui, J.; Chang, C.; Jain, T.; Swanson, J.; McCammon, J. *Biophys. J. Lett.* **2005**, *72* (89), L25.

(47) Procacci, P. S., M.; Barducci, A.; Signorini, G.; Chelli, R. *J. Chem. Phys.* **2006**, *125*, 164101.

(48) Paramore, S.; Ayton, G.; Voth, G. *J. Chem. Phys.* **2007**, *14*, 105105.

(49) Henzler-Wildman, K.; et al. *Nature* **2007**, *450*, 06410.

(50) Muller, C. W.; Schulz, G. E. *J. Mol. Biol.* **1992**, *224* (1), 159.

(51) Arora, K.; Brooks, C., III *Proc. Natl. Acad. Sci. U.S.A.* **2007**, *104*, 18496.

(52) Socci, N. D.; Onuchic, J. N.; Wolynes, P. G. *J. Chem. Phys.* **1996**, *104*, 5860.

(53) Frenkel, D.; Smit, B. Molecular dynamics simulations. In *Understanding Molecular Simulation: From Algorithms to Applications*, 1st ed.; Academic Press: San Diego, CA, 1996; pp 75−88, 377.

(54) Beck, D.; Daggett, V. *Biophys. J.* **2007**, *93*, 3382.

(55) Kevrekidis, I.; Gear, C.; Hummer, G. *AIChE J.* **2004**, *50*, 474.

(56) Givon, D.; Kevrekidis, I.; Kupferman, R. *Commun. Math. Sci.* **2006**, *4*, 707.

(57) Horenko, I.; Hartmann, C.; Schütte, C. *Phys. Rev. E* **2007**, *76*, 016706.

(58) Evensen, G.; van Leeuwen, P. *Mon. Weather. Rev.* **2000**, *128*, 1852.

(59) Vanden-Eijnden, E. *Commun. Pur. Appl. Math* **2003**, *1*, 385.

(60) Zhang, L.; Mykland, P.; Ait-Sahalia, Y. *J. Am. Stat. Assoc.* **2005**, *100*, 1394.

(61) Calderon, C.; Martinez, J.; Carroll, R.; Sorensen, D. submitted2008.

(62) Calderon, C.; Janosi, L.; Kosztin, I. *Technical Report, TR08-24*; CAAM Dept.: Rice University, 2008.

(63) Kou, S.; Xie, X. *Phys. Rev. Lett.* **2004**, *93*, 18.

(64) Ait-Sahalia, Y.; Fan, J.; Peng, H. Social Science Research Network.http://www.stat.iastate.edu/preprint/articles/2006-21.pdf (accessed Oct 1, 2008).

(65) Kloeden, P.; Platen, E. IntroductionIn Numerical Solution of Stochastic Differential Equations, 1st ed.; Springer-Verlag: Berlin, 1999; p 37.

(66) Chandrasekhar, S. *Rev. Mod. Phys.* **1943**, *15*, 1.

(67) El-Ansary, M.; Khalil, H. *SIAM J. Control Optim.* **1986**, *24*, 83.

(68) Skorokhod, A. V. Asymptotic behavior of systems of stochastic equations containing a small parameter. In *Asymptotic Methods in the Theory of Stochastic Differential Equations*, 1st ed.; Amer Mathematical Society: Providence, RI, 1989; p 77.

(69) Krishnan, J.; Runborg, O.; Kevrekidis, I. *Comput. Chem. Eng.* **2004**, *28*, 557.

(70) Erban, R.; Frewen, T.; Wang, X.; Elston, T.; Coifman, R.; Nadler, B.; Kevrekidis, I. *J. Chem. Phys.* **2007**, *126*, 155103.

(71) Pavliotis, G. A.; Stuart, A. M. *J. Stat. Phys.* **2007**, *127*, 741.

(72) Kutoyants, Y. Diffusion processes and statistical problems. In Statistical Inference for Ergodic Diffusion Processes, 1st ed.; Springer: New York, 2004; p50.

(73) Risken, H. Fokker-Planck equation for one variable. In *The Fokker-Planck Equation*, 2nd ed.; Springer-Verlag: Berlin, 1996; p 98.

(74) Chodera, J.; Swope, W.; Pitera, J.; Seok, C.; Dill, K. *J. Chem. Theory Comput.* **2007**, *3*, 26.

(75) Chu, J.-W.; Trout, B. L.; Brooks, B. R. *J. Chem. Phys.* **2003**, *119* (24), 12708.

(76) Michael, S.; Salsbury, F., Jr.; Brooks, C., III *J. Chem. Phys.* **2002**, *116* (24), 10606.

(77) Brooks, B. R.; Bruccoleri, R. E.; Olafson, B. D.; States, D. J.; Swaminathan, S.; Karplus, M. *J. Comput. Chem.* **1983**, *4*, 187.

(78) Marsili, S.; Barducci, A.; Chelli, R.; Procacci, P.; Schettino, V. *J. Phys. Chem. B* **2006**, *110*, 14011.

CT800282A

JCTC Journal of Chemical Theory and Computation

Mechanistic Analysis of the Base-Catalyzed HF Elimination from 4-Fluoro-4-(4′-nitrophenyl)butane-2-one Based on Liquid-Phase Kinetic Isotope Effects Calculated by Dynamics Modeling with Multidimensional Tunneling†

Yongho Kim,[§,II] Aleksandr V. Marenich,[II] Jingjing Zheng,[II] Kyung Hyun Kim,[§] Magdalena Kołodziejska-Huben,[‡] Michał Rostkowski,[‡] Piotr Paneth,*[,‡] and Donald G. Truhlar*[,II]

Institute of Applied Radiation Chemistry, Technical University of Lodz, Zeromskiego 116, 90-924 Lodz, Poland, Department of Chemistry, Kyung Hee University, Yongin-City, Gyeonggi-Do 449-701, Korea, and Department of Chemistry and Supercomputing Institute, University of Minnesota, 207 Pleasant Street SE, Minneapolis, Minnesota 55455-0431

Received August 20, 2008

Abstract: The primary and secondary deuterium kinetic isotope effects as well as leaving-group fluorine kinetic isotope effects have been calculated for the base-promoted elimination of hydrogen fluoride from 4-fluoro-4-(4′-nitrophenyl)butane-2-one in 75% aqueous methanol solution. The elimination was studied for both formate and imidazole as the catalytic base; and reactant and transition state structures and vibrational frequencies have been calculated by including the base explicitly and by including the solvent by an implicit solvation model that includes both electrostatics by class IV charges and first-solvation-shell effects by atomic surface tensions. We used the M06-L density functional for all calculations. The optimized stationary points, the geometry changes along the solution-phase minimum free energy path, and the solution-phase free energy profile indicate that the elimination reaction occurs concertedly but asynchronously via an E1cb-like transition state. Reaction rates were calculated by the equilibrium solvation path method, using variational transition state theory with multidimensional tunneling. The primary deuterium kinetic isotope effects are calculated to be large: 1.67 and 5.13 for formate and imidazole, respectively. The corresponding C_4-secondary deuterium kinetic isotope effects are 1.044 and 1.044, and the leaving group fluorine kinetic isotope effects are respectively 1.020 and 1.015.

Introduction

Enzymes often catalyze proton transfer from the α-carbon of a carbonyl compound by an E1cB mechanism.[1] Shultz et al. found that such reactions can also be catalyzed by an antibody elicited against an ammonium-containing hapten;[2−4] in particular they found a rate enhancement of a factor of 8.8 (compared to the acetate-promoted reaction) for elimination of HF from 4-fluoro-4-(4′-nitrophenyl)butane-2-one (Scheme 1); they found primary H/D kinetic isotope effects (KIEs) of 3.7 and 2.35 for acetate catalysis and the catalytic antibody, respectively. These KIEs rule out the E1 mechanism, in which a rate-limiting detachment of the leaving group precedes a fast proton-transfer step, but the results are consistent with the rate-limiting proton transfer occurring via either a concerted E2 or a stepwise E1cB mechanism.

* Corresponding author e-mail: paneth@p.lodz.pl (P.P.) and truhlar@umn.edu (D.G.T.).

† We dedicate this contribution to Hans-Heinrich Limbach on the occasion of his 65th birthday.

‡ Technical University of Lodz.

§ Kyung Hee University.

II University of Minnesota.

10.1021/ct800345j CCC: $40.75 © 2009 American Chemical Society
Published on Web 12/04/2008

Scheme 1

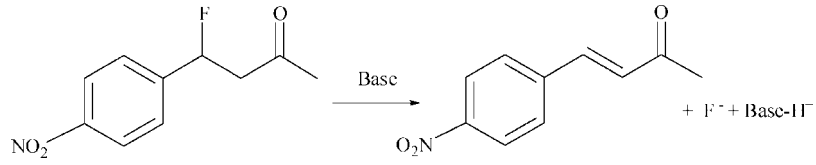

Scheme 2

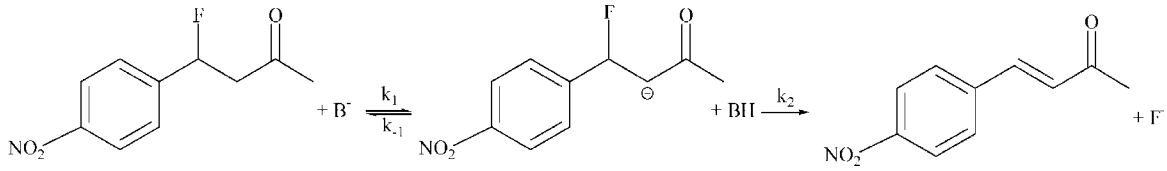

The study of secondary KIEs for such reactions can provide better discrimination between E2 and E1cB mechanisms, as discussed by Saunders[5,6] in conjunction with theoretical fluorine KIEs on model E2 and E1cB elimination reactions.

Based on experimental determinations of primary and secondary deuterium KIEs, and small fluorine KIEs for a set of bases with varying pK_a strengths (formate, acetate, and imidazole) in 75% aqueous methanol solution, Ryberg and Matsson argued that this reaction proceeds via either an E1cB mechanism (Scheme 2) or E1cB-like E2 mechanism.[7] The secondary deuterium KIEs in this study were at position C_4 (atom numbering is illustrated in Figure 1). In the subsequent work, based on deuteration at C_1 and C_3 and the measurement of multiple KIEs, they concluded, based on double isotopic fractionation[8] experiments, that the reaction proceeds by an E1cB mechanism.[9] However their analysis ignores tunneling and variational effects on the location of the transition state. In this respect, we note that the position of the variational transition state of the proton transfer reaction can be different from that of the deuteron transfer case, and furthermore multidimensional tunneling probabilities can be sensitive to secondary substitutions. Ryberg and Matsson's experimental values of the KIEs for the formate and imidazole cases are collected in Table 1, and the present paper will provide theoretical calculations of these values and of other details of the reaction in order to try to understand the mechanistic implications of the KIEs.

Reactions involving charge transfer or charged reactants or products provide an especially difficult challenge to theory because the effects of solvation can be very large.[10−21] Some of us have recently studied[22,23] the ability of electronic structure theory incorporating an implicit solvent, in particular the SM5.42/HF/6−31G(d) model,[24−28] to make reliable predictions of carbon, nitrogen, and oxygen KIEs on the decarboxylation of 4-pyridylacetic acid; however, we were unable to draw definitive conclusions. In later work it was demonstrated that several diverse computational levels cannot theoretically reproduce the experimental KIEs on a simple S_N2 reaction.[29−32] Therefore, it is important to carry out additional studies that allow us to understand the limits of reliability of theoretical KIEs for organic reactions, especially those involving polar or charged reagents. The wealth of experimental data for the title reaction prompts us to test the applicability of theoretical evaluations of KIEs for these elimination reactions, and that is the subject of the present article.

Computational Methods

The first decision to make is the representation of the potential energy surface. We decided to use density functional theory with an implicit solvation model because that is a cost efficient choice for reactions of complex molecules. We chose the M06-L density functional[33] because it is the most accurate available density functional without nonlocal exchange, and local density functionals are less computationally expensive than nonlocal ones for large systems. The present system is large enough that this savings is significant. Furthermore, we have developed an efficient and reasonably accurate implicit universal solvation model, called SM8,[35] that can be used with this functional in general organic solvents. Therefore all electronic structure calculations were carried out with the M06-L density functional and the SM8 solvation model. Furthermore we used the 6−31B(d) basis set[34] because this basis set has slightly more diffuse valence basis functions than the popular 6−31G(d) basis set, and it is therefore possibly more accurate for anions, especially for density functional theory calculations, which are more sensitive than wave function theory to the inclusion of diffuse

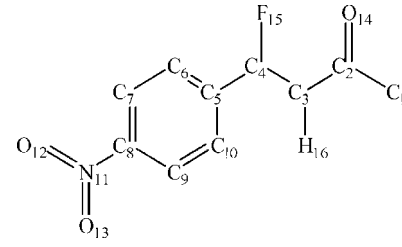

Figure 1. Numbering of atoms in the reactant.

Table 1. Experimental KIEs at 311 K

base	$({}^{H}k/{}^{D}k)_s$[a,b]	${}^{H}k/{}^{D}k$	${}^{18}k/{}^{19}k$[b]
$HCOO^-$	1.038 ± 0.013 (1.009 ± 0.018)	3.2 ± 0.1	1.0037 ± 0.0020
$C_3H_4N_2$	1.014 ± 0.017 (1.010 ± 0.023)	7.5 ± 0.1	1.0013 ± 0.0012

[a] Values not in parentheses are secondary deuterium KIE of hydrogen at C_4. [b] Values in parentheses were obtained for the reactant perdeuterated in positions 1 and 3.

basis functions. In the SM8 calcuations, we used the CM4 M charge model,[36] which has been shown to be much more accurate and much more stable than using population analysis for the solute partial charges. All electronic structure calculations were carried out using the MN-GFM[37] and MN-GSM[38] modules incorporated locally into the *Gaussian03* electronic structure program.[39]

All stationary point geometries were fully optimized in the reaction field of the implicit solvent. Vibrational analysis was performed for each stationary point based on analytical gradients and numerical Hessians. All minima and transition states (TSs) were confirmed to have zero and one imaginary frequency, respectively, and Hessians from these calculations were used for calculations of KIEs by variational[40−42] transition state theory. Since experimentally the reaction was carried out in a binary methanol-water mixture (3:1 v/v), all the parameters used with the solvation models were interpolated linearly from the values for pure solvents. The resulting dielectric constant equals 44.05. Although the rate constants are calculated at 311 K, we used solvation parameters corresponding to 298 K.

We were unable to obtain a stable intermediate structure as shown in Scheme 2 for reaction involving either base at the chosen level of electronic structure theory. Every attempt to locate an intermediate led to C−F bond breaking to generate 4-(4′-nitrophenyl)butene-2-one and fluoride ion. The calculations therefore predict a concerted E2 mechanism. Furthermore, as discussed in more detail below, the conventional transition state has the proton or deuteron partially transferred with the fluoride bond almost intact. Thus the mechanism may be labeled as E1cb-like E2.

The reaction rates of the E2 reaction have been calculated using variational transition state theory[40−42] including a transmission coefficient[43−47] that accounts for multidimensional tunneling. The solvation effects were calculated in the equilibrium solvation path (ESP) approximation,[14] and all rate calculations were carried out by direct dynamics[48−50] with the interpolated variational transition state theory by mapping[51] (IVTST-M) algorithm using the *Gaussrate*[52] program, which is an interface of *Gaussian03*[39] and the *Polyrate*[53] dynamics program.

In the ESP approximation,[14] the stationary points along the minimum free energy path (which we abbreviate, by analogy to the minimum-energy path for gas-phase reactions, as MEP) are calculated in the liquid phase. The MEP corresponds to the path of steepest descent in isoinertial solute cooordinates on a $(3N-6)$-dimensional potental of mean force (where N is the number of atoms in the solute, that is, the total number of atoms in the saddle point structure) called V_2 or U in ref 14; we will call it U. It is evaluated in the zero-order canonical mean shape (CMS-0) approximation.[14,47] In this approximation, U is obtained by adding the gas-phase potential energy of the solute to the standard-state free energy of solvation, and the saddle point on this solute free energy surface will be called the conventional transion state (TS). The signed distance from the TS along the MEP in isoinertial solute coordinate is called the reaction coordinate s. The variational transition state for a canonical ensemble at temperature T is located at the position on the MEP where the standard-state generalized free energy of activation $\Delta G(\mathrm{GT}, s|T)$ is a maximum, when $\Delta G(\mathrm{GT}, s|T)$ is obtained[14,47] by adding the local rovibrational free energy to U. In the present application the local rovibrational free energy consists of the local zero-point vibrational energy of the solute plus the local thermal rotational−vibrational free energy. All vibrational energies and vibrational free energies are computed harmonically from solution-phase frequencies. This yields the canonical variational theory (CVT) rate constant given by[14]

$$k^{\mathrm{CVT}} = \frac{k_B T}{hC^\circ}\exp[-\Delta G^{\mathrm{CVT},0}/RT] \qquad (1)$$

where k_B is the Boltzman constant; h is Planck's constant; C° is the concentration (1 molar) corresponding to the standard state; R is the gas constant; and $\Delta G^{\mathrm{CVT},0}$ is the standard state free energy of activation, which is the maximum along s of $\Delta G(\mathrm{GT}, s|T)$. Conventional transition state theory for a reaction in solution is not clearly defined by traditional treatments, but it is defined here as evaluating the rate constant at the s value that maximizes $U(s|T)$ rather than the one that maximizes $\Delta G(\mathrm{GT}, s|T)$; the variational effect is then defined as the diffference in rate constant due to the difference in the location of the two maxima. A reaction is especially susceptible to variational effects when $U(s|T)$ is rather flat near its maximum, when a reaction is asymmetric (so that the first derivative of the local rovibrational free energy with respect to s evaluated at the maximum of $U(s|T)$ is neither zero by symmetry nor small by near symmetry), or when one is considering higher temperatures (which increase the importance of entropic effects in $U(s|T)$ can also contribute to the local rovibrational free energy). However, these guidelines have their limtations, and one sometimes finds large variational effects even for symmetric reactions at low temperature or for reactions with barriers greater than 10 kcal/mol.

In order to include tunneling, $k^{\mathrm{CVT}}(\mathrm{T})$ is multiplied by a transmission coefficient, κ^{SCT}.

$$k^{\mathrm{CVT/SCT}}(\mathrm{T}) = \kappa^{\mathrm{SCT}}(\mathrm{T})k^{\mathrm{CVT}}(\mathrm{T}) \qquad (2)$$

The transmission coefficient is defined as the ratio of the thermally averaged quantal transmission probability, $P(\mathrm{E})$, to the thermally averaged classical transmission probability for the effective vibrationally adiabatic potential energy along the reaction coordinate.[43,47] The effective vibrationally adiabatic potential energy for the tunneling calculation will be called V_a (it is called V_2 in ref 14); V_a, like U, is calculated in the CMS-0 approximation.[14,47] In this appproximation, the one-dimensional V_a is equal to U plus the local solute zero-point energy along the MEP. (This should not be confused with the one-dimensional generalized free energy of activation profile.) The centrifugal-dominant small-curvature semiclassical adiabatic ground state (CD-SCSAG) tunneling approximation[46,54] was used to calculate $P(\mathrm{E})$; this is called small-curvature tunneling (SCT) for conciseness.

In the IVTST-M algorithm for a solution-phase reaction, the necessary information (free energies, free energy gradients, and free energy Hessians) for the CVT/SCT calculation is computed at a small number of points along the minimum

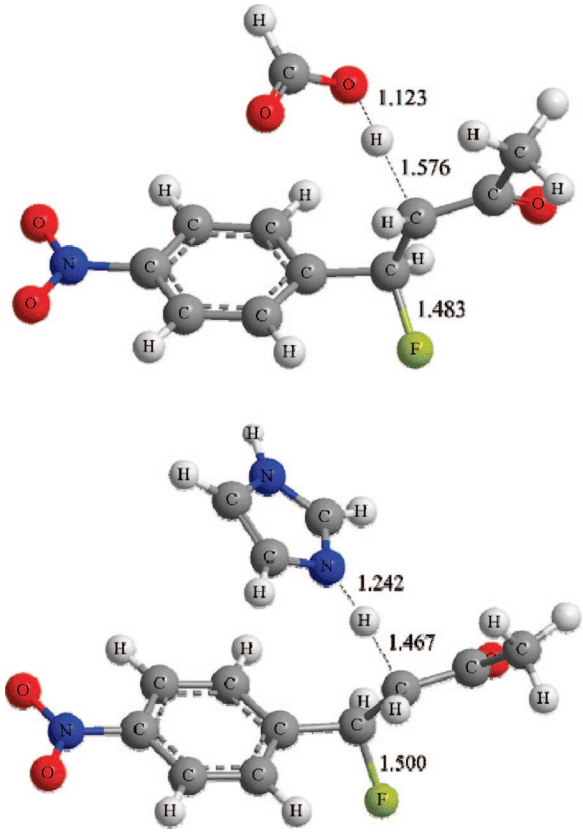

Figure 2. The conventional TS structures for the proton abstraction by formate and imidazole bases calculated at the SM8/CM4M/M06-L/6−31B(d) level.

energy path and fitted to spline functions under tension. We use the notation[51] IVTST-M−*H/G* to denote the number of nonstationary points at which Hessians (*H*) and free energies and gradients (*G*) are calculated. The reaction coordinate for each of the isotopomers was obtained by the RODS algorithm.[51,56]

Results and Discussion

The conventional transition state (TS) structures in solution for the proton abstraction by formate and imidazole bases calculated at the SM8/CM4M/M06-L/6−31B(d) level are illustrated in Figure 2. The imaginary frequencies at the TS are 896i and 1199i cm^{-1} for the reactions with formate and imidazole bases, respectively.

We were able to optimize the intermediate structures successfully in the absence of solvent but were unable to optimize them in solution either with or without the bases. When this was attempted, the C_4−F bond was always broken to generate fluoride ion, which is reasonable since the solvation energy for a small ion is large in a polar solvent. This means that the reaction in solution is concerted at the employed level of electronic structure theory. In terms of the reaction mechanism, it is important to know whether the intermediate is present or not, so further studies to corroborate this prediction would be worthwhile. However, if we assume it is not present, then this reaction becomes an example of the merging[57,58] of the stepwise and concerted mechanisms by the disappearance of the intermediate.

Table 2. Calculated Bond Lengths (Å) and Mayer's Bond Orders for Stationary Points in the Gas Phase and in Solution[a]

	reactants	conventional TS	intermediate	products
		Formate Base		
C_3−H	1.100/*1.100*	1.576/*1.627*	*1.787*	-
	(0.835/*0.895*)	(0.334/*0.333*)	(*0.262*)	
C_4−F	1.415/*1.392*	1.483/*1.451*	*1.456*	-
	(0.501/*0.518*)	(0.454/*0.471*)	(*0.466*)	
C_3−C_4	1.512/*1.516*	1.467/*1.467*	*1.463*	1.349/*1.348*
	(0.937/*0.943*)	(1.046/*1.043*)	(*1.066*)	(1.730/*1.748*)
O−H	-	1.123/*1.102*	*1.049*	0.983/*0.976*
		(0.336/*0.349*)	(*0.426*)	(0.667/*0.706*)
		Imidazole Base		
C_3−H	1.100/*1.100*	1.467/*1.748*	*2.105*	-
	(0.835/*0.895*)	(0.235/*0.355*)	(*0.221*)	
C_4−F	1.415/*1.392*	1.500/*1.400*	*1.398*	-
	(0.501/*0.518*)	(0.472/*0.472*)	(*0.477*)	
C_3−C_4	1.512/*1.516*	1.469/*1.509*	*1.501*	1.349/*1.348*
	(0.937/*0.943*)	(1.038/*0.960*)	(*0.985*)	(1.730/*1.748*)
N−H	-	1.242/*1.127*	*1.055*	1.015/*1.014*
		(0.169/*0.352*)	(*0.507*)	(0.672/*0.693*)

[a] The gas phase values are in italic, and the numbers in parentheses are Mayer bond orders.

Geometric parameters and bond orders for stationary points optimized in the gas phase at the M06-L/6−31B(d) level and in solution by SM8/CM4M/M06-L/6−31B(d) are given in Table 2. Table 2 lists bonds that undergo major changes in the course of the reaction. These include the C_3−H and the O−H (N−H in case of imidazole) bonds, which are broken and formed, respectively, along with the C_4−F bond that is broken in the reaction and the C_3−C_4 bond that becomes a double bond. The corresponding bond orders calculated by the method of Mayer[59] are given in parentheses. Note that the Mayer bond order is calculated from the reference Slater determinant of the density functional calculation, and this is preferred to the Pauling bond order,[60] which is a function only of distance.

Customarily, the analysis of the position of the TS is carried out in terms of its synchronicity and looseness. A transition state is considered synchronous if the bond breaking is as advanced as bond making[61] (often also it is assumed that the total bond order to the central atom is preserved[62]). If the sum of the bond orders to the transferred atom is diminished or increased, the corresponding transition state is called loose or tight, respectively.[61,63] Table 2 shows that in the gas phase the bond order sum of the transferred hydrogen changes from about 0.90 in the reactant to about 0.69 in the intermediate for the formate base reaction and from 0.90 to 0.73 for the imidazole base reaction. The average of these values is 0.80 for formate and 0.82 for imidazole. Table 2 shows that the sum of the hydrogen bond orders at the TS is 0.68 of formate and 0.72 for imidazole. Since these are slightly smaller than the averages mentioned earlier, they indicate a slightly exploded (loose) transition state for the proton transfer step in the gas phase. The same is true for the reactions in solution; in particular, the total bond order at the TS of the imidazole base reaction is only 0.40, which makes it a very loose and polar transition state.

In the gas phase, the reaction mechanism is E1cB, that is, a two-step mechanism. The first step, from reactants to an

Table 3. Calculated Partial Atomic CM4M Charges in Solution and in the Gas Phase at the M06-L/6-31B(d) Level of Theory[a]

		conventional TS		intermediate	
atom	reactants	formate	imidazole	formate	imidazole
C_2	0.35(0.28)	0.31(0.21)	0.27(0.17)	(0.20)	(0.14)
C_3	−0.17(−0.15)	−0.45(−0.29)	−0.31(−0.29)	(−0.29)	(−0.27)
O_{14}	−0.51(−0.36)	−0.58(−0.47)	−0.59(−0.50)	(−0.48)	(−0.52)
F_{15}	−0.25(−0.21)	−0.34(−0.30)	−0.36(−0.23)	(−0.31)	(−0.22)
H_{16}	0.14(0.10)	0.30(0.30)	0.33(0.29)	(0.30)	(0.30)
O_F	−0.59(−0.59)	−0.45(−0.44)	-	(−0.41)	-
N_I	−0.56(−0.44)	-	−0.44(−0.36)	-	(−0.34)

[a] Numbers in parentheses are for the gas phase. Oxygen (O_F) and nitrogen (N_I) atoms are in formate and imidazole, respectively.

intermediate, is rate limiting. The C_3−H bond at the conventional TS of the first step of the formate base reaction has a bond order of 0.33 in the gas phase, which is 89% of the way to the intermediate, and the O−H bond has a bond order of 0.35, which is 82% of its bond order at the intermediate. This indicates that the TS is very late (product-like; the product is an intermediate in this case). In solution, where there is no intermediate, the C_3−H and O−H bond orders at the TS are 0.33 and 0.34, which have changed 60% and 50%, respectively, of their total change in going all the way to products. Therefore the TS in solution is nearly synchronous or slightly late, which is consistent with the change of C_3−H and N/O−H bond lengths between the gas phase and the solution transition states. In contrast the C_3−H and N−H bond orders at the TS of the imidazole base reaction are 0.24 and 0.17, which have changed 72% and 25%, respectively, of their total change in going all the way to products. This analysis of the transition state is most useful when the bond order is approximately preserved in the course of the reaction. If the transition state is very loose or tight, the bond orders for breaking and forming bonds at the TS are very small or large, respectively. In this case the earliness and lateness of the TS does not provide such useful information. Experimentally this analysis of TS character is performed using the α-secondary H/D kinetic isotope effect, which often primarily reflects the changes in the force constant of secondary C−H bonds at the TS. The α-secondary H/D KIE may be a better tool to compare the similarity of the TS with reactants or products than the bond orders of the hydrogen that is being transferred.

As illustrated by the data collected in Table 3 changes in partial charges are primarily concentrated in the reacting fragment of the molecule. The changes in the partial charges of C_2, C_3, and O_{14} from the reactant to the intermediate in the gas phase show that the intermediate has a fairly large enolate character, and the partial charges of the TS in the gas phase are very similar to those of intermediates, which is consistent with the late (enolate-like) transition state. All partial charges of the TS in solution are larger than the corresponding values in the gas phase.

Energetic data for two of the bases are collected in Table 4. For the table, zero of energy is the potential energy of reactants, that is, 4-fluoro-4-(4′-nitrophenyl)butane-2-one infinitely separated form bases. The energy differences between the gas-phase TSs and intermediates are very small, which is also consistent with the late transition state in the gas phase. The solvent effect reduces the barrier height of the imidazole base reaction by about 4 kcal/mol.

Table 4. Energetics of Stationary Points (in kcal/mol)

	gas-phase *V*			solution-phase *U*		
base	R[a]	TS	Int	R[b]	TS	effective barrier[c]
$HCOO^-$	0	−19.3[d]	−19.4	−92.4	−73.0	19.4[c]
$C_3H_4N_2$	0	20.8	19.8	−26.7	−10.2	16.5

[a] Gas-phase reactants, taken as zero of energy for next columns. [b] Solution-phase reactants. [c] *U*(TS) − *U*(R). [d] In the gas phase there is an ion-dipole complex between R and TS; the energy of the TS for $HCOO^-$ is lower than that of the reactant but higher than that of the ion-dipole complex.

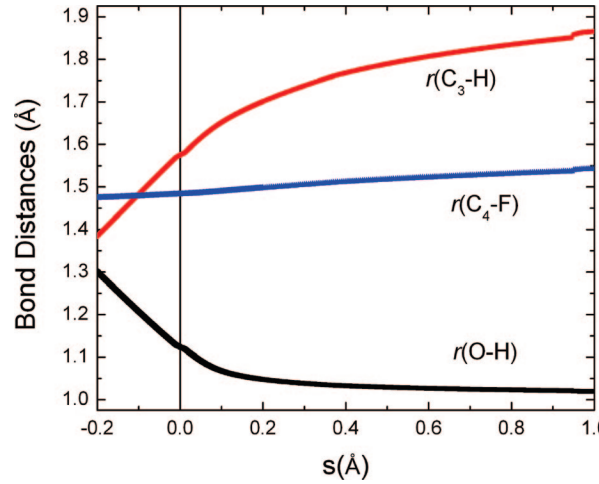

Figure 3. Bond distances along the reaction coordinate for the formate base reaction in solution. The vertical line is at the conventional TS. Negative and positive *s* values represent respectively the reactant side (before transion state) and the product side (after transition state) of the reaction paths.

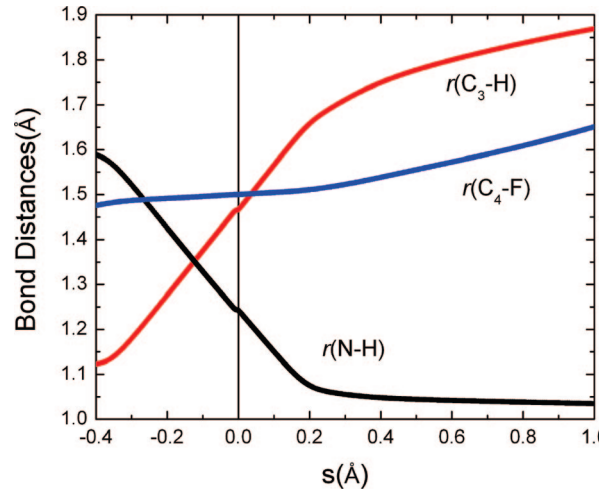

Figure 4. Bond distances along the reaction coordinate for the imidazole base reaction in solution. The vertical line is at the conventional TS. Negative and positive *s* values represent the reactant side and the product side of reaction paths, respectively.

The changes in some geometric parameters along the solution-phase MEP are illustrated in Figures 3 and 4 for the formate and imidazole base reactions, respectively, where *s* is the signed distance along the MEP (with the TS defining $s = 0$) in isoinertial coordinates scaled to a mass of 1 amu.

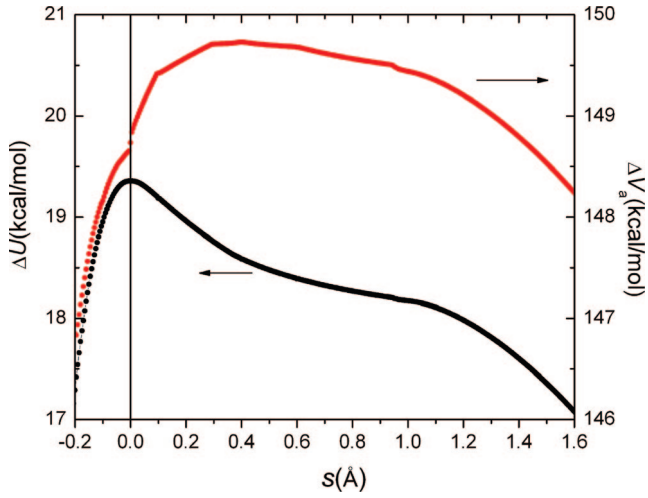

Figure 5. Potential of mean force and vibrationally adiabatic effective potential energy along the reaction coordinate of the HF elimination with formate base calculated by the IVTST-M method. Both curves in the figure are relative to reactants. The vertical line is at the conventional TS. Seven nonstationary Hessian ($s = -0.2, -0.1, 0.1, 0.3, 0.4, 0.6, 0.95$ Å) and 244 energy and gradient points were used [IVTST-M-7/244].

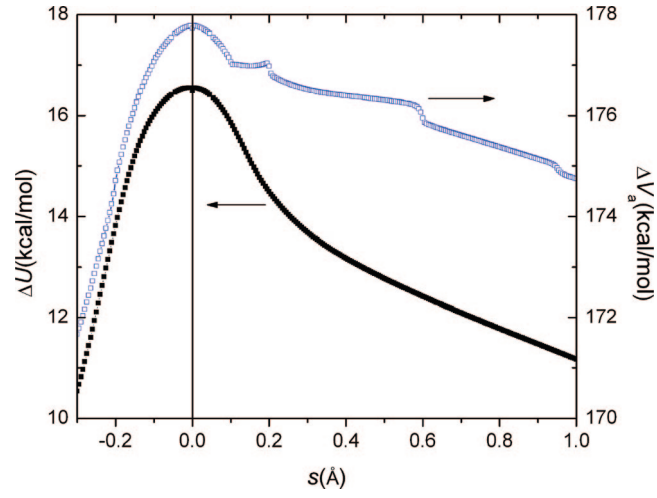

Figure 6. Potential of mean force and vibrationally adiabatic effective potential energy along the reaction coordinate of the HF elimination with imidazole base calculated by the IVTST-M method. Both curves in the figure are relative to reactants. The vertical line is at the conventional TS. Eight nonstationary Hessian ($s = -0.2, -0.1, -0.05, 0.05, 0.1, 0.2, 0.6, 0.95$ Å) and 283 energy and gradient points were used [IVTST-M-8/283].

As shown in Figure 3, the values of the C_3-H and O−H bond lengths cross before the reaction proceeds to a point at $s = -0.2$ Å. At the TS, the O−H distance is much shorter than the C_3-H distance, which is consistent with the late transition state in terms of the proton abstraction. Most of the proton transfer is finished before the point at $s = 0.2$ Å on the reaction path. However the C_4-F distance does not change much in the region of reaction coordinate shown in Figure 3. The bond distances in the imidazole base reaction, as illustrated in Figure 4, are changed in a similar way, except that the point where the C_3-H and O−H bond cross is slightly closer to the TS. Likewise, the transition state is late. Interestingly, the C−F bond length increases more rapidly after the proton transfer is almost finished at $s = 0.2$ Å. These results suggest that the elimination of HF from 4-fluoro-4-(4′-nitrophenyl)butane-2-one occurs asynchronously in a concerted mechanism, E2, with an E1cB-like transition state.

The proton is transferred first and followed by C−F bond cleavage without any intermediate. Specific solvent effects such as hydrogen bonds between solute and hydroxylic solvent are not considered explicitly in this study although to some extent they are implicit in the SM8 solvation model, so further study would be necessary to elucidate their role in the mechanism.

The generalized free energy of activation profile and the vibrationally adiabatic energy curves along the reaction coordinate are illustrated in Figures 5 and 6 for the formate and imidazole base reactions in solution, respectively. In both reactions, the free energies on the reactant side (negative s values) decrease very rapidly as the system leaves the TS, whereas the product side (positive s values) free energies are reduced slowly. In addition, the vibrationally adiabatic energy curve for the elimination by formate is very flat and wide near its maximum at $s = 0.4$ Å. The free energy of activation profiles at 311 K are qualitatively similar in shape to the vibrationally adiabatic curves. As a consequence there is a large variational effect (i.e., a large difference of CVT from conventional TST) for formate, but the variational effect for imidazole is less than 3% for any of the isotopomers studied. For formate the variational transition state is 0.41 Å later than the conventional TS for the all-protium case and 0.62 Å later than the conventional TS for dideuterium substitution at C-3. The variational effect lowers the rate coefficient by a factor of 6.2 for the all-protium case and a factor of 2.2 for dideuterium substitution at C_3. The resulting primary KIEs are shown in Table 5.

Table 5. Calculated Primary H/D KIEs and Ratios of Transmission Coefficients at 311 K[a]

base	k^{TST}	k^{CVT}	κ^{SCT}	$k^{CVT/SCT}$
formate	4.60	1.62	1.02	1.67
imidazole	5.29	5.29	0.97	5.13

[a] Each quantity in the table is the ratio of the values for all-protium HF elimination to that for dideuterium substitution at C_3. TST denotes conventional TS theory.

Table 6. Secondary KIEs and Ratios of Transmission Coefficients at 311 K

	secondary H/D[a]				$^{18}F/^{19}F$			
base	k^{TST}	k^{CVT}	κ^{SCT}	$k^{CVT/SCT}$	k^{TST}	k^{CVT}	κ^{SCT}	$k^{CVT/SCT}$
formate	0.943	1.045	0.999	1.044	1.005	1.021	1.001	1.020
	0.943	1.035	0.997	1.046				
imidazole	1.012	1.014	1.030	1.044	1.006	1.007	1.008	1.015
	1.012	1.012	1.012	1.024				

[a] The upper entry is for D substitution at C_4; the lower entry is for perdeuterated reactants.

We also calculated the secondary deuterium KIEs and the primary fluorine KIEs, and these are in Table 6. Again we see large variational effects for formate. The deuterium KIEs are in better agreement with experiment (see Table 1) than are the fluorine KIEs. For example, for formate, the

experimental result is 0.4% and the simulation gives 2.0%. So evidently something is missing in the theoretical description of these reactions. Perhaps there is another step that is partly rate determining and which does not introduce isotopic fractionation. What the experimental KIEs would seem to be telling us is maybe that most rate limiting hydrogen transfers occur with minor contributions from C−F bond breaking, but if we accepted that interpretation, then the small value of the primary deuterium KIE for formate cannot be explained. So we tentatively base our interpretation mainly on the larger KIEs.

Matsson and co-workers[9] have also provided further interpretation of the KIEs reported in Table 1. The secondary KIEs that they determined for the reactant perdeuterated in positions 1 and 3 are smaller than those for the isotopomers that have protium at these positions; they ascribed this to a mechanistic effect, namely the differences to changes in the commitment on rate constants k_2 and k_{-1} caused by the deuterium KIEs. In their analysis they assumed that the first step of the proton transfer does not exhibit any sizable fluorine KIE. Based on these results they postulated that the reaction proceeds by the E1cb mechanism. Our calculated primary H/D KIEs and ^{18}F/^{19}F KIEs are slightly smaller and larger, respectively, than the corresponding experimental results. The transmission coefficients, κ^{SCT}, for formate and imidazole promoted reactions without isotopic substitutions are 1.06 and 3.50 at 311 K, respectively. The small transmission coefficient for the formate reaction is attributed to the flat effective vibrationally adiabatic potential curve as shown in Figure 5. The tunneling contribution to the KIE, which is the ratio of transmission coefficient of the natural isotopomer to that of the substituted isotopomer, is almost unity for both reactions. The isotopic substitution does not change the tunneling coefficient much in these reactions. The secondary H/D KIEs agree better with experimental values. Interestingly the quasiclassical secondary H/D KIEs, which are from the rate constants without tunneling (that is, from k^{CVT}), become smaller when perdeuterated reactants are used, which means that the small secondary KIEs in experiment using the perdeuterated reactants may not be caused by the change in the commitment of stepwise processes. The smaller KIEs may be just an outcome of the zero-point and thermal vibrational energy changes at the transition state, so they cannot be used as evidence of the stepwise mechanism. The equilibrium secondary H/D KIE is 1.20 for both formate and imidazole promoted reactions. Comparing this value with the quasiclassical secondary H/D KIEs implies early transition states in terms of the force constant change at the C-4 position. Together with our earlier discussion of the lateness of the transition state in terms of the partial charges and the C_3−H bond distances, we postulate that the proton transfer and the fluoride dissociation occur very asynchronously at the level of theory used in this study, and the TS is very similar to the intermediate of the E1cB mechanism if it exists.

Comparison of the results of our calculations with the experimental values led us to a different interpretation from that of Matsson and co-workers. We conclude that the results of the secondary deuterium KIEs and the primary fluorine KIEs indicate that experimentally measured values correspond directly to the intrinsic KIEs on the reaction. The dependence of the observed KIEs on deuteration is in all cases well inside the experimental errors and cannot therefore be conclusive. Our results are in agreement with Thibblin and Ahlberg's[64] suggestion that the secondary leaving group fluorine KIE may also appear on the deprotonation process in the elimination reaction; they ascribed this effect to negative ion hyperconjugation. This was further supported by Saunders' calculations[65,66] of KIEs of the leaving group. Our calculations indicate that the bond order of the C_4−F bond decreases from 0.52 to 0.47 for both formate and imidazole promoted reactions in solution.

The results of the primary deuterium KIEs are also in agreement with the above interpretation, although the quantitative accuracy of the theoretical prediction of these KIEs is lower than of the other two. The size of the primary deuterium KIEs on proton transfer is considered to be a measure of the synchronicity of the transition state. The maximal primary KIE is expected for the most synchronous transition state,[61,67] the situation that occurs when the donor and the acceptor are of equal pK_a. It is interesting to note that in the present case the dependence is opposite; the smallest difference in pK_a is for the imidazole, which is characterized by the largest primary deuterium KIE; however, as mentioned above, the transition state for this reaction is less synchronous than the other.[58] This imbalance deserves further investigations.

Conclusions

We have used M06-L/6−31B(d) level of electronic structure theory with the SM8 solvation model, the CM4M charge model, and CVT/SCT dynamical theory in the equilibrium solvation path approximation to study KIEs on the base promoted elimination of HF from 4-fluoro-4-(4′-nitrophenyl)-butane-2-one. Our results indicate a concerted mechanism with an E1cB-like transition state and highly asynchronous processes for the proton transfer and fluoride dissociation. The tunneling contribution to the KIEs is very small due to very flat effective adiabatic potential energy curves near the transition state.

Acknowledgment. The authors are grateful to Yan Zhao for helpful discussions. These studies were supported by research grants from the State Committee for Scientific Research (KBN Poland) and by the National Science Foundation under Grant No. CHE07-04974. Y. Kim appreciates the financial support in part from the Kyung Hee University.

References

(1) Gerlt, J. A.; Gassman, P. G. *J. Am. Chem. Soc.* **1992**, *114*, 5928.

(2) Shokat, K. M.; Leumann, C. J.; Sugasawara, R.; Schultz, P. G. *Nature* **1989**, *338*, 269.

(3) Shokat, K. M.; Uno, T.; Schultz, P. G. *J. Am. Chem. Soc.* **1994**, *116*, 2261.

(4) Romesberg, F. E.; Flanagan, M. E.; Uno, T.; Schultz, P. G. *J. Am. Chem. Soc.* **1998**, *120*, 5160.

(5) Saunders, W. H., Jr. *J. Org. Chem.* **1997**, *62*, 244.

(6) Saunders, W. H., Jr. *J. Org. Chem.* **1999**, *64*, 861.

(7) Ryberg, P.; Matsson, O. *J. Am. Chem. Soc.* **2001**, *123*, 2712.

(8) Cleland, W. W. In *Enzyme Mechanism from Isotope Effects*; Cook, P. F., Ed.; CRC Press: Boca Raton, 1991; p 247.

(9) Ryberg, P.; Matsson, O. *J. Org. Chem.* **2002**, *67*, 811.

(10) Hwang, J.-K.; Creighton, S.; King, G.; Whitney, D.; Warshel, A. *J. Chem. Phys.* **1988**, *89*, 859.

(11) Sola, M.; Lledos, A.; Duran, M.; Bertran, J.; Abboud, J.-L. M. *J. Am. Chem. Soc.* **1991**, *113*, 2873.

(12) Assfeld, X.; Garapon, J.; Rinaldi, D.; Ruiz-Lopez, M. F.; Rivail, J. L. *THEOCHEM* **1996**, *371*, 107.

(13) Lee, I.; Kim, C. K.; Lee, B.-S.; Kim, C. K.; Lee, H. W.; Han, I.-S. *J. Phys. Org. Chem.* **1997**, *10*, 908.

(14) Chuang, Y.-Y.; Cramer, C. J.; Truhlar, D. G. *Int. J. Quantum Chem.* **1998**, *70*, 887.

(15) Lim, D.; Jenson, C.; Repasky, M. P.; Jorgensen, W. L. *ACS Symp. Ser.* **1999**, *721*, 74.

(16) Cramer, C. J.; Truhlar, D. G. *Chem. Rev.* **1999**, *99*, 2161.

(17) Naka, K.; Sato, H.; Morita, A.; Hirata, F.; Kato, S. *Theor. Chem. Acc.* **1999**, *102*, 165.

(18) McRae, R. P.; Schenter, G. K.; Garrett, B. C.; Svetlicic, Z.; Truhlar, D. G. *J. Chem. Phys.* **2001**, *115*, 8460.

(19) Gronert, S.; Pratt, L. M.; Mogali, S. *J. Am. Chem. Soc.* **2001**, *123*, 3081.

(20) Pliego, J. R., Jr. *J. Mol. Catal. A* **2005**, *239*, 228.

(21) Truhlar, D. G.; Pliego, J. R., Jr. In *Continuum Solvation Models in Chemical Physics*; Mennucci, B., Cammi, R., Eds.; Wiley: Chichester, 2008; p 338.

(22) Sicinska, D.; Paneth, P.; Truhlar, D. G. *J. Phys. Chem. B* **2002**, *106*, 2708.

(23) Sicinska, D.; Truhlar, D. G.; Paneth, P. *J. Am. Chem. Soc.* **2001**, *123*, 7683.

(24) Hariharan, P. C.; Pople, J. A. *Theor. Chim. Acta* **1973**, *28*, 213.

(25) Li, J.; Hawkins, G. D.; Cramer, C. J.; Truhlar, D. G. *Chem. Phys. Lett.* **1998**, *288*, 293.

(26) Li, J.; Zhu, T.; Hawkins, G. D.; Winget, P.; Liotard, D. A.; Cramer, C. J.; Truhlar, D. G. *Theor. Chem. Acc.* **1999**, *103*, 9.

(27) Zhu, T.; Li, J.; Liotard, D. A.; Cramer, C. J.; Truhlar, D. G. *J. Chem. Phys.* **1999**, *110*, 5503.

(28) Chuang, Y.-Y.; Radhakrishnan, M. L.; Fast, P. L.; Cramer, C. J.; Truhlar, D. G. *J. Phys. Chem. A* **1999**, *103*, 4893.

(29) Fang, Y.; Gao, Y.; Ryberg, P.; Eriksson, J.; Kolodziejska-Huben, M.; Dybala-Defratyka, A.; Madhavan, S.; Danielsson, R.; Paneth, P.; Matsson, O.; Westaway, K. C. *Chem. Eur. J.* **2003**, *9*, 2696.

(30) Dybała-Defratyka, A.; Rostkowski, M.; Matsson, O.; Westaway, K. C.; Paneth, P. *J. Org. Chem.* **2004**, *69*, 4900.

(31) Matsson, O.; Dybala-Defratyka, A.; Rostkowski, M.; Paneth, P.; Westaway, K. C. *J. Org. Chem.* **2005**, *70*, 4022.

(32) Fang, Y.; MacMillar, S.; Eriksson, J.; Kołodziejska-Huben, M.; Dybała-Defratyka, A.; Paneth, P.; Matsson, O.; Westaway, K. C. *J. Org. Chem.* **2006**, *71*, 4742.

(33) Zhao, Y.; Truhlar, D. G. *J. Chem. Phys.* **2006**, *125*, 194101.

(34) Lynch, B. J.; Zhao, Y.; Truhlar, D. G. *J. Phys. Chem. A* **2005**, *109*, 1643.

(35) Marenich, A. V.; Olson, R. M.; Kelly, C. P.; Cramer, C. J.; Truhlar, D. G. *J. Chem. Theory Comput.* **2007**, *3*, 2011.

(36) Olson, R. M.; Marenich, A. V.; Cramer, C. J.; Truhlar, D. G. *J. Chem. Theory Comput.* **2007**, *3*, 2046.

(37) Zhao, Y.; Truhlar, D. G. *MN-GFM-version 3.0*; University of Minnesota: Minneapolis, 2006.

(38) (a) Xidos, J. D.; Li, J.; Hawkins, G. D.; Winget, P.; Zhu, T.; Rinaldi, D.; Liotard, D. A.; Cramer, C. J.; Truhlar, D. G.; Frisch, M. J. *MN-GSM-version 99.8*; University of Minnesota, Minneapolis, 2001. (b) Olson, R. M.; Marenich, A. V.; Chamberlin, A. C.; Kelly, C. P.; Thompson, J. D.; Xidos, J. D.; Li, J.; Hawkins, G. D.; Winget, P.; Zhu, T.; Rinaldi, D.; Liotard, D. A.; Cramer, C. J.; Truhlar, D. G.; Frisch, M. J. *MN-GSM-2008*; University of Minnesota: Minneapolis, 2008.

(39) Frisch, M. J.; Trucks, G. W.; Schlegel, H. B.; Scuseria, G. E.; Robb, M. A.; Cheeseman, J. R.; Montgomery, J. A., Jr.; Vreven, T.; Kudin, K. N.; Burant, J. C.; Millam, J. M.; Iyengar, S. S.; Tomasi, J.; Barone, V.; Mennucci, B.; Cossi, M.; Scalmani, G.; Rega, N.; Petersson, G. A.; Nakatsuji, H.; Hada, M.; Ehara, M.; Toyota, K.; Fukuda, R.; Hasegawa, J.; Ishida, M.; Nakajima, T.; Honda, Y.; Kitao, O.; Nakai, H.; Klene, M.; Li, X.; Knox, J. E.; Hratchian, H. P.; Cross, J. B.; Bakken, V.; Adamo, C.; Jaramillo, J.; Gomperts, R.; Stratmann, R. E.; Yazyev, O.; Austin, A. J.; Cammi, R.; Pomelli, C.; Ochterski, J. W.; Ayala, P. Y.; Morokuma, K.; Voth, G. A.; Salvador, P.; Dannenberg, J. J.; Zakrzewski, V. G.; Dapprich, S.; Daniels, A. D.; Strain, M. C.; Farkas, O.; Malick, D. K.; Rabuck, A. D.; Raghavachari, K.; Foresman, J. B.; Ortiz, J. V.; Cui, Q.; Baboul, A. G.; Clifford, S.; Cioslowski, J.; Stefanov, B. B.; Liu, G.; Liashenko, A.; Piskorz, P.; Komaromi, I.; Martin, R. L.; Fox, D. J.; Keith, T.; Al-Laham, M. A.; Peng, C. Y.; Nanayakkara, A.; Challacombe, M.; Gill, P. M. W.; Johnson, B.; Chen, W.; Wong, M. W.; Gonzalez, C.; Pople, J. A. *Gaussian 03*; Gaussian, Inc.: Wallingford, CT, 2004.

(40) Garrett, B. C.; Truhlar, D. G. *J. Chem. Phys.* **1979**, *70*, 1593.

(41) Garrett, B. C.; Truhlar, D. G. *J. Am. Chem. Soc.* **1979**, *101*, 4534.

(42) Truhlar, D. G.; Garrett, B. C. *Acc. Chem. Res.* **1980**, *13*, 440.

(43) Garrett, B. C.; Truhlar, D. G.; Grev, R. S.; Magnuson, A. W. *J. Phys. Chem.* **1980**, *84*, 1730.

(44) Truhlar, D. G.; Isaacson, A. D.; Garrett, B. C. In *Theory of Chemical Reaction Dynamics*; Baer, M., Ed.; CRC Press: Boca Raton, FL, 1985; Vol. 4, p 65.

(45) Truhlar, D. G.; Garrett, B. C. *J. Chim. Phys.* **1987**, *84*, 365.

(46) Liu, Y.-P.; Lynch, G. C.; Truong, T. N.; Lu, D.-h.; Truhlar, D. G.; Garrett, B. C. *J. Am. Chem. Soc.* **1993**, *115*, 2408.

(47) Truhlar, D. G.; Liu, Y.-P.; Schenter, G. K.; Garrett, B. C. *J. Phys. Chem.* **1994**, *98*, 8396.

(48) Baldridge, K. K.; Gordon, M. S.; Steckler, R.; Truhlar, D. G. *J. Phys. Chem.* **1989**, *93*, 5107.

(49) Gonzàlez-Lafont, A.; Truong, T. N.; Truhlar, D. G. *J. Phys. Chem.* **1991**, *95*, 4618.

(50) Truhlar, D. G. In *The Reaction Path in Chemistry; Understanding Chemical Reactivity Series Vol. 16*; Heidrich, D., Ed.; Kluwer: Dordrecht, 1995; p 229.

(51) Corchado, J. C.; Coitiño, E. L.; Chuang, Y.-Y.; Fast, P. L.; Truhlar, D. G. *J. Phys. Chem. A* **1998**, *102*, 2424.

(52) Corchado, J. C.; Chuang, Y.-Y.; Coitiño, E. L.; Ellingson, B. A.; Zheng, J.; Truhlar, D. G. *Gaussrate-version 9.7*; University of Minnesota: Minneapolis, U.S.A., 2007.

(53) Corchado, J. C.; Chuang, Y.-Y.; Fast, P. L.; Hu, W.-P.; Liu, Y.-P.; Lynch, G. C.; Nguyen, K. A.; Jackels, C. F.; Ramos, A. F.; Ellingson, B. A.; Lynch, B. J.; Zheng, J.; Melissas, V. S.; Villa, J.; Rossi, I.; Coitino, E. L.; Pu, J.; Albu, T. V.; Steckler, R.; Garrett, B. C.; Isaacson, A. D.; Truhlar, D. G. *Polyrate-version 9.7*; University of Minnesota: Minneapolis, U.S.A., 2007.

(54) Lu, D.-h.; Truong, T. N.; Melissas, V. S.; Lynch, G. C.; Liu, Y.-P.; Garrett, B. C.; Steckler, R.; Isaacson, A. D.; Rai, S. N.; Hancock, G. C.; Lauderdale, J. G.; Joseph, T.; Truhlar, D. G. *Comput. Phys. Commun.* **1992**, *71*, 235.

(55) Fast, P. L.; Corchado, J. C.; Truhlar, D. G. *J. Chem. Phys.* **1998**, *109*, 6237.

(56) Fast, P. L.; Truhlar, D. G. *J. Chem. Phys.* **1998**, *109*, 3721.

(57) Gandler, J. R.; Jencks, W. P. *J. Am. Chem. Soc.* **1982**, *104*, 1937.

(58) Jia, Z. S.; Rudzinski, J.; Paneth, P.; Thibblin, A. *J. Org. Chem.* **2002**, *67*, 177.

(59) Mayer, I. *Chem. Phys. Lett.* **1983**, *97*, 270. Addendum: **1985**, *117*, 396.

(60) Johnston, H. S. *Adv. Chem. Phys.* **1960**, *3*, 131.

(61) Albery, W. J.; Kreevoy, M. M. *Adv. Phys. Org. Chem.* **1978**, *16*, 87.

(62) Johnston, H. S.; Parr, C. *J. Am. Chem. Soc.* **1963**, *85*, 2544.

(63) Bernasconi, C. F. *Acc. Chem. Res.* **1992**, *25*, 9.

(64) Thibblin, A.; Ahlberg, P. *J. Am. Chem. Soc.* **1977**, *99*, 7926.

(65) Saunders, W. H., Jr. *Chem. Scr* **1975**, *8*, 27.

(66) Saunders, W. H., Jr. *J. Am. Chem. Soc.* **1985**, *107*, 164.

(67) Melander, L.; Saunders, W. H., Jr. *Reaction Rates of Isotopic Molecules*; Wiley and Sons: New York, 1980.

CT800345J

JCTC Journal of Chemical Theory and Computation

Comparison of Semiempirical ZILSH and DFT Calculations of Exchange Constants in Fe_4 Butterfly Complexes

Ted A. O'Brien† and Candace M. Jones*

Department of Chemistry and Chemical Biology, Indiana University-Purdue University Indianapolis, 402 North Blackford Street, Indianapolis, Indiana 46202

Received August 21, 2007

Abstract: Magnetic interactions in a series of tetranuclear Fe^{3+} complexes with the butterfly core structure have been studied with semiempirical ZILSH and density functional theory (DFT) calculations (B3LYP functional). A theoretical analysis of a previously used method of estimating exchange constants from a restricted number of spin configurations reveals systematic errors arising from asymmetry in the complexes, which cause large variations in results with different choices of spin configurations. Correction factors are derived that yield the correct results obtained from full configuration space (FCS) calculations. Exchange constants obtained from DFT FCS calculations for the "body-body" interaction were large and ferromagnetic, in disagreement with values obtained from empirical fits of magnetic susceptibility data for the complexes, established magnetostructural correlations in polynuclear Fe^{3+} complexes, and ZILSH calculations. DFT calculations also gave unreasonably large antiferromagnetic exchange constants for interaction between "wingtip" ions that are not directly bridged, again in disagreement with ZILSH calculations. Estimates of exchange constants for interaction of body and wingtip ions obtained with ZILSH and DFT were similar, with the ZILSH values in slightly better agreement with empirical fits. Considering all interactions, the ZILSH method provides results in better accord with experiment than DFT for these complexes. Additional comparisons of exchange constants obtained with different spin coupling schemes showed that values appropriate for two-center spin eigenfunctions gave consistently better results than values calculated with the local spin operator. The effect of basis set was found to be very small. A brief analysis of these findings is given.

Introduction

Compounds containing multiple, magnetically coupled open shell transition metal ions have been intensively studied because they can display single molecule magnetism.[1−9] These so-called "single molecule magnets" (SMMs) have potential for applications in digital memory storage[10] and quantum computing.[11,12] One property crucial for single molecule magnetism is a large ground-state spin quantum number, which arises from magnetic interactions between transition metal ions with unpaired spins. It is thus vitally important to understand these interactions and the factors that contribute to them, both to describe them in known SMMs and (eventually) to facilitate rational design of SMMs with tailored magnetic properties. Magnetic interactions are usually characterized with the Heisenberg spin model, in which the exchange constant J_{AB} describes the strength and direction of coupling between the spin moments of metal ions labeled "A" and "B". From an experimental perspective, exchange constants are typically found by empirical fitting of the temperature response of the magnetic susceptibility of the complex. This becomes difficult as the number of metal ions (and, hence, number of exchange interactions) increases, leading to problems with obtaining a unique set

* Corresponding author e-mail: canmjone@iupui.edu.
† Deceased March 18, 2008.

10.1021/ct700208m CCC: $40.75 © 2009 American Chemical Society
Published on Web 11/26/2008

of fitting parameters and heavy dependence on the initial parameter values assumed in the fit. There is thus no direct link between experiment and the underlying conceptual model for larger complexes.

Quantum chemistry could in principle be used to assess magnetic interactions between transition metal ions, either to provide corroboration for empirical fits or to independently provide estimates of exchange constants in large, asymmetric complexes. Following early work by Yamaguchi[13,14] and Noodleman,[15−17] exchange constants are typically obtained from theoretical methods by computing the energies of various spin components of the complex defined by different relative orientations of the unpaired spins on the metal centers. These energies are assumed to follow an effective Heisenberg Hamiltonian, and the exchange constants can be solved for simultaneously given energies for an appropriate number of spin components. A number of recent calculations of this sort have been reported, using either density functional theory (DFT; refs 18−29) or the ZILSH method of O'Brien and Davidson.[24,30−36] Both methods have shown some success in these applications but have been systematically compared for only two complexes.[32] Further comparisons are needed to judge the relative merits of the two methods. In this paper we present and compare results obtained for a series of tetranuclear iron compounds with ZILSH and DFT calculations.

There are two important issues to consider when comparing methods. The first of these is accuracy—how well do the methods reproduce exchange constants obtained from fits of magnetic data? Very few direct comparisons of this sort have been made between ZILSH and DFT calculations. ZILSH appeared to be more accurate than DFT for the complex $[Fe_8O_2(OH)_{12}(tacn)_6]^{8+}$,[32] while the opposite was found for the complex $[Mn_{12}(OAc)_{14}(mda)_8]$.[24,29] Cauchy et al. recently reported results of DFT calculations on the complexes $[Fe_4O_2(OAc)_7(bpy)_2]^+$ (**1**), $[Fe_4O_2(O_2CPh)_7(phen)_2]^+$ (**2**), and $[Fe_4O_2(O_2CPh)_8(phen)_2]$ (**3**).[27] These complexes all have the well-known "butterfly" structure (Figure 1), and their magnetic interactions have been experimentally characterized.[37,38] They all have "wingtip-body" interactions with J_{wb} ca. -100 cm^{-1} (see Figure 1) and central, "body-body" interactions with J_{bb} ca. -10 cm^{-1}. Each also has a second-neighbor interaction between wingtip ions that are not directly bridged. The exchange constant for this interaction, J_{ww}, was assumed to be zero in fitting experimental magnetic susceptibility data,[37,38] but DFT calculations indicated these interactions might be significantly antiferromagnetic (J_{ww} ca. -5 to -10 cm^{-1}).[27] Together, complexes **1**−**3** provide a sufficient number of independent exchange constants to allow a thorough comparison of methods.

The second issue to consider in comparing computational methods is the size of complex that can be treated. As size increases calculations become more expensive, both on a per-calculation basis and in terms of the number of calculations that must be carried out; the number of exchange constants increases quadratically with the number of metal ions in the complex. The ZILSH method is based on the efficient semiempirical INDO/S method of Zerner,[39−46] so it can be applied to very large complexes. DFT calculations are much less efficient and become prohibitive for complexes with greater than ten or so transition metal ions present. Recourse is often made in such cases to what could be termed "restricted configuration space" (RCS) calculations, in which exchange constants assumed to have similar values are made equivalent and others neglected. This can greatly reduce the number of exchange constants to be solved for, and hence the number of spin configurations that must be considered compared to the standard "full configuration space" (FCS) approach, but if not done carefully can lead to systematic errors. Cauchy et al. used an RCS formulation for **1**−**3** in which all J_{wb} interactions were assumed to be equivalent.[27] These complexes are small enough that FCS calculations are readily feasible with DFT, allowing a comparison between RCS and FCS methods. The results show that the RCS calculations have systematic errors due to asymmetry in the J_{wb} pathways. Results are also presented for $[Fe_4O_2Cl_2(OAc)_6(bpy)_2]$ (**4**), which is less symmetric than **1**−**3**, and also has been experimentally

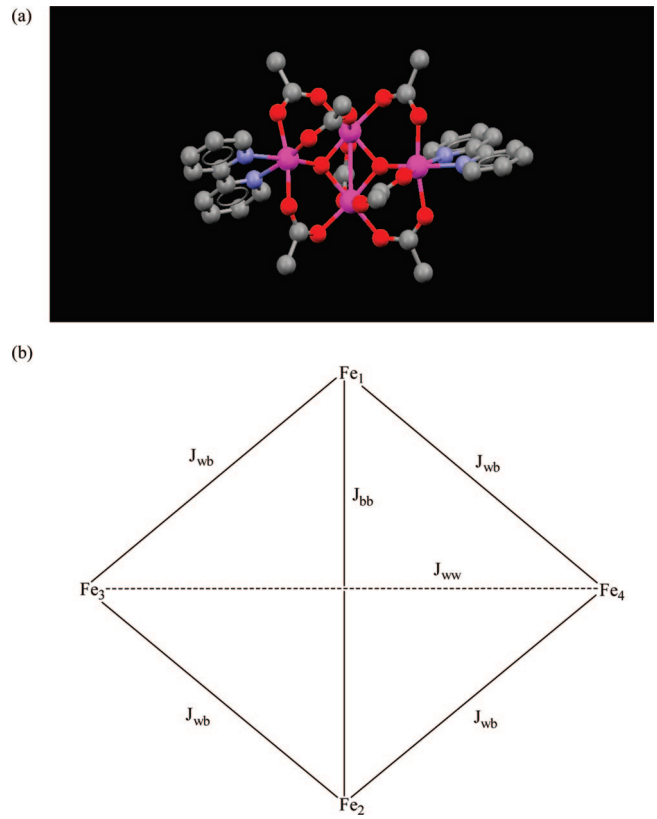

Figure 1. (a) Structure of Fe_4 butterfly complexes: structural diagram of $[Fe_4O_2(OAc)_7(bpy)_2]^+$ (**1**). Hydrogen atoms omitted for clarity. Structure obtained from ref 37. Fe - magenta; O - red; C - gray; N - blue. (b) Schematic representation of core structure with labeling scheme for iron ions and exchange constants. Solid lines represent exchange pathways mediated by bridging ligands. The broken line represents nonbridged second-neighbor interaction between wingtip ions.

characterized.[47] These calculations further illustrate the potential pitfalls of using the RCS method.

Methods of Calculation

A. Full Configuration Space (FCS) and Restricted Configuration Space (RCS) Calculations. The FCS and RCS methods of obtaining exchange constants from quantum chemical calculations both use wave functions (or Kohn−Sham single determinants in the case of DFT calculations) for spin components in which the unpaired spins on certain metal centers are arranged either "spin-up" or "spin-down" with respect to those on other metal centers. For wave function methods (e.g., ZILSH) the electronic Hamiltonian, $\hat{H}$, is assumed to map onto an effective Hamiltonian of the Heisenberg spin form

$$\hat{H} = \hat{H}_0 - \sum_{A<B} J_{AB}\hat{S}_A \cdot \hat{S}_B \tag{1}$$

where A and B label metal centers with nonzero spins, and $\hat{H}_0$ contains all spin-independent terms in the electronic Hamiltonian. Taking expectation values of this effective Hamiltonian for the appropriate number of spin component wave functions provides a set of equations that can be solved simultaneously for the unknown parameters E_0 and the set $\{J_{AB}\}$

$$E^i = E_0 - \sum_{A<B} J_{AB}\langle \hat{S}_A \cdot \hat{S}_B \rangle^i \tag{2}$$

where E^i is the energy of the ith component. In the case of DFT calculations, energies of unrestricted Kohn−Sham determinants are assumed to also follow eq 2.

The spin coupling expectation values $\langle \hat{S}_A \cdot \hat{S}_B \rangle$ in eq 2 might be evaluated with an operator such as Davidson's local spin operator[26,33,48] but often are assigned values assuming formal local spin quantum numbers of the metal centers (e.g., high spin Fe^{3+} ions with five unpaired electrons have $S_A = 5/2$) and that pairs of local spins A and B couple to form two-center spin eigenfunctions. For high spin d^5 Fe^{3+} ions, $\langle \hat{S}_A \cdot \hat{S}_B \rangle$ is then +6.25 for parallel spins A and B or −8.75 for antiparallel spins. These values are assumed even when the complex has more than two spin centers and single determinant wave functions are used in the calculations rather than spin eigenfunctions. The effect of this approximation is discussed in the next section (*vide infra*).

The FCS method uses a number of spin components equal to the number of unknown parameters obtained by allowing A and B to run over all metal centers. It involves no assumptions based on either symmetry (grouping pairwise exchange constants together into equivalent parameters) or magnetic interaction strength (neglecting interactions for metal centers not directly bridged by ligands). The RCS method does make the preceding assumptions—groups of exchange parameters are treated as equivalent parameters, and/or other exchange constants are assumed to be zero. It is often used for larger complexes, because the number of parameters is proportional to the square of the number of metal centers. The set of calculations required for the FCS method thus quickly becomes intractable as the number of metals in the complex increases.

The RCS approach reduces the computational effort required to treat larger complexes, but this is accomplished at the risk of neglecting exchange interactions that might be significant (e.g., second-neighbor interactions). Another more serious problem that can be encountered is that the exchange constants might not be invariant to the choice of spin configurations chosen for the restricted configuration space, and truncation of the configuration space itself might affect the parameters that are obtained. The recent DFT study of tetranuclear Fe^{3+} complexes by Cauchy et al.[37] provides a good illustration of both the RCS approach itself and its associated problems. Its development for complexes **1**−**4** is summarized here.

Given the exchange constants and numbering scheme of Figure 1 for Fe_4 butterfly complexes, the effective Hamiltonian of eq 1 becomes

$$\hat{H}_{eff} = \hat{H}_0 - J_{bb}\hat{S}_1 \cdot \hat{S}_2 - J_{ww}\hat{S}_3 \cdot \hat{S}_4 - J_{wb}(\hat{S}_1 \cdot \hat{S}_3 + \hat{S}_1 \cdot \hat{S}_4 + \hat{S}_2 \cdot \hat{S}_3 + \hat{S}_2 \cdot \hat{S}_4) \tag{3}$$

under the assumption that all J_{wb} interactions are equivalent. This leads to the energy expression

$$E^i = E_0 - J_{bb}\langle \hat{S}_1 \cdot \hat{S}_2 \rangle - J_{ww}\langle \hat{S}_3 \cdot \hat{S}_4 \rangle - J_{wb}(\langle \hat{S}_1 \cdot \hat{S}_3 \rangle + \langle \hat{S}_1 \cdot \hat{S}_4 \rangle + \langle \hat{S}_2 \cdot \hat{S}_3 \rangle + \langle \hat{S}_2 \cdot \hat{S}_4 \rangle) \tag{4}$$

There are thus four unknowns to be solved for, requiring wave functions or densities of four spin components.

Cauchy et al.[37] used the component with all unpaired spins aligned ("high spin", HS), that with the unpaired spins on Fe4 (see Figure 1) reversed relative to all others, and those with unpaired spins on Fe2 and Fe4 or Fe3 and Fe4 reversed. They assumed spin couplings appropriate for two-center spin eigenfunctions, leading to

$$E^{\mathrm{HS}} = E_0 - 6.25J_{bb} - 6.25J_{ww} - 25J_{wb} \tag{5}$$

$$E^4 = E_0 - 6.25J_{bb} + 8.75J_{ww} + 5J_{wb} \tag{6}$$

$$E^{24} = E_0 + 8.75J_{bb} + 8.75J_{ww} + 5J_{wb} \tag{7}$$

The three exchange constants are then found by making appropriate subtractions of these equations and rearranging the resulting expressions. For example, subtracting eq 8 from eq 5 leads to an expression involving only J_{wb} and the known energies E^{HS} and E.[34] Proceeding similarly for the other exchange constants, the following equations are obtained:

$$E^{34} = E_0 - 6.25J_{bb} - 6.25J_{ww} + 35J_{wb} \tag{8}$$

$$J_{wb} = \frac{E^{34} - E^{HS}}{60} \tag{9}$$

$$J_{bb} = \frac{E^{24} - E^4}{15} \tag{10}$$

(These expressions were derived with the subtractions (5)−(8), (6)−(7), and (5)−(6), respectively).

The following development shows that if the wingtip-body exchange couplings are inequivalent, J_{wb} obtained from eq 9 is actually the average of the four distinct wingtip-body couplings J_{13}, J_{14}, J_{23}, and J_{24} ($\overline{J_{wb}}$). Similarly, J_{bb} and J_{ww} obtained from eqs 10 and 11 contain errors arising from

artificially setting all wingtip-body couplings equal. To proceed, eqs 5−8 are recast assuming nonequivalent values for the four wingtip-body interactions, leading to

$$J_{ww} = \frac{E^4 - E^{HS}}{15} - 2J_{wb} = \frac{2E^4 - E^{34} - E^{HS}}{30} \quad (11)$$

$$E^{HS} = E_0 - 6.25J'_{bb} - 6.25J'_{ww} - 6.25(J_{13} + J_{14} + J_{23} + J_{24}) \quad (12)$$

$$E^4 = E_0 - 6.25J'_{bb} + 8.75J'_{ww} - 6.25(J_{13} + J_{23}) + 8.75(J_{14} + J_{24}) \quad (13)$$

$$E^{24} = E_0 + 8.75J'_{bb} + 8.75J'_{ww} - 6.25(J_{13} + J_{24}) + 8.75(J_{14} + J_{23}) \quad (14)$$

Making the same subtractions used above to obtain eqs 5−7 leads to

$$E^{34} = E_0 - 6.25J'_{bb} - 6.25J'_{ww} + 8.75(J_{13} + J_{14} + J_{23} + J_{24}) \quad (15)$$

$$\overline{J_{wb}} = \frac{J_{13} + J_{14} + J_{23} + J_{24}}{4} = \frac{E^{34} - E^{HS}}{60} = J_{wb} \quad (16)$$

$$J'_{bb} = \frac{E^{24} - E^4}{15} + (J_{24} - J_{23}) \quad (17)$$

$$J'_{ww} = \frac{E^4 - E^{HS}}{15} - (J_{14} + J_{24}) \quad (18)$$

Combining eq 17 with eq 10 and eq 18 with eq 11 gives

$$J'_{bb} = J_{bb} + (J_{24} - J_{23}) \quad (19)$$

$$J'_{ww} = J_{ww} + \frac{J_{13} + J_{23} - J_{14} - J_{24}}{2} \quad (20)$$

These equations clearly show that J_{bb} and J_{ww} as proposed by Cauchy et al.[37] provide correct estimates of the body-body and wingtip-wingtip exchange interactions only if the wingtip-body exchange interactions are equivalent. This is not the case for complexes **1**−**4**. It should also be pointed out that experimental determinations of J_{bb} and J_{wb} in butterfly complexes by means of fitting magnetic susceptibility data have also assumed that all J_{wb} interactions are equivalent[37,38,47] and thus involve the same approximations expressed in eqs 16−18.

An additional problem with the RCS method just developed is that the exchange constants are not invariant to the choice of spin components used. This is easily illustrated by considering the component with the spins of Fe2 and Fe3 reversed relative to the others. The energy of this component assuming equivalent J_{wb} interactions is

$$E^{23} = E_0 + 8.75J_{bb} + 8.75J_{ww} + 5J_{wb} \quad (21)$$

which is equal to E^{24} (eq 7) within the RCS model with all J_{wb} assumed to be equivalent. Subtracting eq 21 from eq 6 leads to

$$J_{bb} = \frac{E^{23} - E^4}{15} \quad (22)$$

Clearly, eqs 22 and 10 will lead to different values of J_{bb} unless $E^{23} = E^{24}$, which does not occur in complexes **1**−**4**. Taking complex **3** as an example, values of J_{bb} of -15 cm^{-1} and $+7$ cm^{-1} can be obtained from eqs 10 and 22, respectively (*vide infra*). Similar variance is easily demonstrated for J_{ww} and J_{wb} as well. This problem with variance is discussed further in the next section.

B. Computational Methods. ZILSH calculations on compounds **1**−**4** were performed as described in ref 33. The INDO/S method of Zerner[39−46] was used to obtain unrestricted Hartree−Fock wave functions for the various spin configurations, and expectation values $\langle \hat{S}_A \cdot \hat{S}_B \rangle$ were computed from the wave functions with Davidson's local spin operator.[26,33,48] DFT calculations were performed with the Gaussian03 program,[49] using the B3 exchange functional[50] together with the correlation functional of Lee, Yang, and Parr[51] (B3LYP). Two basis sets were employed, either the all-electron Dunning−Huzinaga double-ζ basis set for light atoms[52] with the Los Alamos effective core potential plus double-ζ valence basis set for iron atoms[53] (LANL2DZ; basis set I) or the all-electron double-ζ DZVP basis set of Alrichs for light atoms[54] and the all-electron triple-ζ TZVP basis set of Alrichs[55] for iron atoms (basis set II). Basis set II was used in ref 27. Spin couplings computed with the ZILSH method are generally similar to those obtained from DFT densities[25,26,33,48] and were used with DFT energies to obtain DFT estimates of the exchange constants. Exchange constants were also computed with all methods assuming spin couplings appropriate for two-center spin eigenfunctions.

Results and Discussion

The goal of this work was to compare FCS and RCS methods for **1**−**4** as well as the performance of the ZILSH and DFT methods with (in the latter case) different basis sets. Calculations were performed with ZILSH and the B3LYP functional with basis sets I and II for seven spin components for all complexes. This allowed for FCS calculations for each complex and RCS calculations with various choices of spin components. The spin components used were the component with all unpaired spins aligned ("high spin"), three components with the unpaired spins on Fe1, Fe2, or Fe4 (see Figure 1) reversed relative to all others,[56] and three components each with unpaired spins on two iron ions reversed relative to all others. The ions with reversed spins in the three cases were Fe2 and Fe3, Fe2 and Fe4, or Fe3 and Fe4. The ZILSH calculations followed the procedure described previously[32,33] and provided energies, spin densities, and spin couplings $\langle \hat{S}_A \cdot \hat{S}_B \rangle^{UHF}$. The latter were calculated with the semiempirical implementation[33] of Davidson's local spin operator.[26,48] The DFT calculations also used a previously described procedure[25] and provided energies and spin densities.

The results of all calculations are presented in Table 1a. Relative energies for each spin component computed with each method are given for each complex in cm^{-1}, along with the absolute energy in atomic units found for the high spin component with each method. The latter were provided to facilitate direct comparisons if other workers seek to repeat these calculations. Raw data (i.e., absolute energies, spin couplings) have not often been presented in the literature on computational studies of exchange interactions in polynuclear complexes, which makes comparative studies like

Table 1. Computational Results for Compounds **1**−**4**[a]

	spin component[b]					
quantity	HS	1	2	4	2,3	2,4	3,4
	A. $[Fe_4O_2(OAc)_7(bpy)_2]^+$ (Compound **1**)						
E (ZILSH)	4532.2[c](−576.33840654)[d]	2137.0	2135.2	2231.9	2153.0	2043.7	0.0
E (B3LYP/I)	4971.8(−3234.36437118)	2675.5	2670.8	2387.5	2527.3	2548.5	0.0
E (B3LYP/II)	5040.0 (−7794.00462476)	2652.8	2646.9	2426.4	2493.0	2560.8	0.0
M_1[e]	4.40 (4.27)	−4.34(−4.22)	4.41(4.27)	4.37(4.24)	4.37(4.25)	4.37(4.25)	4.34(4.22)
M_2	4.40 (4.27)	4.41(4.28)	−4.34(−4.22)	4.37(4.24)	−4.37(−4.25)	−4.37(−4.25)	4.34(4.22)
M_3	4.42 (4.25)	4.39(4.22)	4.39(4.22)	4.42(4.25)	−4.39(−4.21)	4.38(4.21)	−4.35(−4.19)
M_4	4.42(4.25)	4.39(4.22)	4.39(4.22)	−4.35(−4.19)	4.39(4.21)	−4.38(−4.21)	−4.35(−4.19)
$\langle \hat{S}_1 \cdot \hat{S}_2 \rangle$[f]	4.862	−4.769	−4.781	4.781	−4.778	−4.779	4.706
$\langle \hat{S}_1 \cdot \hat{S}_3 \rangle$	4.855	−4.742	4.815	4.811	−4.779	4.769	−4.710
$\langle \hat{S}_1 \cdot \hat{S}_4 \rangle$	4.855	−4.741	4.817	−4.741	4.770	−4.777	−4.709
$\langle \hat{S}_2 \cdot \hat{S}_3 \rangle$	4.855	4.811	−4.744	4.811	4.770	−4.777	−4.709
$\langle \hat{S}_2 \cdot \hat{S}_4 \rangle$	4.854	4.810	−4.746	−4.741	−4.778	4.769	−4.710
$\langle \hat{S}_3 \cdot \hat{S}_4 \rangle$	4.846	4.781	4.770	−4.769	−4.769	−4.767	4.696
	B. $[Fe_4O_2(O_2CPh)_7(phen)_2]^+$ (Compound **2**)						
E (ZILSH)	4846.0[c](−824.53737107)[d]	2208.1	2244.4	2323.0	2168.0	2217.0	0.0
E (B3LYP/I)	5229.4(−4727.58896405)	2686.5	2828.4	2495.9	2674.4	2534.3	0.0
E (B3LYP/II)	5291.4(−9286.34739508)	2665.4	2807.6	2530.5	2688.7	2502.7	0.0
M_1[e]	4.41(4.27)	−4.33(−4.21)	4.41(4.27)	4.37(4.24)	4.37(4.24)	4.37(4.24)	4.34(4.21)
M_2	4.40(4.27)	4.40(4.27)	−4.33(−4.21)	4.37(4.24)	−4.36(−4.24)	−4.37(−4.24)	4.34(4.21)
M_3	4.41(4.24)	4.37(4.21)	4.37(4.21)	4.41(4.24)	−4.37(−4.21)	4.37(4.20)	−4.34(−4.18)
M_4	4.41(4.24)	4.37(4.21)	4.37(4.21)	−4.33(−4.18)	4.37(4.21)	−4.37(−4.21)	−4.33(−4.18)
$\langle \hat{S}_1 \cdot \hat{S}_2 \rangle$[f]	4.833	−4.726	−4.714	4.788	−4.759	−4.688	4.744
$\langle \hat{S}_1 \cdot \hat{S}_3 \rangle$	4.835	−4.743	4.791	4.742	−4.741	4.668	−4.739
$\langle \hat{S}_1 \cdot \hat{S}_4 \rangle$	4.825	−4.725	4.746	−4.718	4.752	−4.687	−4.758
$\langle \hat{S}_2 \cdot \hat{S}_3 \rangle$	4.846	4.795	−4.763	4.786	4.745	−4.683	−4.750
$\langle \hat{S}_2 \cdot \hat{S}_4 \rangle$	4.836	4.768	−4.720	−4.760	−4.761	4.687	−4.760
$\langle \hat{S}_3 \cdot \hat{S}_4 \rangle$	4.840	4.794	4.797	−4.716	−4.755	−4.684	4.748
	C. $[Fe_4O_2(O_2CPh)_8(phen)_2]$ (Compound **3**)						
E (ZILSH)	4461.1[c](−894.32489930)[d]	2007.0	2006.9	2192.6	1830.0	2097.2	0.0
E (B3LYP/I)	5177.0 (−5148.94449971)	2586.8	2586.8	2482.1	2608.8	2276.1	0.0
E (B3LYP/II)	5163.2(−9707.54851198)	2553.0	2553.0	2481.0	2591.8	2252.3	0.0
M_1[e]	4.43(4.28)	−4.36(−4.22)	4.43(4.28)	4.40(4.25)	4.39(4.25)	4.40(4.25)	4.37(4.22)
M_2	4.43(4.28)	4.43(4.28)	−4.36(−4.22)	4.40(4.25)	−4.39(−4.25)	−4.40(−4.25)	4.37(4.22)
M_3	4.45(4.25)	4.41(4.22)	4.41(4.22)	4.45(4.25)	−4.41(−4.21)	4.41(4.21)	−4.37(−4.19)
M_4	4.45(4.25)	4.41(4.22)	4.41(4.22)	−4.37(−4.19)	4.41(4.21)	−4.41(−4.21)	−4.37(−4.19)
$\langle \hat{S}_1 \cdot \hat{S}_2 \rangle$[f]	4.904	−4.788	−4.787	4.866	−4.754	−4.823	4.819
$\langle \hat{S}_1 \cdot \hat{S}_3 \rangle$	4.903	−4.792	4.857	4.862	−4.755	4.815	−4.827
$\langle \hat{S}_1 \cdot \hat{S}_4 \rangle$	4.910	−4.827	4.827	−4.827	4.750	−4.823	−4.825
$\langle \hat{S}_2 \cdot \hat{S}_3 \rangle$	4.896	4.819	−4.816	4.819	4.744	−4.813	−4.818
$\langle \hat{S}_2 \cdot \hat{S}_4 \rangle$	4.903	4.862	−4.789	−4.792	−4.755	4.815	−4.827
$\langle \hat{S}_3 \cdot \hat{S}_4 \rangle$	4.904	4.866	4.859	−4.788	−4.754	−4.823	4.819

	spin component[b]					
quantity	HS	2	3[g]	4	2,3	2,4	3,4
	$[Fe_4O_2Cl_2(OAc)_6(bpy)_2]$ (Compound **4**)						
E (ZILSH)	3815.2[c](−559.84589131)[d]	1401.5	1665.3	2104.6	1557.6	1842.3	0.0
E (B3LYP/I)	4898.3(−3035.99026836)	2271.5	2216.0	2467.7	2309.2	2511.2	0.0
E (B3LYP/II)	4934.4(−8485.97744006)	2221.8	2215.7	2515.9	2296.8	2465.3	0.0
M_1[e]	4.43(4.24)	4.43(4.24)	4.39(4.21)	4.40(4.21)	4.38(4.24)	4.38(4.24)	4.36(4.19)
M_2	4.41(4.27)	−4.34(−4.21)	4.38(4.24)	4.38(4.24)	−4.40(−4.21)	−4.39(−4.21)	4.34(4.21)
M_3	4.42(4.23)	4.38(4.19)	−4.35(−4.16)	4.42(4.22)	−4.38(−4.19)	4.39(4.19)	−4.35(−4.17)
M_4	4.37(4.19)	4.34(4.16)	4.37(4.19)	−4.32(−4.14)	4.35(4.17)	−4.34(−4.16)	4.32(−4.14)
$\langle \hat{S}_1 \cdot \hat{S}_2 \rangle$[f]	4.882	−4.770	4.833	4.848	−4.807	−4.739	4.799
$\langle \hat{S}_1 \cdot \hat{S}_3 \rangle$	4.884	4.801	−4.800	4.812	−4.802	4.730	−4.807
$\langle \hat{S}_1 \cdot \hat{S}_4 \rangle$	4.844	4.802	4.804	−4.758	4.762	−4.718	−4.789
$\langle \hat{S}_2 \cdot \hat{S}_3 \rangle$	4.856	−4.749	−4.737	4.816	4.777	−4.712	−4.774
$\langle \hat{S}_2 \cdot \hat{S}_4 \rangle$	4.816	−4.740	4.737	−4.758	−4.745	4.685	−4.749
$\langle \hat{S}_3 \cdot \hat{S}_4 \rangle$	4.820	4.778	−4.707	−4.730	−4.747	−4.691	4.750

[a] See text for descriptions of methods and basis sets. [b] Indices indicate metals with unpaired spins reversed to all other unpaired spins. See Figure 1 for numbering scheme. "HS" indicates component with all unpaired spins aligned. [c] Relative energy (cm^{-1}). [d] Absolute energy of HS component (a.u.). [e] z component of spin for Fe1 computed from ZILSH component wave function. Values in parentheses obtained from B3LYP/II component density. [f] Spin coupling between Fe1 and Fe2 computed from ZILSH component wave function. [g] This choice of spin components (i.e., using that with spin of Fe3 reversed instead of that with Fe1 reversed) was adopted for **4** for consistent atom labeling with ref 33. The exchange constants obtained with FCS calculations and RCS eqs 9-11 are invariant to this choice.

the one reported here difficult. The high spin component was found to have the highest energy with all methods and basis sets, indicating that exchange interactions in **1**−**4** are predominantly antiferromagnetic. This is discussed further

Table 2. Exchange Constants Obtained for **1**−**4** with RCS Calculations[a] Using B3LYP/II Energies and Spin Couplings for Two-Center Spin Eigenfunctions[b,c]

complex	interaction[d]	FCS	RCS[e]	RCS, corrected[f]
$[Fe_4O_2(OAc)_7(bpy)_2]^+$ (**1**)	$J_{bb} = J_{12}$	+8.7	+9.0 (+8.3)	+8.7
	$J_{ww} = J_{34}$	−8.2	−6.2 (−5.8)	−8.2
	$\overline{J_{wb}}$	−84.0	−84.0 (−80.0)	−84.0
$[Fe_4O_2(O_2CPh)_7(phen)_2]^+$ (**2**)	$J_{bb} = J_{12}$	+6.1	−1.9 (−0.9)	+6.1
	$J_{ww} = J_{34}$	−9.4	−7.7 (−7.2)	−9.4
	$\overline{J_{wb}}$	−88.2	−88.2 (−84.2)	−88.2
$[Fe_4O_2(O_2CPh)_8(phen)_2]$ (**3**)	$J_{bb} = J_{12}$	−1.9	−15.2 (−15.2)	−1.9
	$J_{ww} = J_4$	−8.7	−6.7 (−6.3)	−8.7
	$\overline{J_{wb}}$	−86.1	−86.1 (−82.8)	−86.1
$[Fe_4O_2Cl_2(OAc)_6(bpy)_2]$ (**4**)	$J_{bb} = J_{12}$	+1.0	−3.4	+1.0
	$J_{ww} = J_{34}$	−6.8	+3.2	−6.8
	$\overline{J_{wb}}$	−82.2	−82.2	−82.2

[a] Equations 9-11. [b] The appropriate value for each spin coupling can be obtained from Table 1 by replacing all positive spin couplings with +6.25 and all negative spin couplings with −8.75. [c] All values in cm^{-1}. [d] See Figure 1 for labeling scheme. [e] Values in parentheses from ref 27. [f] Equations 16, 19, and 20.

below in reference to exchange constants obtained from FCS and RCS calculations. The component with unpaired spins on Fe3 and Fe4 reversed relative to the unpaired spins on Fe1 and Fe2 (see Figure 1) was found to have the lowest energy with all methods and basis sets, in accord with previous experimental[37,38,47] and theoretical[27,33] studies of these Fe_4 butterfly complexes.

Local spin densities computed for the iron ions from ZILSH wave functions with the Löwdin scheme[57] are given in Table 1a, along with those found from DFT Kohn−Sham determinants (basis set II) with the Mulliken scheme.[58] The local spin density of an ion is approximately equal to the number of unpaired electrons associated with that ion.[33] All values found with ZILSH are ca. 4.40 in magnitude, close to the formal value of five expected for high spin d^5 Fe^{3+} ions. The values given in Table 1b are reduced below five by spin delocalization and are similar to values obtained with ZILSH for other complexes of Fe^{3+} ions.[32,33,35,36] Values obtained with DFT calculations are similar to the ZILSH values and resemble those reported for similar calculations.[20,27] The signs of the local spin densities indicate the relative directions of spin moments of the iron ions and demonstrate that correct spin distributions were obtained for each spin component with all methods and basis sets.

Spin couplings $\langle \hat{S}_A \cdot \hat{S}_B \rangle^{UHF}$ found from ZILSH wave functions with the local spin operator[26,33,48] (Table 1c) took on values close to ±5, similar to those obtained from ZILSH calculations on other polynuclear Fe^{3+} complexes.[32,33,35,36] One goal of this work is to compare exchange constants obtained in two ways, using spin couplings properly calculated as expectation values of the local spin operator or using spin couplings appropriate for two-center spin eigenfunctions. Values for the latter case for each spin component are given by replacing positive values of $\langle \hat{S}_A \cdot \hat{S}_B \rangle^{UHF}$ in Table 1a with +6.25 and negative values with −8.75. Both choices of spin couplings are used with the energies in Table 1d to compute exchange constants with the FCS method and the RCS method with various sets of spin components. The results are presented and discussed in the following subsections.

A. Comparison of FCS and RCS Methods. Exchange constants obtained with FCS calculations and the RCS method of ref 27 (eqs 9−11) are compared in this subsection. Discussion is limited to results found with energies from B3LYP/II calculations and $\langle \hat{S}_A \cdot \hat{S}_B \rangle$ appropriate for two-center spin eigenfunctions. This allows direct comparison with previously reported results for compounds **1**−**3**.[27] Analogous conclusions would be reached based on results obtained from ZILSH or B3LYP/I calculations and either choice of spin couplings. Exchange constants J_{bb}, J_{ww}, and $\overline{J_{wb}}$ obtained from the data of Table 1a with eqs 9−11 are given in Table 2 for compounds **1**−**4**, along with those reported previously for **1**−**3**.[27] Values obtained with the correction factors of eqs 19 and 20 are also given as well as those found from FCS calculations with the same choice of method, basis set, and spin couplings.

A comparison of exchange constants obtained in this work with those reported previously for compounds **1**−**3**[27] shows very similar results: J_{bb} and J_{ww} agree within 1 cm^{-1}, and $\overline{J_{wb}}$, which is much larger in magnitude, agrees within 4 cm^{-1} (ca. 5%) for every complex. Though direct comparisons are difficult because no raw data were given in ref 27, the small discrepancies likely arise from different methods used for obtaining starting orbitals. We used the procedure described in ref 25, which uses standard starting guesses from the G03 program,[49] while Cauchy et al.[27] used starting guesses from the Jaguar 6.0 program.[59] Additionally, we used the standard G03 SCF algorithm, while they used the quadratically convergent algorithm. The SCF convergence threshold might also play a role. We assumed a threshold of 10^{-8} a.u., compared to the standard threshold of 10^{-4} a.u. employed by the G03 program. The latter threshold corresponds to ca. 20 cm^{-1}, which is on the same order of magnitude as the exchange constants themselves. Again it is difficult to judge whether convergence criteria play a role in the discrepancies in computed exchange constants, as Cauchy et al. did not state the threshold they used in ref 27. Regardless of specific causes for the discrepancies, it is clear that the results found in the present work are substantially the same as those reported by Cauchy et al.

A comparison of exchange constants obtained for compounds **1**−**4** with RCS and FCS calculations (Table 2) shows that there are discrepancies in the values obtained for J_{bb} and J_{ww}, as anticipated from eqs 19 and 20. These discrepancies are small for **1**, which is the least asymmetric complex

Table 3. Limiting Values of Exchange Constants Obtained with RCS Calculations (B3LYP/II) on All Possible Choices of Spin Configurations for Compounds **1**−**4**[a]

compound	**1**	**2**	**3**	**4**
J_{bb} (max)	+9.0	+10.8	+7.4	+16.6
J_{bb} (min)	+4.4	−1.9	−15.2	−16.4
J_{bb} (FCS)	+8.7	+6.1	−1.9	+1.0
J_{ww} (max)	−5.7	+1.6	+2.6	+16.2
J_{ww} (min)	−10.7	−20.3	−20.1	−16.8
J_{ww} (FCS)	−8.2	−9.4	−8.7	−6.8
J_{wb} (max)	−81.8	−81.9	−79.4	−65.7
J_{wb} (min)	−86.2	−94.5	−92.7	−98.7
J_{wb} (FCS)	−84.0	−88.2	−86.1	−82.2

[a] All values in cm^{-1}. See Figure 1 for labeling scheme for exchange constants.

and thus most closely reflects the approximation that all body-wingtip exchange couplings are equal. The discrepancies are larger for the less symmetric compounds, as large as 13.2 cm^{-1} in magnitude for J_{bb} of **3**. The sign of J_{bb} obtained for **2** from the RCS calculations is opposite that found with FCS calculations. The trend in J_{bb} and J_{ww} found with RCS calculations is reversed compared to that found with FCS calculations for **3**. In the case of **4**, the least symmetric compound in the set, the signs of both J_{bb} and J_{ww} found with RCS calculations are reversed relative to those found with FCS calculations, again leading to opposite trends. It is important to note that applying the correction factors of eqs 19 and 20 to J_{bb} and J_{ww} obtained from the RCS calculations leads to the FCS values in every case.[60] This is a clear demonstration that the RCS method does a poor job of recovering the FCS results for the less symmetric compounds.

An additional problem with the RCS method is that the exchange constants obtained are not invariant to the choice of spin components used, as discussed above. Seven spin components are needed for FCS calculations, while only four are needed for RCS calculations. Given energies and spin couplings for seven spin components in Table 1b, thirty-five different choices of four components can be made for RCS calculations. In some of these cases, the result of simultaneous solution of equations similar to eqs 9−11 is indeterminate. This is easily seen when the equations are cast into matrix form to occur when two rows in the square matrix containing the spin couplings are identical. In other cases this does not occur, and a solution for J_{bb}, J_{ww}, and $\overline{J_{wb}}$ is obtained. The crucial point is that these solutions are not the same for different choices of spin components. This is shown in Table 3, which reports limiting values of the exchange constants found for each complex with RCS calculations on all possible choices of four spin components from Table 1a. The results in Table 3 were found using B3LYP/II energies and spin couplings appropriate for two-center spin eigenfunctions; again, similar conclusions would be reached with other choices of method, basis set, and spin coupling scheme. Large variations were found with different choices of spin components used in the RCS calculations, as large as ∼32 cm^{-1} for J_{bb} and J_{ww} of compound **4**, compared to FCS values of +1 cm^{-1} and −7 cm^{-1}, respectively. Again the variations are smallest for **1**, the most symmetric of the four compounds, but even in this case are of substantial size compared to the FCS parameters (e.g., a variation of 5.0 cm^{-1} in magnitude for J_{ww}, compared to the FCS magnitude of 8.2 cm^{-1}). From these results it is clear that exchange constants obtained from one particular choice of spin components are of limited validity.

A very important point in this regard is that despite the large variations in the RCS exchange constants found with different choices of spin components, the FCS values are obtained for *all* sets of spin components when correction terms analogous to those given in eqs 19 and 20 are applied. This is shown in Table 4, which presents RCS equations and correction factors for four different choices of spin components for compound **3**. Exchange constants obtained using B3LYP/II energies and spin couplings appropriate for two-center spin eigenfunctions are given as well, along with corrected values and values obtained from FCS calculations. From the RCS calculations J_{bb} ranges from −15.2 cm^{-1} to +7.4 cm^{-1}, J_{ww} ranges from −20.0 cm^{-1} to +2.6 cm^{-1}, and $\overline{J_{wb}}$ ranges from −92.7 cm^{-1} to −81.4 cm^{-1}. Even so, applying the correction factors leads exactly to the FCS result in every case. This is a convincing demonstration that FCS calculations must be used to obtain a true measure of the performance of a particular method of calculation. In other words, comparisons between various computational methods, and between computational results and experiment, must be made on the basis of FCS calculations if they are to have any validity. This is done for compounds **1**−**4** in the following subsection.

B. Comparisons between Methods and Experiment (FCS Calculations). Exchange constants obtained for **1**−**4** with FCS calculations using different methods, basis sets, and spin coupling schemes are presented in Table 5. They are compared with exchange constants fit to reproduce experimental magnetic susceptibility data[37,38,47] in this section, with the goal of judging which method provides the most accurate picture of magnetic interactions in the complexes. Two general trends that are independent of basis set of spin coupling scheme are immediately apparent in Table 5. First, the body-body interactions J_{bb} found with DFT are uniformly ferromagnetic, while those found with ZILSH are antiferromagnetic. Fits of magnetic susceptibility data for each complex found J_{bb} to be antiferromagnetic,[37,38,47] in better agreement with the ZILSH calculations. It is, however, important to consider that the quality of the fits is relatively insensitive to the value of J_{bb}. In the case of **1**, for example, it was found that J_{bb} was "more positive than −15 cm^{-1}" and likely antiferromagnetic.[37] The experimental results are thus not definitive for these complexes regarding the sign of J_{bb}. Even so, the J_{bb} values from DFT calculations for **1**−**4** are very ferromagnetic, with magnitudes as large as +22 cm^{-1} for **1** found with B3LYP/I energies and $\langle \hat{S}_A \cdot \hat{S}_B \rangle^{UHF}$ values from Table 1a. Such large ferromagnetic interactions are at odds with virtually all salient interpretations of experimental magnetic fata for polynuclear Fe^{3+} complexes, including correlations between exchange constants and geometric parameters in bridging pathways and exchange constants extracted from experimental data for diferric complexes. These are discussed in turn below.

Table 4. RCS Equations and Exchange Constants Found for Compound **3** (B3LYP/II) for Several Choices of Spin Configurations[a]

configurations[b]	RCS	correction	J^{RCS}	J^{RCS}, corrected
HS, 4, 24, 34	$J_{bb} = (E^{24}-E^{4})/15$	$J'_{bb} = J_{bb} + J_{24} - J_{23}$	−15.2	−1.9 (−1.9)[c]
	$J_{ww} = (2E^{4}-E^{HS}-E^{34})/30$	$J'_{ww} = J_{ww} + {}^{1}/_{2}(J_{13} + J_{23} - J_{14} - J_{24})$	−6.7	−8.7 (−8.7)
	$J_{wb} = (E^{34} - E^{HS})/60$	$J_{wb} = J_{wb}$	−86.1	−86.1 (−86.1)
HS, 2, 4, 23	$J_{bb} = (E^{23} - E^{4})/15$	$J'_{bb} = J_{bb} + J_{14} - J_{13}$	+7.4	−1.9
	$J_{ww} = (E^{23} - E^{2})/15$	$J'_{ww} = J_{ww} + J_{23} - J_{13}$	+2.6	−8.7
	$J_{wb} = (E^{2} + E^{4} - E^{23} - E^{HS})/30$	$J_{wb} = {}^{1}/_{2}(J_{wb} + J_{13})$	−90.7	−86.1
2, 4, 24, 34	$J_{bb} = (E^{24} - E^{4})/15$	$J'_{bb} = J_{bb} + J_{24} - J_{23}$	−15.2	−1.9
	$J_{ww} = (E^{24} - E^{2})/15$	$J'_{ww} = J_{ww} + J_{24} - J_{14}$	−20.0	−8.7
	$J_{wb} = (E^{24} + E^{34} - E^{2} - E^{4})/30$	$J_{wb} = {}^{1}/_{2}(J_{wb} + J_{24})$	−92.7	−86.1
1, 4, 23, 34	$J_{bb} = (E^{23}-E^{4})/15$	$J'_{bb} = J_{bb} + J_{14} - J_{13}$	+7.4	−1.9
	$J_{ww} = (E^{23}-E^{1})/15$	$J'_{ww} = J_{ww} + J_{14} - J_{24}$	+2.6	−8.7
	$J_{wb} = (E^{23} + E^{34} - E^{1} - E^{4})/30$	$J_{wb} = {}^{1}/_{2}(J_{wb} + J_{14})$	−81.4	−86.1

[a] All values are given in cm^{-1} and were obtained assuming spin couplings appropriate for two-center spin eigenfunctions. The appropriate value for each spin coupling can be obtained from Table 1 by replacing all positive spin couplings with +6.25 and all negative spin couplings with −8.75. [b] Indices indicate metals with unpaired spins reversed to all other unpaired spins. See Figure 1 for numbering scheme. "HS" indicates component with all unpaired spins aligned. [c] Values obtained from FCS calculations.

Table 5. Exchange Constants Obtained for **1**−**4** with FCS Calculations Using Energies and Spin Couplings Given in Table *1*a[a]

complex	interaction[b]	ZILSH	B3LYP/I	B3LYP/II	exp[c]
$[Fe_4O_2(OAc)_7(bpy)_2]^+$ (**1**)	$J_{bb} = J_{12}$	−11.7 (−8.7)[d]	+21.6 (+12.5)	+15.6 (+8.7)	−17.8
	$J_{ww} = J_{34}$	−2.0 (−2.5)	−12.0 (−9.0)	−10.7 (−8.2)	−
	$J_{wb} = J_{13}$	−115.6 (−73.8)	−132.3 (−84.4)	−134.9 (−86.0)	−
	J_{14}	−121.1 (−77.2)	−127.4 (−81.2)	−128.3 (−81.8)	−
	J_{23}	−121.5 (−73.6)	−131.5 (−83.8)	−131.6 (−83.9)	−
	$\underline{J_{24}}$	−115.5 (−73.6)	−128.8 (−82.1)	−132.2 (−84.3)	−
	J_{wb}	−118.4 (−75.5)	−130.0 (−82.9)	−131.8 (−84.0)	−91.0
$[Fe_4O_2(O_2CPh)_7(phen)_2]^+$ (**2**)	$J_{bb} = J_{12}$	−19.5 (−13.1)	+16.4 (+9.5)	+10.9 (+6.1)	−2.4
	$J_{ww} = J_{34}$	−2.4 (−2.2)	−14.9 (−10.2)	−13.7 (−9.4)	−
	$J_{wb} = J_{13}$	−125.4 (−80.0)	−138.6 (−88.3)	−138.6 (−88.3)	−
	J_{14}	−129.4 (−82.8)	−141.9 (−90.7)	−145.2 (−92.8)	−
	J_{23}	−120.7 (−77.1)	−138.2 (−88.3)	−140.6 (−89.8)	−
	$\underline{J_{24}}$	−129.8 (−83.2)	−126.8 (−81.3)	−127.6 (−81.9)	−
	J_{wb}	−126.3 (−80.8)	−136.4 (−87.2)	−138.0 (−88.2)	−77.6
$[Fe_4O_2(O_2CPh)_8(phen)_2]$ (**3**)	$J_{bb} = J_{12}$	−22.2 (−14.9)	+1.1 (−0.1)	−1.7 (−1.9)	−15.6
	$J_{ww} = J_{34}$	−3.6 (−2.9)	−13.8 (−9.6)	−12.4 (−8.7)	−
	$J_{wb} = J_{13}$	−121.9 (−79.0)	−126.3 (−82.0)	−125.4 (−81.4)	−
	J_{14}	−107.2 (−69.7)	−139.6 (−90.6)	−139.8 (−90.7)	−
	J_{23}	−108.0 (−70.1)	−143.9 (−93.1)	−143.3 (−92.7)	−
	$\underline{J_{24}}$	−121.3 (−78.6)	−122.3 (−79.5)	−122.2 (−79.4)	−
	J_{wb}	−114.6 (−74.4)	−133.0 (−86.3)	−132.7 (−86.1)	−65.7
$[Fe_4O_2Cl_2(OAc)_6(bpy)_2]$ (**4**)	$J_{bb} = J_{12}$	−18.5 (−12.3)	+8.1 (+4.6)	+2.5 (+1.0)	−22
	$J_{ww} = J_{34}$	−1.5 (−1.5)	−10.1 (−7.2)	−9.5 (−6.8)	−
	$J_{wb} = J_{13}$	−100.7 (−64.9)	−125.6 (−81.0)	−126.1 (−81.4)	−
	J_{14}	−63.3 (−40.8)	−102.4 (−65.9)	−102.2 (−65.7)	−
	J_{23}	−119.7 (−76.9)	−141.2 (−90.7)	−145.0 (−93.1)	−
	$\underline{J_{24}}$	−112.4 (−71.7)	−139.5 (−89.0)	−139.1 (−88.7)	−
	J_{wb}	−99.0 (−63.6)	−127.2 (−81.6)	−128.1 (−82.2)	−82

[a] All values in cm^{-1}. [b] See Figure 1 for atom labeling scheme. [c] References 37 (**1**), 38 (**2**, **3**), and 47 (**4**). [d] Values in parentheses obtained assuming spin couplings appropriate for two-center spin eigenfunctions. The appropriate value for each spin coupling can be obtained from Table 1 by replacing all positive spin couplings with +6.25 and all negative spin couplings with −8.75.

Considering first correlations between structural parameters and exchange constants, empirical magnetostructural correlations have been found for both diferric and higher nuclearity Fe^{3+} complexes with substituted and unsubstituted oxo bridging ligands.[36,61−63] The number of distinct bridging pathways considered in these works is quite large, on the order of 85. In all cases, the exchange constant was found to become more antiferromagnetic with decreasing average Fe−O bond distance in the coupling pathway. A dependence on Fe−O−Fe bridging angle was also found,[36,61,62] with the exchange constant becoming more antiferromagnetic with increasing angle. This dependence was especially marked for higher nuclearity complexes[36] but was weaker than the dependence on bond distance in all cases. Although different fitting parameters for the magnetostructural correlation equations were found depending on the complexes considered (i.e., dinuclear or higher nuclearity, substituted vs unsubstituted oxo bridged or both considered together), all of these models predict antiferromagnetic J_{bb} values given the geometric parameters of the body-body pathways in **1**−**4**. The correlation of Cañada-Vilalta et al.[36] is perhaps most applicable for **1**−**4** since it was based on interactions in polynuclear complexes with O^{2-}-mediated exchange interactions as small as -8 cm^{-1}, and it gives estimates of J_{bb} in

the range -13 cm^{-1} to -16 cm^{-1} for **1**−**4**. The other magnetostructural correlations mentioned above[61−63] give even more antiferromagnetic estimates. The large ferromagnetic J_{bb} values found with DFT thus appear to disagree with trends extracted from a great deal of experimental data on dinuclear and higher nuclearity Fe^{3+} complexes.

Turning now to exchange constants extracted from magnetic susceptibilities of diferric complexes, the exchange constant in these cases is directly related to the experimental data since there is only one fitting parameter. A survey of the literature on 65 diferric complexes with substituted and/or unsubstituted oxo bridging ligands with available magnetic susceptibility data showed a very wide range of exchange constants, from -284 cm^{-1} ([(TPP)$_2$Fe$_2$O], TPP = 7,8-dihydro-5,10,15,20-tetraphenylporphyrinate; ref 64) to $+2.4$ cm^{-1} ([(salmp)$_2$Fe$_2$], salmp = 2-bis(salicylidenoamino)methylphenolate; ref 65). It is interesting to note that only one of the observed exchange constants is ferromagnetic, that for [(salmp)$_2$Fe$_2$] with $J = +2.4$ cm^{-1}. This complex has substituted oxo bridging ligands rather than unsubstituted oxo ligands as in **1**−**4**; the latter are known to have interactions that are more antiferromagnetic.[63] The diferric complex also has significantly longer Fe−O bond distances in the bridging pathway (∼2.02 Å vs ∼1.95 Å in **1**−**4**). Given that J becomes more antiferromagnetic with decreasing bond distance,[36,61−63] both factors indicate that J_{bb} in **1**−**4** would be substantially more antiferromagnetic than the value of $+2.4$ cm^{-1} observed for [(salmp)$_2$Fe$_2$] and hence likely have negative signs. Again, the indication is that the J_{bb} values found with DFT are considerably too ferromagnetic. This might be a general tendency, as analogous behavior was found for a similar exchange pathway in the complex $[Fe_8O_2(OH)_{12}(tacn)_6]^{8+}$ (ref 20; see also discussion in ref 32). Additional testing is needed to further investigate this tendency.

Another trend apparent in the exchange constants of Table 5 is that the DFT calculations give strongly antiferromagnetic estimates for the wingtip-wingtip interactions J_{ww} for all four complexes. Again this does not depend heavily on basis set or choice of spin coupling scheme. The ZILSH calculations give estimates that are very weakly antiferromagnetic. Direct comparison with experiment is not possible for this interaction since fits of the magnetic data neglected this interaction.[37,38,47] This was done because the wingtip ions do not interact directly by means of a single-atom bridging mode and were thus assumed to have a negligibly small exchange constant. This is a standard assumption. While there is some experimental evidence that such "second neighbor" interactions might have nonzero exchange interactions (see, e.g., refs 66 and 67), the proposed exchange constants have magnitudes less than 2 cm^{-1}. It seems unlikely that exchange interactions between metal ions that are not directly bridged would be as large in magnitude as the DFT estimates for J_{ww} in **1**−**4**. This is especially true given that J_{ww} is larger in magnitude that J_{bb} for **3** and **4** and of comparable magnitude for **1** and **2**, and the body-body interactions are mediated by single atom bridging ligands. It thus appears that the DFT calculations are overestimating the magnitudes of J_{ww} in **1**−**4**, in contrast to the ZILSH calculations which give much smaller magnitudes for these interactions.

Estimates of $\overline{J_{wb}}$ from the various methods of calculation are more similar than the estimates of J_{bb} and J_{ww}. When comparing computed values to those found from fits of experimental magnetic data, it is important to note that the fits assumed equivalent J_{wb} interactions, so the empirical values should be compared to average values obtained from the FCS calculations. Two factors must be considered in making these comparisons, including choice of method (ZILSH or DFT) and choice of spin coupling scheme. The role of basis set must also be considered for the DFT calculations; this is discussed below. Starting with the choice of method, the ZILSH calculations give better estimates of $\overline{J_{wb}}$ (i.e., closer to the empirical values) than DFT for all four complexes with spin couplings computed from the ZILSH component wave functions and for compounds **2** and **3** with spin couplings appropriate for two-center spin eigenfunctions. Taken together with the results found for J_{bb} and J_{ww} given above, this is a strong indication that the ZILSH calculations provide a picture of magnetic interactions in these complexes that is more consistent with experiment. This was also found to be the case with the complex $[Fe_8O_2(OH)_{12}(tacn)_6]^{8+}$ (ref 32) but not for the complex $[Fe_{14}O_6(bta)_6(OMe)_{18}Cl_6]$, in which DFT calculations gave the correct ground-state spin while ZILSH calculations did not.[68] Clearly comparisons for additional complexes are needed to clarify if one method is consistently more reliable than the other for estimating exchange constants in polynuclear transition metal complexes.

Turning now to choice of spin coupling scheme, in comparisons within the same method DFT calculations give much more accurate estimates of $\overline{J_{wb}}$ with spin couplings appropriate for two-center spin eigenfunctions (Table 5). The ZILSH calculations behave likewise for compounds **1**−**3**, while very similar errors in $\overline{J_{wb}}$ are found with the two coupling schemes for **4**. From a practical standpoint, then, it appears that spin couplings appropriate for two-center spin eigenfunctions give consistently better results. It is unclear why this is the case. O'Brien and Davidson[33] and particularly Clark and Davidson,[25,69,70] among others,[21,71,72] have recently considered this question from a theoretical perspective rather than on the basis of a systematic comparison of calculated and experimental results. While it is not our intention to repeat or extend these theoretical analyses here, some remarks can be made based on the results found for **1**−**4**.

Conceptually, if spin component wave functions are assumed to follow the effective Hamiltonian of eq 1, then spin couplings should properly be evaluated as expectation values of the operator $\hat{S}_A \cdot \hat{S}_B$. O'Brien and Davidson[33] showed that in the formal case of single determinant component wave functions with open-shell MOs centered entirely on the radical centers and identical closed shell ligand MOs for α and β electrons (i.e., no spin delocalization or spin polarization), the same exchange constants describing the true spin states of the system are obtained if the spin couplings are evaluated as expectation values of the local spin operator. Again in the formal case, these expectation values are smaller

in magnitude for single determinant wave functions than for two-center spin eigenfunctions (e.g., ±6.25 vs +6.25/−8.75 for single determinant wave functions and spin eigenfunctions describing two coupled high spin d^5 Fe^{3+} ions, respectively). Exchange constants obtained with the method of simultaneous solution of equations similar to eq 2 above are inversely proportional to the magnitudes of the spin couplings used, since the exchange constants are formally obtained by multiplying a column matrix containing the component energies by the inverse of a square matrix containing the spin couplings. In the formal case, then, use of spin couplings appropriate for two-center spin eigenfunctions should lead to artificially small estimates of the magnitudes of the exchange constants.

The obvious problem with this analysis is that the smaller estimates obtained with two-center spin eigenfunction spin couplings are more consistent with experimental results for $\overline{J_{wb}}$ for **1**−**4**. This could arise from cancelation of errors, as component wave functions for real complexes do not generally meet the formal conditions given above, i.e., unrestricted spin component wave functions do display spin polarization and delocalization. Exchange constants obtained from such wave functions are thus only approximations of the exchange constants describing the true spin eigenstates of a complex. Even if the component wave functions did behave formally, the methods themselves still have intrinsic error; i.e., neither ZILSH nor DFT calculations can be expected to perfectly reproduce magnetic interaction energies. The effect of these various considerations has not been thoroughly elucidated theoretically or on the basis of comparisons between calculated and empirical exchange constants. It is also very important to note that in other cases we have observed that the larger exchange constants found with spin couplings obtained from the local spin operator are more consistent with experiment.[33,68] Further study from both theoretical and practical perspectives is needed to clarify these issues.

A final point to consider is the effect of basis set in the DFT calculations. The larger exchange constants $\overline{J_{wb}}$ found with the two basis sets are very similar (Table 5), with differences on the order of 1 cm^{-1}. The pairwise wingtip-body interactions J_{13}, J_{14}, etc. share this similarity, differing by no more than ∼3% (J_{14} of **2**; J_{23} of **4**) and by about 1 cm^{-1} in all other cases. This level of agreement seems remarkable, given that basis set II is almost twice as large as basis set I (e.g., 1038 vs 622 basis functions for **4**), but it should be recalled that exchange constants are based on differences in energies of spin components with similar local electronic structure (i.e., all open shell metal ions are locally in high spin configurations, though they may be reversed relative to the unpaired spin on another metal ion). It is thus likely that any basis set error—which is itself a somewhat nebulous concept in DFT (e.g., ref 73)—approximately cancels in subtracting to obtain energy differences contributing to $\overline{J_{wb}}$. A clear basis set effect can be seen in the interactions that are not well-described by the DFT calculations, particularly in the J_{bb} interactions. For those the larger basis set consistently provides less ferromagnetic estimates, though the values obtained are still in qualitative disagreement with values obtained from empirical fitting of magnetic susceptibility data.

Conclusions

Exchange constants describing magnetic interactions in tetranuclear Fe^{3+} buttefly complexes **1**−**4** were estimated with semiempirical ZILSH calculations and DFT calculations using the B3LYP functional and two basis sets. Theoretical analysis of a restricted configuration space (RCS) method developed by Cauchy et al.[37] for these complexes showed that systematic errors in the exchange constants were incurred by assuming equivalent wingtip-body interactions J_{wb}. Correction factors were derived and found to exactly reproduce results from full configuration space (FCS) calculations. Additionally it was shown that exchange constants obtained from RCS calculations with different choices of spin configurations had large variances. Again, derived correction factors led exactly to FCS results in all cases. These results indicate that RCS calculations must be handled carefully to prevent significant errors if used in place of FCS calculations.

Comparisons of exchange constants obtained from ZILSH and DFT FCS calculations with those obtained from empirical fits of experimental magnetic susceptibility data were made. It was found that DFT calculations with both basis sets gave strongly ferromagnetic estimates of exchange constants describing interaction of the "body" iron ions (J_{bb}), while ZILSH calculations gave antiferromagnetic estimates. The latter are in much better agreement with empirical values for these complexes as well as estimates from well-known magnetostructural correlations in dinuclear and higher nuclearity Fe^{3+} clusters and empirical values found for diferric complexes. DFT calculations with both basis sets also gave unreasonably strong, antiferromagnetic exchange constants for nonbridged, second-nighbor interactions between wingtip ions (J_{ww}), while ZILSH calculations gave uniformly small estimates. ZILSH and DFT performed similarly for wingtip-body interactions J_{wb}, with the former giving slightly more accurate estimates. Together with the results found for J_{bb} and J_{ww}, these results indicate that the ZILSH method provides exchange constants that are more consistent with experiment for these complexes. Additional comparisons of the two methods are needed to judge their relative abilities to estimate exchange constants in polynuclear transition metal complexes. With further calibration and (perhaps) improvement, these computational methods could make important contributions to ongoing study and development of single molecule magnets.

Comparisons were also made between exchange constants obtained with different spin coupling schemes. Consistently better results were obtained with spin couplings appropriate for two-center spin eigenfunctions rather than couplings obtained as expectation values of the local spin operator evaluated with ZILSH spin component wave functions. A brief conceptual analysis of why this might occur was given. This question needs to be investigated further from both theorectical and practical (i.e., by comparing results against experiment for known complexes) perspectives.

Very small differences were observed when comparing exchange constants obtained from DFT calculations with

basis sets of distinctly different sizes. This likely occurs because basis set errors cancel in subtracting to obtain energy differences in evaluating exchange constants. DFT calculation of exchange constants in larger complexes would be facilitated by using smaller basis sets if the lack of basis set effect observed here is substantiated with additional comparisons.

Acknowledgment. This work was supported by Shared University Research grants from IBM, Inc. to Indiana University. C.M.J. acknowledges funding from the Undergraduate Research Opportunities Program at Indiana University-Purdue University Indianapolis.

References

(1) Sessoli, R.; Tsai, H. L.; Schake, A. R.; Wang, S. Y.; Vincent, J. B.; Folting, K.; Gatteschi, D.; Christou, G.; Hendrickson, D. N. *J. Am. Chem. Soc.* **1993**, *115*, 1804–1816.

(2) Sessoli, R.; Gatteschi, D.; Caneschi, A.; Novak, M. A. *Nature* **1993**, *365*, 141–143.

(3) Sangregorio, C.; Ohm, T.; Paulsen, C.; Sessoli, R.; Gatteschi, D. *Phys. Rev. Lett.* **1997**, *78*, 4645–4648.

(4) Gatteschi, D. *J. Alloys Compd.* **2001**, *317*, 8–12.

(5) Eppley, H. J.; Tsai, H. L.; Devries, N.; Folting, K.; Christou, G.; Hendrickson, D. N. *J. Am. Chem. Soc.* **1995**, *117*, 301–317.

(6) Christou, G.; Gatteschi, D.; Hendrickson, D. N.; Sessoli, R. *MRS Bull.* **2000**, *25*, 66–71.

(7) Caneschi, A.; Gatteschi, D.; Sessoli, R.; Barra, A. L.; Brunel, L. C.; Guillot, M. *J. Am. Chem. Soc.* **1991**, *113*, 5873–5874.

(8) Beltran, L. M. C.; Long, J. R. *Acc. Chem. Res.* **2005**, *38*, 325–334.

(9) Barra, A. L.; Debrunner, P.; Gatteschi, D.; Schulz, C. E.; Sessoli, R. *Europhys. Lett.* **1996**, *35*, 133–138.

(10) Leuenberger, M. N.; Loss, D. *Nature* **2001**, *410*, 789–793.

(11) Troiani, F.; Ghirri, A.; Affronte, M.; Carretta, S.; Santini, P.; Amoretti, G.; Piligkos, S.; Timco, G.; Winpenny, R. E. P. *Phys. Rev. Lett.* **2005**, *94*, 207208.

(12) Troiani, F.; Affronte, M.; Carretta, S.; Santini, P.; Amoretti, G. *Phys. Rev. Lett.* **2005**, *94*, 190501.

(13) Yamaguchi, K. *Chem. Phys. Lett.* **1975**, *33*, 330–335.

(14) Yamaguchi, K.; Fukui, H.; Fueno, T. *Chem. Lett.* **1986**, 625–628.

(15) Noodleman, L.; Norman, J. G. *J. Chem. Phys.* **1979**, *70*, 4903–4906.

(16) Noodleman, L. *J. Chem. Phys.* **1981**, *74*, 5737–5743.

(17) Noodleman, L.; Davidson, E. R. *Chem. Phys.* **1986**, *109*, 131–143.

(18) Zhao, X. G.; Richardson, W. H.; Chen, J. L.; Li, J.; Noodleman, L.; Tsai, H. L.; Hendrickson, D. N. *Inorg. Chem.* **1997**, *36*, 1198–1217.

(19) Soda, T.; Kitagawa, Y.; Onishi, T.; Takano, Y.; Nagao, H.; Yoshioka, Y.; Yamaguchi, K. *Chem. Phys. Lett.* **2000**, *319*, 223–230.

(20) Ruiz, E.; Cano, J.; Alvarez, S. *Chem. Eur. J.* **2005**, *11*, 4767–4771.

(21) Ruiz, E.; Alvarez, S.; Cano, J.; Polo, V. *J. Chem. Phys.* **2005**, 164110.

(22) Rajaraman, G.; Murugesu, M.; Sanudo, E. C.; Soler, M.; Wernsdorfer, W.; Helliwell, M.; Muryn, C.; Raftery, J.; Teat, S. J.; Christou, G.; Brechin, E. K. *J. Am. Chem. Soc.* **2004**, *126*15445–15457.

(23) Rajaraman, G.; Cano, J.; Brechin, E. K.; McInnes, E. J. L. *Chem. Commun.* **2004**, 1476–1477.

(24) Foguet-Albiol, D.; O'Brien, T. A.; Wernsdorfer, W.; Moulton, B.; Zaworotko, M. J.; Abboud, K. A.; Christou, G. *Angew. Chem., Int. Ed. Engl.* **2005**, *44*, 897–901.

(25) Davidson, E. R.; Clark, A. E. *J. Phys. Chem. A* **2002**, *106*, 7456–7461.

(26) Clark, A. E.; Davidson, E. R. *J. Chem. Phys.* **2001**, *115*, 7382–7392.

(27) Cauchy, T.; Ruiz, E.; Alvarez, S. *J. Am. Chem. Soc.* **2006**, *128*, 15722–15727.

(28) Cauchy, T.; Ruiz, E.; Alvarez, S. *Phys. B (Amsterdam, Neth.)* **2006**, *384*, 116–119.

(29) Cano, J.; Costa, R.; Alvarez, S.; Ruiz, E. *J. Chem. Theory Comput.* **2007**, *3*, 782–788.

(30) Tasiopoulos, A. J.; Wernsdorfer, W.; Abboud, K.; Christou, G. *Angew. Chem., Int. Ed. Engl.* **2004**, *43*, 6338–6342.

(31) Stamatatos, T. C.; Christou, A. G.; Jones, C. M.; O'Callaghan, B. J.; Abboud, K. A.; O'Brien, T. A.; Christou, G. *J. Am. Chem. Soc.* **2007**, *129*, 9840–9841.

(32) O'Brien, T. A.; O'Callaghan, B. J. *J. Chem. Theory Comput.* **2007**, *3*, 1275–1283.

(33) O'Brien, T. A.; Davidson, E. R *Int. J. Quantum Chem.* **2003**, *92*, 294–325.

(34) Canada-Vilalta, C.; Streib, W. E.; Huffman, J. C.; O'Brien, T. A.; Davidson, E. R.; Christou, G. *Inorg. Chem.* **2004**, *43*, 101–115.

(35) Canada-Vilalta, C.; O'Brien, T. A.; Pink, M.; Davidson, E. R.; Christou, G. *Inorg. Chem.* **2003**, *42*, 7819–7829.

(36) Canada-Vilalta, C.; O'Brien, T. A.; Brechin, E. K.; Pink, M.; Davidson, E. R.; Christou, G. *Inorg. Chem.* **2004**, *43*, 5505–5521.

(37) McCusker, J. K.; Vincent, J. B.; Schmitt, E. A.; Mino, M. L.; Shin, K.; Coggin, D. K.; Hagen, P. M.; Huffman, J. C.; Christou, G.; Hendrickson, D. N. *J. Am. Chem. Soc.* **1991**, *113*, 3012–3021.

(38) Boudalis, A. K.; Lalioti, N.; Spyroulias, G. A.; Raptopoulous, C. P.; Terzis, A.; Bousseksou, A.; Tangoulis, V.; Tucagues, J. P.; Perlepes, S. P. *Inorg. Chem.* **2002**, *41*, 6474–6487.

(39) Zerner, M. C.; Loew, G. H.; Kirchner, R. F.; Muellerwesterhoff, U. T *J. Am. Chem. Soc.* **1980**, *102*, 589–599.

(40) Ridley, J. E.; Zerner, M. C. *Theor. Chim. Acta* **1973**, *32*, 111–134.

(41) Kotzian, M.; Rosch, N.; Zerner, M. C. *Theor. Chim. Acta* **1992**, *81*, 201–222.

(42) Culberson, J. C.; Knappe, P.; Rosch, N.; Zerner, M. C. *Theor. Chim. Acta* **1987**, *71*, 21–39.

(43) Cory, M. G.; Kostlmeier, S.; Kotzian, M.; Rosch, N.; Zerner, M. C. *J. Chem. Phys.* **1994**, *100*, 1353–1365.

(44) Bacon, A. D.; Zerner, M. C. *Theor. Chim. Acta* **1979**, *53*, 21–54.

(45) Anderson, W. P.; Cundari, T. R.; Zerner, M. C *Int. J. Quantum Chem.* **1991**, *39*, 31–45.

(46) Anderson, W. P.; Cundari, T. R.; Drago, R. S.; Zerner, M. C. *Inorg. Chem.* **1990**, *29*, 1–3.

(47) Wemple, M. W.; Coggin, D. K.; Vincent, J. B.; McCusker, J. K.; Streib, W. E.; Huffman, J. C.; Hendrickson, D. N.; Christou, G. *J. Chem. Soc., Dalton Trans.* **1998**, 719–725.

(48) Davidson, E. R.; Clark, A. E. *Mol. Phys.* **2002**, *100*, 373–383.

(49) Frisch, M. J.; Trucks, G. W.; Schlegel, H. B.; Scuseria, G. E.; Robb, M. A.; Cheeseman, J. R.; Montgomery, J. A., Jr.; Vreven, T.; Kudin, K. N.; Burant, J. C.; Millam, J. M.; Iyengar, S. S.; Tomasi, J.; Barone, V.; Mennucci, B.; Cossi, M.; Scalmani, G.; Rega, N.; Petersson, G. A.; Nakatsuji, H.; Hada, M.; Ehara, M.; Toyota, K.; Fukuda, R.; Hasegawa, J.; Ishida, M.; Nakajima, T.; Honda, Y.; Kitao, O.; Nakai, H.; Klene, M.; Li, X.; Knox, J. E.; Hratchian, H. P.; Cross, J. B.; Adamo, C.; Jaramillo, J.; Gomperts, R.; Stratman, R. E.; Yazyev, O.; Austin, A. J.; Cammi, R.; Pomell, C.; Ochterski, J. W.; Ayala, P. Y.; Morokuma, K.; Voth, G. A.; Salvador, P.; Dannenberg, J. J.; Zakrzewski, V. G.; Dapprich, S.; Daniels, A. D.; Strain, M. C.; Farkas, O.; Malick, D. K.; Rabuck, A. D.; Raghavachari, K.; Foresman, J. B.; Ortiz, J. V.; Cui, Q.; Baboul, A. G.; Clifford, S.; Cioslowski, J.; Stefanov, B. B.; Liu, G.; Liashenko, A.; Piskorz, P.; Komaromi, I.; Martin, R. L.; Fox, D. J.; Keith, T.; Al-Laham, M. A.; Peng, C. Y.; Nanayakkara, A.; Challacombe, M.; Gill, P. M. W.; Johnson, B.; Chen, W.; Wong, M. W.; Gonzalez, C.; Pople, J. A. *Gaussian03, Revision B.05*; Gaussian, Inc.: Pittsburgh, PA, 2003.

(50) Becke, A. D. *J. Chem. Phys.* **1993**, *98*, 5648–5652.

(51) Lee, C.; Yang, W.; Parr, R. G. *Phys. Rev. B* **1988**, *37*, 785–789.

(52) Dunning, T. H.; Hay, P. J. In *Modern Theoretical Chemistry*; H. F. S., III, Ed.; Plenum:New York, 1976; pp 1−28.

(53) Hay, P. J.; Wadt, W. R. *J. Chem. Phys.* **1985**, *82*, 270–283.

(54) Schaefer, A.; Horn, H.; Ahlrichs, R. *J. Chem. Phys.* **1992**, *97*, 2571–2577.

(55) Schaefer, A.; Huber, C.; Ahlrichs, R. *J. Chem. Phys.* **1994**, *100*, 5829–5835.

(56) Components with unpaired spins of Fe2, Fe3, and Fe4 reversed relative to all other unpaired spins were used for 4. This was done to agree with the numbering scheme used for 4 in reference IJQC. All results reported are invariant to this choice.

(57) Löwdin, P.-O. *J. Chem. Phys.* **1950**, *18*, 365–375.

(58) Mulliken, R. S. *J. Chem. Phys.* **1955**, *23*, 1833–1840.

(59) *Jaguar 6.0*; Schrodinger, LLC: New York, 2005.

(60) Corrections were obtained using exchange constants J_{13}, J_{14}, J_{23}, and J_{24} found with FCS calculations (Table 5).

(61) Werner, R.; Ostrovsky, S.; Griesar, K.; Haase, W. *Inorg. Chim. Acta* **2001**, *326*, 78–88.

(62) Weihe, H.; Güdel, H. U. *J. Am. Chem. Soc.* **1997**, *119*, 6539–6543.

(63) Gorun, S. M.; Lippard, S. J. *Inorg. Chem.* **1991**, *30*, 1625–1630.

(64) Strauss, S. H.; Pawlik, M. J.; Skowyra, J.; Kennedy, J. R.; Anderson, O. P.; Spartalian, K.; Dye, J. L. *Inorg. Chem.* **1987**, *26*, 724–730.

(65) Snyder, B. S.; Patterson, G. S.; Abrahamson, A. J.; Holm, R. H. *J. Am. Chem. Soc.* **1989**, *111*, 5214–5223.

(66) Murray, K. *Adv. Inorg. Chem.* **1995**, *43*, 261.

(67) Barra, A. L.; Caneschi, A.; Cornia, A.; Fabrizi de Biani, F.; Gatteschi, D.; Sangregorio, C.; Sessoli, R.; Sorace, L. *J. Am. Chem. Soc.* **1999**, *121*, 5302–5310.

(68) Taguchi, T.; Stamatatos, T. C.; Abboud, K. A.; Jones, C. M.; Poole, K. M.; O'Brien, T. A.; Christou, G. *Inorg. Chem.* **2008**, *47*, 4095–4108.

(69) Davidson, E. R.; Clark, A. E. *Phys. Chem. Chem. Phys.* **2007**, *9*, 1881–1894.

(70) Davidson, E. R.; Clark, A. E *Int. J. Quantum Chem.* **2005**, *103*, 1–9.

(71) Reiher, M. *Faraday Discuss.* **2007**, *135*, 97–124.

(72) Adamo, C.; Barone, V.; Bencini, A.; Broer, R.; Filatov, M.; Harrison, N. M.; Illas, F.; Malrieu, J. P.; Moreira, I. d. p. R. *J. Chem. Phys.* **2006**, *124*, 107101.

(73) Boese, A. D.; Martin, J. M. L.; Handy, N. C. *J. Chem. Phys.* **2003**, *118*, 3005–3014.

CT700208M

JCTC Journal of Chemical Theory and Computation

Automatic Selection of Integral Thresholds by Extrapolation in Coulomb and Exchange Matrix Constructions

Elias Rudberg, Emanuel H. Rubensson, and Paweł Sałek*

Department of Theoretical Chemistry, School of Biotechnology, Royal Institute of Technology, SE-10691 Stockholm, Sweden

Received June 9, 2008

Abstract: We present a method to compute Coulomb and exchange matrices with predetermined accuracy as measured by a matrix norm. The computation of these matrices is fundamental in Hartree-Fock and Kohn-Sham electronic structure calculations. We show numerically that, when modern algorithms for Coulomb and exchange matrix evaluation are applied, the Euclidean norm of the error matrix ε is related to the threshold value τ as $\varepsilon = c\tau^{\alpha}$. The presented extrapolation method automatically selects the integral thresholds so that the Euclidean norm of the error matrix is at the requested accuracy. This approach is demonstrated for a variety of systems, including protein-like systems, water clusters, and graphene sheets. The proposed method represents an important step toward complete error control throughout the self-consistent field calculation as described in [*J. Math. Phys.* **2008**, *49*, 032103].

1. Introduction

In large scale Hartree-Fock and Kohn-Sham electronic structure calculations, the Coulomb matrix J and the exchange matrix K are computed using various computational approximations for which threshold values must be chosen carefully in order to achieve a result of desired accuracy without performing unnecessary work. Cauchy-Schwarz screening of integrals and multipole approximations are frequently used to control errors in individual matrix elements ε_{ij}.[1−10] Such approximations are governed by a threshold value τ: whenever a contribution to a matrix element is predicted to be smaller than τ, that contribution is neglected. Thus, choosing a smaller τ generally gives a more accurate result. However, smaller thresholds come with a performance penalty, affecting the timings by orders of magnitude—see Figure 1. One faces here a tradeoff between accuracy and performance. Therefore, the value of τ has to be selected with care.

In practice, it is preferable to control the error in the entire matrix rather than individual contributions. Recently, it has been found that controlling the accuracy in the electron density amounts to controlling the Euclidean norm of the error matrix for each approximation.[11] The Euclidean norm of a matrix A is defined as $||A||_2 = \max_{||x||_2=1}||Ax||_2$. The self-consistent field iterations are in ref 11 seen as a sequence of rotations of the occupied subspace, which uniquely defines the electron density for a given basis set. Errors coming from computational approximations, such as Cauchy-Schwarz screening of integrals and multipole approximations, are characterized as erroneous rotations. An erroneous rotation can be quantified by the canonical angles $\Theta(\mathcal{X},\tilde{\mathcal{X}})$ between

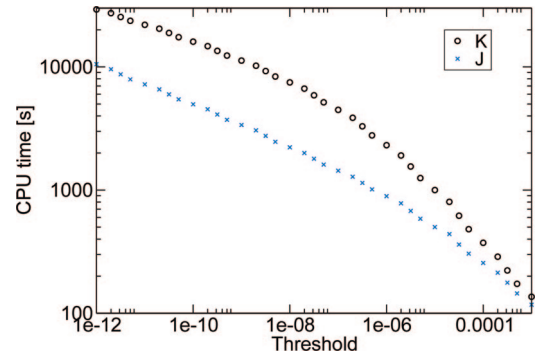

Figure 1. The CPU time needed to evaluate Coulomb and exchange matrices as functions of the threshold value τ. These are example timings measured for a HF/3−21G calculation on an insulin molecule.

* Corresponding author e-mail: pawsa@theochem.kth.se.

10.1021/ct8002145 CCC: $40.75 © 2009 American Chemical Society
Published on Web 12/09/2008

the exact subspace $\mathcal{X}$ and the perturbed subspace $\tilde{\mathcal{X}}$. Using matrix perturbation theory,[16,17] we show in ref 11 that controlling an erroneous rotation, as measured by the canonical angles, amounts to controlling the Euclidean norm of the error matrix E and knowing the band gap ξ:

$$||\sin \Theta(\mathcal{X}, \tilde{\mathcal{X}})||_2 \leq \frac{||E||_2}{\xi - ||E||_2} \quad (1)$$

The band gap ξ can be efficiently computed as a byproduct of density matrix purification.[12] Provided that the norms of the error matrices can be controlled, all approximations can be governed by a single parameter, specifying the desired accuracy in the electron density, thus eliminating the need for ad-hoc chosen threshold values. See ref 11 for details. Along the lines of ref 11, we have previously presented truncation strategies for density matrix purification based on analytical error bounds of the canonical angles between exact and perturbed subspaces.[18] In this article, we aim to provide a method for similar control of the Coulomb and exchange matrix calculations.

One possible way of attacking this problem is using the Frobenius norm: the above-mentioned methods for screening away individual contributions can be used to compute upper bounds of the error in matrix elements, provided that the number of neglected contributions is accounted for. These upper bounds ε_{ij} are in turn related to the error in the total matrix using the Frobenius norm

$$||E||_F = \sqrt{\sum_{ij} \varepsilon_{ij}^2} \quad (2)$$

Formally, the Frobenius norm $||E||_F$ could be used to estimate the Euclidean norm $||E||_2$ for a matrix E of size n using

$$\frac{1}{\sqrt{n}} ||E||_F \leq ||E||_2 \leq ||E||_F \quad (3)$$

Such estimation is however too loose for practical use, at least for large systems. Also, useful upper bounds of error matrix elements ε_{ij} may be difficult to come by. These difficulties cause the screening methods to be used in a qualitative way only: different screening thresholds are tried empirically until working ones are found. Such an approach does not guarantee scalability to larger systems.

In this article, we present a method to determine the relationship between the threshold value and the Euclidean norm of the error matrix in an automatic fashion, using extrapolation. Our method can be executed at run-time to select integral thresholds for J and K. These thresholds will be sufficiently tight to not obstruct the SCF convergence while requiring only necessary work.

2. Interaction Screening in Point Charge Model

In order to understand better the screening process, we study a simplified, classical model consisting of N discrete charges $\{\rho_i\}$ with coordinates $\{r_i\}$. We consider computation of the potential generated by such a charge distribution, when ignoring in the computations contributions smaller than a threshold value τ. Our goal is to find out how the error introduced in the screening process depends on τ. We choose the charges to have nonuniform distributions. It has been found that the distribution of density matrix elements for a nonconducting material follows an exponential function.[21] Therefore, we consider first the distribution $\rho_i = e^{-\gamma x_i}$ where x_i are random numbers uniformly distributed in the [0, 1] interval and γ is a parameter determining the spread of the distribution. The expression for the Coulomb potential V_p measured at R_p is

$$V_p = \sum_{i=1}^{N} \frac{\rho_i}{|r_i - R_p|} \quad (4)$$

We insert the formula for ρ_i to obtain the screening error which we define as the normalized sum of all ignored contributions:

$$\varepsilon_p(\tau) = \frac{1}{N} \sum_{i=1}^{N} \begin{cases} \dfrac{exp(-\gamma x_i)}{|r_i - R_p|}, & \dfrac{exp(-\gamma x_i)}{|r_i - R_p|} < \tau \\ 0, & \dfrac{exp(-\gamma x_i)}{|r_i - R_p|} \geq \tau \end{cases} \quad (5)$$

For large values of N, we can approximate the value of $\varepsilon_p(\tau)$ with an integral over the variable x. Let us also assume that all denominators are of the same order and do not affect substantially the screening process and can therefore be moved out of the integration $|r_i - R_p| \approx P_p$. We get

$$\varepsilon_p(\tau) \approx \frac{1}{P_p} \int_{\exp(-\gamma x)/P_p < \tau}^{1} e^{-\gamma x} dx = \frac{1}{P_p} \int_{\log((P_p\tau)^{-1/\gamma})}^{1} e^{-\gamma x} dx \quad (6)$$

$$= \frac{1}{P_p} \left[-\frac{1}{\gamma} e^{-\gamma x} \right]_{\log((P_p\tau)^{-1/\gamma})}^{1} \quad (7)$$

$$= \frac{1}{P_p \gamma} [P_p \tau - e^{-\gamma}] \quad (8)$$

The second term $e^{-\gamma}$ is the smallest charge present in the system. We can assume it is sufficiently small compared to the applicable values of τ and interaction with it is always screened away. We then obtain a compact formula

$$\varepsilon_p(\tau) \approx \frac{1}{\gamma} \tau \quad (9)$$

Let us repeat this derivation for another charge distribution. We take this time a set of random charges $\rho_i = x_i^2$ where x_i are random numbers uniformly distributed in the [0, 1] interval. We make the same approximations as for the other charge distribution, that is assume that the denominator does not affect the screening, and that we can replace the discrete sum with an integral. We get the final expression

$$\varepsilon_p(\tau) \approx \frac{1}{P_p} \int_0^{x^2/P_p < \tau} x^2 dx = \frac{1}{3\sqrt{P_p}} \tau^{3/2} \quad (10)$$

A pattern can be observed: the screening error for both studied charge distributions has the form

$$\varepsilon(\tau) = c\tau^{\alpha} \quad (11)$$

where c and α are some constants, and where the form of the charge distribution will affect the exponent α of the formula. We note that the functional form in eq 11 is routinely used for numerical estimation of truncation errors

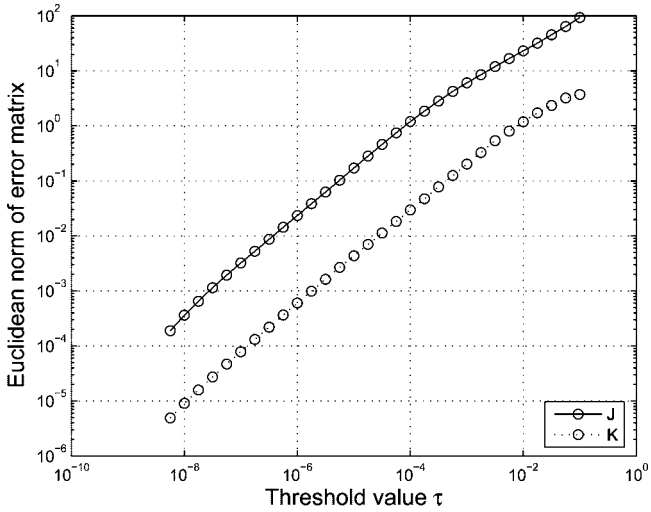

Figure 2. Errors versus threshold values for *J* and *K* matrix calculations on a water cluster containing 156 water molecules, using the 6−31G** basis set. Matrices computed at $\tau = 10^{-9}$ were used as reference for computing the error matrices.

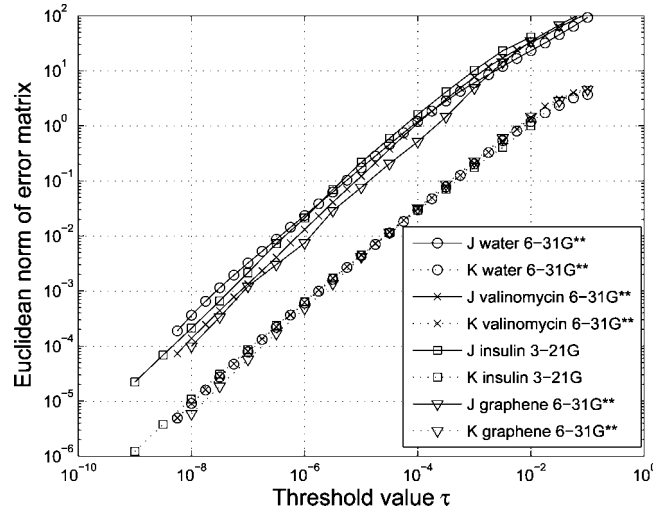

Figure 3. Errors versus threshold values for *J* and *K* matrix calculations for the four different test systems.

in finite difference and finite element methods.[22] In that context, the expression is commonly written ch^{α} where h is the mesh constant.

The presented interaction screening model can be used more or less directly to simulate the effects of screening on the Euclidean norm of the Coulomb error matrix. A particular charge distribution corresponds then to a magnitude distribution of density matrix elements. Simple-minded (4-center integral based) evaluation of the Coulomb matrix in turn corresponds to the pairwise evaluation of the classical potential as above. If we have used an orthogonal set of delta functions as the basis, the Coulomb matrix becomes diagonal, and the Euclidean norm of the error matrix can be computed exactly as the largest perturbation of the diagonal matrix elements. We have therefore a reason to presume that the screening error will behave as given by eq (11).

3. Numerical Error Estimates

After establishing the likely functional form of the error as given by eq (9), let us study the actual numerical error made in calculations of Coulomb and exchange matrices in Gaussian basis sets. We will consider the difference between the computed matrix J and the exact matrix J_{exact}

$$E = J - J_{exact} \tag{12}$$

and analogously for K. We will refer to the matrix E as the *error matrix* and consider the Euclidean norm of E, $\varepsilon \equiv ||E||_2$. Once the relation $\varepsilon(\tau)$ has been determined, its inverse $\tau(\varepsilon)$ can be used to choose τ so that the resulting error ε ends up at the requested accuracy.

Figure 2 shows the Euclidean norm of the error matrix for different values of τ for computations of J and K for a water cluster containing 156 water molecules, using the 6−31G** basis set. The calculations reported in this work were performed with the Ergo program,[19,20] with multipole approximations for the Coulomb matrix according to ref 8 and an algorithm for the exchange matrix essentially as described in ref 3. Matrices calculated at $\tau = 10^{-9}$ were used as reference for the computation of error matrices. For threshold values smaller than 10^{-3} the logarithmic plot in Figure 2 is nearly linear for both J and K, indicating that the relationship between the threshold τ and the error ε is of the form given by eq (11). Thus it appears that eq (11), which was derived for the Coulomb case, is also valid for the error in the exchange matrix. This is promising for our purposes here: once the values of the constants c and α have been established, we can easily select the threshold value τ so that the error in the computed Coulomb or exchange matrix is controlled

$$\tau(\varepsilon_{req}) = \left(\frac{\varepsilon_{req}}{c}\right)^{\frac{1}{\alpha}} \tag{13}$$

where ε_{req} is the requested accuracy when the error is measured as the Euclidean norm of the error matrix.

So far we have only seen that eq (11) is valid for one particular water cluster, for small enough values of τ. It remains to investigate the relationship between τ and ε for other systems, in order to see if our scheme is generally applicable. Figure 3 displays collected curves for a number of systems: same water cluster as above ($H_{312}O_{156}$), valinomycin ($C_{54}N_6O_{18}H_{90}$), insulin ($C_{247}N_{62}O_{74}S_6H_{367}$), and a small graphene sheet ($C_{96}H_{24}$). In all cases the behavior of the error with respect to the threshold value τ is essentially in accordance with eq (11). However, the numbers c and α vary somewhat for different systems. In our calculations, we get $0.88 \leq \alpha \leq 1.00$. This is close to the value $\alpha = 1$ obtained in Section 2 for an exponential distibution of charges and thus agrees with earlier findings regarding the distribution of density matrix elements.[21] Values of c are implementation-dependent. Therefore, in order to control errors using eq (13), practical implementations should investigate the behavior of errors for the particular system and basis set in question. If we assume that the functional form in eq (11) is valid in all cases, it is sufficient to calculate three matrices using different threshold values in order to find values for the constants c and α: the most accurate calculation is used as reference, while the two others provide two points on the graph

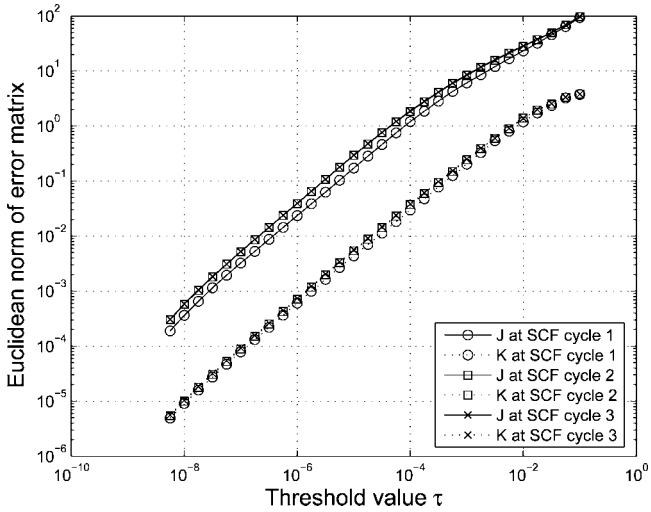

Figure 4. Errors versus threshold values for a Hartree-Fock calculation on a water cluster containing 156 water molecules, using the 6−31G** basis set. Matrices computed at $\tau = 10^{-9}$ were used as reference for computing the error matrices. Results for self-consistent field cycles 1, 2, and 3 are shown. There is some change going from cycle 1 to 2, while the results for cycle 3 are essentially the same as for cycle 2.

allowing for calculation of c and α. Figure 3 suggests that the three calculations needed to determine the error behavior can be done at rather low accuracy, since the graphs appear linear already for thresholds τ as large as 10^{-3}. Thus, these three calculations will be relatively cheap if high accuracy is needed in the final result.

We have also investigated how the behavior of errors changes during the self-consistent field iterations. Figure 4 shows the error behavior for the same water cluster as in Figure 2, but this time for three self-consistent field cycles. The calculation was performed at the Hartree-Fock level with basis set 6−31G**, with a starting guess density projected from a previous 3−21G calculation. There is a significant difference between the electron density in the first cycle compared to the second cycle, with the density affecting the offset c but leaving the slope α virtually unchanged. This has an effect on the error behavior: errors are somewhat smaller in the first iteration compared to the second. However, in the third iteration (and in all subsequent iterations) the error curves are essentially the same as for the second iteration. Therefore, performing three calculations of J and K to assess the error behavior in cycle 2 would in this case provide values for the constants c and α that would be valid in all subsequent iterations. Our test calculations on other systems show similar trends regarding the changes in different self-consistent field cycles: only the first cycle gives a change in density large enough to have a significant effect on the behavior of errors in the J and K matrices, when the starting guess is taken from a 3−21G calculation. This is good news from a performance point of view: since a self-consistent field calculation typically requires at least 5−10 iterations, the extra effort needed to find values for c and alpha becomes only a small fraction of the total time since those values can then be reused throughout the whole self-consistent field calculation.

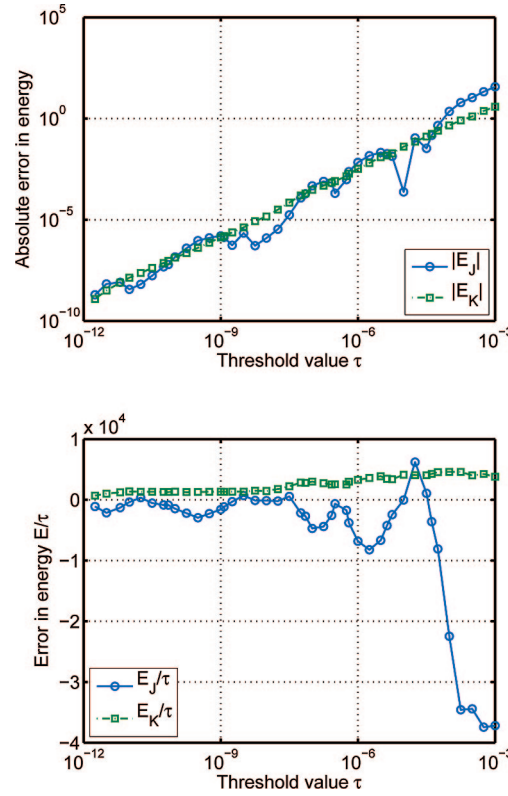

Figure 5. The error in the Coulomb and exchange energies as a function of the screening parameter τ. The values have been obtained for the first SCF cycle of a HF/6−31G** calculation on the valinomycin molecule. The same density matrix was used for all values of τ. The upper panel displays the absolute values of the errors in the exchange and Coulomb energies. The lower displays the energy error divided by the corresponding threshold value.

4. Selecting Threshold Values by Extrapolation

Based on the observations in the previous section, we propose the following scheme for error control in J and K matrix constructions: first, three low-accuracy matrix evaluations $X_{i=1,2,3}$, $X \in \{J, K\}$ are done in order to assess the error behavior, where different indices correspond to calculations with different threshold values $\tau_{i=1,2,3}$. The CPU time required to evaluate these matrices is only a small fraction of the CPU time required for a high-accuracy evaluation, see Figure 1. An optimized code could accelerate the process even further by computing all three at once rather than doing three separate matrix evaluations. Next, error matrices $E_{j=1,2}$ are computed and the coefficients c and α can be determined:

$$E_1 = X_3 - X_1, E_2 = X_3 - X_2 \tag{14}$$

$$\alpha = \frac{\log \|E_2\| - \log \|E_1\|}{\log \tau_2 - \log \tau_1}, c = \|E_1\| \tau_1^{-\alpha} \tag{15}$$

Having evaluated the parameters c and α and given the requested accuracy ε_{req} of the matrices in the norm of choice, the integral threshold can be trivially determined from eq (13). Provided that the density is reasonably close to convergence, this assessment of errors and evaluation of c and α constants needs to be done only once, so that the

matrices can thereafter be computed with a requested accuracy using eq (13). Although our approach is not based on analytical error bounds, it is in practice applicable to most systems of interest; apart from the systems described above, we have also investigated water clusters of sizes varied between 9 and 156 water molecules and polypeptide helices of sizes between 54 and 418 atoms as well as different basis sets of double- and triple-zeta quality with and without polarization functions. We have not encountered any case where the behavior of errors in approximate Coulomb and exchange matrices is not well described by eq (11). In early iterations, when the density still changes a lot in each step, the extrapolation can be performed in every SCF step or since the choice of threshold values is less critical at that stage, transferred from previous cycles. After a few steps, when the structure of the density matrix has stabilized, the extrapolation coefficients can be straightforwardly reused. Generally, as seen in Figure 3, the differences in c and α for different systems are not very large.

It is worth noting that at the same threshold value, the error in the exchange matrix is in our implementation 1−2 orders of magnitude lower—it is therefore beneficial to use different thresholds for Coulomb and exchange calculations. In general, the error in the exchange matrix depends in a remarkably predictable fashion on the chosen threshold value. The errors for the Coulomb matrix display some scatter of the c value, but the slope α remains practically the same.

The scheme for selecting threshold values for computation of the matrices J and K proposed here may also be applicable to computation of the exchange-correlation matrix in Kohn-Sham calculations, provided that the accuracy is governed by one continuous parameter. The hierarchical cubature grid generation scheme developed by Challacombe[23] may be suitable for this, since it needs only a single parameter to determine the quality of the grid.

5. Concluding Remarks

We present an adaptive method for choosing the screening threshold in calculation of the Coulomb and exchange matrices. This method can be directly incorporated into the single-threshold SCF scheme proposed in ref 11.

The scheme for Coulomb and exchange matrix error control presented in this work does not make any assumptions about the actual calculation method of J and K matrices apart from ability to control its accuracy with a single threshold. It is important to note that the precise positions and slopes of the error curves presented in this article are dependent on details in the specific implementation; for example if screening of integrals is done for basis function products or for products of Gaussian primitives. Parameters such as box sizes and maximum order of multipole expansions may also affect the results. Thus, values for the constants c and α should be determined separately for each implementation. We also note that for the proposed scheme to work for multipole methods, the method must be such that a single threshold value governs the accuracy, with the maximum degree of multipole expansion being a parameter affecting performance but not limiting the accuracy.[5−8]

Since many SCF optimization schemes are based on the energy,[13−15] it is tempting to select thresholds by extrapolation based on the errors in Coulomb and exchange energies. Unfortunately, the Coulomb energy, as computed in our implementation, behaves unpredictably as a function of τ, see Figure 5. Therefore extrapolation based on the Coulomb energy seems difficult.

The presented method allows us to automatically select threshold values to control the error in the Coulomb and exchange matrices given some desired accuracy $||E||_2 < \varepsilon_{req}$. The requested accuracy ε_{req} should be determined from the band gap and the desired accuracy in the electron density as described in ref 11. Using that strategy for error control, the matrices are computed accurately enough to ensure convergence, but, at the same time, the performance is not hampered by excessively tight thresholds. We have recently presented analytical error bounds with accompanying truncation strategies for density matrix purification.[18] Combined with the present work this will allow for self-consistent field calculations without need for ad-hoc chosen threshold values.

Finally, we would like to stress that the presented extrapolation scheme is based on on-the-fly numerical error estimates. Achieving strict error control based on analytical error bounds for Coulomb and exchange matrix construction remains an open challenge.

References

(1) Häser, M.; Ahlrichs, R. Improvements on the direct SCF method. *J. Comput. Chem.* **1989**, *10*, 104.

(2) Schwegler, E.; Challacombe, M.; Head-Gordon, M. Linear scaling computation of the Fock matrix. II. Rigorous bounds on exchange integrals and incremental Fock build. *J. Chem. Phys.* **1997**, *106*, 9708.

(3) Ochsenfeld, C.; White, C. A.; Head-Gordon, M. Linear and sublinear scaling formation of Hartree-Fock-type exchange matrices. *J. Chem. Phys.* **1998**, *109*, 1663.

(4) Lambrecht, D. S.; Ochsenfeld, C. Multipole-based integral estimates for the rigorous description of distance dependence in two-electron integrals. *J. Chem. Phys.* **2005**, *123*, 184101.

(5) Challacombe, M.; Schwegler, E.; Almlöf, J. Fast assembly of the Coulomb matrix: A quantum chemical tree code. *J. Chem. Phys.* **1995**, *104*, 4685.

(6) Challacombe, M.; Schwegler, E. Linear scaling computation of the Fock matrix. *J. Chem. Phys.* **1996**, *106*, 5526.

(7) Schwegler, E.; Challacombe, M.; Head-Gordon, M. A multipole acceptability criterion for electronic structure theory. *J. Chem. Phys.* **1998**, *109*, 8764.

(8) Rudberg, E.; Sałek, P. Efficient implementation of the fast multipole method. *J. Chem. Phys.* **2006**, *125*, 084106.

(9) Izmaylov, A. F.; Scuseria, G. E.; Frisch, M. J. Efficient evaluation of short-range Hartree-Fock exchange in large molecules and periodic system. *J. Chem. Phys.* **2006**, *125*, 104103.

(10) Ángyán, J. G.; Gerber, I.; Marsman, M. Spherical harmonic expansion of short-range screened Coulomb interactions. *J. Phys. A* **2006**, *39*, 8613.

(11) Rubensson, E. H.; Rudberg, E.; Sałek, P. Rotations of occupied invariant subspaces in self-consistent field calculations. *J. Math. Phys.* **2008**, *49*, 032103.

(12) Rubensson, E. H.; Zahedi, S. Computation of interior eigenvalues in electronic structure calculations facilitated by density matrix purification. *J. Chem. Phys.* **2008**, *128*, 176101.

(13) Kudin, K. N.; Scuseria, G. E.; Cancés, E. A black-box self-consistent field convergence algorithm: One step closer. *J. Chem. Phys.* **2002**, *116*, 8255.

(14) Thøgersen, L.; Olsen, J.; Yeager, D.; J,rgensen, P.; Sałek, P.; Helgaker, T. The trust-region self-consistent field method: Towards a black-box optimization in Hartree-Fock and Kohn-Sham theories. *J. Chem. Phys.* **2004**, *121*, 16.

(15) Thøgersen, L.; Olsen, J.; Köhn, A.; J,rgensen, P.; Sałek, P.; Helgaker, T. The trust-region self-consistent field method in Kohn-Sham density-functional theory. *J. Chem. Phys.* **2005**, *123*, 074103.

(16) Davis, C.; Kahan, W. M. The rotation of eigenvectors by a perturbation. III. *SIAM J. Numer. Anal.* **1970**, *7*, 1.

(17) Stewart, G. W.; Sun, J.-g. *Matrix Perturbation Theory*; Reinboldt W., Siewiorek, D., Eds.; Academic Press: San Diego, CA, 1990.

(18) Rubensson, E. H.; Rudberg, E.; Sałek, P. Density matrix purification with rigorous error control. *J. Chem. Phys.* **2008**, *128*, 074106.

(19) Rudberg, E.; Rubensson, E. H.; Sałek, P. *Ergo, a quantum chemistry program for large-scale self-consistent field calculations, version 1.6*; Stockholm, 2007.

(20) Rudberg, E.; Rubensson, E. H.; Sałek, P. Hartree-Fock calculations with linearly scaling memory usage. *J. Chem. Phys.* **2008**, *128*, 184106.

(21) Maslen, P. E.; Ochsenfeld, C.; White, C. A.; Lee, M. S.; Head-Gordon, M. Locality and sparsity of ab initio one-particle density matrices and localized orbitals. *J. Phys. Chem. A.* **1998**, *102*, 2215.

(22) Iserles, A. *A First Course in the Numerical Analysis of Differential Equations*; Crighton D. G., Eds.; Cambridge University Press: Cambridge, United Kingdom, 1996.

(23) Challacombe, M. Linear scaling computation of the Fock matrix. V. Hierarchical Cubature for numerical integration of the exchange-correlation matrix. *J. Chem. Phys.* **2000**, *113*, 10037.

CT8002145

JCTC Journal of Chemical Theory and Computation

Performance of Several Density Functional Theory Methods on Describing Hydrogen-Bond Interactions

Li Rao,[†] Hongwei Ke,[‡] Gang Fu,[†] Xin Xu,*[,†] and Yijing Yan[‡]

State Key Laboratory for Physical Chemistry of Solid Surfaces, Center for Theoretical Chemistry, Department of Chemistry, College of Chemistry and Chemical Engineering, Xiamen University, Xiamen 361005, China, and Department of Chemistry, Hong Kong University of Science and Technology, Kowloon, Hong Kong

Received June 21, 2008

Abstract: We have investigated eleven density functionals, including LDA, PBE, mPWPW91, TPSS, B3LYP, X3LYP, PBE0, O3LYP, B97−1, MPW1K, and TPSSh, for their performances on describing hydrogen bond (HB) interactions. The emphasis has been laid not only on their abilities to calculate the intermolecular hydrogen bonding energies but also on their performances in predicting the relative energies of intermolecular H-bonded complexes and the conformer stabilities due to intramolecular hydrogen bondings. As compared to the best theoretical values, we found that although PBE and PBE0 gave the best estimation of HB strengths, they might fail to predict the correct order of relative HB energies, which might lead to a wrong prediction of the global minimum for different conformers. TPSS and TPSSh did not always improve over PBE and PBE0. B3LYP was found to underestimate the intermolecular HB strengths but was among the best performers in calculating the relative HB energies. We showed here that X3LYP and B97−1 were able to give good values for both absolute HB strengths and relative HB energies, making these functionals good candidates for HB description.

1. Introduction

Hydrogen-bond (HB) interactions play a very important role in biochemistry. With the rapid development of biochemistry and pharmacology, the field of the first principle computational study has grown enormously. Traditional *ab initio* methodology, such as Møller−Plesset perturbation approach (MP2, MP4),[1,2] and coupled-cluster theory (CCSD(T)),[3] *etc.* can yield a highly accurate description of HB interactions, provided that large basis sets are used. However, the dramatic increase in computational cost with the size of systems limits their applications to just benchmark calculations of small molecules. Density functional theory (DFT) offers a promising alternative to the wave function-based methods.[4] Particularly, Becke's three parameter scheme,[5] B3LYP, has made great success in predicting the ground-state electronic structures, reaction energetics, molecular geometries, and so forth.[4] However, it is now well documented that B3LYP is unsatisfactory for the calculation of HB binding energies.[6−11] It has a tendency to underestimate HB strength, and errors accumulate for large systems involving multiple HB interactions.[9] New functionals were continually developed.[12−27] Some representatives are PBE,[12] mPWPW91,[15] O3LYP,[22] B97−1,[17] TPSS,[25] TPSSh,[26] X3LYP,[27] *etc*. These functionals were claimed to be a significant improvement over B3LYP in this or that aspect (see Table 1).[12−27] Several authors have explored the feasibility of these functionals on the description of HB interactions (see Table 2).[6−11,26] For example, Zhao and Truhlar[11] have performed an extensive test for the HB behaviors of forty-four functionals with three different basis sets against the so-called HB6/04 database. The HB6/04 set contains six HB systems, $(NH_3)_2$, $(HF)_2$, $(H_2O)_2$, NH_3/H_2O, $(HCONH_2)_2$, and $(HCOOH)_2$, with HB strengths ranging from ∼13 to ∼68 kJ/mol using data calculated by the W1 or W2 theory[28] as references. According to an integrated performance, based on the mean absolute deviations (MADs) of HB binding energies calculated by

* Corresponding author e-mail: xinxu@xmu.edu.cn.
[†] Xiamen University.
[‡] Hong Kong University of Science and Technology.

10.1021/ct800237n CCC: $40.75 © 2009 American Chemical Society
Published on Web 12/04/2008

Table 1. Functionals Examined in the Present Work

name	year	HF%	type	ex corr	comments
PBE	1996	0	GGA	PBE ex PBE corr	Improves over PW91.[12]
PBE0	1996	25	hybrid GGA	PBE ex PBE corr	Not far from the most reliable functionals including heavy parametrization.[14] Multiply bonded systems are most improved.[13]
mPWPW91	1998	0	GGA	mPW ex PW91 corr	Significantly improves the long-range behavior. Allows to obtain remarkable results both for covalent and noncovalent interactions.[15]Can provide the binding states of the rare gas, although the calculated binding energies cannot reproduce the experimental trend in binding energies.[16]
B97−1	1998	21	hybrid GGA	B97−1 ex B97−1 corr	Improves over B3LYP and B97.[17] Performs well on electrical properties.[18] Performs well on kinetics.[19]
MPW1K	2000	42.8	hybrid meta-GGA	mPW ex PW91 corr	Reduces the mean unsigned error in reaction barrier heights by a factor of 2.4 over mPW1PW91 and by a factor of 3 over B3LYP.[20] Works very well on kinetics.[21]
O3LYP	2001	11.61	hybrid GGA	OPTX ex LYP corr	Substantially improves over B3LYP.[22] Is overall better than B3LYP, albeit not by much.[23] Outperforms B3LYP in most fields but failed in hydrogen bond systems.[24]
TPSS	2003	0	meta-GGA	TPSS ex TPSS corr	Gives generally excellent results for a wide range of systems and properties, correcting overestimated PKZB bond lengths in molecules, hydrogen-bonded complexes, and ionic solids.[25]
TPSSh	2003	10	hybrid meta-GGA	TPSS ex TPSS corr	In some cases surpasses in accuracy the best available semiempirical approximations such as B3LYP, B3PW91, and VSXC.[26]
X3LYP	2004	21.8	hybrid GGA	X ex. LYP corr	Improves over B3LYP especially for hydrogen-bonded and van der Waals complexes. Will be useful for predicting ligand binding in proteins and DNA.[27]

three basis sets of different sizes with and without counterpoise corrections, PBE was concluded to be the best functional for HB; while PBE0 was the best hybrid GGA, VSXC[29] the best meta-GGA and MPW1K,[11] is the best performer with the DIDZ (desert-island double-ζ) basis set. In agreement with our previous results,[24] OPTX was concluded to be unsuitable for HB calculations. Staroverov et al.[26] has examined the performance of sixteen functionals, focusing on the new generation of nonempirical functional TPSS. It was concluded that TPSS is the most reliable nonhybrid functional for dissociation energies and geometries of H-bonded systems. The hybrid functionals are more accurate than their nonhybrid counterparts, although TPSSh surpasses TPSS only for geometries.[26]

It should be pointed out that all of the above works focused only on the absolute deviation of the binding energy from the corresponding reference value for an intermolecular hydrogen-bond.[6−11,26] The accuracy of each functional for the description of the relative HB binding energies was not examined. It is, however, the relative binding energies that determine the best binding interaction mode among different configurations. Furthermore, the functional performance for the intramolecular HB interactions has not yet been systematically investigated. Such intramolecular HB can play a decisive role in determining the conformer structure of a biomolecule.

In the present work, we have examined the performances of eleven DFT methods — LDA (SVWN5),[30,31] PBE, mPWPW91, TPSS, B3LYP, X3LYP, PBE0, O3LYP, B97−1, MPW1K, and TPSSh—to describe HB interactions. Fourteen model systems have been chosen to simulate the intermolecular HB interactions frequently appearing between the main function groups of amino acids (i.e., amino, hydroxyl, carboxyl, and peptide bond groups) in biochemical systems. Special attention has been paid to the relative HB strengths for different bonding interactions originating from the same pair of monomers. The functional performance for intramolecular HB interactions has been examined by looking into the conformer stability of three amino acids (glycine, proline, and serine). Three Ramachandran conformers of glycine dipeptide have been chosen as examples to demonstrate the interplay of HB and van der Waals (vdW) interactions in the biosystems.

The remainder of this paper is organized as follows. In section 2, we show the details of our calculations. In section 3, we present our results and discussion. In the last section, we give the conclusions.

2. Computational Details

2.1. Reference Value of Intermolecular HB Binding Energy—D_e^{SAPT}. It is nontrivial to establish a reliable reference set for HB from experiments, where theory shows its power. The literature data are often taken from the expensive methods such as CCSD(T) extrapolated to the complete basis set limit or the Wn theory.[11,32] We show here that the reference values for intermolecular HBs can be obtained satisfactorily by a relatively cheaper method, the symmetry-adapted perturbation theory (SAPT). SAPT was designed to calculate the interaction energy of a dimer, consisting of two arbitrary closed-shell monomers.[33,34] In SAPT, the interaction energy was expressed as a sum of a set of perturbative corrections, and each correction results from a different physical effect (*i.e.*, electrostatic, polarization, dispersion, and exchange).

The SAPT model we employed here is approximately equivalent to the fourth order many body perturbation theory (see eq 9 in ref 33). The geometries were first optimized by MP2(full)/aug-cc-pVDZ.[35,36] The basis set used in SAPT interaction energy calculations was aug-cc-pVTZ basis

Table 2. Representative Assessments of the DFTs' Abilities on Describing Hydrogen Bonded Interactions

author and year	functionals	systems	studied properties	methods for reference values	author's conclusions
Tuma, C.; Handy, N. C 1999[6]	B3LYP, B97−1, PBE0, HCTH, BLYP, PBE, LDA, and HTCH38	$(HF)_2$, $(HCl)_2$, $(H_2O)_2$, (CO)(HF), (OC)(HF), (FH)(NH_3), (ClH)(NH_3), (H_2O)(NH_3), (H_3O^+)(H_2O)	binding energy	CCSD(T)/ aug-cc-pVTZ or aug-cc-pVQZ BSSE corrected	Although the hybrid methods performed well in general, the new HCTH38 functional as a pure GGA predicted binding energies of better quality than the B3LYP functional.
Rabuck, A. D.; Scuseria, N. C. 2000[7]	B3LYP, BHLYP, PBE, VSXC, and PBE0	$(HF)_2$, $(HCl)_2$, $(H_2O)_2$, (HF)(HCN), (HF)(H_2O), (CN^-)(H_2O), (OH^-)(H_2O), (HCC^-)(H_2O), (H_3O^+)(H_2O), (NH_4^+)(H_2O)	binding energy and geometry	experiment and MP2 BSSE corrected	Overall, the hybrid functionals which contain a portion of Hartree−Fock exchange (B3LYP, BHLYP, and PBE0) yield the most accurate results. The kinetic-energy-density-dependent functionals, VSXC and meta-GGA, are significantly less accurate.
Sherer, E. C.; Cramer, C. J. 2003[8]	BLYP, B3LYP, mB3LYP, mPWPW91, and mPW1PW91	six base pairs for all DFTs and another 22 base pairs for mPWPW91/MIDI!	interaction enthalpies	MP2/6−31G(d)//HF/ 6−31G(d) and experiment BSSE corrected	At the pure and hybrid density functional levels, mPWPW91/MIDI! performed most satisfactorily.
Staroverov V. N.; Scuseria G. E.; Tao, J. M.; Perdew, J. P. 2003[26]	16 DFT methods, including LDSA, PW91, PBE, PBE0, PKZB, TPSS, and TPSSh	$(HF)_2$, $(HCl)_2$, $(H_2O)_2$, (HF)(HCN), (HF)(H_2O), (CN^-)(H_2O), (OH^-)(H_2O), (HCC^-)(H_2O), (H_3O^+)(H_2O), (NH_4^+)(H_2O)	binding energy and geometry	DFT/ 6−311++G(3df,3pd) and MP2/ 6−311++G(3df,3pd)	TPSS is the most reliable nonhybrid functional. It also represents a dramatic improvement over PKZB. The hybrid functionals are more accurate than their nonhybrid counterparts, although TPSSh surpasses TPSS only for geometries.
Xu, X.; Goddard, W. A. 2004[9]	SVWN, BLYP, BP86, BPW91, PW91, mPWPW, PBE, XLYP, BHLYP, B3LYP, B3P86, B3PW91, PW1PW, mPW1PW, PBE0, and X3LYP	H_2O monomer and H_2O dimer	geometry, vibrational frequencies, bond energy, dipole moment, kinetics, polarizability	experiment and CCSD(T)(FULL)/ IO275 extrapolations to the complete basis set; BSSE corrected	The best overall performance is given by X3LYP, comparing with the exact values, suggesting that X3LYP should be generally useful for predicting accurate properties for systems dominated by hydrogen bonding, electrostatics, and van der Waals (dispersion) interactions, such as ligand/protein complexes.
Frey, J. A.; Leutwyler, S. 2005[10]	BLYP, B3LYP, X3LYP, PBE, PW91, and mPWPW91	(formamide)$_2$ and (2-pyridone)$_2$	binding energy	MP2/CBS	PW91 consistently gives the best agreement with the MP2 basis-set limit binding energies, closely followed by PBE. The mPWPW91, B3LYP, and the recently proposed X3LYP functionals are in less good agreement.
Zhao, Y.; Truhlar, D. G. 2005[11]	44 DFT methods, including PBE, PBE0, B3P86, MPW1K, B97−1, BHLYP, and X3LYP.	$(HF)_2$, $(NH_3)_2$, $(H_2O)_2$, NH_3/H_2O, $(HCONH_2)_2$, $(HCOOH)_2$	binding energy	W1 and W2 theory[25]	Among the tested methods, the PBE, PBE0, B3P86, MPW1K, B97−1, and BHandHLYP functionals give good performance for hydrogen bondings.

set[35,36] modified by removing the f and g functions. The recommended MC+BS approach was used.[33,34] A bond function of 3s2p1d was added, centered in the H-bond area. The keyword scfcp was used to correct the basis set

Table 3. Comparison between Results of SAPT and Wn for the Benchmark Database HB6/04[a]

	$(NH_3)_2$	$(HF)_2$	$(H_2O)_2$	$(NH_3)(H_2O)$	$(HCONH_2)_2$	$(HCOOH)_2$	MAD[c]
D_e^{SAPT}	13.01	18.54	20.29	26.48	61.17	66.90	0.6
HB6/04[b]	13.18	19.12	20.79	26.82	62.51	67.57	

[a] Units: kJ/mol. [b] Benchmark database HB6/04 was introduced by Zhao and Truhlar in ref 11; the values of $(NH_3)_2$, $(HF)_2$, $(H_2O)_2$, and $(NH_3)(H_2O)$ are W2 results, and the values of $(HCONH_2)_2$ and $(HCOOH)_2$ are W1 results. [c] MAD are calculated using Wn values as references.

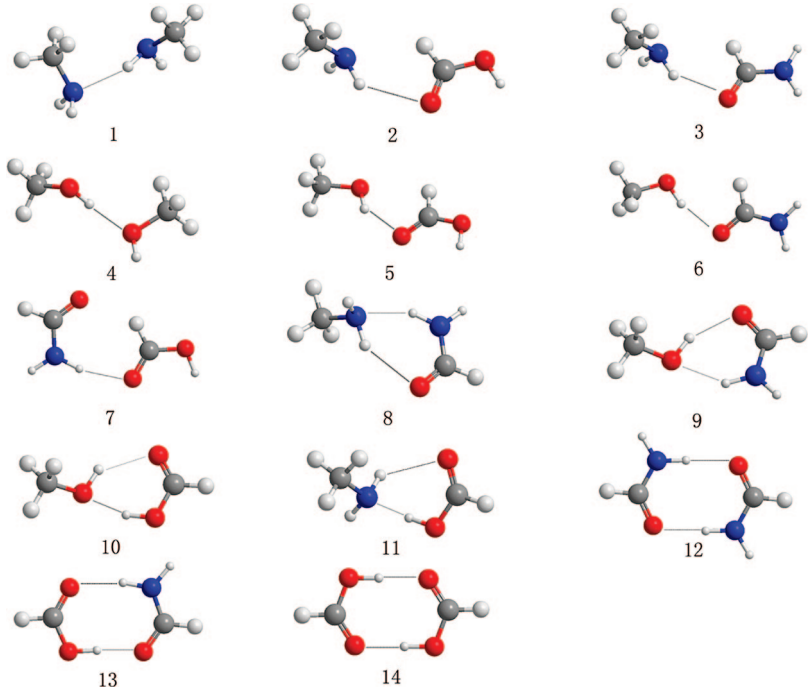

Figure 1. Fourteen intermolecular H-bonded complexes. Color codes: O (red), N (blue), C (dark gray), and H (light gray).

superposition errors (BSSE). The original SAPT results are equivalent to the vertical bond dissociation energies, that is, such SAPT calculations do not consider the structure relaxation energy, which results from the difference between the geometry of the isolated monomer and the geometry of the monomer in the dimer. On the other hand, the HB binding energies for DFT were calculated by using the supermolecular model. To facilitate the comparison with the DFT results, we calculated the relaxation energy at the MP4(SDTQ)/aug-cc-pVTZ//MP2(full)/aug-cc-pVDZ level and added it to the SAPT results to obtain the SAPT supermolecular binding energy D_e^{SAPT} (see eq 1)

$$D_e^{SAPT} = -E_{int}^{SAPT} + (E_{monomer}^{A} - E_{dimer}^{A}) + (E_{monomer}^{B} - E_{dimer}^{B}) \quad (1)$$

where $E_{monomer}^{A}$ and E_{dimer}^{A} are the calculated energies adopting the optimized geometry of the isolated monomer and the geometry of the monomer in the dimer, respectively. This methodology has been applied to the HB06/04 database.[11] The results are shown in Table 3. Clearly, SAPT achieved a similar accuracy for the HB binding energies as the Wn theory, with a MAD of 0.6 kJ/mol.

2.2. Intermolecular HB Complexes. The HB complexes shown in Figure 1 were chosen to simulate the intermolecular HBs between the main function groups of amino acids (i.e., amino, hydroxyl, carboxyl, and peptide bond group).[37] They are representatives of HB interactions most frequently appearing in biochemical systems. Each dimer in D1-D7 contains a single XH...Y HB, where X, Y = N or O. Each dimer in D8-D11 contains a cyclic XH...Y HB, where X (N or O) acts both as a proton donor and acceptor. Such kinds of HBs are believed to play an important role in proton transfer reactions. Each dimer in D12-D14 contains two XH...Y HBs that form a cycle. HB interactions in D12-D14 are usually strong.

We do not include XH...π interactions in our testing set. This type of interactions deserves special attention for its biologic significance.[38] While the electrostatic interaction is mainly responsible for the attraction in the conventional XH...Y HBs, the major source of attraction in the XH...π interaction is the dispersion interaction,[39] and it is well-known that the commonly used LDA and GGA, designed for nonuniform electron gases, fail to capture the essence of vdW energies.[40] Hence the conclusion of the present work should be taken with caution for the biological systems containing aromatic side-chains.

2.3. Conformational Analysis for Amino Acids and Glycine Dipeptide. Amino acids and peptides are building blocks of proteins. From the simplest glycine to more complex peptides, each molecule may have many conformers. These conformers are stabilized by intramolecular HBs, which are counterbalanced by destabilizing steric strain and lone-pair electron-repulsion interaction. The performance of the DFT methods on describing the intramolecular HB

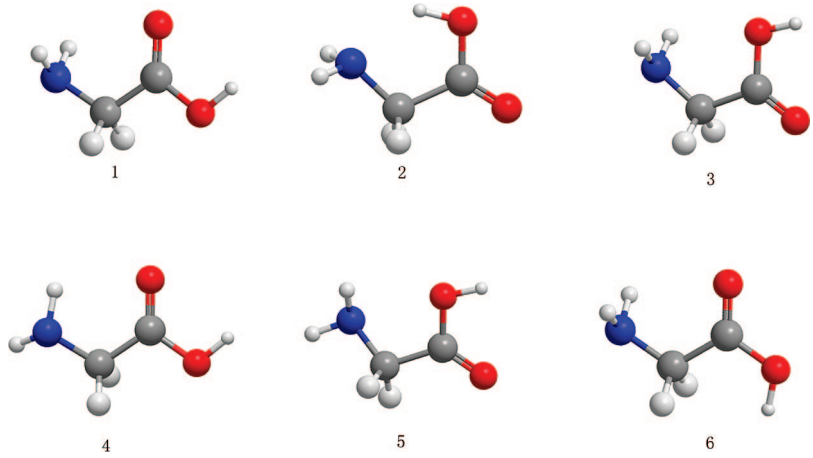

Figure 2. Six conformers of gaseous glycine. Color codes: O (red), N (blue), C (dark gray), and H (light gray).

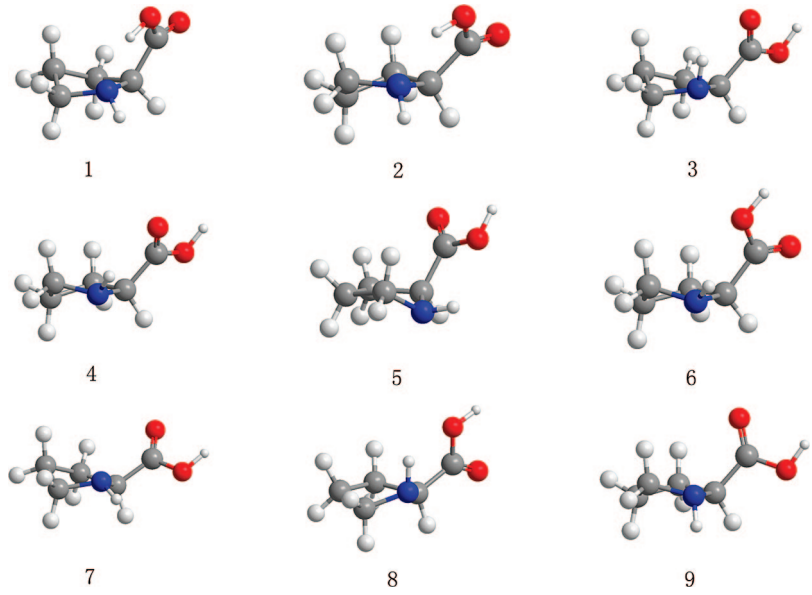

Figure 3. Nine conformers of gaseous proline. Color codes: O (red), N (blue), C (dark gray), and H (light gray).

interactions may be judged via the conformational analysis of the amino acids. We selected six conformers of glycine,[41] nine conformers of proline,[42] and twelve conformers of serine,[43] where some of their accurate energetics are available in the literature.[41,42] The geometries are depicted in Figures 2, 3, and 4, respectively.

While single amino acids provide simple examples of intramolecular HBs, small peptides are better representatives of proteins. Figure 5 depicted three conformers of glycine dipeptide.[44] However, it should be noted that there may exist $\pi-\pi$ interactions, resulting from each amide plane of the polypeptide backbone. The interplay between HB interactions and vdW interactions is very important in a bioapplication, which poses a great challenge to DFT.

2.4. Computational Methods. Eleven DFT methods, including LDA, PBE, mPWPW91, TPSS, B3LYP, X3LYP, PBE0, O3LYP, B97−1, MPW1K, and TPSSh, have been examined here. At the beginning, we have also included VSXC. It turned out VSXC has a strong tendency to overestimate CH...Y (Y = N or O) interactions, which frequently led to failure of optimizations or wrong structures. Hence VSXC's results are not presented in this paper.

All geometries were optimized with the 6−311++G-(2d,2p) basis sets.[45,46] Analytical vibrational frequency calculations were performed to ensure that each minimum is a true local minimum, containing only positive frequencies. For HB complexes, single point calculations with the 6−311++G(3df,2pd) basis sets[45−47] were employed to calculate the zero-point-exclusive binding energies, D_e, which were then compared to the corresponding reference values to check validity of a functional. Relative energies of the different HB conformations made from the same pair of monomers were calculated by subtracting the binding energies (which is equivalent to the subtractions of the total energies). Functional performances were evaluated based on MADs as well as variance analysis (VAR) from the reference data.

For conformational analysis of the amino acids and glycine dipeptide, the geometries and energies were obtained with the 6−311++G(2d,2p) basis sets. The reference values were

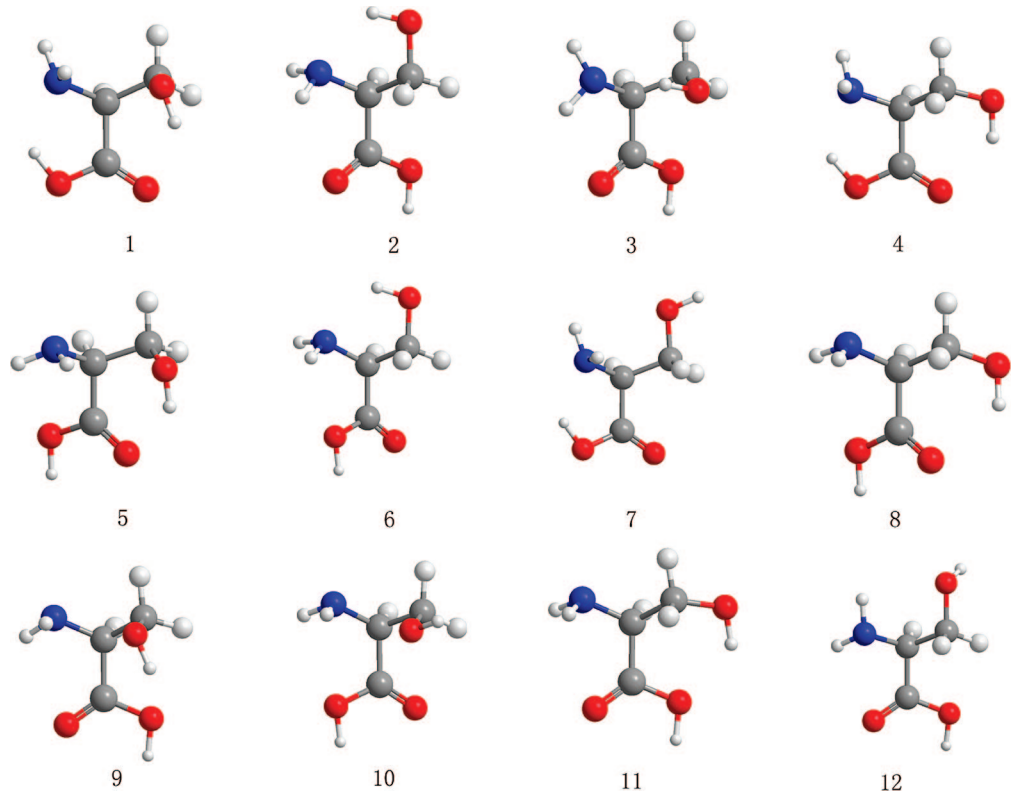

Figure 4. Twelve conformers of gaseous serine. Color codes: O (red), N (blue), C (dark gray), and H (light gray).

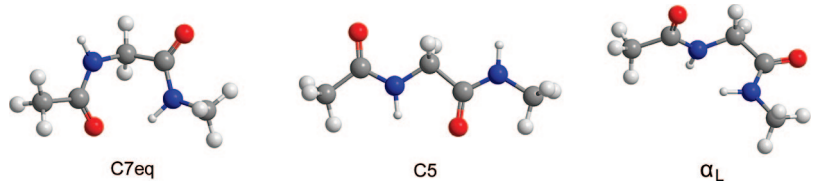

Figure 5. Three Ramachandran conformers of glycine dipeptide. Color codes: O (red), N (blue), C (dark gray), and H (light gray).

calculated by using the G3 theory, which were then compared with the high level *ab initio* results in the literatures.[41,42]

In the present work, the SAPT interaction energy calculations were performed by using the SAPT2006 program package.[33] All other calculations were performed by using the Gaussian 03 program package.[48]

3. Results and Discussion

3.1. Intermolecular Hydrogen Bonded Complexes. *3.1.1. HB Binding Energies.* Table 4 shows the calculated binding energies of fourteen HB dimers as shown in Figure 1. With respect to D_e^{SAPT}, errors of LDA are dramatic, ranging from 10 to 50 kJ/mol. On average, LDA overestimates the bond strength of a single HB by 15 kJ/mol. But errors are more than tripled when forming a cyclic HB complex (i.e., D13 or D14 in Table 4 and Figure 1), which comprises two HBs. GGAs significantly amend this error. MADs of the PBE and PBE0 functionals are only 2.55 and 2.64 kJ/mol, respectively, being the best functionals as claimed by Zhao and Truhlar.[11] MADs associated with TPSS and TPSSh are 5.09 and 5.10 kJ/mol, which argue the advantage of meta-GGAs for the description of HBs.[26] Table 4 shows that B97−1 and X3LYP are the second best performers, giving MADs of 3.24 and 3.77 kJ/mol, respectively. Even though mPW was claimed to have improved behavior in low density (large gradient) regions,[11−15] which is important for HB, MADs associated with mPW are 4.34 (MPW1K) and 5.69 kJ/mol (mPWPW91). B3LYP's performance is actually not far from mPWPW91, leading to a MAD of 6.07 kJ/mol. A severe underestimation (about 10−23 kJ/mol) can be found with O3LYP (Table 4), reconfirming the conclusion that O3LYP cannot be recommended for treating HB systems.[11,24]

As seen from Figure 6 and Table 4, the functional performance based on the VAR data is not identical to that based on MADs. As HB strengths for D1-D14 are ranging from 16 to 67 kJ/mol, a small VAR associated with a method may suggest that this method is able to deal with HB of varying strength on an equal footing. From Table 4, it is clear that LDA leads to too high VAR (178.71 kJ^2/mol^2), as errors may accumulate for multiple HB complexes. Errors associated with O3LYP (VAR = 23.30 kJ^2/mol^2) are also very large, rendering it again an unsuitable method for HBs. MPW1K (VAR = 3.30) improves over mPWPW91 (VAR = 5.56 kJ^2/mol^2), even though the former was originally fitted against the kinetic data.[11] The larger portion of the exact

Table 4. Binding Energies of the Intermolecular Hydrogen-Bonded Complexes[a]

dimer[b]	D1	D2	D3	D4	D5	D6	D7	D8	D9	D10	D11	D12	D13	D14	MAD	VAR[e]
LDA	31.43	28.93	33.11	39.06	38.01	46.85	55.31	63.77	72.24	83.76	89.61	96.30	110.07	119.51	26.47	178.71
PBE	13.93	13.81	15.82	21.88	19.41	26.19	30.42	35.61	39.66	45.65	54.94	59.12	66.36	69.25	2.55	6.94
mPWPW91	11.09	10.67	12.47	19.08	16.28	23.01	26.11	31.42	35.27	41.30	50.88	54.10	61.38	64.22	5.69	5.56
TPSS	11.31	11.28	12.93	19.54	16.67	23.43	27.00	31.79	36.03	42.51	50.90	55.05	62.36	65.31	5.09	5.79
B3LYP	10.29	11.51	13.35	19.46	17.53	23.77	27.99	29.75	35.02	39.87	46.99	53.64	60.50	62.30	6.07	2.59
X3LYP	11.88	13.31	15.23	21.21	19.50	25.77	30.50	32.05	37.61	42.55	48.83	56.61	63.64	65.56	3.77	3.08
PBE0	13.01	14.06	16.02	21.25	19.83	26.36	31.30	34.31	38.83	44.22	52.72	58.66	66.02	68.74	2.64	4.35
O3LYP	6.78	7.32	8.62	13.51	12.05	17.24	18.62	20.71	23.10	26.69	36.78	38.87	43.76	44.02	15.65	23.30
B97−1	13.64	14.69	16.48	21.21	19.87	25.90	31.34	33.56	37.57	42.09	50.25	56.94	63.22	64.85	3.22	1.27
MPW1K	11.05	12.68	14.52	19.62	18.58	24.94	29.79	31.55	36.40	41.71	49.54	55.94	63.60	66.40	4.35	3.30
TPSSh	11.16	11.60	13.27	19.44	17.03	23.66	27.62	31.53	35.87	41.99	50.23	55.06	62.35	65.17	5.10	4.51
D_e^{SAPT}[c]	16.36	18.95	21.21	22.89	22.93	28.74	36.40	37.11	40.17	43.39	54.14	61.17	66.65	66.90		
W1[d]												62.51		67.57		

[a] Units: kJ/mol. [b] The structures of D1-D14 are depicted in Figure 1. [c] D_e^{SAPT} refers to the SAPT supermolecular binding energies, obtained by the combination of the SAPT interaction energies and the corresponding structural relaxation energies at MP4 (see eq 1). [d] W1 values are taken from ref 11. [e] VAR = $[n\sum X^2 - (\sum X)^2]/n(n-1)$, where X is the difference between DFT results and the corresponding SAPT results, and $n = 14$. Units: kJ^2/mol^2.

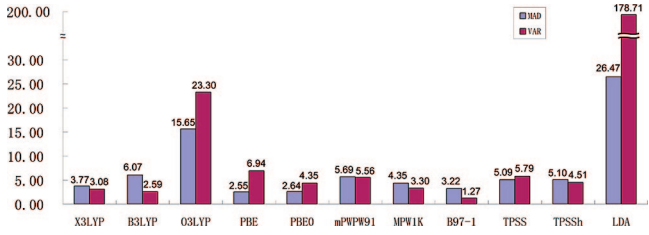

Figure 6. Statistic data of DFTs on binding energy calculations of fourteen intermolecular hydrogen-bonded complexes. MAD (mean absolute deviation) in kJ/mol and VAR (variance) in kJ^2/mol^2.

exchange should contribute to the improvement. Significantly, the best performers, based on the VAR data, are B97−1 (1.27), B3LYP (2.59), and X3LYP (3.08 kJ^2/mol^2). On the other hand, VARs of PBE (6.94) and PBE0 (4.35 kJ^2/mol^2) are considerably high. This may be related to the fact that PBE and PBE0 overshoot the target values of D_e^{SAPT} such as those in D10 and D14 but underestimate HB strengths of other conformers. From Table 4, we see that TPSS improves over PBE, having a smaller VAR of 5.79 kJ^2/mol^2. A smaller VAR may suggest that errors be more systematic. This property is very important when the relative energies rather than the absolute energies are concerned. We will see this in the following discussion.

3.1.2. Relative HB Energies. Complexes D11 and D2 are formed with the same pair of monomers. The geometric difference between them is the reorganization of hydrogen bonds. The same relationship can be found between other four pairs of monomers (i.e. D8 and D3, D10 and D5, D9 and D6, D13 and D7). Table 5 summarizes the reorganization energies obtained by using SAPT and various flavors of DFT methods. MADs for these five pairs with respect to the SAPT values are also presented. Clearly, B97−1, B3LYP, and X3LYP are the best performers, giving MADs less than 1.5 kJ/mol.

In terms of MAD of the relative HB energies, data in Table 5 show that there is a general improvement over the calculated HB data as listed in Table 4. This is understandable, as errors associated with a functional may cancel out, to some extent, when we take the difference of two HB systems. On the other hand, we should note that errors can

Table 5. Relative Energies between Dimers Made of the Same Pair of Monomers[a]

dimer[b]	D11-D2	D8-D3	D10-D5	D9-D6	D13-D7	MAD
LDA	60.68	30.65	45.75	25.39	54.77	20.80
PBE	41.09	19.79	26.23	13.47	35.94	4.64
mPWPW91	40.21	18.91	25.02	12.22	35.27	3.68
TPSS	39.62	18.86	25.84	12.60	35.35	3.80
B3LYP	35.48	16.40	22.38	11.21	32.55	1.05
X3LYP	35.48	16.82	23.05	11.84	33.14	1.42
PBE0	38.66	18.28	24.39	12.47	34.73	3.05
O3LYP	29.46	12.09	14.64	5.86	25.15	5.23
B97−1	35.56	17.11	22.22	11.67	31.84	1.05
MPW1K	36.86	17.03	23.14	11.51	33.81	1.80
TPSSh	38.64	18.26	24.96	12.20	34.74	3.11
D_e^{SAPT}[c]	35.19	15.90	20.46	11.46	30.25	

[a] Units: kJ/mol. [b] The structures are depicted in Figure 1. Each dimer pair differs only in interaction modes. [c] MAD are calculated using SAPT values as references.

be irregular. Take D11-D2 as an example, errors may depend on type and strength of the HB interactions. Hence, different errors encounter at a single HB of the N−H...O type of 16 kJ/mol as in D2 and a cyclic HB of the O...H−N...H−O type of 52 kJ/mol as in D11. Clearly, the accuracy of a functional to describe the relative HB binding energies is very important, as the relative binding energies play a decisive role in determining the best binding interaction mode among different configurations.

As compared data in Tables 5 and 4, we see that the largest improvement (10.42 kJ/mol) on the description of the relative HB strength is seen for O3LYP. Nevertheless, a MAD of 5.23 kJ/mol still ranks O3LYP as the second poorest method other than LDA. Noteworthily, PBE and PBE0 provide an exception. Instead of error cancelation, errors accumulate for the relative binding energy predictions, leading to MADs of 4.64 and 3.05 kJ/mol, respectively. We conclude that such a disturbing behavior significantly downplays the role of PBE and PBE0 for the description of a biosystem, where HB interactions of different types and strengths compete with each other.

3.1.3. Hydrogen Bond Distances. We also looked into the hydrogen bond distances predicted by each DFT method. Table 6 shows that there is a simple correlation between the calculated H-bond distance and the calculated binding energy,

Table 6. Hydrogen Bond Distances (DH...A[b]) of the Intermolecular Hydrogen-Bonded Complexes[a]

	1 NH...N	2 NH...OC	3 NH...OC	4 OH...O	5 OH...OC	6 OH...OC	7 NH...OC	8 NH...N	9 OH...OC	10 OH...O	11 OH...N	12 NH...OC	13 OH...OC	14 OH...OC
LDA	1.99	2.09	2.00	1.71	1.81	1.70	1.76	1.76	1.65	1.49	1.45	1.62	1.41	1.37
PBE	2.21	2.42	2.19	1.89	1.99	1.87	1.97	1.95	1.86	1.69	1.62	1.81	1.59	1.59
mPWPW91	2.25	2.50	2.21	1.91	1.99	1.88	1.99	1.96	1.87	1.69	1.63	1.82	1.60	1.60
TPSS	2.25	2.52	2.21	1.90	1.99	1.88	1.98	1.97	1.87	1.70	1.66	1.82	1.61	1.61
B3LYP	2.29	2.45	2.22	1.93	2.02	1.91	2.02	2.03	1.92	1.75	1.70	1.87	1.65	1.67
X3LYP	2.27	2.41	2.20	1.91	2.02	1.90	2.00	2.02	1.91	1.75	1.70	1.86	1.64	1.66
O3LYP	2.52	2.96	2.46	2.07	2.16	2.03	2.19	2.11	2.05	1.82	1.72	1.98	1.71	1.73
PBE0	2.23	2.39	2.19	1.90	1.99	1.87	1.97	1.98	1.88	1.71	1.65	1.83	1.61	1.62
B97−1	2.28	2.44	2.23	1.93	2.05	1.92	2.02	2.02	1.93	1.76	1.69	1.87	1.65	1.67
MPW1K	2.26	2.40	2.19	1.91	2.00	1.88	1.98	2.00	1.89	1.73	1.68	1.84	1.62	1.63
TPSSh	2.25	2.49	2.21	1.90	1.99	1.88	1.98	1.98	1.87	1.71	1.67	1.83	1.61	1.62

[a] Units: Å. [b] DH...A is the shortest hydrogen-accepter distance in each complex.

Table 7. Relative Energies of Six Conformers of Glycine Given by DFTs with 6-311++G(2d,2p)[a]

conformer[b]	1p	2n	3n	4n	5n	6p	MAD[d]
LDA	0.00	−11.19	6.30	1.60	11.13	20.22	3.84 (3.66)
PBE	0.00	−2.27	6.17	5.10	11.83	19.41	1.68 (1.31)
mPWPW91	0.00	−1.96	6.18	5.36	11.92	19.52	1.61 (1.28)
TPSS	0.00	−2.06	6.09	5.43	11.61	19.71	1.56 (1.23)
B3LYP	0.00	2.50	6.72	5.56	11.63	21.08	0.41 (0.66)
X3LYP	0.00	2.47	6.76	5.42	11.57	21.21	0.40 (0.65)
O3LYP	0.00	3.20	6.63	6.18	11.95	20.29	0.71 (0.84)
PBE0	0.00	0.53	6.91	5.19	12.24	20.77	0.78 (0.90)
B97−1	0.00	2.00	6.68	5.74	11.96	20.58	0.59 (0.59)
MPW1K	0.00	2.47	7.35	5.39	12.47	21.78	0.71 (1.06)
TPSSh	0.00	−0.82	6.42	5.42	11.76	20.26	1.17 (1.04)
G3	0.00	2.68	6.98	5.25	10.66	20.75	–
'best' literature value[c]	0.00	2.05	6.70	5.15	10.51	19.76	0.43

[a] Units: kJ/mol. [b] See Figure 2 for structures. The labeling scheme was introduced by Császár who used p to denote conformers of C_s symmetry and n to those of C_1 symmetry.[41] [c] The 'best literature value' is Császár's 'final prediction',[41] which is the extrapolation of the MP2 energy to the infinite-order. [d] MADs are given with respect to the G3 values. Numbers in parentheses are MADs with respect to the 'best' literature values.

i.e., a method that predicts a stronger H-bond always gives a shorter H-bond distance. For example, the H-bond distances obtained by X3LYP are systematically shorter than those of B3LYP. This is consistent with the trend that B3LYP generally underestimates HB energies. Hence, O3LYP gives the longest H-bond distances and the lowest binding energies, while LDA give the shortest H-bond distances and the highest binding energies.

3.2. Conformational Analysis of Amino Acids. *3.2.1. Glycine.* Table 7 shows the relative energies of six selected conformers of gaseous glycine (see Figure 2). We follow the labeling scheme introduced by Császár who used p to denote conformers of C_s symmetry and n to those of C_1 symmetry.[41] Our calculated values by the G3 theory compare well with Császár's 'final prediction', which is the extrapolation of the MP2 energy to the infinite-order with an estimated maximum error of ~1.2 kJ/mol. We anticipate that the G3 values are more accurate, as it is extrapolated to QCISD(FULL,T)/6−311+G(3d2f,2df,2p) plus an empirical high level correction. The MAD data with respect to G3 in Table 7 seem to suggest that all functionals, other than PBE and mPWPW91, work well, with X3LYP, B3LYP, and B97−1 being better than others (MADs = 0.40−0.59 kJ/mol). There is a significant improvement for B3LYP to estimate the relative HB energies. Even O3LYP leads to only a MAD of 0.71 kJ/mol. Noteworthily, LDA, PBE, mPWPW91, and TPSS give MADs larger than 1.50 kJ/mol, respectively. In fact, these functionals fail to correctly predict the most stable conformer, erroneously putting 2n lower in energy than 1p. Even though PBE, mPWPW91, and TPSS have been suggested to be good performers for HB,[11,26] clearly, such a conclusion has to be taken with caution based on our present results.

3.2.2. Proline. Table 8 shows the relative energies of nine conformers of gaseous proline (see Figure 3). The 'best' literature values were taken from ref 42. These are from the focal-point approach, by extrapolating the RHF and MP2 energies to the complete basis set limit, appending coupled-cluster energy increments to the extrapolated results, and finally adding the core correlation corrections and relativistic

Table 8. Relative Energies of Nine Conformers of Proline Given by DFTs with 6-311++G(2d,2p)[a]

conformer[b]	1	2	3	4	5	6	7	8	9	MAD[d]
LDA	0.00	4.21	19.59	20.51	26.74	26.74	31.05	28.96	32.59	12.00 (12.58)
PBE	0.00	2.14	11.39	11.48	18.39	19.00	20.52	20.18	21.17	4.09 (4.33)
mPWPW91	0.00	2.08	11.22	11.19	18.36	18.71	20.20	19.82	20.76	3.86 (4.10)
TPSS	0.00	2.18	11.28	11.14	17.88	18.36	19.86	19.73	20.70	3.69 (3.93)
B3LYP	0.00	1.75	6.89	6.15	13.61	13.87	14.22	15.24	15.60	0.93 (0.47)
X3LYP	0.00	1.84	6.83	6.13	13.47	13.87	14.19	15.35	15.71	0.88 (0.41)
O3LYP	0.00	1.18	6.05	5.54	13.93	13.33	14.21	14.02	15.32	1.48 (0.96)
PBE0	0.00	2.48	8.97	8.66	15.97	16.96	17.81	18.84	19.41	2.11 (2.42)
MPW1K	0.00	2.60	7.27	6.63	14.38	15.40	15.75	17.78	17.95	0.86 (1.05)
B97−1	0.00	1.93	7.37	7.03	13.94	14.68	15.55	15.99	16.63	0.53 (0.49)
TPSSh	0.00	2.33	10.30	9.91	16.81	17.49	18.66	19.14	19.92	2.83(3.10)
G3	0.00	3.56	7.11	7.43	13.43	14.72	14.90	16.67	16.57	–
'best' literature value[c]	0.00	2.20	6.64	6.80	13.19	14.68	14.78	15.48	15.97	0.58

[a] Units: kJ/mol. [b] See Figure 3 for structures. [c] The 'best' literature values are from ref 42, which are the extrapolation of the CCSD(T) energies to the infinite-order. The value for conformer 7 was miscalculated to be 18.54 kJ/mol. We updated it here as 14.78 kJ/mol. See text for more details. [d] MADs are given with respect to the G3 values. Numbers in parentheses are MADs with respect to the 'best' literature values.

Table 9. Relative Energies of Twelve Conformers of Serine Given by DFTs with 6-311++G(2d,2p)[a]

conformer[b]	1	2	3	4	5	6	7	8	9	10	11	12	MAD[c]
LDA	0.00	9.51	9.68	−5.11	14.45	18.08	9.04	20.54	24.41	30.47	22.47	33.04	9.81
PBE	0.00	3.35	7.13	0.03	9.18	10.46	8.81	13.38	14.96	20.01	16.66	22.52	3.46
mPWPW91	0.00	3.04	7.14	0.27	9.01	10.02	8.45	13.01	14.60	19.50	16.36	22.15	3.21
TPSS	0.00	3.16	7.13	0.62	8.47	10.03	8.76	12.70	14.71	19.49	16.52	22.71	3.16
B3LYP	0.00	0.56	3.95	1.47	5.83	7.46	7.74	8.56	10.25	14.05	12.33	17.60	1.09
X3LYP	0.00	0.73	3.82	1.42	5.81	7.70	7.93	8.62	10.32	14.13	12.41	17.68	1.02
O3LYP	0.00	−0.54	4.63	2.23	6.78	6.25	7.20	8.56	9.44	13.84	12.16	16.98	1.44
PBE0	0.00	2.65	5.36	1.02	8.59	10.11	8.91	11.80	13.10	17.57	15.48	21.23	2.29
MPW1K	0.00	1.97	4.27	1.69	7.50	9.60	8.91	10.40	11.80	15.83	14.51	20.25	1.34
B97−1	0.00	1.23	4.66	1.57	6.77	8.30	8.42	9.66	10.96	15.28	13.12	19.09	1.01
TPSSh	0.00	2.87	6.33	1.03	8.36	9.92	8.75	12.13	13.85	18.38	15.98	22.01	2.66
G3	0.00	1.79	2.93	3.02	5.49	8.81	9.39	9.43	9.59	12.96	13.46	18.74	

[a] Units: kJ/mol. [b] See Figure 4 for structures. [c] MADs are given with respect to the G3 values.

corrections. The uncertainty of these final values was estimated to be 2 kJ/mol. Our G3 values are also listed in Table 8. We anticipate that the G3 values are less accurate due to the finite basis set effect. There is, however, an inconsistency among data of ref 42 for conformer 7. We recalculated the MP2/cc-pVTZ data and concluded that the energy reported in ref 42 for conformer 7 is in error. Our final value following the same focal-point approach[42] led to 14.78, instead of 18.54 kJ/mol.

The MAD data with respect to the best numbers show that the results of X3LYP, B3LYP, and B97−1 (0.41−0.49 kJ/mol) are much better than those of PBE and mPWPW91 (4.33 and 4.10 kJ/mol, respectively). MAD of PBE is ten times larger than that of X3LYP. For conformers 3−9, PBE and mPWPW91 significantly underestimate their stabilities.

All DFT methods correctly predict that conformer 1 is the global minimum, and the trend of relative stabilities of different conformers is generally correct. However, there are some notable exceptions. While conformers 3 and 4 have comparable stabilities, the reference value suggests that conformer 3 is more stable than conformer 4. All DFT methods, except LDA and PBE, predict the reverse relative stability. From Table 8, we see that LDA, PBE, and TPSS erroneously predict that conformer 8 is more stable than conformer 7. O3LYP also reverses the relative stability of 5 and 6 as well as 7 and 8.

3.2.3. Serine. Table 9 shows the relative energies of twelve conformers of gaseous serine (see Figure 4). We calculate the reference values by using the G3 theory, as there are no reliable and accurate reference data available in the literature. MADs of X3LYP, B3LYP, and B97−1 are around 1 kJ/mol, being the best performers. LDA is again the worst performer (MAD = 9.81 kJ/mol). MADs of PBE, mPWPW91, and TPSS are 3.46, 3.21, and 3.16 kJ/mol, respectively, being unsatisfactory. O3LYP leads to a MAD of 1.44 kJ/mol. Nevertheless, it erroneously predicts conformer 2, instead of conformer 1, as the global minimum. X3LYP, B3LYP, and B97−1 generally give the correct trend for the relative stability of different conformers, although they reverse the trend between conformers 3 and 4 as well as conformers 10 and 11. From Table 9, we can see that LDA, PBE, PBE0, mPWPW91, TPSS, and TPSSh fail to give a qualitative trend. They reverse the trend between conformers 10 and 11 and mess up conformers from 2 to 7. Hence these functionals may not be suitable for the description of intramolecular HB interactions.

Taking all three amino acids into consideration (Tables 7−9), we may conclude that as the complexity of the amino acid increases, the accuracy of PBE, PBE0, mPWPW91, TPSS, or TPSSh decreases. The performance of X3LYP, B3LYP, and B97−1 is stable, giving MADs of 1 kJ/mol or less in conformational analysis of all three amino acids, holding promise for the study of HBs of peptides and proteins, which are linkages of amino acids.

3.2.4. Glycine Dipeptide. Table 10 shows the relative energies of three Ramachandran conformers of gaseous

Table 10. Relative Energies of Three Ramachandran Conformers of Glycine Dipeptide Given by DFTs with 6-311++G(2d,2p)[a]

conformer[a]	C7	C5	α_L	MAD[b]
LDA	0.00	7.29	14.81	1.34
PBE	0.00	2.75	8.85	3.92
mPWPW91	0.00	2.54	8.58	4.16
TPSS	0.00	3.20	8.99	3.62
B3LYP	0.00	1.14	8.79	4.75
X3LYP	0.00	1.38	9.17	4.44
O3LYP	0.00	−1.19	5.73	7.45
PBE0	0.00	0.96	8.62	4.93
MPW1K	0.00	−0.31	8.19	5.78
B97−1	0.00	1.64	8.53	5.09
TPSSh	0.00	2.24	8.78	4.21
G3	0.00	6.91	12.52	

[a] Units: kJ/mol. [a] See Figure 5 for structures. [b] MADs are given with respect to the G3 values.

glycine dipeptide (see Figure 5). We followed the labeling scheme in ref 44, using C7eq, C5, and α_L to label the H-bonded cycle conformer, the unfolded conformer, and the "L" conformer. The structures were taken from ref 44 and reoptimized by using each method examined here. It is known that the α_R conformer is not an energy minimum for dipeptide,[49] so this conformer is not considered in this work. We calculated the reference values by using the G3 theory.

Though all functionals, except O3LYP and MPW1K, gave the right trend for the relative energy, none of them, with the exception of LDA, gave results which were quantitatively similar to those of the G3 theory. From the results and discussion in the preceding sections, we see that B97−1, X3LYP, and B3LYP are capable of giving a good description of the relative bond strengths of HB interactions, the degraded performance for these functionals for dipeptide has to be attributed to their limitations in the description of inter-residual nonbonded interactions.[49] It should be noted that there are π electrons, delocalized in the orbitals that are perpendicular to the amide plane. According to the Ramachandran map, the C5 conformer has (Φ, $\Psi \approx 180°$, 180°), the C7eq conformer has (Φ, $\Psi \approx -60°$, 60°), and the α_L conformer has (Φ, $\Psi \approx 60°$, 60°). Hence, the $\pi-\pi$ interactions are minimized in C5 and maximized in C7eq, while the strength of the $\pi-\pi$ interaction in α_L is placed in the middle of the three. To take effective error cancelations for the dispersion interactions, one may choose α_L as the reference conformer, such that MADs are reduced to 2.64−2.89 kJ/mol for B97−1, X3LYP, and B3LYP from the original 4.44−4.75 kJ/mol as shown in Table 10 where C7eq is used as the reference conformer.

For the performance of other functionals, it is a result from error cancelations (or accumulations) for the description of HB and vdW interactions. Hence, the interplay between HB and vdW interactions is very important in a bioapplication, which poses a great challenge to DFT. Significantly, LDA, being so poor for the description of HBs and vdWs[11] either alone, gave a very good performance in the case of glycine dipeptide (see Table 10). It would be interesting to see how effectively this error cancelation can carry on for the description of longer peptides.

4. Conclusion

We have examined the performance of some popular DFT methods (i.e., LDA, PBE, mPWPW91, TPSS, B3LYP, X3LYP, PBE0, O3LYP, B97−1, MPW1K, and TPSSh) on describing hydrogen-bond interactions. Here the emphasis has been laid not only on functionals' abilities to calculate the intermolecular hydrogen bonding energies but also on their performances of predicting the relative energies of intermolecular H-bonded complexes and the conformer stabilities due to intramolecular hydrogen bondings. As compared to the best theoretical values, we conclude the following:

(1) In terms of the intermolecular hydrogen bonding energies, PBE and PBE0 give the smallest MADs. These two functionals, however, always lead to large errors for the prediction of the relative energies, giving wrong orders of intermolecular binding configurations and intramolecular conformations. Such conclusions can also be applied to mPWPW91 and MPW1K. TPSS and TPSSh did not always improve over PBE and PBE0.

(2) B3LYP, especially O3LYP, has a severe tendency to underestimate the intermolecular HB bindings. However, errors tend to cancel out in the predictions of relative HB energies and conformational energy differences. Errors associated with O3LYP are usually too large, lending this functional to not be recommended for bioapplications, whereas errors associated with B3LYP are usually small for relative HB energies, showing the value of this functional.

(3) X3LYP and B97−1 treat well all of the HB systems examined here. Not only do they give good results for intermolecular HB energies but also they are the best performers on calculating the relative energies of intermolecular HB complexes and amino acid conformers. We anticipate these functionals be good for systems where hydrogen bondings of varying types and strengths are all important.

(4) The interplay between HB and vdW interactions is very important in a bioapplication, which poses a great challenge to DFT. Other newer functionals (especially, the M06 series),[50] which are very promising but have not yet been available in the commercialized Gaussian package, will be examined in due time.

Acknowledgment. This work was supported by the National Natural Science Foundation of China (20525311, 20533030, 10774126, 20433030) and the Ministry of Science and Technology (2004CB719902, 2007CB815206).

References

(1) Head-Gordon, M.; Pople, J. A.; Frisch, M. J. *Chem. Phys. Lett.* **1988**, *153*, 503–506.

(2) Krishnan, R.; Pople, J. A. *Int. J. Quantum Chem.* **1978**, *14*, 91–100.

(3) Pople, J. A.; Head-Gordon, M.; Raghavachari, K. *J. Chem. Phys.* **1987**, *87*, 5968–5975.

(4) Sousa, S. F.; Fernandes, P. A.; Ramos, M. J. *J. Phys. Chem. A* **2007**, *111*, 10439–10452.

(5) Becke, A. D. *J. Chem. Phys.* **1993**, *98*, 5648–5652.

(6) Tuma, C.; Boese, A. D.; Handy, N. C. *Phys. Chem. Chem. Phys.* **1999**, *1*, 3939–3947.

(7) Rabuck, A. D.; Scuseria, G. E. *Theor. Chem. Acc.* **2000**, *104*, 439–444.

(8) Sherer, E. C.; York, D. M.; Cramer, C. J. *J. Comput. Chem.* **2003**, *24*, 57–67.

(9) Xu, X.; Goddard, W. A. *J. Phys. Chem. A* **2004**, *108*, 2305–2313.

(10) Frey, J. A.; Leutwyler, S. *Chimia* **2005**, *59*, 511–516.

(11) Zhao, Y.; Truhlar, D. G. *J. Chem. Theory Comput.* **2005**, *1*, 415–432.

(12) Burke, K.; Ernzerhof, M.; Perdew, J. P. *Phys. Rev. Lett.* **1996**, *77*, 3865–3868.

(13) Burke, K.; Ernzerhof, M.; Perdew, J. P. *Chem. Phys. Lett.* **1997**, *265*, 115–120.

(14) Adamo, C.; Barone, V. *J. Chem. Phys.* **1999**, *110*, 6158–6170.

(15) Adamo, C.; Barone, V. *J. Chem. Phys.* **1998**, *108*, 664–675.

(16) Kurita, N.; Sekino, H. *Int. J. Quantum Chem.* **2003**, *91*, 355–362.

(17) Hamprecht, F. A.; Cohen, A. J.; Tozer, D. J.; Handy, N. C. *J. Chem. Phys.* **1998**, *109*, 6264–6271.

(18) Cohen, A. J.; Tantirungrotechai, Y. *Chem. Phys. Lett.* **1999**, *299*, 465–472.

(19) Andersson, S.; Gruning, M. *J. Phys. Chem. A* **2004**, *108*, 7621–7636.

(20) Lynch, B. J.; Fast, P. L.; Harris, M.; Truhlar, D. G. *J. Phys. Chem. A* **2000**, *104*, 4811–4815.

(21) Zhao, Y.; Pu, J. Z.; Lynch, B. J.; Truhlar, D. G. *Phys. Chem. Chem. Phys.* **2004**, *6*, 673–676.

(22) Cohen, A. J.; Handy, N. C. *Mol. Phys.* **2001**, *99*, 607–615.

(23) Baker, J.; Pulay, P. *J. Chem. Phys.* **2002**, *117*, 1441–1449.

(24) Xu, X.; Goddard, W. A. *J. Phys. Chem. A* **2004**, *108*, 8495–8504.

(25) Tao, J.; Perdew, J. P.; Staroverov, V. N.; Scuseria, G. E. *Phys. Rev. Lett.* **2003**, *91*, 146401.

(26) Staroverov, V. N.; Scuseria, G. E.; Tao, J.; Perdew, J. P. *J. Chem. Phys.* **2003**, *119*, 12129.

(27) Xu, X.; Goddard, W. A. *Proc. Natl. Acad. Sci. U.S.A.* **2004**, *101*, 2673–2677.

(28) Martin, J. M. L.; Oliveira, G. *J. Chem. Phys.* **1999**, *111*, 1843–1856.

(29) Voorhis, T. V.; Scuseria, G. E. *J. Chem. Phys.* **1998**, *109*, 400–410.

(30) Slater, J. C. *Quantum Theory of Molecular and Solids. Vol. 4: The Self-Consistent Field for Molecular and Solids*; McGraw-Hill: New York, 1974.

(31) Vosko, S. H.; Wilk, L.; Nusair, M. *Can. J. Phys.* **1980**, *58*, 1200.

(32) Zhao, Y.; Truhlar, D. G. *J. Chem. Theory Comput.* **2007**, *3*, 289–300.

(33) SAPT2006: An Ab Initio Program for Many-Body Symmetry-Adapted Perturbation Theory Calculations of Intermolecular Interaction Energies and its user's manual by R. Bukowski, W. Cencek, P. Jankowski, B. Jeziorski, M. Jeziorska, S. A. Kucharski, V. F. Lotrich, A. J. Misquitta, R. Moszynski, K. Patkowski, R. Podeszwa, S. Rybak, K. Szalewicz, H. L. Williams, R. J. Wheatley, P. E. S. Wormer, and P. S. Zuchowski.

(34) Jeziorski, B.; Moszynski, R.; Szalewicz., K. *Chem. Rev.* **1994**, *94*, 1887–1930.

(35) Dunning, T. H., Jr. *J. Chem. Phys.* **1989**, *90*, 1007–1023.

(36) Kendall, R. A.; Dunning, T. H., Jr.; Harrison, R. J. *J. Chem. Phys.* **1992**, *96*, 6796–6806.

(37) Kim, K. S.; Friesner, R. A. *J. Am. Chem. Soc.* **1997**, *119*, 12952–12961.

(38) Mignon, P.; Loverix, S.; Steyaert, J.; Geerlings, P. *Nucleic Acids Res.* **2005**, *33*, 1779–1789.

(39) Tsuzuki, S.; Fujii, A. *Phys. Chem. Chem. Phys.* **2008**, *10*, 2584–2594.

(40) Kohn, W.; Meir, Y.; Makarov, D. E. *Phys. Rev. Lett.* **1998**, *80*, 4153–4156.

(41) Csaszar, A. G. *J. Am. Chem. Soc.* **1992**, *114*, 9568–9575.

(42) Czinki, E.; Csaszar, A. G. *Chem. Eur. J.* **2003**, *9*, 1008–1019.

(43) Lambie, B.; Ramaekers, R.; Maes, G. *J. Phys. Chem. A* **2004**, *108*, 10426–10433.

(44) Could, I. R.; Cornell, W. D.; Hillier, I. H. *J. Am. Chem. Soc.* **1994**, *116*, 9250–9256.

(45) Krishan, A.; Binkley, J. S.; Seeger, R.; Pople, J. A. *J. Chem. Phys.* **1980**, *72*, 650–654.

(46) Clark, T.; Chandrasekhar, J.; Schleyer, P. v. R. *J. Comput. Chem.* **1983**, *4*, 294–301.

(47) Frisch, M. J.; Pople, J. A.; Binkley, J. S. *J. Chem. Phys.* **1984**, *80*, 3265–3269.

(48) Frisch, M. J.; Trucks, G. W.; Schlegel, H. B.; Scuseria, G. E.; Robb, M. A.; Cheeseman, J. R.; Montgomery, J. A., Jr.; Vreven, T.; Kudin, K. N.; Burant, J. C.; Millam, J. M.; Iyengar, S. S.; Tomasi, J.; Barone, V.; Mennucci, B.; Cossi, M.; Scalmani, G.; Rega, N.; Petersson, G. A.; Nakatsuji, H.; Hada, M.; Ehara, M.; Toyota, K.; Fukuda, R.; Hasegawa, J.; Ishida, M.; Nakajima, T.; Honda, Y.; Kitao, O.; Nakai, H.; Klene, M.; Li, X.; Knox, J. E.; Hratchian, H. P.; Cross, J. B.; Adamo, C.; Jaramillo, J.; Gomperts, R.; Stratmann, R. E.; Yazyev, O.; Austin, A. J.; Cammi, R.; Pomelli, C.; Ochterski, J. W.; Ayala, P. Y.; Morokuma, K.; Voth, G. A.; Salvador, P.; Dannenberg, J. J.; Zakrzewski, V. G.; Dapprich, S.; Daniels, A. D.; Strain, M. C.; Farkas, O.; Malick, D. K.; Rabuck, A. D.; Raghavachari, K.; Foresman, J. B.; Ortiz, J. V.; Cui, Q.; Baboul, A. G.; Clifford, S.; Cioslowski, J.; Stefanov, B. B.; Liu, G.; Liashenko, A.; Piskorz, P.; Komaromi, I.; Martin, R. L.; Fox, D. J.; Keith, T.; Al-Laham, M. A.; Peng, C. Y.; Nanayakkara, A.; Challacombe, M.; Gill, P. M. W.; Johnson, B.; Chen, W.; Wong, M. W.; Gonzalez, C.; Pople, J. A. *Gaussian 03, revision C.01*; Gaussian, Inc.: Pittsburgh, PA, 2003.

(49) Improta, R.; Barone, V. *J. Comput. Chem.* **2004**, *25*, 1333–1341.

(50) Zhao, Y.; Truhlar, D. G. *Acc. Chem. Res.* **2008**, *41*, 157–167.

CT800237N

JCTC Journal of Chemical Theory and Computation

Influence of Guest−Host Interactions on the Structural, Energetic, and Mössbauer Spectroscopy Properties of Iron(II)tris(2,2′-bipyridine) in the Low-Spin and High-Spin States: A Density-Functional Theory Study of the Zeolite-Y Embedded Complex

Alfredo Vargas, Andreas Hauser, and Latévi Max Lawson Daku*

Département de Chimie Physique, Université de Genève, 30 quai Ernest-Ansermet, CH-1211, Genève 4, Switzerland

Received July 18, 2008

Abstract: Density functional theory is applied within a supramolecular approach to the study of the guest−host interactions in $[Fe(bpy)_3]^{2+}$@Y and their influence on the structural, energetic, and ^{57}Fe Mössbauer spectroscopy properties of the encapsulated $[Fe(bpy)_3]^{2+}$ complex in the low- and high-spin states. The structures of the isolated complex and the supramolecular model used for $[Fe(bpy)_3]^{2+}$@Y were optimized in both spin-states using different generalized gradient approximation (PBE, HCTH, OLYP) and hybrid (B3LYP*, O3LYP) functionals. The results obtained are consistent with one another and show that, in either spin-state, the structure of $[Fe(bpy)_3]^{2+}$ shrinks and distorts upon encapsulation. Still, the structural changes experienced by the complex in a given spin-state remain limited, especially in that they do not lead to a substantial variation of the ^{57}Fe quadrupole splitting, whose calculated values are in very good agreement with avalaible experimental data. The decomposition of the guest−host interaction energy into its electrostatic, Pauli and orbital contributions shows that the bonding between the complex and the supercage is more electrostatic than covalent. The ability of modern functionals to accurately describe the interactions explains the remarkable consistency of the results obtained with the various functionals. In particular, although the functionals perform very differently for the determination of the high-spin/low-spin energy difference ΔE^{el}_{HL} in $[Fe(bpy)_3]^{2+}$ and $[Fe(bpy)_3]^{2+}$@Y, they consistently predict that the encapsulation entails a destabilization of the high-spin state with regard to the low-spin state of $\Delta(\Delta E^{el}_{HL}) = 2500$ cm^{-1}. Using for $[Fe(bpy)_3]^{2+}$ the CASPT2 value of $\Delta E^{el}_{HL} = 3700$ cm^{-1} [Pierloot, K.; Vancoillie, S. *J. Chem. Phys.* 2006, *125*, 124303; Pierloot, K.; Vancoillie, S. *J. Chem. Phys.* 2008, *128*, 034104], we obtain for the high-spin/low-spin energy difference in $[Fe(bpy)_3]^{2+}$@Y, a best ab initio estimate of $\Delta E^{el}_{HL} = 6200$ cm^{-1}.

1. Introduction

The increasing demand on new functional materials for use in advanced nanoscale technologies makes the control of the wide range of properties of transition metal compounds a more than ever attractive goal. In this respect, varying the environment of transition metal complexes, hence the involved guest−host interactions, proves to be an efficient means to finely tune their electronic properties, as this will be exemplified here for the title complex $[Fe(bpy)_3]^{2+}$ (bpy = 2,2′-bipyridine). This is a low-spin (LS) d^6 complex, that is, its electronic ground-state corresponds to the ligand-field $^1A_1(t_{2g}^6)$ state, while the ligand-field high-spin (HS) $^5T_2(t_{2g}^4E_g^2)$ state lies

* To whom correspondence should be addressed. E-mail: max.lawson@unige.ch.

10.1021/ct800284g CCC: $40.75 © 2009 American Chemical Society
Published on Web 12/17/2008

too high in energy to become thermally populated. As in the case of the spin-crossover systems, the population of the metastable HS state can be achieved by photoexcitation, and the kinetics of the subsequent HS → LS relaxation can be followed by time-resolved absorption spectroscopy.[1] However, because of the larger HS−LS zero-point energy difference ($\Delta E^{\circ}_{HL} = E^{\circ}_{HS} - E^{\circ}_{LS}$), the relaxation dynamics reported for the LS $[Fe(bpy)_3]^{2+}$ complex are faster than for spin-crossover compounds. Thus, while the low-temperature tunnelling rate constants, $k_{HL}(T \rightarrow 0)$, are between 10^{-6} and 10^{-1} s^{-1} for spin-crossover compounds, they take on values between 10^4 and 10^8 s^{-1} for the title complex doped into a series of photophysically inert crystalline hosts.[2−5] The HS → LS relaxation is described by the theory of nonadiabatic multiphonon relaxation (see ref 1 and references therein). The quantitative analysis of the low-temperature relaxation dynamics reported for $[Fe(bpy)_3]^{2+}$ within this framework showed that the different environments provided by these hosts make ΔE°_{HL} vary between 2500 and 5000 cm^{-1}.[6,7]

In passing from the LS to the HS state, the metal−ligand bond length of $[Fe(bpy)_3]^{2+}$ increases by $\Delta r_{HL} = r_{HS} - r_{LS} \approx 0.2$ Å, and concomitantly, the molecular volume increases by $\Delta V_{HL} = V_{HS} - V_{LS} \approx 20$ Å^3.[6,8] This is caused by the promotion of two electrons from the metallic nonbonding orbital levels of octahedral t_{2g} parentage into the antibonding ones of e_g parentage. The molecular volume of the complex being larger in the HS state than in the LS state, the drastic manner in which the environment influences the HS−LS zero-point energy difference can be rationalized in terms of an internal or chemical pressure exerted by the environment of the hosts on the $[Fe(bpy)_3]^{2+}$ guest, which destabilizes the HS state with respect to the LS state. The concept of chemical pressure is of widespread use in solid-state physics and in solid-state chemistry as it offers an appealing parallel between the effect of the external pressure on a specific property of a material and the effect on this same property of a lattice volume variation obtained by chemical changes (see, e.g., refs 9−11). Nevertheless, as discussed in refs 12 and 13, for instance, chemical and physical pressures are not necessarily equivalent. Of special interest to us is the concept of chemical pressure that was shown by Hauser et al. to provide insight not only into the manner in which the relative energies of the ligand-field states of the title complex but also that of the complexes $[M(bpy)_3]^{2+}$ (M = Ru, Co) and, hence, into how their electronic properties can be tuned by guest−host interactions.[5] Still, it does not give a detailed picture of the effective interactions, which we aim at providing with the present study of $[Fe(bpy)_3]^{2+}$ encapsulated in the supercage of zeolite Y ($[Fe(bpy)_3]^{2+}$@Y).

As recently reviewed by Gol'tsov,[14] zeolites with encapsulated transition metal complexes are very convenient materials for investigating guest−host interactions and their influence on the physical and chemical properties of the encapsulated complexes. Zeolites provide well-defined rigid and stable frameworks with cavities of various sizes and shapes, so that the encapsulation of transition metal complexes in these cavities allows us to vary their environment in a controlled manner. The supercage of zeolite Y has a diameter of about 13 Å and openings of approximatively 7.4 Å,[15] which allows the encapsulation of organometallic molecules of a similar size, such as tris(2,2′-trisbipyridine) complexes, using a ship-in-a-bottle synthesis. [16,17]

The physicochemical properties of thus synthesized zeolite-Y embedded LS $[Fe(bpy)_3]^{2+}$ complexes have been investigated by several research groups.[18−22] X-ray diffractometry (XRD) possibly combined with UV−vis reflectance,[18,19,21] IR,[21,22] or solid-state NMR[22] spectroscopies helped evidence the formation of the complex within the supercages of zeolite Y. ^{57}Fe Mössbauer absorption spectroscopy was employed as well. This spectroscopy is an efficient tool for probing spin crossover in iron systems.[23−27] For the title LS complex, it allows the characterization of the distortion undergone upon encapsulation. Thus, in the first-ever reported study of $[Fe(bpy)_3]^{2+}$@Y by Quayle et al., two samples containing 5.3 and 13 Fe ions per unit cell were investigated.[18] From the Mössbauer spectroscopy study of the sample with the low iron loading, $[Fe(bpy)_3]^{2+}$ was found to represent about 88% of the iron content and to be characterized by an isomer shift of $\delta = 0.63$ mm s^{-1} and a quadrupole splitting of $\Delta E_Q = 0.34$ mm s^{-1}. While this value of ΔE_Q is similar to those found for $[Fe(bpy)_3]^{2+}$ in other matrices, that of δ is larger than the literature value of 0.3−0.5 mm s^{-1}. This difference was ascribed to the influence of the high electron density within the zeolite lattice on the polarizable ligands.[18] The analysis of the Mössbauer spectrum of the second sample gave also $[Fe(bpy)_3]^{2+}$ as the dominant iron species, with an abundance of ∼55%. Its Mössbauer parameters, $\delta = 0.46$ mm s^{-1} and $\Delta E_Q = 0.35$ mm s^{-1}, are in line with those observed for the complex in other environments. In an other study, Vankó et al.[20] investigated three samples wherein $[Fe(bpy)_3]^{2+}$ was found by Mössbauer spectroscopy to represent 38, 56, and 100% of the iron content and to be characterized by $\delta = 0.32$ mm s^{-1} and $\Delta E_Q = 0.32$ mm s^{-1}. Given that the ΔE_Q values thus determined for $[Fe(bpy)_3]^{2+}$@Y are very similar to those found for the complex in other matrices, it especially follows from these Mössbauer studies that the complex does not undergo major distortions upon encapsulation.[28]

Interestingly, the trigonal symmetry of the complex turns out to be preserved in the supercage. This could be inferred from the IR spectroscopy study of $[Fe(bpy)_3]^{2+}$@Y.[21] This is also supported by the EPR spectroscopy study of $[Fe(bpy)_3]^{3+}$@Y obtained by in situ oxidation, the recorded spectrum being indeed characteristic of the trigonal LS $[Fe(bpy)_3]^{3+}$ complex.[18] Consequently, to theoretically investigate the influence of the second coordination sphere on the properties of $[Fe(bpy)_3]^{2+}$ in zeolite Y, we adopted the supramolecular model of C_3 symmetry shown in Figure 1. This one consists of the complex and the surrounding Si and O atoms that define the supercage. The valence of the Si atoms has been saturated with H atoms. Finally, the orientation of the complex is such that its trigonal axis coincides with one C_3 axis of the supercage, which has an ideal T_d symmetry. As shown below, the study of this model within density functional theory (DFT)[29−33] allowed us to get major new insights into the nature of the guest−host interactions in $[Fe(bpy)_3]^{2+}$@Y and into their influence on the structural,

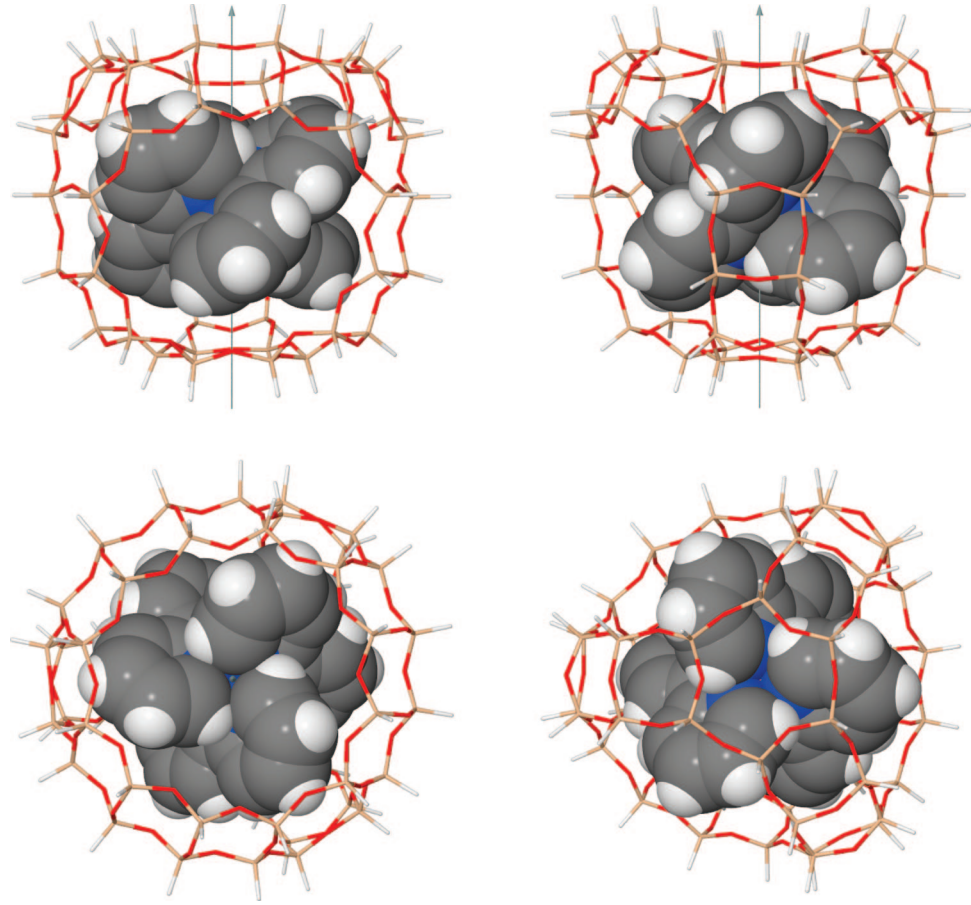

Figure 1. Supramolecular model used to investigate $[Fe(bpy)_3]^{2+}$@Y: the trigonal axis of $[Fe(bpy)_3]^{2+}$ coincides with one of the C_3 axes of the supercage that cross opposite six- and twelve-membered oxygen rings. The top drawings are side views of the models that are related to each other by a 180° rotation about the main C_3 axis; the bottom drawings are views from the top (bottom left) and from the bottom (bottom right).

energetic, and Mössbauer spectroscopy properties of the complex in the LS and in the metastable HS state.

Few studies have dealt with the experimental characterization of the metastable HS state of the zeolite-Y embedded complex. Vankó et al.[34−36] used ^{57}Fe Mössbauer emission spectroscopy to investigate $[^{57}Co(bpy)_3]^{2+}$ encapsulated in the supercages of zeolite Y. They thus showed that three nucleogenic ^{57}Fe species are formed after the electron capture ^{57}Co(EC) ^{57}Fe nuclear decay: the LS $[^{57}Fe(bpy)_3]^{2+}$ and LS $[^{57}Fe(bpy)_3]^{3+}$ complexes and a HS iron(II) complex with a damaged coordination sphere. In similar investigations performed on the system $[^{57}Co/Mn(bpy)_3](PF_6)_2$ by Deisenroth et al.,[3,37] Mössbauer emission spectroscopy could be used to show the formation of a fourth species, namely, the ligand-field HS $[^{57}Fe(bpy)_3]^{2+}$ complex and to follow the dynamics of the subsequent HS → LS relaxation. The absence of the ligand-field HS state of $[^{57}Fe(bpy)_3]^{2+}$ in the Mössbauer emission spectra of $[^{57}Co(bpy)_3]^{2+}$@Y was therefore ascribed by Vankó et al. to the very short lifetime τ_{HS} of this state in zeolite Y, which results from the strong increase of ΔE°_{HL} upon encapsulation and which prevents its detection with this spectroscopic technique. Nevertheless, from the time-integral Mössbauer emission spectroscopy intensity data of $[^{57}Co(bpy)_3]^{2+}$@Y, Vankó et al. were able to determine for τ_{HS} an upper limit of 60 ns or equivalently a lower limit of 1.67×10^7 s^{-1} for $k_{HL}(T \rightarrow 0)$.[36]

2. Computational Details

The Gaussian03 program package[38] was used to optimize the geometries of the isolated $[Fe(bpy)_3]^{2+}$ complex, the supercage, and the $[Fe(bpy)_3]^{2+}$@Y model. The calculations were run with the symmetry constrained to C_3. The OLYP,[39,40] B3LYP*,[41−43] HCTH,[44] O3LYP, [45] and PBE[46,47] exchange-correlation (XC) functionals were employed in combination with the $\mathcal{G}$ basis set of Gaussian-type orbital (GTO) functions. In this basis set, the H atoms are described by the Pople double-ζ polarized 6−31G** basis set.[48,49] For the heavy atoms, the compact effective potentials (CEPs) of Stevens et al. are used to describe the atomic core electrons, while the valence electrons are described with associated GTO basis sets of double-ζ polarized quality, for the C, Si, O, and N atoms, (CEP-31G* basis set), and of triple-ζ quality for the Fe atom, (CEP-121G basis set). [50,51] The optimization calculations were performed with the default convergence criteria, and it proved necessary to resort to a large integration grid consisting of 99 radial shells and 770 angular points per shell.

To get insight into the guest−host interactions in $[Fe(bpy)_3]^{2+}$@Y, we have analyzed the interaction energy between the complex and the supercage using the bonding energy decomposition scheme implemented in the Amsterdam Density Functional (ADF) program package.[52,53] The

calculations were performed on the optimized OLYP/$\mathcal{G}$ geometries with the OLYP functional and the all-electron TZP basis set of triple-ζ polarized quality from the ADF Slater-type orbital (STO) basis set database, thereafter referred to as the $\mathcal{G}$ basis set. The ADF package was also used for the determination of the ^{57}Fe quadrupole splitting of the free and encapsulated $[Fe(bpy)_3]^{2+}$ complex. This one was derived from the electric field gradient (EFG) at the iron center obtained by scalar relativistic (SR) calculations carried out within the zeroth-order relativistic approximation (ZORA), as well as within the ZORA-4 approximation, which incorporates the small component density.[54] The EFG calculations were performed with the all-electron ZORA relativistic TZP basis set, (referred to below as the $\mathcal{J}_R$ basis set), and the OLYP and PBE functionals. In all calculations with the ADF package, we could not make use of the C_3 symmetry of the involved structures because this point group is not supported. All these calculations were therefore performed in C_1 symmetry. A high accurracy parameter "accint" of 6 was also used. Note that for the characterization of the free or embedded complex in the HS state, it was also necessary to apply electron smearing to help the calculations converge; the smearing parameter "smearq" being set to the small value of 0.003 Ha.

The Jmol program[55,56] was used for visualizing the molecular structures.

3. Results and Discussion

3.1. Characterization of $[Fe(bpy)_3]^{2+}$@Y in the Low-Spin State. *3.1.1. Structural Properties.* For all XC functionals used, the optimization of the structure of the isolated complex in C_3 symmetry led to an optimized geometry of D_3 symmetry. In these calculated LS geometries of $[Fe(bpy)_3]^{2+}$, as well as in others that are considered subsequently, the arrangement of the ligands around the iron center are characterized by the following structural parameters: the Fe−N and Fe−N′ metal−ligand bond lengths, the distance C_2-C_2' (see Figure 2 for the atom labeling) between the pyridinyl moieties, and the angles defined in Figure 3.

The values found for these structural parameters in the optimized LS geometries of free $[Fe(bpy)_3]^{2+}$ are reported in Table 1, along with those found in the X-ray structure of the LS complex.[57] Note that the experimental geometry of the complex in $[Fe(bpy)_3](PF_6)_2$ is of D_3 symmetry and that we therefore verify in this case: $\theta = \theta'$ and Fe−N = Fe−N′, as in the case of the optimized geometries. The inspection of Table 1 shows that the calculated LS geometries are consistent with one another and in good agreement with experiment. Actually, the optimized geometries of $[Fe(bpy)_3]^{2+}$ tend to be slightly more expanded than the experimental one, as reflected by the somewhat larger optimized iron−nitrogen and C_2-C_2' bond lengths. This discrepancy is the result of the neglect of the packing and counterion effects in our calculations performed in the gas phase.

Given the confining environment provided by the supercage of zeolite-Y, the results of the calculations performed for determining the structure of $[Fe(bpy)_3]^{2+}$@Y may exhibit a strong dependence on the choice of the starting geometry.

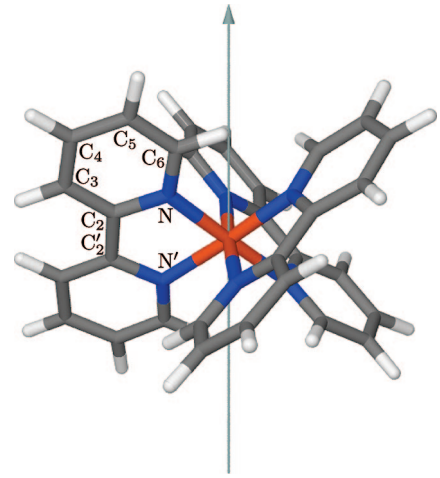

Figure 2. Atom labeling used for the complex: the atoms with primed labels belong to the equivalent pyridinyl moieties which, in the supercage, are oriented toward the six-membered ring at the bottom of the supercage (see Figure 1). Note that H_i and H_i' refer to the hydrogen atoms bound to atoms C_i and C_i', respectively ($i = 3,\ldots, 6$).

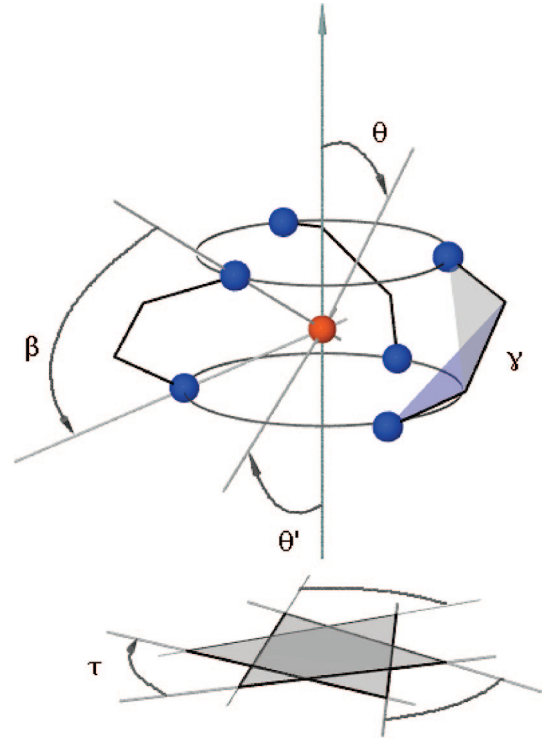

Figure 3. Angles characterizing the arrangement of the ligands around the iron center in $[Fe(bpy)_3]^{2+}$: $\beta = N-Fe-N'$ is the bite angle; $\gamma = N-C_2-C_2'-N'$ is the dihedral angle between the ligand moieties; τ is the twist angle; θ (respectively, θ') is the angle between the z-axis and the generator of the cone on which the nitrogen atoms labeled N (respectively, N′) are located.

The influence of this choice has been thoroughly investigated by carrying out a series of geometry optimizations at the OLYP/$\mathcal{G}$ level. The details of this analysis are given in the Supporting Information. The most stable optimized geometry thus obtained proves to be 11 220 cm^{-1} lower in energy than the LS reference configuration defined as the LS $[Fe(bpy)_3]^{2+}$ complex and the supercage taken separately and relaxed at

Table 1. Selected Bond Lengths (Å) and Angles (deg) Characterizing the Geometry of the LS $[Fe(bpy)_3]^{2+}$ Complex: Results of Geometry Optimization Calculations Performed on the Isolated and on the Zeolite-Y Embedded Complex[a]

		Fe−N	Fe−N′	C_2-C_2'	β	γ	τ	θ	θ'
OLYP/$\mathscr{G}$	$[Fe(bpy)_3]^{2+}$	1.993	1.993	1.477	81.4	3.7	54.7	58.6	58.6
	$[Fe(bpy)_3]^{2+}$@Y	1.956	1.986	1.473	82.2	7.5	56.9	57.7	60.3
HCTH/$\mathscr{G}$	$[Fe(bpy)_3]^{2+}$	1.981	1.981	1.472	81.5	3.6	54.7	58.6	58.6
	$[Fe(bpy)_3]^{2+}$@Y	1.951	1.976	1.468	82.3	6.0	56.9	57.8	60.1
PBE/$\mathscr{G}$	$[Fe(bpy)_3]^{2+}$	1.972	1.972	1.482	82.2	3.0	53.6	58.2	58.2
	$[Fe(bpy)_3]^{2+}$@Y	1.955	1.965	1.479	82.7	3.5	56.4	57.8	59.0
O3LYP/$\mathscr{G}$	$[Fe(bpy)_3]^{2+}$	2.002	2.002	1.481	81.2	3.5	54.7	58.7	58.7
	$[Fe(bpy)_3]^{2+}$@Y	1.966	1.994	1.476	82.0	7.2	56.7	57.8	60.1
B3LYP*/$\mathscr{G}$	$[Fe(bpy)_3]^{2+}$	2.010	2.010	1.490	81.4	2.7	54.7	58.4	58.4
	$[Fe(bpy)_3]^{2+}$@Y	1.986	2.000	1.486	82.1	3.7	55.8	57.9	59.3
exptl[b]	$[Fe(bpy)_3](PF_6)_2$	1.967	1.967	1.471	81.8	6.4	53.6	57.8	57.8

[a] The values found for these structural parameters in the X-ray structure of the LS compound $[Fe(bpy)_3](PF_6)_2$ are also given for comparison purpose. [b] Taken from ref 57.

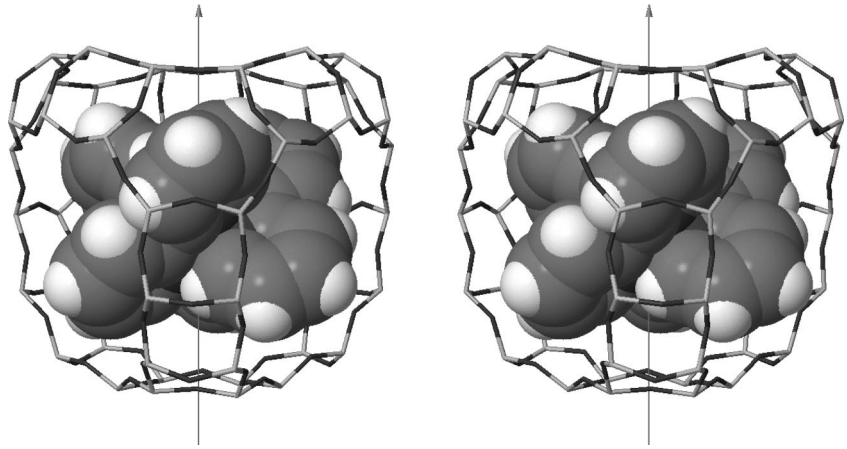

Figure 4. Stereoscopic view of the most stable structure determined for the LS $[Fe(bpy)_3]^{2+}$@Y system at the OLYP/$\mathscr{G}$ level (see text).

the same theoretical level. Figure 4 gives a stereoscopic view of this calculated structure that we also used as starting point in the optimization calculations performed with the other functionals for characterizing the LS $[Fe(bpy)_3]^{2+}$@Y system.

Figure 4 shows that the orientation of the complex within the supercage helps minimize the steric repulsion between the two subsystems. Thus, for each bipyridine, the $C_i'-H_i'$ (i = 3, 4, 5) and C_3-H_3 bonds face a twelve-membered window and point into the void. Likewise, the C_4-H_4 bond points toward the center of the six-membered window which, along with the previously mentioned twelve-membered window, are bisected by the average plane of the ligand. In addition, the C_5-H_5 bond points toward the twelve-membered opening on the top (i.e., the one crossed by the C_3 axis), whereas the C_6-H_6 and C_6-H_6 and $C_6'-H_6'$ bonds are inwardly directed. This optimal arrangement of the complex within the supercage is preserved in passing to the other calculated LS geometries of $[Fe(bpy)_3]^{2+}$@Y, which actually are quite close to the OLYP/$\mathscr{G}$ geometry shown in Figure 4. For all these computed geometries, selected bond lengths and angles characterizing the first coordination sphere of the encapsulated LS complex are summarized in Table 1. The comparison of these structural data with their counterparts for the isolated LS complex shows that the complex does not undergo a tremendous distortion upon encapsulation. This can also be inferred from the superposition in Figure 5A of its geometries in the gas phase and in the supercage.

Figure 5A also shows that there is a slight shrinkage of the geometry of the LS complex upon encapsulation. Thus, depending on the considered theoretical level, there is a shortening of the Fe−N and Fe−N′ bonds of 0.017−0.037 and 0.005−0.010 Å, respectively, and to a lesser extent that of the C_2-C_2' bond of between 0.003 and 0.005 Å. Actually, for the different theoretical levels used, the decrease of the Fe−N bond length is about 2−6 times larger than the decrease of the Fe−N′ bond length. For each ligand, given that the pyridinyl moiety with the "N" labeled nitrogen atom comes the closest to the wall of the supercage, the pronounced shrinking of the Fe−N bond, as well as the accompanying noticeable decrease of the ligand cone angle θ provide an efficient means for minimizing the steric repulsion between this pyridinyl moiety and the supercage. Although the Fe−N′ bond length is far less affected by the encapsulation than the Fe−N bond length, one observes an increase of the cone angle θ' of ∼1° to ∼2°, which is made possible thanks to the space made available to the corresponding pyridinyl moiety through the twelve-membered opening that faces it. The encapsulation has also little influence on the bite angle β since the value found for the encapsulated complex differs by less than 1% from the optimal gas-phase value. For the complex to fit at best within the supercage, the twist angle τ substantially increases by about 1−3° depending on the functional used. Similarly, the dihedral

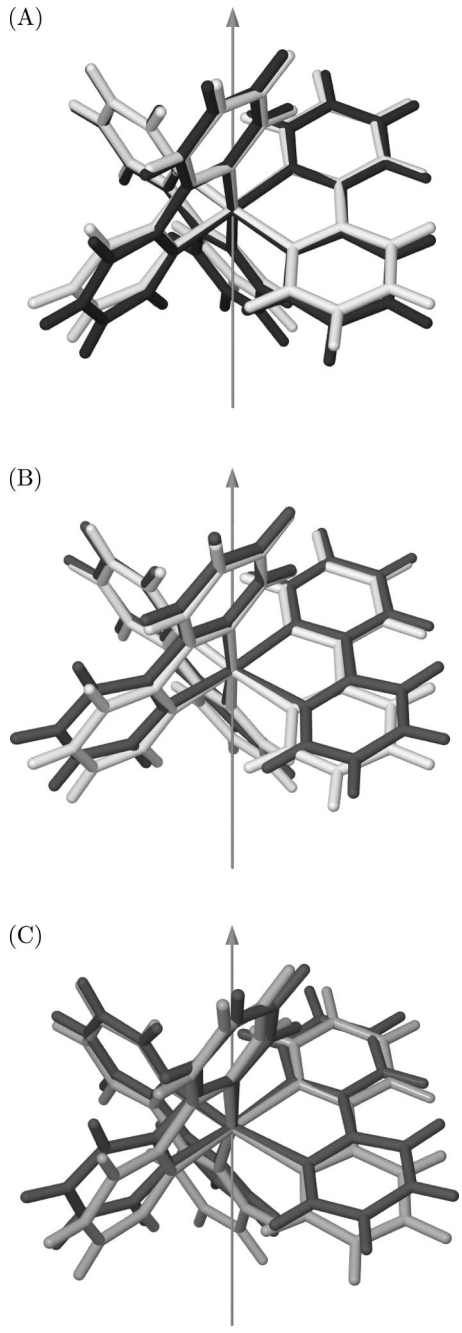

Figure 5. Superimposed geometries of $[Fe(bpy)_3]^{2+}$ showing the structural variations undergone by the complex upon a change of spin-states and/or upon encapsulation (OLYP/$\mathscr{G}$ results): (A) optimized LS geometry of the isolated complex (black) and its geometry as found in the most stable optimized LS geometry of $[Fe(bpy)_3]^{2+}$@Y (white); (B) this latter LS geometry (white) and the geometry of the complex as found in the optimized HS geometry of $[Fe(bpy)_3]^{2+}$@Y (gray); (C) geometry of the HS encapsulated complex (gray) and geometry of the isolated complex in the HS state (light gray).

angle γ increases by a factor of about 2, passing from ~3.5° to ~7°. The increase of γ is however not as large in the case of the results obtained with the PBE and B3LYP* functionals. Actually, the use of these two functionals leads to the smallest γ values for the complex both in the gas phase and in the supercage.

Finally, our results show that the geometry of the LS complex only undergoes a slight distortion upon encapsulation. For the complex, the concomitant energy change is limited as illustrated by the fact that, at the OLYP/$\mathscr{G}$ level, the passing from the relaxed geometry of the isolated complex to that of the encapsulated complex translates into a small energy increase of 1391 cm^{-1}. Similarly, the structural changes experienced by the supercage upon the inclusion of the LS complex are minimal and give rise to an increase of its energy by 3393 cm^{-1} (OLYP/$\mathscr{G}$ level). These changes are illustrated in Figure 6A by the superposition of the geometries of the supercage before and after the inclusion of the LS complex, which indeed prove to be very close. In summary, our results show that the encapsulation of the LS $[Fe(bpy)_3]^{2+}$ complex in the supercage of zeolite Y does not entail major geometric distortions neither for the complex nor for the supercage.

3.1.2. ^{57}Fe Mössbauer Quadrupole Splitting. As pointed out in the Introduction, ^{57}Fe Mössbauer spectroscopy has proven to be an efficient tool for investigating $[Fe(bpy)_3]^{2+}$@Y and especially for providing a measure of the distortion of the encapsulated complex through the determination of the quadrupole splitting ΔE_Q for the ^{57}Fe $I = 3/2$ excited nuclear state. From a computational point of view, ΔE_Q is obtained from the calculation of the eigenvalues of the traceless electric field gradient (EFG) tensor, $V_{\alpha\alpha}$ with $\alpha = x,\ y,\ z$ and $|V_{zz}| \geq |V_{yy}| \geq |V_{xx}|$, according to the relation

$$\Delta E_Q = \frac{eQV_{zz}}{2} \times \sqrt{1 + \frac{\eta^2}{3}} \tag{1}$$

where e is the electron charge, Q is the quadrupole moment of the ^{57}Fe nucleus in its $I = 3/2$ excited state,[58] where $Q =$ 0.14 barn, (1 barn = 10^{-28} m ^{2}), and

$$\eta = \left| \frac{V_{xx} - V_{yy}}{V_{zz}} \right| \tag{2}$$

is the asymmetry parameter of the EFG tensor.

We proceeded to the determination of the principal values of the EFG tensor for $[Fe(bpy)_3]^{2+}$ and $[Fe(bpy)_3]^{2+}$@Y in the LS spin state by carrying out SR calculations within the ZORA and ZORA-4 approximations. For the LS $[Fe(bpy)_3]^{2+}$@Y system, the calculations performed either on the whole system or on the $[Fe(bpy)_3]^{2+}$ subsystem gave EFG components and also ΔE_Q values that agree to within less than 1%. This could be established from calculations performed at the OLYP/$\mathscr{J}_R$ and PBE/$\mathscr{J}_R$ levels using the structural description of the LS $[Fe(bpy)_3]^{2+}$@Y system obtained at the OLYP/$\mathscr{G}$ level, as well as from calculations performed at the PBE/$\mathscr{J}_R$ level using the PBE/$\mathscr{G}$ structural description of the system (data not shown). Consequently, the determination of the EFG components and hence that of the quadrupole splitting at the iron center in $[Fe(bpy)_3]^{2+}$@Y can be very accurately done without including the second coordination sphere in the calculations. That is, the influence of the environment provided by the zeolite Y on the EFG at the metallic center may be considered as being exclusively caused by the distortion of the first coordination sphere entailed by the encapsulation. The vanishing contribution of the second coordination sphere to the EFG is probably caused

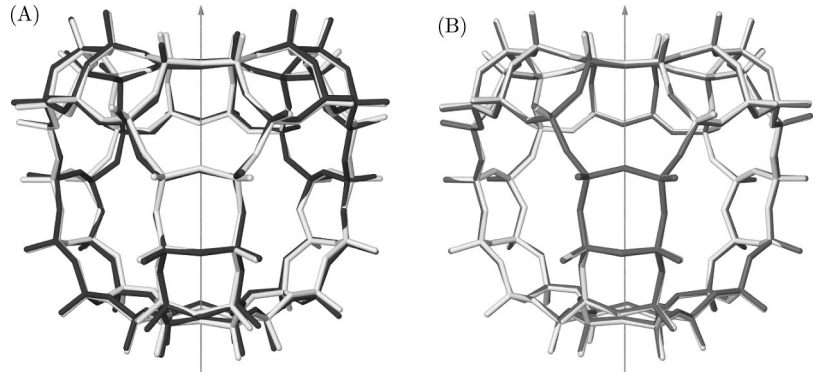

Figure 6. Superimposed geometries of the supercage showing its structural changes upon the inclusion of the LS or HS $[Fe(bpy)_3]^{2+}$ complex (OLYP/$\mathscr{G}$ results): (A) optimized geometry of the supercage in the gas phase (black) and its geometry as found in the optimized LS geometry of $[Fe(bpy)_3]^{2+}$@Y (white); (B) this latter geometry (white) and the geometry of the supercage as found in the optimized HS geometry of $[Fe(bpy)_3]^{2+}$@Y (gray).

by the central position of the iron atom within the supercage which has an ideal T_d symmetry. In passing to the real $[Fe(bpy)_3]^{2+}$@Y system, the lattice contribution to the EFG at the metallic center of $[Fe(bpy)_3]^{2+}$ remains vanishing because of the location of the iron atom at or in the close vicinity of a tetrahedral site of the cubic lattice. This allows the direct comparison of the theoretical results obtained for the ^{57}Fe quadrupole splitting of the encapsulated complex with the experimental ones.

Note that all EFG components and ΔE_Q values given below for $[Fe(bpy)_3]^{2+}$@Y in either spin-state were obtained from calculations carried out with the geometry of the encapsulated complex. This is the case for the results reported for the LS $[Fe(bpy)_3]^{2+}$@Y in Table 2, which also give the results obtained for the isolated LS $[Fe(bpy)_3]^{2+}$ complex. For both LS systems, the magnitudes of the calculated quadrupole splittings are in very good agreement with the experimental estimate of 0.3−0.4 mm s^{-1} determined for the LS complex in various media.[18,3,20−22]

The determination of the EFG components and thereof of ΔE_Q actually exhibits a negligible dependence on the choice of the functional. This could be inferred from the results of calculations performed at the OLYP/$\mathscr{S}_R$ and PBE/$\mathscr{S}_R$ levels (see Supporting Information, Table S1). Table 2 gives the results obtained at the OLYP/$\mathscr{S}_R$ level from the calculations carried out on the OLYP/$\mathscr{G}$, PBE/$\mathscr{G}$, HCTH/$\mathscr{G}$, O3LYP/$\mathscr{G}$, and B3LYP*/$\mathscr{G}$ structures. Its inspection shows that the dependence of the results on the use of the ZORA or ZORA-4 scheme is also neglibible because both schemes lead to values of the EFG components and of ΔE_Q which differ by at most ∼1%. The influence of the methods used being thus vanishingly small, we can draw the following general conclusions.

The calculated EFG tensor exhibits an axial symmetry: $V_{xx} = V_{yy}$ ($\eta = 0$), in agreement with the trigonal symmetry of the investigated systems. The calculations having been performed within C_1 symmetry, this attests to the adequacy of the integration grid that has been used (see section 2) and to the high numerical accuracy thus achieved for the determination of the EFG. The sign of V_{zz}, or equivalently that of ΔE_Q (eq 1), is found to be negative. It has not been established so far and its experimental determination requires that the Mössbauer spectroscopy measurements be done under an applied magnetic field.

Table 2. Calculated Principal Values of the Electric Field Gradient Tensor, $V_{\alpha\alpha}$ ($\alpha = x, y, z$, in a.u.) and Quadrupole Splitting ΔE_Q (mm s^{-1}) at the Iron Center for $[Fe(bpy)_3]^{2+}$ and $[Fe(bpy)_3]^{2+}$@Y in the LS Manifold: Results of SR Calculations Performed at the OLYP/$\mathscr{S}_R$ Level on the Optimized HCTH/$\mathscr{G}$, O3LYP/$\mathscr{G}$, and B3LYP*/$\mathscr{G}$ Structures

		V_{zz}	$V_{xx} = V_{yy}$	ΔE_Q
OLYP/$\mathscr{G}$ geometries				
ZORA	$[Fe(bpy)_3]^{2+}$	−0.280	0.140	−0.397
	$[Fe(bpy)_3]^{2+}$@Y	−0.222	0.111	−0.313
ZORA-4	$[Fe(bpy)_3]^{2+}$	−0.283	0.141	−0.400
	$[Fe(bpy)_3]^{2+}$@Y	−0.224	0.112	−0.317
PBE/$\mathscr{G}$ geometries				
ZORA	$[Fe(bpy)_3]^{2+}$	−0.276	0.138	−0.390
	$[Fe(bpy)_3]^{2+}$@Y	−0.263	0.131	−0.372
ZORA-4	$[Fe(bpy)_3]^{2+}$	−0.278	0.139	−0.393
	$[Fe(bpy)_3]^{2+}$@Y	−0.265	0.132	−0.375
HCTH/$\mathscr{G}$ geometries				
ZORA	$[Fe(bpy)_3]^{2+}$	−0.283	0.141	−0.400
	$[Fe(bpy)_3]^{2+}$@Y	−0.241	0.120	−0.341
ZORA-4	$[Fe(bpy)_3]^{2+}$	−0.285	0.143	−0.403
	$[Fe(bpy)_3]^{2+}$@Y	−0.243	0.122	−0.344
O3LYP/$\mathscr{G}$ geometries				
ZORA	$[Fe(bpy)_3]^{2+}$	−0.275	0.138	−0.390
	$[Fe(bpy)_3]^{2+}$@Y	−0.223	0.111	−0.315
ZORA-4	$[Fe(bpy)_3]^{2+}$	−0.278	0.139	−0.393
	$[Fe(bpy)_3]^{2+}$@Y	−0.225	0.113	−0.318
B3LYP*/$\mathscr{G}$ geometries				
ZORA	$[Fe(bpy)_3]^{2+}$	−0.268	0.134	−0.379
	$[Fe(bpy)_3]^{2+}$@Y	−0.253	0.127	−0.359
ZORA-4	$[Fe(bpy)_3]^{2+}$	−0.270	0.135	−0.382
	$[Fe(bpy)_3]^{2+}$@Y	−0.256	0.128	−0.362

For the isolated LS complex, $\Delta E_Q \approx -0.39 \pm 0.01$ mm s^{-1}. Upon encapsulation, the magnitude of ΔE_Q decreases to an extent which proves to depend on the theoretical level used for the determination of the considered geometry of the LS $[Fe(bpy)_3]^{2+}$@Y system (Table 2). This evidence that the degree of distortion predicted for the encapsulated complex should be considered as varying noticeably with the functional used, although the different geometries predicted for the LS $[Fe(bpy)_3]^{2+}$@Y model system may be considered at first glance as being quite close to one another

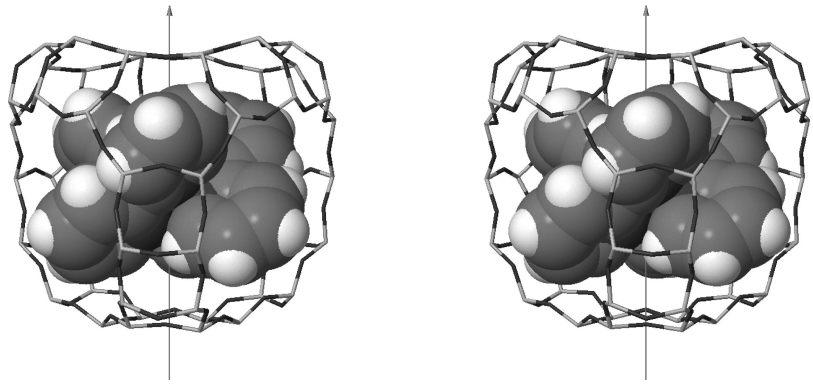

Figure 7. Stereoscopic view of the optimized OLYP/$\mathscr{G}$ geometry of the HS $[Fe(bpy)_3]^{2+}$@Y system.

Table 3. Selected Bond Lengths (Å) and Angles (deg) Characterizing the Geometry of the HS $[Fe(bpy)_3]^{2+}$ Complex: Results of Geometry Optimization Calculations Performed on the Isolated and on the Zeolite-Y Embedded Complex

		Fe−N	Fe−N′	C_2-C_2'	β	γ	τ	θ	θ'
OLYP	$[Fe(bpy)_3]^{2+}$	2.244	2.244	1.499	73.9	6.0	47.1	60.7	60.7
	$[Fe(bpy)_3]^{2+}$@Y	2.174	2.230	1.493	75.4	13.7	51.7	57.7	65.2
HCTH	$[Fe(bpy)_3]$	2.233	2.233	1.495	74.0	6.0	47.1	60.6	60.6
	$[Fe(bpy)_3]$ @Y	2.177	2.222	1.490	75.4	12.3	51.8	58.0	65.0
PBE	$[Fe(bpy)_3]^{2+}$	2.195	2.195	1.502	75.5	5.6	47.1	59.8	59.8
	$[Fe(bpy)_3]^{2+}$@Y	2.160	2.181	1.499	76.5	9.0	51.3	58.3	62.8
O3LYP	$[Fe(bpy)_3]^{2+}$	2.237	2.237	1.498	73.9	5.4	46.9	60.6	60.6
	$[Fe(bpy)_3]^{2+}$@Y	2.178	2.226	1.493	75.2	12.8	51.5	57.8	65.2
B3LYP*	$[Fe(bpy)_3]^{2+}$	2.214	2.214	1.505	75.0	4.3	47.1	59.8	59.8
	$[Fe(bpy)_3]^{2+}$@Y	2.177	2.200	1.501	76.0	8.2	51.0	58.2	63.4

(Table 1). The ratio of the metal−ligand bond lengths Fe−N/Fe−N′ constitutes an immediate and relevant measure of the degree of distortion of the trigonal complex, which furthermore can be readily correlated with the values found for the quadrupole splitting.

This ratio thus takes for the isolated LS complex a value of one (1.000), as imposed by the molecular D_3 symmetry, and the results of the different EFG calculations lead to $\Delta E_Q \approx -0.39$ mm s^{-1} to within $\pm$ 0.01 mm s^{-1}. In passing to the encapsulated LS complex of C_3 symmetry, the Fe−N/Fe−N′ ratio decreases, taking the values of 0.995, 0.993, 0.987, 0.986, and 0.985 for the geometries obtained with the PBE, B3LYP*, HCTH, O3LYP, and OLYP functionals, respectively. The quadrupole splittings determined from these geometries vary monotonically with the Fe−N/Fe−N′ ratio, taking the values of $\Delta E_Q \approx -0.38$, -0.36, -0.34, -0.32, and -0.32 mm s^{-1}, respectively. That is, there is a negative correlation between the Fe−N/Fe−N′ ratio and the value ΔE_Q. Hence, as anticipated above, the quadrupole splitting ΔE_Q increases with the distortion of the complex. Finally, Vankó et al. having established that $|\Delta E_Q| \approx 0.32$ mm s^{-1} for the LS $[Fe(bpy)_3]^{2+}$@Y compound,[20] the observed correlation suggests that the OLYP, O3LYP, and HCTH functionals perform better for the description of the structure of the zeolite-Y embedded LS complex than the PBE and B3LYP* functionals.

3.2. Characterization in the High-Spin State. *3.2.1. Structural Properties.* The optimization calculations performed with the Gaussian package for characterizing $[Fe(bpy)_3]^{2+}$ and $[Fe(bpy)_3]^{2+}$@Y in the ligand-field HS $^5T_2(t_{2g}^4E_g^2)$ state led to their characterization in the HS ^{5}A trigonal component. The other trigonal HS component of ^{5}E symmetry is not available through such calculations. This indeed requires the use of fractional occupation numbers, which actually is not implemented in the current version of the Gaussian package, except as an intermediate step in the self-consistent field convergence strategy. For the two investigated systems, given that the $^5A \leftrightarrow {}^5E$ change of states consists mainly in an electronic rearrangement within the nonbonding metallic levels of octahedral Fe(t_{2g}) parentage, one can assume that the HS components are close in energy and that they exhibit similar geometries, as effectively shown for the isolated complex in a previous study.[6] The characterization thus achieved for the structures and the energetics of $[Fe(bpy)_3]^{2+}$ and $[Fe(bpy)_3]^{2+}$@Y in the ^{5}A state therefore extends to the ^{5}E component of the HS state as well.

For the HS $[Fe(bpy)_3]^{2+}$@Y system, the optimization calculations were performed first with the OLYP functional. This led to an optimized geometry wherein the orientation of the complex within the supercage is identical to the optimal one observed in the most stable structure of LS $[Fe(bpy)_3]^{2+}$@Y (see Figure 7). We therefore did not carry out further calculations for investigating the influence of the choice of the initial geometry on the outcome of the optimization calculations and used the optimized OLYP/$\mathscr{G}$ geometry of HS $[Fe(bpy)_3]^{2+}$@Y as starting point in the subsequent minimizations performed with the other functionals. As for the isolated complex, the calculations performed within C_3 led to final HS geometries of effective D_3 symmetry.

The selected bond lengths and angles reported in Table 3 for the isolated (respectively, encapsulated) complex show that the optimized HS geometries of $[Fe(bpy)_3]^{2+}$ (respectively, $[Fe(bpy)_3]^{2+}$@Y) are consistent with one another. For

the isolated complex, these structural data also compare very well with those previously reported for $[Fe(bpy)_3]^{2+}$ in the HS state.[6] As for $[Fe(bpy)_3]^{2+}$@Y, the optimized HS geometries resemble the OLYP/$\mathcal{G}$ one shown in Figure 7. In both cases, the major structural change undergone by $[Fe(bpy)_3]^{2+}$ upon the LS → HS change of spin-states is the lengthening of the iron−ligand bond, which follows from the promotion of two electrons from the nonbonding metallic levels of Fe(t_{2g}) parentage into the antibonding metallic level of Fe(e_g) parentage. The comparison of Tables 1 and 3 shows that this increase, Δr_{HL}, of the iron−nitrogen distance in $[Fe(bpy)_3]^{2+}$ and in $[Fe(bpy)_3]^{2+}$@Y is on the average between 0.20 and 0.25 Å, depending on the functional. For the isolated complex, the large increase of the metal−ligand bond length is accompagnied by a slight lengthening of the C_2-C_2' bond of ∼0.02 Å and by relatively large variations of the angles β, γ, τ, and $\theta = \theta'$, which reflect the structural changes and spatial rearrangements undergone by the ligands upon the LS → HS conversion, so as to maintain the metal−ligand bonding interactions optimal. For the encapsulated complex, concomitant with the increase of the metal−ligand bonds, there is likewise a ∼0.02 Å increase of the C_2-C_2' bond length and significant changes in the values of the angular parameters β, γ, τ, and θ'; the value of the cone angle θ remaining close to its LS value. The structural changes thus undergone by the ligands can also be seen in Figure 5B. Interestingly, the large expansion experienced by the guest complex upon the LS → HS spin-state conversion hardly affects the structure of the supercage because of the rigidity of this host. This is illustrated in Figure 6B by the nearly perfect match of the OLYP/$\mathcal{G}$ LS and HS geometries of the supercage; the latter being less stable than the former by 312 cm^{-1} only.

Inspection of Table 3 shows that the geometry of the HS $[Fe(bpy)_3]^{2+}$ complex contracts upon encapsulation, as exemplified in Figure 5C by the superposition of the OLYP/$\mathcal{G}$ geometries of the HS complex in the gas phase and in the supercage of zeolite Y. Depending on the considered theoretical level, this shrinkage of the geometry of the HS complex translates into a decrease of the Fe−N and Fe−N′ bond lengths of about 0.04−0.07 and 0.01 Å, respectively, and also into a small decrease of the C_2-C_2' bond length (<0.01 Å). The angular parameters used to describe the arrangement of the ligands in the HS geometry are also noticeably influenced by the encapsulation. The cone angle θ thus decreases by 1.5−3.0°, while the other cone angle, θ', increases by 3.0−4.6°. Concurrently, the bite angle β and the twist angle τ increase by 1.0−1.5° and 3.9−4.7°, respectively. The dihedral angle γ also substantially increases by 6.3−7.7°, except in the case of the results obtained with the PBE and B3LYP* functionals, wherein far smaller increases of 3.5° and 3.9°, respectively, are predicted for γ. As previously observed during the investigation of the structural properties of the LS complex, the use of PBE and B3LYP* functionals leads to the smallest predicted γ values for the isolated and the encapsulated HS complex.

These structural changes experienced by the HS complex to fit at best within the supercage are similar to but more pronounced than those undergone by the LS complex upon encapsulation. This clearly follows from the fact that the molecular volume of $[Fe(bpy)_3]^{2+}$ is larger in the HS state than in the LS state. The more pronounced distortion undergone by the complex in the HS state upon encapsulation can also be inferred from the comparison of Figure 5, parts A and C, which show the superimposed OLYP/$\mathcal{G}$ geometries of the isolated and of the encapsulated complex in the LS and HS states, respectively. On a similar note, the passing from the OLYP/$\mathcal{G}$ geometry of the isolated complex to the one of the encapsulated complex is associated to an energy increase of 3740 cm^{-1} for the complex in the HS state, whereas this energy increase was found to amount to 1391 cm^{-1} only for the complex in the LS state.

Table 4. Calculated Principal Values of the Electric Field Gradient Tensor, $V_{\alpha\alpha}$ ($\alpha = x, y, z$, in au), and Quadrupole Splitting ΔE_Q (mm s^{-1}) at the Iron Center for $[Fe(bpy)_3]^{2+}$ and $[Fe(bpy)_3]^{2+}$@Y in the ^{5}E Component of the HS State: Results of SR Calulations Performed at the OLYP/$\mathcal{S}_R$ Level[a]

		V_{zz}	$V_{xx} = V_{yy}$	ΔE_Q
OLYP/$\mathcal{G}$ geometries				
ZORA	$[Fe(bpy)_3]^{2+}$	0.938	−0.469	1.328
	$[Fe(bpy)_3]^{2+}$@Y	0.989	−0.495	1.400
ZORA-4	$[Fe(bpy)_3]^{2+}$	0.936	−0.468	1.324
	$[Fe(bpy)_3]^{2+}$@Y	0.986	−0.493	1.396
PBE/$\mathcal{G}$ geometries				
ZORA	$[Fe(bpy)_3]^{2+}$	0.938	−0.469	1.327
	$[Fe(bpy)_3]^{2+}$@Y	0.966	−0.483	1.367
ZORA-4	$[Fe(bpy)_3]^{2+}$	0.936	−0.468	1.324
	$[Fe(bpy)_3]^{2+}$@Y	0.963	−0.482	1.363
HCTH/$\mathcal{G}$ geometries				
ZORA	$[Fe(bpy)_3]^{2+}$	0.946	−0.473	1.338
	$[Fe(bpy)_3]^{2+}$@Y	0.991	−0.495	1.402
ZORA-4	$[Fe(bpy)_3]^{2+}$	0.943	−0.472	1.334
	$[Fe(bpy)_3]^{2+}$@Y	0.988	−0.494	1.398
O3LYP/$\mathcal{G}$ geometries				
ZORA	$[Fe(bpy)_3]^{2+}$	0.941	−0.471	1.332
	$[Fe(bpy)_3]^{2+}$@Y	0.991	−0.495	1.402
ZORA-4	$[Fe(bpy)_3]^{2+}$	0.939	−0.470	1.328
	$[Fe(bpy)_3]^{2+}$@Y	0.988	−0.494	1.397
B3LYP*/$\mathcal{G}$ geometries				
ZORA	$[Fe(bpy)_3]^{2+}$			
	$[Fe(bpy)_3]^{2+}$@Y	0.968	−0.484	1.369
ZORA-4	$[Fe(bpy)_3]^{2+}$			
	$[Fe(bpy)_3]^{2+}$@Y	0.965	−0.483	1.366

[a] Note that we were not able to make converge the calculations performed on the B3LYP*/ $\mathcal{G}$ geometry of $[Fe(bpy)_3]^{2+}$.

3.2.2. ^{57}Fe Mössbauer Quadrupole Splitting. The SR calculations performed with the ADF package within C_1 for the determination of the EFG at the iron site of the isolated or the encapsulated HS $[Fe(bpy)_3]^{2+}$ complex converged all to the ^{5}E trigonal component of the HS state. The results of these calculations carried out at the OLYP/$\mathcal{S}_R$ level on the geometries of the free and of the encapsulated HS complex are summarized in Table 4. Note that the choice of the functional proves to have little influence on the results since the EFG calculations similarly performed at the PBE/$\mathcal{S}_R$ level on the PBE/$\mathcal{G}$ and OLYP/$\mathcal{G}$ geometries gave results that differ by 2% at most from those similarly obtained with the OLYP functional.

There is a fairly good consistency among the results given in Table 4. The calculated EFG tensors exhibit an axial symmetry ($V_{xx} = V_{yy}$), in agreement with the trigonal

symmetry of the investigated system. The sign of V_{zz}, hence that of ΔE_Q, is found to be positive and was not experimentally determined so far. Further inspection of Table 4 shows that $\Delta E_Q \approx 1.33$ mm s^{-1} for the isolated complex in the ^{5}E state and that it increases in passing to the $[Fe(bpy)_3]^{2+}$@Y system in the ^{5}E state, as a consequence of the distortion entailed by the encapsulation. As previously noticed for the LS complex, this increase of ΔE_Q upon encapsulation depends on the XC functional used for optimizing the considered HS geometry of the $[Fe(bpy)_3]^{2+}$@Y system. That is, the degree of distortion predicted for the encapsulated complex both in the LS and in the HS state depends on the functional used.

The ratio Fe−N/Fe−N′ gives a measure of the distortion of the trigonal $[Fe(bpy)_3]^{2+}$ complex: the smaller it is, the more distorded the geometry of the complex. It takes the values 0.990, 0.990, 0.980, 0.978, and 0.975 for the HS geometries of $[Fe(bpy)_3]^{2+}$@Y obtained with the PBE, B3LYP*, HCTH, O3LYP, and OLYP, respectively. Meanwhile, for the encapsulated complex in the ^{5}E state the calculated values of the quadrupole splitting are $\Delta E_Q \approx 1.37$ for the PBE and B3LYP* geometries, and $\Delta E_Q \approx 1.40$ for the HCTH, O3LYP, and OLYP geometries. For $[Fe(bpy)_3]^{2+}$@Y in the LS state, we could infer from the comparison of the calculated and experimental values of ΔE_Q that the HCTH, O3LYP, and OLYP probably perform better for the description of the structure of the encapsulated LS complex than the PBE and B3LYP* functionals. Given that the distortions predicted for the encapsulated complex in the HS state follow the same trend as the one observed in the LS state, this conclusion can actually be extended to the description of the geometry of the encapsulated HS complex. That is, the HCTH, O3LYP, and OLYP functionals very likely perform better for the description of the structure of the encapsulated complex in either spin state than the PBE and B3LYP* functionals.

The above results and their discussion are valid for $[Fe(bpy)_3]^{2+}$ and $[Fe(bpy)_3]^{2+}$@Y in the ^{5}E component of the HS state only. For the determination of the EFG tensors of both systems in the ^{5}A state, we were not able to make converge the calculations performed within C_1 to this component of the HS state. For the isolated complex, we nevertheless could do so by carrying out the calculations with the molecular symmetry constrained to the effective D_3 symmetry and the occupations of the Kohn−Sham levels appropriately chosen (see ref 6). These calculations performed on all the available HS geometries of $[Fe(bpy)_3]^{2+}$ at the OLYP/$\mathcal{J}_R$ level gave ^{57}Fe ΔE_Q values of between −2.69 and −2.66 mm s^{-1}, depending on the considered geometry. The quadrupole splitting of the encapsulated complex in the ^{5}A state obviously deviates from this gas-phase value of about −2.7 mm s^{-1}. However, as observed for $[Fe(bpy)_3]^{2+}$ in the LS and in the HS ^{5}E state, it should remain close to this value because the HS geometries of the complex in the gas phase and in the supercage stay close. The $^5E \rightarrow {}^5A$ internal conversion mainly involves an electronic rearrangement within the metallic levels of nonbonding octahedral Fe(t_{2g}) parentage. As pointed out by Lawson Daku et al.,[6] this change of states translates into the transfer of electron density from the xy-plane to along the trigonal z-axis, which explains the change of sign and of magnitude found for ΔE_Q in passing from the ^{5}E to the ^{5}A state.

The Mössbauer parameters of the HS complex have been experimentally determined by Deisenroth et al. from the Mössbauer emission spectroscopy study of [^{57}Co/$Mn(bpy)_3](PF_6)_2$.[3] In this matrix, they measured for the nucleogenic HS $[^{57}Fe(bpy)_3]^{2+}$ complex a quadrupole splitting of $|\Delta E_Q| = 1.17$ mm s^{-1}. The ΔE_Q values calculated for the complex in the ^{5}E state are in fairly good agreement with this value. We can therefore conclude that the ^{5}E state is the lowest-lying component of the HS state of the complex doped into $[Co(bpy)_3](PF_6)_2$. For the isolated complex, note that the two components of the HS state were shown to be nearly degenerate and that its molecular volume was shown to be slightly larger in the ^{5}A state (∼22 Å^3) than in the ^{5}E state (∼20 Å^3).[6] Consequently, on the basis of this molecular volume difference, the fact that the ^{5}E state is found to be the lowest-lying HS component of $[Fe(bpy)_3]^{2+}$ doped into $[Co(bpy)_3](PF_6)_2$ can be ascribed to the chemical pressure experienced by the complex which destabilizes the ^{5}A state with regard to the ^{5}E state. Note that this energy ordering of the trigonal components of the HS state: $E(^5E) \lesssim E(^5A)$, is probably the same for $[Fe(bpy)_3]^{2+}$ in the confining environment provided by the supercage of zeolite Y.

3.3. High-Spin/Low-Spin Energy Difference. *3.3.1. Determination of the Change in the Spin-State Energetics upon Encapsulation and of the Experienced Chemical Pressure.* The large number of atoms (229) of the model system devised for investigating the guest−host interactions in $[Fe(bpy)_3]^{2+}$@Y precludes the use of computationally demanding high-level ab initio methods. In contrast, with a computational cost formally identical to that of the Hartree−Fock method, DFT methods can efficiently be applied to the study of such large systems. However, although they perform quite well for the study of numerous properties of transition metal complexes,[59] they tend to dramatically fail when it comes to the accurate evaluation of the relative energies of the different spin-states of these systems.[6,7,60−76] This failure of the current density-functional approximations manifests itself in the present case by the large spread of the calculated values of the HS−LS electronic energy difference, ΔE^{el}_{HL}, in $[Fe(bpy)_3]^{2+}$ and in $[Fe(bpy)_3]^{2+}$@Y, which are given in Table 5A.

These values were obtained from the results of the optimization calculations performed with the Gaussian package as the energy difference between the LS ^{1}A state and the ^{5}A trigonal component of the HS state, to which the results obtained using Gaussian are restricted. They range from −811 to 10087 cm^{-1} for $[Fe(bpy)_3]^{2+}$ and from 1941 to 12004 cm^{-1} for $[Fe(bpy)_3]^{2+}$@Y. The very various performances thus exhibited by the different XC functionals with regard to the determination of ΔE^{el}_{HL} and, more generally, with regard to the issue of the spin-state energetics in transition metal complexes, have been discussed in details by different authors (see, for instance, refs 6, 61, 64, 65, 68, 70, and 74). A further discussion of this delicate issue is beyond the scope of the present study. We rather focus on

the change $\Delta(\Delta E^{el}_{HL})$ in ΔE^{el}_{HL} upon encapsulation, which is given by

$$\Delta(\Delta E^{el}_{HL}) = \Delta E^{el}_{HL}[Y] - \Delta E^{el}_{HL}[\varnothing] \quad (3)$$

In the above equation, we introduce the notation $X[\varnothing]$ and $X[Y]$ to refer to the values of a quantity X for $[Fe(bpy)_3]^{2+}$ in the gas phase and in the supercage of zeolite Y, respectively. The values found for $\Delta(\Delta E^{el}_{HL})$ are summarized in Table 5B. There is a remarkably good consistency between these values, which are positive and spread over the narrow range of 1917−2934 cm^{-1}. The positive values show that the HS state is destabilized with regard to the LS state upon encapsulation. Their convergence can be related to the fact that the choice of the functional tends to have a weak influence on the difference of two ΔE^{el}_{HL} values (see ref 70). In the present case, it also demonstrates that the different functionals tend to perform equally well for the evaluation of the influence of the guest−host interactions in $[Fe(bpy)_3]^{2+}$@Y on the HS−LS energy difference, although they perform very differently for the calculation of this energy difference.

$\Delta(\Delta E^{el}_{HL})$ can be divided into three contributions: $\Delta E^{dist}_{HL}\{Fe\}$, $\Delta E^{dist}_{HL}\{Y\}$, and ΔE^{int}_{HL}. $\Delta E^{dist}_{HL}\{Fe\}$ is the energy difference

$$\Delta E^{dist}_{HL}\{Fe\} = E^{dist}_{HS}\{Fe\} - E^{dist}_{LS}\{Fe\} \quad (4)$$

where $E^{dist}_{LS}\{Fe\}$ (respectively, $E^{dist}_{HS}\{Fe\}$) is the energy required to bring the isolated complex in the LS (respectively, HS) state from its relaxed geometry to its distorted geometry at the minimum of $[Fe(bpy)_3]^{2+}$@Y in the LS (respectively, HS) state. $\Delta E^{dist}_{HL}\{Y\}$ is for the supercage the counterpart of $\Delta E^{dist}_{HL}\{Fe\}$ for the complex.

$$\Delta E^{dist}_{HL}\{Y\} = E^{dist}_{HS}\{Y\} - E^{dist}_{LS}\{Y\} \quad (5)$$

where $E^{dist}_{LS}\{Y\}$ (respectively, $E^{dist}_{HS}\{Y\}$) is the energy needed to bring the supercage from its relaxed geometry to its geometry after the inclusion of $[Fe(bpy)_3]^{2+}$ in the LS (respectively, HS) state. The contributions $\Delta E^{dist}_{HL}\{Fe\}$ and $\Delta E^{dist}_{HL}\{Y\}$ sum up to a global geometric distortion term, ΔE^{dist}_{HL}.

The last contribution ΔE^{int}_{HL} to $\Delta(\Delta E^{el}_{HL})$ is the change in the guest−host interaction energy upon the LS → HS change of spin-states. It is given by

$$\Delta E^{int}_{HL} = E^{int}_{HS} - E^{int}_{LS} \quad (6)$$

where E^{int}_{LS} (respectively, E^{int}_{HS}) is the interaction energy between the supercage and the guest complex in the LS (respectively, HS) state at the minimum of the whole system. The values found at the different theoretical levels for ΔE^{dist}_{HL} and $\Delta E^{int}_{HL} = \Delta(\Delta E^{el}_{HL}) - \Delta E^{dist}_{HL}$ are summarized in Table 5, along with the values found for $\Delta E^{dist}_{HL}\{Fe\}$ and $\Delta E^{dist}_{HL}\{Y\}$.

Of the two contributions, ΔE^{dist}_{HL} and ΔE^{int}_{HL}, to $\Delta(\Delta E^{el}_{HL})$, ΔE^{dist}_{HL} is the one responsible for the observed dispersion of ∼1000 cm^{-1} in the calculated $\Delta(\Delta E^{el}_{HL})$ values. The values found for ΔE^{int}_{HL} indeed exhibit a remarkably weak to negligible dependence on the theoretical level used and average to $\Delta E^{int}_{HL} \approx 1300$ cm^{-1}. Meanwhile, the values found for ΔE^{dist}_{HL} range from 671 to 1593 cm^{-1} depending on the functional used. Inspection of Table 5 also shows that $\Delta E^{dist}_{HL}\{Fe\}$ is the major contribution to ΔE^{dist}_{HL}, with $\Delta E^{dist}_{HL}\{Y\}$ being 4 to 7 times smaller than $\Delta E^{dist}_{HL}\{Fe\}$. The small positive values found for $\Delta E^{dist}_{HL}\{Y\}$ show that the slight structural changes of the supercage in $[Fe(bpy)_3]^{2+}$@Y entailed by the LS → HS change of spin-states and the concomitant expansion of the $[Fe(bpy)_3]^{2+}$ guest translate only into a weak destabilization of the host.

The geometric changes undergone by $[Fe(bpy)_3]^{2+}$ upon encapsulation are more pronounced in the HS state than in the LS state. The fact that the calculated values of $\Delta E^{dist}_{HL}\{Fe\}$ are positive (i.e., $E^{dist}_{LS}\{Fe\} < E^{dist}_{HS}\{Fe\}$) shows that these changes are also more destabilizing in the HS state than in the LS state. Figure 8 gives the plots of $E^{dist}_{LS}\{Fe\}$ and $E^{dist}_{HS}\{Fe\}$ against the ratios $\xi_{LS} = r_{LS}[Y]/r_{LS}[\varnothing]$ and $\xi_{HS} = r_{HS}[Y]/r_{HS}[\varnothing]$, respectively, where r_Γ designates the average iron−nitrogen bond length in the Γ manifold (Γ = LS, HS).

One notes in Figure 8 that (a) $E^{dist}_\Gamma\{Fe\}$ increases with decreasing ξ_Γ (Γ = LS, HS) and (b), regardless of the considered spin-state, the calculated values of ξ_Γ decrease in the order: PBE > B3LYP* > HCTH > O3LYP > OLYP. This ordering is also the one found for the LS and HS values of the ratio Fe−N/Fe−N′ in $[Fe(bpy)_3]^{2+}$@Y, which gives a measure of the predicted distortion of the geometry of the encapsulated complex: the smaller the Fe−N/Fe−N′ ratio, the more distorted the geometry of $[Fe(bpy)_3]^{2+}$ (see above). Consequently, for a given functional, ξ_Γ is a relevant measure of both the shrinkage and the distortion predicted for the geometry of $[Fe(bpy)_3]^{2+}$ in the Γ state upon encapsulation.

Table 5. Spin-State Energetics: Calculated Values (cm^{-1}) of (A) the HS−LS Electronic Energy Difference ΔE^{el}_{HL} in $[Fe(bpy)_3]^{2+}$ and in $[Fe(bpy)_3]^{2+}$@Y; (B) the Change $\Delta(\Delta E^{el}_{HL})$ in ΔE^{el}_{HL} upon Encapsulation; (C) the Contributions ΔE^{int}_{HL} and ΔE^{dist}_{HL} to $\Delta(\Delta E^{el}_{HL})$; and (D) the Terms $\Delta E^{dist}_{HL}\{Fe\}$ and $\Delta E^{dist}_{HL}\{Y\}$ into which ΔE^{dist}_{HL} Divides

	PBE/$\mathscr{G}$	B3LYP*/$\mathscr{G}$	HCTH/$\mathscr{G}$	O3LYP/$\mathscr{G}$	OLYP/$\mathscr{G}$
		(A) HS−LS electronic energy difference ΔE^{el}_{HL}			
$[Fe(bpy)_3]^{2+}$	+10 087	+3849	+141	−811	+3660
$[Fe(bpy)_3]^{2+}$@Y	+12 004	+5925	+2687	+1941	+6594
		(B) Change in ΔE^{el}_{HL} upon encapsulation			
$\Delta(\Delta E^{el}_{HL})$	+1917	+2076	+2546	+2752	+2934
		(C) $\Delta(\Delta E^{el}_{HL}) = \Delta E^{int}_{HL} + \Delta E^{dist}_{HL}$			
ΔE^{int}_{HL}	+1246	+1267	+1621	+1286	+1331
ΔE^{dist}_{HL}	+671	+809	+925	+1466	+1593
		(D) $\Delta E^{dist}_{HL} = \Delta E^{dist}_{HL}\{Fe\} + \Delta E^{dist}_{HL}\{Y\}$			
$\Delta E^{dist}_{HL}\{Fe\}$	+583	+679	+571	+1181	+1291
$\Delta E^{dist}_{HL}\{Y\}$	+88	+130	+354	+285	+312

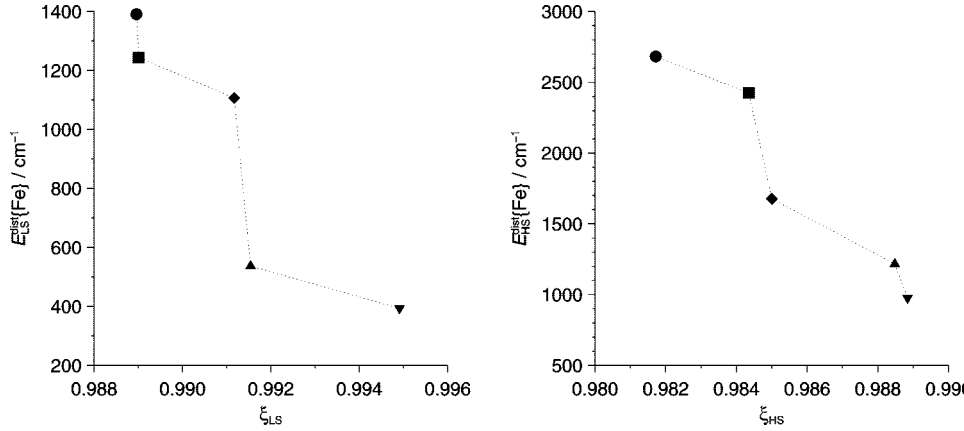

Figure 8. Plots of $E_{LS}^{dist}\{Fe\}$ against ξ_{LS} (left) and of $E_{HS}^{dist}\{Fe\}$ against ξ_{HS} (right) for the different XC functionals used: PBE/$\mathscr{G}$(▼), B3LYP*/$\mathscr{G}$(▲), HCTH/$\mathscr{G}$(♦), O3LYP/$\mathscr{G}$(■), and OLYP/$\mathscr{G}$(●) results (lines serve to highlight the trends among the functionals).

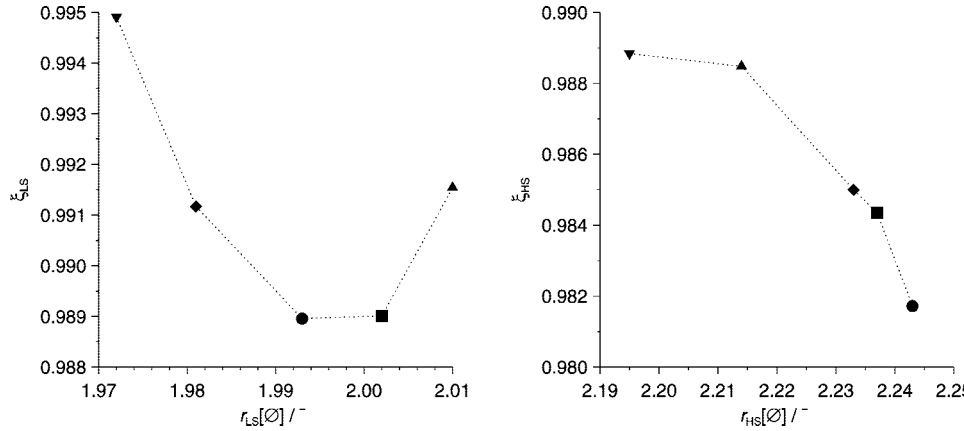

Figure 9. Plots of ξ_{LS} against $r_{LS}[\varnothing]$ (left) and of ξ_{HS} against $r_{HS}[\varnothing]$ (right) for the different XC functionals used: PBE/$\mathscr{G}$(▼), B3LYP*/$\mathscr{G}$(▲), HCTH/$\mathscr{G}$(♦), O3LYP/$\mathscr{G}$(■), and OLYP/$\mathscr{G}$(●) results (lines serve to highlight the trends among the functionals).

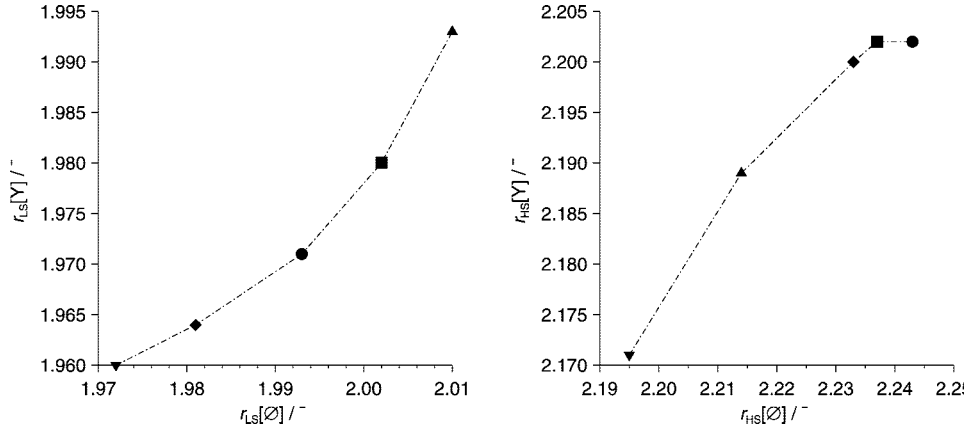

Figure 10. Plots of $r_{LS}[Y]$ against $r_{LS}[\varnothing]$ (left) and of $r_{HS}[Y]$ against $r_{HS}[\varnothing]$ (right) for the different XC functionals used: PBE/$\mathscr{G}$(▼), B3LYP*/$\mathscr{G}$(▼), HCTH/$\mathscr{G}$(♦), O3LYP/$\mathscr{G}$(■) and OLYP/$\mathscr{G}$(●) results (lines serve to highlight the trends among the functionals).

It thus follows that $E_{\Gamma}^{dist}\{Fe\}$ increases with the predicted degree of shrinking and distortion of the Γ geometry of $[Fe(bpy)_3]^{2+}$ as measured by ξ_{Γ} (Γ = LS, HS).

Can the above correlation between the calculated values of $E_{\Gamma}^{dist}\{Fe\}$ and ξ_{Γ} (Γ = LS, HS) be related to a particular tendency among the functionals? As shown in Figure 9, ξ_{HS} turns out to be a decreasing function of $r_{HS}[\varnothing]$. Note also in Figure 10 that $r_{\Gamma}[Y]$ is an increasing function of $r_{\Gamma}[\varnothing]$ (Γ = LS, HS). For the complex in the HS state, we therefore observe the following trend among the functionals: the calculated $E_{HS}^{dist}\{Fe\}$ value is larger, the longer the predicted iron−nitrogen bond in the HS state. However, this trend is not observed for the complex in the LS state since ξ_{LS} does not vary monotonously with $r_{LS}[\varnothing]$ (Figure 9). Consequently, the influence of the choice of the XC functional on the calculated values of $E_{\Gamma}^{dist}\{Fe\}$ and ξ_{Γ} cannot be explained only by the tendency of the functionals to give more or less long metal−nitrogen bonds for $[Fe(bpy)_3]^{2+}$ in either spin state.

Actually, $E_{\Gamma}^{dist}\{Fe\}$ and ξ_{Γ} (Γ = HS, LS) are related not only to the extent of the structural changes which the complex in the Γ state must undergo to fit best into the supercage but also to the ability of the supercage to more or less readily host the complex in this spin state. This follows from the fact that the guest−host interactions in $[Fe(bpy)_3]^{2+}$@Y, at the origin of the structural changes experienced by the supercage and the complex, depend on the match between the void volume of the supercage and the volume of the complex, for which the metal−ligand distance provides an immediate measure. In addition, besides its influence on the description of the complex, the choice of the functional obviously also affects the description of the supercage and that of the guest−host interactions in $[Fe(bpy)_3]^{2+}$@Y. Therefore, the correlated variations in the predicted values of $E_{\Gamma}^{dist}\{Fe\}$ and ξ_{Γ} reflect the subtle interplay between the influence of the functionals on the description of the supercage, hence of its void volume, and their influence on the description of $[Fe(bpy)_3]^{2+}$ in the Γ state, hence of its volume.

We noticed that the correlation between $E_{HS}^{dist}\{Fe\}$ and ξ_{HS} also translates into a correlation between $E_{HS}^{dist}\{Fe\}$ and $r_{HS}[\varnothing]$. Such an observation implies that, in the HS state, the variations introduced by the use of the different functionals in the description of $[Fe(bpy)_3]^{2+}$ prevail over the manner in which these functionals influence the description of the supercage. The most plausible explanation is that the volume ofthe HS complex is so large that, with its encapsulation, the maximum capacity of the supercage regarding the inclusion of a tris(2,2′-bipyridine) complex is reached. This is nicely illustrated by the plot in Figure 10 of the predicted values of $r_{HS}[Y]$ against those of $r_{HS}[\varnothing]$. This tendency curve indeed has a negative curvature and presents at large $r_{HS}[\varnothing]$ values a plateau which suggests for $r_{HS}[Y]$ an upper limit of ∼2.202 Å. Note in passing the contrasting positive curvature of the tendency curve obtained for the LS complex of lesser volume by plotting the calculated values of $r_{LS}[Y]$ against those of $r_{LS}[\varnothing]$. We thus understand that the shrinkage and the distortion undergone by the structure of the HS complex are all the more pronounced ($\xi_{HS}\downarrow$) and destabilizing ($E_{HS}^{dist}\{Fe\}\uparrow$) that, first and foremost, the predicted gas-phase structure is expanded ($r_{HS}[\varnothing]\uparrow$).

The values predicted for $\Delta(\Delta E_{HL}^{el})$ with the various GGA and hybrid approximations to the universal XC functional average to 2445 cm^{-1} and present a standard deviation of 435 cm^{-1}. As this will be emphasized later on in the analysis of the guest−host interactions in $[Fe(bpy)_3]^{2+}$@Y, the physics of the embedding of $[Fe(bpy)_3]^{2+}$ in zeolite Y in either spin-state is quantitatively captured by the approximate functionals. We therefore propose as a fair estimate of $\Delta(\Delta E_{HL}^{el})$

$$\Delta(\Delta E_{HL}^{el}) = 2500 \pm 1000\ cm^{-1} \quad (7)$$

3.3.2. Analysis of the Guest−Host Interactions in $[Fe(bpy)_3]^{2+}$@Y. To get insight into the physics of the involved guest−host interactions, we analyzed them using the bonding energy decomposition scheme implemented in the ADF package.[53,77] This decomposition scheme is similar to the energy decomposition analysis proposed by Morokuma within the Hartree−Fock approximation,[78−80] and closely follows the one introduced within DFT by Ziegler and Rauk using the extended transition state method.[81−83] It has been successfully applied to the analysis of different bonding situations, as recently reviewed by Bickelhaupt and Baerends,[77] and by Frenking and co-workers.[84,85] Before giving our results, we briefly present the physically meaningful contributions to bonding interaction energies that are obtained with this partitioning scheme and refer the reader to the above reviews for detailed discussions of these contributions.

The bond dissociation energy between two fragments A and B, in our case, $[Fe(bpy)_3]^{2+}$ and the supercage, is divided into two major contributions E^{prep} and E^{int}. E^{prep} is the energy necessary to promote the fragments from their equilibrium geometry and electronic ground-state to their geometry and electronic state in the interacting system AB. Note that, for $[Fe(bpy)_3]^{2+}$@Y, we have already discussed the geometric contributions $E_{\Gamma}^{dist}\{Fe\}$ and $E_{\Gamma}^{dist}\{Y\}$ to E^{prep} (Γ = LS, HS). As for the electronic contribution to E^{prep}, we are in principle concerned with its determination only when dealing with $[Fe(bpy)_3]^{2+}$@Y in the HS state. E^{int} is the instantaneous interaction energy between the prepared fragments. It can be broken down into three main components

$$E^{int} = E^{elstat} + E^{Pauli} + E^{orb} \quad (8)$$

E^{elstat} corresponds to the classical electrostatic interaction between the unperturbed charge distributions of the prepared fragments, the overall density being the simple superposition of the fragment densities. E^{Pauli} corresponds to the Pauli repulsion, which is responsible for any steric repulsion between the fragments. It is the energy change that arises upon going from the simple superposition of the fragment densities to the wave function that obeys the Pauli principle through the antisymmetrization and normalization of the product of the fragment wave functions. Last, E^{orb} is the orbital interaction energy, that is, the energy gained by allowing the electron density to fully relax. It potentially includes the contributions from all conceivable stabilizing orbital interactions (electron pair bonding, charge transfer, polarization) and can be further decomposed into the contributions from the irreducible representations of the interacting system. Given that the calculations with ADF cannot be done using the C_3 symmetry of the $[Fe(bpy)_3]^{2+}$@Y model, the partitioning of E^{orb} into the contributions from the e and a representations is not accessible.

The corresponding ADF calculations are single-point calculations performed at the OLYP/$\mathcal{S}$ level on optimized OLYP/$\mathcal{G}$ geometries. The $\mathcal{G} \rightarrow \mathcal{S}$ change of basis sets does not influence the description of the spin-states energetics. Indeed, the HS−LS energy differences obtained with these single-point calculations are $\Delta E_{HL}^{el}[\varnothing]$ = 3049 cm^{-1} and $\Delta E_{HL}^{el}[Y]$ = 5836 cm^{-1}, leading to $\Delta(\Delta E_{HL}^{el})$ = 2787 cm^{-1}, in excellent agreement with the OLYP/$\mathcal{G}$ results of Table 5. Note that the calculations targeted at the characterization of the HS state converged toward its ^5E component.

For $[Fe(bpy)_3]^{2+}$@Y taken in a given geometry, the guest−host interactions are not affected by the electronic rearrangements within the metallic d orbitals. This can be

Table 6. Analysis of the Guest−Host Interactions in $[Fe(bpy)_3]^{2+}$@Y in the LS and HS States: Results of Calculations Performed at the OLYP/$\mathcal{J}$ Level Using the OLYP/$\mathcal{G}$ Optimized LS and HS Geometries (cm^{-1})

	E_Γ^{elstat}	E_Γ^{Pauli}	E_Γ^{orb}	E_Γ^{int}
Γ = LS	−15558	+17442	−12158	−10275
Γ = HS	−15251	+18099	−11874	−9026
	ΔE_{HL}^{elstat}	ΔE_{HL}^{Pauli}	ΔE_{HL}^{orb}	ΔE_{HL}^{int}
	+307	+657	+284	+1249

concluded from the energies of LS ↔ HS vertical transitions in $[Fe(bpy)_3]^{2+}$@Y, which can be calculated by considering either the whole system or the $[Fe(bpy)_3]^{2+}$ subsystem only. Thus, at the OLYP/$\mathcal{G}$ optimized LS geometry of $[Fe(bpy)_3]^{2+}$@Y, the OLYP/$\mathcal{J}$ values found for the energy of the LS → HS Franck−Condon excitation are 18 296 and 17 956 cm^{-1}, when the calculations are performed on the entire system and on the complex, respectively. Similarly, at the HS geometry of $[Fe(bpy)_3]^{2+}$@Y, the calculated energies of the LS ← HS Franck−Condon excitation are 4375 and 4397 cm^{-1}, respectively. The fact that the guest−host interactions at a fixed geometry of $[Fe(bpy)_3]^{2+}$@Y do not depend on the ligand-field state of $[Fe(bpy)_3]^{2+}$ originates from the strongly local character of vertical d−d excitations. Given this insensitivity of the guest−host interactions to the nature of the ligand-field state of the complex, we can identify them as closed-shell interactions between the first coordination sphere provided by the bipyridine ligands and the second coordination sphere defined by the supercage under the polarizing effects of the iron dication.

The fact that such interactions are accurately described by most modern XC functionals is the reason as to why there is a remarkably good consistency between the results obtained with the various functionals for the influence of encapsulation on the structural, energetic ($\Delta(\Delta E_{HL}^{el})$) and Mössbauer spectroscopy properties of $[Fe(bpy)_3]^{2+}$. The guest−host interactions at any given geometry of $[Fe(bpy)_3]^{2+}$@Y can simply be characterized in the LS manifold. We proceeded this way for analyzing the guest−host interactions at the LS as well as at the HS geometry of $[Fe(bpy)_3]^{2+}$@Y. Table 6 summarizes the results. In either spin-state, the attractive components of the interaction energy, E_Γ^{elstat} and E_Γ^{orb}, are smaller in magnitude than the Pauli repulsion E_Γ^{Pauli}, but together they do more than compensate this latter, thus leading to overall stabilizing guest−host interactions $E_\Gamma^{int} < 0$ (Γ = LS, HS). One also notes that E_Γ^{elstat} is larger in magnitude than E_Γ^{orb}: that is, the bonding between the complex and the supercage in the two spin-states is more electrostatic than covalent. Upon the LS → HS change of spin-states, the guest−host interactions become less stabilizing, with a predicted increase of $\Delta E_{HL}^{int} = +1249$ cm^{-1}, which is in very good agreement with the previously determined ΔE_{HL}^{int} values (Table 5).

As a consequence of the expansion of the complex upon the LS → HS transition, the Pauli repulsion increases. This interaction corresponds to four-electron two-orbital destabilizing interactions, which are all the more destabilizing the larger the orbital overlap. The expansion of $[Fe(bpy)_3]^{2+}$ indeed brings the ligands and the supercage closer to each other, thus increasing the overlap between the molecular orbitals (MOs) of the supercage and those of the complex. However, the increase of the Pauli repulsion accounts only for ∼53% of ΔE_{HL}^{int}. The electrostatic and orbital interactions both become also less attractive, and the corresponding energy increases account for ∼25% and ∼22% of ΔE_{HL}^{int}, respectively. The increase of the electrostatic interaction shows that the electronic and nuclear repulsions between the two subsystems increase with respect to the attractive interactions between the electronic charge distribution of one subsystem with the nuclei of the other. In passing from the LS to the HS state, the distortions experienced by the complex and, to a far lesser extent, by the supercage are accompanied by changes in the energies and shapes of their MOs. These changes, combined with the unavailability of the decomposition of the orbital interaction into the contributions from the representations a and e, prevent determination of the reasons as to the observed variation of the orbital interaction.

Noticing the insensivity of the guest−host interactions to the spin-state of $[Fe(bpy)_3]^{2+}$, we substituted the Fe^{2+} ion with the $4d^6$ Ru^{2+} and $3d^{10}$ Zn^{2+} ions to assess the influence of the nature of the transition metal dication on these interactions.[86] Thus, using the OLYP/$\mathcal{G}$ optimized geometry of LS $[Fe(bpy)_3]^{2+}$@Y, the analysis of the guest−host interactions in the Fe^{2+} → Zn^{2+} substituted $[Zn(bpy)_3]^{2+}$@Y system at the OLYP/$\mathcal{J}$ level gives $E_{LS}^{int} = -10\,287$ cm^{-1} with $E_{LS}^{elstat} = -15\,569$ cm^{-1}, $E_{LS}^{Pauli} = 17\,697$ cm^{-1}, and $E_{LS}^{orb} = -12\,415$ cm^{-1}. For the Fe^{2+} → Ru^{2+} substituted LS $[Ru(bpy)_3]^{2+}$@Y system, we similarly obtain $E_{LS}^{int} = -10\,282$ cm^{-1} with $E_{LS}^{elstat} = -15\,613$ cm^{-1}, $E_{LS}^{Pauli} = 17\,853$ cm^{-1}, and $E_{LS}^{orb} = -12\,523$ cm^{-1}. For either substituted $[M(bpy)_3]^{2+}$@Y system (M = Fe, Zn), the value of the bonding energy between the $[M(bpy)_3]^{2+}$ complex and the supercage and those of its three components perfectly match those obtained from the analysis of the guest−host interactions in the original LS $[Fe(bpy)_3]^{2+}$@Y system (Table 6). This shows that, for a given geometry of a transition metal system $[M(bpy)_3]^{2+}$@Y, the interactions between the $[M(bpy)_3]^{2+}$ complex and the supercage depend neither on the spin state of the transition metal dication M^{2+} nor on its nature.

Finally, the whole destabilization $\Delta(\Delta E_{HL}^{el})$ of the HS state with regard to the LS state upon encapsulation can be viewed as resulting from the need to keep the decrease ΔE_{HL}^{int} of the stabilizing guest−host interactions minimal, at the expense ΔE_{HL}^{dist} of increased distortions of the two moieties of $[Fe(bpy)_3]^{2+}$@Y upon the LS → HS transition. The distortions undergone by the complex give the dominant contribution to ΔE_{HL}^{dist} (Table 5). In this respect, let us point out the fact that, in both spin states, but especially in the HS state, the encapsulation of $[Fe(bpy)_3]^{2+}$ is accompanied by large deformations along the γ angular coordinate (Tables 1 and 3), which actually are associated with floppy modes.[6] Hence, while the sizable increase of the molecular volume of $[Fe(bpy)_3]^{2+}$ entailed by the LS → HS change of spin-states is at the origin of the influence of the encapsulation on the spin-state energetics, the ability of the complex to thus readily

distort along such floppy modes helps moderate this destabilizing influence.

3.3.3. HS−LS Energy Difference and the Low-Temperarure Dynamics of the HS → LS Relaxation in [Fe(bpy)$_3$]$^{2+}$@Y. Pierloot and Vancoillie recently demonstrated the feasability of high-level wave function-based calculations with the CASPT2 method and extensive basis sets for the determination of the HS−LS electronic energy difference in the isolated $[Fe(bpy)_3]^{2+}$ complex, as well as in other iron(II) complexes of similar size.[69,75] Their studies, based on single-point CASPT2 calculations on DFT-optimized LS and HS geometries, led, for the gas-phase value of ΔE^{el}_{HL} in $[Fe(bpy)_3]^{2+}$, to the currently most accurate ab initio estimate of[69,75]

$$\Delta E^{el}_{HL}[\varnothing] = 3700 \pm 1000\ cm^{-1} \quad (9)$$

Using eq 3 and the independent estimates of $\Delta(\Delta E^{el}_{HL})$ and $\Delta E^{el}_{HL}[\varnothing]$, we obtain for the value of ΔE^{el}_{HL} in the zeolite-Y encapsulated complex a best ab initio estimate of

$$\Delta E^{el}_{HL}[Y] = 6200 \pm 1500\ cm^{-1} \quad (10)$$

The comparison of the calculated $\Delta E^{el}_{HL}[Y]$ values given in Table 5A with the above estimate shows that there is a remarkably good agreement for the results obtained with the OLYP and B3LYP* functionals. This follows from the fact (i) that these two functionals perform well for the determination of $\Delta E^{el}_{HL}[\varnothing]$ in $[Fe(bpy)_3]^{2+}$, as also previously reported,[6,67,69,75] and (ii) that the different functionals give $\Delta(\Delta E^{el}_{HL})$ values that are very consistent with one another.

The low-temperature dynamics of the HS → LS relaxation in the $[Fe(bpy)_3]^{2+}$@Y compound are determined by the HS−LS zero-point energy difference $\Delta E^{\circ}_{HL}[Y]$. This one divides into an electronic contribution, $\Delta E^{el}_{HL}[Y]$, whose predicted value is given above, and a vibrational contribution, $\Delta E^{vib}_{HL}[Y]$. Within our approach to the theoretical study of $[Fe(bpy)_3]^{2+}$@Y, the determination of this latter contribution rigorously requires that a vibrational analysis be performed for the whole model system in the LS and in the HS state. However, given that the supercage is hardly affected by the structural changes undergone by the complex upon the LS → HS change of spin states, this computationally demanding task is avoided by considering the supercage as being rigid and, afterward, by taking $\Delta E^{vib}_{HL}[Y]$ as being caused by the shifts in the vibrational frequencies centered on the encapsulated complex upon the LS → HS change of spin-states. Because of the weakening of the metal−ligand bond in passing from the LS to the HS state, $\Delta E^{vib}_{HL}[Y]$ is negative. Furthermore, the structure of the encapsulated complex in either spin-state remaining close to that of the isolated complex in the same spin manifold, it is reasonable to assume that $\Delta E^{vib}_{HL}[Y]$ is comparable in magnitude to $\Delta E^{vib}_{HL}[\varnothing]$, the vibrational contribution to the HS−LS zero-point energy difference of the isolated complex. A value of $\Delta E^{vib}_{HL}[\varnothing] = -875\ cm^{-1}$ was previously reported.[6] Actually, $|\Delta E^{vib}_{HL}[Y]|$ is probably slightly smaller than $|\Delta E^{vib}_{HL}[\varnothing]|$ because the shrinkage of the structure of the complex entailed by the encapsulation is larger in the HS state than in the LS state. We therefore propose for $\Delta E^{vib}_{HL}[Y]$ a model value of $\Delta E^{vib}_{HL}[Y] = -800\ cm^{-1}$. This gives for ΔE°_{HL} in $[Fe(bpy)_3]^{2+}$@Y a best estimate of

$$\Delta E^{\circ}_{HL}[Y] = 5400 \pm 1500\ cm^{-1} \quad (11)$$

On the basis of the HS → LS relaxation theory,[7] we could deduce from this $\Delta E^{\circ}_{HL}[Y]$ value that the lifetime $\tau_{HS}[Y]$ of the metastable HS state in $[Fe(bpy)_3]^{2+}$@Y is below 10 ns.

4. Concluding Remarks

The application of DFT to the study of the guest−host interactions in $[Fe(bpy)_3]^{2+}$@Y within a supramolecular approach allowed us to gain major new insights into the nature of these interactions and into their influence on the structural, energetic and Mössbauer spectroscopy properties of the complex in the LS and HS states. The main results and conclusions are summarized below.

(1) Guest−Host Interactions. The guest−host interactions at a given geometry of $[Fe(bpy)_3]^{2+}$@Y do not depend on the spin state of the complex. We ascribed this to the fact that the vertical d−d excitations involved in a change of ligand-field states have a strongly local character. By substituting Fe^{2+} with Ru^{2+} and Zn^{2+}, we also showed that varying the nature of the transition metal dication does not affect the guest−host interactions. These interactions are closed-shell interactions between the first coordination sphere provided by the 2,2′-bipyridine ligands and the second coordination sphere defined by the supercage under the polarizing effects of the transition metal dication. They are accurately described by most modern functionals, and in this respect, the different GGA (PBE, HCTH, OLYP) and hybrid (B3LYP*, O3LYP) functionals used very consistently predict an increase in the interaction energy of $\Delta E^{int}_{HL} \approx 1300\ cm^{-1}$ upon the LS → HS transition.

The analysis of the guest−host interaction energy at the LS and HS geometries of[5] $[Fe(bpy)_3]^{2+}$@Y showed that these interactions are stabilizing and that the resulting bonding is more electrostatic than covalent. In passing from the LS to the HS state, there is an increase of the Pauli or steric repulsion, which is expected from the expansion of the complex upon this change of spin states. The Pauli repulsion however contributes only to about half of ΔE^{int}_{HL}. The electrostatic and orbital interactions also become less stabilizing and their increases contribute almost equally to the remaining part of ΔE^{int}_{HL}.

(2) Structural Properties. Our results show that, upon encapsulation, the structure of the complex shrinks and distorts to an extent which increases in passing from the LS to the HS state. The supercage also undergoes geometric changes so as to host the $[Fe(bpy)_3]^{2+}$ complex, but its structure turns out to hardly evolve upon the LS → HS change of spin-states and the concomitant expansion of its guest. A relevant measure of the structural changes experienced by the complex proves to be the ratio $\xi_\Gamma = r_\Gamma[Y]/r_\Gamma[\varnothing]$, where r_Γ is the average iron−nitrogen bond length in the Γ state (Γ = LS, HS). The smaller the ratio, the more

pronounced the structural changes. Because of the approximate nature of the functionals used, the calculated geometries exhibit small but noticeable differences, and varying degrees of distortion and shrinkage are observed. In either spin state, these last ones are found to increase with the functionals in the order PBE < B3LYP* < HCTH < O3LYP < OLYP. Still, the shrinkage and distortion experienced by the complex in either spin state are not such that this translates into a sizable variation of the quadrupole splitting ΔE_Q at the iron center.

(3) ^{57}Fe Quadrupole Splitting. The values of ΔE_Q in LS and HS $[Fe(bpy)_3]^{2+}$ and $[Fe(bpy)_3]^{2+}$@Y were obtained from the results of relativistic EFG calculations performed at the OLYP level within the ZORA and ZORA-4 approximations on the different optimized geometries. The two relativistic approximations give very similar results and the remarkable consistency observed among the results of EFG calculations performed with the OLYP and PBE functionals suggests that the choice of the XC functional has a negligible influence on the results.[87] For $[Fe(bpy)_3]^{2+}$@Y, ΔE_Q could accurately be calculated by considering the $[Fe(bpy)_3]^{2+}$ subsystem only. The contribution of the outer coordination sphere to the EFG at the iron center was indeed shown to be vanishing. The main trend observed in both spin-states is that, as a consequence of the shrinking and distortion undergone by the complex, the quadrupole splitting increases in passing from the isolated complex of D_3 symmetry to the encapsulated complex of C_3 symmetry: $\Delta E_Q[\varnothing] < \Delta E_Q[Y]$.

The increase of ΔE_Q upon encapsulation depends on the predicted degree of shrinking and distortion experienced by the complex. In the LS state, $\Delta E_Q[\varnothing] \cong -0.38$ mm s^{-1} and $\Delta E_Q[Y]$ varies between -0.37 and -0.32 mm s^{-1} depending on the functional used in the optimization calculations. In the HS state, we have $\Delta E_Q[\varnothing] \cong 1.33$ mm s^{-1} and $\Delta E_Q[\varnothing] \cong -2.68$ mm s^{-1} for $[Fe(bpy)_3]^{2+}$ in the ^5E and ^5A HS states, respectively. For HS $[Fe(bpy)_3]^{2+}$@Y, the EFG could be calculated for the ^5E state only, and this gives $\Delta E_Q[Y]$ values of between 1.37 and 1.40 mm s^{-1} depending on the considered HS geometry. For the complex in the ^5A state, we expect similar increases of the quadrupole splitting upon encapsulation. Deisenroth et al. determined for the HS complex in the $[Co(bpy)_3](PF_6)_2$ matrix $|\Delta E_Q| = 1.17$ mm s^{-1}.[3] The good agreement between this value and those determined for the complex in the ^5E state shows that this state is the lowest-lying component of the HS state for $[Fe(bpy)_3]^{2+}$ doped into $[Co(bpy)_3](PF_6)_2$. The molecular volume of $[Fe(bpy)_3]^{2+}$ is slightly larger in the ^5A state than in the ^5E state and the two HS states are nearly degenerate in the isolated complex.[6] Consequently, the energy ordering observed for the two components of the HS state in the $[Co(bpy)_3](PF_6)_2$ matrix can be ascribed to the chemical pressure exerted by the environment, which destabilizes the ^5A state with respect to the ^5E state. Given the confining environment provided by the supercage of zeolite Y, we expect this same energy ordering in $[Fe(bpy)_3]^{2+}$@Y.

(4) Spin-State Energetics. The XC functionals used perform very differently for the determination of the HS−LS energy difference ΔE^{el}_{HL} in both $[Fe(bpy)_3]^{2+}$ and $[Fe(bpy)_3]^{2+}$@Y. However, thanks to their converging performances for the accurate description of the guest−host interactions in $[Fe(bpy)_3]^{2+}$@Y, they perform very similarly for predicting the change of this energy difference upon encapsulation: $\Delta(\Delta E^{el}_{HL}) = +2500 \pm 1000$ cm^{-1}.

Of the two components ΔE^{int}_{HL} and ΔE^{dist}_{HL} of $\Delta(\Delta E^{el}_{HL})$, the latter is the one responsible for the uncertainty in the determination of $\Delta(\Delta E^{el}_{HL})$. While $\Delta E^{int}_{HL} \approx 1300$ cm^{-1} at all levels, the calculated values of the geometric contribution ΔE^{dist}_{HL} noticeably depend on the functionals used (Table 5). $\Delta E^{dist}_{HL} = E^{dist}_{HS} - E^{dist}_{LS}$, where E^{dist}_{Γ} is the energy needed to bring the Γ complex and the supercage from their gas-phase geometries to their geometries in Γ $[Fe(bpy)_3]^{2+}$@Y (Γ = LS, HS). The calculated E^{dist}_{Γ} values increase with the degree of shrinkage and distortion predicted for the complex in a given spin state. Their dispersion reflects the varying errors made with the different functionals in describing both subsytems at and in the vicinity of the minima of their potential energy surfaces. The propagation of this dispersion to the calculated ΔE^{dist}_{HL} values shows that the errors made in determining E^{dist}_{LS} and E^{dist}_{HS} with a given functional tend to only partly compensate when it comes to evaluate ΔE^{dist}_{HL}. This implies that improving the accuracy in the determination of $\Delta(\Delta E^{el}_{HL})$ requires the use of functionals which accurately describe the geometries of transition metal complexes in different spin-states. Note that the $\Delta(\Delta E^{el}_{HL})$ values obtained with the very various functionals used actually average to 2445 cm^{-1} with a standard deviation of $\sigma = 435$ cm^{-1}. Consequently, improving the accuracy of the description of the geometries of $[Fe(bpy)_3]^{2+}$ in both spin states should not lead to a significant change in the $\Delta(\Delta E^{el}_{HL})$ best estimate of 2500 cm^{-1}, but rather mainly help reduce the uncertainty of ± 1000 cm^{-1} (i.e., $\sim 2\sigma$) put on this value.

Finally, from our calculated $\Delta(\Delta E^{el}_{HL})$ value and the CASPT2 estimate of ΔE^{el}_{HL} in the isolated complex,[69,75] $\Delta E^{el}_{HL}[\varnothing] = 3700 \pm 1000$ cm^{-1}, we could obtain for ΔE^{el}_{HL} in $[Fe(bpy)_3]^{2+}$@Y a best ab initio estimate of $\Delta E^{el}_{HL}[Y] = 6200 \pm 1500$ cm^{-1}. Our supramolecular approach to the study of the guest−host interactions in $[Fe(bpy)_3]^{2+}$@Y and their influence on the physicochemical properties of $[Fe(bpy)_3]^{2+}$ allowed us to quantitatively capture the whole picture. The conclusions thus drawn regarding the influence of the confining environment provided by the supercage on the relative energies of the ligand-field states of $[Fe(bpy)_3]^{2+}$ readily extend to other $[M(bpy)_3]^{2+}$@Y systems. This immediately follows from the insensi-

tivity of the guest−host interactions, at a given geometry of $[M(bpy)_3]^{2+}$@Y, to the nature of the transition metal cation. So, upon the encagement of a d^n $[M(bpy)_3]^{2+}$ complex, a ligand-field state originating from a $t_{2g}^{n-p-1}e_g^{p+1}$ configuration will be destabilized with regard to a ligand-field state originating from the $t_{2g}^{n-p}e_g^{p}$ ($p \leq n-1$). Indeed, the equilibrium geometry of the complex is more expanded in the former state than in the latter. However, given that the equilibrium geometries of the complex in these states depend on the nature of the transition metal, the variations of the relative energies of the ligand-field states can only be determined through dedicated studies. Our supramolecular approach is thus being applied to the study of $[Co(bpy)_3]^{2+}$@Y to determine how the guest−host interactions turn the intermediate-field $[Co(bpy)_3]^{2+}$ complex with usually a HS ground-state into a spin-crossover system.

This approach can be applied to the study of the physicochemical properties of zeolite-Y encapsulated complexes other than tris(2,2′-bipyridine) complexes. For instance, it would help rationalize the observation made by Maruszewski et al. that the encapsulation entails an increase in energy of the excited d−d quencher state in $[Ru(bpy)_3]^{2+}$ but also in other Ru(II) polypyridine complexes of similar size.[90] But, more generally, it can be used to address the prediction of the influence of the environments provided by different hosting cavities on the physicochemical properties of a given complex. In this respect, zeolites provide cavities of very various sizes and shapes.[91,92] Metal−organic frameworks (MOFs) are also appealing porous materials,[93−96] Alkordi et al. having recently reported the encagement of metalloporphyrins into a zeolite-like MOF.[97] Hence, there is a wide applicability of the supramolecular approach used for investigating $[Fe(bpy)_3]^{2+}$@Y, which makes it quite promising for exploring and tailoring the properties of inclusion compounds of transition metal complexes.

Acknowledgment. This work has benefited from the financial supports of the Swiss National Science Foundation and the MAGMANet NoE of the European Union (contract NMP3-CT-2005-515767-2). We acknowledge supercomputer time at the Centro Svizzero di Calcolo Scientifico (CSCS) in the framework of the CSCS project entitled "Photophysics and Photochemistry of Transition Metal Compounds: Theoretical Approaches". We also warmly thank Claudio Redaelli and Maria Grazia Giuffreda of the CSCS for valuable technical support and Bob Hanson for his valuable support in the use of the Jmol program.

Supporting Information Available: Influence of the starting geometry on the outcome of the geometry optimization of $[Fe(bpy)_3]^{2+}$@Y, influence of the choice of the functional on the calculation of the quadrupole splitting, LS and HS geometries of $[Fe(bpy)_3]^{2+}$@Y calculated at the OLYP/$\mathcal{G}$ level and scripts which allow their visualization using the Jmol program. This material is available free of charge via the Internet at http://pubs.acs.org.

References

(1) Hauser, A. *Top. Curr. Chem.* **2004**, *234*, 155–198.

(2) Hauser, A. *Chem. Phys. Lett.* **1990**, *173*, 507–512.

(3) Deisenroth, S.; Hauser, A.; Spiering, H.; Gütlich, P. *Hyperfine Interact.* **1994**, *93*, 1573–1577.

(4) Schenker, S.; Hauser, A.; Wang, W.; Chan, I. Y. *Chem. Phys. Lett.* **1998**, *297*, 281–286.

(5) Hauser, A.; Amstutz, N.; Delahaye, S.; Sadki, A.; Schenker, S.; Sieber, R.; Zerara, M. *Struct. Bonding (Berlin)* **2004**, *106*, 81–96.

(6) Lawson Daku, L. M.; Vargas, A.; Hauser, A.; Fouqueau, A.; Casida, M. E. *ChemPhysChem* **2005**, *6*, 1393–1410.

(7) Hauser, A.; Enachescu, C.; Lawson Daku, M.; Vargas, A.; Amstutz, N. *Coord. Chem. Rev.* **2006**, *250*, 1642–1652.

(8) Gawelda, W.; Pham, V.-T.; Benfatto, M.; Zaushitsyn, Y.; Kaiser, M.; Grolimund, D.; Johnson, S. L.; Abela, R.; Hauser, A.; Bressler, C.; Chergui, M. *Phys. Rev. Lett.* **2007**, *98*, 057401.

(9) Nishikiori, S.; Yoshikawa, H.; Sano, Y.; Iwamoto, T. *Acc. Chem. Res.* **2005**, *38*, 227–234.

(10) Sugi, M.; Matsumoto, Y.; Kimura, N.; Komatsubara, T.; Aoki, H.; Terashima, T.; Uji, S. *Phys. Rev. Lett.* **2008**, *101*, 056401.

(11) Espallargas, G. M.; Brammer, L.; Allan, D. R.; Pulham, C. R.; Robertson, N.; Warren, J. E. *J. Am. Chem. Soc.* **2008**, *130*, 9058–9071.

(12) Sampathkumaran, E. V.; Dhar, S. K.; Malik, S. K. *J. Phys. C: Solid State Phys.* **1987**, *20*, L53–L56.

(13) Lawson Daku, L. M.; Hagemann, H. *Phys. Rev. B* **2007**, *76*, 014118.

(14) Gol'tsov, Y. G. *Theor. Exp. Chem.* **1999**, *35*, 183–197.

(15) Payra, P.; Dutta, P. K. In *Handbook of Zeolite Science and Technology*; Auerbach, S. M., Carrado, K. A., Dutta, P. K., Eds.; Marcel Dekker Publishing: New York, 2003, pp 1−19.

(16) DeWilde, W.; Peeters, G.; Lunsford, J. H. *J. Phys. Chem.* **1980**, *84*, 2306–2310.

(17) Herron, N. *Inorg. Chem.* **1986**, *25*, 4714–4717.

(18) Quayle, W. H.; Peeters, G.; De Roy, G. L.; Vansant, E. F.; Lunsford, J. H. *Inorg. Chem.* **1982**, *21*, 2226–2231.

(19) Umemura, Y.; Minai, Y.; Tominaga, T. *J. Chem. Soc., Chem. Commun.* **1993**, 1822–1823.

(20) Vankó, G.; Homonnay, Z.; Nagy, S.; Vértes, A.; Pál-Borbély, G.; Beyer, H. K. *Chem. Commun.* **1996**, 785–786.

(21) Umemura, Y.; Minai, Y.; Tominaga, T. *J. Phys. Chem. B* **1999**, *103*, 647–652.

(22) Vijayalakshmi, R.; Kulshreshtha, S. K. *Microporous Mesoporous Mater.* **2008**, *111*, 449–454.

(23) Gütlich, P.; Hauser, A.; Spiering, H. *Angew. Chem., Int. Ed. Engl.* **1994**, *33*, 2024–2054.

(24) Zhang, Y.; Oldfield, E. *J. Phys. Chem. A* **2003**, *107*, 4147–4150.

(25) Gütlich, P.; Goodwin, H. A. *Top. Curr. Chem.* **2004**, *233*, 1–47.

(26) Paulsen, H.; Schünemann, V.; Trautwein, A. X.; Winkler, H. *Coord. Chem. Rev.* **2005**, *249*, 255–272.

(27) Remacle, F.; Grandjean, F.; Long, G. J. *Inorg. Chem.* **2008**, *47*, 4005–4014.

(28) Umemura et al.[19,21] predicted that the Mössbauer spectroscopic features of $[Fe(bpy)_3]^{2+}$@Y are $\delta = 0.5$ mm s^{-1} and $\Delta E_Q = 1.4-1.5$ mm s^{-1}. Recently, Vijayalakshmi and Kulshreshtha[22] also reported for the encapsulated complex, $\delta = 0.37$ mm s^{-1} and $\Delta E_Q = 0.81$ mm s^{-1}. These values of the quadrupole splitting are significantly larger than that of $\Delta E_Q \approx 0.3$ mm s^{-1} determined for $[Fe(bpy)_3]^{2+}$@Y by Quayle et al.[18] and by Vankó et al.[20] Hence, according to these results, one would draw the conclusion that the complex becomes strongly distorted in the zeolite Y. However, Vankó et al. demonstrated that such Mössbauer features cannot be assigned to $[Fe(bpy)_3]^{2+}$@Y but rather to uncomplexed iron cations located in the small cavities of the zeolite framework.[20] To this end, they blocked these cavities with La^{3+} ions before proceeding to the bottle-in-a-ship synthesis of $[Fe(bpy)_3]^{2+}$@Y. By proceeding so, they obtained $[Fe(bpy)_3]^{2+}$ as the unique included iron species, as attested for by the Mössbauer spectrum of the final compound which consists of a single quadrupole doublet with a narrow linewidth of 0.25 mm s^{-1} and with $\delta = 0.32$ mm s^{-1} and with $\Delta E_Q = 0.32$ mm s^{-1}.

(29) Hohenberg, P.; Kohn, W. *Phys. Rev.* **1964**, *136*, B864–B871.

(30) Kohn, W.; Sham, L. J. *Phys. Rev.* **1965**, *140*, A1133–A1138.

(31) Parr, R. G.; Yang, W. *Density-Functional Theory of Atoms and Molecules*; Oxford University Press: New York, 1989.

(32) Dreizler, R. M.; Gross, E. K. U. *Density Functional Theory, An Approach to the Quantum Many-Body Problem*; Springer-Verlag: New York, 1990.

(33) Koch, W.; Holthausen, M. C. *A Chemist's Guide to Density Functional Theory*; Wiley-VCH: New York, 2000.

(34) Homonnay, Z.; Vankó, G.; Vértes, A.; Nath, A.; Spiering, H.; Gütlich, P. *Hyperfine Interact.* **1998**, *113*, 331–339.

(35) Vankó, G.; Homonnay, Z.; Nagy, S.; Vértes, A.; Spiering, H.; Gütlich, P. *J. Chem. Phys.* **1998**, *108*, 8472–8478.

(36) Vankó, G.; Nagy, S.; Homonnay, Z.; Vértes, A. *Hyperfine Interact.* **2000**, *126*, 163–167.

(37) Deisenroth, S.; Spiering, H.; Nagy, D. L.; Gütlich, P. *Hyperfine Interact.* **1998**, *113*, 351–355.

(38) Frisch, M. J.; Trucks, G. W.; Schlegel, H. B.; Scuseria, G. E.; Robb, M. A.; Cheeseman, J. R.; Montgomery, J. A., Jr.; Vreven, T.; Kudin, K. N.; Burant, J. C.; Millam, J. M.; Iyengar, S. S.; Tomasi, J.; Barone, V.; Mennucci, B.; Cossi, M.; Scalmani, G.; Rega, N.; Petersson, G. A.; Nakatsuji, H.; Hada, M.; Ehara, M.; Toyota, K.; Fukuda, R.; Hasegawa, J.; Ishida, M.; Nakajima, T.; Honda, Y.; Kitao, O.; Nakai, H.; Klene, M.; Li, X.; Knox, J. E.; Hratchian, H. P.; Cross, J. B.; Bakken, V.; Adamo, C.; Jaramillo, J.; Gomperts, R.; Stratmann, R. E.; Yazyev, O.; Austin, A. J.; Cammi, R.; Pomelli, C.; Ochterski, J. W.; Ayala, P. Y.; Morokuma, K.; Voth, G. A.; Salvador, P.; Dannenberg, J. J.; Zakrzewski, V. G.; Dapprich, S.; Daniels, A. D.; Strain, M. C.; Farkas, O.; Malick, D. K.; Rabuck, A. D.; Raghavachari, K.; Foresman, J. B.; Ortiz, J. V.; Cui, Q.; Baboul, A. G.; Clifford, S.; Cioslowski, J.; Stefanov, B. B.; Liu, G.; Liashenko, A.; Piskorz, P.; Komaromi, I.; Martin, R. L.; Fox, D. J.; Keith, T.; Al-Laham, M. A.; Peng, C. Y.; Nanayakkara, A.; Challacombe, M.; Gill, P. M. W.; Johnson, B.; Chen, W.; Wong, M. W.; Gonzalez, C.; Pople, J. A. *Gaussian 03*, revision B.03/D.01; Gaussian, Inc.: Pittsburgh, PA, 2003.

(39) Lee, C.; Yang, W.; Parr, R. G. *Phys. Rev. B* **1988**, *37*, 785–789.

(40) Handy, N. C.; Cohen, A. J. *Mol. Phys.* **2001**, *99*, 403–412.

(41) Reiher, M.; Salomon, O.; Hess, B. A. *Theor. Chem. Acc.* **2001**, *107*, 48–55.

(42) Salomon, O.; Reiher, M.; Hess, B. A. *J. Chem. Phys.* **2002**, *117*, 4729–4737.

(43) Reiher, M. *Inorg. Chem.* **2002**, *41*, 6928–6935.

(44) Boese, A. D.; Handy, N. C. *J. Chem. Phys.* **2001**, *114*, 5497–5503.

(45) Cohen, A. J.; Handy, N. C. *Mol. Phys.* **2001**, *99*, 607–615.

(46) Perdew, J. P.; Burke, K.; Ernzerhof, M. *Phys. Rev. Lett.* **1996**, *77*, 3865–3868.

(47) Perdew, J. P.; Burke, K.; Ernzerhof, M. *Phys. Rev. Lett.* **1997**, *78*, 1396.

(48) Hehre, W. J.; Ditchfield, R.; Pople, J. A. *J. Chem. Phys.* **1972**, *56*, 2257–2261.

(49) Hariharan, P. C.; Pople, J. A. *Theor. Chim. Acta* **1973**, *28*, 213–222.

(50) Stevens, W. J.; Basch, H.; Krauss, M. *J. Chem. Phys.* **1984**, *81*, 6026–6033.

(51) Stevens, W. J.; Krauss, M.; Basch, H.; Jasien, P. G. *Can. J. Chem.* **1992**, *70*, 612–630.

(52) *Amsterdam Density Functional Program*, release ADF2004.01; Theoretical Chemistry, Vrije Universiteit: Amsterdam, The Netherlands, 2004; http://www.scm.com (accessed Nov 2, 2008).

(53) te Velde, G.; Bickelhaupt, F. M.; Baerends, E. J.; Fonseca Guerra, C.; van Gisbergen, S. J. A.; Snijders, J. G.; Ziegler, T. *J. Comput. Chem.* **2001**, *22*, 931–967.

(54) van Lenthe, E.; Baerends, E. J. *J. Chem. Phys.* **2000**, *122*, 8279–8292.

(55) Jmol: An open-source Java viewer for chemical structures in 3D. http://www.jmol.org (accessed Nov 2, 2008).

(56) McMahon, B.; Hanson, R. M. *J. Appl. Crystallogr.* **2008**, *41*, 811–814.

(57) Dick, S. *Z. Kristallogr.—New Cryst. Struct.* **1998**, *213*, 356.

(58) Schwerdtfeger, P.; Söhnel, T.; Pernpointner, M.; Laerdahl, J. K.; Wagner, F. E. *J. Chem. Phys.* **2001**, *115*, 5913–5924.

(59) *Principles and Applications of Density Functional Theory in Inorganic Chemistry I, II*; Kaltsoyannis, N., McGrady, J. E., Eds.; Springer-Verlag: Berlin, Germany, 2004.

(60) Paulsen, H.; Duelund, L.; Winkler, H.; Toftlund, H.; Trautwein, A. X. *Inorg. Chem.* **2001**, *40*, 2201–2204.

(61) Ghosh, A.; Taylor, P. R. *Curr. Opin. Chem. Biol.* **2003**, *7*, 113–124.

(62) Paulsen, H.; Trautwein, A. X. *Top. Curr. Chem.* **2004**, *235*, 197–219.

(63) Deeth, R. J.; Fey, N. *J. Comput. Chem.* **2004**, *25*, 1840–1848.

(64) Fouqueau, A.; Mer, S.; Casida, M. E.; Lawson Daku, L. M.; Hauser, A.; Mineva, T. *J. Chem. Phys.* **2004**, *120*, 9473–9486.

(65) Fouqueau, A.; Casida, M. E.; Lawson Daku, L. M.; Hauser, A.; Neese, F. *J. Chem. Phys.* **2005**, *122*, 044110.

(66) Smith, D. M. A.; Dupuis, M.; Straatsma, T. P. *Mol. Phys.* **2005**, *103*, 273–278.

(67) Ganzenmüller, G.; Berkaïne, N.; Fouqueau, A.; Casida, M. E. *J. Chem. Phys.* **2005**, *122*, 234321.

(68) Vargas, A.; Zerara, M.; Krausz, E.; Hauser, A.; Lawson Daku, L. M. *J. Chem. Theory Comput.* **2006**, *2*, 1342–1359.

(69) Pierloot, K.; Vancoillie, S. *J. Chem. Phys.* **2006**, *125*, 124303.

(70) Zein, S.; Borshch, S. A.; Fleurat-Lessard, P.; Casida, M. E.; Chermette, H. *J. Chem. Phys.* **2007**, *126*, 014105.

(71) Krivokapic, I.; Zerara, M.; Lawson Daku, M.; Vargas, A.; Enachescu, C.; Ambrus, C.; Tregenna-Piggott, P.; Amstutz, N.; Krausz, E.; Hauser, A. *Coord. Chem. Rev.* **2007**, *251*, 364–378.

(72) Conradie, J.; Ghosh, A. *J. Chem. Theory Comput.* **2007**, *3*, 689–702.

(73) Guillon, T.; Salmon, L.; Molnár, G.; Zein, S.; Borshch, S.; Bousseksou, A. *J. Phys. Chem. A* **2007**, *111*, 8223–8228.

(74) Scherlis, D. A.; Cococcioni, M.; Sit, P.; Marzari, N. *J. Phys. Chem. B* **2007**, *111*, 7384–7391.

(75) Pierloot, K.; Vancoillie, S. *J. Chem. Phys.* **2008**, *128*, 034104.

(76) Marti, K. H.; Ondík, I. M.; Moritz, G.; Reiher, M. *J. Chem. Phys.* **2008**, *128*, 014104.

(77) Bickelhaupt, F. M.; Baerends, E. J. *Rev. Comput. Chem.* **2000**, *15*, 1–86.

(78) Morokuma, K. *J. Chem. Phys.* **1971**, *55*, 1236–1244.

(79) Kitaura, K.; Morokuma, K. *Int. J. Quantum Chem.* **1976**, *10*, 325–340.

(80) Morokuma, K. *Acc. Chem. Res.* **1977**, *10*, 294–300.

(81) Ziegler, T.; Rauk, A. *Theoret. Chim. Acta* **1978**, *46*, 1–10.

(82) Ziegler, T.; Rauk, A. *Inorg. Chem.* **1979**, *18*, 1558–1565.

(83) Ziegler, T.; Rauk, A. *Inorg. Chem.* **1979**, *18*, 1755–1759.

(84) Frenking, G.; Fröhlich, N. *Chem. Rev.* **2000**, *100*, 717–774.

(85) Frenking, G.; Wichmann, K.; Fröhlich, N.; Loschen, C.; Lein, M.; Frunzke, J.; Rayón, V. M. *Coord. Chem. Rev.* **2003**, *238*−*239*, 55–82.

(86) The Zn and Ru atoms were described by the $\mathcal{J}$ basis set. For Ru, the core electrons were frozen up to the 3d level.

(87) The largest source of uncertainty in the determination of ΔE_Q most likely comes from the value of the quadrupole moment of the ^{57}Fe $I = 3/2$ excited state. We use the value of $Q = 0.14$ barn determined by Schwerdtfeger et al.,[58] while Pyykkö[88] recommends the value of $Q = 0.16$ barn found by Dufek et al.[89] The 14% difference between these two values provides an estimate of the relative error made in our evaluation of ΔE_Q.

(88) Pyykkö, P. *Mol. Phys.* **2008**, *106* (16−18), 1965–1974, 10.1080/00268970802018367.

(89) Dufek, P.; Blaha, P.; Schwarz, K. *Phys. Rev. Lett.* **1995**, *75*, 3545–3548.

(90) Maruszewski, K.; Strommen, D. P.; Kincaid, J. R. *J. Am. Chem. Soc.* **1993**, *115*, 8345–8350.

(91) Database of Zeolite Structures. http://www.iza-structure.org/databases (accessed Nov 1, 2008).

(92) Meier, W. M.; Olsen, D. H.; Baerlocher, C. *Atlas of Zeolite Structure Types*; Elsevier: London, 1996.

(93) Seidel, S. R.; Stang, P. J. *Acc. Chem. Res.* **2002**, *35*, 972–983.

(94) Fujita, M.; Tominaga, M.; Hori, A.; Therrien, B. *Acc. Chem. Res.* **2005**, *38*, 369–378.

(95) Tranchemontagne, D. J.; Ni, Z.; O'Keeffe, M.; Yaghi, O. M. *Angew. Chem., Int. Ed.* **2008**, *47*, 5136–5147.

(96) Sakai, N.; Matile, S. *Angew. Chem., Int. Ed.* **2008**, *47* (50), 9603–9607, 10.1002/anie.200803300.

(97) Alkordi, M. H.; Liu, Y.; Larsen, R. W.; Eubank, J. F.; Eddaoudi, M. *J. Am. Chem. Soc.* **2008**, *130*, 12639–12641.

CT800284G

JCTC Journal of Chemical Theory and Computation

Gradient Projection Method for Constraint Optimization and Relaxed Energy Paths on Conical Intersection Spaces and Potential Energy Surfaces

Bernhard Dick*

Institut für Physikalische and Theoretische Chemie, Universität Regensburg, D 93040 Regensburg, Germany

Received July 29, 2008

Abstract: A gradient projection algorithm is presented that permits the application of several constraints during geometry optimization on electronic potential energy surfaces (PES) or conical intersection (CI) seams. The algorithm generalizes the idea recently published in this journal (Sicilia et al. *J. Chem. Theory Comput.* **2008**, *4*, 257) for the optimization of conical intersection geometries. Singular value decomposition is used to transform all constraints, including those related to maintaining the CI, to a new set of constraints with orthogonal gradients. The constraints need not be satisfied at the initial geometry but will be upon convergence. A procedure is presented that determines relaxed energy paths (REP) connecting two reference structures on a potential energy surface, or the conical intersection space, without the need to assign an internal coordinate as the reaction coordinate. Examples are presented of optimizations of minimum energy structures and REPs in the CI space and REPs on a single electronic PES.

1. Introduction

During the last two decades it has been increasingly recognized that conical intersections (CIs) play a decisive role in many photochemical reactions.[1] This has also led to much interest in calculating the geometries of critical points within the conical intersection subspace. The algorithms developed so far can be roughly grouped into three families: Techniques that minimize a Lagrangian including the constraints to maintain the degeneracy of the crossing states,[2−8] gradient projection techniques,[9−14] and a method using a penalty function.[15] Recently, a comparison of these three techniques has been performed employing a semiempirical Hamiltonian.[16] This study found that the Lagrange-Newton technique needed the smallest number of iterations to converge to the minimum energy point of the conical intersection. The gradient projection technique needed usually more iterations but converged to the same result, whereas the penalty function method frequently converged to a slightly different geometry and energy. Based on the convergence performance, the Lagrange-Newton method should be the first choice. However, as discussed in refs 16 and 17, Newton−Raphson programs usually employed in quantum mechanical programs cannot be easily adapted to this technique, whereas the modifications required by the projection technique are straightforward. Also, the Hessian of the Langrangian function has negative eigenvalues for each constraint. Hence the popular Broyden-Fletcher-Goldfarb-Shanno (BFGS) update formula[18] for positive definite Hessian matrices cannot be used.

Recently, Sicilia et al. published a modified version[17] of the gradient projection technique that showed greatly improved convergence properties compared to the original technique of Bearpark et al.[9] (which was the one used in the comparative study mentioned above).[16] This modified method was also used in combination with a projection technique[19] that imposes a geometry constraint by using only that part of the search direction which is perpendicular to the gradient of the constraint. As a consequence the constraint will be fixed at the initial value. In this way points on a relaxed energy path (REP) within the conical intersection space were calculated. Apparently the method by Sicilia et al.[17] treats the constraints associated with maintaining the degeneracy between two electronic states differently from

* Corresponding author e-mail: Bernhard.Dick@chemie.uni-regensburg.de.

10.1021/ct8003029 CCC: $40.75 © 2009 American Chemical Society
Published on Web 12/08/2008

an additional geometrical constraint. Care has to be taken to avoid cancelation errors that can arise when the gradient vector of the constraint is not orthogonal to the branching space.[19]

Here we present a generalization of the principle idea of ref 17 with the following properties:

1) All constraints, including those pertaining to the conical intersection, are treated in the same fashion. The algorithm can also be used for constrained optimization on a single electronic state, or for a triple degeneracy.

2) Several constraints on structural parameters (bond lengths, bond angles, or dihedral angles) or other functions of geometry (e.g., moments of inertia) can be specified at the same time.

3) A constraint can be any linear or nonlinear function of geometrical parameters for which the gradient can be calculated. For example, the projection of the geometry onto the difference vector between two reference structures can be fixed. This will lead to the REP between these two structures without the need to identify a prominent internal coordinate as the reaction coordinate.

4) The algorithm avoids problems associated with the fact that the projected Hessian does not have full rank.

5) The constraints need not be satisfied by the initial geometry but will be met upon convergence.

2. Outline of the Constrained Optimization Method

We begin with a brief review of the recent algorithm of Sicilia et al.[17] The aim is to minimize the average energy of two electronic states

$$F = \frac{1}{2}(E_1 + E_2) \tag{1}$$

subject to the two constraints

$$C^{(1)} = (E_1 - E_2) = 0 \tag{2}$$

$$C^{(2)} = H_{12} = 0 \tag{3}$$

where H_{12} is the interstate coupling matrix element. Both energies and the interstate coupling matrix element are functions of a set of N geometrical variables $\mathbf{r} = \{x_1, x_2, \cdots, x_N\}$. The original gradient projection method of Bearpark et al.[9] makes steps along the direction of a modified gradient

$$\mathbf{g}_M = \mathbf{P}\mathbf{g}_0 + \frac{2(E_1 - E_2)}{|\mathbf{g}^{(1)}|}\mathbf{g}^{(1)} \tag{4}$$

In this expression, $\mathbf{g}_0$ is the gradient of F with respect to $\mathbf{r}$, $\mathbf{g}^{(j)}$ is the gradient of the constraint $C^{(j)}$, and $\mathbf{P}$ is a projection operator that projects the component of $\mathbf{g}_0$ perpendicular to the plane spanned by $\mathbf{g}^{(1)}$ and $\mathbf{g}^{(2)}$.

The recent improvement of this technique makes use of the Hessian matrix $\mathbf{H}$ of the problem. The algorithm switches between two modes, depending on the size of the energy difference. If this is larger than a given threshold, the gradient of eq 4 is used to calculate the step $\mathbf{d}$ according to

$$\mathbf{d} = -\mathbf{H}^{-1}\mathbf{g}_M \tag{5}$$

When the energy difference is below the threshold, the modified Hessian

$$\mathbf{H}_M = \mathbf{PHP} + (1 - \mathbf{P})\mathbf{A}(1 - \mathbf{P}) \tag{6}$$

is used, where $\mathbf{A}$ is a diagonal matrix with large diagonal elements. The procedure remedies the fact that the projected Hessian $\mathbf{PHP}$ has rank $N - 2$ and can hence not be inverted. The step is given by

$$\mathbf{d} = -\mathbf{H}_M^{-1}(\mathbf{P}\mathbf{g}_0) + \frac{E_1 - E_2}{|\mathbf{g}^{(1)}|^2}\mathbf{g}^{(1)} \tag{7}$$

In summary: above the threshold, the gradient of the energy difference is added to the projected gradient of the function F to be optimized, and the full Hessian is used. Below the threshold, the projected and rank-corrected Hessian is used, and a term proportional to the gradient of the energy difference is added to the step. Only $E_1 - E_2$ and $\mathbf{g}^{(1)}$ are used in eqs 4 and 7, i.e., the step or gradient are not modified for nonvanishing H_{12} or $\mathbf{g}^{(2)}$.

When a further constraint is added to these equations, care must be taken to ensure that application of the constraint leaves the projected gradient of the optimized function $\mathbf{P}\mathbf{g}_0$ orthogonal to the gradient of the energy difference, $\mathbf{g}^{(1)}$. This is important to ensure that upon minimization of the gradient $\mathbf{g}_M$ not only the sum of both terms goes to zero but also each term separately.[19] When the various gradient vectors $\mathbf{g}^{(k)}$ are not orthogonal, their corresponding projection operators

$$\mathbf{P}^{(k)} = 1 - \frac{\mathbf{g}^{(k)}\mathbf{g}^{(k)T}}{|\mathbf{g}^{(k)}|^2} = 1 - \mathbf{e}^{(k)}\mathbf{e}^{(k)T} \tag{8}$$

do not commute. (The superscript T indicates the transposed vector or matrix, and $\mathbf{e}$ indicates a unit vector.) It was concluded in ref 19 that the direction of the gradient of the additional constraint must be projected from $\mathbf{g}_0$, $\mathbf{g}^{(1)}$, and $\mathbf{g}^{(2)}$ prior to forming the projected gradient $\mathbf{P}\boldsymbol{g}_0$ of eq 4. Apparently the result will depend on the order in which projections are applied when several constraints are imposed and the corresponding gradients are not orthogonal.

Our generalization of the algorithm, which will be described next, avoids this problem. Our method is applicable to a generalized form of eq 1 for the definition of the optimized function, e.g.

$$F = \frac{1}{m}\sum_{j=1}^{m} E_j \tag{9}$$

With $m = 1$ a single electronic state is optimized, whereas $m = 2$ or $m = 3$ correspond to a double or triple degeneracy. This involves $(m - 1)$ constraints for the energy differences and $m(m - 1)/2$ constraints for the coupling matrix elements between all of these states. In addition to these, further constraints can be applied, e.g. on internal coordinates (bond lengths, bond angles, dihedral angles) or more generalized coordinates as discussed in the next section. We define a matrix $\mathbf{G}$ whose columns are given by the gradient vectors of all constraints that should be satisfied

$$\mathbf{G} = \{\mathbf{g}^{(1)}, \mathbf{g}^{(2)}, \cdots, \mathbf{g}^{(L)}\} \tag{10}$$

$$G_{jk} = \frac{\partial}{\partial x_j} C^{(k)} \tag{11}$$

The first two are those given in eq 2; the other can be constrained internal coordinates or other functions of the coordinates of the molecule. The dimension of this matrix is $N \times L$, where N is the number of geometrical variables, and L is the number of constraints. We assume that the number of constraints is smaller than the number of variables, i.e. $L < N$. Next this matrix is decomposed by singular value decomposition (SVD) according to

$$\mathbf{G} = \mathbf{U}\mathbf{S}\mathbf{V}^T \tag{12}$$

This decomposition is always possible, and efficient numerical algorithms exist. The matrices on the RHS of eq 12 have the following properties: Matrix **S** is a diagonal $L \times L$ matrix with positive elements. In the following we assume that they are arranged in descending order. Matrix **U** is a $N \times L$ matrix whose columns are normalized and orthogonal to each other. Finally, matrix **V** is an orthogonal $L \times L$ matrix, i.e.

$$\mathbf{U}^T\mathbf{U} = \mathbf{V}^T\mathbf{V} = \mathbf{V}\mathbf{V}^T = 1 \tag{13}$$

The column vectors of **U** thus form an orthonormal basis for the set of gradient vectors $\mathbf{g}^{(k)}$. The number of diagonal elements for which the ratio S_m/S_1 is above a certain threshold can be considered as the effective rank of **G**, and all basis vectors $\mathbf{u}^{(k)}$ for which this ratio is smaller than the threshold are neglected.[20] For this (potentially reduced) set of vectors the matrix **S** can be inverted, and eq 12 can be rewritten as

$$\mathbf{U} = \mathbf{G}\mathbf{V}\mathbf{S}^{-1} \tag{14}$$

Next we define linear combinations of the original constraints as

$$B^{(m)} = \sum_{j=1}^{L} C^{(j)} V_{jm} \tag{15}$$

Their gradients are given by

$$\frac{\partial}{\partial x_k} B^{(m)} = \sum_{j=1}^{L} \frac{\partial}{\partial x_k} C^{(j)} V_{jm} = \sum_{j=1}^{L} G_{kj} V_{jm} = S_m U_{km} \tag{16}$$

Thus the column vector $\mathbf{u}^{(m)}$ gives the direction of the gradient of $B^{(m)}$, and S_m is its length. In summary, the set of nonorthogonal gradient unit vectors $\mathbf{e}^{(j)} = \mathbf{g}^{(j)}/|\mathbf{g}^{(j)}|$, gradient lengths $|\mathbf{g}^{(j)}|$, and constraints $C^{(j)}$ has been transformed to an orthogonal set $\{\mathbf{u}^{(m)}, S_m, B^{(m)}\}$ from which linear dependencies have been removed.

The set of vectors $\mathbf{u}^{(m)}$ is now split into two: Set 1 contains those vectors for which $B^{(m)}/S_m$ is below a given threshold, and set 2 contains the remaining vectors. Also, two projection operators are defined

$$\mathbf{P} = 1 - \mathbf{U}\mathbf{U}^T \tag{17}$$

$$\mathbf{P}^{(1)} = 1 - \mathbf{U}^{(1)}\mathbf{U}^{(1)T} \tag{18}$$

Thus **P** projects onto the orthogonal complement of the subspace of all constraints, whereas $\mathbf{P}^{(1)}$ projects out only the components of set 1. In analogy to the method of ref 17, the gradient of the optimized function is now modified by first projecting out all contributions of the constraints and then adding contributions for those constraints that are above threshold

$$\mathbf{g}_S = \mathbf{P}\mathbf{g}_0 + 2\sum_{j}^{set2} B^{(j)}\mathbf{u}^{(j)} \tag{19}$$

It should be noted that the additional contribution to the gradient would also arise if the square of the constrained $(B^{(j)})^2$ should be minimized. Except for the first iteration, the unprojected Hessian **H** is updated at this point by the BFGS formula.[17,18] The next step taken by the algorithm is calculated from a modified Hessian without the contribution of those constraints which are below threshold

$$\mathbf{H}_S = \mathbf{P}^{(1)}\mathbf{H}\mathbf{P}^{(1)} \tag{20}$$

Note that no term was added like in eq 6 which makes the projected Hessian again full rank. This is not needed since instead of inverting the matrix the equation system

$$\mathbf{H}_S\mathbf{d}_S = -\mathbf{g}_S \tag{21}$$

is solved by a linear least-squares algorithm. This algorithm finds the shortest vector $\mathbf{d}_S$ that minimizes the sum of squares $|\mathbf{H}_S\mathbf{d}_S + \mathbf{g}_S|^2$. Finally, the step for the next iteration is calculated by adding the contributions of the constraints in set 1 as

$$\mathbf{d} = \mathbf{d}_S - \sum_{j}^{set1} \frac{B^{(j)}}{S_j}\mathbf{u}^{(j)} \tag{22}$$

3. Relaxed Energy Paths

Relaxed energy paths (REP) connecting two critical points are frequently calculated with the technique of a relaxed scan. For this purpose, an internal coordinate of the system is identified that changes monotonously and by a considerable amount along the path between two reference structures. The REP is then obtained by a sequence of constrained optimizations for a set of fixed values of this internal coordinate.

The gradient projection method outlined above is easily employed for this purpose. Since the constrained variable need not have the intended value at the beginning, each point of the REP can be started from the previously optimized point. This can be done for a single electronic potential energy surface or for the intersection space of two states.

Such a scan of one internal coordinate combined with optimization of all other coordinates requires that the projection of the REP onto the internal coordinate varies monotonously along the REP. This is not always the case, and an example will be presented in the Discussion section. Sometimes a reaction involves the collective change of several internal coordinates none of which makes a dominant contribution to the REP. Hence the possibility of finding a more general approach was considered. In particular we are interested in a strategy that connects two given points in configuration space by a REP.

An ideal algorithm would automatically identify a geometrical constraint, given by a single parameter α, such that the optimized structure for $\alpha = 0$ corresponds to the initial structure $\mathbf{r}_1$ of the REP. Optimizing the structure at $\alpha = 1$ should lead to the final structure $\mathbf{r}_2$ of the REP. Here two alternatives are presented that appear suitable for this purpose.

The first fixes the projection of the structure onto the distance vector $\Delta\mathbf{r} = \mathbf{r}_2 - \mathbf{r}_1$ between the initial and the final point of the REP. The constraint to be minimized is then

$$C = \frac{(\mathbf{r} - \mathbf{r}_1)\Delta\mathbf{r}}{|\Delta\mathbf{r}|^2} - \alpha \tag{23}$$

This constraint involves the coordinates of the system in absolute space. As will be shown in the application section, this formula was successful in several cases but requires that rotation and translation of the whole system is suppressed. This can be simply achieved by additional constraints but can altogether be avoided by using a constraint that makes use only of internal coordinates of the system. Our second proposal for a constraint is of this kind.

$$C = \frac{1}{N_b}\sum_{\{ij\}} \frac{d_{ij} - d_{ij}^{(1)}}{d_{ij}^{(2)} - d_{ij}^{(1)}} - \beta \tag{24}$$

In this expression, $d_{ij}^{(k)}$ is the distance between atoms i and j in structure k. The summation is performed over all bonds with an absolute change $|d_{ij}^{(2)} - d_{ij}^{(1)}|$ above a threshold, which is usually set as a certain fraction of the largest change. N_b is the number of these bonds. This formula is especially useful in cases where the main contribution of the reaction coordinate shifts from one internal coordinate to another one along the relaxed scan. Equation 24 can easily be extended to include other internal coordinates like bond angles or dihedral angles.

4. Computational Details

The algorithm was coded into a FORTRAN program that acts as an interface to the quantum chemical program GAMESS[21] optimized for the Windows operation system.[22] It generates the appropriate input files, starts GAMESS, and extracts the required energies and energy gradients from the GAMESS output files. The constraints and their gradients are calculated in the external program. Singular value decomposition is performed by the routine DGESDD from the LaPack library,[23] the linear least-squares problem of eq 20 is solved by the routine DGELSD from the same library.

The program always operates on the mass- and symmetry-weighted unique Cartesian coordinates of the system. When the norm of the calculated geometry step was larger than a given value d_{max}, the step was rescaled accordingly. Iteration was stopped when the norm of the gradient vector and the step were both below a certain threshold, which was set to 0.003 for all calculations in this work. The threshold on the condition number of the gradient matrix was set such that the vectors $\mathbf{u}^{(m)}$ with $S_m/S_1 < 10^{-6}$ were neglected. The threshold for including a vector in set 1 was $B^{(m)}/S_m < 5 \times 10^{-3}$. With this setting the constraints were satisfied to within $10^{-6}-10^{-8}$ units, and energies changed by less than 10^{-6} Hartree during the last few steps.

5. Results and Discussion

5.1. Convergence. We have chosen the CI between S_0 and S_1 of fulvene as an example in order to permit comparison with the work of Bearpark et al.[19] The first

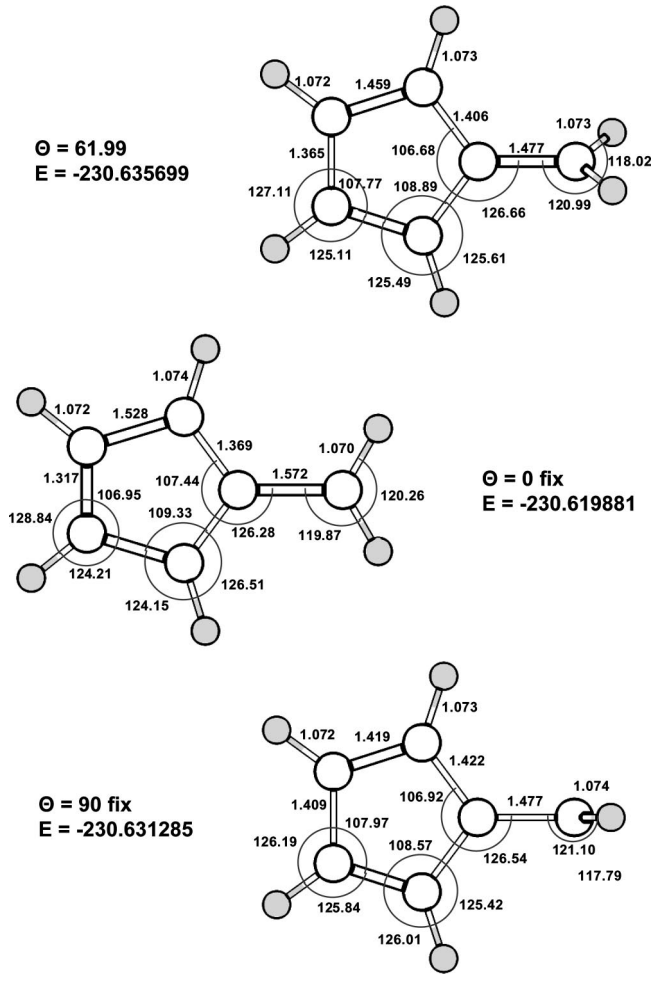

Figure 1. Optimized bond lengths (Angstrom units) and angles (in degrees) for the minimum energy point of the S_0/S_1 conical intersection in fulvene without geometrical constraint (top), with fixed dihedral angle $\theta = 0°$ (middle), and with fixed dihedral angle $\theta = 90°$ (bottom).

geometry of this CI reported by Dreyer and Klessinger[35] has the exocyclic CH_2 group oriented perpendicular to the ring (CI_{Perp}). Bearpark et al.[32] arrived at the same conclusion but showed in addition that the intersection exists for all twist angles up to the planar structure. Later it was recognized that a C_2-symmetric structure with a twist angle of $\approx 63°$ (CI_{63}) is ≈ 2.3 kcal mol^{-1} lower in energy.[34] The relaxed energy path connecting the planar and the perpendicular structures on the seam has been presented in ref 19, and it is this calculation that we take as the benchmark here. It should, however, be mentioned that recently a C_1-symmetric structure has been presented[33] that is still 0.003 kcal mol^{-1} lower in energy than CI_{63}.

In our calculation, the same CASSCF(6,6)/6−31G* type of wave function and C_2 symmetry as in ref 19 was employed. Optimizations were performed for the minimum energy point of the CI without constraint and with the dihedral angle between the five-membered ring and the CH_2 group constrained to $\theta = 0°$ and $\theta = 90°$, respectively. All optimizations were started from the geometry of the electronic ground-state optimized at the RHF/6−31G* level.

The optimized bond lengths and angles of the three structures are shown in Figure 1. They compare well with

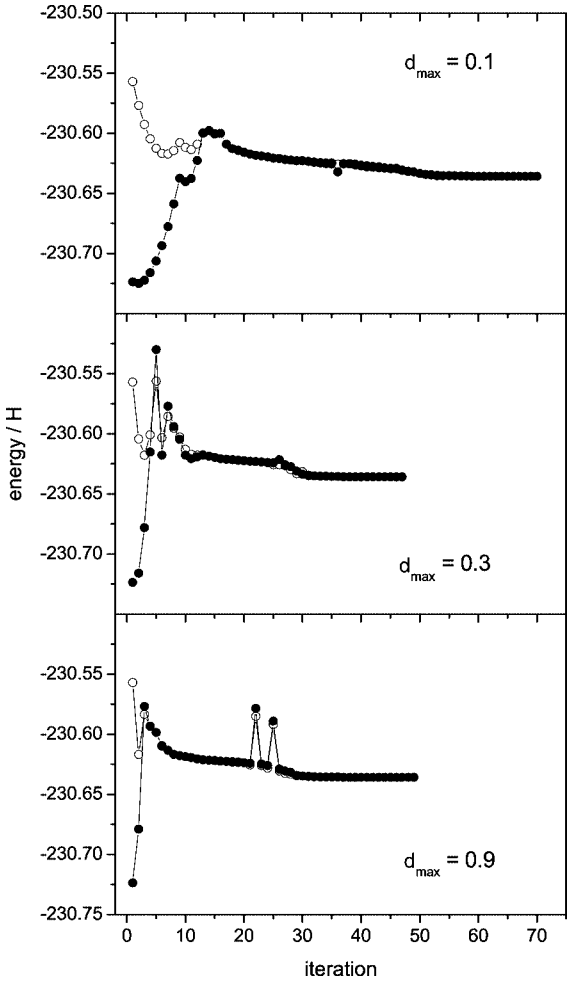

Figure 2. Convergence behavior of the algorithm for optimization of the S_0/S_1 conical intersection in fulvene without geometrical constraint. Three different values for the norm of the largest step d_{max} were used. Full and open symbols represent ground-state and excited-state energies, respectively.

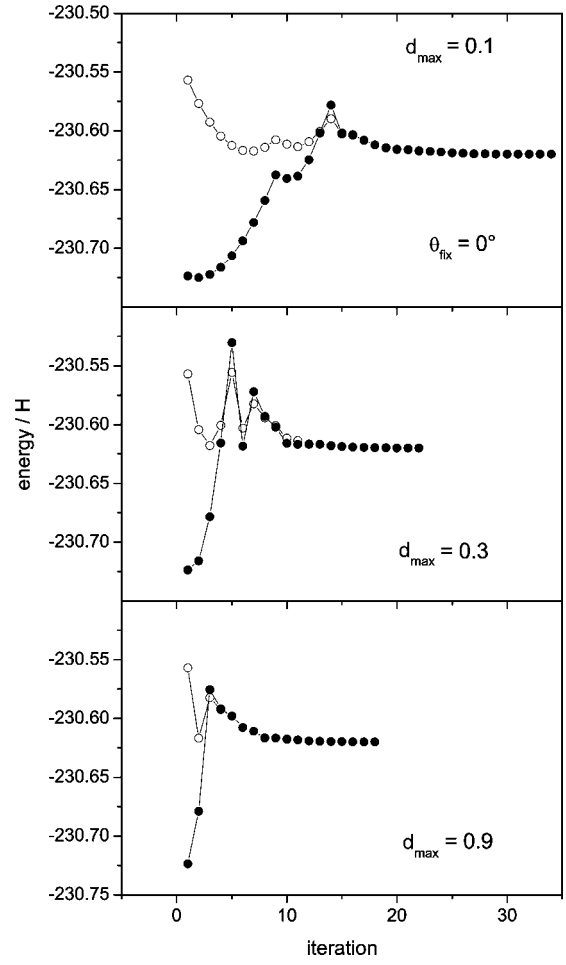

Figure 3. Convergence behavior of the algorithm for optimization of the S_0/S_1 conical intersection in fulvene with fixed dihedral angle $\theta = 0°$. Three different values for the norm of the largest step d_{max} were used. Full and open symbols represent ground-state and excited-state energies, respectively.

those reported by Bearpark et al.[19] However, we perform separate state specific CASSCF calculations for the S_0 and the S_1 states, which belong to different irreducible representations of the C_2 point group. This ensures orthogonality of the two wave functions but allows for different optimized orbitals. As a consequence, our energies are slightly lower than those reported in ref 19.

Each optimization was repeated three times with the setting of the maximum allowed step size d_{max} successively increased by a factor of 3, beginning with $d_{max} = 0.1$ Å. The observed convergence behavior is shown in Figures 2−4.

Without geometrical constraint and with the smallest allowed step size $d_{max} = 0.1$ Å (upper panel in Figure 2), the degeneracy is found after 12 steps, with the energy difference below 1 mH from this point on. Convergence requires 58 more steps during which the energy of both states relaxes by 36 mH. When the smallest allowed step size is increased to $d_{max} = 0.3$ Å (middle panel in Figure 2), the degeneracy is again found after 12 steps within 1 mH. However, the energies show large oscillations during the first few steps, which can even bring the A-state considerably above the B-state. Convergence is reached after a total of 47 steps, with almost the same energy (6 μH lower) than in the previous run. Interestingly, with an even larger value of $d_{max} = 0.9$ Å (lower panel in Figure 2) convergence to the degeneracy is already reached after 3 steps, and the initial oscillations disappear. The final energy after 48 steps is 2 μH lower than in the previous case, and the splitting of the states amounts to 6×10^{-8} H.

A similar behavior is observed for the optimization with the dihedral angle $\theta = 0°$ fixed (Figure 3). Convergence is slow but smooth with $d_{max} = 0.1$ Å, it becomes faster but shows initial oscillations with $d_{max} = 0.3$ Å, and performs best with $d_{max} = 0.9$ Å, requiring only 17 steps. The fast convergence is mainly due to the fact that the fixed dihedral angle had initially already the required value.

However, the algorithms performs also well when the dihedral angle is initially far away from the target value, as seen in Figure 4 for the target $\theta = 90°$. With a small step size the simultaneous optimization toward $\Delta E = 0$ and $\theta = 90°$ apparently leads into a structural region where the energy is much too high, but the algorithm finally finds its way down to the optimized perpendicular structure of fulvene. The escape in that unfavorable region is much shorter when larger steps are allowed ($d_{max} = 0.3$ Å, middle panel in Figure 4),

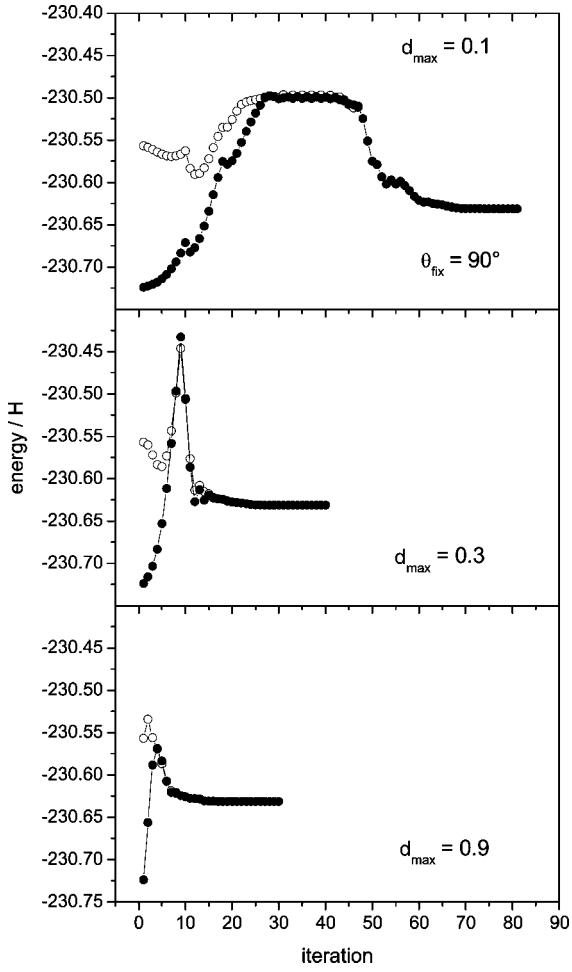

Figure 4. Convergence behavior of the algorithm for optimization of the S_0/S_1 conical intersection in fulvene with fixed dihedral angle $\theta = 90°$. Three different values for the norm of the largest step d_{max} were used. Full and open symbols represent ground-state and excited-state energies, respectively.

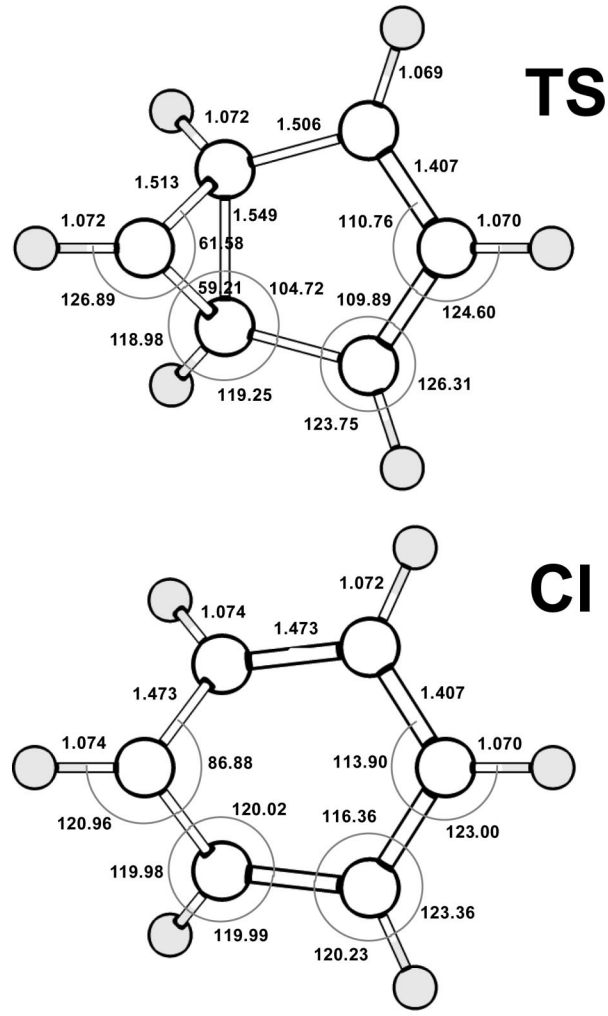

Figure 5. Structures of the optimized S_0/S_1 conical intersection (CI) of benzene and the transition state (TS) between two benzvalene isomers. Bond lengths are given in Angstroms, bond angles in degrees.

and convergence is again fastest with the largest allowed step size of $d_{max} = 0.9$ Å (lower panel in Figure 4).

As a common feature of all these convergence studies one observes that convergence is smooth once the degeneracy has been reached to within a few mH. Only in one case (lower panel of Figure 2) two short excursions (one step each) occurred into an unfavorable region of the PES before the system continued to convergence. In this case very large steps (0.9 Å) were permitted. It might be that in this case the Hessian was not yet well balanced after only 20 updates. In the early phase of the optimization where the two states are widely apart, oscillations and excursions in highly excited regions are more frequent, especially when large step sizes are permitted. Hence one can expect even better convergence behavior when the maximum allowed step size is dynamically adjusted according to the splitting of the states and the success of the previous steps taken by the algorithm.

The algorithm does not always go easily to the conical intersection of interest when started from a point far away. E.g., the optimization of the S_0/S_1 conical intersection of benzene seems to depend strongly on the precise structure used as the starting point. Using different distortions from the ground-state structure as starting structures our algorithm optimized to various local minima of the CI. This might be improved by using a more sophisticated guess for the initial Hessian (in this paper a diagonal matrix is used throughout) or dynamically adjusting the trust radius for the Newton-Raphson step. Alternatively, the degeneracy of interest can be located quickly by an algorithm based on the idea of Longuet-Higgins loops.[24] For the discussion of the underlying principles see refs 25−29. As an example a CASSCF(8,7)/DZV calculation of the S_0/S_1 conical intersection of benzene is shown below.[30] This CI is encircled by a loop that has benzene and two of its benzvalene isomers as its anchors.[26] The structure of the transition state between the two benzvalene isomers is shown in Figure 5. It has A″ symmetry in the C_S point group. Classifying the states of benzene with reference to the same mirror plane, the ground-state has A′ symmetry. Along a path between these two structures that conserves the mirror plane the two states must hence cross. This crossing is located within three steps by a bisection algorithm as shown in the upper part of Figure 6. Since this algorithm does not require gradients, each iteration is even faster than those of the optimization algorithm. Starting from this structure the present algorithm smoothly converges to

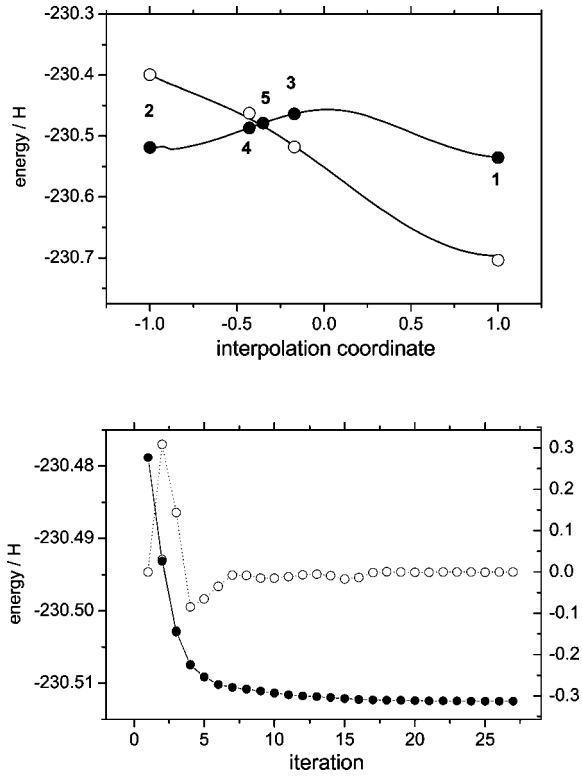

Figure 6. Upper part: Search for the crossing seam along the coordinate defined as the linear interpolation between the structures of benzene (1) and the transition state between two benzvalene isomers (2). The points (3-5) indicate the steps taken by the search algorithm to locate the degeneracy. Open symbols represent the A′ state, full symbols the A″ state. The full lines represent the two electronic potential energy curves. Lower part: Convergence of the optimization of the CI. Full symbols: energy (in Hartree units, left scale) of the degenerate pair of states, open symbols: Splitting of the states (in milli-Hartree units, right scale).

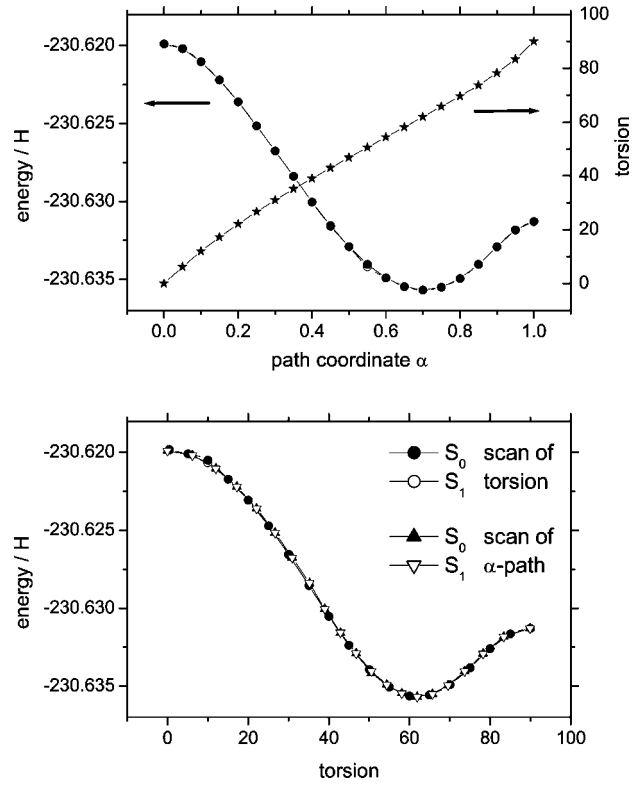

Figure 7. REP connecting the planar and the perpendicular structures of fulvene on the S_0/S_1 conical intersection seam. Upper panel: Energies (left scale) and torsional angle θ (right scale) of the optimized REP along the path coordinate α (eq 23). Lower panel: Energies of the REP as function of the torsional angle. Circles are optimized at equidistant points along θ, and triangles are the results of the path calculated along the path coordinate α defined in eq 23.

the optimized structure of the CI while maintaining the degeneracy within less than 0.3 mH, as seen in the lower part of Figure 6. The structural parameters of the optimized CI are given in Figure 5. They compare well with those presented in the first report on this CI by Palmer at al.[31]

5.2. Relaxed Energy Paths. As first example we present calculations of the REP connecting the planar and perpendicular transition states on the intersection space for the CI between S_0 and S_1 of fulvene. The same basis and active space as in the previous section was used. The REP was calculated along the torsional coordinate θ (19 equidistant points with 5° distance) and also along the path coordinate α defined in eq 23 (21 points with distance of 0.05). Both runs were started from the optimized planar CI geometry and required a total of 107 function evaluations for all points to converge. The results are displayed in Figure 7. The upper panel shows the energy values of the relaxed scan at fixed values of the generalized path coordinate α defined in eq 23 (left scale). The torsional angle at the optimized points increases monotonously with the path parameter α (right scale). The lower panel shows the same REP, now calculated along equidistant points with fixed torsional angle. These data are represented by circles. The data from the scan along α have been included in this plot at the appropriate torsional angles and are shown as triangles. Apparently both scans walked along the same REP.

It should be mentioned that the use of the path parameter α requires the application of further constraints since it is defined in terms of absolute coordinates in $3N$ space. Hence a given projection of the shift $\mathbf{r} - \mathbf{r}_1$ onto the difference vector $\mathbf{r}_2 - \mathbf{r}_1$ between the two reference structures could be achieved by a rotation or translation of the whole molecule. This must be suppressed by fixing components of the center of mass **R** and off-diagonal elements of the inertial tensor **I**. In the present case with C_2-symmetry these conditions were $R_z = 0$ and $I_{xy} = 0$.

As a second example the tautomerization reaction on the PES of the electronic ground-state in propandial was studied. All calculations were performed with CASSCF(10,7)/6−31G** wave functions. The active space consisted of the 5 valence π-orbitals and two σ-orbitals representing the O−H bond and the oxygen lone pair, respectively. The optimized structures of one of the two equivalent ground-state tautomers and the transition state (TS) are shown in Figure 8. The REP was first explored by performing a relaxed scan with the distance r_{19} as the parameter (for the numbering of atoms see Figure 8). The REP obtained in this way is shown by the open circles in Figure 9. Beginning with the value $r_{19} =$ 1.99 Å, the energy rises monotonously with smaller values of r_{19} and reaches a maximum near $r_{19} = 1.2$ Å, in

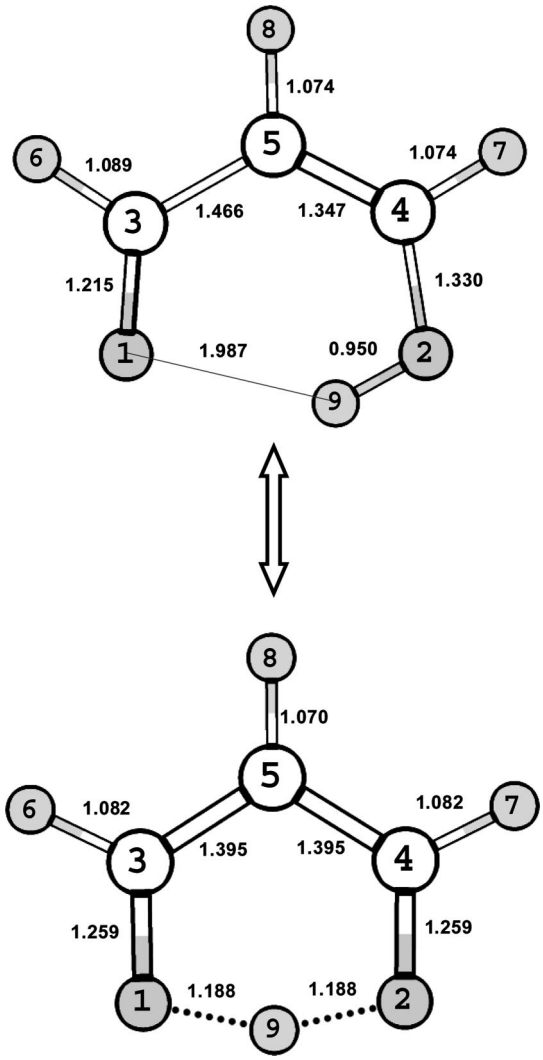

Figure 8. Optimized structures of the electronic ground state (top) and the transition state (bottom) of the enol form of propandial. Bond lengths are given in Angstroms, bond angles in degrees.

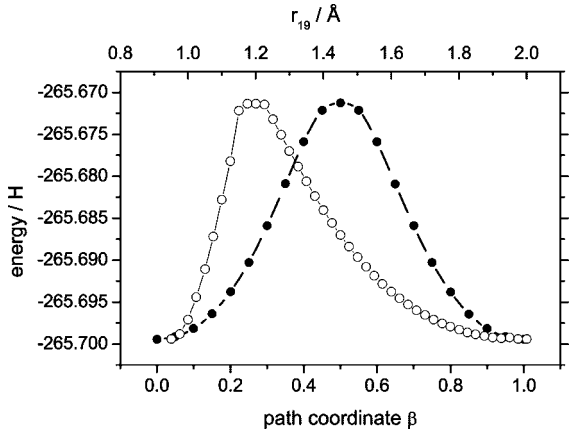

Figure 9. Energy profile on the S_0 potential energy surface connecting the two enol forms of propandial. Open circles (upper axis): relaxed scan along r_{19}. Full cirlces (lower axis): relaxed scan along the path coordinate β defined in eq 24.

accordance with the structure of the TS. The REP then decays quickly to the initial energy value, now at the other tautomer of the ground state. The REP appears unsymmetric: The

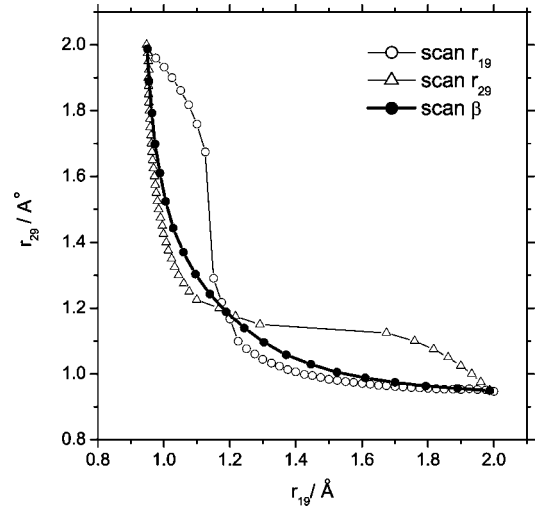

Figure 10. Projection of the REP between the two enol forms of propandial onto the plane spanned by the two distances between the migrating H-atom and the two O-atoms. Open circles: Path followed by a relaxed scan with equidistant steps in r_{19}. Open triangles: Path followed by a relaxed scan with equidistant steps in r_{29}. Full circles: Path followed by a relaxed scan with equidistant steps in the path coordinate β defined in eq 24.

change of the O−H distance amounts to 0.80 Å on one side of the TS but only 0.24 Å at the other side. Figure 10 reveals another problem with this type of relaxed scan. This figure shows the projection of the path onto the plane spanned by the two OH distances. The path mentioned above is represented by the open circles. Beginning with $r_{19} = 1.99$ Å the path shows only very little change in the other distance r_{29}, so that the reaction coordinate is well represented by the internal coordinate r_{19}. However, shortly after passing through the TS, the distance r_{29} changes by a large amount of 0.4 Å, whereas r_{19} changes by only 0.025 Å. Apparently, in this region, r_{19} has only a small projection on the reaction coordinate and is a bad choice for the parameter of a relaxed scan. In addition, the path obtained when following r_{19} is not symmetric with respect to the exchange of r_{19} and r_{29}. This becomes apparent when the data points corresponding to the scan in the opposite direction, now with equidistant steps in r_{29}, is included in the plot (represented by the open triangles). Such a symmetry is, however, expected from the fact that the two minima correspond to equivalent structures. Hence we conclude that the REP calculated as a relaxed scan along either of the two O−H distance coordinates deviates from the true REP due to the switch between the dominant contributions of the two internal coordinates to the reactions coordinate.

In this case the path coordinate β defined in eq 24 performs much better. The energy profile, shown by the full circles in Figure 9, is symmetric around $\beta = 0.5$, which corresponds to the TS structure. For each optimized point along this path the pairs of distances of the hydrogen atom to both oxygen atoms are plotted in Figure 10 as full circles. It is obvious that this path is symmetric with respect to the exchange of these two bond lengths. It is also seen that the point for $\beta = 0.5$ is at the crossing point of the two paths discussed before. Hence, all three paths go through the same TS, as is also

apparent from the same peak height of the energy profiles in Figure 9.

6. Conclusions

An algorithm has been presented for optimization of molecular structures subject to geometric and energetic constraints. The algorithm is a generalization of a recently published method developed in particular for the optimization of conical intersections. The two algorithms are identical for the particular case that a conical intersection is optimized, the interstate coupling gradient vanishes (e.g., due to symmetry), and no additional geometrical constraints are used. The algorithm presented here treats all constraints in an equivalent way. Hence a term is added to the projected gradient (eq 19) or the search step (eq 22) when the interstate coupling matrix element or its gradient does not vanish. The original algorithm adds such a term only for the energy difference. Since the interstate coupling gradient is not available in the GAMESS program, all examples used in the present study were chosen such that the interstate coupling vanishes by symmetry.

The algorithm works well with and without an additional geometry constraint, even when the starting geometry is far from satisfying the constraint. The algorithm apparently tolerates rather large step sizes, and rescaling the steps to a smaller size frequently leads to a worse performance, although the converged results are very similar. Still better convergence behavior can be expected from strategies that dynamically adjust the maximum step size depending on the performance of the previous steps.

The algorithm usually works well with a diagonal matrix for the initial Hessian matrix, but the use of a more realistic Hessian was also studied. E.g., when the Hessian of the RHF-optimized ground-state of fulvene was used to initiate the optimization of the conical intersection, a much faster convergence was found for the full optimization and the optimization with the constraint of $\theta = 0$. However, convergence was much slower in the case $\theta = 90°$. Apparently the Hessian for the planar structure is a bad guess for the perpendicular CI structure.

Since the number of variables and the size of the Hessian matrix are not modified, the algorithm should be easily incorporated into existing Newton-Raphson type optimization routines in quantum chemical programs.

Acknowledgment. This work has been supported by the Fonds der Chemischen Industrie.

References

(1) Domcke, W.; Yarkony, D. R.; Köppel, H. *Conical Intersections: Electronic Structure, Dynamics & Spectroscopy*; World Scientific Publishing Co.: Singapore, 2004.

(2) Yarkony, D. R. *J. Chem. Phys.* **1990**, *92*, 2457.

(3) Yarkony, D. R. *J. Phys. Chem. A* **2004**, *108*, 3200.

(4) Manaa, M. R.; Yarkony, D. R. *J. Chem. Phys.* **1993**, *99*, 5251.

(5) Anglada, J. M.; Bofill, J. M. *J. Comput. Chem.* **1996**, *18*, 992.

(6) De Vico, L.; Olivucci, M.; Lindh, R. *J. Chem. Theory Comput.* **2005**, *1*, 1029.

(7) Dallos, M.; Lischka, H.; Shepard, R.; Yarkony, D. R.; Szalay, P. G. *J. Chem. Phys.* **2004**, *120*, 7330.

(8) Ragazos, I. N.; Robb, M. A.; Bernardi, F.; Olivucci, M. *Chem. Phys. Lett.* **1992**, *197*, 217.

(9) Bearpark, M. J.; Robb, M. A.; Schlegel, H. B. *Chem. Phys. Lett.* **1994**, *223*, 269.

(10) Toniolo, A.; Ben-Nun, M.; Martinez, T. J. *J. Phys. Chem. A* **2002**, *106*, 4679.

(11) Chachiyo, T.; Rodriguez, J. H. *J. Chem. Phys.* **2005**, *123*, 094711.

(12) Yamazaki, S.; Kato, S. *J. Chem. Phys.* **2005**, *123*, 114510.

(13) Izzo, R.; Klessinger, M. *J. Comput. Chem.* **2000**, *21*, 52.

(14) Page, C. S.; Olivucci, M. *J. Comput. Chem.* **2003**, *24*, 298.

(15) Ciminelli, C.; Granucci, G.; Persico, M. *Chem. Eur. J.* **2004**, *10*, 2327.

(16) Keal, T. W.; Koslowski, A.; Thiel, W. *Theor. Chem. Acc.* **2007**, *118*, 837.

(17) Sicilia, F.; Blancafort, L.; Bearpark, M. J.; Robb, M. A. *J. Chem. Theory Comput.* **2008**, *4*, 257.

(18) Fletcher, R. *Practical methods of optimization*; Wiley: Chichester, 1987.

(19) Bearpark, M. J.; Blancafort, L.; Paterson, M. J. *Mol. Phys.* **2006**, *104*, 1033.

(20) A set of orthogonal vectors spanning the space of the constraints gradients can also be generated by Gram-Schmidt orthogonalization. In this case care has to be taken to detect linear dependencies. The advantage of SVD is that, in addition to providing an orthogonal space, the magnitudes of the gradient vectors is transformed to the weights S_m.

(21) (a) Schmidt, M. W.; Baldridge, K. K.; Boatz, J. A.; Elbert, S. T.; Gordon, M. S.; Jensen, J. H.; Koseki, S.; Matsunaga, N.; Nguyen, K. A.; Su, S. J.; Windus, T. L.; Dupuis, M.; Montgomery, J. A. *J. Comput. Chem.* **1993**, *14*, 1347. (b) GordonM. S.; SchmidtM. W. In *Theory and Applications of Computational Chemistry, the first forty years*; Dykstra, C. E., Frenking, G., Kim, K. S., Scuseria, G. E., Eds.; Elsevier: Amsterdam, 2005.

(22) (a) Granovsky, A. A. *PC GAMESS version 7.0*. http://classic.chem.msu.su/gran/gamess/index.html (accessed Oct. 28, 2008). (b) Nemukhin, A. V.; Grigorenko, B. L.; Granovsky, A. A. *Moscow Univ. Chem. Bull.* **2004**, *45*, 75.

(23) http://www.netlib.org/lapack/ (accessed Oct. 28, 2008).

(24) Dick, B.; Haas, Y.; Zilberg, S. *Chem. Phys.* **2008**, *347*, 65.

(25) (a) Herzberg, G.; Longuet-Higgins, H. C. *Discuss. Faraday Soc.* **1963**, *35*, 77. (b) Longuet-Higgins, H. C. *Proc. Roy. Soc., London A* **1975**, *344*, 147.

(26) Zilberg, S.; Haas, Y. *Chem. Eur. J.* **1999**, *5*, 1755.

(27) (a) Zilberg, S.; Haas, Y. *Chem. Phys.* **2000**, *259*, 249. (b) Haas, Y.; Zilberg, S. *Adv. Chem. Phys.* **2002**, *124*, 433. (c) Haas, Y.; Cogan, S.; Zilberg, S *Int. J. Quantum Chem.* **2005**, *102*, 961. (d) Zilberg, S.; Haas, Y. *J. Phys. Chem. A* **2003**, *107*, 1222.

(28) The loop approach has been critisized by Vanni et al.[29] These authors conclude in particular that it will be difficult to transform that idea into a computer algorithm. A detailed comparison of the approaches presented by Zilberg and Haas with that of Vanni et al. is far beyond the scope of the present paper. Here it should suffice to note that the Zilberg/Haas

approach did work in many cases, in particular when symmetry could be used.

(29) Vanni, S.; Garavelli, M.; Robb, M. A. *Chem. Phys.* **2008**, *347*, 46.

(30) The minimum active space is CAS(6,6). The bisection algorithm makes, however, very large jumps in configuration space. E.g., the CAS for benzene is started with the orbitals of the TS structure. I observed that in these searches the MCSCF converges faster when the active space is slightly larger than minimal. In the present case one additional occupied orbital was enough.

(31) Palmer, I. J.; Ragazos, I. N.; Bernardi, F.; Olivucci, M.; Robb, M. A. *J. Am. Chem. Soc.* **1993**, *115*, 673.

(32) Bearpark, M. J.; Bernardi, F.; Olivucci, M.; Robb, M. A.; Smith, B. R. *J. Am. Chem. Soc.* **1996**, *118*, 5254.

(33) Sicilia, F.; Bearpark, M. J.; Blancafort, L.; Robb, M. A. *Theor. Chem. Acc.* **2007**, *118*, 241.

(34) Paterson, M. J.; Bearpark, M. J.; Robb, M. A.; Blancafort, L.; Worth, G. A. *J. Chem. Phys.* **2004**, *121*, 11562.

(35) Dreyer, J.; Klessinger, M. *J. Chem. Phys.* **1994**, *101*, 10655.

CT8003029

JCTC Journal of Chemical Theory and Computation

SEST: Simulated Electronic Structure Theory

Joshua W. Hollett* and Raymond A. Poirier

Department of Chemistry, Memorial University of Newfoundland, St. John's, Newfoundland A1B 3X7, Canada

Received August 11, 2008

Abstract: A novel approach to empirically modeling the electronic structure of molecules is introduced. The theory is based on relationships between molecular orbital energy components and the average distance between electrons and electrons and nuclei. The electron−electron and electron-nucleus distances are subsequently related to interatomic distances which provides a means for modeling the electronic structure of molecules. The general energy expression for a simulated electronic structure theory is defined, along with the functional form of the interatomic distance dependent energy functions. The theory is used to model the hydrogen molecule, the first-row hydrides, and ethane. The models, which have the correct RHF/6−31G(d) optimized geometries, also fit the RHF/6−31G(d) energy at equilibrium and the UHF/6−31G(d) energy at the bond dissociation limit as well as some vibrational frequencies.

1. Introduction

Molecular mechanics methods are widely used to study problems in a variety of research fields, from nanotechnology[1] to molecular biology.[2] In conventional molecular mechanics the total energy of a molecule is divided into different components; bond stretching, E_s, angle bending, E_b, torsional interactions, E_{tor}, van der Waals interactions, E_{vdW}, and electrostatic interactions, E_{elec}.[3]

$$E_{tot}(R) = E_s + E_b + E_{tor} + E_{vdW} + E_{elec} \quad (1)$$

Some formulations may use other energy terms to describe phenomena, such as hydrogen bonding, that are not described well by the existing terms. The functional form of these energy terms and the empirical parameters that occur in the functions are known as a force field. Given the functional form of a molecular mechanics force field, the empirical parameters are defined through fitting of experimental or *ab initio* data.

The major advantage of molecular mechanics methods over *ab initio*, density functional, or semiempirical methods is their computational efficiency. Molecular mechanics allows for the study of large systems and dynamics, where it is unfeasible or strictly impossible to use other approaches. The flexibility of force fields which may be tuned to various classes of compounds allows for quite accurate calculations. However, on the other hand, the specificity of the force fields makes studies on unknown compounds inaccurate and unpredictable. This lack of transferability of specific atom-atom interactions is due to contamination by the molecular environment, which is, indirectly, a result of neglecting the electronic structure. The absence of electrons and orbitals also poses problems for chemical calculations. It is not possible to study reaction mechanisms with molecular mechanics or many other properties related to the electronic structure, such as magnetic properties, excitations, electron transport, and electrical conductivity. A partial solution to such a problem is through a combined quantum mechanics and molecular mechanics (QM/MM) approach.[4]

A hybrid QM/MM approach is common in the study of reactions involving large systems, such as enzyme catalysis or organic reactions in solution. The general scheme behind a QM/MM calculation is to treat the region of interest, or importance, with a quantum mechanical calculation, and the rest of the system is treated with molecular mechanics. In some applications the solvent may be treated with molecular mechanics, while the reacting molecules are treated quantum mechanically, or for large molecules, like enzymes, the active site may be QM, while the rest of the molecule is MM. The Hamiltonians, and energy, of these hybrid systems are divided into QM, MM, and QM/MM parts. How the two different regions interact, QM/MM, is defined in several ways.[5]

* Corresponding author phone: (709)737-8752; fax: (709)737-3702; e-mail: jhollett@mun.ca.

10.1021/ct800433r CCC: $40.75 © 2009 American Chemical Society
Published on Web 12/12/2008

Since the initial appearance of molecular mechanics almost a century ago,[6] most of the development of the theory has been focused on parametrization (i.e., developing force fields for different classes of compounds), while the general formulation of molecular mechanics has remained relatively the same. This has led to accurate modeling of a wide variety of large systems in many research fields. However, the problems associated with the absence of electronic structure are still present. While methods such as QM/MM provide a partial solution to such a problem, there may be other approaches. This study explores such an idea. Rather than the molecular mechanics approach to molecular modeling, modeling of electronic structure is performed. The theory presented provides a different approach to modeling potential energy surfaces, where the energy components associated with electron pairs and individual electrons are functions of the nuclear coordinates.

2. Theory

2.1. Simulated Electronic Structure Theory (SEST). A theory which includes electrons explicitly will have an energy expression that differs significantly from conventional molecular mechanics (eq 1) and more closely resembles the electronic Hamiltonian (eq 2, in atomic units)

$$\hat{H}_e = -\sum_{i=1}^{N}\frac{1}{2}\nabla_i^2 - \sum_{i=1}^{N}\sum_{A=1}^{M}\frac{Z_A}{r_{iA}} + \sum_{i=1}^{N}\sum_{j>i}^{N}\frac{1}{r_{ij}} \quad (2)$$

where N is the number of electrons, and M is the number of nuclei. The SEST energy expression can be expressed as a sum of atomic contributons, V_{atomic}, and contributions from atom-atom, $V_{\text{atom-atom}}$, atom-lone pair, $V_{\text{atom-lone pair}}$, and lone pair-lone pair, $V_{\text{lone pair-lone pair}}$, interactions.

$$V(R) = V_{\text{atomic}} + V_{\text{atom-atom}} + V_{\text{atom-lone pair}} + V_{\text{lone pair-lone pair}} \quad (3)$$

The electronic kinetic energy is included through the virial theorem (see discussion at the end of this section). Each energy term is further subdivided into electron−electron, electron−nuclear, and nuclear−nuclear potential energy, $V = V^{ee}+V^{Ne}+V^{NN}$.

The atomic energy, which does not depend on the nuclear coordinates, accounts for the energy associated with atoms and their own electrons. Each atom has its own electrons corresponding to the neutral atom. The electronic configuration of each atom follows a Lewis dot structure approach. For example, a sp^3 carbon atom has four unpaired, valence electrons, and a pair of core electrons. Also, a sp^3 nitrogen atom has three unpaired valence electrons, a lone pair, and a pair of core electrons. The atomic energy term is calculated as a sum over the contributions of individual nuclei, $V_{\text{atomic}} = \sum_{A=1}^{M} V_A$, where M is the total number of nuclei

$$V_A = \sum_{a\in A} 2V_{Aa}^{Ne} + \sum_{i\in A} V_{Ai}^{Ne} + \sum_{a\in A}\left\{\sum_{\substack{b\in A\\ b\le a}}(2-\delta_{ab})V_{ab}^{ee} + \sum_{i\in A} V_{ai}^{ee}\right\} + \sum_{i\in A}\sum_{\substack{j\in A\\ j<i}}\frac{1}{2}V_{ij}^{ee} + \sum_{\mu\in A} V_{\mu\mu}^{ee} \quad (4)$$

where a and b are pairs of core electrons, i and j are valence electrons, and μ is a lone pair. Each atom has nuclear-electron potential energy associated with its nucleus, A, and its electrons, V_{Aa}^{Ne} and V_{Ai}^{Ne}. Each atom also has electron−electron potential energy due to its electrons, V_{ab}^{ee}, V_{ai}^{ee}, and V_{ij}^{ee} as well as the potential energy of the electrons in each of its lone pairs, $V_{\mu\mu}^{ee}$. The potential energy, $V_{\mu\mu}^{ee}$, due to each lone pair is included in the atomic energy because, like the atomic energy, it is distance independent.

The distance dependent energy terms include $V_{\text{atom-atom}}$, $V_{\text{atom-lone pair}}$, and $V_{\text{lone pair-lone pair}}$. The atom-atom interaction energy is the sum of the interactions between each atom pair, $V_{\text{atom−atom}} = \sum_{A=1}^{M}\sum_{B<A} V_{AB}(R_{AB})$

$$V_{AB}(R_{AB}) = \frac{Z_A Z_B}{R_{AB}} + \sum_{a\in A} 2V_{Ba}^{Ne}(R_{AB}) + \sum_{a\in B} 2V_{Aa}^{Ne}(R_{AB}) + \sum_{i\in A} V_{Bi}^{Ne}(R_{AB}) + \sum_{i\in B} V_{Ai}^{Ne}(R_{AB}) + \sum_{a\in A}\left\{\sum_{b\in B} 2V_{ab}^{ee}(R_{AB}) + \sum_{i\in B} V_{ai}^{ee}(R_{AB})\right\} + \sum_{b\in B}\sum_{i\in A} V_{bi}^{ee}(R_{AB}) + \sum_{\substack{i\in A\\ (i\in c)}}\left\{\sum_{\substack{j\in B\\ (j\notin c)}}\frac{1}{2}V_{ij}^{ee}(R_{AB}) + \sum_{\substack{j\in B\\ (j\in c)}} V_{ij}^{ee}(R_{AB})\right\} \quad (5)$$

where c denotes a bond between atoms A and B. This interatomic energy includes core electron pairs and valence electrons of one atom attracted to another, V_{Ba}^{Ne}, V_{Aa}^{Ne}, V_{Bi}^{Ne}, and V_{Ai}^{Ne}, and potential energy between electrons of different atoms, V_{ab}^{ee}, V_{ai}^{ee}, V_{bi}^{ee}, and V_{ij}^{ee}. The atom-lone pair interaction energy is given by $V_{\text{atom−lone pair}} = \sum_{A=1}^{M}\sum_{\mu=1}^{L} V_{A\mu}(R_{A\mu})$, where L is the total number of lone pairs, and

$$V_{A\mu}(R_{A\mu}) = 2V_{A\mu}^{Ne}(R_{A\mu}) + \sum_{a\in A} 2V_{a\mu}^{ee}(R_{A\mu}) + \sum_{i\in A} V_{i\mu}^{ee}(R_{A\mu}) \quad (6)$$

There is nuclear attraction potential energy between atom A and lone pair μ, $V_{A\mu}^{Ne}$, and electron−electron potential energy, $V_{a\mu}^{ee}$ and $V_{i\mu}^{ee}$. The lone pair−lone pair interaction energy consists of only electron−electron potential energy, where $V_{\text{lone pair−lone pair}} = \sum_{\mu=1}^{L}\sum_{\nu<\mu} V_{\mu\nu}$.

$$V_{\mu\nu} = 2V_{\mu\nu}^{ee}(R_{\mu\nu}) \quad (7)$$

This formulation of simulated electronic structure theory contains no electronic kinetic energy terms. It was found that kinetic energy terms were not required to accurately model the systems studied thus far. However, kinetic energy, like electron-nucleus potential energy (Section 2.2), correlates quite well with the average distance between an electron and a nucleus. Therefore, it is possible to include terms to model kinetic energy in future development of the theory, if desired. In order to calculate the energy of a molecular system, $E(R)$, without the kinetic energy of the electrons, it is assumed that the virial coefficient, which is the negative ratio of the potential and kinetic energy, $c_v = -V/T$, is constant over the entire potential energy surface.

$$E(R) = \frac{(c_v - 1)}{c_v}V(R) \quad (8)$$

In this study the equilibrium geometries and energies of the molecules were fit to RHF/6−31G(d) values; therefore, the

virial coefficient is set to the value obtained from the equilibrium geometry at RHF/6−31G(d).

2.2. The Average Interparticle Distance and Modeling Molecular Orbital Energy Components. Simulated electronic structure theory models the PESs of molecular systems, in which the energy contribution of electron pairs and individual electrons are functions of the nuclear coordinates. It is useful to obtain parameters for these models as well as insight on how the energy contributions per electron pair and individual electron depend on molecular geometry, from *ab initio* models of electronic structure. Such properties are easily examined at the Hartree−Fock level of theory. The closed-shell Hartree−Fock (RHF) energy is given as

$$E_{\mathrm{HF}} = \sum_{a=1}^{N/2} 2h_a + \sum_{a=1}^{N/2}\sum_{b=1}^{N/2} 2J_{ab} - K_{ab} \tag{9}$$

where N is the number of electrons, h_a is the one-electron energy, J_{ab} is the Coulomb energy, and K_{ab} is the exchange energy, associated with molecular orbitals (MOs) a and b. The one-electron energy, $h_a = T_a + V_a$, consists of kinetic energy

$$T_a = \langle a|-\frac{1}{2}\nabla_1^2|a\rangle \tag{10}$$

and nuclear-electron attraction potential energy

$$V_a = \langle a|-\sum_{A=1}^{M}\frac{Z_A}{r_{1A}}|a\rangle \tag{11}$$

The Coulomb and exchange energy are calculated from two-electron integrals.

$$J_{ab} = \langle ab|ab\rangle \tag{12}$$

$$K_{ab} = \langle ab|ba\rangle \tag{13}$$

In recent work,[7] it was found that the Coulomb energy could be modeled with a one-electron property of MOs, the average interelectronic distance, δr_{12}. The Coulomb energy, J_{ab}, associated with any two MOs is inversely proportional to the average distance between an electron in MO a and an electron in MO b, $(\delta r_{12})_{ab}$, which is given by

$$(\delta r_{12})_{ab} = \sqrt{\langle ab|r_{12}^2|ab\rangle} \tag{14}$$

The relationship

$$J_{ab} \approx \frac{\alpha}{(\delta r_{12})_{ab}} \tag{15}$$

has severe deviations for the canonical MOs (CMOs) of HF theory, due to delocalized core MO pairs. However, if localized MOs (LMOs) are used the relationship is followed quite closely, Figure 1.

A similar relationship has been found between the nuclear-electron attraction potential energy, V_a (eq 11), and the average distance between an electron and a nucleus, δr_{aA}, which is calculated analogously to $(\delta r_{12})_{ab}$.[8]

$$\delta r_{aA} = \sqrt{\langle a|r_{1A}^2|a\rangle} \tag{16}$$

The nuclear-electron potential energy, V_a, may be separated into contributions from individual nuclei, V_{aA}, where $\sum_{A=1}^{M} V_{aA} = V_a$. The nuclear-electron potential energy between MO a and nucleus A is related to δr_{aA} through the equation

$$V_{aA} \approx -\gamma\frac{Z_A}{\delta r_{aA}} \tag{17}$$

The relationship has the same deviations for CMOs as seen with J_{ab} and $(\delta r_{12})_{ab}$ and performs quite well for LMOs, Figure 2.

It should be noted that while the overall correlation in Figures 1 and 2 is good, $r^2 = 0.997$ and 0.995 respectively, individual deviations approach 1 hartree for the relationship between J_{ab} and $(\delta r_{12})_{ab}$ and 25 hartrees for V_{aA} and δr_{aA}. These errors are quite large on the scale of reaction energetics. However, these deviations involve core MOs, which correspond to the core electron pairs of SEST, for which the energy terms are constant parameters and therefore do not depend upon the above relationships. Furthermore, it is the qualitative result, which is most relevant to an empirically parametrized SEST. The Coulomb and electron−

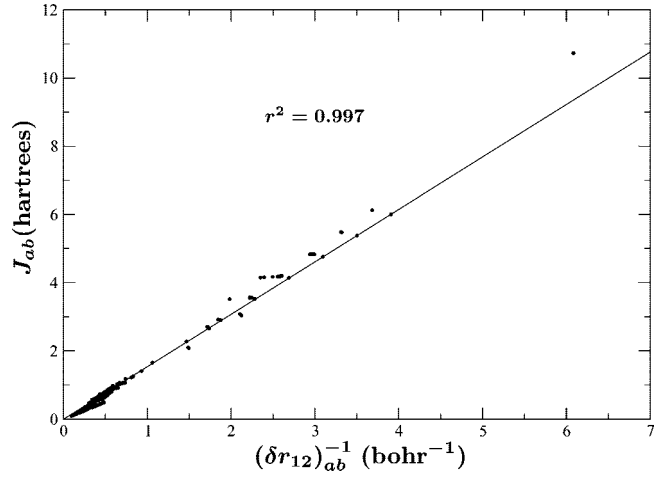

Figure 1. Relationship between Coulomb energy, J_{ab}, and the average distance between two electrons, $(\delta r_{12})_{ab}$ (eq 14), for two electron ions to molecules with up to 58 electrons (RHF/6−31G(d), LMO). From ref 7.

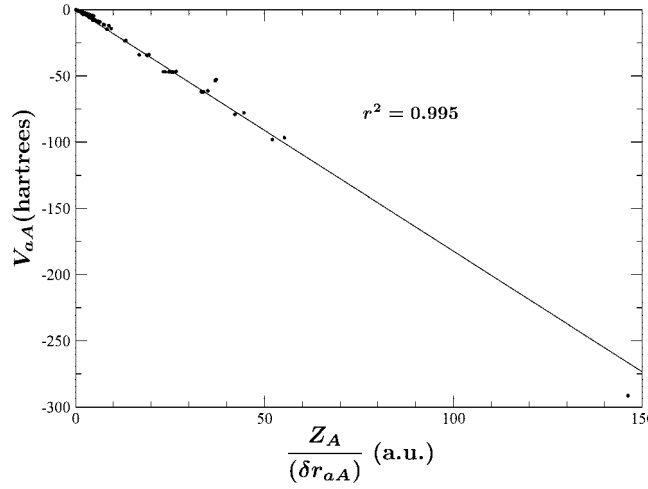

Figure 2. Relationship between electron−nuclear attraction energy, V_{aA}, and the average distance between an electron and a nucleus, δr_{aA} (eq 16), for two electron ions to molecules with up to 58 electrons (RHF/6−31G(d), LMO).

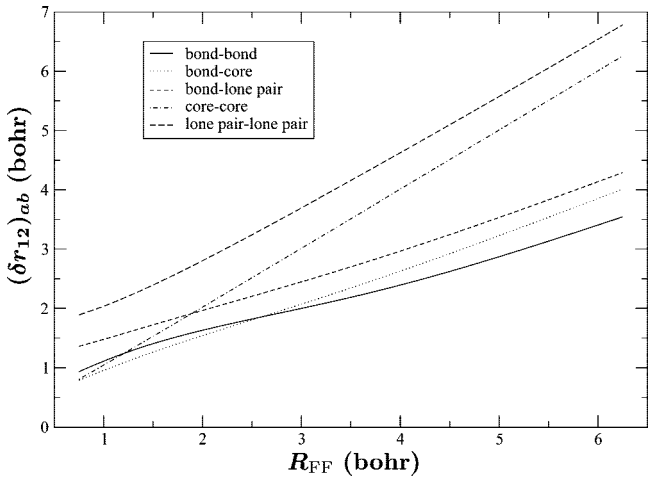

Figure 3. Relationship between the average distance between two electrons, $(\delta r_{12})_{ab}$, and the fluorine−fluorine distance, R_{FF}, in F_2 (RHF/6−31G(d), LMO). Includes a = bond b = bond, a = bond b = core, a = core b = core, and a = lone pair b = lone pair (from separate nuclei).

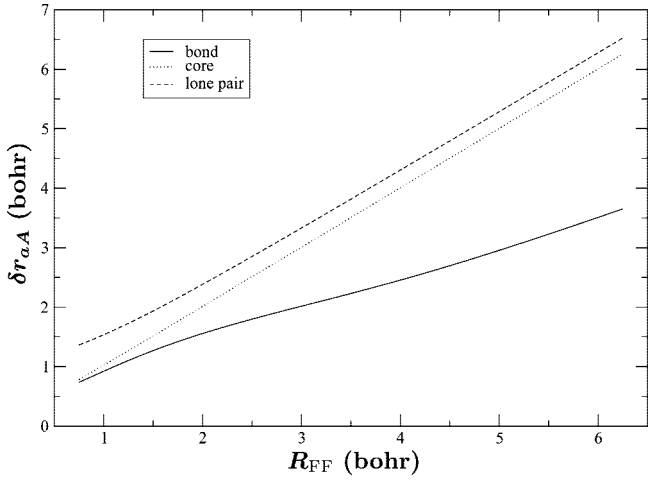

Figure 4. Relationship between the average distance between an electron and a nucleus, δr_{aA}, and the fluorine−fluorine distance, R_{FF}, in F_2 (RHF/6−31G(d), LMO). Includes a = bond, core, and lone pair.

nuclear potential energy are quantities calculated from integrating over the electronic distribution. Although as a result of the relationships just mentioned, to some approximation electrons have average positions with respect to each other and with respect to the nuclei. Furthermore, these average positions, and hence distances, may be used to approximate components of the HF energy per MO. An immediate question following such deductions is how do these average interparticle distances change with changing molecular structure.

In general, the average interparticle distances, $(\delta r_{12})_{ab}$ and δr_{aA}, are linearly related to interatomic distance. This relationship is illustrated in Figures 3 and 4, with F_2.

It is expected that such a relationship would be most critical for atoms which are bonded to each other. Changing bond length significantly affects the electronic structure of a molecule, especially around the two bonded atoms, and even more for a diatomic. While this may be the case, it is seen in Figures 3 and 4 that the interparticle distances very closely follow a linear relationship with the fluorine−fluorine distance. However, for shorter bond lengths (<1.5 bohr) there is slight curvature in the lone pair-lone pair $(\delta r_{12})_{ab}$ and lone pair δr_{aA} curves which is due to the lone pairs on different fluorine atoms bending away from each other as the bond length decreases. It is also observed in both figures that distances involving electrons in the bond show slight curvature. In both the bond-bond $(\delta r_{12})_{ab}$ and bond δr_{aA} curves, the slope is less around the equilibrium bond length ($(R_{FF})_e$ = 2.54 bohr) than that at the shorter and longer R_{FF} distances. Nonetheless, this relationship, even as an approximation, is a powerful tool.

The ability to relate the average interparticle distances to atomic distances has important consequences. For a given molecular structure, not only will these relationships provide an estimate of MO energy components but also they will provide a means of predicting an *average* picture of the electronic structure.

2.3. Functional Form. It was seen in Section 2.1 that the SEST energy expression, eq 3, contains terms which depend on atom-atom, atom-lone pair, and lone pair-lone pair distances. The functional form of these distance dependent terms determines the success of applying SEST. Following the relationships observed in Figures 3 and 4, the interparticle distances, $(\delta r_{12})_{ab}$ and δr_{bA}, are taken to be linear functions of the interatomic distance, R_{AB}

$$(\delta r_{12})_{ab} = \lambda R_{AB} + \sigma \tag{18}$$

and

$$\delta r_{bA} = \omega R_{AB} + \kappa \tag{19}$$

where MO a is localized on atom A, MO b is localized on atom B, or one of them (a or b) is the bond between A and B, and λ, σ, ω, and κ are constants for each unique pair of MOs. As observed in Figures 3 and 4, the relationships involving bonding MOs are approximate. However, an exact model of *ab initio* electronic structure through interatomic distances is not the goal, neither is it possible.

The LMO potential energy components are related to the interatomic distance through the linear relationships above and the relationships seen earlier (Figures 1 and 2). Substitution of eq 18 into eq 15 yields

$$J_{ab} \approx \frac{\alpha}{\lambda R_{AB} + \sigma} \tag{20}$$

While, substitution of eq 19 into eq 17 gives

$$V_{bA} \approx \frac{-\gamma Z_A}{\omega R_{AB} + \kappa} \tag{21}$$

The above equations are used to derive the general form of the SEST distance dependent functions.

Given electron pairs a and b, where a is localized on atom A and b is localized on atom B, the electron−electron potential energy between the two pairs of electrons is given by

$$V_{ab}^{ee}(R_{AB}) = \frac{(V_{ab}^{ee})_e((R_{AB})_e - r_{ab}^{ee})}{R_{AB} - r_{ab}^{ee}} \tag{22}$$

where $(R_{AB})_e$ is an equilibrium interatomic distance, r_{ab}^{ee} is a constant parameter, and $(V_{ab}^{ee})_e$ is the potential energy at the equilibrium distance. Also, as the interatomic distance, R_{AB}, approaches infinity the potential energy term vanishes. The SEST electron−electron potential energy function is chosen to model the total HF electron−electron potential energy (eq 9)

$$V_{ab}^{ee}(R_{AB}) \approx 2J_{ab} - K_{ab} \tag{23}$$

although it is only the Coulomb energy, J_{ab}, which is inversely proportional to the average interelectronic distance, $(\delta r_{12})_{ab}$ (eq 15). The functional form is derived using localized molecular orbitals (LMOs),[15] in which case the exchange energy, K_{ab}, is minimal. Therefore the approximation in eq 23 is considered valid. The electron-nucleus potential energy is calculated in a similar fashion.

$$V_{Ba}^{Ne}(R_{AB}) = \frac{\left(V_{Ba}^{Ne}\right)_e\left((R_{AB})_e - r_{Ba}^{Ne}\right)}{R_{AB} - r_{Ba}^{Ne}} \tag{24}$$

While the functions given in eqs 22 and 24 are for pairs of electrons, a and b, functions for individual electrons, i and j, and any combination of pairs and individual electrons (*e.g.* $V_{ai}^{ee}(R_{AB})$) take the same form, albeit with different parameter values. The parameters of these functions are derived from the LMOs of the *ab initio* electronic structure of a molecule.

It is recognized that positive values of the parameters r_{ab}^{ee}, r_{Ba}^{Ne}, etc., result in singularities in the potential energy surface for positive values of R_{AB}. While fitting a potential energy surface, parameters with values larger than $^1/_2(R_{AB})_e$ are avoided, and values smaller than this threshold are dealt with using a piecewise function.

$$V_{AB}(R_{AB}) = \begin{cases} V^{NN}(R_{AB}) + V^{Ne}(R_{AB}) + V^{ee}(R_{AB}), & \text{if } R_{AB} > r_{AB}^{\max} + \delta \\ V^{NN}(R_{AB}) + V^{Ne}(r_{AB}^{\max} + \delta) + V^{ee}(r_{AB}^{\max} + \delta), & \text{if } R_{AB} \le r_{AB}^{\max} + \delta \end{cases} \tag{25}$$

$$V_{A\mu}(R_{A\mu}) = \begin{cases} V^{Ne}(R_{A\mu}) + V^{ee}(R_{A\mu}), & \text{if } R_{A\mu} > r_{A\mu}^{\max} + \delta \\ V^{Ne}(r_{A\mu}^{\max} + \delta) + V^{ee}(r_{A\mu}^{\max} + \delta) + V^{ee}(R_{A\mu} + r_i) - V^{ee}(r_{A\mu}^{\max} + \delta + r_i), & \text{if } R_{A\mu} \le r_{A\mu}^{\max} + \delta \end{cases} \tag{26}$$

The largest positive value for a given atom-atom interaction or atom-lone pair interaction is $r^{\max}$ (e.g., $r_{AB}^{\max} = \max\{r_{Ai}^{Ne}, r_{Ba}^{Ne}, r_{ij}^{ee}, \ldots\}$). The argument $R_{A\mu}+r_i$ (eq 26) denotes that for each given function of the form in eqs 22 and 24 the value of the specific r_i parameter is added to $R_{A\mu}$, thus removing r_i from the denominator.

2.4. Determining the Parameters. In this study the parameters of the distance dependent functions (eqs 22 and 24) along with the constant energy terms (eq 4) are derived from *ab initio* calculations. The LMO energy components, V_{aA}, J_{ab}, and K_{ab}, are used to define the constant energy terms, V_A, and the equilibrium energy terms, $(V_{AB})_e$, $(V_{A\mu})_e$, and $(V_{\mu\nu})_e$. For electron pairs belonging to the same atom (core electrons), or a lone pair, the energy is taken to be equal to the corresponding LMO energy component. For example

$$(V_{ab}^{ee})_e = 2J_{ab}^{\mathrm{LMO}} - K_{ab}^{\mathrm{LMO}} \tag{27}$$

and

$$V_{Aa}^{Ne} = V_{aA}^{\mathrm{LMO}} \tag{28}$$

Energy terms for individual electrons, the bonding electrons, require the partitioning of LMO energy components. The energy expression for ammonia may be used to illustrate an energy partitioning scheme.

$$V_{NH_3} = V_N + 3V_H + 3V_{NH} + 3V_{HH} + V_{N\mu} + 3V_{H\mu} \tag{29}$$

The lone pair of nitrogen is denoted μ. The terms V_N and V_H are the atomic energies of nitrogen and hydrogen, respectively

$$V_N = 2V_{Na}^{Ne} + 3V_{Ni}^{Ne} + V_{aa}^{ee} + 3V_{ai}^{ee} + 3\left(\frac{1}{2}V_{ij}^{ee}\right) + V_{\mu\mu}^{ee} \tag{30}$$

where a is the pair of core electrons of nitrogen, and i and j denote valence electrons of nitrogen.

$$V_H = V_{Hk}^{Ne} \tag{31}$$

where k is the hydrogen electron. The atom-atom interaction energy terms are V_{NH} and V_{HH}

$$V_{NH} = \frac{Z_N Z_H}{R_{NH}} + 2V_{Ha}^{Ne}(R_{NH}) + 2V_{Hj}^{Ne}(R_{NH}) + V_{Hi}^{Ne}(R_{NH}) + V_{Nk}^{Ne}(R_{NH}) + V_{ak}^{ee}(R_{NH}) + 2\left(\frac{1}{2}V_{jk}^{ee}(R_{NH})\right) + V_{ik}^{ee}(R_{NH}) \tag{32}$$

where a is the pair of core electrons of nitrogen, i is the valence electron of nitrogen in this NH bond, j is a valence electron of nitrogen not in this bond, and k is the hydrogen electron. The hydrogen−hydrogen nonbonded interaction energy is described as

$$V_{HH} = \frac{Z_H Z_H}{R_{HH}} + 2V_{Hi}^{Ne}(R_{HH}) + \frac{1}{2}V_{ij}^{ee}(R_{HH}) \tag{33}$$

Finally, $V_{N\mu}$ and $V_{H\mu}$ are the atom-lone pair interaction terms

$$V_{N\mu} = 2V_{N\mu}^{Ne}(R_{N\mu}) + 2V_{a\mu}^{ee}(R_{N\mu}) + 3V_{i\mu}^{ee}(R_{N\mu}) \tag{34}$$

$$V_{H\mu} = 2V_{H\mu}^{Ne}(R_{H\mu}) + V_{k\mu}^{ee}(R_{H\mu}) \tag{35}$$

The derivation of the parameters for the electron-nucleus and electron−electron potential energy terms from LMO energy values is given in Tables 1 and 2, respectively.

Similar schemes are used to partition the energies of the bonding electrons of other molecules. In some cases there may be a point in which the partition is arbitrary and is defined intuitively (see V_{ai}^{ee} and $(V_{i\mu}^{ee})_e$ in Table 2). Also, the partitioning of the energy for V_{Ni}^{Ne} (Table 1) and V_{di}^{ee} (Table 2) ensures that dissociation of a single bond leads to the UHF/6−31G(d) potential energy of the dissociated products. It is important to note that, for the equilibrium structure, the MO energy components, V_{aA}^{LMO} and V_{ab}^{LMO}, can be recovered exactly. For example

$$V_{cd}^{LMO} = \frac{1}{2}V_{ij}^{ee} + 2\left(\frac{1}{2}V_{ik}^{ee}(R_{NH})\right) + V_{kl}^{ee}(R_{HH}) \qquad (36)$$

where i and j denote bonding electrons of nitrogen, and k and l are hydrogen electrons. Furthermore, for a distorted geometry an approximation to the MO energy components may be calculated.

It is not surprising that a theory which parametrizes the energy of individual electrons and electron pairs derives the parameters from *ab initio* LMO calculations. SEST, an alternative approach to modeling PESs, shares the same premise of molecular mechanics, which is that certain functions and parameters are transferable from one molecule to another. The transferability of the properties of LMOs has been known for decades,[9,10] and work is currently being done to apply this transferability to linear scaling, divide, and conquer methods.[11−13]

The other parameters of the distance dependent functions, $(R_{AB})_e$, r_{ABa}^{Ne}, r_{AiBj}^{ee}, etc., are defined through fitting of the equilibrium geometry, $\partial E(R_e)/\partial R = 0$, and the vibrational frequencies.

Table 1. Derivation of SEST Electron-Nucleus Potential Energy Parameters for Ammonia from RHF/6-31G(d) LMO Energy Components[a]

parameter	eq	derived from [b]
V_{Na}^{Ne}	30	V_{aN}^{LMO}
$(V_{Ha}^{Ne})_e$	32	V_{aH}^{LMO}
$(V_{N\mu}^{Ne})_e$	34	$V_{\mu N}^{LMO}$
$(V_{H\mu}^{Ne})_e$	35	$V_{\mu H}^{LMO}$
$(V_{Hj}^{Ne})_e$	32	$2V_{dH}^{LMO} - V_{Hi}^{Ne}(R_{HH})$[c]
V_{Ni}^{Ne}	30	$V_{NH_2}^{Ne} - 2(V_{Na}^{Ne} + 2(V_{Ha}^{Ne})_e + 2V_{dN}^{LMO} + 2V_{dH}^{LMO} + 2V_{dH}^{LMO} + (V_{N\mu}^{Ne})_e + 2(V_{H\mu}^{Ne})_e) - 2(V_{Hj}^{Ne})_e$[d]
$(V_{Nk}^{Ne})_e$	32	$2V_{dN}^{LMO} - V_{Ni}^{Ne}$
$(V_{Hl}^{Ne})_e$	32	$2V_{dH}^{LMO} - V_{Hk}^{Ne}$

[a] μ denotes the lone pair of nitrogen, a denotes the pair of core electrons of nitrogen, c denotes a bond involving the specified atom, d denotes a bond not involving a specified atom (i.e., another bond), i and j denote valence electrons of nitrogen, and k denotes electron of hydrogen. [b] Terms of the form V^{LMO} denote energy values taken from LMOs of an *ab initio* calculation. [c] $V_{Hj}^{Ne}(R_{HH})$ denotes electron-nucleus potential energy of previously defined HH nonbonded interaction, calculated at the equilibrium ammonia HH distance, R_{HH}. [d] $V_{NH_2}^{Ne}$ denotes total electron-nucleus potential energy of the radical amine calculated at UHF/6−31G(d).

Table 2. Derivation of SEST Electron−Electron Potential Energy Parameters for Ammonia from UHF/6-31G(d) LMO Energy Components[a]

parameter	eq	derived from [b]
V_{aa}^{ee}	30	V_{aa}^{LMO}
$V_{\mu\mu}^{ee}$	30	$V_{\mu\mu}^{LMO}$
$(V_{a\mu}^{ee})_e$	34	$V_{a\mu}^{LMO}$
V_{di}^{ee}	intermediate term[c]	$\{V_{NH_2}^{ee} - V_{aa}^{ee} - 2V_{cc}^{LMO} - 2V_{cd}^{LMO} - 4V_{ca}^{LMO} - V_{\mu\mu}^{ee} - 4V_{c\mu}^{LMO} - 2(V_{a\mu}^{ee})_e\}(2 + (V_{ca}^{LMO}/V_{cd}^{LMO}) + (V_{c\mu}^{LMO}/V_{cd}^{LMO}))^{-1}$[d]
V_{ai}^{ee}	30	$V_{di}^{ee}(V_{ca}^{LMO}/V_{cd}^{LMO})$
$(V_{i\mu}^{ee})_e$	34	$V_{di}^{ee}(V_{c\mu}^{LMO}/V_{cd}^{LMO})$
$(V_{k\mu}^{ee})_e$	35	$2V_{c\mu}^{LMO} - (V_{i\mu}^{ee})_e$
$(V_{ak}^{ee})_e$	32	$2V_{ca}^{LMO} - V_{ai}^{ee}$
V_{dk}^{ee}	intermediate term[c]	$2V_{cd}^{LMO} - V_{di}^{ee}$
$(V_{jk}^{ee})_e$	32	$2V_{dk}^{ee} - V_{ij}^{ee}(R_{HH})$[e]
V_{ij}^{ee}	30	$2V_{di}^{e} - (V_{jk}^{ee})_e$
$(V_{ik}^{ee})_e$	32	V_{cc}^{LMO}

[a] μ denotes the lone pair of nitrogen, a denotes the pair of core electrons of nitrogen, c denotes a bond involving the specified electron, d denotes a bond not involving the specified electron (i.e., another bond), i and j denote valence electrons of nitrogen, and k denotes electron of hydrogen. [b] Terms of the form V^{LMO} denote energy values taken from LMOs of an *ab initio* calculation (where $V_{ab}^{LMO} = 2J_{ab}^{LMO} - K_{ab}^{LMO}$). [c] Intermediate terms used to simplify expressions for some energy parameters. [d] $V_{NH_2}^{ee}$ denotes total electron−electron potential energy of the radical amine calculated at UHF/6−31G(d). [e] $V_{ij}^{ee}(R_{HH})$ denotes electron−electron potential energy of previously defined HH nonbonded interaction, calculated at the equilibrium ammonia HH distance, R_{HH}.

Table 3. SEST and RHF/6-31G(d) Vibrational Frequencies for the First-Row Hydrides

		frequency (cm^{-1})	
system	ν	RHF/6−31G(d)	SEST
BeH_2	1	761	540
	2	763	540
	3	2107	2240
	4	2324	2324
BH_3	1	1225	1085
	2	1305	1218
	3	1306	1218
	4	2694	3033
	5	2816	2817
	6	2818	2817
CH_4	1	1487	1862
	2	1488	1862
	3	1488	1862
	4	1702	1485
	5	1702	1485
	6	3196	3891
	7	3303	3305
	8	3305	3305
	9	3307	3305
NH_3[a]	1	1214	2294
	2	1849	1980
	3	1851	1980
	4	3690	5001
	5	3825	3825
	6	3826	3825
H_2O[a]	1	1829	2237
	2	4070	5658
	3	4191	4191
HF[a]	1	4362	4362

[a] Molecules with lone pairs have lone pair vibrational modes. These modes are not shown, they are of the order 10^4-10^8 cm^{-1} and easily distinguished from the real modes.

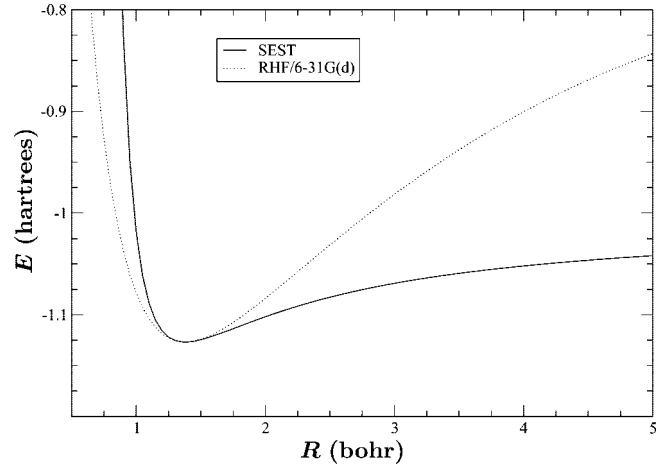

Figure 5. Dissociation curve for H_2 (SEST and RHF/6−31G(d)).

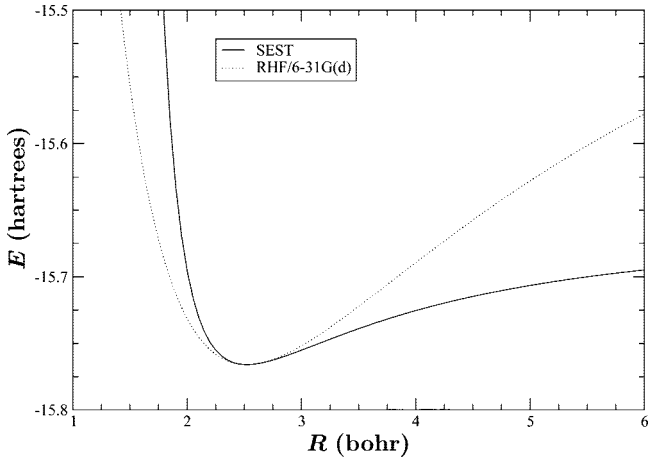

Figure 6. Dissociation curve for the BeH bond of BeH_2 (SEST and RHF/6−31G(d)).

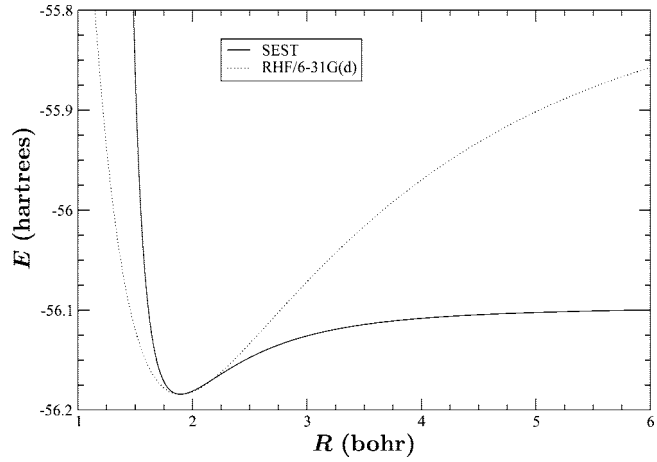

Figure 9. Dissociation curve for the NH bond of NH_3 (SEST and RHF/6−31G(d)).

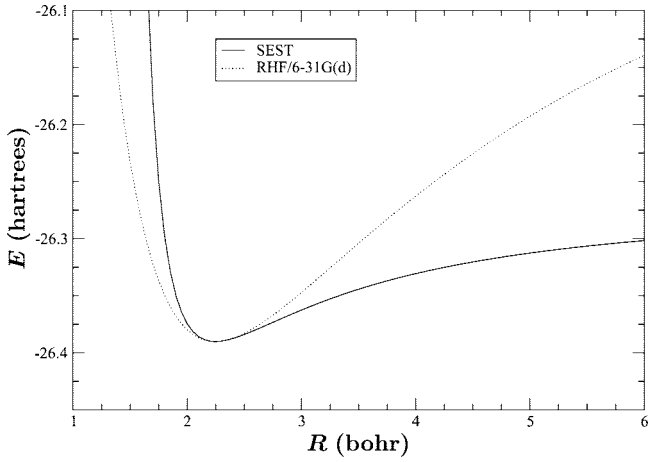

Figure 7. Dissociation curve for the BH bond of BH_3 (SEST and RHF/6−31G(d)).

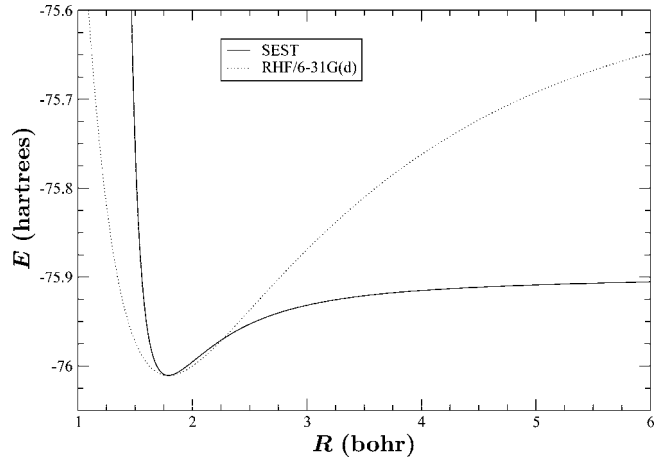

Figure 10. Dissociation curve for the OH bond of H_2O (SEST and RHF/6−31G(d)).

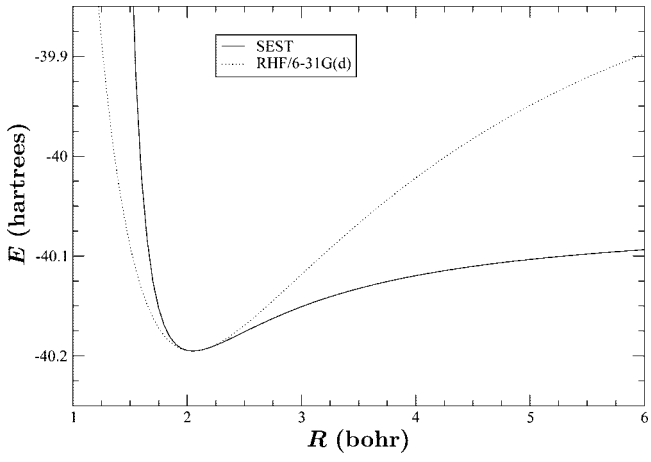

Figure 8. Dissociation curve for the CH bond of CH_4 (SEST and RHF/6−31G(d)).

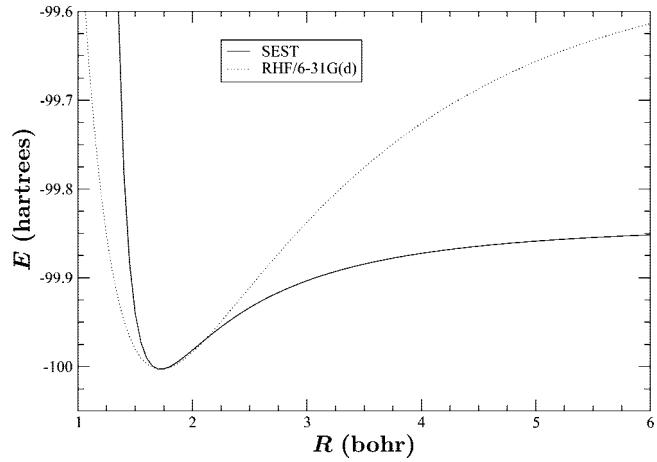

Figure 11. Dissociation curve for HF (SEST, RHF/6−31G(d)).

3. Method

Simulated Electronic Structure Theory (SEST) was implemented within the MUNgauss program.[14] The geometries of the molecules studied were optimized at RHF/6−31G(d), and the energies and MO properties were also calculated at RHF/6−31G(d). The energies of the products of bond dissociaton were calculated at UHF/6−31G(d). Localized molecular orbitals were obtained through Boys localization.[15]

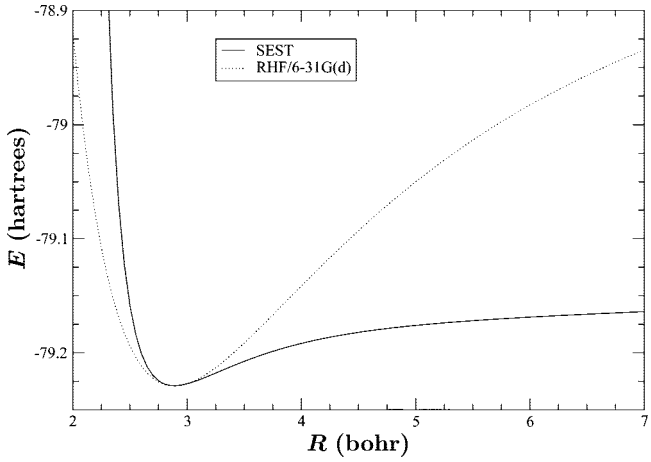

Figure 12. Dissociation curve for the CC bond of ethane (SEST and RHF/6−31G(d).

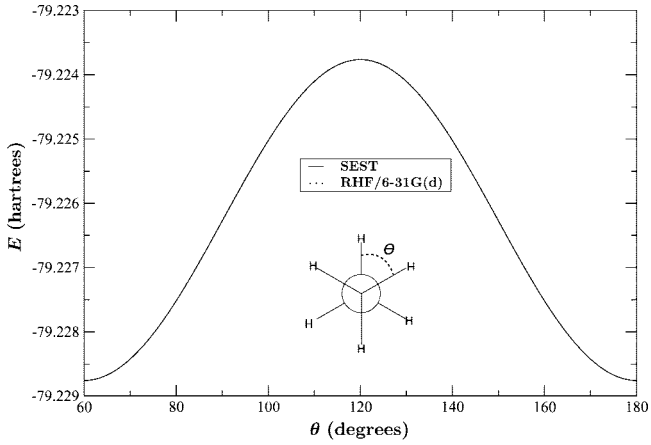

Figure 13. Rigid rotation about the CC bond of ethane (SEST and RHF/6−31G(d)).

4. Results and Discussion

4.1. Hydrogen Molecule and the First-Row Hydrides. An initial demonstration of SEST is given through modeling *ab initio* calculations on small molecules, such as the hydrogen molecule and the first-row hydrides. The SEST energy expression for the hydrogen molecule is

$$V_{H_2}(R_{HH}) = 2V^{Ne}_{Hi} + \frac{Z_H Z_H}{R_{HH}} + 2V^{Ne}_{HHi}(R_{HH}) + V^{ee}_{HiHj}(R_{HH}) \quad (37)$$

The SEST model of H_2 fits the RHF/6−31G(d) energy at the equilibrium bond length, $(R_{HH})_e = 1.380$ bohr. At the dissociation limit, $R_{HH} \rightarrow \infty$ the energy approaches the UHF/6−31G(d) potential energy of the dissociated products, $2V_H$, multiplied by the factor $(c_v-1)/c_v$, where c_v is the virial coefficient of the equilibrium structure (eq 8). The result is a dissociation energy which is 8 millihartrees smaller than the actual UHF/6−31G(d) dissociation energy. This could be corrected by first scaling the potential energy of the dissociated products (2H), before defining the energy parameters of the SEST model of H_2. However, the purpose of the study is to illustrate the ability of the SEST model to qualitatively dissociate correctly (unlike RHF); the actual dissociation energy is adjustable. The SEST vibrational frequency of H_2 is set to that of the RHF/6−31G(d) calculation, 4646 cm^{-1}. The hydrogen molecule energy expression (eq 37) has only two parameters, r^{Ne}_{HHi} and r^{ee}_{HiHj}, which in this case are used to fit the first and second derivatives of the RHF/6−31G(d) wave function at the equilibrium bond length. The fit to equilibrium geometry and frequency is achieved by setting the parameters r^{Ne}_{HHi} and r^{ee}_{HiHj} to 0.27291230 bohr and 0.68583812 bohr, respectively. Similarly, for the first-row hydrides, SEST can model the HF equilibrium geometries and some frequencies and allow for qualitatively correct dissociation of bonds.

Bond dissociation in the SEST models of the first-row hydrides resembles the potential energy curve of H_2. In all cases the equilibrium geometry and energy of the SEST model is identical to the RHF/6−31G(d) values, and, therefore, these values are not reported. Also for all systems, the dissociation of a single bond leads to the UHF/6−31G(d) potential energy of the dissociated products, multiplied by $(c_v-1)/c_v$. As previously mentioned, SEST provides an approximation to the energy components $2J_{ab}-K_{ab}$ and V_a, for all MOs, for any point along the potential energy surface (dissociation curve). In this study, it is only the equilibrium values which have been fit exactly. Exact dissociation energies can be obtained with appropriate scaling. The ultimate goal of such a theory would be to accurately model several points along the bond dissociation curve as well as various points over the entire potential energy surface (i.e., conformational changes). An improved SEST model would use an *ab initio* method such as GVB to obtain dissociation energy curve parameters and first and second energy derivatives. However, the source for defining parameters is not limited to *ab initio* calculations. A SEST approach could involve empirical parameters from experiment or a combination of *ab initio* and empirical parameters.

Using the SEST formulation of this study, it is possible to fit some vibrational frequencies of the SEST models of the first-row hydrides to RHF/6−31G(d) values (Table 3).

For each hydride model there is a hydrogen−hydrogen (HH) nonbonding function. In an effort to explore the transferability of these functions, the same HH nonbonding function is used for all molecules. It was found that if the same HH nonbonding function is used, it is only possible to fit some of the vibrational frequencies.

For this study, the parameters of the AH bonding functions, where A is Be, B, C, N, O, or F, as well as the atom-lone pair, lone pair-lone pair interaction functions, were adjusted to fit the asymmetric stretch vibrational modes of the first-row hydrides. For BeH_2, ν_4 is the asymmetric stretch (Table 3). The error in the lower frequencies ranges from 133 to 223 cm^{-1}. For the rest of the hydrides it is seen that the asymmetric stretches are fit exactly; however, the symmetric stretch is always overestimated. The BH_3 model overestimates the symmetric stretch, ν_4, by 339 cm^{-1}, and the error in the lower frequencies is less than 140 cm^{-1}. For CH_4 the symmetric stretch is overestimated by 695 cm^{-1}, while the error in the other frequencies ranges from 217 cm^{-1} to 375 cm^{-1}. The overestimation of the symmetric stretch is greater for the molecules with lone pairs. The NH_3 model has a symmetric stretch which is 1311 cm^{-1} larger than the RHF/

6−31G(d) value. Also, the frequency of the out-of-plane bending mode, ν_1, is overestimated by 1080 cm^{-1}, while the error in the other two modes is only 130 cm^{-1}. For H_2O, the symmetric stretch, ν_2, and the bending mode, ν_1, are also overestimated, by 1588 cm^{-1} and 408 cm^{-1}, respectively. These overestimations are due to the HH nonbonding interaction. For the symmetric stretches, the out-of-plane bend of NH_3, and the angle bend of H_2O, it is the HH distances which are changing the most. It appears that the HH nonbonding interaction is too strong for these vibrational modes. However, upon investigation of the SEST model of CH_4, it was found that having a HH nonbonding function for a specific molecule does not necessarily correct the problem. By defining parameters specifically for the HH nonbonding interaction of CH_4, vibrational modes 1, 2, 3, and 6 to 9 (Table 3) were fit to the RHF/6−31G(d) values to within 5 cm^{-1}. However, vibrational modes 4 and 5 were underestimated by 942 cm^{-1}. This suggests, that in order to fit all the vibrational frequencies of a molecule, modification of the functional form of at least the HH nonbonding interaction is required.

In the SEST model, lone pairs have their own coordinates, and therefore they also have vibrational frequencies. A mass of 0.0001 amu is assigned to the lone pairs in frequency calculations, which keeps the lone pair modes distinguishable and uncoupled from the real modes. With the exception of an out-of-plane bend, lone pair vibrational mode of HF, $\nu_{lp} = 5.7 \times 10^4$ cm^{-1}, the lone pair vibrational modes are 4 to 5 orders of magnitude larger than the real modes.

4.2. Ethane. It is essential that any modeling approach, which is intended for large systems, accurately describes carbon−carbon (CC) bonds. SEST can model the RHF/6−31G(d) equilibrium structure of ethane and the dissociation of the CC bond to $2CH_3$, UHF/6−31G(d) (see Figure 12).

The SEST model of ethane is constructed using newly defined CC bond and CH nonbonding functions, along with the previously defined HH nonbonding function and a modified CH bond function, from methane. The CH bond function of the SEST model of methane contains two nonzero parameters, $r^{ee}_{CiHj} = 1.29131654$ bohr and $r^{Ne}_{HCi} = 0.86020816$ bohr. In order to fit the equilibrium geometry of ethane the CH bond function is slightly modified, the value of a third parameter, r^{Ne}_{CHi}, is adjusted from 0 to −0.04518330 bohr. Such an approach could be applied to the construction of a SEST force field. The parameters defined through modeling the first-row hydrides could be considered starting points for models of CH bonds, OH bonds, etc. Especially in the case of hydrocarbons, parameters can be defined for small aliphatic systems, and as they are extended the parameters are adjusted to some limiting, *ideal* value.

From the CC bond dissociation curve (Figure 12), it is seen that it is similar to that of the hydrides. Besides fitting the equilibrium geometry and qualitatively dissociating the CC bond correctly, the SEST model fits the rigid rotation about the CC bond in ethane. The same HH nonbonding function (same parameters) which is used for the first-row hydrides is used in the ethane model, which reproduces the potential energy curve for the rigid rotation about the CC bond at RHF/6−31G(d) exactly (Figure 13).

As a consequence, the vibrational mode which involves rotation about the CC bond, that has a value of 335 cm^{-1} at RHF/6−31G(d), has a value of 326 cm^{-1} for the SEST model. Also, through adjustment of CC bond parameters, the CC bond stretch vibrational mode, 1063 cm^{-1} at RHF/6−31G(d), is fit exactly. The differences between SEST and RHF for the other vibrational frequencies range from 10 cm^{-1} to 1000 cm^{-1}. The fitting of all such vibrational frequencies requires more investigation and experimentation with parameters, and possibly functional forms.

5. Conclusions

It is indeed possible to implement a model of the electronic structure of a molecule that depends solely on atomic distances. It is shown that Simulated Electronic Structure Theory can accurately model MO energy components of equilibrium structures as well as the dissociation of bonds while providing an approximation of the MO energy components along the potential energy surface. In this study the kinetic energy of the electrons is neglected to simplify the energy expression. However, the inclusion of the kinetic energy is quite feasible and would likely lead to similar results. Also, the model in this study fits the RHF/6−31G(d) equilibrium energies and geometries exactly and the UHF/6−31G(d) energy of the products of bond dissociation, multiplied by the factor $(c_v-1)/c_v$. The motivation for defining parameters from these levels of theory is due to availability and how quickly results can be obtained. More accurate SEST models could be obtained through use of higher levels of theory, GVB, Configuration Interaction, etc. It is also not necessary to define parameters from *ab initio* calculations; parameters may be empirically defined to fit experimental data. How parameters are defined will likely be determined by the intended use of the model.

It was seen that while this formulation of SEST fits the equilibrium structures and energies and dissociation energies, it only fits some of the HF vibrational frequencies. The design of a SEST version that accurately predicts all the vibrational frequencies of molecules may be possible. However, the SEST version presented in this study, the parameters and the functional form, will not predict all the vibrational frequencies of most molecules. It is suggested that the use of a modified functional form may solve this problem, especially in the case of nonbonding functions. An in-depth investigation of the dependence of the vibrational frequencies on functional form is required.

Further work is also required on the generation of a SEST force field. The advantage of a theory in which parameters are derived from *ab initio* calculations is the ability to automate the generation of a force field. The wave functions of a test set of molecules could be used to determine the parameters of bonding and nonbonding functions, according to a standard energy partitioning scheme and through fitting of the equilibrium structures and vibrational frequencies.

Finally, the most important aspect of the SEST approach is the explicit inclusion of the electrons. A molecular modeling theory which includes electronic structure has significant

advantages over existing molecular mechanics methods. While this study showed that the relative positions of electrons and nuclei are related to atomic distances and consequently the MO energy components, there are other properties related to the average interparticle distances. Similar to how the energy is related to the molecular structure, electronic properties such as dipole moment could also be modeled. Of course, as seen in this study, the inclusion of electrons allows for the breaking and forming of bonds and hence a theory that may be used to study kinetics. A simulated electronic structure theory creates many possibilities, and much future work is required to explore them all.

References

(1) Coluci, V. R.; Dantas, S. O.; Jorio, A.; Galvao, D. S. *Phys. Rev. B* **2007**, *75*, 075417.

(2) Boas, F. E.; Harbury, P. B. *J. Mol. Biol.* **2008**, *380*, 415–424.

(3) Bowen, J. P.; Allinger, N. L. *Reviews in Computational Chemistry, Molecular Mechanics: The Art and Science of Parameterization*; Lipkowitz, K. B., Boyd, D. B., Eds.; VCH Publishers, Inc.: New York, NY, 1991; Vol. 2, pp 81−97.

(4) Warshel, A.; Levitt, M. *J. Mol. Biol.* **1976**, *103*, 227–249.

(5) Amara, P.; Field, M. J. *Combined Quantum Mechanical and Molecular Mechanical Potentials, Encyclopedia of Computational Chemistry*, 2nd ed.; Kollman, P., Allinger, N., Eds.; Wiley: New York, 1998; Vol. 1, pp 431−436.

(6) Andrews, D. H. *Phys. Rev.* **1930**, *36*, 544–554.

(7) Hollett, J. W.; Poirier, R. A. *J. Theor. Comput. Chem.* **2007**, *6*, 13–22.

(8) Hollett, J. W.; Poirier, R. A. *J. Mol. Model.* **2008**, in press.

(9) Epstein, I. R. *J. Chem. Phys.* **1970**, *53*, 4425–4436.

(10) Garmer, D. R.; Stevens, W. J. *J. Phys. Chem.* **1989**, *93*, 8263–8270.

(11) Liu, S.; Pérez-Jordá, J. M.; Yang, W. *J. Chem. Phys.* **2000**, *112*, 1634–1644.

(12) Li, W.; Li, S. *J. Chem. Phys.* **2005**, *122*, 194109.

(13) Genoni, A.; Sironi, M. *Theo. Chem. Acc.* **2004**, *112*, 254–262.

(14) Poirier, R. A.; Hollett, J. W. *MUNgauss (Fortran 90 version)*; Chemistry Department, Memorial University of Newfoundland, St. John's, NL A1B 3X7. With contributions from S. D. Bungay, A. El-Sherbiny, T. Gosse, D. Keefe, A. Kelly, C. C. Pye, D. Reid, M. Shaw, Y. Wang, J. Xidos.

(15) Boys, S. F. *Quantum Theory of Atoms, Molecules and the Solid State*; Löwdin, P. O., Ed.; Academic Press: New York, 1966; pp 263−280.

CT800433R

JCTC Journal of Chemical Theory and Computation

Electronic Structure Calculations under Periodic Boundary Conditions Based on the Gaussian and Fourier Transform (GFT) Method

Tomomi Shimazaki* and Yoshihiro Asai

National Institute of Advanced Industrial Science and Technology (AIST), Umezono 1-1-1, Tsukuba Central 2, Tsukuba, Ibaraki 305-8568, Japan

Received August 12, 2008

Abstract: We developed the Gaussian and Fourier transform method for crystalline systems. In this method, the Hartree (Coulomb) term of valence electron contribution is taken into account by solving the Poisson equation based on Fourier transform technique. We compared the band structures obtained by the Hartee-Fock (HF) approximation and the density functional theory (DFT). We used three different types of density functional approximations such as the local density approximation (LDA), generalized gradient approximation (GGA), and hybrid density functional. In this paper, we confirm that our calculation technique yields similar results to previous studies.

I. Introduction

The crystal orbital (CO) method based on the Gaussian basis set has been developed for first-principle calculations under the periodic boundary condition (PBC),[1−9] where the direct lattice sum of the Hartree term is the most time-consuming part of the calculation due to the slow decay of the Coulomb potential. The cutoff technique[10] and the fast multipole method (FMM)[5,11−14] have been used for resolving this problem. In this paper, we employ the Fourier transform for calculating the Hartree term. The Fourier transform technique provides an exact solution for the Hartree term under the periodic boundary conditions, and therefore this feature is a major advantage for band calculations in crystalline systems. In our technique, the direct lattice sum calculation based on the Gaussian basis set is used for determining the "core" Hartree (Coulomb) term employed to describe the core electrons. We also discuss the effective core potential (ECP) technique for the "core" term in this paper. On the other hand, the electron density of the valence electrons is represented by the auxiliary plane wave basis set, and the Poisson equation is solved by using the Fourier transform (FT) in order to obtain the "valence" Hartree (Coulomb) term. Therefore, we refer to our technique as the Gaussian and Fourier Transform (GFT) method in this paper. It should be noted that while the GFT method is similar to previous studies, its details are different. For example, Lippert et al. reported the Gaussian and augmented plane wave (GAPW) method,[15,16] in which both the Gaussian function and the plane wave are used as representations of the valence electron density, and the core electrons are eliminated by introducing atomic pseudopotentials. Moreover, Krack et al. extended the GAPW method to all-electron calculations.[17] The GPW method, which is a sister version of the GAPW method, was reported by VandeVondele et al.,[18] and Füsti-Molnár et al. adopted an the auxiliary plane wave technique in the Fourier transform Coulomb (FTC) method.[19] In addition, Kurashige et al. reported the adaptive density portioning technique (ADPT) for efficient Fourier transform calculations.[20] Other techniques for large molecular systems have been reported.[21−24] On the other hand, Wieferink et al. employed the Gaussian function and the Fourier transform in order to obtain the k-dependent energy band structure,[25,26] and some applications have been reported.[27,28] While they used pseudopotentials, in this paper we show not only the use of effective core potential but also an explicit treatment of core electrons. In the following section, we explain the details of the GFT method. In Section III, we show the energy band structure of diamond obtained with our method and compare those results with previous studies, and a summary is presented in Section V.

* Corresponding author e-mail: t-shimazaki@aist.go.jp.

10.1021/ct800329m CCC: $40.75 © 2009 American Chemical Society
Published on Web 11/25/2008

II. Theory

A. Gaussian and Fourier Transform (GFT) Method. In this section, we explain the GFT method for crystalline systems. The Bloch function (crystal orbital) is defined as the linear combination of atomic orbitals (LCAO) expansion as follows[1,2]

$$b_j^{\mathbf{k}}(\mathbf{r}) = \frac{1}{\sqrt{K}} \sum_{\alpha}^{M} \sum_{\mathbf{Q}}^{K} \exp(i\mathbf{k}\cdot\mathbf{Q}) d_{\alpha,j}^{\mathbf{k}}(\mathbf{k}) \chi_{\alpha}^{\mathbf{Q}} \tag{1}$$

where $\mathbf{Q}$ is the translation vector. The total number of cells is $K = K_1K_2K_3$, where K_1, K_2, and K_3 are the number of cells in the direction of each crystal axis, and $\mathbf{k}$ is the wave vector. $\chi_{\alpha}^{\mathbf{Q}} = \chi_{\alpha}(\mathbf{r} - \mathbf{Q} - \mathbf{r}_{\alpha})$ is the α-th atomic orbital (AO), whose center is displaced from the origin of the unit cell at $\mathbf{Q}$ by $\mathbf{r}_{\alpha}$. In this paper, we use Greek letters to indicate the indexes of the atomic orbitals. $d_{\alpha,j}^{\mathbf{k}}$ is the LCAO coefficient, which is obtained from the following Schrödinger equation, and j is the suffix for the molecular orbital (MO).

$$\mathbf{h}(\mathbf{k})\mathbf{d}_j^{\mathbf{k}} = \lambda_j^{\mathbf{k}} \mathbf{S}(\mathbf{k})\mathbf{d}_j^{\mathbf{k}} \tag{2-1}$$

$$\mathbf{d}_j^{\mathbf{k}} = (d_{1,j}^{\mathbf{k}} \quad d_{2,j}^{\mathbf{k}} \quad \cdots \quad d_{\alpha,j}^{\mathbf{k}} \quad \cdots \quad d_{M,j}^{\mathbf{k}})^T \tag{2-2}$$

$$\mathbf{h}(\mathbf{k}) = \sum_{\mathbf{Q}}^{K} \exp(i\mathbf{k}\cdot\mathbf{Q})\mathbf{h}(\mathbf{Q}) \tag{2-3}$$

$$\mathbf{S}(\mathbf{k}) = \sum_{\mathbf{Q}}^{K} \exp(i\mathbf{k}\cdot\mathbf{Q})\mathbf{S}(\mathbf{Q}) \tag{2-4}$$

$$\mathbf{d}_j^{\mathbf{k}*T}\mathbf{S}(\mathbf{k})\mathbf{d}_{j'}^{\mathbf{k}} = \delta_{j,j'} \tag{2-5}$$

Here, the Hamiltonian and the overlap matrices are given by $[\mathbf{h}(\mathbf{Q})]_{\alpha\beta} = \langle \chi_{\alpha}^{\mathbf{Q}_1} | \hat{h} | \chi_{\beta}^{\mathbf{Q}_2} \rangle$ and $[\mathbf{S}(\mathbf{Q})]_{\alpha\beta} = \langle \chi_{\alpha}^{\mathbf{Q}_1} | \chi_{\beta}^{\mathbf{Q}_2} \rangle$, respectively. $\hat{h}$ is the one-electron Hamiltonian operator, and $\mathbf{Q} = \mathbf{Q}_2 - \mathbf{Q}_1$. The Bloch functions satisfy the following orthonormal relation, $\langle b_{j'}^{\mathbf{k}'}(\mathbf{r}) | b_j^{\mathbf{k}}(\mathbf{r}) \rangle = \delta_{\mathbf{k}',\mathbf{k}}\delta_{j',j}$.

The one-electron Hamiltonian matrix is composed of the following terms.

$$\mathbf{h}(\mathbf{Q}) = \mathbf{T}(\mathbf{Q}) + \mathbf{V}_{NA}(\mathbf{Q}) + \mathbf{V}_{Hartree}(\mathbf{Q}) + \mathbf{V}_{XC}(\mathbf{Q}) \tag{3}$$

Here, $\mathbf{T}(\mathbf{Q})$ represents the kinetic term, whose matrix element is obtained from $[\mathbf{T}(\mathbf{Q})]_{\alpha\beta} = \langle \chi_{\alpha}^{\mathbf{0}} | -(1/2)\nabla^2 | \chi_{\beta}^{\mathbf{Q}} \rangle$. $\mathbf{V}_{NA}(\mathbf{Q})$ is the nuclear attraction term, $\mathbf{V}_{Hartree}(\mathbf{Q})$ is the Hartree term, and $\mathbf{V}_{XC}(\mathbf{Q})$ is the exchange correlation term. In this paper, we divided $\mathbf{V}_{NA}(\mathbf{Q}) + \mathbf{V}_{Hartree}(\mathbf{Q})$ into core and valence contributions as follows.

$$\mathbf{V}_{NA}(\mathbf{Q}) + \mathbf{V}_{Hartree}(\mathbf{Q}) = \mathbf{V}_{NA}^{core}(\mathbf{Q}) + \mathbf{V}_{Hartree}^{core}(\mathbf{Q}) + \mathbf{V}_{SR-NA}^{valence}(\mathbf{Q}) + \mathbf{V}_{LR-NA}^{valence}(\mathbf{Q}) + \mathbf{V}_{Hartree}^{valence}(\mathbf{Q}) \tag{4}$$

The above equation is obtained by simply dividing the terms into core and valence contributions, where $\mathbf{V}_{NA}^{core}(\mathbf{Q})$ and $\mathbf{V}_{Hartree}^{core}(\mathbf{Q})$ are the nuclear attraction and Hartree terms for the core contribution, respectively. $\mathbf{V}_{SR-NA}^{valence}(\mathbf{Q})$ and $\mathbf{V}_{LR-NA}^{valence}(\mathbf{Q})$ are the short-range (SR) and long-range (LR) nuclear attraction terms, respectively, for the valence contribution. $\mathbf{V}_{Hartree}^{valence}(\mathbf{Q})$ is the Hartree term for the valence contribution. We will discuss the details of these terms later. The division into core and valence contributions is an essential concept in the GFT method. In this method, two different techniques are adopted for calculating the Coulomb interactions. The electron−electron and electron−nuclear interactions of the core contribution are directly determined based on the conventional quantum chemical (direct lattice sum) calculations. We will discuss the GFT method together with the effective core potential (ECP) in the next section. On the other hand, the interactions of valence contribution are considered by using the Poisson equation and the Fourier transform. The core electrons are strongly localized, and the direct lattice sum calculation is therefore more suitable. If we apply the Fourier transform to the core contribution, many plane waves are required. On the other hand, the lattice sum calculation for the valence contribution requires excessively long CPU times due to the long-range behavior of the Coulomb interactions. Therefore, the Fourier transform approach is more efficient for valence contribution, whereas the GFT method gives the exact solution for long-range Coulomb interactions. In other words, each of these two different techniques compensates for disadvantages of the other one.

In order to divide the terms into core and valence contributions, we introduce the following core and valence electron densities.

$$\rho(\mathbf{r}) = \sum_{\alpha}\sum_{\beta}\sum_{\mathbf{Q}_1,\mathbf{Q}_2} \mathbf{D}_{\alpha\beta}(\mathbf{Q}_2 - \mathbf{Q}_1)\chi_{\beta}^{\mathbf{Q}_2}(\mathbf{r})\chi_{\alpha}^{\mathbf{Q}_1}(\mathbf{r}) = \sum_{\alpha}\sum_{\beta}\sum_{\mathbf{Q}_1,\mathbf{Q}_3} \mathbf{D}_{\alpha\beta}(\mathbf{Q}_3)\chi_{\alpha}^{\mathbf{Q}_1}(\mathbf{r})\chi_{\beta}^{\mathbf{Q}_1+\mathbf{Q}_3}(\mathbf{r}) = \rho^{core}(\mathbf{r}) + \rho^{valence}(\mathbf{r}) \tag{5-1}$$

$$\rho^{core}(\mathbf{r}) = \sum_{\alpha}^{core}\sum_{\beta}^{core}\sum_{\mathbf{Q}_1,\mathbf{Q}_3} \mathbf{D}_{a\beta}(\mathbf{Q}_3)\chi_{\alpha}^{\mathbf{Q}_1}(\mathbf{r})\chi_{\beta}^{\mathbf{Q}_1+\mathbf{Q}_3}(\mathbf{r}) + \sum_{\alpha}^{core}\sum_{\beta}^{valence}\sum_{\mathbf{Q}_1,\mathbf{Q}_3} \mathbf{D}_{a\beta}(\mathbf{Q}_3)\chi_{\alpha}^{\mathbf{Q}_1}(\mathbf{r})\chi_{\beta}^{\mathbf{Q}_1+\mathbf{Q}_3}(\mathbf{r}) + \sum_{\alpha}^{valence}\sum_{\beta}^{core}\sum_{\mathbf{Q}_1,\mathbf{Q}_3} \mathbf{D}_{a\beta}(\mathbf{Q}_3)\chi_{\alpha}^{\mathbf{Q}_1}(\mathbf{r})\chi_{\beta}^{\mathbf{Q}_1+\mathbf{Q}_3}(\mathbf{r}) \tag{5-2}$$

$$\rho^{valence}(\mathbf{r}) = \sum_{\alpha}^{valence}\sum_{\beta}^{valence}\sum_{\mathbf{Q}_1,\mathbf{Q}_3} \mathbf{D}_{\alpha\beta}(\mathbf{Q}_3)\chi_{\alpha}^{\mathbf{Q}_1}(\mathbf{r})\chi_{\beta}^{\mathbf{Q}_1+\mathbf{Q}_3}(\mathbf{r}) \tag{5-3}$$

Here, $\rho(\mathbf{r})$ is the total electron density, and $\rho^{core}(\mathbf{r})$ and $\rho^{valence}(\mathbf{r})$ are the core and valence electron densities, respectively. The density matrix is obtained from the following equation

$$\mathbf{D}_{\alpha\beta}(\mathbf{Q}) = \frac{1}{K}\sum_{\mathbf{k}}\sum_{j} f_{FD}(E_F - \lambda_j^{\mathbf{k}}) d_{\alpha,j}^{\mathbf{k}*} d_{\beta,j}^{\mathbf{k}} \exp(i\mathbf{k}\cdot\mathbf{Q}) \tag{6}$$

where $f_{FD}(E_F - \lambda_j^{\mathbf{k}})$ and E_F are the Fermi-Dirac distribution function and the Fermi energy, respectively. The Hartree potential is divided into core and valence contributions on the basis of eqs (5-1), (5-2), and (5-3) as follows.

$$V_{Hartree}(\mathbf{r}) = \int \frac{\rho(\mathbf{r}')}{|\mathbf{r} - \mathbf{r}'|} d\mathbf{r}' = \int \frac{\rho^{core}(\mathbf{r}')}{|\mathbf{r} - \mathbf{r}'|} d\mathbf{r}' + \int \frac{\rho^{valence}(\mathbf{r}')}{|\mathbf{r} - \mathbf{r}'|} d\mathbf{r}' \equiv V_{Hartree}^{core}(\mathbf{r}) + V_{Hartree}^{valence}(\mathbf{r}) \tag{7}$$

The "core" Hartree term for crystalline systems is determined from the "core" contribution of the density matrix as follows

$$[\mathbf{V}_{Hartree}^{core}(\mathbf{Q})]_{\alpha\beta} = \langle\chi_\alpha^{\mathbf{0}}|V_{Hartree}^{core}|\chi_\beta^{\mathbf{Q}}\rangle = \sum_\gamma^{core}\sum_\delta^{core}\sum_{\mathbf{Q}_1,\mathbf{Q}_2}\mathbf{D}_{\gamma\delta}(\mathbf{Q}_1-\mathbf{Q}_2)\langle\chi_\alpha^{\mathbf{0}}\chi_\gamma^{\mathbf{Q}_1}|\chi_\beta^{\mathbf{Q}}\chi_\delta^{\mathbf{Q}_2}\rangle + \sum_\gamma^{core}\sum_\delta^{valence}\sum_{\mathbf{Q}_1,\mathbf{Q}_2}\mathbf{D}_{\gamma\delta}(\mathbf{Q}_1-\mathbf{Q}_2)\langle\chi_\alpha^{\mathbf{0}}\chi_\gamma^{\mathbf{Q}_1}|\chi_\beta^{\mathbf{Q}}\chi_\delta^{\mathbf{Q}_2}\rangle + \sum_\gamma^{valence}\sum_\delta^{core}\sum_{\mathbf{Q}_1,\mathbf{Q}_2}\mathbf{D}_{\gamma\delta}(\mathbf{Q}_1-\mathbf{Q}_2)\langle\chi_\alpha^{\mathbf{0}}\chi_\gamma^{\mathbf{Q}_1}|\chi_\beta^{\mathbf{Q}}\chi_\delta^{\mathbf{Q}_2}\rangle \quad (8\text{-}1)$$

$$\langle\chi_\alpha^{\mathbf{0}}\chi_\gamma^{\mathbf{Q}_1}|\chi_\beta^{\mathbf{Q}}\chi_\delta^{\mathbf{Q}_2}\rangle = \int\int\chi_\alpha^{\mathbf{0}}(\mathbf{r}_1)\chi_\beta^{\mathbf{Q}}(\mathbf{r}_1)\frac{1}{r_{12}}\chi_\gamma^{\mathbf{Q}_1}(\mathbf{r}_2)\chi_\delta^{\mathbf{Q}_2}(\mathbf{r}_2)d\mathbf{r}_1d\mathbf{r}_2 \quad (8\text{-}2)$$

where $r_{12} = |\mathbf{r}_1 - \mathbf{r}_2|$. The lattice sum over a small number of sites is required since the core electrons are strongly localized around the center of the nucleus and their charges are thus perfectly compensated by the core nuclear charges. We will discuss the "valence" Hartree term later. The nuclear attractive potential is also divided into core and valence contributions as follows.

$$V_{NA}(\mathbf{r}) = \sum_A\frac{Z_A}{|\mathbf{r}-\mathbf{R}_A|} = \sum_A\frac{Z_A^{core}}{|\mathbf{r}-\mathbf{R}_A|} + \sum_A\frac{Z_A^{valence}}{|\mathbf{r}-\mathbf{R}_A|} \equiv V_{NA}^{core}(\mathbf{r}) + V_{NA}^{valence}(\mathbf{r}) \quad (9)$$

Here, Z_A is the nuclear charge for atom number A. The "core" nuclear charge Z_A^{core} is defined as follows.

$$Z_A^{core} = \sum_{\alpha\in A}^{core}\sum_\beta^{core}\sum_{\mathbf{Q}}\mathbf{D}_{a\beta}(\mathbf{Q})\mathbf{S}_{\beta a}(\mathbf{Q}) + \sum_{\alpha\in A}^{core}\sum_\beta^{valence}\sum_{\mathbf{Q}}\mathbf{D}_{a\beta}(\mathbf{Q})\mathbf{S}_{\beta a}(\mathbf{Q}) + \sum_{\alpha\in A}^{valence}\sum_\beta^{core}\sum_{\mathbf{Q}}\mathbf{D}_{a\beta}(\mathbf{Q})\mathbf{S}_{\beta a}(\mathbf{Q}) \quad (10)$$

The remaining charge is assigned as the "valence" nuclear charge $Z_A^{valence}$ as follows.

$$Z_A^{valence} = Z_A - Z_A^{core} \quad (11)$$

The "core" nuclear attraction term is obtained as follows.

$$[\mathbf{V}_{NA}^{core}(\mathbf{Q})]_{\alpha\beta} = -\langle\chi_\alpha^{\mathbf{0}}|V_{NA}^{core}|\chi_\beta^{\mathbf{Q}}\rangle = -\langle\chi_\alpha^{\mathbf{0}}|\sum_A\frac{Z_A^{core}}{|\mathbf{r}-\mathbf{R}_A|}|\chi_\beta^{\mathbf{Q}}\rangle \quad (12)$$

Note that the "core" and "valence" nuclear charges are renewed in each self-consistent field (SCF) cycle.

Next, we discuss the "valence" contribution of the nuclear attraction and the Hartree terms. In the GFT method, the "valence" nuclear attractive potential is divided into short-range (SL) and long-range (LR) contributions, where $V_{NA}^{valence} = V_{SR-NA}^{valence} + V_{LR-NA}^{valence}$. For that purpose, we adopt the following error function (erf) and complementary error function (erfc).

$$\frac{1}{r} = \frac{erf(wr)}{r} + \frac{erfc(wr)}{r} \quad (13\text{-}1)$$

$$erf(wr) = \int_0^{wr}\exp(-t^2)dt \quad (13\text{-}2)$$

The short-range (SR) "valence" nuclear attraction term is determined from the complementary error function (erfc) and the "valence" nuclear charges $Z_A^{valence}$ as follows.

$$[\mathbf{V}_{SR-NA}^{valence}(\mathbf{Q})]_{\alpha\beta} = -\langle\chi_\alpha^{\mathbf{0}}|V_{SR-NA}^{valence}|\chi_\beta^{\mathbf{Q}}\rangle = -\langle\chi_\alpha^{\mathbf{0}}|\sum_A\frac{Z_A^{valence}erfc(\sqrt{\eta}|\mathbf{r}-\mathbf{R}_A|)}{|\mathbf{r}-\mathbf{R}_A|}|\chi_\beta^{\mathbf{Q}}\rangle \quad (14)$$

It is also necessary to calculate the long-range (LR) nuclear attraction term corresponding to the valence nuclear charge, which is given by the error function, $Z_A^{valence}erf(\eta^{1/2}|\mathbf{r}-\mathbf{R}_A|)/|\mathbf{r}-\mathbf{R}_A|$. The term is considered together with the "valence" Hartree term, as seen below. The sum of the "valence" Hartree and the long-range "valence" nuclear attraction terms, i.e., $\mathbf{V}_{LR-NA}^{valence}(\mathbf{Q})+\mathbf{V}_{Hartree}^{valence}(\mathbf{Q})$, is obtained from the following Poisson equation.

$$[\mathbf{V}_{Hartree}^{valence}(\mathbf{Q}) + \mathbf{V}_{LR-NA}^{valence}(\mathbf{Q})]_{\alpha\beta} = \langle\chi_\alpha^{\mathbf{0}}|V_{Hartree}^{valence} + V_{LR-NA}^{valence}|\chi_\beta^{\mathbf{Q}}\rangle = \langle\chi_\alpha^{\mathbf{0}}|V_{PE}(\mathbf{r})|\chi_\beta^{\mathbf{Q}}\rangle = [\mathbf{V}_{PE}(\mathbf{Q})]_{\alpha\beta} \quad (15\text{-}1)$$

$$\nabla^2V_{PE}(\mathbf{r}) = -4\pi\left[-\rho^{valence}(\mathbf{r}) + \sum_A Z_A^{valence}\left(\frac{\eta}{\pi}\right)^{\frac{3}{2}}\times\exp(-\eta|\mathbf{r}-\mathbf{R}_A|^2)\right] \equiv -4\pi\rho_{Total}^{valence}(\mathbf{r}) \quad (15\text{-}2)$$

The first term in eq (15-2) corresponds to the valence electrons, and the second term corresponds to the valence nuclear charges. In order to obtain these equations, we used the relation, $-\nabla^2(erf(\eta^{1/2}r)/r) = 4\pi(\eta/\pi)^{3/2}\exp(-\eta r^2)$.

In the Hartree−Fock approximation, the Fock exchange term $\mathbf{V}_X(\mathbf{Q})$ is obtained as follows.

$$[\mathbf{V}_X^{Fock}(\mathbf{Q})]_{\alpha\beta} = -\sum_\gamma\sum_\delta\sum_{\mathbf{Q}_1,\mathbf{Q}_2}\mathbf{D}_{\gamma\delta}(\mathbf{Q}_1-\mathbf{Q}_2)\langle\chi_\alpha^{\mathbf{0}}\chi_\beta^{\mathbf{Q}}|\chi_\gamma^{\mathbf{Q}_1}\chi_\delta^{\mathbf{Q}_2}\rangle \quad (16)$$

It should be noted that the determination of the Fock exchange term may be the most time-consuming part when we employ a fast evaluation technique for the Hartree term, such as the Fourier transform method and the fast multipole method (FMM). Although Izmaylov et al. tackled this problem and proposed an efficient evaluation technique of short-range Fock exchange term,[7] we simply estimate the Fock exchange term by truncating the sum of eq (16) in this paper.

B. Effective Core Potential (ECP). When we employ the effective core potential (ECP) together with the GFT method, the core electron density, $\rho^{core}(\mathbf{r})$, and nuclear charges, Z_A^{core}, become zero, and the ECP term, $\mathbf{V}_{ECP}$, is replaced instead of $\mathbf{V}_{Hartree}^{core} + \mathbf{V}_{NA}^{core}$ as follows.

$$\mathbf{h}(\mathbf{Q}) = \mathbf{T}(\mathbf{Q}) + \mathbf{V}_{ECP}(\mathbf{Q}) + \mathbf{V}_{NA-SR}^{valence}(\mathbf{Q}) + \mathbf{V}_{NA-LR}^{valence}(\mathbf{Q}) + \mathbf{V}_{Hartree}^{valence}(\mathbf{Q}) + \mathbf{V}_{XC}(\mathbf{Q}) \quad (17)$$

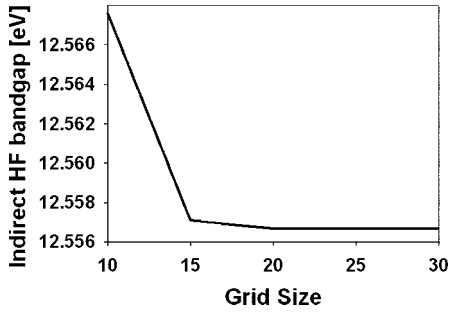

Figure 1. Changes of the indirect HF energy band gap with respect to the FFT grid size. The number of horizontal axis indicates the $N \times N \times N$ FFT grid. In this paper, we employ the $25 \times 25 \times 25$ FFT grid, and therefore we can confirm its numerical accuracy.

Table 1. Comparison of Calculated Direct and Indirect Bandgaps of Diamond Based on GFT Methods and Experimental Data

bandgap	HF	SVWN	BLYP	B3LYP	exp
direct [eV]	14.6	5.9	5.7	7.4	7.3
indirect [eV]	12.6	4.2	4.4	6.0	5.48

The total energy per unit cell is obtained as follows.

$$E_{cell} = \sum_{\mathbf{Q}} Tr[\mathbf{D}(\mathbf{Q})\{\mathbf{T}(\mathbf{Q}) + \mathbf{V}_{ECP}(\mathbf{Q})\}] + \frac{2\pi}{N_{FT}^2 V_{cell}} \sum_{(\mathbf{G}\neq\mathbf{0})} \frac{|\rho^{valence}(\mathbf{G})|^2}{G^2} - \frac{4\pi}{N_{FT}} \sum_{A}^{cell} \sum_{(\mathbf{G}\neq\mathbf{0})} \frac{Z_A^{valence}\rho^{valence}(\mathbf{G})}{G^2} \exp(i\mathbf{G}\cdot\mathbf{R}_A) + \frac{2\pi}{V_{cell}} \sum_{A}^{cell}\sum_{A'}^{cell} \sum_{(\mathbf{G}\neq\mathbf{0})} \frac{Z_A^{valence} Z_{A'}^{valence}}{G^2} \exp\left(-\frac{G^2}{4\eta} + i\mathbf{G}\cdot\mathbf{R}_A\right) + \sum_{A}^{cell}\sum_{A'}^{cell} \sum_{(\mathbf{R}_A-\mathbf{R}_{A'}-\mathbf{Q}\neq\mathbf{0})} \frac{Z_A^{valence} Z_{A'}^{valence} erfc(\sqrt{\eta}|\mathbf{R}_A - \mathbf{R}_{A'} - \mathbf{Q}|)}{|\mathbf{R}_A - \mathbf{R}_{A'} - \mathbf{Q}|} - \left[\sum_{A}^{cell} (Z_A^{valence})^2\right]\sqrt{\frac{\eta}{\pi}} - \frac{1}{2}\left[\sum_{A}^{cell} Z_A^{valence}\right]^2 \frac{\pi}{\eta V_{cell}} + E_{XC} \quad (18)$$

Here, $\mathbf{G}$ is the reciprocal lattice vector. E_{XC} is the unit cell exchange-correlation energy, which is written as $E_{XC} = 0.5\sum_{\mathbf{Q}} Tr[\mathbf{D}(\mathbf{Q})\mathbf{V}_X^{Fock}(\mathbf{Q})]$ in the Hartree−Fock approximation. N_{FT} is the number of grids for the Fourier transform. In this paper, we adopt the Fast Fourier Transform (FFT) algorithm, and thus $\rho^{valence}(\mathbf{G}) = \sum_{\mathbf{r}_g} \rho^{valence}(\mathbf{r}_g) \exp(-i\mathbf{G}\cdot\mathbf{r}_g)$, where $\mathbf{r}_g$ is the grid point.

C. Recursion Relation. We discuss a technique for calculating eq (15-1). $V_{PE}(\mathbf{r})$ is expanded by plane waves by using the Fourier transform in the GFT method.

$$V_{PE}(\mathbf{r}) = \frac{1}{N_{FT}} \sum_{(\mathbf{G}\neq 0)} \frac{v_{PE}(\mathbf{G})}{G^2} \exp(i\mathbf{G}\cdot\mathbf{r}) \quad (19)$$

Here, $v_{PE}(\mathbf{G}) = 4\pi\sum_{\mathbf{r}_g} \rho_{Total}^{valence}(\mathbf{r}_g) \exp(-i\mathbf{G}\cdot\mathbf{r}_g)$ is the Fourier coefficient. Equation (15-1) can be rewritten using the Fourier coefficients as follows.

$$[\mathbf{V}_{Hartree}^{valence}(\mathbf{Q}) + \mathbf{V}_{LR-NA}^{valence}(\mathbf{Q})]_{\alpha\beta} = \frac{1}{N_{FT}} \sum_{(\mathbf{G}\neq 0)} \frac{v_{PE}(\mathbf{G})}{G^2} \langle \chi_\alpha^{\mathbf{0}} | \exp(i\mathbf{G}\cdot\mathbf{r}) | \chi_\beta^{\mathbf{Q}} \rangle \quad (20)$$

In order to calculate eq (20), we use the following recursion relation (cf. Appendix A).

$$\langle \mathbf{a} + \mathbf{1}_\xi | \exp(i\mathbf{G}\cdot\mathbf{r}) | \mathbf{b} \rangle = \left(P_\xi - R_\xi^A + \frac{iG_\xi}{2p}\right)\langle \mathbf{a} | \exp(i\mathbf{G}\cdot\mathbf{r}) | \mathbf{b} \rangle + \frac{1}{2p} N_\xi(\mathbf{a}) \langle \mathbf{a} - \mathbf{1}_\xi | \exp(i\mathbf{G}\cdot\mathbf{r}) | \mathbf{b} \rangle + \frac{1}{2p} N_\xi(\mathbf{b}) \langle \mathbf{a} | \exp(i\mathbf{G}\cdot\mathbf{r}) | \mathbf{b} - \mathbf{1}_\xi \rangle \quad (21\text{-}1)$$

$$\langle \mathbf{0} | \exp(i\mathbf{G}\cdot\mathbf{r}) | \mathbf{0} \rangle = \exp(-\mu|\mathbf{R}_A - \mathbf{R}_B|^2)\left(\frac{\pi}{p}\right)^{\frac{3}{2}} \times \exp\left(-\frac{G^2}{4p}\right)\exp(i\mathbf{G}\cdot\mathbf{P}) \quad (21\text{-}2)$$

$$|\mathbf{a}\rangle = (x - R_x^A)^{a_x}(y - R_y^A)^{a_y}(z - R_z^A)^{a_z} \exp(-g_a|\mathbf{r} - \mathbf{R}_A|^2) \quad (21\text{-}3)$$

$$p = g_a + g_b \quad (21\text{-}4)$$

$$\mu = \frac{g_a g_b}{g_a + g_b} \quad (21\text{-}5)$$

Here, $\mathbf{R}_A = (R_x^A R_y^A R_z^A)$, $\mathbf{a} = (a_x a_y a_z)$, $N_\xi(a) = a_\xi$, and $\mathbf{1}_\xi = (\delta_{x\xi}\delta_{y\xi}\delta_{z\xi})$ utilizing Kronecker's delta. $\mathbf{P} = (g_a\mathbf{R}_A + g_b\mathbf{R}_b)/(g_a + g_b)$. ξ represents one of x, y, or z. This recursion relation is an expansion of the Obara and Saika (OS) technique for atomic orbital (AO) integers. Note that the analytical technique based on this recursion relation provides highly efficient estimations for $\mathbf{V}_{Hartress}^{valence}(\mathbf{Q}) + \mathbf{V}_{LR-NA}^{valence}(\mathbf{Q})$.

We use the standard FFT algorithm, where the scaling is $O(N_{FT}\log N_{FT})$ and the scaling for atomic orbital integrations is $O(M^2 N_{FT})$ when we employ the above recursion relation. The fast multipole method (FFM) with a Gaussian basis set also yields a linear scaling estimation for the Hartree term.[5] In this respect, the GFT method may become an alternative for the FMM to calculate the Hartree term under the periodic boundary condtions. It should be noted that the GFT method cannot rigorously take into account isolated molecular systems because of the periodicity of plane wave.

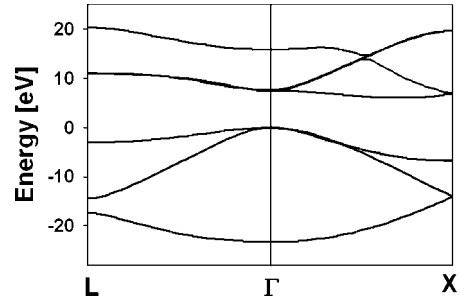

Figure 2. Energy band structure of diamond calculated by using the B3LYP functional.

III. Test Calculations

A. Diamond. In this section, we examine the energy band structure for a cubic bulk diamond on the basis of the GFT method. We have calculated the band energy by using the HF method and some DFT functionals. We employ three different types of DFT functionals such as the local density approximation (LDA), the generalized gradient approximation (GGA), and the hybrid functional. The Slater[29]-Vosko-Wilk-Nusair[30] (SVWN) and Becke[31,32]-Lee-Yang-Parr (BLYP) functionals are adopted for the LDA and the GGA calculations, respectively. We examine the B3LYP functional in the hybrid DFT method,[33] and we use the 6−21G* basis set proposed by Catti et al. for all calculations in this section.[34] Furthermore, we set the lattice constant to 3.57 Å and employ 25 × 25 × 25 k-points and 25 × 25 × 25 mesh grid points for the FFT procedure in order to calculate eq (20). We confirm the validity of the FFT grid size in Figure 1. We also checked the dependence of bandgap value on the truncation conditions. When we take into account the lattice integrals up to third neighboring cells, i.e. (7 × 7 × 7) cells, the value of the diamond's direct bandgap determined with the B3LYP functional is 7.35378 eV. On the other hand, a different truncation, which takes into account the second neighboring cells, yields 7.35358 eV. These calculated bandgap values are enough converged to discuss the property, and thus we employ the truncation condition of third neighboring cells in this paper. It should be noted that the "valence" Coulomb term in the GFT method is exactly determined because of the use of the Fourier transform. The truncation conditions affect only the Fock exchange and "core" Hartree terms.

Table 1 summarizes the direct and indirect (minimum) bandgaps determined by using the HF, SVWN, BLYP, and B3LYP methods. In this paper, the direct bandgap is defined as the eigenvalue energy difference between the top of the valence band and the bottom of the conduction band at $\mathbf{k} = 0$, and the indirect bandgap is the (minimum) energy difference between the top of the valence band and the bottom of the conduction band. We also show the corresponding values obtained from experiments in Table 1 and the B3LYP energy band structure in Figure 2. The SVWN functional underestimates the bandgaps in comparison with the experimental values, which is a well-known problem for LDA. There are no major differences between the LDA (SVWN) and GGA (BLYP) calculations. The GFT-SVWN method yields 5.5 eV for the direct bandgap and 4.2 eV for the indirect (minimum) bandgap. On the other hand, the direct and indirect bandgaps determined with the linear muffin-tin-orbital (LMTO) method are 5.7 and 4.1 eV, respectively.[35] The linear augmented plane wave (LAPW) method yields 5.6 and 4.0 eV for the direct and indirect bandgaps, respectively.[36] The plane-wave basis set calculation yields 5.57 and 3.90 eV for the same bandgaps.[37] From these calculations, we can confirm that the GFT-LDA method yields almost the same values with these calculations. On the other hand, the GFT-HF method overestimates the bandgap, yielding values for the direct and indirect bandgaps of 14.6 and 12.6 eV, respectively. On the other hand, the LMTO-HF method yields 14.6 eV for the direct bandgap and 12.6 eV for the indirect bandgap.[35] The LAPW-HF method yields 14.7 and 12.4 eV for the same values.[36]

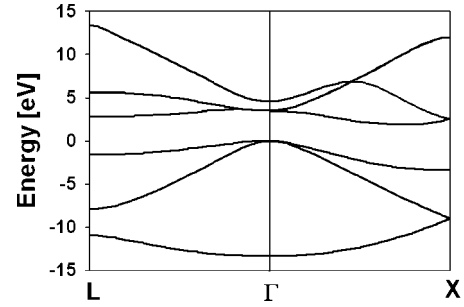

Figure 3. Energy band structure of silicon calculated by using the B3LYP functional.

Table 2. Exponents α (in a.u.) and the Coefficients *c* of the Gaussian Basis Set

	$\alpha_{s,p}$	c_s	c_p		α_d	c_d
			Si			
SP	1.10	−0.40	0.70	D	0.65	1.00
	0.30	1.00	1.00			
SP	0.18	1.00	1.00			
			Ga			
SP	0.90	−0.30	0.60	D	0.55	1.00
	0.19	−0.10	0.50			
SP	0.14	1.00	1.00			
			As			
SP	1.10	−0.40	0.70	D	0.65	1.00
	0.21	−0.20	0.50			
SP	0.18	1.00	1.00			

The B3LYP functional includes 80% of the Slater local density approximation $\mathbf{V}_X^{Slater}$ and 72% of the Becke88(B88)-type gradient correction $\Delta\mathbf{V}_X^{B88}$. In addition, 20% of the Fock exchange term is mixed into the functional. It was determined by Becke in 1993[33] that three parameters in the B3LYP functional reproduce the properties of molecules and the atoms of the G1 database.[38,39]

$$\mathbf{V}_{XC}^{B3LYP} = 0.8\mathbf{V}_X^{Slater} + 0.72\Delta\mathbf{V}_X^{B88} + 0.2\mathbf{V}_X^{Fock} + \mathbf{V}_C^{B3LYP} \tag{22-1}$$

$$\mathbf{V}_C^{B3LYP} = 0.19\mathbf{V}_C^{VWN} + 0.81\mathbf{V}_C^{LYP} \tag{22-2}$$

Here, $\mathbf{V}_C^{VWN}$ and $\mathbf{V}_C^{LYP}$ are the VWN and LYP correlation terms, respectively. There are only a few studies based on the B3LYP functional for crystalline systems. The direct and indirect bandgaps determined with the GFT-B3LYP method are 7.4 and 6.0 eV, respectively, while the crystal orbital (CO) method with the B3LYP functional yields 5.8 eV for the indirect bandgap.[40] In this regard, the B3LYP functional reproduces the experimental bandgap well. The nonlocal nature of the Fock exchange potential may be essential for reproducing the properties of semiconductors and insulators.

B. Silicon and GaAs. We show calculation results for silicon and GaAs in this section. We employ the effective core potential proposed by Labelo et. al for those calculations.[41,42] The exponents and the contraction coefficients of the atomic orbital for silicon, Ga, and As are summarized in Table 2. We employ 5.43 Å and 5.65 Å as the lattice constants for silicon and GaAs, respectively. The same values used in the previous section are adopted for other calculation parameters, such as k-point sampling and FFT-grid mesh grid points. Figures 3 and 4 show the energy band structure of silicon

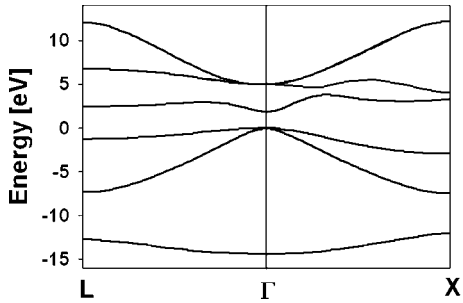

Figure 4. Energy band structure of GaAs calculated by using the B3LYP functional.

Table 3. Comparison of Calculated Direct and Indirect Bandgaps of Silicon Based on GFT Methods and Experimental Data

bandgap	HF	SVWN	BLYP	B3LYP	exp
direct [eV]	8.3	2.2	2.4	3.5	3.4
indirect [eV]	6.4	0.48	0.90	1.9	1.17

Table 4. Comparison of Calculated Direct Bandgap of GaAs Based on GFT Methods and Experimental Data

bandgap	HF	SVWN	BLYP	B3LYP	exp
direct [eV]	6.8	0.84	0.88	1.8	1.63

and GaAs, respectively. These figures are determined by the GFT-B3LYP method. We show the direct and indirect (minimum) bandgaps of silicon determined based on the HF, SVWN, BLYP, and B3LYP methods in Table 3. Table 3 also has experimentally obtained bandgaps. Similarly, we summarize the direct bandgap of GaAs in Table 4, where the direct bandgap of GaAs is the same with the minimum energy difference between the conduction and valence bands. The GFT-SVWN method yields 0.48 eV for the indirect bandgaps of silicon. In comparison, the plane wave (PW) basis set, the LMTO method, and the LAPW method yield 0.45 eV, 0.5 eV, and 0.5 eV for the property, respectively.[35−37] The GFT-HF method yields 6.4 eV for the indirect bandgap, and the LMTO and LAPW methods yield 5.6 and 6.3 eV for the property, respectively.[35,36] On the other hand, the direct bandgap of GaAs is determined as 0.84 eV based on the GFT-SVWN method, and the PW method and the LMTO method yield 0.67 eV and 0.83 eV for the same value, respectively.[43] The LDA(SVWN) and GGA(BLYP) methods underestimate the bandgaps, and the HF method overestimates the property. The tendency is the same current with the diamond's calculations. We also summarize the cohesive energies of silicon and GaAs determined with the SVWN, BLYP, B3LYP, HF methods in Table 5. The calculated values based on the DFT methods are close to the experimentally obtained cohesive energy. From these calculations, we conclude that the GFT method can yield results very similar to those of previous studies.

We have discussed only the B3LYP functional in this paper, but it should be noted that the HSE functional, which possesses a screened exchange term, was successfully applied to various systems.[13,44−47] In addition, Henderson et al. recently reported the middle-range Hartree−Fock-type exchange potential for the HISS functional.[48,49] The importance of the screened exchange term has been addressed through these studies. The screening effect on the exchange term may be essential to improve the description of the electronic structure of molecules and crystalline systems, and a discussion for the screening effect will be found in the literature.[50]

Table 5. Comparison of Calculated Cohesive Energy of Silicon and GaAs Based on GFT Methods and Experimental Data

cohesive energy [eV]	HF	SVWN	BLYP	B3LYP	exp
silicon	4.1	5.8	4.6	4.7	4.63
GaAs	3.1	6.8	4.2	4.5	6.52

VI. Summary

We have discussed the GFT method in relation to crystalline systems under the periodic boundary conditions, and applied this method to the energy band structure calculations for the diamond, silicon, and GaAs. The HF method overestimates the bandgap, while both the LDA(SVWN) and GGA(BLYP) methods underestimate it, although the B3LYP method reproduces the bandgap well in the case of diamond. The result indicates that the hybrid DFT methods, such as B3LYP, are useful for improving the molecular (material) properties of extended systems as well as isolated molecular systems. A discussion of the first-principle calculation studies for other materials on the basis of our technique will be provided elsewhere.

Acknowledgment. The authors would like to thank Prof. So Hirata of the University of Florida and Dr. Shoji Ishibashi of the National Institute of Advanced Industrial Science and Technology (AIST) for discussions on the DFT method.

Appendix A. Recursion Relation

In this Appendix, we derive the recursion relation of eq (22-1). The left term of eq (22-1) is expanded from the Gaussian product rule as follows.

$$\begin{aligned}\langle \mathbf{a}|\exp(i\mathbf{G}\cdot\mathbf{r})|\mathbf{b}\rangle &= \int\int\int (x-R_x^A)^{a_x}(y-R_y^A)^{a_y}(z-R_z^A)^{a_z}\times \\ &\exp(-g_a|\mathbf{r}-\mathbf{R}_A|^2)\times(x-R_x^B)^{b_x}(y-R_y^B)^{b_y}(z-R_z^B)^{b_z}\times \\ &\exp(-g_b|\mathbf{r}-\mathbf{R}_B|^2)\exp(i\mathbf{G}\cdot\mathbf{r})d\mathbf{r} = \exp(-\mu|\mathbf{R}_A-\mathbf{R}_B|^2)\times \\ &\int\int\int (x-R_x^A)^{a_x}(y-R_y^A)^{a_y}(z-R_z^A)^{a_z}(x-R_x^B)^{b_x}(y-R_y^B)^{b_y}\times \\ &(z-R_z^B)^{b_z}\exp(-p|\mathbf{r}-\mathbf{P}|^2)\exp(i\mathbf{G}\cdot\mathbf{r})d\mathbf{r} \\ &= \exp(-\mu|\mathbf{R}_A-\mathbf{R}_B|^2)I_xI_yI_z \quad \text{(A-1)}\end{aligned}$$

Here,

$$\begin{aligned}I_\xi(a_\xi,b_\xi) &= \int_{-\infty}^{\infty}(\xi-R_\xi^A)^{a_\xi}(\xi-R_\xi^B)^{b_\xi}\exp(-p(\xi-P_\xi)^2+iG_\xi\xi)d\xi \\ &= \sum_{\substack{m,n \\ m+n \text{ is even}}}\binom{a_\xi}{m}\binom{b_\xi}{n}\xi^{m+n}\pi\left(P_\xi-R_\xi^A+\frac{iG_\xi}{2p}\right)^{a_\xi-m}\times \\ &\left(P_\xi-R_\xi^B+\frac{iG_\xi}{2p}\right)^{b_\xi-n}(m+n-1)!!\times \\ &\sqrt{\pi/p}\,2^{-(m+n)/2}p^{-(m+n)}\exp\left(-\frac{G_\xi^2}{4p}+iG_\xi P_\xi\right) \\ &\equiv \sum_{\substack{m,n \\ m+n \text{ is even}}}\binom{a_\xi}{m}\binom{b_\xi}{n}L_\xi(a_\xi,b_\xi,m,n) \quad \text{(A-2)}\end{aligned}$$

In order to derive the recursion relation, we use the following first derivation of the equation.

$$\frac{1}{2g_a}\frac{\partial I_\xi(a_\xi,b_\xi)}{\partial R_\xi^A}=\frac{1}{2g_a}\sum_{\substack{m,n\\ m+n \text{ is even}}}\binom{a_\xi}{m}\binom{b_\xi}{n}L_\xi(a_\xi-1,b_\xi,m,n)\times$$
$$(a_\xi-m)\left(\frac{g_a}{p}-1\right)+\frac{1}{2g_a}\sum_{\substack{m,n\\ m+n \text{ is even}}}\binom{a_\xi}{m}\binom{b_\xi}{n}L_\xi(a_\xi,b_\xi-1,m,n)\times$$
$$(b_\xi-n)\frac{g_a}{p}+\frac{1}{2g_a}\frac{iG_\xi g_a}{p}I_\xi(a_\xi,b_\xi)$$
$$=a_\xi\left(\frac{1}{2p}-\frac{1}{2g_a}\right)I_\xi(a_\xi-1,b_\xi)+\frac{b_\xi}{2p}I_\xi(a_\xi,b_\xi-1)+\frac{iG_\xi}{2p}I_\xi(a_\xi,b_\xi) \quad \text{(A-3)}$$

Here, we used the following equation.

$$\binom{a_\xi}{m}(a_\xi-m)=\frac{a_\varsigma(a_\xi-1)\cdots(a_\xi-m+1)}{m(m-1)\cdots 1}(a_\xi-m)$$
$$=a_\xi\binom{a_\xi-1}{m} \quad \text{(A-4)}$$

We obtain the recursion relation from the above equations and $\partial|\mathbf{a}\rangle/\partial R_\xi^A=2g_a|\mathbf{a}+\mathbf{1}_\xi\rangle-N_\xi(\mathbf{a})|\mathbf{a}-\mathbf{1}_\xi\rangle$ as follows.

$$\langle\mathbf{a}+\mathbf{1}_\xi|\exp(i\mathbf{G}\cdot\mathbf{r})|\mathbf{b}\rangle=\frac{1}{2g_a}\frac{\partial}{\partial R_\xi^A}\langle\mathbf{a}|\exp(i\mathbf{G}\cdot\mathbf{r})|\mathbf{b}\rangle$$
$$+\frac{1}{2g_a}N_\xi(\mathbf{a})\langle\mathbf{a}-\mathbf{1}_\xi|\exp(i\mathbf{G}\cdot\mathbf{r})|\mathbf{b}\rangle$$
$$=\frac{-\mu}{g_a}(R_\xi^A-R_\xi^B)\langle\mathbf{a}|\exp(i\mathbf{G}\cdot\mathbf{r})|\mathbf{b}\rangle$$
$$+a_\xi\left(\frac{1}{2p}-\frac{1}{2g_a}\right)\langle\mathbf{a}-\mathbf{1}_\xi|\exp(i\mathbf{G}\cdot\mathbf{r})|\mathbf{b}\rangle+$$
$$\frac{b_\xi}{2p}\langle\mathbf{a}|\exp(i\mathbf{G}\cdot\mathbf{r})|\mathbf{b}-\mathbf{1}_\xi\rangle$$
$$+\frac{iG_\xi}{2p}\langle\mathbf{a}|\exp(i\mathbf{G}\cdot\mathbf{r})|\mathbf{b}\rangle+\frac{1}{2g_a}N_\xi(\mathbf{a})\langle\mathbf{a}-\mathbf{1}_\xi|\exp(i\mathbf{G}\cdot\mathbf{r})|\mathbf{b}\rangle$$
$$=\left(P_\xi-R_\xi^A+\frac{iG_\xi}{2p}\right)\langle\mathbf{a}|\exp(i\mathbf{G}\cdot\mathbf{r})|\mathbf{b}\rangle$$
$$+\frac{1}{2p}N_\xi(\mathbf{a})\langle\mathbf{a}-\mathbf{1}_\xi|\exp(i\mathbf{G}\cdot\mathbf{r})|\mathbf{b}\rangle+$$
$$\frac{1}{2p}N_\xi(\mathbf{b})\langle\mathbf{a}|\exp(i\mathbf{G}\cdot\mathbf{r})|\mathbf{b}-\mathbf{1}_\xi\rangle \quad \text{(A-5)}$$

Here, we used $-(R_\xi^A-R_\xi^B)(\mu/g_a)=P_\xi-R_\xi^A$.

References

(1) Pisani, C.; Dovesi, R.; Roetti, C. *Hartree-Fock Ab Initio Treatment of Crystallline Systems*; Springer-Verlag: Berlin, 1988; pp 32−46.

(2) Ladik, J. J. *Phys. Rep.* **1999**, *313*, 171.

(3) Hirata, S.; Iwata, S. *J. Chem. Phys.* **1997**, *107*, 10075.

(4) Hirata, S.; Head-Gordon, M.; Bartlett, R. J. *J. Chem. Phys.* **1999**, *111*, 10774.

(5) Kudin, K. N.; Scuseria, G. E. *Phys. Rev. B* **2000**, *61*, 16440.

(6) Ayala, P. Y.; Kudin, K. N.; Scuseria, G. E. *J. Phys. Chem.* **2001**, *115*, 9698.

(7) Izmaylov, A. F.; Scuseria, G. E.; Frisch, M. J. *J. Chem. Phys.* **2006**, *125*, 104103.

(8) Maschio, L.; Usvyat, D.; Manby, F. R.; Casassa, S.; Pisani, C.; Schutz, M. *Phy. Rev. B* **2007**, *76*, 075101.

(9) Izmaylov, A. F.; Scuseria, G. E. *Phys. Chem. Chem. Phys.* **2008**, *10*, 3421.

(10) Pisani, C.; Dovesi, R. *Int. J. Quantum Chem.* **1980**, *17*, 501.

(11) Delhalle, J.; Piela, L.; Bredas, J.-L.; Andre, J.-M. *Phys. Rev. B* **1980**, *22*, 6254.

(12) Helgaker, T.; Jorgensen, P.; Olsen, J. *Molecular Electronic-Structure Theory*; John Wiley & Sons, Ltd.: Chichester, 2000; pp 405−425.

(13) Krukau, A. V.; Vydrov, O. A.; Izmaylov, A. F.; Scuseria, G. E. *J. Chem. Phys.* **2006**, *125*, 224106.

(14) Izmaylov, A. F.; Scuseria, G. E. *J. Chem. Phys.* **2007**, *127*, 144106.

(15) Lippert, G.; Hutter, J.; Parrinello, M. *Mol. Phys.* **1997**, *92*, 477.

(16) Lippert, G.; Hutter, J.; Parrinello, M. *Theor. Chem. Acc.* **1999**, *103*, 124.

(17) Krack, M.; Parrinello, M. *Phys. Chem. Chem. Phys.* **2000**, *2*, 2105.

(18) VandeVondele, J.; Krack, M.; Mohamed, F.; Parrinello, M.; Chassaing, T.; Hutter, J. *Comput. Phys. Commun.* **2004**, *167*, 103.

(19) Füsti-Molnár, L.; Pulay, P. *J. Chem. Phys.* **2002**, *117*, 7827.

(20) Kurashige, Y.; Nakajima, T.; Hirao, K. *Chem. Phys. Lett.* **2006**, *417*, 241.

(21) Chen, X.; Langlois, J.-M.; Goddard, W. A., III *Phys. Rev. B* **1995**, *52*, 2348.

(22) Ordejon, P.; Artacho, E.; Soler, J. M. *Phys. Rev. B* **1996**, *53*, R10441.

(23) Delley, B. *J. Phys. Chem.* **1996**, *100*, 6107.

(24) Kurashige, Y.; Nakajima, T.; Hirao, K. *J. Chem. Phys.* **2007**, *126*, 144106.

(25) Wieferink, J.; Kruger, P.; Pollmann, J. *Phys. Rev. B* **2006**, *74*, 205311.

(26) Wieferink, J.; Kruger, P.; Pollmann, J. *Phys. Rev. B* **2007**, *75*, 153305.

(27) Baumeier, B.; Kruger, P.; Pollmann, J. *Phys. Rev. B* **2007**, 085407.

(28) Baumeier, B.; Kruger, P.; Pollmann, J. *Phys. Rev. B* **2007**, *76*, 205404.

(29) Slater, J. C. *Phys. Rev.* **1951**, *81*, 385.

(30) Vosko, S. H.; Wilk, L.; Nusair, M. *Can. J. Phys* **1980**, *58*, 1200.

(31) Becke, A. D. *Phys. Rev. A* **1988**, *38*, 3098.

(32) Lee, C.; Yang, W.; Parr, R. G. *Phys. Rev. B* **1988**, *37*, 785.

(33) Becke, A. D. *J. Chem. Phys.* **1993**, *98*, 5648.

(34) Catti, M.; Pavese, A.; Dovesi, R.; Saunders, V. R. *Phys. Rev. B* **1993**, *47*, 9189.

(35) Svane, A. *Phys. Rev. B* **1987**, *35*, 5496.

(36) Massidda, S.; Posternak, M.; Baldereschi, A. *Phys. Rev. B* **1993**, *48*, 5058.

(37) Godby, R. W.; Schluter, M.; Sham, L. J. *Phys. Rev. B* **1988**, *37*, 10159.

(38) Pople, J. A.; Head-Gordon, M.; Fox, D. J.; Raghavachari, K.; Curtiss, L. A. *J. Chem. Phys.* **1989**, *90*, 5622.

(39) Curtiss, L. A.; Jones, C.; Trucks, G. W.; Raghavachari, K.; Pople, J. A. *J. Chem. Phys.* **1990**, *93*, 2537.

(40) Muscat, J.; Wander, A.; Harrison, N. M. *Chem. Phys. Lett.* **2001**, *342*, 397.

(41) Stevens, W. J.; Basch, H.; Krauss, M. *J. Chem. Phys.* **1984**, *81*, 6026.

(42) Stevens, W. J.; Krauss, M.; Basch, H.; Jasien, P. G. *Can. J. Chem.* **1992**, *70*, 612.

(43) Agrawal, B. K.; Yadav, P. S.; Kumar, S.; Agrawal, S. *Phys. Rev. B* **1995**, *52*, 4896.

(44) Heyd, J.; Scuseria, G. E.; Ernzerhof, M. *J. Chem. Phys.* **2003**, *118*, 8207.

(45) Brothers, E. N.; Izmaylov, A. F.; Normand, J. O.; Barone, V.; Scuseria, G. E. *J. Chem. Phys.* **2008**, *129*, 011102.

(46) Heyd, J.; Peralta, J. E.; Scuseria, G. E.; Martin, R. L. *J. Chem. Phys.* **2005**, *123*, 174101.

(47) Vydrov, O. A.; Heyd, J.; Krukau, A. V.; Scuseria, G. E. *J. Chem. Phys.* **2006**, *125*, 074106.

(48) Henderson, T. M.; Izmaylov, A. F.; Scuseria, G. E.; Savin, A. *J. Chem. Phys.* **2007**, *127*, 221103.

(49) Henderson, T. M.; Izmaylov, A. F.; Scuseria, G. E.; Savin, A. *J. Chem. Theory Comput.* **2008**, *4*, 1254.

(50) Shimazaki, T.; Asai, Y. *Chem. Phys. Lett.* **2008**, *466*, 91.

CT800329M

JCTC Journal of Chemical Theory and Computation

A Few Comments on the Application of Density Functional Theory to the Calculation of the Magnetic Structure of Oligo-Nuclear Transition Metal Clusters

Alessandro Bencini and Federico Totti*

Dipartimento di Chimica, Università degli Studi di Firenze, Firenze, Italy

Received September 2, 2008

Abstract: First principle calculations of the magnetic structure of high nuclearity clusters appears challenging in order to validate fits of magnetic experiments. Density Functional Theory (DFT)-Broken Symmetry approach pair became, in the past few years, the most widely applied computational tool to investigating the chemical-physical properties of complex systems, in particular magnetic molecular compounds. However, the application of the Broken Symmetry formalism requires the knowledge of the energies of $2^N/2$ single Slater determinants, and this task can easily become difficult for large *N*. Three main approximations are therefore usually done in order to limit the computational efforts: the model dimer approach (MDA), the doped cluster approach (DCA), and the minimum cluster approach (MCA). The whole cluster approach (WCA) will be also applied as reference and in order to check the importance of spin Hamiltonian high order terms. A systematic comparison between these different approaches has been, therefore, performed. Since this study is aimed for being of help in choosing the best method of calculation, we check here the validity of the above approaches by computing the magnetic structure of some test systems: the tetrahedral system $(HeH)_4$ and linear $[Cu(II)]_3$ and $[Mn(II)]_4$ complexes.

Introduction

Density Functional Theory (DFT) became, in the past few years, the most widely applied computational tool to investigating the chemical-physical properties of complex systems,[1−4] and particular attention was devoted to the understanding of the magnetic properties of molecular aggregates.[5] The "unusual" properties of these *molecular magnets*, as Olivier Khan[6] called them in 1993, are related to the common nature of their ground and excited states, which always consist of a manifold of states of different spin multiplicities nearly degenerate with respect to the temperature quantum *k*T (∼200 cm^{-1} at room temperature). A few paramagnetic molecules were discovered to show (at sufficiently low temperatures) hysteresis of the magnetization mimicking the bulk magnets behavior. These molecules appeared, therefore, possible precursors of building blocks for future molecular-sized storage devices.[7] These *Single Molecule Magnets* (SMM) are high nuclearity clusters, also called *molecular nanomagnets*, like $Mn_{12}(\mu_3\text{-}O)_{12}(CH_3COO)_6(H_2O)_4$,[8] whose magnetic hysteresis is due to the *magnetization tunneling* between the quantum states of the ground spin manifold.[9] The complete description of the electronic structure of magnetic systems can be achieved only within a relativistic formalism. However, the complexity of *n*-electron relativistic approaches prevents its application even to fairly complex systems. Calculations are therefore usually performed using a simpler, nonrelativistic, Hamiltonian, eventually including scalar relativistic effects on the valence electrons. Coupling between spins and orbital angular momenta (*spin−orbit coupling* (SOC)), in the case of orbitally nondegenerate ground states, is included via perturbation theory.[10] Notwithstanding these simplifications, calculation of magnetic properties remains a formidable task. It requires a computational approach that is capable of handling systems of chemical complexity and includes both static and dynamic electron correlation required to describing the many-body problem. Indeed, the main difficulty which arises in these cases is the correct definition of the different

* Corresponding author e-mail: federico.totti@unifi.it.

10.1021/ct800361x CCC: $40.75 © 2009 American Chemical Society
Published on Web 12/10/2008

spin states of the paramagnetic cluster. The highest spin state, in which all the majority spins, say α, of the individual paramagnetic centers are aligned parallel, is usually called the *ferromagnetic state* of the cluster, $|F>$. This state can be generally represented, in a molecular orbital framework, with a single Slater determinant formed by n_β doubly occupied molecular orbitals and $(n_\alpha - n_\beta)$ singly occupied α molecular orbitals (n_α and n_β being the number of α and β electrons, respectively), using either a spin unrestricted or a restricted open shell formalism. This state, neglecting the small spin contamination due to the unrestricted formalism, is an eigenstate of the total spin operator, $\mathbf{S}^2$ ($\mathbf{S} = \Sigma\mathbf{S_i}$), with eigenvalue $S_{max} = [n_\alpha(n_\alpha+1)]/4$. Another state, the *antiferromagnetic state*, $|AF>$, is, in general, written down with one single Slater determinant in which the spins of the individual centers are aligned antiparallel to each other and represents the state with the smallest spin multiplicity. This determinant, however, is not an eigenstate of the total spin operator, but only of its z component, S_z, with eigenvalue $M_S = (n_\alpha - n_\beta)/2$. In general, all the eigenstates of $\mathbf{S}^2$ that correspond to states with spin multiplicity $S_k < S_{max}$ are linear combinations of eigenstates of S_z with eigenvalue s_k. To properly describe these states, therefore, multiconfiguration SCF (MC-SCF) (also called multireference (MR-SCF)) approaches must be applied. The method most widely used to define the multireference wave function is the complete active space method (CAS), also called full optimized reaction space (FORS). The correlation between the electrons introduced in this way is called *static* or *long-range* correlation. The correct energy of the eigenfunction is computed by adding the effect of all the other electrons in the molecule (*dynamic* or *short-range* correlation) through the use of *post*-HF configuration interaction (CI) on the multiconfigurational wave function either explicitly (MR-CI, DDCI,...) or perturbatively (CASPT2, MRPT, MRQDPT,...).[11] All of these approaches need big computational resources and can be applied only to rather small molecules.[12]

Molecular magnets can be experimentally studied by a number of techniques, the more common being magnetization measurements, electron magnetic resonances, and heat-capacity calorimetry. In all cases, the interpretation of their physical properties is performed using an effective Hamiltonian that, in the case of magnetic properties, acts on spin variables (*Spin Hamiltonian*, SH). The eigenvalues of the SH match exactly the low energy spectrum of the magnetic systems by incorporating proper parameters, whose values are derived from the experiments and from theoretical methods. Calculations of the magnetic properties are therefore devoted to calculating the SH parameters with quantum mechanical methods. For most molecular magnets, the magnetic properties arise from the collectivization of magnetic moments localized onto a given atom or ion or groups of atoms, called *magnetic centers*. When the orbital contribution to the individual magnetic moments is negligible, i.e. all the magnetic centers have orbitally nondegenerate ground states rather well isolated from excited states, they behave like Curie paramagnets. In these cases, it is possible to associate each center with a magnetic moment $\mu_k^2 = g_k^2\mu_B^2 S_k(S_k+1)$, where S_k is the spin quantum number of center k, g_k contains the SOC contribution to the magnetization, and μ_B^2 is the Bohr magneton. A convenient form of the SH to be used in these cases is[13]

$$\mathrm{H_{Spin}} = \sum_{i<j} \mathbf{S_i}\cdot\mathbf{J_{ij}}\cdot\mathbf{S_j} + \sum_k H_{S_k} \quad (1)$$

The first term in the right-hand side in (1) is the quadratic coupling between the magnetic moments localized on the centers i and j bearing spins $\mathbf{S_i}$ and $\mathbf{S_j}$, respectively. The coupling is parametrized by the *exchange coupling tensor*, $\mathbf{J_{ij}}$. This is a second-rank tensor that includes all the physics of the magnetic coupling. Higher order terms involving fourth-order powers of the spin operators are allowed by symmetry, and their form and calculation will be discussed later in the text. H_{S_k} represents the low lying energy levels of the magnetic center k and their interaction with the magnetic field. This Hamiltonian, neglecting any interaction with nuclear moments, can be expressed, in generalized form, as a sum of terms of the type $B^{l_B}S_k^{l_S}$ (l_B and l_S non-negative integers; $l_S \le 2S_k$), where l_B+l_S is even to preserve time-reversal symmetry.[14] Although l_B is in principle unbounded, terms with $l_B > 1$ are seldom included. The term with $l_B = 1$, linear with $\mathbf{B}$, and $l_S = 1$ is the *linear Zeeman interaction* of the localized spins $\mathbf{S_k}$ with the external magnetic field, $\mathbf{B}$. When $S_k \ge 1$, terms with $l_B = 0$ and $l_S = 2(,4,...)$ must be considered that represent the *zero-field splitting* (ZFS) of the ground-state of the *k-th* magnetic center. A widely used form of H_{S_k}, including only quadratic terms with $l_B = 0$ and $l_S = 2$, is

$$H_{S_k} = \mu_B\mathbf{B}\cdot\mathbf{g_k}\cdot\mathbf{S_k} + \mathbf{S_k}\cdot\mathbf{D_k}\cdot\mathbf{S_k} \quad (2)$$

The exchange coupling tensor can be conventionally decomposed as

$$\mathbf{J_{ij}} = J\mathbf{E} + \mathbf{S_{ij}} + \mathbf{A_{ij}} \quad (3)$$

where $\mathbf{E}$ is the unit tensor, $\mathbf{S_{ij}}$ is the symmetric traceless $(\mathbf{J}_{ij}+\mathbf{J}_{ji})/2$-$\mathrm{Tr}(\mathbf{J}_{ij})/3$ tensor, $\mathbf{A_{ij}}$ is the antisymmetric tensor $(\mathbf{J}_{ij}-\mathbf{J}_{ji})/2$, and $J = \mathrm{Tr}(\mathbf{J}_{ij})/3$ is referred to as the (isotropic) *exchange coupling constant*. A conventional form for (1) is

$$\mathrm{H_{Spin}} = \sum_{i<j}[J_{ij}\mathbf{S_i}\cdot\mathbf{S_j} + \mathbf{d_{ij}}\cdot\mathbf{S_i}\times\mathbf{S_j} + \mathbf{S_i}\cdot\mathbf{D_{ij}}\cdot\mathbf{S_j}] + \sum_k \mu_B\mathbf{B}\cdot\mathbf{g_k}\cdot\mathbf{S_k} + \mathbf{S_k}\cdot\mathbf{D_k}\cdot\mathbf{S_k} \quad (4)$$

The overall exchange interaction is decomposed into the isotropic or Heisenberg−Dirac-vanVleck (HDvV) interaction,[15] the anisotropic interaction, and the antisymmetric or Dzialozshinsky-Moryia interaction,[16] respectively. All of these interactions arise from two main mechanisms: direct *through-space* magnetic interactions and electron−electron (*through-bond*) correlation effects. The first mechanism is small, in transition-metal complexes, and it is often neglected in the calculation of the exchange parameters. It can be modeled as a classical dipolar (the simplest) interaction between localized magnetic moments and has the greatest effect on the anisotropic term. The second mechanism determines the isotropic exchange, which is often the leading term in the SH. Anisotropic and antisymmetric interactions are due to spin−orbit coupling mixing of excited states into

the ground state and are generally much smaller than the HDvV interaction. They influence the magnetic properties only at low temperatures, the antisymmetric interaction being responsible of the spin canting in antiferromagnets.[6] In Hamiltonian (4), the local zero-field splitting terms, $\mathbf{S_k \cdot D_k \cdot S_k}$, can have a relevant role. Similarly to the anisotropic magnetic interactions, they arise from spin−spin (dipolar) coupling and from spin−orbit coupling effects on each magnetic center and can significantly alter the pattern of the low lying energy levels. In transition-metal complexes the spin−spin interaction is usually much smaller than the spin−orbit coupling. Hamiltonian (2) was derived by the use of second order perturbation theory, higher order perturbations corresponding to term with $l_S > 4$.[17]

In many cases, the zero field splitting is smaller than the other terms. This is particularly true in paramagnetic centers with an odd number of electrons, where the time reversal symmetry imposes a Kramers doublet as the ground state (in the absence of external magnetic fields). In magnetic centers with even number of electrons, zero-field splitting effects can be large enough to be observable at high temperatures.[18] First principle calculation of single zero field splitting is a challenging field of research[19] that was up to now mainly confined to Ligand Field Theory.[20]

In a few cases a SH simpler than HDvV can be used to interpret the magnetic properties. This typically occurs in paramagnetic centers with odd electrons, when SOC is dominant in determining the low energy level spectrum of the magnetic centers. In this situation one isolated Kramers doublet can be the ground state. Strong magnetic anisotropy is then present, and the Lenz-Ising model Hamiltonian,[21] $H_{LI} = \sum_{i<j} J_{ij} \mathbf{S}_{iz} \cdot \mathbf{S}_{jz}$, can be applied provided that all the matrix elements of the spin−spin coupling operators between the two ground level states of each magnetic center vanish. Examples of *Ising-like* magnets can be typically found among the rare earths compounds[22] like dysprosium ethyl sulfate, $Dy(C_2H_5SO_4)_3 \cdot 9H_2O$, and in some high spin cobalt(II) linear chain compounds.[23,24]

The commonest way to experimentally determining the SH parameters of a molecular magnet is the fitting of the temperature (and/or magnetic field) dependence of its magnetization. The main computational difficulty is the diagonalization of the SH matrix to obtaining the eigenvectors,[25] since the matrix dimension rapidly grows with the number of magnetic centers of the clusters and their spins. Single ion ZFS and anisotropic or antisymmetric interactions cause smaller effects on the energy spectrum than the isotropic interaction. They produce effects that are measurable only at low temperatures when excited states start to depopulate. These effects are usually better observed with spectroscopies (EPR, Mössbauer) or calorimetric and low temperature magnetization techniques. In the high temperature range, the magnetic properties are therefore mainly influenced by the relative population of the spin multiplets of the cluster. A convenient working formula to compute the magnetic susceptibility of paramagnetic samples is

$$\chi = \frac{N_A g^2 \mu_B^2}{3kT} \frac{\sum_S S(S+1)(2S+1) e^{-E(S)/kT}}{\sum_S (2S+1) e^{-E(S)/kT}} \quad (5)$$

where $E(S)$ are the eigenvalues of the HDvV SH that depend on the isotropic J_{ij}'s value. Equation 5 can be fitted to the measured values of χ, and the exchange coupling constants can in principle be measured. It has to be mentioned that in deriving eq 5 a g value common to all the spin states was assumed. This approximation is generally done in order to reduce the number of parameters to fit, and it is generally not further verified. However, it can be argued that g and J values are correlated, and a different choice of g could produce different values of J_{ij}.

Magnetic anisotropy is anyway an important factor to be explored theoretically. In SMM, for example, high easy-axis anisotropy is required to "block" spontaneous reorientation of the magnetization of the magnetic units. Furthermore, feeble magnetic interactions between adjacent molecules are to be present as a prerequisite to recording magnetic bits independently in each molecule. The modeling of these last interactions and the calculation of SOC effects are challenging fields for the computational chemist.[26]

In the following part of this report we will discuss the mapping of the isotropic part of the HDvV spin Hamiltonian of eq 4 with DFT approaches. Binuclear transition-metal complexes received much attention because DFT allowed the reproduction of experimental data with *semiquantitative* accuracy at the computational cost of few SCF convergences on single Slater determinants. With the term *semiquantitative* we mean that the spin multiplicity of the ground states of the complexes was reproduced, and the energy of the next excited states was found in fair agreement (from a few percent to ±50%) with the experimental data. It is quite well established in the literature that the best agreement with the experimental data is reached using the Broken Symmetry (BS) approach, developed by L. Noodleman and J. G. Norman,[27] together with the B3LYP hybrid functional[28] and valence triple-ζ basis functions. Within the BS approach the energy of the low spin state (pure spin state) of the complex, that is the state mostly affected by static electron correlation effects, is approximately computed as a projection from a state of mixed spin and space symmetry (the BS state) obtained by an independent SCF calculation.[29] Within this formalism, it is, in principle, possible to handle clusters with nuclearity higher than 2. Using the HDvV Hamiltonian of eq 4, the number of independent coupling constants[30] can be $N(N-1)/2$ unless symmetry is present to reduce this number. It is apparent that, when $N > 2$, the system becomes rapidly overparameterized making meaningless any fitting procedure. A magnetic symmetry is always imposed to reduce the number of parameters. It often happens that the data can be fit with different magnetic topologies, since a multiparameter function can have many equivalent minima. The *a priori* calculation of the magnetic structure of high nuclearity clusters appears therefore challenging in order to validate fits of experiments.[31] Application of the BS formalism requires the knowledge of the energies of $2^N/2$ single Slater determinants, and this task can easily become difficult

for large N. Three main approximations are therefore usually done in order to limit the computational efforts:

1. The Model Dimer Approach (MDA). The magnetic exchange coupling constants are computed on simple binuclear model complexes build up to mimicking the various exchange pathways in the cluster.

2. The Doped Cluster Approach (DCA). BS calculations are performed on model clusters in which all the magnetic centers except two have been substituted with diamagnetic ions.

3. The Minimum Cluster Approach (MCA). The minimum number of BS determinants (equal to the number of independent magnetic coupling constants required by the symmetry) and the highest spin determinant are computed on the whole cluster.

To the best of our knowledge, no systematic comparison between these different approaches has been yet performed. Since this study is aimed for being of help in choosing the best method of calculation, we check here the validity of the above approaches by computing the magnetic structure of some test systems.

In the following we will first comment on the BS formalism, and later we will present and discuss the magnetic structure of the model tetrahedral system $(HeH)_4$ and of linear $[Cu(II)]_3$ and $[Mn(II)]_4$ complexes.

The Broken Symmetry Formalism

Binuclear Complexes. For two interacting magnetic centers with localized spins $\mathbf{S_1}$ and $\mathbf{S_2}$, the HDvV spin Hamiltonian of eq 4 takes the form

$$\mathrm{H_{HDvV}} = J_{12}\mathbf{S_1}\cdot\mathbf{S_2} \tag{6}$$

and acts on the $\{(2S_1+1)(2S_2+1)\}$ dimensional product space $\{|S_1m_1\rangle|S_2m_2\rangle \equiv |S_1m_1S_2m_2\rangle\}$ with $-S_1 \le m_1 \le S_1$ and $-S_2 \le m_2 \le S_2$. Hamiltonian (6) commutes with $\mathbf{S}^2$ and S_z, $\mathbf{S} = \mathbf{S_1}+\mathbf{S_2}$; therefore, its eigenvectors can be labeled using the expectation values of $\mathbf{S}^2$ and S_z. In order to compute the J_{12} parameter the energies of all the S spin multiplets, $|S_1-S_2| \le S \le S_1 + S_2$, should be computed at the quantum mechanical level and compared with the eigenstates of (6). Assuming, however, the general validity of (6), only the energies of the highest spin state, $S_{max} = S_1 + S_2$, and of the lowest spin one, $S_{min} = S_1-S_2$, are to be calculated. When the magnetic centers are in the highest spin states (*high spin complexes*), the state corresponding to $S = S_{max}$ is usually well described by one single Slater determinant. The state corresponding to $S = S_{min} = |S_1-S_2|$ is, on the contrary, a linear combination of Slater determinants that are eigenstates of S_z with eigenvalue S_{min}. Without spin contamination from excited states the coefficients of this linear combination are the Wigner or Clebsch-Gordon coefficients appearing in the theory of the angular momentum.[27b] It is apparent that the energy of this state can be exactly computed only using multireference SCF approaches. The Difference Dedicated Configuration Interaction (DDCI), developed in the past few years by Malrieu et al.,[32] allowed accurate calculation of the exchange coupling constants in several binuclear transition-metal complexes.[33] Although the configuration space of DDCI is considerably reduced with respect to a full CI calculation, the applications to clusters with $N > 2$ are still rare.[34]

Using the DFT approach the calculation of the energy of the $S = S_{min}$ state is not possible due to the single-determinant nature of the Kohn−Sham implementation. However, in the spin-polarized or unrestricted formalism, the energy of one single Slater determinant build up with open shell magnetic orbitals localized onto the two magnetic centers and bearing the magnetic electrons with opposite spins can be written as a weighted average of the energies of the pure spin multiplets.[27,29] This determinant, the Broken Symmetry (BS) determinant, is an eigenstate of S_z with eigenvalue $M_s = S_1 - S_2$, and the magnetic coupling constant can be obtained, neglecting the usually small spin contamination of the $S = S_{max}$ state, by

$$J_{12} = \frac{E(S_{max}) - E(BS)}{2S_1S_2} \tag{7}$$

Equation 7 was originally derived using spin projection operators on the unrestricted BS determinant in the approximation that the α magnetic orbitals on center 1 and the β magnetic orbitals on center 2 are orthogonal, $S_{ij}^{\alpha\beta} = 0$ $\forall(i \in 1, j \in 2)$, and can be a good approximation when $(S_{ij}^{\alpha\beta})^2 \ll 1$.[27b] Application of (7) to a number of transition-metal binuclear complexes, particularly copper(II) complexes, was found to give J_{12} values larger than the experimental ones, and an alternative formula was used[35] that read

$$J_{12}^{un} = \frac{E(S_{max}) - E(BS)}{2S_1S_2 + S_2} \;\forall\; (S_1 \ge S_2) \tag{8}$$

Equation 8 can be derived[27a] by spin projection from the unrestricted BS determinant under the condition $(S_{ij}^{\alpha\beta})^2 = 1$. In this case, the BS determinant is also an eigenfunction of $\mathbf{S}^2$, that for $S_1 = S_2$, corresponds to the singlet state of the complex. Using eq 8 one is assuming that the energy of the BS state computed with DFT is the energy of a pure spin state. We have here indicated the exchange coupling constant J_{12}^{un}, *un* meaning *un*-projected formula. This equation was successfully applied in the case of strong covalent bonding interaction between the magnetic centers.[36] It must be stressed that the BS determinant is strongly spin contaminated. For a single Slater determinant built with spatially orthogonal α and β electrons the expectation value of $\mathbf{S}^2$ is given by $(n_\alpha \ge n_\beta)$:[37]

$$\langle \mathbf{S^2} \rangle_{SD} = \left(\frac{n_\alpha - n_\beta}{2}\right)^2 + \left(\frac{n_\alpha + n_\beta}{2}\right) = \langle S_z \rangle^2 + S_{max} \tag{9}$$

For the BS determinant of two $S_1 = S_2 = 5/2$ spins this value is $\langle \mathbf{S^2} \rangle_{SD} = 5$. Comparison with $\langle \mathbf{S^2} \rangle$ computed on the unrestricted BS determinant, $\langle \mathbf{S^2} \rangle_{BS}$, with the value obtained by eq 9 gave an estimate of the deviation from the conditions under which eqs 7 and 8 were derived, i.e. of the overlap between the magnetic orbitals. Equations have been suggested correcting (7) to account for the overlap between the magnetic orbitals through the calculation of $\langle \mathbf{S^2} \rangle_{BS}$ and of $\langle \mathbf{S^2} \rangle$ in the high-spin state, $\langle \mathbf{S^2} \rangle_{HS}$.[38,39,29e] In particular, in the Approximate Projection (AP) method[39] the working equation for the calculation of the exchange coupling constants is

$$J_{12}^{AP} = 2\frac{E(S_{max}) - E(BS)}{\langle \mathbf{S^2} \rangle_{HS} - \langle \mathbf{S^2} \rangle_{BS}} \quad (10)$$

The use of eq 10 generally gives J values comprised between J_{12}^{un} and J_{12}, only in slight better agreement with experimental findings.

The theoretical foundations of eqs 7 and 8 were subject to some discussions,[40,41] and there is not in the literature a general agreement on their use.[42] In a number of cases a nice agreement with the experimental data was usually reached using eq 8 in conjunction with the B3LYP functional[35] (in some cases a mixing of HF exchange between 33% and 50% was found to give better results[43] than the 20% used by B3LYP), and we in general prefer to adopt the strategy of applying both of the formulas to obtain upper and lower limiting values for J_{12}.

A generalization[44] of the spin projection approach can be obtained considering that both the high-spin and the unrestricted BS wave functions are eigenstates of S_z, with eigenvalues $M_S = S_{max}$ and $|S_1 - S_2|$, respectively. A one-to-one correspondence can thus be established between the diagonal elements of H_{HDvV} (6), on the product basis $\{|S_1 s_1\rangle|S_2 \pm s_2\rangle \equiv |S_1 s_1 S_2 \pm s_2\rangle\}$, and the energy of the BS states. The expectation values of (6) coincide with the eigenvalues of the Ising, H_{LI}, Hamiltonian, and the above procedure is often referred to as the mapping of the unrestricted-BS wave functions with H_{LI},[45] even if this Hamiltonian cannot be applied to describing the magnetic properties of the complex.

Clusters. The exchange interactions in a cluster with N magnetic centers is usually phenomenologically interpreted using the HDvV Hamiltonian of eq 4 including interactions only between adjacent centers, except in the case of linear clusters in which coupling between the terminal atoms is generally included. In the general cases, $N(N-1)/2$ exchange coupling constants need to be determined. Ovchinnikov and Labanowski[46] developed a spin projection technique to express the energies of the spins states of a cluster as a weighted average of the energy of the highest spin state and those of the unrestricted Slater determinants corresponding to $M_S = S$ with $|S_1 - S_2 - \cdots - S_N| \leq S < (S_1 + S_2 + S_N)$. Application of this technique to clusters with $S_i > 1/2$ easily becomes rather cumbersome. A procedure easier to handle is obtained by mapping the diagonal elements of H_{HDvV} (or equivalently mapping the eigenvalues of the H_{LI} Hamiltonian), $\langle \Pi_i S_i m_i | \sum_{i<j} J_{ij} S_i \cdot S_j | \Pi_j S_j m_j \rangle = \sum_{i<j} J_{ij} m_i m_j$ for $m_i = \pm s_i$ and $m_j = \pm s_j$, to the energies of appropriate BS states, as already done for the binuclear case. At variance with the binuclear case, this mapping cannot now be one-to-one since one has to compute $N(N-1)/2$ exchange coupling constant and has $2^N/2$ independent determinants, hence $2^N - 2/2$ energy differences. For a *4*-nuclear cluster, for example, the number of exchange coupling constants is 6 to be obtained by 7 energy differences that become 28 and 127, respectively, for a *8*-nuclear system.

The energy of the ket $|s_{max}\rangle = \Pi_{i<j}|S_i s_i S_j s_j\rangle$ is easily computed as $E(S_{max}) = \sum_{i<j} J_{ij} s_i s_j$ and the energy difference with a ket, $|s>$, with spin projection $s < s_{max}$ can be written in general form as

$$\Delta E(S_{max} - s) = \sum_{i<j} (2J_{ij}|s_i s_j|)\lambda_{ij} \quad (11)$$

where $\lambda_{ij} = 0$ if s_i and s_j have the same sign in $|s>$ and 1 otherwise. Equating (11) to the energy differences between the high spin and the BS states with the appropriate value of s yields all the equations needed to compute the J_{ij} values, as it will be discussed later.

A number of more complex approaches based on the concept of local spins have been recently proposed to compute the exchange coupling constants in clusters.[47] The results of these procedures are close to those obtained by the above reviewed approaches, and we will not discuss these models any longer in the present paper.

As already found for dinuclear complexes, the application of (11) often results in exchange coupling constants larger than the experimental values. A modified equation in which (8) is used to express the SH energy difference on the left-hand side of (11) has been proposed:[48]

$$\Delta E(S_{max} - s) = \sum_{i<j} J_{ij}(2|s_i s_j| + s_j)\lambda_{ij} \; (s_i \geq s_j) \quad (12)$$

While (8) can be justified if, for some reason, DFT energies of BS states match those of pure spin multiplets, eq 12 cannot receive this support. In the general case, in fact, the energies of the spin states of a cluster cannot be computed in analytical form since the HDvV SH is not diagonal in the intermediate spin coupling space. Furthermore to any $s < s_{max}$ a number of different BS determinant can be written that cannot be uniquely assigned to the particular S state. It is therefore misleading referring to (12) as to the nonprojected formula for clusters,[48] and (12) should be used, if one likes, as some kind of working equation not theoretically justified.

Benchmark Calculations of the Exchange Coupling Constants

The H_4He_4 cluster. The H−He−H binuclear paramagnetic system has been widely used to test theoretical models of superexchange interaction between two $S_i = S_j = 1/2$ paramagnetic centers.[49] We have performed calculations on the cubane-like cluster shown in Figure 1 at various H−He distances.

All the adjacent H−He bond distances were kept equal to each other, resulting in a tetrahedral arrangement of the H_4 and He_4 subunits. The spin Hamiltonian describing the magnetic structure of this cluster is

$$H_{Td} = J(\mathbf{S_1 \cdot S_2} + \mathbf{S_1 \cdot S_3} + \mathbf{S_1 \cdot S_4} + \mathbf{S_2 \cdot S_3} + \mathbf{S_2 \cdot S_4} + \mathbf{S_3 \cdot S_4}) \quad (13)$$

which can be written in the equivalent form

$$H_{Td} = \frac{J}{2}(\mathbf{S^2} - \sum_i \mathbf{S_i^2}) \quad (14)$$

The eigenvalues of eq 6 depend only on the total spin S:

$$E_{Td}(S) = \frac{J}{2}S(S+1) - \frac{3J}{2} \quad (15)$$

Note that the constant term $-3J/2$ is not important in this framework, since only the energy differences are important.

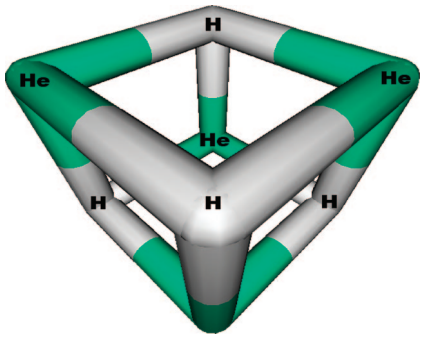

Figure 1. The H_4He_4 model cluster.

Application of the BS approach requires the calculations of the unrestricted energies of the 8 Slater determinants shown in the following:[50]

M_S	determinant
2	$\|HS\rangle = \|++++\rangle$
1	$\|IS1\rangle = \|-+++\rangle$ $\|IS2\rangle = \|+-++\rangle$ $\|IS3\rangle = \|++-+\rangle$ $\|IS4\rangle = \|+++-\rangle$
0	$\|LS1\rangle = \|-+++-\rangle$ $\|LS2\rangle = \|-+-+\rangle$ $\|LS3\rangle = \|++--\rangle$

The intermediate spin, *IS,* determinants corresponding to $M_s = 1$ are obtained from the high spin configuration by one-spin flip. Two-spin flips yielded the low spin determinants, *LS*, with $M_s = 0$. Using eq 11 we get two equations defining J

$$\Delta E(2-1) = \frac{3J}{2} \tag{16}$$

$$\Delta E(2-0) = 2J \tag{17}$$

that can be used to compute the exchange coupling constant. The results of the DFT calculations for several H−He distances are shown in Table 1. Only for H−He distances larger than 1.5 Å eqs 16 and 17 are simultaneously verified. At shorter distances the J values computed with these equations, J_{2-1} and J_{2-0} respectively, significantly differ from each other. This shows that deviations from the spin ladder required by Hamiltonian (13) can be found. Since at any distance the degeneracy among each of the $M_S = 1$ and $M_S = 0$ states, which is expected because the T_d symmetry of the cluster, is preserved, these deviations cannot be ascribed to inaccuracy of the SCF convergences. It is apparent that the MCA scheme, in which only one of eqs 16 or 17 is used to compute J, cannot be safely applied in the whole range of bond distances.

Table 1. Distance Dependence of the J Value[a] (cm^{-1}) Computed for the H_4He_4 Cluster

d_{H-He}	J_{2-1}	J_{2-0}	J_{2-1}-J_{2-0}
5.000	0.10	0.10	0.00
4.000	2.61	2.61	0.00
3.000	36.92	36.89	0.03
2.000	78.09	78.19	−0.01
1.750	43.93	43.94	−0.01
1.625	202.40	201.70	0.71
1.500	854.70	829.60	25.10
1.375	2800.73	2564.65	236.05

[a] J_{2-1}: value computed through eq 16; J_{2-0}: value computed through eq 17.

Table 2. Distance Dependence of the J_{1234} Value Computed for the H_4He_4 Cluster[a]

d_{H-He}	J	J_{1234}	$\|J_{1234}/J\|$
5.000	0.10	0.00	0.00
4.000	2.61	0.00	0.00
3.000	36.92	−0.16	0.00
2.000	78.09	0.54	0.01
1.750	43.93	0.06	0.00
1.624	202.40	−3.50	0.02
1.500	854.70	−134.01	0.16
1.375	2800.73	−1259.11	0.45

[a] Since the J computed with eqs 16 and 17 are fairly consistent up to $d_{H-He} = 1.625$ Å (see Table 1), we chose to report the J computed with only eq 16. J_{1234} is computed from eq 18.

Table 3. Computed Exchange Coupling Constants for H_2He_2 (MDA) and H_2He_6 (DCA) Model Systems at Several H−He Bond Distances and Comparison with Full Cluster Calculations

	H_2He_2	H_2He_6	H_4He_4
d_{H-He}	J_{12}[a]	J_{12}[a]	J[b]
5.000	0.04	0.09	0.10
4.000	1.29	2.56	2.61
3.000	18.94	37.03	36.92
2.000	42.92	75.94	78.09
1.750	19.69	50.93	43.93
1.625	117.81	249.17	202.40
1.500	557.21	1091.90	854.70
1.375	1935.80	3726.80	2800.73

[a] Computed with eq 7. J_{12}^{yg} from eq 8 is half of this value. [b] Values from Table 2.

Additional terms that are commonly neglected can be added to the Hamiltonian (13), namely the biquadratic interactions. This can be done with the four-spin biquadratic interaction Hamiltonian[51,52] $J_{ijkl}\sum_{ijkl}[(\mathbf{S_i}\cdot\mathbf{S_j})(\mathbf{S_k}\cdot\mathbf{S_l})+(\mathbf{S_i}\cdot\mathbf{S_l})-(\mathbf{S_j}\cdot\mathbf{S_k})+(\mathbf{S_i}\cdot\mathbf{S_k})(\mathbf{S_j}\cdot\mathbf{S_l})]$, where the summation runs on the three nuclear configurations invariant in the T_d symmetry group: the three coupling constants being equal, $J_{ijkl} = J_{1234} = J_{1423} = J_{1324}$. Adding this term to eq 13, modifies eq 16 that becomes

$$\Delta(2-1) = \frac{3}{2}J + \frac{3}{8}J_{1234} \tag{18}$$

This spin ladder can be matched exactly with the parameters shown in Table 2. The exchange interaction is antiferromagnetic in the whole range of distances, and J increases on decreasing the H−He distance. The four-spin biquadratic exchange increases upon shortening the bond and can be as large as 45% of J.

In order to look at the performances of the model dimer, MDA, and doped cluster, DCA, approaches, we performed DFT calculations on the binuclear model system H_2He_2 (MDA) and on the model cluster H_2He_6 (DCA). The results of the calculations are summarized in Table 3. The computed exchange coupling constants are all positive (antiferromagnetic interaction) independently on the approximation in use, but it appears that DCA is closer to the full cluster calculation. For H−He distances shorter than 1.65 Å also the DCA results significantly deviates from the full clusters results. This can be attributed to the increasing importance of the four-center biquadratic exchange interaction and/or

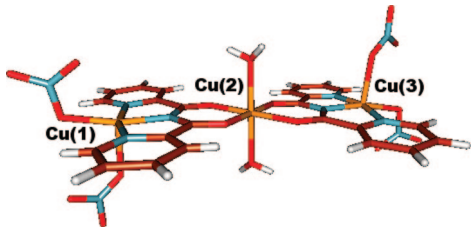

Figure 2. Molecular structure of the $[Cu(bpca)_2(H_2O)_2\{Cu(NO_3)_2\}_2]$ cluster (bpca = bis(2-pyridylcarbonyl)amine).

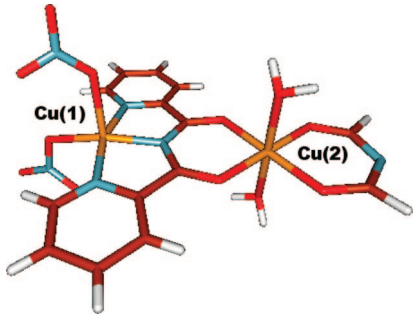

Figure 3. Dinuclear model of $[Cu(bpca)_2(H_2O)_2\{Cu(NO_3)_2\}_2]$ used in the MDA calculations.

some polarization effects not accounted in the DCA. The computed values of $\langle \mathbf{S^2} \rangle$ for the high spin state in the MDA and DCA is $\langle \mathbf{S^2} \rangle_1 = 2.00$ independent of the H−He distance, showing that no appreciable spin contamination due to the unrestricted nature of the wave function is present, a result commonly found in DFT. The corresponding values for the BS state deviate from the value 1 expected from eq 9 below $d_{H-He} = 1.75$ Å. The corresponding values for $d_{H-He} = 1.625$, 1.50, and 1.375 Å are $\langle \mathbf{S^2} \rangle_0 = 0.99$, 0.97, 0.89, respectively. Application of eq 10 does not significantly ameliorate the agreement between the DCA results and the full cluster calculations.

Linear Three Spins: The $[Cu(bpca)_2(H_2O)_2\{Cu(NO_3)_2\}_2]$ Complex (bpca = bis(2-pyridylcarbonyl)amine). The magnetic properties of the trinuclear $[Cu(bpca)_2(H_2O)_2\{Cu(NO_3)_2\}_2]$ complex[53] were satisfactorily interpreted using the spin Hamiltonian

$$H_{123} = J_{12}(\mathbf{S_1} \cdot \mathbf{S_2} + \mathbf{S_2} \cdot \mathbf{S_3}) + J_{13}(\mathbf{S_1} \cdot \mathbf{S_3}) \qquad (19)$$

that takes into account the crystallographic C_i symmetry of the molecule (J_{12}=J_{23}), following the atom numbering indicated in Figure 2. Calculation of the exchange coupling constants was performed in the model dimer approach (MDA) using the model dimer shown in Figure 3, in which one bpca ligand was substituted by one N-formylimidoformate molecule.

The doped cluster approach (DCA) was applied by substituting one Cu^{II} ion with one Zn^{II} ion in turn in the structure of Figure 2. Two symmetry independent doped clusters models were obtained indicated as Cu(1)Cu(2)Zn and Cu(1)ZnCu(3). Due to the crystallographic C_i symmetry, only two BS determinant with $M_S = 1/2$, namely $|BS1> = |+-+>$ and $|BS1> = |++->$,[50] are required to compute the J_{ij} values of the whole cluster. In this case, therefore, the whole cluster approach (WCA) and the minimum cluster approach (MCA) are identical. The relevant equations to be used in this approach follow from eq 11 as

$$\Delta E\left(\frac{3}{2} - BS_1\right) = J_{12};\ \Delta E\left(\frac{3}{2} - BS_2\right) = \frac{J_{12} + J_{13}}{2} \qquad (20)$$

The J_{ij} values computed with the different approaches are reported in Table 4 and compared to the experimental findings. The close match between J_{12} and J_{12}^{AP} is due to the fact that $\langle \mathbf{S^2} \rangle_{BS}$ and $\langle \mathbf{S^2} \rangle_{HS}$ were computed very close to the theoretical values of 1.0 and 2.0, respectively. This shows that the BS state is a equal mixture of the singlet and triplet state, as expected in the weak covalent limit, and that the spin contamination of the triplet state is negligible.

J_{12}^{un} in MDA and DCA closely match the experimental J_{12} value, as already often found for other Cu(II) complexes, but the value of J_{13} is uncorrectly reproduced by DCA. The WCA calculations reproduced the alternation in sign of the J's value, but $|J_{12}|$ is quite far from the experiment.

Table 4. Computed J_{12} and J_{13} Values (cm^{-1}) with Different Approaches

	J_{12}	J_{13}
MDA[a]	−25.0 (−12.5;−25.0)	−
DCA[a]	−29.0 (−14.5;−29.0)	−5.71 (−2.85;−5.66)
WCA	−50.7	7.68
exp.	*−14.1*	*5.7*

[a] Computed with eq 7. The values reported in parentheses were computed with eq 8 for J_{12}^{un} and eq 10 for J_{12}^{AP}, respectively.

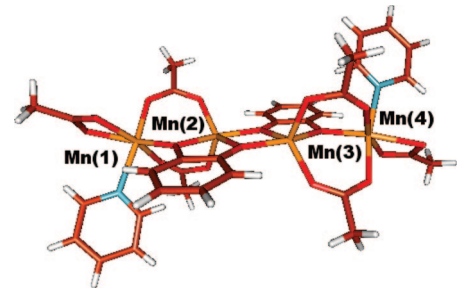

Figure 4. Molecular structure of the $[Mn_4(OAc)_6(py)_2(cat)_2]^{2-}$ cluster anion.

Linear Four Spins: The $[Mn_4(OAc)_6(py)_2(cat)_2]^{2-}$ (OAc = acetate, py = pyridine, cat = catecholate dianion) Complex. This cluster is one of the few linear clusters containing high-spin Mn(II) ions. This system seemed therefore particularly useful to test the consistency of different computational approaches since high spin Mn(II) has an orbitally nondegenerate ground state, $^6A_1$, that is also the only possible sextet state. This fact minimizes the effects of spin−orbit coupling and assures that the ground-state can be described with one Slater determinant. The linear geometry renders the various coupling constants different from each other, and large relative deviations are expected. The magnetic properties of this compound have not yet been measured; therefore, comparison with experiment will not be possible.

The molecular structure of the cluster[54] is schematically shown in Figure 4 together with the numbering scheme of

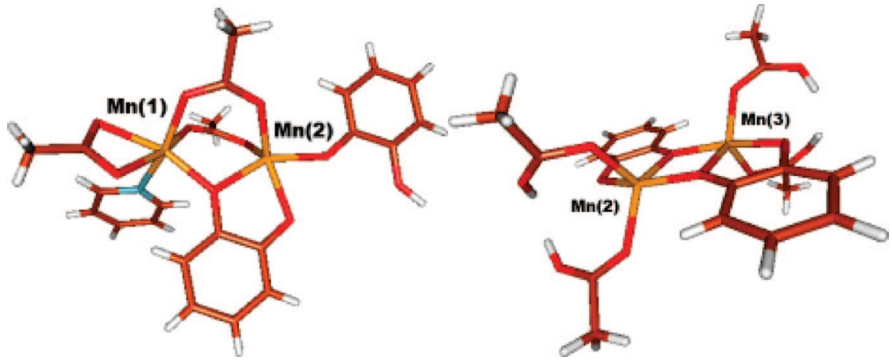

Figure 5. Dinuclear models of $[Mn_4(OAc)_6(py)_2(cat)_2]^{2-}$ used in the MDA calculations.

the Mn(II) atoms. Since the molecule is centrosymmetric, the appropriate spin Hamiltonian is

$$H_{1234} = J_{12}(\mathbf{S_1}\cdot\mathbf{S_2} + \mathbf{S_3}\cdot\mathbf{S_4}) + J_{23}(\mathbf{S_2}\cdot\mathbf{S_3}) + J_{13}(\mathbf{S_1}\cdot\mathbf{S_3} + \mathbf{S_2}\cdot\mathbf{S_4}) + J_{14}(\mathbf{S_1}\cdot\mathbf{S_4}) \quad (21)$$

The 8 possible Slater determinants take the form shown in the following:[50]

M_S	determinant
10	$\|HS\rangle = \|++++\rangle$
5	$\|IS1\rangle = \|-+++\rangle$ $\|IS2\rangle = \|+-++\rangle$ $\|IS3\rangle = \|++-+\rangle$ $\|IS4\rangle = \|+++-\rangle$
0	$\|LS1\rangle = \|-++-\rangle$ $\|LS2\rangle = \|-+-+\rangle$ $\|LS3\rangle = \|++--\rangle$

The energies of the intermediate spin states were found to be degenerate in couples according to the C_i symmetry of the complexes; therefore, $E(IS1) = E(IS4)$ and $E(IS2) = E(IS3)$, leaving 5 independent energy differences to compute the 4 spin Hamiltonian parameters. The relevant equations, obtained by application of eq 11, are shown in Table 5 together with the computed DFT energy differences.

In the MDA, the dimers shown in Figure 5 were used. The exchange between Mn(1) and Mn(2) (equal to that between Mn(3) and Mn(4)) is propagated by two μ_2-OAc^- ions and one μ_1-Cat^{2-} ion (Figure 5 left); the model dimer for this interaction being $[Mn_2(OAc)_3(py)(Cat)(CatH)]^{2-}$. The second exchange pathway, between Mn(3) and Mn(4), is due to two bridging μ_1-Cat^{2-} ions (Figure 5 right) and is modeled by the $[Mn_2(HOAc)_4(Cat)_2]$ dimer.

In the DCA, four model dinuclear species were obtained by substituting two Mn(II) centers with diamagnetic Sn(II): MnMnSnSn, SnMnMnSn, MnSnMnSn, and MnSnSnMn. They permit the DCA calculation of J_{12}, J_{23}, J_{13}, and J_{14}, respectively.

WCA and MCA calculations were performed on the structure shown in Figure 4. In the Minimum Cluster Approach we need to choose 4 equations among the 5 possibilities shown in Table 5. This leads to 5 sets of equations that can be solved separately yielding 5 sets of possible J_{ij} values. If the system were exact, the five sets of solutions would be identical and equal to the WCA calculation. The results of the calculations are collected in Table 6.

WCA calculations are customarily performed assuming *a priori* the magnetic spin topology in order to reduce the number of exchange coupling constants, and, hence, the number of BS states, to be computed. In the general cases, it is impossible to determine the cluster's spin topology from experiments, due to overparameterization problems, and theoretical tools are mandatory to meaningfully solve the problem. This can be achieved, within DFT, by applying a procedure previously described[55] that consists in computing all the m energy differences between the high spin states and the possible BS determinants, $\Delta E^{DFT}(S_{max}-s)$; building up a system of equations using (11); extracting the $\{J_{ij}\}$ set that minimizes the test function $f = \sum_s[\Delta E^{DFT}(S_{max}-s) - \Delta E(S_{max}-s)]^2$, being 0 in the case of a perfect match between the SH expectation values and the BS energies.[56] From this procedure one obtains the J_{ij} values that best fit the DFT energies, together with their standard deviations. It is computationally heavy to applying this formalism to large clusters and a simplified procedure, in which only one subset of all the possible BS energies is evaluated, was applied.[57,58]

For the linear Mn_4 cluster the spin topology one can assume is obtained neglecting J_{13} and J_{14} in (21), and we can check here the quality of this approximation. We have therefore 5 energy differences that can be used to computing up to a maximum of 4 exchange coupling constants. The results of the calculations are reported in Table 7. As expected, J_{12} and J_{23} are larger than the other two coupling constants. The inclusion of J_{13} and J_{14} in turn into the fitting procedure causes f to decrease without significantly altering the J_{12} and J_{23} values that average to 47.7 cm^{-1} and −5.5

Table 5. Energy Differences Used To Compute the Exchange Coupling Constants for $[Mn_4(OAc)_6(py)_2(cat)_2]^{2-}$

E(HS)-E(X)=	J_{12}	J_{23}	J_{13}	J_{14}	ΔE (cm^{-1})
IS1	25/2		25/2	25/2	603.8
IS2	25/2	25/2	25/2		530.0
LS1	25		25		1191.7
LS2	25	25/2		25/2	1123.7
LS3		25/2	25	25/2	−65.6

Table 6. J_{ij} Values (cm^{-1}) of $[Mn_4(OAc)_6(py)_2(cat)_2]^{2-}$ Computed with MCA[a] Using Different Sets of BS States[a]

set	**1**	**2**	**3**	**4**	**5**
J_{12}	47.26	48.0	48.0	47.62	47.68
J_{23}	−5.27	−5.27	−5.98	−5.98	−5.27
J_{13}	0.40	−0.31	0.40	0.05	0.05
J_{14}	0.64	0.64	−0.08	0.64	−0.08

[a] The different MCA sets were obtained with the equations E(HS)-E(X) (see Table 6) with X: *set* **1** = {*IS1*,*IS2*,*LS1*,*LS2*}; *set* **2** = {*IS1*, *IS2*,*LS1*,*LS3*}; *set* **3** = {*IS1*,*IS2*,*LS2*,*LS3*}; *set* **4** = {*IS1*,*LS1*,*LS2*,*LS3*}; *set* **5** = {*IS2*,*LS1*,*LS2*,*LS3*}.

Table 7. J_{ij} Values[a] (cm^{-1}) of $[Mn_4(OAc)_6(py)_2(cat)_2]^{2-}$ Computed with WCA with the Different Spin Hamiltonian Topologies[b]

J_{12}	J_{23}	J_{13}	J_{14}	f
47.73(2)	−5.38(6)	–	–	62.3
47.68(3)	−5.45(9)	0.11(3)	–	51.2
47.65(3)	−5.6(1)	0.08(3)	0.3(1)	28.1

[a] $f = \sum_s[\Delta E^{DFT}(S_{max}-s)-\Delta E(S_{max}-s)]^2$, see text. Standard deviations are shown in parentheses. [b] *i.e.* number of different J's taken into consideration in the SH.

cm^{-1} respectively. It has to be noted that even in the fit with all the four parameters f is still different from 0 (28.8 cm^{-1}).

In Table 8 a comparison between the J values computed at the different level of approximation is presented. In all the calculations J_{12} is the leading antiferromagnetic interaction, except when the DCA is applied. In this latter case J_{14} is the greatest term of the SH. This result is, of course, wrong and shows that the diamagnetic metal ions can be noninnocent partners in transmitting the superexchange interactions. The MDA results do not reproduce the sign alternation between J_{12} and J_{23} computed with WCA. MCA calculations are dependent on the chosen BS set (Table 7); in any case J_{12} and J_{23} compare well with the values obtained with WCA, and differences are seen only on the J_{13} and J_{14} values. Test calculations on systems with larger J values than the present ones must be performed in order to check if this is a general trend. Other spin topologies than the linear one also have to be checked in order to be able to generalize these results.

In the WCA calculations the match between DFT and SH energies is not perfect even if SH is considered with all the parameters free. This fact can be due to an internal inconsistency of the BS approach or to the inadequacy of the SH in the form given in eq 21. As already done for the H_4He_4 model system, higher order (biquadratic) terms can be added to (21). These terms can be two-centers or four-centers that in C_i symmetry become

$$H^2_{bq} = j_{12}[(\mathbf{S_1}\cdot\mathbf{S_2})^2 + (\mathbf{S_3}\cdot\mathbf{S_4})^2] + j_{23}(\mathbf{S_2}\cdot\mathbf{S_3})^2 + j_{13}[(\mathbf{S_1}\cdot\mathbf{S_3})^2 + (\mathbf{S_2}\cdot\mathbf{S_4})^2] + j_{14}(\mathbf{S_1}\cdot\mathbf{S_4})^2 \quad (22)$$

and

$$H^4_{bq} = J_{1234}(\mathbf{S_1}\cdot\mathbf{S_2})(\mathbf{S_3}\cdot\mathbf{S_4}) \quad (23)$$

The effect of these terms on the energies of the cluster can cause deviations from the HDvV behavior. Within the BS formalism it would be impossible to handle with these effects since the number of parameters easily exceed the number of available BS energies. The calculation of the energies of the spin states, which requires MR-CI approaches, is needed for an evaluation of the importance of these interactions.[59] However it is important to note that eq 22 only adds a constant term, $j_{bq} = (625/16)[2j_{12}+j_{23}+2j_{13}+j_{14}]$, to the diagonal elements of the HDvV matrix and does not contribute to the energy differences of Table 5. Therefore the effect of H^2_{bq} cannot be extracted from BS calculations. The expectation value of H^4_{bq} is nonzero only for the $|IS1>$ and $|IS2>$ states, whose relative energies in Table 5 must be modified adding $25j_{1234}/8$. Inserting this new parameter, the relative energies of Table 5 can be reproduced with $J_{12} = 47.62\ cm^{-1}$, $J_{23} = -6.6\ cm^{-1}$, $J_{13} = 0.05\ cm^{-1}$, $J_{14} = 0.3\ cm^{-1}$, and $J_{1234} = 1.4\ cm^{-1}$.

Computational Details

Calculations have been performed using the NWCHEM 5.0 program package, as developed and distributed by Pacific Northwest National Laboratory, P.O. Box 999, Richland, WA 99352 U.S.A., and funded by the U.S. Department of Energy.[60] 6−311G** basis sets[61] were applied to H and He atoms for the calculations on the model $(HeH)_4$ cluster. LANL2DZ Gaussian basis set[62] with their correspondent LANL2 pseudopotential were used for calculations on $[Cu(bpca)_2(H_2O)_2\{Cu(NO_3)_2\}_2]$ except for H atoms to which a 31G basis was applied. All electron Ahlrichs TZV basis sets[63] were used for the Mn cluster calculations except for H atoms to which a 311G basis was applied. All the basis sets came with the NWCHEM package. The hybrid B3LYP functional,[28] as implemented in NWCHEM 5.0, was used in all cases. The grid parameter was set to xfine, and the energies converged to 10^{-8} hartree.

Concluding Remarks

We have shown that the BS formalism give an internally consistent set of equations that can be used to determine the topology of the magnetic interactions in paramagnetic transition-metal clusters. Solving the whole set of BS equations allows the calculation of the exchange coupling parameters avoiding the indetermination that can be caused by an *a priori* choice of one particular subset, and the uncertainties on the computed values can be estimated from the least-squares fitting procedure. At least for the cases we computed here, these uncertainties arise from higher order terms that are not included in the HDvV spin Hamiltonian. BS formalism cannot be used to compute the biquadratic two-centers terms since their diagonal contributions in the spin Hamiltonian matrix is a constant but can be used to estimating the three and four center contributions.

We have seen that application of the BS formalism requires independent SCF convergences on several Slater determinants corresponding to the possible distributions of spin densities on the magnetic center. These convergences are prone to instability, and some criteria should be followed to

Table 8. Comparison between J_{ij} Values (cm^{-1}) Computed for $[Mn_4(OAc)_6(py)_2(cat)_2]^{2-}$ with MDA, DCA, MCA, and WCA

calculation model	J_{12}	J_{23}	J_{13}	J_{14}
MDA[b]	53.8(44.8;53.7)	19.2(16.0;19.2)	–	–
DCA[b]	33.1(27.6;33.1)	35.0(28.3;35.2)	14.1(11.7;14.0)	72.9(60.7;72.8)
MCA[a]	47.26	−5.3	0.4	0.6
WCA	47.65(3)	−5.6(1)	0.08(3)	0.3(1)

[a] *Set* **1** was chosen among the results shown in Table 6. [b] Computed with eq 7. The values reported in parentheses are J^{vq}_{12} and J^{AP}_{12}, respectively (see eqs 8 and 10).

being sure that the correct solution is found. Often a number of orbitals are close in energy in the SOMO-LUMO region. Visual inspection of the magnetic orbitals is possible only when their number is limited; this was not easily possible already for the Mn_4 cluster. Here we choose the quality of a SCF convergence looking at the spin density (Mulliken and/or Löwdin) of the metals and at the value of $\langle \mathbf{S^2} \rangle_{BS}$ and $\langle \mathbf{S^2} \rangle_{HS}$. The computed values of the spin densities and of the expectation values of $\mathbf{S}^2$ for $[Cu(bpca)_2(H_2O)_2\{Cu(NO_3)_2\}_2]$ and $[Mn_4(OAc)_6(py)_2(cat)_2]^{2-}$ are reported in Tables S1−S4. For Cu(II) spin densities were found to vary between 0.60 au to 0.66 au to be compared with the fully localized value of 1; for the Mn(II) complex spin densities were found to vary between 4.58 au and 4.67 au against a fully localized value of 5. The use of the WCA permits also the judging about the correctness of the SCF convergence, since we have found that when an incorrect energy is introduced into the BS set of equations a large error (hundreds of wavenumbers) is usually computed in the least-squares procedure.

Acknowledgment. This research was supported by the FIRB04 RBNE033KMA and NE MAGMANet NMP3-CT-2005-515767.

Supporting Information Available: MDA copper spin densities (SD) and $<S^2>$ values for $[Cu(bpca)_2(H_2O)_2\{Cu(NO_3)_2\}_2]$ (Table S1); DCA copper/zinc atoms spin densities (SD) and $<S^2>$ values for $[Cu(bpca)_2(H_2O)_2\{Cu(NO_3)_2\}_2]$ (Table S2); MDA manganese/tin atoms spin densities (SD) and $<S^2>$ value for $[Mn_4(OAc)_6(py)_2(cat)_2]^{2-}$) (Table S3); and DCA manganese/tin atoms spin densities (SD) and $<S^2>$ values for $[Mn_4(OAc)_6(py)_2(cat)_2]^{2-}$ (Table S4). This material is available free of charge via the Internet at http://pubs.acs.org.

References

(1) *Reviews of Modern Quantum Chemistry*; Sen, K. D., Ed.; World Scientific: Singapore, 2002; Vol. II, p 1247.

(2) Harvey, J. N. *Struct. Bonding (Berlin)* **2004**, *112*, 151.

(3) Siegbahn, P. E. M.; Borowski, T. *Acc. Chem. Res.* **2006**, *39*, 729.

(4) Bencini, A. *Inorg. Chim. Acta* **2008**, doi: 10.1016/j.ica.2008.03.076.

(5) Itoh, K.; Kinoshita, M. *Molecular Magnetism, New Magnetic Materials*; Gordon and Breach Science Pub.: Tokyo, 2000.

(6) Kahn, O. *Molecular Magnetism*; VCH Publisher: New York, 1993.

(7) Sessoli, R.; Gatteschi, D.; Caneschi, A.; Novak, M. A. *Nature* **1993**, *115*, 1804.

(8) Lis, T. *Acta Crystallogr., Sect. B: Struct. Crystallogr. Cryst. Chem.* **1980**, *36*, 2042.

(9) Friedman, J. R.; Sarachik, M. P.; Tejada, J.; Ziolo, R. *Phys. Rev. Lett.* **1996**, *76*, 3830. (b) Thomas, L.; Lionti, F.; Ballou, R.; Gatteshi, D.; Sessoli, R.; Barbara, B. *Nature (London)* **1996**, *383*, 145.

(10) Neese, F.; Petrenko, T.; Ganyushin, D.; Olbrich, G. *Coord. Chem. Rev.* **2007**, *251*, 288.

(11) Jensen, F. *Introduction to Computational Chemistry*, 2nd ed.; John Wiley & Sons: 2006; Chapter 4, p 98.

(12) (a) Fink, K.; Wang, C.; Staemmler, V. *Inorg. Chem.* **1999**, *38*, 3847. (b) Illas, F.; Moreira, I. de P. R.; de Graaf, C.; Barone, V. *Theor. Chem. Acc.* **2000**, *104*, 265. (c) Castell, O.; Caballol, R. *Inorg. Chem.* **1999**, *38*, 668. (d) Cabrero, J.; de Graaf, C.; Bordas, E.; Caballol, R.; Malrieu, J.-P. *Chem. Eur. J.* **2003**, *9*, 2307. (e) Calzado, C. J.; Malrieu, J.-P. *Phys. Rev. B* **2004**, *69*, 094435. (f) Bordas, E.; Caballol, R.; de Graaf, C. *J. Mol. Struct.: THEOCHEM* **2005**, *727*, 173. (g) Wang, M.; Wang, B.; Chen, Z. C. *J. Mol. Struct.: THEOCHEM* **2007**, *816*, 103.

(13) Bencini, A.; Gatteschi, D. *EPR of Exchange Coupled Systems*; Springer-Verlag: Berlin, Heidelberg, 1990.

(14) (a) Bleaney, B. *Proc. Phys. Soc. London, Sect. A* **1959**, *205*, 135. (b) Koster, G. F.; Statz, H. *Phys. Rev.* **1959**, *113*, 445. (c) McGavin, D. G.; Tennant, W. C.; Weil, J. A. *J. Magn. Reson.* **1990**, *87*, 92.

(15) In the literature equivalent form of the HDvV Hamiltonian are used with $-2J_{ij}$, $-J_{ij}$, and $2J_{ij}$ in the place of our notation J_{ij}. Care must be taken in checking the appropriate form of the SH when comparing data from different sources. In the convention used in this paper *antiferromagnetic coupling* corresponds to a *positive* J_{ij} value.

(16) (a) Stevens, K. W. H. *Rev. Mod. Phys.* **1953**, *25*, 166. (b) Kanamori, J. In *Magnetism*; Rado, G. T., Suhl, H., Eds.; Academic Press: New York, 1963; Vol. 1, p 127. (c) Dzialozshinsky, I. *J. Phys. Chem. Solids* **1958**, *4*, 241. (d) Moryia, T. In *Magnetism*; Rado, G. T., Suhl, H., Eds.; Academic Press: New York, 1963; Vol. 1, p 86.

(17) Griffith, J. S. *The Theory of Transition Metal Ions*; Cambridge University Press: 1961.

(18) Boča, R. *Coord. Chem. Rev.* **2004**, *248*, 757.

(19) (a) Neese, F.; Solomon, E. I. *Inorg. Chem.* **1998**, *37*, 6569. (b) Neese, F. *J. Chem. Phys.* **2007**, *127*, 164112.

(20) (a) Gerloch, M.; McMeeking, R. F. *J. Chem. Soc., Dalton Trans.* **1975**, 2443. (b) Banci, L.; Bencini, A.; Benelli, C.; Gatteschi, D.; Zanchini, C. *Struct. Bonding (Berlin)* **1982**, *52*, 37. (c) Bencini, A.; Benelli, C.; Gatteschi, D. *Coord. Chem. Rev.* **1984**, *60*, 131. (d) Bencini, A.; Ciofini, I.; Uytterhoeven, M. G. *Inorg. Chim. Acta* **1998**, *274*, 90.

(21) Brush, S. G. *Rev. Mod. Phys.* **1967**, *39*, 883.

(22) Wolf, W. P. *Braz. J. Phys* **2000**, *30*, 794.

(23) Losee, D. B.; McElearney, J. N.; Shankle, G. E.; Carlin, R. L.; Creswell, P. J.; Robinson, W. T. *Phys. Rev. B* **1973**, *8*, 2185.

(24) Foner, S.; Frankel, R. B.; Reiff, W. M.; Wong, H.; Long, G. J. *J. Chem. Phys.* **1978**, *68*, 4781.

(25) Borras-Almenar, J. J.; Clemente-Juan, J. M.; Coronado, E.; Tsukerblat, B. S. *Inorg. Chem.* **1999**, *38*, 6081.

(26) Pederson, M. R.; Khanna, S. N. *Phys. Rev. B* **1999**, *60*, 9566.

(27) (a) Noodleman, L.; Norman, J. G., Jr. *J. Chem. Phys.* **1979**, *70*, 4903. (b) Noodleman, L. *J. Chem. Phys.* **1981**, *74*, 5737.

(28) Becke, A. D. *J. Chem. Phys.* **1993**, *98*, 5648.

(29) (a) Noodleman, L.; Peng, C. Y.; Case, D. A.; Mouesca, J. M. *Coord. Chem. Rev.* **1995**, *144*, 199. (b) Noodleman, L.; Davidson, E. R. *Chem. Phys.* **1986**, *109*, 131. (c) Soda, T.; Kitagawa, Y.; Onishi, T.; Takano, Y.; Shigeta, Y.; Nagao, H.; Yoshioka, Y.; Yamaguchi, K. *Chem. Phys. Lett.* **2000**, *319*, 223. (d) Illas, F.; Moreira, I. de P. R.; de Coen, C.; Barone, V. *Theor. Chem. Acc.* **2000**, *104*, 265. (e) Ciofini, I.; Daul, C. A.; Bencini, A. Modeling Molecular Magnetism. In *Recent Advances in DFT Methods*; Barone, V., Bencini, A.,

Fantucci, P., Eds.; World Scientific: Singapore, 2002; Vol. 1, Part III, p 106. (f) Ruiz, E.; Rodrìguez-Fortea, A.; Cano, J.; Alvarez, S.; Alemany, P. *J. Comput. Chem.* **2003**, *24*, 982.

(30) Here we refer to the number of couples of *i*,*j* magnetic centers. This number can be further reduced by considering only adjacent magnetic centers. This is not usually a good choice, since experimentalists found that long-range interactions can significantly ameliorate the fitting of the magnetic data. Typical examples are linear, or almost linerar, trimers and tetramers in which the interactions between the extremes of the chains are usually included.

(31) Bencini, A.; Dei, A.; Sangregorio, C.; Totti, F.; Vaz, M. G. F. *Inorg. Chem.* **2003**, *42*, 8065.

(32) Miralles, J.; Daudey, J. P.; Caballol, R.; Malrieu, J. P. *Chem. Phys.* **1993**, *172*, 33.

(33) Calzado, C. J.; Cabrero, J.; Malrieu, J. P.; Caballol, R. *J. Chem. Phys.* **2002**, *116*, 2728.

(34) Bastardis, R.; Guihéry, N.; de Graaf, C. *Phys. Rev. B* **2007**, *76*, 132412.

(35) Ruiz, E.; Alemany, P.; Alvarez, S.; Cano, J. *J. Am. Chem. Soc.* **1997**, *119*, 1297. (b) Ruiz, E.; Cano, J.; Alvarez, S.; Alemany, P. *J. Comput. Chem.* **1999**, *20*, 1391.

(36) Albonico, C.; Bencini, A. *Inorg. Chem.* **1988**, *27*, 1934.

(37) Szabo, A.; Ostlund, N. S. Modern Quantum Chemistry; Dover Publications: 1996.

(38) In the absence of spin contamination from excited states the expected value is $S(S+1)$.

(39) Soda, T.; Kitagawa, Y.; Onishi, T.; Takano, Y.; Shigeta, Y.; Nagao, H.; Yoshioka, Y.; Yamaguchi, K. *Chem. Phys. Lett.* **2000**, *319*, 223.

(40) Ruiz, E.; Alvarez, S.; Cano, J.; Polo, V. *J. Chem. Phys.* **2005**, *123*, 164110.

(41) Adamo, C.; Barone, V.; Bencini, A.; Broer, R.; Filatov, M.; Harrison, N. M.; Illas, F.; Malrieu, J. P.; Moreira, I. d. P. R. *J. Chem. Phys.* **2006**, *124*, 107101.

(42) (a) Sorkin, A.; Iron, M. A.; Truhlar, D. G. *J. Chem. Theory Comput.* **2008**, *4*, 307 and references therein. (b) Reiher, M. *Faraday Discuss.* **2007**, *135*, 97 and references therein.

(43) Cabrero, J.; Calzado, C. J.; Maynau, D.; Caballol, R.; Malrieu, J. P. *J. Phys. Chem. A* **2002**, *106*, 8146.

(44) (a) Noodleman, L.; Case, D. A.; Sontum, S. F. *J. Chim. Phys.* **1989**, *86*, 743. (b) Mousca, J. M.; Chen, J. L.; Noodleman, L.; Bashford, D.; Case, D. A. *J. Am. Chem. Soc.* **1994**, *116*, 11898.

(45) Moreira, I. de P. R.; Illas, F. *Phys. Chem. Chem. Phys.* **2006**, *8*, 1645.

(46) Ovchinnikov, A. A.; Labanovski, J. K. *Phys. Rev. A* **1996**, *53*, 3946.

(47) (a) Shoji, M.; Koizumi, K.; Kitagawa, Y.; Kawakami, T.; Yamanaka, S.; Okumura, M.; Yamaguchi, K. *Chem. Phys. Lett.* **2006**, *432*, 343. (b) O'Brien, T. A.; O'Callaghan, J. *J. Chem. Theory Comput.* **2007**, *3*, 1275.

(48) Ruiz, E.; Rodríguez-Fortea, A.; Cano, J.; Alvarez, S.; Alemany, P. *J. Comput. Chem.* **2003**, *24*, 982.

(49) (a) Hart, J. R.; Rappé, A. K.; Gorun, S. M.; Upton, T. H. *J. Phys. Chem.* **1992**, *96*, 6264. (b) Bencini, A.; Totti, F.; Daul, C. A.; Doclo, K.; Fantucci, P.; Barone, V. *Inorg. Chem.* **1997**, *36*, 5022. (c) Ciofini, I.; Adamo, C.; Barone, V.; Berthier, G.; Rassat, A. *Chem. Phys.* **2005**, 309–133.

(50) All the other possible determinants that can be obtained flipping all the spins in each of the presented determinants will not be considered as they are degenerate to their respective completely flipped counterparts.

(51) Boèa, R. *Theoretical Foundations of Molecular Magnetism, Current Methods in Inorganic Chemistry*; Elsevier: Amsterdam, 1999; Vol. 1.

(52) (a) Calzado, C. J.; Malrieu, J. P. *Phys. Rev. B* **2004**, *69*, 094435. (b) Calzado, C. J.; de Graaf, C.; Bordas, E.; Caballol, R.; Malrieu, J. P. *Phys. Rev. B* **2003**, *67*, 132409.

(53) Carlucci, L.; Ciani, G.; Maggini, S.; Proserpio, D. M.; Sessoli, R. Manuscriptto be submitted for publication.

(54) Reynolds, R. A., III; Coucouvanis, D. *Inorg. Chem.* **1998**, *37*, 170.

(55) (a) Bencini, A.; Totti, F. *Int. J. Quantum Chem.* **2005**, *101*, 819. (b) Totti, F.; Bencini, A. Is Still the Heisenberg Spin Hamiltonian Reliable for Multi-nuclear Paramagnetic Clusters? In *CECAM Workshop, Models and Theory for Molecular Magnetism*; Lyon, 2006.

(56) DFT energies were obtained converging to 10^{-8} hartree. We estimate therefore an error at least 0.004 cm^{-1} on the energy differences, and this value is assumed as 0.

(57) Kortus, J.; Hellberg, C. S.; Pederson, M. R. *Phys. Rev. Lett.* **2001**, *86*, 3400.

(58) (a) Cano, J.; Costa, R.; Alvarez, S.; Ruiz, E. *J. Chem. Theory Comput.* **2007**, *3*, 782. (b) Ruiz, E.; Cauchy, T.; Cano, J.; Costa, R.; Tercero, J.; Alvarez, S. *J. Am. Chem. Soc.* **2008**, *130*, 7420.

(59) Bencini, A.; Totti, F. *Inorg. Chim. Acta* **2008**, doi:10.1016/j.ica.2008.03.033.

(60) (a) Straatsma, T. P.; Aprà, E.; Windus, T. L.; Bylaska, E. J.; de Jong, W.; Hirata, S.; Valiev, M.; Hackler, M.; Pollack, L.; Harrison, R.; Dupuis, M.; Smith, D. M. A.; Nieplocha, J.; Tipparaju,V.; Krishnan, M.; Auer, A. A.; Brown, E.; Cisneros, G.; Fann, G.; Früchtl, H.; Garza, J.; Hirao, K.; Kendall, R.; Nichols, J.; Tsemekhman, K.; Wolinski, K.; Anchell, J.; Bernholdt, D.; Borowski, P.; Clark, T.; Clerc, D.; Dachsel, H.; Deegan, M.; Dyall, K.; Elwood, D.; Glendening, E.; Gutowski, M.; Hess, A.; Jaffe, J.; Johnson, B.; Ju, J.; Kobayashi, R.; Kutteh, R.; Lin, Z.; Littlefield, R.; Long, X.; Meng, B.; Nakajima, T.; Niu, S.; Rosing, M.; Sandrone, G.; Stave, M.; Taylor, H.; Thomas, G.; van Lenthe, J.; Wong, A.; Zhang, Z. *NWChem, A Computational Chemistry Package for Parallel Computers, Version 4.6*; Pacific Northwest National Laboratory: Richland, WA, U.S.A. 99352-0999, 2004. (b) Kendall, R. A.; Aprà, E.; Bernholdt, D. E.; Bylaska, E. J.; Dupuis, M.; Fann, G. I.; Harrison, R. J.; Ju, J.; Nichols, J. A.; Nieplocha, J.; Straatsma, T. P.; Windus, T. L.; Wong, A. T. High Performance Computational Chemistry: an Overview of NWChem a Distributed Parallel Application. *Comput. Phys. Commun.* **2000**, *128*, 260–283.

(61) McLean, A. D.; Chandler, G. S. *J. Chem. Phys.* **1980**, *72*, 5639.

(62) Hay, P. J.; Wadt, W. R. *J. Chem. Phys.* **1985**, *82*, 270.

(63) Ahlrichs, R.; May, K. *Phys. Chem. Chem. Phys.* **2000**, *2*, 943.

CT800361X

JCTC Journal of Chemical Theory and Computation

Br···O Complexes as Probes of Factors Affecting Halogen Bonding: Interactions of Bromobenzenes and Bromopyrimidines with Acetone

Kevin E. Riley,*[,†,‡] Jane S. Murray,[§,||] Peter Politzer,[§,||] Monica C. Concha,[§] and Pavel Hobza[†]

Institute of Organic Chemistry and Biochemistry, Academy of Sciences of the Czech Republic, Center for Biomolecules and Complex Molecular Systems and Department of Physical Chemistry, Palacky University, 771 46 Olomouc, Czech Republic, Department of Chemistry, P.O. Box 23346, University of Puerto Rico, Rio Piedras, PR 00931, Department of Chemistry, University of New Orleans, New Orleans, Louisiana 70148, and Department of Chemistry, Cleveland State University, Cleveland, Ohio 44115

Received October 1, 2008

Abstract: Halogen bonding is a unique type of noncovalent binding phenomenon in which a halogen atom interacts attractively with an electronegative atom such as oxygen or nitrogen. These types of interactions have been the subject of many recent investigations because of their potential in the development of new materials and pharmaceutical compounds. Recently, it was observed that most halogen bonding interactions in biological contexts involve close contacts between a halogen bound to an aromatic ring and a carbonyl oxygen on a protein's backbone structure. In this work we investigate interactions of substituted bromobenzenes and bromopyrimidines with acetone to ascertain the effects of various substituents upon the strengths of these interactions. It was found that replacement of ring hydrogens in these systems has dramatic effects upon the interaction strengths of the resulting complexes, which have interaction energies between −1.80 and −7.11 kcal/mol. Examination of the electrostatic potentials of the substituted bromobenzene and bromopyrimidine monomers indicates that the addition of substituents has a large influence upon the most positive electrostatic potential on the surface of the interacting bromine and thus modulates these halogen bonding interactions. Results obtained using the symmetry-adapted perturbation theory (SAPT) interaction energy decomposition procedure also indicate that electrostatic interactions play the key role in these halogen bonding interactions. These results have important implications in drug design and crystal engineering. Halogen bonds have been a subject of great interest in these fields because of their unique noncovalent bonding characteristics.

Introduction

It is widely known that intermolecular and intramolecular noncovalent interactions are very important for the structures and stabilities of a broad range of molecular complexes and crystals. The hydrogen bond, the chief mode of interaction of which is through electrostatic and charge-transfer (delocalization) forces, has been the subject of many investigations and can be said to be the best characterized type of noncovalent interaction. The role of dispersion (and stacking) forces throughout many facets of chemistry has received an increasing amount of attention in the past decade or so. In recent years, halogen bonds, which share many properties with hydrogen bonds (although perhaps having a larger dispersive contribution), have been recognized as playing

* To whom correspondence should be addressed. E-mail: kev.e.riley@gmail.com.

† Academy of Sciences of the Czech Republic, Center for Biomolecules and Complex Molecular Systems and Department of Physical Chemistry, Palacky University, 771 46 Olomouc, Czech Republic.

‡ University of Puerto Rico.

§ University of New Orleans.

|| Cleveland State University.

10.1021/ct8004134 CCC: $40.75 © 2009 American Chemical Society
Published on Web 12/18/2008

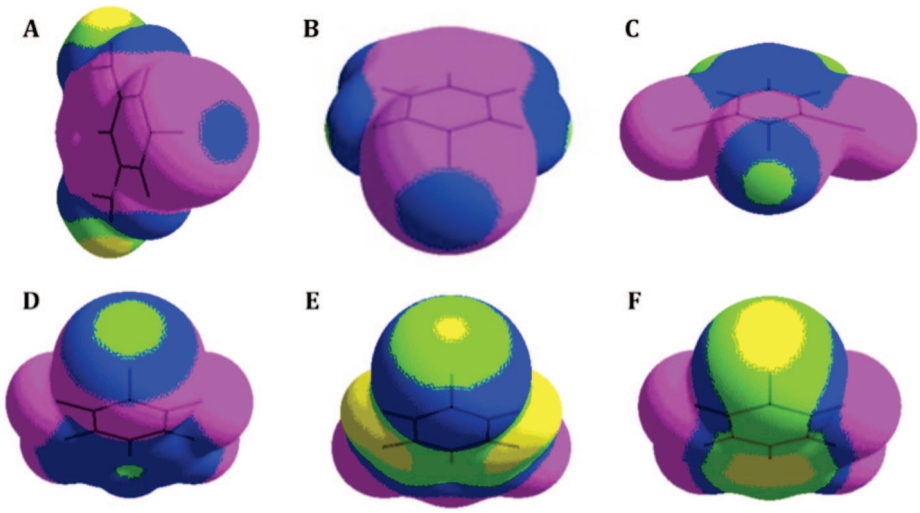

Figure 1. Electrostatic potentials of selected bromobenzene molecules in order of increasing Br $V_{S,max}$: (A) 3,5-diaminobromobenzene, (B) bromobenzene, (C) 2,6-dicyanobromobenzene, (D) pentafluorobromobenzene, (E) *meta*-$C_6O_2H_3Br$ (**2**), (F) C_6O_4HBr (**3**). Color ranges, in kcal/mol, are purple, negative; blue, from 0 to 15; green, from 15 to 30; yellow, from 30 to 42. The bromine is facing the viewer in each plot.

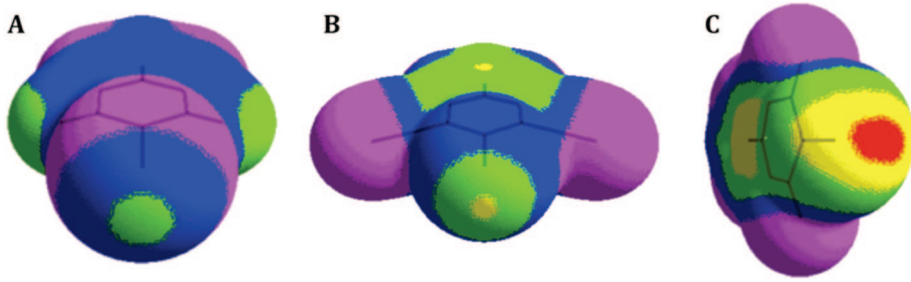

Figure 2. Electrostatic potentials of selected substituted bromopyrimidine molecules in order of increasing Br $V_{S,max}$: (A) 5-bromopyrimidne, (B) 5-bromo-4,6-dicyanopyrimidine, (C) $C_4N_2O_2HBr$ (**4**). Color ranges, in kcal/mol, are purple, negative; blue, from 0 to 15; green, from 15 to 30; yellow, from 30 to 42; red, greater than 42. The bromine is facing the viewer in each plot.

key roles in a wide variety of chemical systems. The phenomenon of halogen bonding has been a subject of particular interest within the fields of biochemistry [1,2] and materials science.[2,3] These types of interactions have recently been the subject of many theoretical [1,4−16] and experimental [17−19] investigations and promise to be of considerable significance in the development of novel chemical species with unique properties that may prove to be invaluable throughout chemistry and, more specifically, in drug design and crystal engineering. The importance of halogen bonds within various areas of scientific research is widely recognized, and this mode of interaction has been the subject of several recent review and perspectives articles.[3,4,20,21]

A halogen bond is a short-range RX···YZ interaction, where X is a halogen (typically chlorine, bromine, or iodine) that is part of the molecule RX and YZ is a Lewis base; Y is often an atom, such as oxygen, nitrogen, or sulfur, that has a lone pair.[3,4] Halogen bonds can be said to be analogous in many ways to hydrogen bonds (of the form RH···YZ) and are often treated in a similar manner. In both hydrogen bonding and halogen bonding, the donor (R) and the acceptor (Y) tend to be electronegative. For both hydrogen and halogen bonds, the distances H···Y and X···Y are generally less than the sum of the van der Waals radii of these atoms.

Because both halogen atoms and halogen bond acceptors (Y) are electronegative and are typically viewed as being negatively charged, the existence of halogen bonds is surprising and counterintuitive. However, studies of the electrostatic potentials of halogen-containing molecules by Brinck et al.,[5] Auffinger et al.,[1] and Politzer et al. [4,6] show that the larger halogens bound to carbon (and some other elements) often have a region of positive potential on the extension of the covalent bond to the halogen atom, that is, on the side of the halogen opposite to R (see the bromines in Figures 1B and 2A (bromobenzene and 5-bromopyrimidine)). The remainder of the halogen normally has also a negative region of potential, forming a ring around its lateral sides, except for cases where the molecule has one or more strongly electron-withdrawing groups.[6] The region of positive potential on a halogen's surface is often described as a positive σ-hole,[7] and has also been termed the electropositive crown.[1] The electrostatic attraction between the σ-hole and the negative Lewis base is the origin of halogen bonding. A halogen's σ-hole becomes larger and more positive as the size of the halogen increases, with a corresponding tendency for a halogen bond to become stronger.[4,6] Fluorine, the smallest (and most electronegative) halogen, rarely forms an electropositive crown, and thus does not normally

participate in halogen bonding. It has also been observed that the size and positive strength of the σ-hole tend to increase as R becomes more electron withdrawing.[4,6] Very recently, it has been demonstrated that covalently bonded atoms in Groups V and VI can also exhibit positive σ-holes and interact through these with Lewis bases.[8−10] It is interesting to note that the phenomenon of halogen bonding is attributable to a nonuniform atomic electron density and a corollary to this is that halogen bonds can only be properly treated using methods capable of accurately describing electron densities. Thus, molecular mechanics and molecular dynamics methods, which are based on parametrized force fields, would be expected to fail in describing halogen-bonding interactions.

The presence of a positive σ-hole on a halogen indicates that noncovalent interactions between that halogen and an electronegative atom should be highly electrostatic in nature. However, it should be kept in mind that halogen atoms, which are large and have large polarizabilities, would also be expected to interact with other chemical species through dispersion. In a recent work, the interactions between fluorinated and nonfluorinated halomethanes and formaldehyde (as well as methanol) were studied using high-level computational methods, including symmetry-adapted perturbation theory (SAPT).[11] It was found that these types of halogen-bonding interactions depend strongly upon both electrostatic and dispersion contributions. The relative magnitudes of these are highly dependent upon the identity of the halogen X and the number of fluorine substituents in R, with the relative contribution of the electrostatic term increasing for larger X and higher degrees of fluorine substitution. These bonding tendencies correspond to the presence of larger and more positive σ-holes.

Halogen bonds involving oxygen as the acceptor Y are especially interesting in biochemistry because they are, by a large margin, the most common types of halogen bonds involved in protein−ligand interactions. Recently, Auffinger and co-workers carried out a crystallographic database survey of short halogen−oxygen distances[1] and found that 81 out of 113 X···O interactions involved carbonyl oxygens (the database contained 66 protein structures and 6 nucleic acid structures from the protein data bank). These interactions generally involved a protein's backbone carbonyl group (78 out of 81). Interactions involving hydroxyl oxygens were also fairly common (18 out of 113). In 73 of the 78 protein−ligand complexes that involve a carbonyl oxygen as the acceptor (∼94%), the halogen X is bonded to an aromatic or heterocyclic aromatic ring.

Clearly, halogen bonds in which R is aromatic (and heterocyclic aromatic) and Y is a carbonyl oxygen are among the most important in biological systems. In this work, we investigated the effects of various substituents on the electrostatic potentials (especially in the region of the halogen σ-holes), optimal complex geometries, and binding energies of bromobenzene−acetone and bromopyrimidine−acetone complexes. The substitution of various chemical groups on the aromatic rings in these complexes has a large effect on the halogen's interactive behavior and thus could be used in the design of novel (pharmaceutical) ligands. Here we attempt to determine some of the fundamental rules for modifying a halogen bond's character via ring substitution.

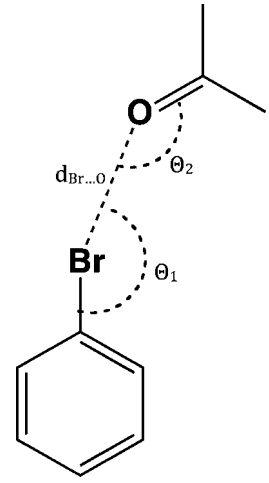

Figure 3. Schematic representation of $C_6H_5Br\cdots O{=}C(CH_3)_2$ halogen bond.

Computational Methods

General. Halogen bonds are multifaceted types of interactions that depend strongly upon both electrostatic and dispersion forces. We have used several techniques to describe the halogen bonds occurring between variously substituted bromobenzenes and bromopyrimidines as donors and acetone as the acceptor. To study the geometrical and energetic parameters that govern these halogen bonds, we have obtained optimized intermolecular geometries and binding energies with the MP2 method and a mixed basis set, which describes bromine using the pseudopotential-based aug-cc-pVDZ-PP and all other atoms with aug-cc-pVDZ. This approach is adopted because aug-cc-pVDZ-PP implicitly accounts for relativistic effects, which may influence halogen bonding interactions with such a large atom. We have computed the electrostatic potentials of all of the substituted bromobenzenes and bromopyrimidines, as well as that of acetone, at the B3PW91/6−31G(d,p) level. Finally, symmetry-adapted perturbation theory (SAPT) computations were performed to assess the relative contributions of dispersion and electrostatic (as well as induction and exchange) forces to the overall halogen bonding interactions. SAPT computations were performed using the aug-cc-pVDZ basis set.

Complete optimization of each of the halogen-bonding complexes described here proved to be too time-consuming and computationally costly to be practical. As a way to decrease the cost of these calculations, we divided the optimizations into two parts, first the monomers individually and then the dimer geometries in a self-consistent manner, using the optimal monomer geometries. The former were determined using the B3LYP/6-31G* method. To obtain optimal dimer geometries, the relative orientations of the monomers were systematically varied until the MP2/aug-cc-pVDZ(aug-cc-pVDZ-PP) binding energies reached self-consistency, as follows (see Figure 3 for geometric parameters):

1. The $d_{Br\cdots O}$ distance is changed by increments of 0.05 Å.

2. The angle θ_2 is varied by increments of one degree. θ_1 was assumed to be 180° for all complexes considered. The

validity of this assumption has been explored, and the results are described in the Results section. It should be noted that we have carried out a complete optimization for the case of the (unsubstituted) benzene-acetone complex at the MP2/aug-cc-pVDZ level of theory (CP corrected, no pseudopotential), the resulting geometrical parameters for this optimized complex are $d_{Br\cdots O} = 3.13$ Å, $\theta_2 = 120.6°$, and $\theta_1 = 179.3°$; the geometrical values obtained using our "by-hand" method are $d_{Br\cdots O} = 3.15$ Å, $\theta_2 = 120°$, and $\theta_1 = 180°$ (by definition). We believe that the optimization procedure used here is sufficient to obtain final geometries that are very close to the potential energy minima for these complexes and that, given the present purpose of comparing halogen bonds with various aromatic substituents, the results obtained using this method will describe the important trends in terms of the effects of substituents on geometrical parameters. We will also note here that we carried out another optimization for the benzene−acetone complex using the DFT/B3LYP/6−31+G* method to determine whether or not a lower level method, which does not describe dispersion interaction contributions very well, could systematically be used for the purposes of geometry optimization in this study. It was found that the final geometry parameters obtained at this level of theory are as follows: $d_{Br\cdots O} = 3.30$Å, $\theta_2 = 130.7°$, and $\theta_1 = 178.9°$. These results are rather far from those obtained at the MP2/aug-cc-pVDZ level, with a $\Delta\theta_2$ of about 10° and $\Delta d_{Br\cdots O}$ of 0.13 Å. With this result in mind, we determined that the optimization of these complexes using DFT methods would not be appropriate for this study.

Interaction energies were calculated at the MP2/aug-cc-pVDZ/aug-cc-pVDZ-PP level of theory, which has been shown to give results that are at least semiquantitative for halogen bonds,[11] although there is a tendency to underestimate the strengths of the interactions. This is more pronounced for weak halogen bonds (which are generally more dispersive in nature) and becomes less important for strong ones (which are generally more electrostatic). ΔE is given by

$$\Delta E = E_{complex} - (E_{acetone} + E_{brominederivative}) \qquad (1)$$

Here the counterpoise method was used to account for the basis set superposition error (for binding energies and optimization computations).[22]

In this work, our halogen bond donors are bromobenzene and bromopyrimidine derivatives and are listed in Tables 1 and 2. We have included a variety of functional groups (NH_2, OH, F, Cl, CN, and =O) in different combinations. It should be noted that among these are some carbonyl derivatives that may be unrealistic and might not exist for any extended period of time in nature (Table 2). The purpose of these unlikely structures, identified in Table 2 as **1**, **2**, **3**, and **4**, was to investigate the halogen bonding behavior of extreme examples of the bromobenzene and bromopyrimidine frameworks.

To compare the strengths of hydrogen bonds for complexes that are structurally similar to some of the halogen bonding complexes studied here, we have computed geometries and binding energies for the benzene−acetone and pentafluorobenzene−acetone complexes using the MP2/aug-cc-pVDZ method. The results obtained for these complexes can be directly compared with those for the bromobenzene-acetone and pentafluorobromobenzene-acetone complexes.

Table 1. Computed Bromine $V_{S,max}$ Values for a Series of Brominated Benzenes and Pyrimidines, and Interaction Energies, Optimized Br···O Separations, and Angles θ_2, for Their Complexes with Acetone[a]

molecule	Br $V_{S,max}$	interaction energy	Br···O separation	Br···O=C angle θ_2
bromobenzenes				
3,5-diaminobromobenzene	4.9	−1.80	3.15	120
para-aminobromobenzene	5.8	−2.02	3.10	121
meta-aminobromobenzene	7.1	−2.08	3.15	120
bromobenzene	9.7	−2.23	3.15	120
ortho-aminobromobenzene	9.9	−2.55	3.10	121
3,5-dihydroxybromobenzene	11.5	−2.25	3.10	121
ortho-chlorobromobenzene	12.9	−2.50	3.10	121
para-chlorobromobenzene	13.8	−2.52	3.10	121
meta-chlorobromobenzene	13.9	−2.53	3.10	121
3,5-difluorobromobenzene	15.7	−2.93	3.00	125
2,6-dicyanobromobenzene	22.1	−4.39	2.95	123
pentafluorobromobenzene	23.4	−4.08	2.95	124
3,5-dicyanobromobenzene	25.4	−3.71	2.95	127
bromopyrimidines				
2-bromopyrimidine	10.0	−2.46	3.05	121
5-bromopyrimidine	19.2	−3.24	3.00	125
5-bromo-4,6-dicyanopyrimidine	31.4	−5.04	2.75	125

[a] The $V_{S,max}$ and the interaction energies are in kcal/mol, Br···O separations in angstroms, and angles θ_2 in degrees.

Table 2. Computed Bromine $V_{S,max}$ Values for Four Brominated Carbonyl-Containing Heterocycles, and Interaction Energies, Optimized Br···O Separations, and Angles θ_1 and θ_2, for Their Complexes with Acetone[a]

Molecule	Br $V_{S,max}$	Interaction energy	Br...O separation	Br...O=C angle θ_2
1 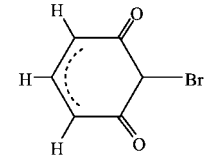	15.1	−2.63	3.00	119
2 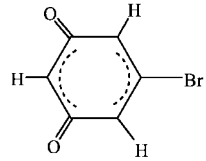	31.7	−4.30	2.95	129
3 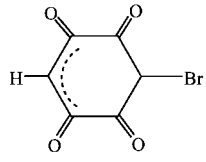	38.5	−4.56	2.95	123
4 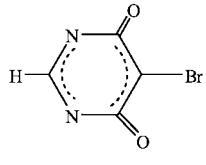	45.6	−7.11	2.80	129

[a] The $V_{S,max}$ and the interaction energies are in kcal/mol, Br···O separations in angstroms, and angles θ_2 in degrees.

Electrostatic Potential $V(\mathbf{r})$. The electrostatic potential $V(\mathbf{r})$ that the electrons and nuclei of a molecule create at any point $\mathbf{r}$ in the surrounding space is given by eq 2.

$$V(\mathbf{r}) = \sum_A \frac{Z_A}{|\mathbf{R}_A - \mathbf{r}|} - \int \frac{\rho(\mathbf{r}')d\mathbf{r}'}{|\mathbf{r}' - \mathbf{r}|} \quad (2)$$

Z is the charge on nucleus A, located at $\mathbf{R}_A$, and $\rho(\mathbf{r})$ is the electronic density function of the molecule. $V(\mathbf{r})$ is positive in those regions in which the dominant contribution is that of the nuclei, negative where it is that of the electrons. The electrostatic potential is a physical observable, which can be determined experimentally by diffraction techniques[23,24] as well as computationally.

When using $V(\mathbf{r})$ to analyze noncovalent interactions, we normally compute it on the surface of the molecule, which we take, following Bader et al.,[24] to be the 0.001 au (electrons/bohr^3) contour of the molecule's electronic density. A surface defined as a three-dimensional contour of $\rho(\mathbf{r})$ has the advantage that it reflects features specific to that molecule, for example, lone pairs, π electrons, strained bonds, etc.

In a series of studies, it has been demonstrated that a variety of condensed phase physical properties that depend upon noncovalent interactions can be expressed quantitatively in terms of the features characterizing $V(\mathbf{r})$ on a molecular surface, which we label $V_S(\mathbf{r})$.[26,27] For example, empirical measures of hydrogen bond donating and accepting tendencies correlate well with the most positive values ($V_{S,max}$) associated with hydrogens and the most negative ($V_{S,min}$) on basic sites.[28]

SAPT Methodology. The SAPT method[31] permits the separation of interaction energies into physically meaningful components, such as those arising from dispersion, electrostatics, induction, and exchange. The SAPT interaction energy is given by eq 3.

$$E_{int} = E^1_{pol} + E^1_{ex} + E^2_{ind} + E^2_{ex-ind} + E^2_{disp} + E^2_{ex-disp} \quad (3)$$

Some of these terms can be combined to give commonly understood physical quantities. In this work, we define the following:
$E(\text{elec}) = E^1_{pol}$
$E(\text{ind}) = E^2_{ind} + E^2_{ex-ind}$
$E(\text{disp}) = E^2_{disp} + E^2_{ex-disp}$
$E(\text{exch}) = E^1_{ex}$ These four quantities refer to, respectively, the electrostatic, induction, dispersion and exchange contributions to the overall interaction energy.

In this work, we have utilized the SAPT technique to study the relative contributions of the various interaction energy terms in halogen-bonding systems. The systems studied here are relatively large, thus the only reasonable basis set that could be used for these computations is the aug-cc-pVDZ basis of Dunning. It should be noted that when SAPT is used with this medium -sized basis set, contributions from dispersion will generally be underestimated by approximately 10%−15%. The version of the SAPT method employed in this study utilizes electronic densities determined at the Hartree−Fock level.

All interaction energies and SAPT computations were carried out using the Molpro electronic structure package (M06).[30]

Results

Tables 1 and 2 give (a) the computed bromine $V_{S,max}$ values for a series of individual brominated benzene and pyrimidine derivatives, (b) their interaction energies with acetone, (c) the optimum Br···O separations, and (d) the angles θ_1 and θ_2. Here it can be seen that, as stated in the Introduction, the substitution of various groups onto the bromobenzene and bromopyrimidine rings has a very large effect upon halogen bond strengths. Computed interaction energies range from −1.80 (3,5-diaminobromobenzene) to −7.11 kcal/mol ($C_4N_2O_2HBr$, **4**). There are several other important aspects of these data that can immediately be seen in these tables. One of the most pronounced patterns is the relationship between interaction energies and Br $V_{S,max}$ values: Higher $V_{S,max}$ (more positive σ-holes) result in complexes that are more strongly bound. Also apparent is that the presence of electron-withdrawing groups on the aromatic rings results in higher bromine $V_{S,max}$ values and more negative interaction energies, while the electron-donating NH_2 substituent leads to weaker interactions. In terms of geometries, there are two prevailing trends: the bromine−oxygen separation ($d_{Br\cdots O}$) contracts and the angle θ_2 become larger as the interaction energy increases in magnitude (the latter of these two relationships shows only moderate correlation). Note that the Br···O separations, $d_{Br\cdots O}$, are all less than the sum of the bromine and oxygen van der Waals radii, 3.37 Å,[29] consistent with the occurrence of a noncovalent interaction.

Relation of Electrostatic Potentials to Interaction Energies. Figures 1 and 2 show the electrostatic potentials on the molecular surfaces of nine of the molecules listed in Tables 1 and 2. In each case, the $V_{S,max}$ on the bromine is along the extension of its C−Br bond. The bromine $V_{S,max}$ tends to increase relative to the parent molecule bromobenzene as electron-attracting components are introduced; these may be substituents (Figure 1) or ring nitrogens (Figure 2).

Figure 1 displays, in order of increasing $V_{S,max}$, the electrostatic potentials on the molecular surfaces of six of the bromobenzene derivatives. 3,5-diaminobromobenzene, Figure 1A, has the weakest $V_{S,max}$ in Tables 1 and 2, consistent with the electron-donating nature of the amino group. Moving on to electron-withdrawing substituents, we see that the five fluorines in pentafluorobromobenzene, Figure 1D, make the σ-hole more positive ($V_{S,max}$ = 23.4 kcal/mol) than do the two ortho cyano groups in 2,6-dicyanobromobenzene ($V_{S,max}$ = 22.1 kcal/mol), shown in Figure 1C. In the bromopyrimidine framework, however, in which the electron-attracting power of the cyano groups is complemented by that of two ring nitrogens, putting two ortho cyano groups on 5-bromopyrimidine framework, Figure 2B, increases the bromine $V_{S,max}$ to 31.4 kcal/mol. Finally, the introduction of carbonyl oxygens further strengthens the bromine σ-holes; C_6O_4HBr (**2**) and $C_4N_2O_2HBr$ (**4**), in Figures 1E and 2C, have $V_{S,max}$ of 38.5 and 45.6 kcal/mol, respectively. The latter is the most-positive bromine $V_{S,max}$ computed in this work.

The bromines in Figures 1A−D and 2A are more typical than are the others in Figures 1 and 2 in that they have rings of negative electrostatic potential around their lateral sides, while the surfaces of the bromines in Figures 1E and F and 2B and C are completely positive. These latter potentials are a consequence of the strongly electron-withdrawing substituents on the rings and have been noted earlier for bromine and other halogens in such environments.[6] For the molecules in Tables 1 and 2, we find that the more characterstic rings of negative electrostatic potential are no longer present after the bromine $V_{S,max}$ reaches about 30 kcal/mol.

As mentioned earlier, the data in Tables 1 and 2 show a general tendency for the interaction energies to increase in magnitude as the computed $V_{S,max}$ prior to interaction become more positive. There are some exceptions, primarily involving those molecules having ortho substituents. In such cases, there are often secondary interactions (favorable or unfavorable) between the acetone and the ortho groups that affect the interaction energies.[32] For a striking example, consider 3,5-dicyanobromobenzene and 2,6-dicyanobromobenzene (Table 1). 3,5-dicyanobromobenzene, which has its cyano groups meta to the bromine, has a $V_{S,max}$ of 25.4 kcal/mol. The interaction energy with acetone is −3.7 kcal/mol. Its ortho isomer, 2,6-dicyanobromobenzene, has a slightly weaker $V_{S,max}$ of 22.1 kcal/mol, yet a stronger interaction energy with acetone, −4.4 kcal/mol. This can be explained by looking at the surface electrostatic potential of 2,6-dicyanobromobenzene in Figure 1C. The negative potentials of the cyano nitrogens overlap with that on the lateral sides of the bromine, creating extended negative regions that can interact favorably with one or more acetone hydrogens. This complements the C═O···Br interaction, resulting in a more negative ΔE than for the 3,5-dicyano case.

An ortho substituent may also affect the bromine $V_{S,max}$ and hence ΔE through an overlapping of potentials. Thus the slightly lower bromine $V_{S,max}$ in *ortho*-chlorobromobenzene compared to the meta and para isomers may be caused by the chlorine's negative potential overlapping with the positive one of the bromine σ-hole.

Figure 4 shows a plot of interaction energy versus bromine $V_{S,max}$ for the 13 molecules lacking bulky ortho substituents. The correlation is remarkably good, with a correlation coefficient of 0.976. This demonstrates the importance of the positive σ-hole, as reflected by the computed bromine $V_{S,max}$, in determining the energetics of the C−Br···O halogen bonds. When all 20 molecules are included, the correlation coefficient drops slightly to 0.956. These correlations indicate the role that electrostatics plays in these interactions, whether or not there are secondary ones.

Relation of Binding Energies to Geometric Parameters. Figures 5−7 show the potential energy curves for five of the complexes, with respect to three geometrical parameters: the bromine−oxygen separation ($d_{Br\cdots O}$), the Br···O−C angle (θ_2), and the C−Br···O angle (θ_1). These complexes are those of acetone with 3,5-diaminobromobenzene, bromobenzene, pentafluorobromobenzene, *meta*-$C_6O_2H_3Br$ (**2**), and $C_4N_2O_2HBr$ (**4**). These complexes are examples of halogen bonding interactions ranging from very weak (3,5-diaminobromobenzene, $\Delta E = \mu 1.80$ kcal/mol) to very strong (**4**, $\Delta E = \mu 7.11$ kcal/mol). The general tendency for stronger halogen bonds to have shorter optimum Br···O separations can clearly be seen in Figure 5. It is also interesting to note that these halogen bonding interactions act over a relatively large distance, with the stronger ones still discernible at a radial distance of 7.0 Å.

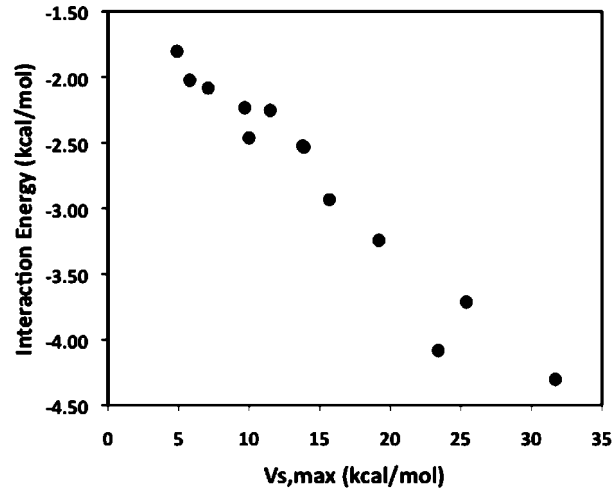

Figure 4. Plot of interaction energy vs bromine $V_{S,max}$ for the 13 molecules without ortho substituents (other than F). $R = 0.976$.

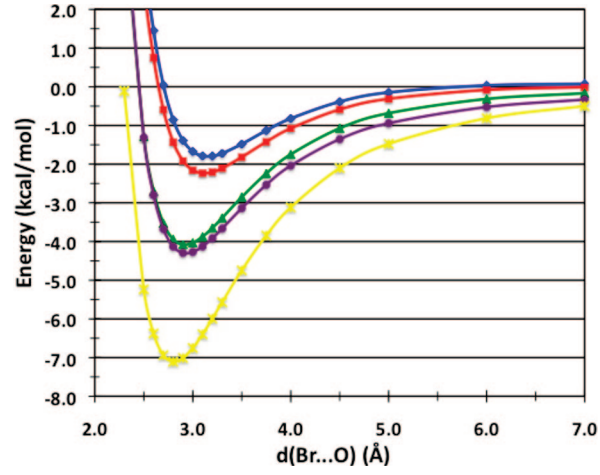

Figure 5. Potential energy curves for interaction energies with acetone as a function of the Br···O separation for complexes of 3,5-diaminobromobenzene (blue), bromobenzene (red), pentafluorobenzene (green), *meta*-$C_6O_2H_3Br$, **2** (purple), and $C_4N_2O_2HBr$, **4** (yellow).

The curves given in Figure 6 show that the interaction energy behaves is a shallow function of the Br···O−C angle (θ_2) between the values of approximately 115° and 180°. For these complexes, the difference between the interaction energies at the optimum angle and at 180° ranges from −0.32 (**2**) to −0.81 kcal/mol (3,5-diaminobromobenzene). As indicated in Tables 1 and 2, there is some tendency for the optimum Br···O−C angles to be larger for complexes with stronger interaction energies than for more weakly bound ones. These phenomena can be explained by looking at the electrostatic potential on the molecular surface of acetone, shown in Figure 8. The most striking feature is the strong

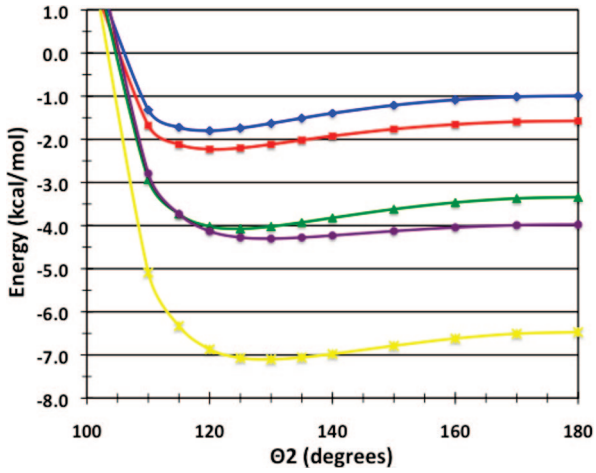

Figure 6. Potential energy curves for interaction energies with acetone as a function of the Br···O=C angle angle θ_2 for complexes of 3,5-diaminobromobenzene (blue), bromobenzene (red), pentafluorobenzene (green), *meta*-$C_6O_2H_3Br$, **2** (purple), and $C_4N_2O_2HBr$, **4** (yellow).

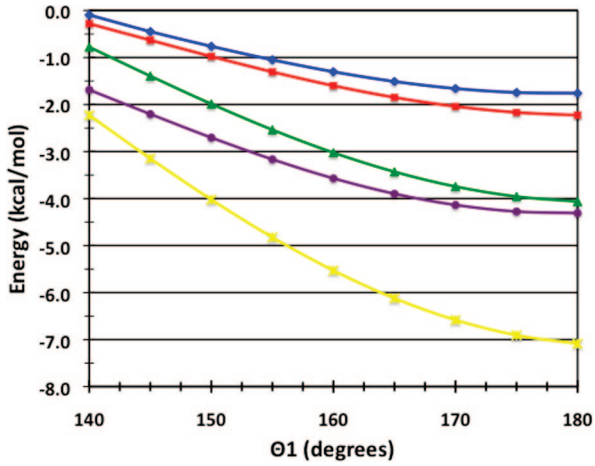

Figure 7. Potential energy curves for interaction energies with acetone as a function of the C−Br···O angle angle θ_1 for complexes of 3,5-diaminobromobenzene (blue), bromobenzene (red), pentafluorobenzene (green), *meta*-$C_6O_2H_3Br$, **2** (purple), and $C_4N_2O_2HBr$, **4** (yellow).

Figure 8. Electrostatic potential of acetone. Color ranges, in kcal/mol, are purple, more negative than −35; blue, from −35 to −30; green, from −30 to −20; yellow, from −20 to 0; red, greater than 0. The oxygen is toward the viewer.

band of negative potential, shown in purple, along the outer portion of the oxygen, extending 60° to either side of the C=O bond. This region has two minima, $V_{S,min}$, with values of −36.6 kcal/mol; however they are very shallow minima. This explains the fact that, although our calculations find the preferred C=O···Br angles for complexes with acetone to be between 119° and 129°, the binding energies remain fairly strong as these angles increase from their optimum values to 180°. The slight trend of the optimum binding angle for more strongly interacting complexes to be larger may be attributable to the fact that stronger halogen bonding interactions are generally more electrostatic in nature and thus the bromine σ-hole has a greater tendency to align with the most negative regions in the space surrounding the carbonyl oxygen. These carbonyl oxygen global minima (V_{min}) are at angles (C−O−V_{min}) of ∼127°.

A final observation that can be made from the data in Figure 6 is that the potential energy curve for the **2**···acetone complex is significantly shallower (although much more negative) than that of the pentafluorobromobenzene complex. The electrostatic potentials for these two molecules (Figure 1D and E) show that **2** does not have a typical σ-hole, with a ring of negative potential around the bromine. The fact that the entire bromine is positive in **2** allows it to interact attractively with the acetone oxygen over a wider range of angles.

Figure 7 shows binding energies as functions of the C−Br···O angle (θ_1). For all of the complexes, the optimum value of θ_1 is 180°, which corresponds to the optimal alignment of the bromine σ-hole with the carbonyl oxygen. The strengths of the interactions decrease rather sharply as θ_1 contracts, with ΔE for the weaker interactions (3,5-diaminobromobenzene and bromobenzene) reaching negligible values at 140°. This trend can clearly be attributed to the fact that the bromine σ-holes are no longer oriented toward the carbonyl negative charge density at low θ_1. As might be expected, the interaction energy falls off more slowly for the **2**···acetone complex than for that of pentafluorobromobenzene. This is the result of the overall positive potential found on the bromine atom of **2**, which can have an attractive electrostatic interaction over a wider range of the θ_1.

On the other hand, the strength of the **4**···acetone complex is highly dependent upon the strong electrostatic interaction with the more localized positive σ-hole of the bromine ($V_{S,max}$ = 45.6 kcal/mol). Figure 2C shows that the region of maximum positive potential on the bromine of **4** is relatively small. This explains the relatively sharp falloff for the interaction energy of this complex as a function of θ_1.

Comparison of Halogen Bonding and Hydrogen Bonding. It is interesting to compare the properties of halogen bonds with their, more ubiquitous, counterparts, hydrogen bonds. These types of intermolecular interactions evidently share several characteristics, most notably, both are interactions that occur between two atoms, which distinguishes them from general dispersion interactions and stacking interactions, which generally involve several atoms on both monomers. Another characteristic shared by both these types of noncovalent interactions is a large contribution of electrostatic forces to the overall interaction, although it should be noted that the electrostatic contribution to hydrogen bonding interactions is generally greater than that for most halogen bonding interactions.

Table 3 shows the interaction energies, $d_{X\cdots O}$ distances, and X···O−C (θ_2) angles for the complexes of bromoben-

Table 3. Comparison of Halogen-Bonding and Hydrogen-Bonding Geometrical Parameters and Binding Energies[a]

molecule	interaction energy	X···O separation	X···O=C angle θ_2
halogen bond			
bromobenzene	−2.23	3.15	120
pentafluorobromobenzene	−4.08	2.95	124
hydrogen bond			
benzene	−2.01	2.50	113
pentafluorobenzene	−3.99	2.25	130

[a] The interaction energies are in kcal/mol, Br···O separations in angstroms, and angles θ_2 in degrees.

Table 4. Computed Symmetry-Adapted Perturbation Theory (SAPT) Interaction Energy Decomposition Values for Halogen-Bonding Complexes[a]

SAPT term	$C_6H_5Br\cdots O{=}C(CH_3)_2$	$HC_4N_2O_2Br\cdots O{=}C(CH_3)_2$
E(elec.)	−2.44	−10.10
E(ind.)	−0.61	−1.90
E(disp.)	−2.56	−3.67
E(exch.)	3.69	8.28
E(SAPT)	−1.92	−7.39

[a] In kcal/mol.

zene, pentafluorobromobenzene, benzene, and pentafluorobenzene with acetone. Here it can be seen that, for both cases, the halogen-bonding interactions are predicted to be slightly stronger than the hydrogen-bonding interactions; in the unsubstituted case (bromobenzene and benzene), the halogen bonding interaction energy is about 0.2 kcal/mol lower than that for the hydrogen bonding case, while the difference is about 0.1 kcal/mol for the fluorine substituted complexes. As would be expected, the $d_{X\cdots O}$ distances are substantially shorter for the hydrogen-bonding complexes (by 0.65−0.70 Å). Interestingly, the X···O−C angle is larger for the bromobenzene complex than for the benzene one by seven degrees, while for the fluorine substituted complexes the X···O−C is six degrees smaller for the halogen bonding complex compared to the hydrogen bonding one. These results may be a result of intermolecular interactions, likely to be more important when the molecules are closer together, as they are in the hydrogen bonding cases.

SAPT Results. Table 4 gives interaction energy decompositions in terms of symmetry-adapted perturbation theory (SAPT/aug-cc-pVDZ) for the complexes of bromobenzene and **4** with acetone. The most important aspect of these data is the fact that the interaction of **4** is much more electrostatic in nature than that of bromobenzene (by about a factor of 4). This result is not unexpected because the bromine $V_{S,max}$ for **4** is so much larger than that of bromobenzene (see Tables 1 and 2 and Figures 1B and 2C). The other three SAPT terms are also larger for **4** than for bromobenzene. The increase in induction is most likely caused by a larger degree of charge transfer for the **4**···acetone complex. The increases in both the dispersion and exchange terms can be attributed to the fact that in the **4**···acetone complex, the bromine is in much closer to the acetone oxygen than in the bromobenzene complex.

These results are in agreement with those in earlier work by Riley and Hobza.[11] There it was found that in the interaction of unsubstituted bromomethane with formaldehyde, the SAPT electrostatic term contributes about 26% less than the dispersion term. Upon substitution of three fluorines to bromomethane to form F_3CBr, the size and positive potential of the bromine σ-hole increases significantly. Likewise, the electrostatic component of the interaction increases considerably, contributing about 37% *more* than dispersion.

Conclusions

The main conclusion to be drawn from this investigation is that the strength and character of halogen-bonding interactions can be influenced to a great extent through the introduction of various substituents onto an aromatic ring bearing bromine (or presumably other halogens such as chlorine and iodine). The range of interaction energies for the substituent configurations used in this study is quite large, varying from −1.80 kcal/mol (3,5-diaminobromobenzene) to −7.11 kcal/mol ($C_4N_2O_2HBr$, **4**). This result has great implications in the fields of drug design and crystal engineering, in which halogen bonding interactions have been the subject of intense research because of their unique properties and their potential in the development of novel pharmaceuticals and materials.

The principal mechanism for the modulation of halogen bond strengths by aromatic substitution involves changes in the electron density on bromine. It can be seen by studying the electrostatic potentials of these molecules that the presence of electron-withdrawing and -donating substituents greatly affects the electrostatic potential in the space around bromine (and the rest of the system). The introduction of different substituents into these systems produces a broad spectrum of bromine $V_{S,max}$ values (which measure the maximum positive potential found on the bromine surface), ranging from 4.9 kcal/mol (3,5-diaminobromobenzene) to 45.6 kcal/mol ($C_4N_2O_2HBr$, **4**). These $V_{S,max}$ values correlate very well with interaction energies, showing that the electrostatic properties of a possible halogen-bonding molecule are critical to its binding behavior. These findings are supported by SAPT interaction energy decompositions, which demonstrate that the electrostatic component of halogen bonding changes substantially upon substitution of a strong electron-withdrawing group or ring atom.

In cases where an electron-donating substituent (NH_2), no substituent (H), and weakly electron-withdrawing substituents (OH, Cl) are present, the bromine exhibits a conventional σ-hole, which varies greatly in size and in positive potential ($V_{S,max}$) and for which the bromines have rings of negative potentials around their lateral sides. For stronger electron-withdrawing substituents (=O, CN), the entire bromine acquires a positive potential, with a higher $V_{S,max}$, which leads to very stable halogen-bonding interactions. As would be expected, electron-donating groups tend to weaken halogen bonding, while electron-withdrawing substituents lead to stronger interactions. It should also be noted that for (unsubstituted and substituted) bromopyrimidines, which contain two electron-attracting nitrogens within their aromatic rings, the σ-hole is generally larger and more positive than for the corresponding bromobenzene structures.

As was expected, the optimum C−Br···O angles for halogen bonding complexes was found to be 180° (Figure 7), corresponding to an optimal interaction between the acetone oxygen and the bromine σ-hole. The strengths of these interactions decrease rather sharply as the C−Br···O angle becomes smaller and the σ-hole can no longer interact with =O. The C=O···Br angles for these complexes were observed to be in the range between 119° and 129°, with a tendency for stronger halogen-bonding interactions to assume larger angles. This trend is most likely attributable to the fact that stronger halogen bonds, with σ-holes that are more positive, will have a stronger tendency to line up with the most negative region of the acetone oxygen (found at a C=O···Br angle of ∼127°).

Acknowledgment. This work was a part of the research project No. Z40550506 of the Institute of Organic Chemistry and Biochemistry, Academy of Sciences of the Czech Republic, and it was supported by Grants LC512 and MSM6198959216 from the Ministry of Education, Youth and Sports of the Czech Republic. The support of Praemium Academiae, Academy of Sciences of the Czech Republic, awarded to P.H. in 2007 is also acknowledged. K.R. gratefully acknowledges the support of the NSF EPSCOR program (EPS-0701525).

References

(1) Auffinger, P.; Hays, F. A.; Westhof, E.; Ho, P. S. *Proc. Natl. Acad. Sci. U.S.A.* **2004**, *101*, 16789–16794.

(2) Metrangolo, P.; Neukirsch, H.; Pilati, T.; Resnati, G. *Acc. Chem. Res.* **2005**, *38*, 386–395.

(3) Halogen Bonding with Dihalogens and Interhalogens, in Halogen Bonding. In *Fundamentals and Applications*; Metrangolo, P., Resnati, G., Eds.; Structure and Bonding 126; Springer: Berlin, 2008.

(4) Politzer, P.; Lane, P.; Concha, M. C.; Ma, Y.; Murray, J. S. *J. Mol. Model.* **2007**, *13*, 305–311.

(5) Brinck, T.; Murray, J. S.; Politzer, P. *Int. J. Quantum Chem., Quantum Biol. Symp.* **1992**, *19*, 57–64.

(6) Politzer, P.; Murray, J. S.; Concha, M. C. *J. Mol. Model.* **2007**, *13*, 643–650.

(7) Clark, T.; Hennemann, M.; Murray, J. S.; Politzer, P. *J. Mol. Model.* **2007**, *13*, 291–296.

(8) Murray, J. S.; Lane, P.; Politzer, P *Int. J. Quantum Chem.* **2007**, *107*, 3046–3052.

(9) Murray, J. S.; Lane, P.; Clark, T.; Politzer, P. *J. Mol. Model.* **2007**, *13*, 1033–1038.

(10) Politzer, P.; Murray, J. S.; Lane, P *Int. J. Quantum Chem.* **2007**, *107*, 3046–3052s.

(11) Riley, K. E.; Hobza, P. *J. Chem. Theory Comput.* **2008**, *4*, 232–242.

(12) Riley, K. E.; Merz, K. M. *J. Phys. Chem. A* **2007**, *111*, 1688–1694.

(13) Lommerse, J. P. M.; Stone, A. J.; Taylor, R.; Allen, F. H. *J. Am. Chem. Soc.* **1996**, *118*, 3108–3116.

(14) Lu, Y. X.; Zou, J. W.; Wang, Y. H.; Yu, Q. S. *J. Mol. Struct. Theochem* **2006**, *767*, 139–142.

(15) Poleshchuk, O. K.; Branchadell, V.; Brycki, B.; Fateev, A. V.; Legon, A. C. *J. Mol. Struct. Theochem* **2006**, *760*, 175–182.

(16) Palusiak, M.; Grabowski, S. *J. Struct. Chem.* **2008**, *19*, 5–11.

(17) Chopra, D; Thiruvenkatam, V.; Manjunath, S. G.; Row, T. N. G. *Cryst. Growth Des.* **2007**, *7*, 868–874.

(18) Corradi, E.; Meille, S. V.; Messina, M. T.; Metrangolo, P.; Resnati, G. *Ang. Chem., Int. Ed.* **2000**, *39*, 1782–1786.

(19) Glaser, R.; Chen, N. J.; Wu, H.; Knotts, N.; Kaupp, M. *J. Am. Chem. Soc.* **2004**, *126*, 4412–4419.

(20) Metrangolo, P.; Resnati, G. *Science* **2008**, *321*, 918–919.

(21) *Halogen Bonding: Fundamentals and Applications*; Metrangolo, P., Resnati, G. Eds.; Structure and Bonding 126; Springer: Berlin, 2008.

(22) Boys, S. F.; Bernardi, F. *Mol. Phys.* **1970**, *19*, 553–566.

(23) Stewart, R. F. *Chem. Phys. Lett.* **1979**, *65*, 335–342.

(24) *Chemical Applications of Atomic and Molecular Electrostatic Potentials*; Politzer, P., Truhlar, D. G., Eds.; Plenum, New York, 1981.

(25) Bader, R. F. W.; Carroll, M. T.; Cheeseman, J. R.; Chang, C. *J. Am. Chem. Soc.* **1987**, *109*, 7968–7979.

(26) Murray, J. S.; Politzer, P. *J. Mol. Struct. (Theochem)* **1998**, *425*, 107–114.

(27) Politzer, P.; Murray, J. S. *Fluid Phase Equilib.* **2001**, *185*, 129–137.

(28) Hagelin, H.; Murray, J. S.; Brinck, T.; Berthelot, M.; Politzer, P *Can. J. Chem.* **1995**, *73*, 483–488.

(29) Jeziorski, B.; Moszynski, R.; Szalewicz, K. *Chem. Rev.* **1994**, *94*, 1887–1930.

(30) Werner, H. J.; Knowles, P. J.; Lindh, R.; Manby, F. R.; Schütz, M.; Celani, P.; Korona, T.; Rauhut, G.; Amos, R. D.; Bernhardsson, A.; Berning, A.; Cooper, D. L.; Deegan, M. J. O.; Dobbyn, A. J.; Eckert, F.; Hampel, C.; Hetzer, G.; Lloyd, A. W.; McNicholas, S. J.; Meyer, W.; Mura, M. E.; Nicklaβ; A.; Palmieri, P.; Pitzer, R.; Schumann, U.; Stoll, H.; Stone, A. J.; Tarroni, R.; T., T. *Molpro*, version 2006.1; 2006.

(31) Bondi, A. *J. Phys. Chem.* **1964**, *68*, 441–451.

(32) Clark, T.; Murray, J. S.; Lane, P.; Politzer, P. *J. Mol. Model.* **2008**, *14*, 689–697.

CT8004134

JCTC Journal of Chemical Theory and Computation

Computation of Local and Global Properties of the Electron Localization Function Topology in Crystals

J. Contreras-García, A. Martín Pendás, and J. M. Recio*

MALTA-Consolider Team and Departamento de Química Física y Analítica, Universidad de Oviedo, E-33006 Oviedo, Spain

B. Silvi

Laboratoire de Chimie Théorique (UMR-CNRS 7616), Université Pierre et Marie Curie, 3 rue Galilée 94200-Ivry sur Seine, France

Received October 6, 2008

Abstract: We present a novel computational procedure, general, automated, and robust, for the analysis of local and global properties of the electron localization function (ELF) in crystalline solids. Our algorithm successfully faces the two main shortcomings of the ELF analysis in crystals: (i) the automated identification and characterization of the ELF induced topology in periodic systems, which is impeded by the great number and concentration of critical points in crystalline cells, and (ii) the localization of the zero flux surfaces and subsequent integration of basins, whose difficulty is due to the diverse (in many occasions very flat or very steep) ELF profiles connecting the set of critical points. Application of the new code to representative crystals exhibiting different bonding patterns is carried out in order to show the performance of the algorithm and the conceptual possibilities offered by the complete characterization of the ELF topology in solids.

I. Introduction

Due to the high coordination indexes and to the numerous atom−atom contacts, the presence of different bonding types is a common and genuine feature of solids which hampers their characterization when compared with the molecular realm. Performing a rigorous qualitative and quantitative classification of these bonds, based on a unique theoretical formalism, has revealed itself to be a challenge and a source of debate.[1] The localization of orbitals leads to ambiguities in many solid-state problems,[2] a reason for which the topological analysis in real space has been shown to be a very fruitful approach in the last few decades. Among these methods, the widest-spread approach has been to consider the topological analysis of the electron density (AIM) as developed by Bader and co-workers,[3,4] according to which the existence of a bond is associated to the presence of a bond path in the stable structure of the solid. It has also been long recognized that chemical insight into the nature of the chemical bond can be gained by resorting to the electron localization function (ELF).[5]

The topological analysis of ELF, although spread among molecules, has been scarce in the solid state due to the major computational difficulties imposed by periodicity.[5−7] Some noticeable applications concern relevant geophysical problems, as the identification of favored docking sites in SiO_2 polymorphs,[8,9] whereby protons were found to prefer the proximities of lone pairs. However, the ability of this function to reflect interactions, as well as the translational symmetry of crystalline systems, leads to an intricate pattern of ELF critical points and of irregular ELF profiles that hamper their automated localization and the integration of the related basins in which the 3D space of the unit cell is divided.

Our work has been focused on the development of a computational algorithm attempting to fulfill the gap existing between the ELF topological analyses of bonding in the molecular and the crystalline realms. A thoughtful analysis of the nature of the problem is critical thereto. It was already recognized by Nathaniel et al.[10] that algorithms coming from

* Corresponding author. E-mail: mateo@fluor.quimica.uniovi.es.

10.1021/ct800420n CCC: $40.75 © 2009 American Chemical Society
Published on Web 12/15/2008

Bader analyses mainly fail at the inner and outer core, whose sphericity remains practically unaltered under the crystal environment, leading to nearly degenerated surfaces and critical point clustering. A hybrid algorithm that combines previous methods and a new approach for the determination of the local and global properties of the core topology is proposed for the complete determination of the ELF topology. Due to the intricate and heterogeneous nature of the function, special emphasis has been given to the design of a robust algorithm, of applicability to a wide variety of crystal bonding patterns.

The organization of the paper is as follows. First, we will introduce the basic concepts of the ELF topology stressing the computational difficulties associated with the main differences between the ELF in the molecular and the crystalline realms. Then, we explain the algorithms devised to overcome these problems for the localization of critical points and the integration of basins. Next, some examples of bonding analyses in prototypical solids will be presented to show the robustness and performance of the method. Finally, conclusions will be drawn and future applications advanced.

II. ELF Topological Analysis in Crystals

The electron localization function (ELF) was originally designed by Becke and Edgecombe to identify "localized electronic groups in atomic and molecular systems".[11] It relies, through its kernel, to the laplacian of the conditional same spin pair probability scaled by the homogeneous electron gas kinetic energy:

$$\chi_\sigma(\mathbf{r}) = \frac{D_\sigma(\mathbf{r})}{D_\sigma^0(\mathbf{r})} \tag{1}$$

in which

$$D_\sigma(\mathbf{r}) = \tau_\sigma(\mathbf{r}) - \frac{1}{4}\frac{(\rho_\sigma(\mathbf{r}))^2}{\rho_\sigma(\mathbf{r})}$$

appears to be the difference of the actual definite positive kinetic energy $\tau_\sigma(\mathbf{r})$ and the von Weizsäcker kinetic energy functional,[12] whereas

$$D_\sigma^0(\mathbf{r}) = \frac{3}{5}(6\pi^2)^{2/3}\rho_\sigma^{5/3}(\mathbf{r})$$

is the kinetic energy density of the homogeneous electron gas. This formulation led Savin to propose an interpretation of ELF in terms of the local excess kinetic energy due to the Pauli repulsion, enabling its calculation from Kohn−Sham orbitals.[2,13,14] Orbital based interpretations of ELF have been proposed by Burdett[15] and more recently by Nalewajski et al.[16] who considered the nonadditive interorbital Fisher information. Another route pioneered by Dobson[17] explicitly considers the pair functions. It has been independently developed by Kohout et al.[18,19] and by one of us[20] allowing the extension of ELF to correlated wave functions.[21]

From a simple statistical viewpoint, the concept of electron density localization at a given position $\mathbf{r}$ relies on the standard deviation of the electron density integrated over a sampling volume $V(\mathbf{r})$ encompassing the reference point and containing a given quantity of matter, in other words a given charge q. The smaller the standard deviation, the higher the localization. Instead of the standard deviation, it is advantageous to use its square, the variance σ^2, which can be expressed as the expectation value of the variance operator:[22]

$$\langle \widehat{\mathrm{cov}}(V(\mathbf{r}), V(\mathbf{r}))\rangle = \bar{\Pi}(V(\mathbf{r}), V(\mathbf{r})) - \bar{N}(V(\mathbf{r}))\left(\bar{N}(V(\mathbf{r})) - 1\right) = \bar{\Pi}(V(\mathbf{r}), V(\mathbf{r})) - q^2 + q \tag{2}$$

in which $\bar{N}(V(\mathbf{r})) = q$ and $\bar{\Pi}(V(\mathbf{r}), V(\mathbf{r}))$ are respectively the one particle and two particle densities integrated over the sample $V(\mathbf{r})$. In the expression of the variance given above, only $\bar{\Pi}(V(\mathbf{r}), V(\mathbf{r}))$ is function of the position and therefore $-q^2 + q$ can be regarded as a constant and deleted. The integrated pair density is the sum of an opposite spin contribution, $2\bar{\Pi}^{\alpha\beta}(V(\mathbf{r}),V(\mathbf{r}))$ almost proportional to q^2 and of a same spin contribution $\bar{\Pi}^{\alpha\alpha}(V(\mathbf{r}), V(\mathbf{r})) + \bar{\Pi}^{\beta\beta}(V(\mathbf{r}), V(\mathbf{r}))$ which has numerically been shown proportional to a function of the position, say $c_\pi(\mathbf{r})$, times $q^{5/3}$. In the limit $q = 0$, the ratio

$$\frac{\bar{\Pi}(V(\mathbf{r}), V(\mathbf{r}))}{q^{5/3}}$$

tends to the spin pair composition, $c_\pi(\mathbf{r})$, a local function independent of the size of the sample.[20] The ability of this function to localize "electronic groups" can be illustrated by a very simple example in which two α and two β spin electrons are confined in a box of volume Ω. For the sake of simplicity we assume the electron density probability to be uniform, i.e. $\rho(\mathbf{r}) = 4/\Omega$ without spin polarization ($\rho^\alpha(\mathbf{r}) = \rho^\beta(\mathbf{r}) = 2/\Omega$), such as the opposite spin pair functions, $\Pi^{\alpha\beta}(\mathbf{r}_1, \mathbf{r}_2) = \Pi^{\beta\alpha}(\mathbf{r}_1, \mathbf{r}_2) = 4/\Omega^2$ are constant. This model enables to consider two localization cases. On the one hand, the opposite spin pairs are delocalized over the box and the same spin pair functions are constant: $\Pi^{\alpha\alpha}(\mathbf{r}_1, \mathbf{r}_2) = \Pi^{\beta\beta}(\mathbf{r}_1, \mathbf{r}_2) = 2/\Omega^2$ and therefore $c_\pi(\mathbf{r})$ is also constant. On the other hand, each opposite spin pair occupies one-half of the box such as the following:

$$\Pi^{\alpha\alpha}(\mathbf{r}_1, \mathbf{r}_2) = \Pi^{\beta\beta}(\mathbf{r}_1, \mathbf{r}_2) = \begin{cases} 0 & \mathbf{r}_1, \mathbf{r}_2 \in \text{ same half box} \\ 4/\Omega^2 & \mathbf{r}_1, \mathbf{r}_2 \in \text{ different half boxes} \end{cases} \tag{3}$$

It follows that

$$c_\pi(\mathbf{r}) \begin{cases} = 0 & \mathbf{r} \notin \text{ the boundary} \\ \propto 4/\Omega^2 & \mathbf{r} \in \text{ the boundary} \end{cases} \tag{4}$$

which enables one to locate the boundary between the two opposite spin pair regions.

For the Hartree−Fock wave function, it can be easily demonstrated[20] that

$$\chi_\sigma(\mathbf{r}) \approx c_\pi(\mathbf{r}) \tag{5}$$

The localization function itself is obtained through the transformation of $\chi_\sigma(\mathbf{r})$ into a Lorentzian function

$$\eta(\mathbf{r}) = \frac{1}{1 + \chi_\sigma^2(\mathbf{r})} \tag{6}$$

so that it tends to 1 in those regions where the localization is high and to small values at the boundaries between such regions.

The arguments developed above indicate that $\eta(\mathbf{r})$ can be used to recover regions of space associated to electron pairs as they emerge in the Lewis's description.[23] The dynamical system theory[24] has been used in this context to provide a partition of the direct geometrical space into non overlapping basins of attractors[25,26] which can be thought of as electronic domains corresponding to the chemical entities of the Lewis's picture. Moreover, it has been recently shown that the electrostatic repulsions between these basins provide a justification of the valence shell electron pair repulsion (VSEPR) rules.[27] The ELF basins belong either to the core or valence shells of atoms in molecules. The valence basins V(A, ...) encompassing a given atomic core basin C(A) (which can be constituted by K, L, ... shells) form the valence shell of atom A. In agreement with the Lewis's picture V(A, ...) may belong to several atomic shells. The synaptic order of a valence basin is the number of atomic shells to which it belongs. The hierarchy of the ELF basin is given by the bifurcation diagrams[28,29] which provide the connectivity of the different fragments of the investigated system.

Within the dynamical system framework, pioneered by Bader for the analysis of the electron density,[3] a formal analogy is made between a vector field bounded on a manifold and a velocity field. In the present case, the vector field is the gradient field of the ELF, $\nabla\eta(\mathbf{r})$, and the manifold the 3-dimensional geometrical space. This is the reason why this point is also known as attractor of the gradient field. Attractors belong to a subset of special points of the field, named critical points (CPs), characterized by a null gradient. Contrary to wandering points ($\nabla\eta \neq 0$) critical points may act as a source or a sink of more than one gradient path, depending on their nature. The number of nonzero eigenvalues of the Hessian, or rank, determines its dimensionality, and the sum of the signs of the Hessian eigenvalues characterizes the capability to receive or send gradient paths. In a stable 3D topology, this gives rise to the following possibilities: (3, −3) for local maxima or attractors, (3, +3) for local minima, and (3, −1) and (3, +1) for saddle points in one or two dimensions, respectively.

Indeed, two types of topological information are obtained: local and global. Local information is gathered by evaluating density properties at distinctive points where the gradient vanishes. Global information is acquired from volume integration of property densities over spatial fragments. Since the topological analysis of the ELF gradient field[25,26] yields basins that can be associated to Lewis entities, the integration of the density (ρ) over their volume (Ω_i) assigns a population ($\bar{N}$) to bonds, lone pairs and atomic shells:

$$\bar{N}(\Omega_i) = \int_{\Omega_i} \rho(\mathbf{r})\mathrm{d}\mathbf{r} \tag{7}$$

In spite of the lack of a clear physical significance of the definition of the zero flux surfaces of ELF, it was demonstrated by Kohout and Savin[30] that these populations follow the expected values and tendencies from the Aufbau principle and the VSEPR theory.

The properties of the gradient dynamical system are complemented in the context of the ELF topology with the interpretation derived from the *f*-domain[28] concept, that enables chemical units in the system to be recovered, as well as to characterize the basins according to common chemical knowledge. Introduced by Mezey[31] within the AIM framework, the concept of an *f*-domain accounts for the volume enclosed by an isosurface of a certain value of $\eta = f$. As the value f increases, successive splitting of the initial domains take place until all of them contain one, and only one, attractor. This process in called reduction (and the final domains, irreducible), and the order in which it takes place reveals the nature of the interactions taking place in the system and the relationship between basins. The turning points of the splitting corresponds to that of the highest (3, −1) point of the separatrix connecting the basins. According to the value of η at these nodes, also known as *bips* (bond interaction points),[32] a bifurcation tree can be constructed that reveals the basin hierarchy at a glance. The difficulties that the localization of all the bips entail in solids have refrained the use of bifurcation diagrams for their bond analysis in spite of the wide range of possibilities this would obviously offer[5] due to the intricate and colorful bonding patterns present in the solid state.

There are several factors that draw a clear line between the molecular and the crystalline realms as far as the study of their topology is concerned. On the one hand, and due to the periodicity of the solid, an infinite number of critical points is expected. The search has to be, therefore, limited to a finite part of the solid (generally the unit cell or one part of it). This fact obliges the implementation of periodic contour conditions that ensure the recuperation of the points escaping this region of space. Furthermore, for the electron localization function defined over the crystalline unit cell, the Morse relationship that holds reads as follows:

$$n_{(3,-3)} - n_{(3,-1)} + n_{(3,+1)} - n_{(3,+3)} = 0 \tag{8}$$

$$n_{(3,-3)} \geq 1, \quad n_{(3,-1)} \geq 3, \quad n_{(3,+1)} \geq 3, \quad n_{(3,+3)} \geq 1 \tag{9}$$

being n the number of critical points of a given type. Just like in the topology of molecules, the (3, −3) positions are associated to Lewis entities of the crystal. The existence of (3, +3) points is ensured by the Weierstrass theorem, which accordingly enforces the presence of the whole set of types of critical points of rank 3 (eq 9).

The split of the critical points imposed by symmetry had already been observed when passing from the atomic to the molecular state. The neighboring atoms force the degenerated atomic ELF maxima to collapse onto nondegenerated ones.[25] Due to the high coordinations in solid state, great concentration of critical points cluster in small volumes. This great variety and amount of critical points per unit cell sets the main algorithmic difference between solids and molecules.[4] Thus, algorithms as the one used in AIMPAC[33] where critical points are searched by an exhaustive formation of pairs, trios, and quartets of atoms are not suitable due to the translational periodicity of the system, and new algorithms have to be designed that benefit from the properties induced by the translational symmetry. For example, the periodicity of the solid ensures the cancellation of the gradient at the fixed

Wyckoff positions, providing some a priori information on the CPs of the system. As far as integrations are concerned, the periodicity in the solid assures finite values for all the basins in the crystal, so that no thresholds are needed to delimit volumes because all basin properties are well defined.

III. Algorithm

A. Construction of the Critical Point List. The clustering of critical points that takes place in the ELF topology of crystals gives rise to two undesirable computational features: (i) finding a great number of solutions of a non linear system of equations within a small interval of the domain of the variables and (ii) being able to accurately discard equivalent solutions. Since the valence region has been found to be exhaustively tracked by algorithms analogous to those employed for the analysis of the topology induced by the electron density, the complete characterization of the ELF topology in the solid requires a hybrid method, with a combination of core−valence approaches. In the first place, we have resorted to a recursive and exhaustive method implemented in our laboratory[34] for the construction of the critical point list of the electron density field of crystals. It starts with the division of the unit cell (or its irreducible part) into all the irreducible tetrahedra it is formed of. Then, all the 0−3-dimensional simplexes are generated in order to perform an iterative barycentric search in each of them: a critical point is searched inside the N simplex that gives rise to a new subdivision into $N + 1$ simplexes that share this barycenter as a common vertex. An infinite recurrence is avoided by introducing a limiting number of subdivisions. This method would ideally be able to localize all the critical points of the crystal, as long as the algorithm is able to find one critical point, if present, inside a simplex. This is the case of the valence region but not of the cores. As the simplexes evolve toward the core regions, the concentration of steep gradients is such that the recursive procedure fails in exhausting the solutions.

However, the landscape of the ELF topology in the cores is extremely simple and constant from one crystal to another, enabling to devise a complementary search that completes the set of critical points found in the first step.[10] Cores are characterized by a nearly spherical shape of the shells enclosed within it. Provided that this structure remains nearly unperturbed in the crystalline environment, we can perform a second CP search around the nuclei, seeding the shell radii as starting points. In order to devise a completely automated search, these positions are internally approximated around a spherical grid by the $\partial\eta(\theta, \phi)/\partial r = 0$ points. The resulting hybrid method turns out to be highly efficient and able to automatically provide complete sets of critical points. Ill cases are mainly related to heavy elements inner cores, whose shells are very abrupt. Although these points do not provide chemical insights, a wise set of parameters provided by the user in order to accurately determine the shell radii and discard equivalent positions would provide the fussy user with the answer.

If the first search is carried out in the irreducible Wigner Seitz cell, some of the borders of the tetrahedra may coincide, leading to redundant critical points. Repeated critical points would also be found according to their multiplicity in the restricted second search and in the barycentric one, were it carried out in the unit cell. Thus, all temporal positions are subsequently filtered for repetitions with the help of punctual symmetry operations and applying cutoffs to avoid redundancies due to numerical inaccuracies. To the best of our knowledge, this algorithm has been the first to provide complete lists of critical points of the ELF induced topology. Not only does it output the position of the maxima for the ulterior integration of their basins, but it also informs about the delocalization between them.

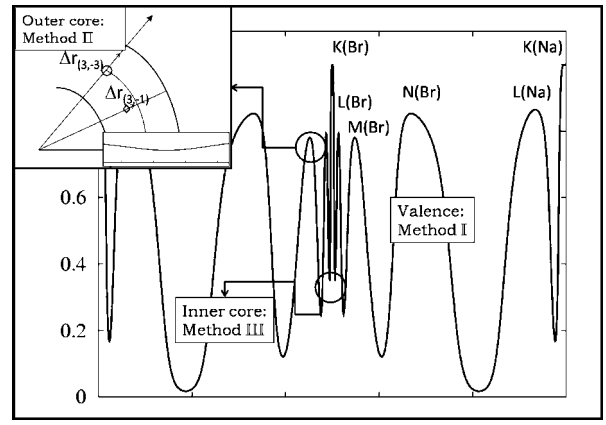

Figure 1. Zone of application of each of the methods described in the text in the NaBr crystal. Method I is able to resolve the valence topology (4th N-shell of Br^- and L-shell of Na^+) flat profiles in the shell basins in the θ, ϕ direction represented in the inset are avoided by means of method II, that enables a more accurate and fast integration of the Br^- outercore. The localization of the quasi-degenerated zero flux surfaces in the inner core of Br^- K-shell is avoided by the spherical approximation of method III.

The concepts of localization domain and bifurcation tree have been rarely used in the solid state, in spite of their potentiality, due to the difficult determination of the bip points by graphical approaches. In fact, its use was already encouraged by Gatti in order to shed light into the nature of the interactions governing the structure of molecular solids.[5] The complete characterization of the topology of the ELF gradient offered by our core−valence algorithm holds the key for a direct construction of bifurcation trees[35] within the crystalline realm, as proved in our recent studies on the pressure behavior of BeO phases[36] and the CO_2 polymerization.[37]

B. Basin Integration. The integration of the basins of the electron density has been the object of numerous publications due to the difficulty of reaching a balance between computational time and accuracy. The first attempts, led by Biegler-König et al.,[33,38] were based on the spatial localization of the zero flux surfaces. Less time-consuming proposals were subsequently put forward by the group of Popelier et al., who devised numerous ingenious ways to tackle the problem, from the analytical fitting of the surfaces[39,40] to the discretization of basins into polyhedra.[41] Grids have also been a very popular modality[33,38] due to their speed. Indeed, the integration of more complex topologies has been mainly addressed by means of the later

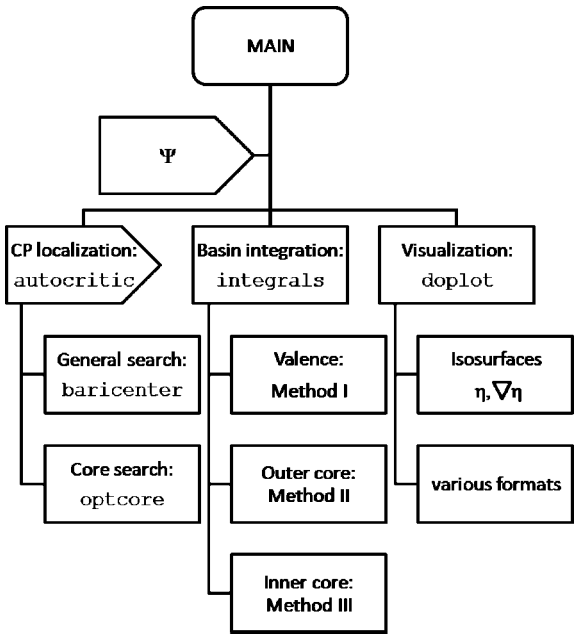

Figure 2. Schematic figure of the code operation.

approach[42,43] to the detriment of accuracy.[44] Since sharp as well as nearly degenerated basins are a common feature of the ELF induced topology, we have decided to recover the more accurate ELF basins properties, as well as an explicit picture of their shape provided by the first set of methods, which are known to deal properly with complicated basin shapes and heterogeneous function profiles, and then using chemical knowledge to properly solve the problem.

Valence basins occupy broad spaces and their profiles are smooth enough to be accurately tracked by the type of methods mentioned above. Its ability to integrate valence basins is highlighted in Figure 1 as the proper method to obtain basin properties of the 4th N-shell of Br^- in NaBr under the name of method I. Due to the colorful valence shapes depending on the bonding type, the bisection method[40] has been preferred due to its accuracy, and in spite of its computational cost. First, and making use of the previous algorithm for the determination of the (3, −3) points, a mapping is carried out for each attractor, centering at its location a polar coordinate system. Then, this sphere is divided into a regular $n_\theta \times n_\phi$ grid, whose radial lengths are found according to the flux lines properties. Since all the gradient paths that end up at the given attractor belong to its basin, it suffices to bracket the point $r(\theta, \phi)$ at which the flux lines start leading to another (3, −3) point. Given the fact that we have reduced the problem to one dimension, a bisection search is, due to its reliability, mostly suited for this task. It should be noted that the wide range of valence basin shapes difficulties an automated setting of the bisection initial limits and would boost Newton−Raphson weaknesses at long distances, so the point fulfilling the condition $\partial\eta/\partial r = 0$ can be used as the first approximation for setting the limits. Finally, and once the radial limit has been found, the Gaussian−Legendre quadrature, proposed by Biegler-König et al., is used for the integration of the coordinates.[33,38]

It is always said that the bisection search succeed by mediation of the mean value theorem. However, it must be noted that the bisection method defined above is coupled to a flux integration for the bracketing process. It is at this step that the above method finds difficulties in some topologies. More specifically, and as advanced above, the integration of core shells entails serious problems due to the planarity of the ELF profile around the shells (see inset for the direction perpendicular to the NaBr interionic axis in Figure 1). The nearly nonzero derivative distorts the Newton−Raphson flux integration, that in the best of these cases provides an inaccurate attractor position, complicating the coordinates comparison for the bisecant point discarding, or even worse integrates to a wrong point. The punctual core attractors of the crystal (shells > K) descend from a perturbation induced by the environment of the atomic shells in vacuo, where they are organized in a degenerated sphere. The potential from the nearby attractors gives rise to a collapse onto the (3, −3) shell attractors. This is due to the changes in the density and the kinetic energy upon the long-range influence of an external potential. These increments are magnified along the interattractor direction (r), where the term $\partial\phi/\partial r$ is vanishingly small, being ϕ the interacting molecular orbital.[45] This steepest increase in the density and decrease in the kinetic energy in the parallel direction gives rise to an increase in the ELF and, therefore, to the attractor collapse on the internuclear line. In general, the greater the potential, the larger the deformation and the easier the integration of the shell basin. As depicted in the inset for method II in Figure 1, the deviation of the (3, −3) points is greater than that of the connecting (3, −1) points. This is easily taken into account by the perturbative changes explained above, whose effect is shifting the attractor towards the source of the potential.

If more shells are present in the core, the intermediate ones are subject to the attractive potential from the neighboring nuclei as well as the repulsive potential from other shell attractors, and more complicated topological patterns may arise (e.g. ligand opposed core charge concentrations).[46,47] However, in these cases, the distances are large enough as to induce very little deformations and the spherical shape is nearly preserved. Hence, once again, the most complicated computational situations arise from inner core shells of heavy atoms as well as from ionic interactions. A change of gradient search procedure is not convenient due to the fact that the integration only fails along a certain angular interval. Therefore, a complementary integration method seems more appropriate. At this point, a previous proposal of the authors[48] to take the basin shells of solids as one chemically meaningful superbasin holds the key for the design of the integration procedure. From a conceptual point of view, the partition of core into basins is a mere consequence of symmetry. Furthermore, it has been shown that this split is not chemically meaningful[48] but just a mere artifact induced by the symmetry. If all the basins belonging to the same shell are integrated together, the approximated sphericity, for which the above bisection was developed, is recovered, and so are the curved ELF profiles. This algorithm is designated as method II in Figure 1 and is most appropriate for the integration of densities in outer shells, such as the M- and L-shell of Br^- on the figure. Besides, this method increases the accuracy of the integrations, other-

Table 1. Set of Critical Points Found for an Ionic (fcc LiF, $a = 4.017$ Å) and a Covalent Crystal (diamond C, $a = 3.102$ Å)[a]

LiF							C (diamond)						
Type	*x*	*y*	*z*	M	η	CHM	Type	*x*	*y*	*z*	M	η	CHM
(3, −3)	0.0000	0.0000	0.0000	4	0.9999	C(Li)	(3, −3)	0.1250	0.1250	0.1250	8	0.9999	C(C)
(3, −3)	0.5000	0.5000	0.5000	4	0.9999	C(F)	(3, −3)	0.0000	0.2500	0.2500	16	0.9352	V(C,C)
(3, −3)	0.0000	0.1256	0.5000	24	0.8555	V(F)	(3, −1)	0.0745	0.3750	0.3750	48	0.5954	C−V
(3, −1)	0.5000	0.2500	0.2500	24	0.0280	F−F	(3, −1)	0.0710	0.1790	0.1783	32	0.0833	V−V
(3, −1)	0.5000	0.4114	0.4114	48	0.8549	V(F)−V(F)	(3, +1)	0.2403	0.2403	0.2405	32	0.4675	ring
(3, −1)	0.1805	0.0000	0.0000	24	0.1463	Li−F	(3, +1)	0.0293	0.1250	0.1250	48	0.0736	ring
(3, −1)	0.4548	0.0000	0.0000	24	0.1303	C(F)−V(F)	(3, +1)	0.2500	0.2500	0.5000	16	0.0427	ring
(3, +1)	0.1804	0.3196	0.3196	32	0.1533	ring	(3, +3)	0.3750	0.3750	0.3750	8	0.0236	cage
(3, +1)	0.0000	0.3576	0.3576	48	0.0095	ring	(3, +3)	0.1829	0.1829	0.1779	32	0.0670	cage
(3, +1)	0.4277	0.5723	0.5723	32	0.8548	ring							
(3, +1)	0.4681	0.4681	0.4988	48	0.1303	ring							
(3, +3)	0.2500	0.2500	0.2500	8	0.0129	cage							
(3, +3)	0.1210	0.3790	0.3790	32	0.0083	cage							
(3, +3)	0.4739	0.0261	0.9739	32	0.1303	cage							
Morse				0							0		

[a] Positions (*x*, *y*, *z*), multiplicities (M), ELF value at the CP (η), and chemical meaning (CHM) are collected.

Table 2. Set of Critical Points Found for a Metallic (fcc Al, $a = 4.086$ Å) and a Molecular Crystal ($Pa\bar{3}$ N_2, $a = 5.0$ Å)[a]

Al							N_2						
type	*x*	*y*	*z*	M	η	CHM	type	*x*	*y*	*z*	M	η	CHM
(3, −3)	0.0000	0.0000	0.0000	4	0.9999	K(Al)	(3, −3)	0.0530	0.0530	0.0530	8	0.9999	C(N)
(3, −3)	0.5000	0.5000	0.2738	24	0.6805	V(Al)	(3, −3)	0.0226	0.4774	0.4553	24	0.8867	V(N, N)
(3, −3)	0.3035	0.3035	0.0000	48	0.7234	V(Al)	(3, −3)	0.6402	0.3598	0.8629	8	0.9868	V(N)
(3, −3)	0.0000	0.4246	0.5000	24	0.8697	L(Al)	(3, −3)	0.4626	0.0374	0.5000	24	0.8842	V(N, N)
(3, −1)	0.2500	0.5000	0.2500	24	0.3011	V−V	(3, −1)	0.4022	0.9025	0.4401	24	0.7187	V(N)−V(N, N)
(3, −1)	0.4440	0.0000	0.4495	96	0.8697	L-L	(3, −1)	0.2155	0.5415	0.2721	24	0.0050	N_2−N_2
(3, −1)	0.3402	0.3402	0.1520	96	0.6379	V−V	(3, −1)	0.9734	0.5266	0.4734	8	0.1227	C−V
(3, −1)	0.4467	0.4467	0.0000	48	0.8696	L−L	(3, −1)	0.4200	0.9200	0.5801	8	0.1334	C−V
(3, −1)	0.0000	0.0000	0.9723	24	0.1891	C−V	(3, +1)	0.3507	0.3507	0.3507	8	0.0003	ring
(3, +1)	0.3281	0.3281	0.3232	32	0.0691	ring	(3, +1)	0.1740	0.3713	0.2015	24	0.0007	ring
(3, +1)	0.4100	0.4100	0.8838	96	0.0486	ring	(3, +1)	0.0081	0.4925	0.3435	24	0.6382	ring
(3, +1)	0.5000	0.0258	0.4900	96	0.1891	ring	(3, +1)	0.0000	0.5000	0.5000	4	0.8664	ring
(3, +3)	0.2500	0.2500	0.2500	8	0.0391	cage	(3, +1)	0.5301	0.4700	0.9075	24	0.0543	ring
(3, +3)	0.1729	0.5000	0.5000	24	0.0470	cage	(3, +3)	0.2890	0.2890	0.2890	8	0.0002	cage
(3, +3)	0.5000	0.5000	0.5000	4	0.0004	cage	(3, +3)	0.5000	0.5000	0.5000	4	0.0001	cage
							(3, +3)	0.9275	0.5727	0.4900	24	0.0540	cage
							(3, +3)	0.4901	0.9230	0.5669	24	0.0532	cage
							(3, +3)	0.0771	0.0099	0.0667	24	0.0532	cage
Morse sum				0							0		

[a] Positions (*x*, *y*, *z*), multiplicities (M), ELF value at the CP (η), and chemical meaning (CHM) are collected.

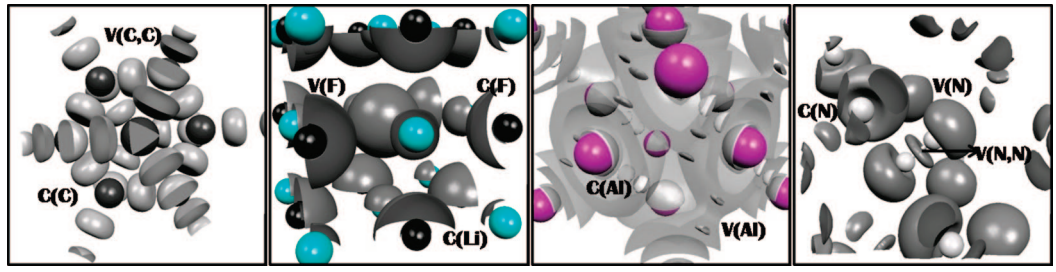

Figure 3. Schematic ELF profile of the various type of solids (see text): (a) diamond, (b) LiF, (c) Al, (d) N_2.

wise endangered by the low performance of the quadrature at high density cusp points,[40] and fastens the general procedure, since less integrals in low symmetry crystals are needed. For this purpose, the assignation of basin attractors to a certain nucleus turns out to be crucial, allowing the bipartition procedure to be applicable in spite of the basin attractor and the center of integration not being the same.

As the number of shells increases, the potential induced by the environment is screened and the inner shells remain degenerated. Hence, the above bipartition procedures are no longer applicable, since it fails to accurately locate the extremes. Furthermore, the bracketing of the bisection becomes extremely complicated due to the clustering of inner separatrices. The combination of the above algorithms is to be complemented by a third method in the case of heavy

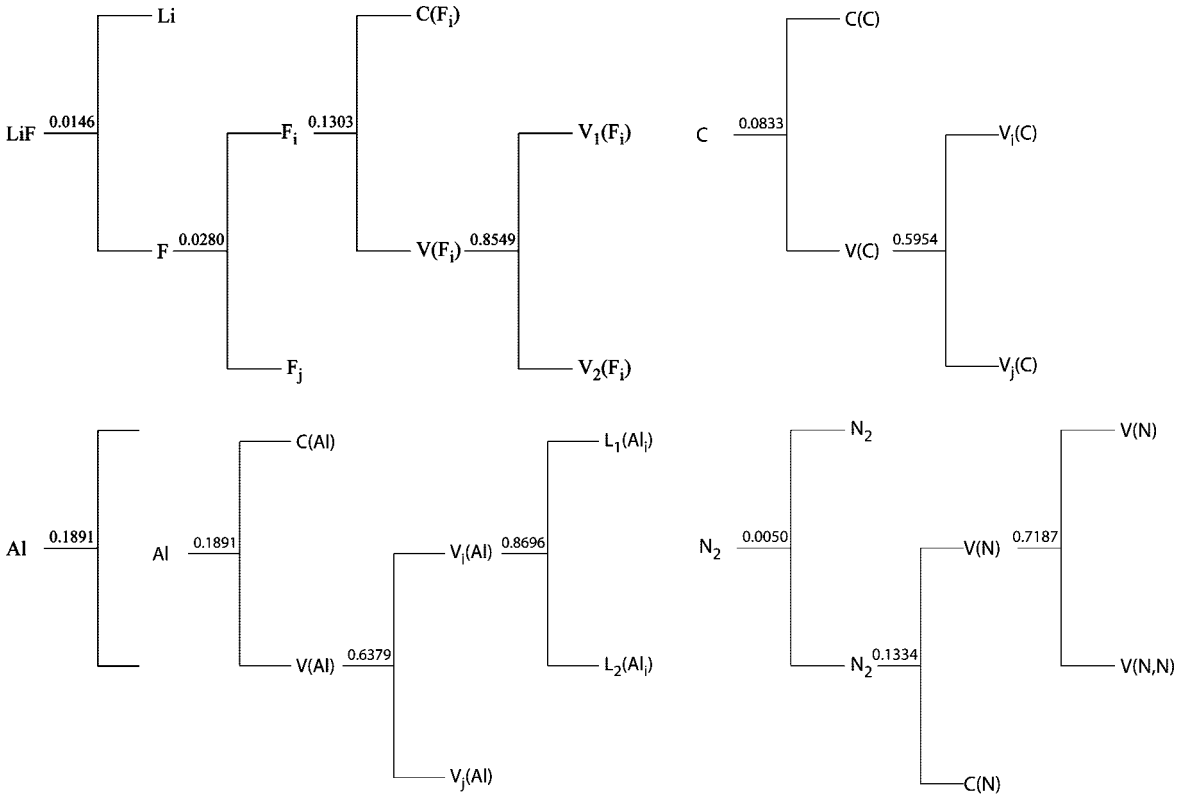

Figure 4. Bifurcation tree for LiF, C, Al, and N_2. The crystal data is as in Tables 1 and 2, respectively.

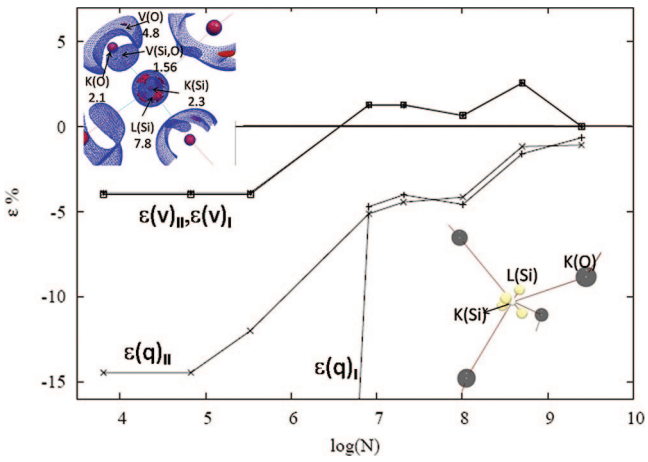

Figure 5. Convergence of ELF basin charges in the cristobalite phase of SiO_2 for an $n = n_r \times n_\theta \times n_\phi$ grid. The meaning of the basin labels is illustrated in the upper left inset: K stands for the 1st shell, L, for the 2nd, V(Si, O), for bond, and V(O), for lone pair. Curves present the relative error, ϵ (%), in the integration of charges (ϵ_q) and volumes (ϵ_v) according to both methods of integration (labeled I and II). Inset in the right bottom corner is an illustration of the complementary tetrahedral distribution of oxygens (black) and L-shell maxima (yellow online).

elements (from the 3rd and 4th rows downward). Taking into account that the problems in these shells arise from their spherical shape, the approximation (method III) of $\partial\eta/\partial\vec{r}$ by $\partial\eta/\partial r$ becomes a reasonable approach to the correct answer, as depicted in Figure 1 for the 1st K-shell of Br^-.

All the program features and main operation routines are schematized in Figure 2. First, the autocritic routine localizes the critical points of the cell by means of the combined core−valence algorithm. The characterization of the topology induced by the ELF gradient is used for studying the interactions in the solid. Then, the basin integration implemented in integrals is coupled to the CP search (represented by the arrow shape in the diagram) and makes use of all three algorithms described above to provide charge and volume values associated to the maxima found in the first step. Finally, the construction of η and $\nabla\eta$ grids with the doplot routine enables the bonding pattern of the solid to be visually analyzed.

IV. Performance

A. Critical Points. Lists of critical points for compounds representative of ionic, covalent, metallic, and molecular bonding are gathered in Tables 1 and 2. Multiplicities, referred to in the tables as "M", have to be taken into account to check the Morse sum. The corresponding ELF pictures and bifurcation trees are displayed in Figures 3 and 4. As explained above, these trees have a dual purpose in the analysis of the bonding: on the one hand, they highlight chemical units, and on the other hand, they unveil the nature of the interaction between them.

LiF in Table 1a is characterized by the absence of bond basins, only showing core and valence closed-shell basins (C(Li), C(F), and V(F)) whose shape approach that of a sphere (see Figure 3), as can be shown from the small variance in the critical point distance to the nucleus. It should be noted that, contrary to some early ideas, clear quantifiable ELF topological difference arises for the polarity of ionic compounds. Among these compounds, polarity can be viewed as an especial orientation of the valence toward the

Table 3. Calculated Charges (q_i) and Volumes (V_i) of ELF Basins in LiF (fcc, $a = 4.017$ Å) C (diamond, $a = 3.56$ Å), Al (fcc, $a = 4.086$ Å), and N_2 ($Pa\bar{3}$, $a = 5.0$ Å) for an $n_r \times n_\theta \times n_\phi$ grid of $30 \times 15 \times 15$[a]

	LiF		C		Al		N_2	
basin	q_i	V_i	q_i	V_i	q_i	V_i	q_i	V_i
core(A)	2.03	14.02	2.08	0.79	10.01	9.89	2.08	0.45
core(B)	2.15	0.17						
bond			1.98	20.39			3.50	26.48
lone pair							3.18	159.34
valence	7.81	98.57			2.99	111.64		
ε	−0.1%	−1.3%	+0.08%	−2.3%	−0.4%	0.3%	+0.2%	0.9%

[a] Errors (ϵ) in percent are with respect to the total volume and number of electrons per formula unit. A and B stand for Li and F, respectively.

atoms with whom it is bonded. The difference between the ELF values at the maxima and intrashell bip points gives an idea of the delocalization between the basins of the valence:[48] $\Delta\eta^{\mathrm{val}} = \eta^{\mathrm{val}}_{(3,-3)} - \eta^{\mathrm{val}}_{(3,-1)_{\mathrm{intra}}}$. Further information on the calculation of ionic polarity can be found by another article of the authors,[48] where this index is applied in order to track the subtle variation of ionicity along the B1 → B3 of BeO. In Figure 4, the hierarchy of the basins for LiF is built from these results. It can be seen that the first reduction corresponds to cation−anion separation at a very low ELF value (represented in the tables as Li−F) so that the crystal has no common valence. The stabilization of the compound comes therefore from electrostatic grounds. The high value at which the F valence domains are split clearly shows that they form one meaningful chemical unit, that is, the L-shell.

A covalent solid like diamond (Table 1 and Figure 3) displays a continuous 3D-network of tetrahedrically coordinated carbons, C(C), bound together by means of single-bond basins, V(C, C). The first domain separation (Figure 4) gives rise to cores and a common valence, formed by the bonds, at ELF = 0.08 (C(C)−V(C, C)). The valence domain is separated into irreductible bond basins at 0.59 (V(C, C)−V(C, C)). It can be seen from Figure 3 that metallic Al is formed of two shells (C(Al) and V(Al)). The quantitative results in Table 2a show that the valence of the atom is spread over the crystal, giving rise to low ELF maxima. Furthermore, the valence bips also show a value close to 0.5, so that the resulting bifurcation tree reveals a nearly continuous and planar valence (Figure 4) The observation of this planarity in the valence ELF in many metals led Silvi and Gatti to establish the characterization of metallic bond in terms of the delocalization window: $^6\Delta\eta\mathrm{val} = \eta^{\mathrm{val}}_{(3,-3)} - \eta^{\mathrm{val}}_{(3,-1)}$, yielding 0.043 for the Al. As far as N_2 is concerned, the value of ELF at the intermolecular points (named "N_2−N_2" in Table 2) is crucial in order to study the relationship between the molecular units. As reflected in Figure 4, the van der Waals forces that stabilize the crystal give rise to a first reduction into N_2 molecular units at this very low intermolecular ELF value, whereas the covalency within molecules is revealed by the common valence they share (formed by bonds, V(N, N), and lone pairs V(N)).

Overall, the relevance of the (3, −1) points and the necessity of a reliable code for the localization of all the valence critical points, cannot be overemphasized. Furthermore, the identification and characterization of the complete set of critical points are of capital importance in the study of chemical change by means of the catastrophe theory, a field that up to now, and due to the lack of a computational method, was restricted to the molecular realm.[49,50]

B. Basin Integration. The cristobalite phase of silica has been chosen to exemplify the performance of the integrations. It constitutes one of the simplest examples whereby all kinds of ELF basins can be found.[47] Cristobalite SiO_2 presents three maxima of ELF near the oxygen centers. One corresponds to the lone pair basin with 4.8 electrons. The other two are bonding basins sharing an average of 1.56 electrons with each of the silicon centers to which O is coordinated (see upper left inset in Figure 5). Silicon inner cores (with 2.3 electrons) are surrounded by the L-shell split in 4 maxima, giving a total charge for the outer core of 7.8 electrons. These maxima are located against the positions of the oxygens[47] (see bottom right inset in Figure 5), corresponding to a feature of the laplacian called ligand opposed core charge concentrations (LOCCC).[46] Hence, they reflect in an indirect and subtle way the 4-fold coordination of Si in cristobalite.

The integration grid for each basin consisted from 5 to 40 points for the radial and angular integrations, respectively. The logarithm of the total number of grid points is represented on the x axis of Figure 5. A convergence to the tenths of electrons and hundredths of volume atomic units, which is enough for most common applications, is usually found by a mixture of methods I and II (and III if heavy elements are present) with a $n_r \times n_\theta \times n_\phi$ grid of $30 \times 15 \times 15$ points. In spite of the modest amount of points, this grid provides volumes that fill up the volume of the cristobalite unit cell with errors around 0.8%. Greater deviations are encountered in the charge due to core integrations, where the high density value at the quadrature points gives rise to bigger inaccuracies. Indeed, the convergence obtained in the volume integration of SiO_2 with both methods is nearly the same, but it decreases when charge density is integrated from 1.1% to 0.7% if both methods are combined (see Figure 5). Deviations are also expected in specially challenging cases where the low symmetry of the cell or the split of multiple bonds demand greater grids. The number of gradient evaluations is of the order of 10^5 for each nonequivalent basin or group of basins, so any additional simplification of the integration turns out to be extremely valuable. In this sense, method number II for outer core integrations not only gives rise to greater accuracy but also provides great time saving by integrating all atomic shells together and requiring smaller grids. Another way to fasten the calculations is the use of cell symmetry: the

integration of basins occupying high symmetry Wyckoff positions can be limited to the irreducible angular part.

In order to check the applicability of integrations to different bonding patterns, the representative examples presented in the previous section have been considered following the hybrid procedure and using the selected 30 × 15 × 15 grid. Results are compiled in Table 3. It can be seen that the quantitative picture recovered by ELF in the solid state is in agreement with chemical expectations. The ionic nature of LiF is observed in its closed shell basins with a charge transfer of 0.97 electrons. The Ne-like core with 10 electrons in aluminum is perfectly recovered, as well as the metallic valence surrounding it, formed by unsaturated basins of small charge. The high pressure molecular phase of N_2 keeps a strong N−N bond with a charge of 3.5 electrons and voluminous lone pairs that fill the space and hold 3.18 electrons each. Lower population than that of a formal triple bond is expected due to the pressure induced charge flow from the bond basin to the lone pair and to the presence of resonant structures.[37] In the case of diamond, perfect electron pairs are found, according to the perfect covalency of the compound and the absence of resonant forms. The last row of Table 3 reveals that the percent error in the integrations stays below 0.5% in the charge and 2.5% in the volume, confirming the ability of the new algorithm to provide accurate charges and volumes for ELF basins in a wide range of solids. We firmly believe that the hereby proposed method will enable to extend the quantitative topological ELF analysis of bonding to the solid state, where the appearance of complex bonding structures claims for such approaches.

V. Conclusions

An algorithm for the complete characterization of the topology induced by ELF in solids, including identification and characterization of all critical points and basin integration, is put forward. It is based on the fact that this topology is characterized for having two regions with different topological features: on the one hand, the valence, which can be determined following previous crystalline topological methods, and on the other hand, the core, whose sphericity holds the key for designing new automated algorithms. The robustness of the approach is proved across a wide range of applications, where the relevancy of a thorough determination of the local and global properties of the electron localization function is well set. The next step toward a deeper understanding of bond in solids and its dynamical change involves the calculation of probabilities[51] and localization/delocalization indexes,[29,52] dependent on higher order density matrices.

Acknowledgment. Financial support from the Spanish MEC and FEDER programs under projects MAT2006-13548-C02-02 and CTQ-2006-02976 and Programa Ingenio 2010 under the MALTA-Consolider CSD2007-00045 project are gratefully acknowledged. J.C.-G. thanks the Spanish MEC for a FPU postgraduate grant.

References

(1) Mori-Sánchez, P.; Martín Pendás, A.; Luaña, V. *J. Am. Chem. Soc.* **2002**, *124*, 14721.

(2) Savin, A.; Jepsen, O.; Flad, J.; Andersen, O. K.; Preuss, H.; von Schnering, H. G. *Angew. Chem., Int. Ed. Engl.* **1992**, *31*, 187.

(3) Bader, R. F. W. *Atoms in Molecules: A Quantum Theory*; Oxford Univ. Press: Oxford, 1990.

(4) Martín Pendás, A.; Costales, A.; Luaña, V. *Phys. Rev. B* **1997**, *55*, 4275.

(5) Gatti, C. *Zeit. Kristallogr.* **2005**, *220*, 399.

(6) Silvi, B.; Gatti, C. *J. Phys. Chem. A* **2000**, *104*, 947.

(7) Savin, A. *J. Phys. Chem. Solids* **2004**, *65*, 2025.

(8) Gibbs, G. V.; Cox, D. F.; Boisen, M. B., Jr.; Downs, R. T.; Ross, N. L. *Phys. Chem. Minerals* **2003**, *30*, 305.

(9) Gibbs, G. V.; Cox, D. F.; Ross, N. L. *Phys. Chem. Minerals* **2004**, *31*, 232.

(10) Nathaniel, O.; Malcom, J.; Popelier, P. L. A. *J. Comput. Chem.* **2003**, *24*, 437.

(11) Becke, A. D.; Edgecombe, K. E. *J. Chem. Phys.* **1990**, *92*, 5397.

(12) von Weizsäcker, C. F. *Z. Phys.* **1935**, *96*, 431.

(13) Savin, A.; Becke, A. D.; Flad, J.; Nesper, R.; Preuss, H.; von Schnering, H. G. *Angew. Chem., Int. Ed. Engl.* **1991**, *30*, 409.

(14) Savin, A.; Nesper, R.; Wengert, S.; Fässler, T. F. *Angew. Chem., Int. Ed. Engl.* **1997**, *36*, 1809.

(15) Burdett, J. K.; McCormick, T. A. *J. Phys. Chem. A* **1998**, *102*, 6366.

(16) Nalewajski, R. F.; Koster, A. M.; Escalante, S. *J. Phys. Chem. A* **2005**, *109*, 10038.

(17) Dobson, J. F. *J. Chem. Phys.* **1991**, *94*, 4328.

(18) Kohout, M.; Pernal, K.; Wagner, F. R.; Grin, Y. *Theor. Chem. Acc.* **2004**, *112*, 453.

(19) Kohout, M.; Pernal, K.; Wagner, F. R.; Grin, Y. *Theor. Chem. Acc.* **2005**, *113*, 287.

(20) Silvi, B. *J. Phys. Chem. A* **2003**, *107*, 3081.

(21) Matito, E.; Silvi, B.; Duran, M.; Solà, M. *J. Chem. Phys.* **2006**, *125*, 024301.

(22) Silvi, B. *Phys. Chem. Chem. Phys.* **2004**, *6*, 256.

(23) Lewis, G. N. *Valence and the Structure of Atoms and Molecules*; Dover: New York, 1966.

(24) Abraham, R. H.; Marsden, J. E. *Foundations of Mechanics*; Addison Wesley: Reading, MA, 1994.

(25) Silvi, B.; Savin, A. *Nature* **1994**, *371*, 683.

(26) Häussermann, U.; Wengert, S.; Nesper, R. *Angew. Chem., Int. Ed. Engl.* **1994**, *33*, 2069.

(27) Martín Pendás, A.; Francisco, E.; Blanco, M. A. *Chem. Phys. Lett.* **2008**, *454*, 396.

(28) Calatayud, M.; Andrés, J.; Beltrán, A.; Silvi, B. *Theor. Chem. Acc.* **2001**, *105*, 299.

(29) Savin, A.; Silvi, B.; Colonna, F. *Can. J. Chem.* **1996**, *74*, 1088.

(30) Kohout, M.; Savin, A. *Int. J. Quantum Chem.* **1996**, *60*, 875.

(31) Mezey, P. G. *Can. J. Chem.* **1993**, *72*, 928.

(32) Kohout, M.; Wagner, F. R.; Grin, Y. *Theor. Chem. Acc.* **2002**, *108*, 150.

(33) Biegler-Köonig, F. W.; Bader, R. F. W.; Tang, T.-H. *J. Comput. Chem.* **1982**, *3*, 317.

(34) Otero de la Roza; A.; Blanco, M. A.; Martín Pendás; A.; Luaña, V. *Comput. Phys. Commun.* **2009**, *180*, 157.

(35) Silvi, B. *J. Mol. Struct.* **2002**, *614*, 3.

(36) Contreras-García, J.; Martín Pendás, A.; Silvi, B.; Recio, J. M. *J. Phys. Chem. Solids* **2008**, *69*, 2204.

(37) Contreras-García, J.; Silvi, B.; Martín Pendás, A.; Recio, J. M. *J. Phys. Chem. B*, in press.

(38) Biegler-König, F. W.; Nguyen-Dang, T. T.; Tal, Y.; Bader, R. F. W. *J. Phys. B: Atom. Molec. Phys.* **1981**, *14*, 2739.

(39) Popelier, P. L. A. *Mol. Phys.* **1996**, *87*, 1169.

(40) Popelier, P. L. A. *Comput. Phys. Commun.* **1998**, *108*, 180.

(41) Rafat, M.; Popelier, P. L. A. *J. Comput. Chem.* **2007**, *28*, 2602.

(42) Noury, S.; Krokidis, X.; Fuster, F.; Silvi, B. *Comput. Chem.* **1999**, *23*, 597.

(43) Nathaniel, O.; Malcom, J.; Popelier, P. L. A. *J. Comput. Chem.* **2003**, 24.

(44) Henkelman, G.; Arnaldsson, A.; Jonsson, H. *Comput. Mater. Sci.* **2006**, *36*, 354.

(45) Feinberg, M. J.; Ruedenberg, K. *J. Chem. Phys.* **1971**, *54*, 1495.

(46) Bytheway, I.; Gillespie, R. J.; Tang, T.-H.; Bader, R. F. W. *Inorg. Chem.* **1995**, *34*, 2407.

(47) Gracia, L.; Contreras-García, J.; Beltrán, A.; Recio, J. M. *High Pres. Res.*, in press.

(48) Contreras-García, J.; Silvi, B.; Martín Pendás, A.; Recio, J. M. *J. Phys. Chem. B* **2008**, *112*, 9787.

(49) Krokidis, X.; Noury, S.; Silvi, B. *J. Phys. Chem. A* **1997**, *101*, 7277.

(50) Polo, V.; Andres, J.; Castillo, R.; Berski, S.; Silvi, B. *Chem.—Eur. J.* **2004**, *10*, 5165.

(51) Savin, A. *J. Chem. Sci.* **2005**, *117*, 473.

(52) Chesnut, D. B. *Chem. Phys.* **2001**, *271*, 9.

CT800420N

JCTC Journal of Chemical Theory and Computation

An Effective Hamiltonian Molecular Orbital-Valence Bond (MOVB) Approach for Chemical Reactions as Applied to the Nucleophilic Substitution Reaction of Hydrosulfide Ion and Chloromethane

Lingchun Song,*,† Yirong Mo,*,‡ and Jiali Gao*,†

Department of Chemistry, Digital Technology Center and Supercomputing Institute, University of Minnesota, Minneapolis, Minnesota 55455, and Department of Chemistry, Western Michigan University, Kalamazoo, Michigan 49008

Received October 7, 2008

Abstract: An effective Hamiltonian mixed molecular orbital and valence bond (EH-MOVB) method is described to obtain accurate potential energy surfaces for chemical reactions. Building upon previous results on the construction of diabatic and adiabatic potential surfaces using *ab initio* MOVB theory, we introduce a diabatic-coupling scaling factor to uniformly scale the *ab initio* off-diagonal matrix element H_{12} such that the computed energy of activation from the EH-MOVB method is in agreement with the target value. The scaling factor is very close to unity, resulting in minimal alteration of the potential energy surface of the original MOVB model. Furthermore, the relative energy between the reactant and product diabatic states in the EH-MOVB method can be improved to match the experimental energy of reaction. A key ingredient in the EH-MOVB theory is that the off-diagonal matrix elements are functions of all degrees of freedom of the system and the overlap matrix is explicitly evaluated. The EH-MOVB method has been applied to the nucleophilic substitution reaction between hydrosulfide and chloromethane to illustrate the methodology, and the results were matched to reproduce the results from *ab initio* valence bond self-consistent-field (VBSCF) calculations. The diabatic coupling (the off-diagonal matrix element in the generalized secular equation) has small variations along the minimum energy reaction path in the EH-MOVB model, whereas it shows a maximum value at the transition state and has nearly zero values in the regions of the ion-dipole complexes from VBSCF calculations. The difference in the diabatic coupling stabilization is attributed to the large overlap integral in the computationally efficient MOVB method.

1. Introduction

Previously, we described a mixed molecular orbital and valence bond (MOVB) theory,[1−3] in which effective diabatic states are constructed by a block-localized wave function (BLW) method at the *ab initio* level.[4−11] In this approach, molecular orbitals (MOs) are strictly localized within individual fragments of a molecular system according to the specific Lewis resonance structure of the reactant or product state configuration. At the same time the block-localized MOs are delocalized within each fragment, making the MOVB method extremely efficient in comparison with *ab initio* valence bond self-consistent-field (VBSCF) methods.[12−16] In MOVB, the localized diabatic states are coupled to result in an avoid-crossing at the transition state and the ground-state adiabatic potential energy surface.[1−3,17] Key features of the MOVB theory include (1) that MOs within each fragment are orthogonal, which makes computation efficient, and (2) that MOs between different fragments are nonorthogonal, which retains important characteristics of valence

* Corresponding author e-mail: songx184@umn.edu (L.S.), yirong.mo@wmich.edu (Y.M), and jgao@umn.edu (J.G.).

† University of Minnesota.

‡ Western Michigan University.

10.1021/ct800421y CCC: $40.75 © 2009 American Chemical Society
Published on Web 12/15/2008

bond (VB) theory. In the first limiting case in which there is one fragment, MOVB reduces exactly to the Hartree−Fock theory or Kohn−Sham density functional theory. In the second limiting case in which MOs are localized on atoms, the MOVB becomes an *ab initio* VBSCF model. The MOVB method can be regarded as the simplest *ab initio* VB variant, and its computational accuracy depends on the basis functions used and the coupling between diabatic states in a specific reaction. The aim of this paper is to develop an effective Hamiltonian strategy to yield accurate results on the computed reaction barrier. We make use of the second-order nucleophilic substitution (S_N2) reaction between HS^- and CH_3Cl in the gas phase to illustrate this approach.

The most widely used empirical model in computer simulations is the empirical valence bond (EVB) approach introduced by Warshel and Weiss,[18] in which the reactant and product diabatic states are represented by molecular mechanics force field. For chemical reactions, a modified Morse potential is used to describe the potential energy profile for a given bond dissociation process.[19] Although multiple state configurations can be constructed, a two-state model is typically employed, representing the reactant and the product diabatic state, respectively. A key assumption of the EVB model is that the diabatic states are treated as orthogonal states, thereby, resulting in a simple secular equation independent of the overlap integral between the reactant and product wave functions.[18,19c] This is necessary because in such an implicit model wave functions are not available. The impact of this assumption can be relieved by adjusting the off-diagonal matrix element, H_{12}, which is approximated by an exponential function or simply by a constant value, adjusted to yield the desired barrier height. Consequently, the EVB potential constructed this way can reproduce the experimental activation barrier exactly.

Recently, Hong et al.[20a] described an interesting frozen density functional theory (FDFT) model in which the total electron density of a system is separated into fragmental densities, similar to the MOVB approach in the definition of the wave functions for the diabatic states.[1] Hong et al. defined the diabatic coupling by back calculation of the delocalized ground-state energy E_g, assuming that the overlap between the two states is zero; $H_{12} = [(E_g - H_{11})(E_g - H_{22})]^{1/2}$. The FDFT method has been applied to an S_N2 reaction and a proton transfer process in water.[20] In this approach, the density of a diabatic state is determined at a given configuration and kept frozen throughout the entire reaction profile.[20] The frozen densities are considered to be an arbitrary mathematical definition without any relationship.[20b] Nevertheless, one notices that the adiabatic ground-state energy E_g can become higher than that of the reactant diabatic state in the FDFT model (see Figure 1 of ref 20a), which would result in an imaginary value for the diabatic coupling H_{12}. Thus, it appears to be necessary to impose certain requirements, including an approximate but explicit consideration of the overlap,[21] when densities are separated or kept frozen. It seems that ab initio molecular orbital and valence bond methods described here have a unique advantage that the diabatic states are well-defined with specific physical properties that can be related to the traditional concepts of chemical bonding.[3,12,17]

It has been noted that the use of a constant value or a simple exponential function of one or few degrees of freedom for the off-diagonal matrix element is not flexible enough to fit both structure and vibrational frequencies at the transition state.[22] To overcome this difficulty, which could be important for studying reaction dynamics including computation of kinetic isotope effects, a variety of algorithms have been proposed. Chang and Miller used a generalized Gaussian function to model the resonance integral by fitting the structure and vibrational frequencies at the transition state.[23] This approach has been extended to a multistate empirical valence bond (MS-EVB) model for modeling proton transfer reactions.[24−26] Recently, Schlegel and co-workers further improved the Chang-Miller model by introducing a product of Gaussian and polynomial functions,[22,27] which is aided by a remarkably efficient fitting procedure. The latter method was demonstrated to yield chemically accurate potential energy surfaces for a number of reactions. In yet another optimization approach, Truhlar and co-workers employed an interpolation scheme to reproduce the energy, gradient, and Hessian from *ab initio* methods.[28−30]

Of course, *ab initio* valence bond (VB) theory can be directly used to construct diabatic and adiabatic states;[12−16,31] however, there is no straightforward formulism to derive a simple two state model,[3,32−36] representing the reactant and product diabatic states that are often used in force-field calculations. In addition, these calculations are too expensive for application to large molecules and chemical reactions in solution. Recently, we describe an approach for deriving a two-state model[3] by constructing the two diabatic states from *ab initio* multiconfigurational valence bond (VBSCF) theory,[16,37,38] and this theoretical model was used to compare results obtained from the MOVB theory.[3] We showed that the effective diabatic states can be optimized by two complementary variational approaches, resulting in two limiting scenarios. In the first case, the diabatic states are constructed by optimizing the wave function of each diabatic state to yield the minimum diabatic energy; we call these states the variational diabatic configurations (VDC).[1−3] It appears that one of the requirements for computing H_{12} in ref 21a (see eq 4 of that paper) is to obtain such states, although that approach was described in a constrained DFT model.[21a] Alternatively, the diabatic states can be obtained as a result of the variational optimization of the valence bond wave function of the adiabatic ground state. We call these diabatic states the consistent diabatic configurations (CDC).[3] Comparison between the MOVB results with those obtained using *ab initio* VBSCF theory for a model S_N2 reaction between ammonia and methylammonium ion shows that the two methods are in excellent accord in describing both the VDC and CDC diabatic states. However, the barrier heights for chemical reactions from MOVB calculations are typically a few kilocalories per mole higher than high-level *ab initio* results that include dynamic correlation.

In this paper, we show that the MOVB method can be constructed to yield the barrier height for a chemical reaction

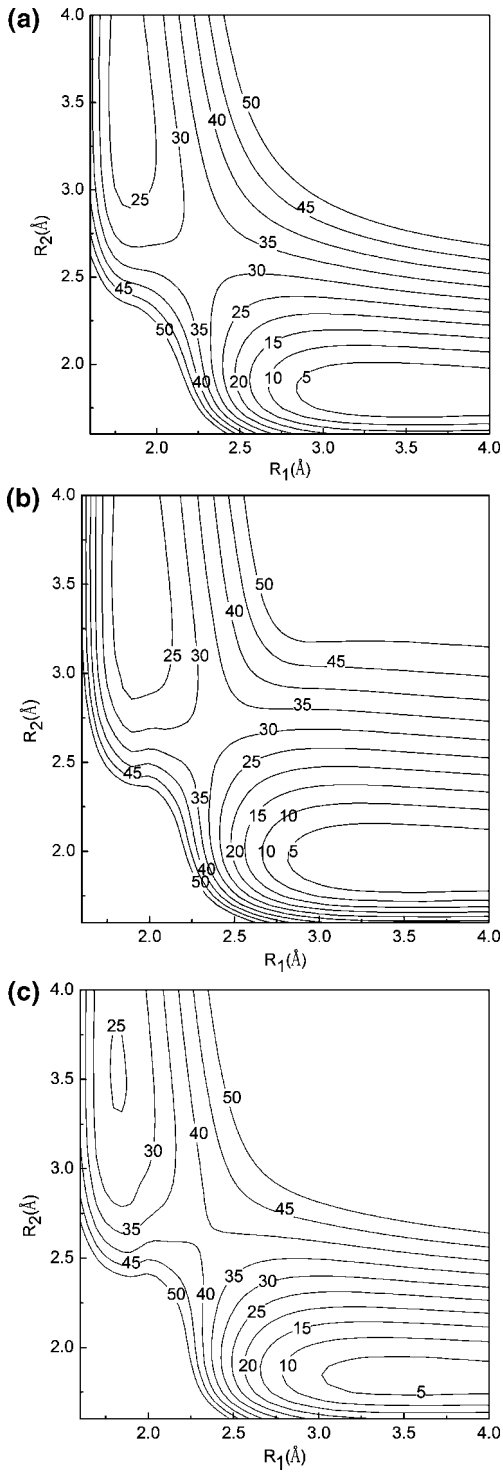

Figure 1. Computed adiabatic ground-state potential energy surface for nucleophilic substitution reaction of $HS^- + CH_3Cl \rightarrow HSCH_3 + Cl^-$ determined using (A) HF/6−31G(d), (B) VBSCF(6)/6−31G(d), and (C) CDC-MOVB(2)/6−31G(d) methods. The 6−31G(d) basis set is used throughout, which will be omitted in other figures. The reaction coordinate R_1 represents the distance between the central carbon and the chlorine atom, and R_2 specifies the distance between the sulfur atom and the central carbon atom. Energies are given in kcal/mol and distances are given in angstroms. The energy of the fully separated product is chosen as the reference (zero) energy. This convention is used throughout this paper.

Scheme 1. Schematic Representation of the Valence Bond Structures for the S_N2 Reaction between HS^- and CH_3Cl

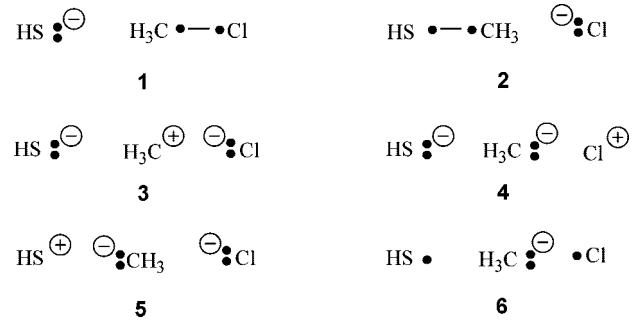

in exact agreement with experimental or high-level *ab initio* results. This can be accomplished by introducing a scaling factor to the exchange integral between the two diabatic states, which has minimal effects on the shape of the overall potential energy surface. We call this method the effective Hamiltonian MOVB (EH-MOVB) model. Note that the principles of constructing effective Hamiltonian valence bond theory have been used in numerous other contexts.[22−30,39−45] In the following, we first present the theory to systematically reduce *ab initio* valence bond configurations into a two effective state model. Then, the mixed molecular orbital and valence bond (MOVB) theory is reviewed, followed by a summary of computation. Results and discussions are presented next. Finally, the paper concludes with a summary of the major findings of this study and future perspectives.

2. Method

In this section, we first describe *ab initio* valence bond self-consistent-field (VBSCF) method employed in the present study as the high-level calibration target, although any other methods can be used. Then, we summarize key features of the mixed molecular orbital and valence bond (MOVB) theory for constructing diabatic and adiabatic potential surfaces and the effective Hamiltonian approach for obtaining accurate barrier height and energy of reaction for a chemical reaction.

A. Self-Consistent-Field Valence Bond (VBSCF) Theory. For the S_N2 reaction between HS^- and H_3CCl, we consider the VB active space formed by four electrons, two from the nucleophile and two from the covalent bond between the central carbon and the leaving group chloride ion, and 3 hybridized (or polarized) atomic orbitals located on the sulfur, the central carbon, and the leaving group, respectively. Thus, a total of six VB structures can be written (Scheme 1) to form the VB wave function of the diabatic ground state. Specifically, states **1** and **2** are the covalent Heitler-London structures for the reactant and product states, respectively, each of which is represented by two Slater determinants.[46] Furthermore, each Lewis bond, the C−Cl bond in the reactant state and the S−C bond in the product state, consists of two ionic configurations, corresponding to the electron pair localized on a single atom; they are described by structures **3** and **4** and structures **3** and **5**, respectively. Finally, configuration **6** represents the spin pairing interactions between an electron localized on the

nucleophilic group and one electron on the leaving group with the substrate central carbon orbital doubly occupied.

The VB wave function Φ for the S_N2 reaction between hydrosulfide ion and chloromethane is written as a linear combination of the six configurations depicted in Scheme 1:[13,14,47]

$$\Phi = \sum_{K=1}^{6} a_K \Psi_K \tag{1}$$

where Ψ_K is a Heilter-Lonton-Slater-Pauling (HLSP) function, and a_K is the coefficient for state K. In the VBSCF theory,[16,37,38] both the state coefficients $\{a_K\}$ in eq 1 and orbital coefficients of each VB structure $\{\Psi_K\}$ are simultaneously optimized to yield the minimum energy of the system. In this calculation, the VB atomic orbitals are the same in all configurations. The accuracy of VBSCF results is similar to that of the complete active space self-consistent field (CASSCF) method,[48] and these calculations include partial static electron correlation effects for electrons in the active space. Dynamic correlation effects can be introduced in VB calculations by relaxing the restriction on VB orbitals to allow them "breath" in different VB configurations.[14,49−51]

B. Mixed Molecular Orbital and Valence Bond (MOVB) Theory. In the mixed molecular orbital and valence bond (MOVB) method,[1−3,52,53] we use one Slater determinant with block-localized molecular orbitals to define individual VB configuration or Lewis resonance structure, called a diabatic state.[4−11] The Slater determinant can be self-consistently derived at both the Hartree−Fock and DFT levels. For example, the reactant state of the S_N2 reaction between HS^- and CH_3Cl is defined as the Lewis bond structure of the substrate $\{CH_3Cl\}$ in the presence of the "spectator" nucleophilic ion $\{HS^-\}$

$$\{\text{HS-}\}\{\text{CH3Cl}\};\Psi^R_{\text{MOVB}} = \hat{A}\{\chi^R_{\text{HS}}\chi^R_{\text{CH}_3\text{Cl}}\} \tag{2}$$

where Ψ^R_{MOVB} is the MOVB wave function for the reactant diabatic state, $\hat{A}$ is an antisymmetrizing operator, and χ^R_{HS} and $\chi^R_{\text{CH}_3\text{Cl}}$ are direct products of molecular orbitals for the fragments $\{HS^-\}$ and $\{CH_3Cl\}$, respectively, constructed under the restriction that they are linear combinations of atomic orbitals located within the corresponding fragment. Furthermore, the MOs within each fragment are constrained to be orthogonal, but they are nonorthogonal between different fragments. These features are illustrated by the transformation matrix

$$\mathbf{C}^R = \begin{pmatrix} \mathbf{C}^R_{\text{HS}} & 0 \\ 0 & \mathbf{C}^R_{\text{CH}_3\text{Cl}} \end{pmatrix} \tag{3}$$

where $\mathbf{C}^R_{\text{HS}}$ and $\mathbf{C}^R_{\text{CH}_3\text{Cl}}$ are matrices of orbital coefficients of the occupied molecular orbitals for the two fragments.[2] Note that the total number of electrons within each fragment is also fixed according to the corresponding Lewis structure and there is no chemical bond between the two fragments in the present case.

Similarly, the product state is defined as the Lewis bond structure of the product $\{HSCH_3\}$ in the presence of the "spectator" ion of the leaving group $\{Cl^-\}$

$$\{\text{HSCH3}\}\{\text{Cl-}\};\Psi^P_{\text{MOVB}} = \hat{A}\{\chi^P_{\text{HSCH}_3}\chi^P_{\text{Cl}}\} \tag{4}$$

where Ψ^P_{MOVB} is the MOVB wave function for the product diabatic state, and $\chi^P_{\text{HSCH}_3}$and χ^P_{Cl} are direct products of molecular orbitals for the $\{HSCH_3\}$ and $\{Cl^-\}$ fragments, respectively.

The MOVB wave function for the adiabatic ground-state is written as a linear combination of the diabatic states

$$\Phi_{\text{MOVB}} = a^R\Psi^R_{\text{MOVB}} + a^P\Psi^P_{\text{MOVB}} \tag{5}$$

where a^R and a^P are the configurational coefficients for the reactant and product diabatic state, respectively.[4,5] The potential energy of the adiabatic ground-state is the lower energy root of the secular equation

$$\begin{vmatrix} H^{\text{R}}_{11} - V & H_{12} - S_{12}V \\ H_{12} - S_{12}V & H^{\text{P}}_{22} - V \end{vmatrix} = 0 \tag{6}$$

where V is the adiabatic potential energy, H^R_{11} and H^P_{22} are the Hamiltonian matrix elements for the reactant and product diabatic states, respectively, H_{12} is the exchange integral, and $S^R_{12} = <\Psi^R_{\text{MOVB}}|\Psi^P_{\text{MOVB}}>$ is the overlap integral between the two effective states.

The reactant and product diabatic states Ψ^R_{MOVB} and Ψ^P_{MOVB} can be individually optimized, giving rise to the variational diabatic configurations (VDC),[1−3,52,53] and they can be used as basis functions to obtain the VDC-MOVB adiabatic ground-state energy with the optimization of the configurational coefficients a^R and a^P only. However, such a configuration interaction approach in the VDC-MOVB model is not a variational method. The VDC diabatic states are useful for a variety of applications; if one is interested in electronic resonance effects such as hyperconjugation stabilization of carbocations, the aromaticity of benzene and derivatives, or charge transfer effects in cation-π interactions, the VDC energies are variational for the charge localized diabatic configurations, which can be used to compare with the charge delocalized adiabatic state.[1,2,6,9,10,54−59]

When the wave function of eq 5 is variationally optimized both in terms of the configurational coefficients a^R and a^P and in terms of the molecular orbital coefficients (eq 3) to yield the minimum energy of the adiabatic ground state, the resulting MOVB diabatic states are called the consistent diabatic configurations (CDC).[3] The CDC-MOVB computational procedure is similar to that used in conventional multiconfiguration self-consistent field (MCSCF) method or *ab initio* VBSCF method, and the gradients of the adiabatic potential energy can be conveniently determined for use in geometry optimization and in molecular dynamics simulation. We note that the CDC-MOVB method is the appropriate computational approach for studying properties associated with the adiabatic ground-state such as the reaction barrier for a chemical reaction and the solvent reorganization energy. In this paper, we restrict out discussions on the CDC-MOVB method for the adiabatic ground state.

For comparison, each of the corresponding MOVB diabatic states Ψ^R_{MOVB} and Ψ^P_{MOVB} is represented by a single Slater determinant, whereas in *ab initio* VBSCF theory each state is described by three Heitler-London structures and four Slater determinants (Scheme 1). This emphasizes the com-

Table 1. Computed Binding Energies (kcal/mol) for the Formation of the Ion-Dipole (ΔE_1) Complex, the Barrier Height Relative to the IP Complex ($\Delta E^{\ddagger}$), the Relative Energy between the Reactant and Product Ion-Dipole Complexes (ΔE_2), and the Net Energy of Reaction (ΔE_{rxn}) between the Product and Reactant States for the S_N2 Reaction between Hydrosulfide and Chloromethane

	HF	B3LYP	MP2	CCSD (T)	VBSCF (6)[a]	MOVB (2)[a]	EH-MOVB (2)[a]
ΔE_1	–9.3	–11.2	–9.9	–9.9	–9.9	–8.8	–10.7
$\Delta E^{\ddagger}$	9.7	1.5	9.9	8.0	9.6	15.3	9.6
ΔE_2	–21.8	–18.7	–21.9	–21.5	–21.1	–22.0	–20.9
ΔE_{rxn}	–24.9	–22.3	–24.8	–24.5	–25.0	–25.0	–24.3

[a] The value in parentheses is the number of structures used in the calculation.

putational efficiency of MOVB. In addition, the MOVB adiabatic ground-state defined by eq 5 does not include VB state **6** in Scheme 1, and it has been shown that exclusion of this state does not affect the energy of the adiabatic ground-state significantly in *ab initio* VBSCF calcualtions.[3]

C. Effective Hamiltonian MOVB. The MOVB method has bee used to study a number of nucleophilic substitution reactions and proton transfer processes both in the gas phase and in aqueous solution.[1−3,52−54] While the overall MOVB results on diabatic states and the adiabatic ground-state are in good agreement with those obtained from *ab initio* VBSCF calculations, the computed barrier heights from MOVB are typically a few kilocaleries per mole greater than high-level *ab initio* results that include electron correlations. For example, the computed barriers for the reaction of HS^- and CH_3Cl are 9.7, 9.9, 8.0, and 9.6 kcal/mol at the HF, MP2, CCSD(T), and VBSCF levels of theory using the 6−31G(d) basis set (density functional theory using the B3LYP model produces an unrealistically low barrier of 1.5 kcal/mol), but the CDC-MOVB model yields an energy barrier of 15.3 kcal/mol (Table 1). To overcome this small nagging problem in MOVB, but at the same time to retain the shape of the potential energy surface which is in accord with high-level results (Figure 1), we introduce a scaling parameter to adjust the off-diagonal Hamiltonian matrix element H_{12}

$$H_{12}^{\mathrm{EH}} = \beta H_{12} \tag{7}$$

where H_{12}^{EH} is the effective Hamiltonian (EH) off-diagonal matrix element, and β is the diabatic coupling scaling constant to account for static correlations that are not fully accounted for in MOVB states and dynamic correlations that are not included as well as the use of a specific basis set. In such an EH-MOVB model, we retain the good qualitative and quantitative results for the diabatic states, i.e., the diagonal matrix elements H_{11}^R and H_{22}^P, in the MOVB model. We also retain the qualitative features of the off-diagonal matrix element H_{12}, but we choose a β value to reproduce exactly the barrier height of the target potential, derived either from experiment or from high-level *ab initio* calculations. In principle, the approach is similar to that used in effective Hamiltonian valence bond methods to parameterically model the *ab initio* matrix elements to reproduce the exact high-level results.[22−30,39−45]

In addition, if the energy of reaction, which is the energy difference between the product state and the reactant state

Scheme 2. Definition and Relative Energies

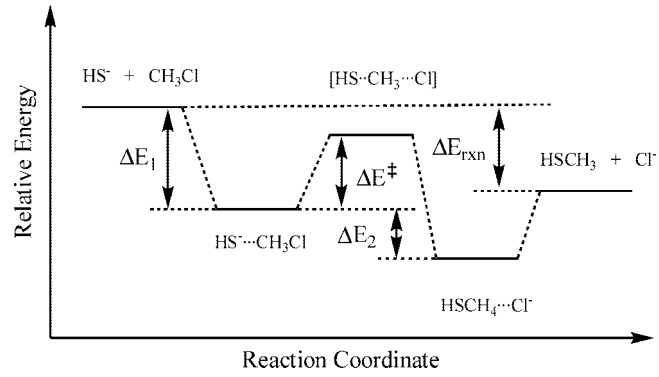

from the MOVB model, is not in good agreement with experiment, we can also adjust the EH-MOVB result to match the experimental value. Here, we employ a strategy that was used in the EVB model by Warshel and co-workers by introducing a shift-parameter in the diagonal matrix element H_{22}^P. Let ΔE_{exp} be the experimental energy of reaction and ΔE_{MOVB} be the energy of reaction determined from the original MOVB method, which is roughly the difference between the energies of the two diabatic state, $\Delta E_{\mathrm{MOVB}} \approx H_{22}^P(\mathbf{R}^P) - H_{11}^R(\mathbf{R}^R)$, at their respective geometries $\mathbf{R}^R$ and $\mathbf{R}^P$. Then, in EH-MOVB, the product state matrix element is adjusted by an energy shift-parameter $\Delta\varepsilon$ as follows:

$$H_{22}^{\mathrm{EH}} = H_{22}^P + \Delta\varepsilon = H_{22}^P + (\Delta E_{\mathrm{exp}} - \Delta E_{\mathrm{MOVB}}) \tag{8}$$

In the EH-MOVB model, the energy of the adiabatic ground-state is determined by using the modified secular equation

$$\begin{vmatrix} H_{11}^{\mathrm{R}} - V & \beta H_{12} - S_{12}V \\ \beta H_{12} - S_{12}V & H_{22}^{\mathrm{P}} + \Delta\varepsilon - V \end{vmatrix} = 0 \tag{9}$$

In eq 9, with the introduction of two parameters, the EH-MOVB method can be adjusted to reproduce exactly the experimental energy of activation and energy of reaction. We note that this parameter calibration approach has been used by Warshel and co-workers.[18−21] The difference here is that the diabatic coupling scaling parameter uniformly modifies the entire multidimensional surface rather than a simple constant or a single-variable function.[19] The value of the diabatic coupling scaling parameter is found to be in the order of 1.0005 for many reactions, and the value for the present S_N2 process is 1.00064; the value close to unity is a further indication that the shape of the potential energy surface is minimally affected, while the barrier height is reduced by about 6 kcal/mol.

3. Computational Details

All calculations are carried out using a modified version of the Xiamen Valence Bond (XMVB)[16] program and Gaussian03.[60] The 6−31G(d) basis set is used throughout all calculations. Geometries for the S_N2 reaction between HS^- and CH_3Cl along the reaction coordinate defined below are optimized using the 6−31G(d) basis set at each level of theory. In VBSCF and BOVB calculations, the inner electrons are frozen at the Hartree−Fock level, and 22 valence electrons are treated in VB calculations.[61]

To describe the change in energy and wave function of the two Lewis bond states as the reaction takes place, we define the reaction coordinate here as the difference between the bond length of the central carbon and the leaving group R(C−Cl) and that of the nucleophile and the central carbon R(S−C):

$$R_c = R_1(\mathrm{C-Cl}) - R_2(\mathrm{S-C}) \quad (10)$$

Of course, one can use other definitions to monitor the progress of the reaction, including the difference between the corresponding bond orders or energies of the two Lewis bond states. The geometrical variable, corresponding to the asymmetric bond stretch coordinate, is a good choice and of chemical intuition.

4. Results and Discussion

The main goal of this study is to develop an effective Hamiltonian approach so that quantitatively accurate results can be obtained from MOVB calculations using a two-state model with a modest basis set. We aim not only to obtain accurate results for the reaction barrier and the overall energy of reaction in comparison with high-level *ab initio* results but also to ensure that the structure and the potential energy surface are adequately represented. First, we compare the adiabatic potential energy surface from *ab initio* VBSCF theory with that from MOVB calculations as a function of the bond lengths that are broken and formed in the S_N2 reaction of hydrosulfide and chloromethane. Then, we discuss the qualitative features and quantitative results for the individual diabatic configurations and the diabatic coupling integral.

A. Adiabatic Potential Energy Surface. Figure 1 illustrates the two-dimensional potential energy surfaces as functions of the S−C bond length between the nucleophile and the central carbon and the C−Cl distance between the central carbon and the leaving group, which are constructed by using three different levels of theory, including HF, VBSCF(6), and MOVB(2) methods, all with the 6−31G(d) basis set. The number in parentheses specifies the number of VB configurations used in the corresponding theory. In addition, the relative energies at key stationary points are summarized in Table 1 with definitions of the energy terms depicted in Scheme 2. The computational methods include the Moller−Plesset second order perturbation (MP2) theory, coupled cluster at the CCSD(T) level, and the hybrid B3LYP density function model. Overall, the results from all theoretical levels are in agreement, except for the B3LYP model which yields a surprisingly low barrier. The computed barrier heights ($\Delta E^{\ddagger}$) at the transition state relative to the reactant ion-dipole complex are 9.7, 9.9, 8.0, and 9.6 kcal/mol at the HF, MP2, CCSD(T), and VBSCF(6) level of theory, respectively, and the energy differences between the two ion-dipole complexes (ΔE_2) are −21.8, −21.9, −21.5, and −21.1 kcal/mol, respectively. The computed overall energies of reaction for the separated reactants and products are in good accord among these theoretical models. For comparison, the original CDC-MOVB(2) method yields a reaction barrier of 15.3 kcal/mol, an energy difference between the dipole complex of −22.0 kcal/mol, and an energy of reaction (ΔE_{rxn}) of −5.9 kcal/mol. Thus, the overall performance of the MOVB(2) method is good in comparison with VBSCF results; however, the reaction barrier is overestimated by 5.7 kcal/mol relative to that of VBSCF(6) calculations. Comparison of the energy contours in Figure 1 shows that the qualitative features of the two-state MOVB(2) model are also in good accord with those obtained from HF and VBSCF(6) optimizations. This suggests that the original MOVB(2) model only needs to be slightly adjusted by lowering the barrier height by 5.7 kcal/mol but, at the same time, retaining the general qualitative features of the potential energy surface. This can be achieved within the effective Hamiltonian framework, and we have optimized the diabatic-coupling scaling parameter β in the EH-MOVB model to yield the result from *ab initio* VBSCF(6) theory. Since the relative energies between the ion-dipole complexes and the separated reactants and products are already in good accord with the VBSCF(6) values, we have decided to use an energy leveling correction of zero for the present system. The parameters in the EH-MOVB model are listed in Table 2, and the final EH-MOVB(2) results are given in Table 1. As can be seen, the exchange integral is only scaled by a factor of 0.06% of the original values.

Table 2. Diabatic Coupling Scaling Parameter and the Relative Energy Shift for the Diabatic State Used in the EH-MOVB(2)/6-31+G(d,p) Method for the S_N2 Reaction between Hydrosulfide and Chloromethane[a]

β (unitless)	$\Delta\varepsilon$ (kcal/mol)
1.00064	0.0

[a] Energies are given in kcal/mol.

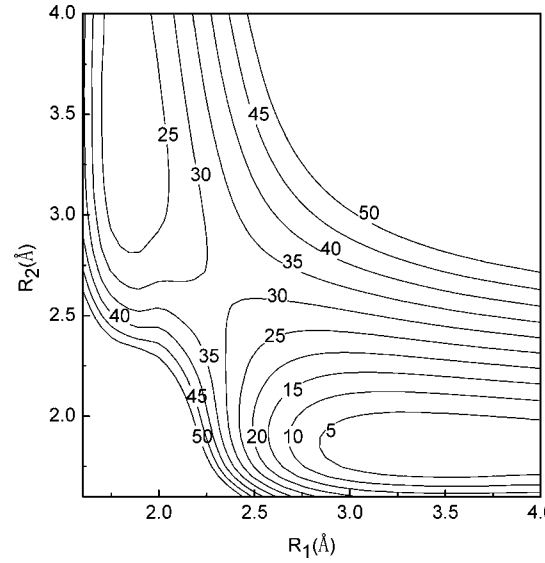

Figure 2. Adiabatic ground-state potential energy surface computed using the EH-MOVB model for the reaction of $HS^- + CH_3Cl \rightarrow HSCH_3 + Cl^-$.

The EH-MOVB potential energy surface for the reaction of HS^- and CH_3Cl is depicted in Figure 2, which may be compared with the *ab initio* valence bond results in Figure 1b. The original MOVB surface shows somewhat narrower contours about the minima for the two ion-dipole complexes than the VBSCF results. On the other hand, the energy contours determined using the EH-MOVB method are found

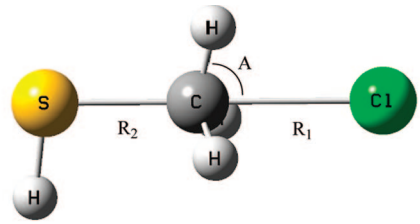

	Reactant			Transition State			Product		
	R_1	R_2	A	R_1	R_2	A	R_1	R_2	A
HF	1.828	3.451	107.97	2.267	2.601	93.57	3.461	1.832	69.88
EH-MOVB	1.820	3.553	108.10	2.272	2.886	96.76	3.521	1.830	69.95
VBSCF	1.922	3.468	106.44	2.484	2.052	76.94	3.542	1.926	71.16

Figure 3. Key geometrical parameters for the reactant-state ion-dipole complex, the transition state, and the product ion-dipole complex optimized at the HF, EH-MOVB, and VBSCF levels of theory.

to be in good accord with the VBSCF(6) results (Figure 1b). Key geometrical parameters for the optimized transition state using different methods are shown in Figure 3. Specifically the S−C and C−Cl distances are 2.05 and 2.48 Å from VBSCF(6) theory and are 2.89 and 2.27 Å from EH-MOVB(2) optimizations. While VBSCF and EH-MOVB show large difference in the S–C bond length, the agreement between HF and EH-MOVB is reasonable. The bond angles for the hydrogen atoms that are inverted in configuration show similar trends among these three methods (Figure 3).

The energy contours for the reactant and product diabatic states are shown in Figures 4 and 5. Clearly, the shapes of these potential energy surfaces are in good agreement between the EH-MOVB and VBSCF models, although the energy contours for product diabatic state from VBSCF(6) calculations appear to be somewhat more tightly grouped. It is interesting to notice that the minimum energy paths along the coordinate of the nucleophile approaching the substrate from the upper left corner in Figures 4a and 5a mirror nicely with that of the adiabatic potential energy surface, but it deviates markedly beyond the transition state region. Of course, the energy path on the product side is more appropriately described by the product diabatic state, and it is illustrated in Figures 4b and 5b. The diabatic states are coupled, and the resulting resonance stabilization energy, also called diabatic coupling, to lower the energy of the diabatic states to yield the adiabatic potential energy surface can be defined by

$$B(\mathbf{R}) = H_{12}^{\mathrm{EH}}(\mathbf{R}) - S_{12}(\mathbf{R})V(\mathbf{R}) \qquad (11)$$

where $\mathbf{R}$ specifies the coordinates of all atoms in the system, $V(\mathbf{R})$ is the potential energy surface of the adiabatic ground state, $H_{12}^{\mathrm{EH}}(\mathbf{R})$ is the effective Hamiltonian off-diagonal matrix element, and $S_{12}(\mathbf{R})$ is the overlap matrix.

Shown in Figure 6 are the contour maps for the diabatic coupling both from the VBSCF(6) and the EH-MOVB(2) method. Inspecting the two diabatic coupling maps, one immediately notices that they are qualitatively different despite the fact that the potential surfaces for the adiabatic states are very similar (Figures 1b and 2). In the EH-MOVB(2) model, the energy contours for the diabatic coupling follow roughly in the direction parallel to the minimum energy path (MEP) of the adiabatic potential energy surface (Figure 2), whereas, in VBSCF theory, the isoenergy contour curves trace nearly perpendicularly to the MEP path. Thus, the diabatic coupling in the EH-MOVB

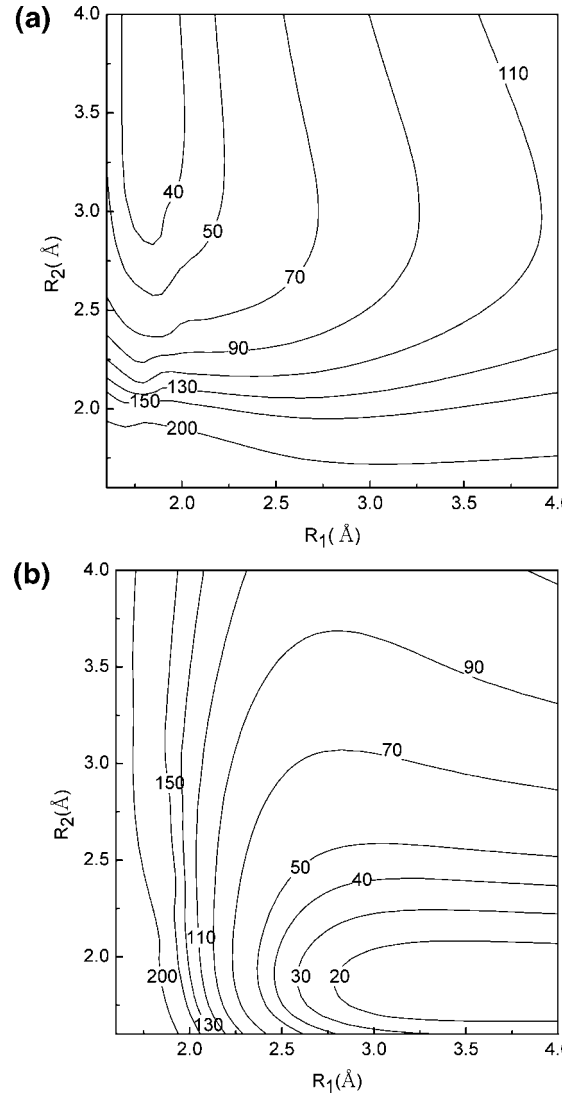

Figure 4. EH-MOVB consistent diabatic configurations for the reactant (a) and product (b) state. Energies are given in kcal/mol.

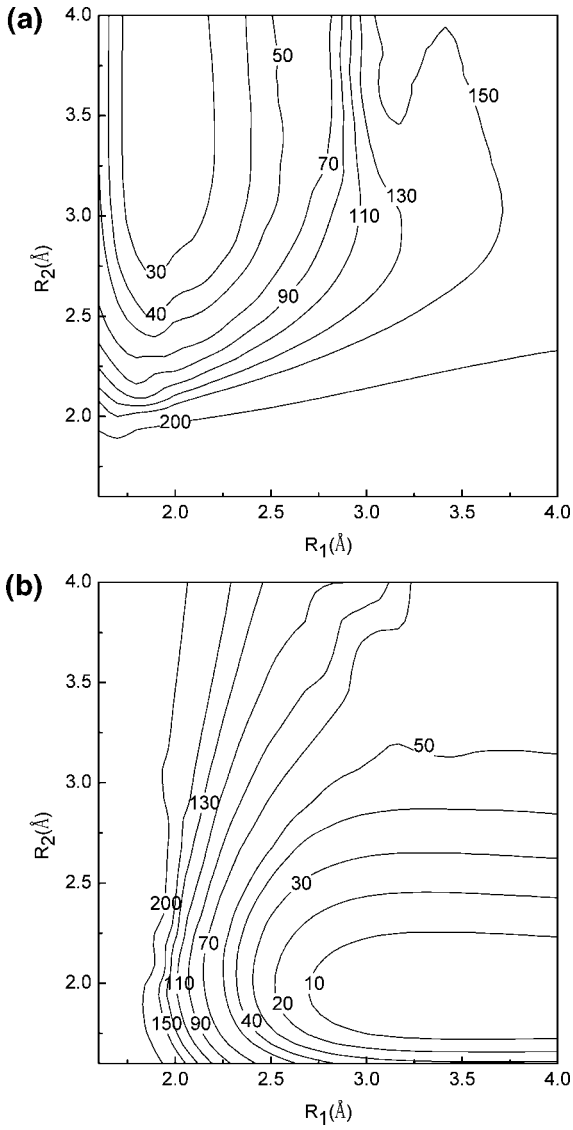

Figure 5. VBSCF consistent diabatic configurations for the reactant (a) and product (b) state. Energies are given in kcal/mol.

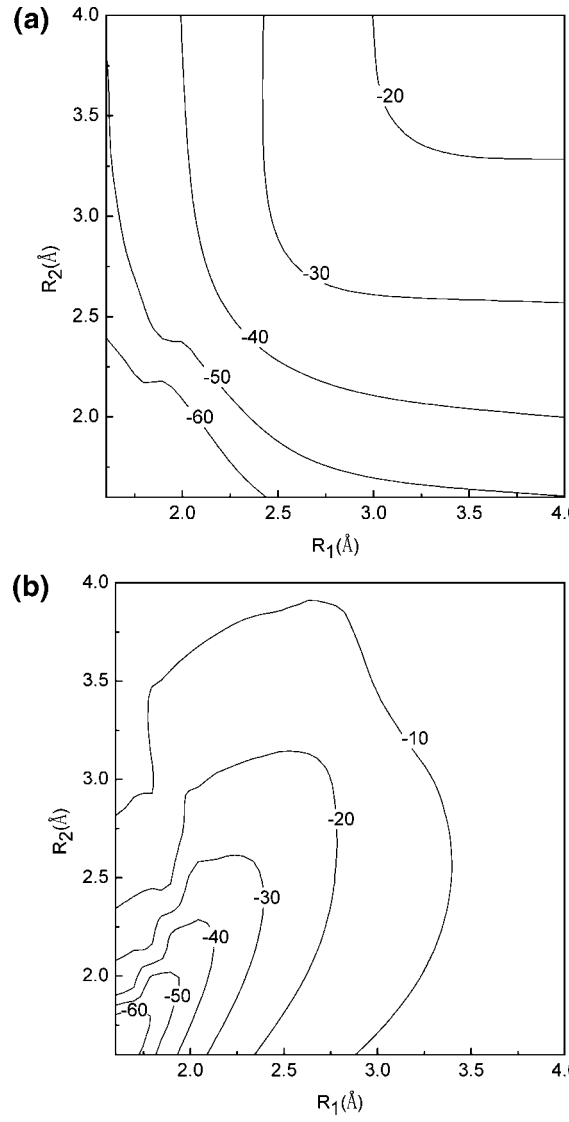

Figure 6. Computed resonance energy also called diabatic coupling (kcal/mol) for the S_N2 reaction of hydrosulfide and chloromethane using (a) the CDC-MOVB method and (b) the CDC-VBSCF approach.

model has rather small variations along the MEP path coordinate, but the VBSCF diabatic coupling has a maximum at the transition state and is nearly zero at the reactant and product state (Figure 7). The difference is due to the relatively large contributions from the same ionic configuration (State 3 in Scheme 1) both in the reactant and product diabatic states in the MOVB method, resulting in greater overlap between the two states along the entire reaction coordinate. Consequently, the diabatic coupling (eq 10) shows small changes. On the other hand the overlap integral shows greater variation with geometry changes in VBSCF theory, and this dependence can be modeled by an exponential function along the MEP coordinate. Obviously, this exponential dependence is different away from the MEP, and the diabatic coupling is in general a function of all atomic coordinates (eq 10), rather than a single reaction coordinate. Interestingly, both a constant value and an exponential function have been used to mimic the diabatic coupling in applications of the EVB model.[18,19]

B. Variational Diabatic States. The diabatic potential energy surfaces for the reactant and product states can be obtained in two different ways.[3] When the diabatic states are generated as a result of variational minimization of the energy of the adiabatic ground state, they are consistent diabatic configurations (CDC).[3] Alternatively, the energy of each individual diabatic state can be variationally minimized, and such variational diabatic configurations (VDC) represent the potential energy surfaces of the diabatic states ($\varepsilon_1 = H_{11}$, $\varepsilon_2 = H_{22}$),[1−3] which should be distinguished from the diagonal matrix elements (H_{11}, H_{22}) from the CDC states. This distinction is important because if one uses molecular fragments as models to parametrize the potential energy functions for the diabatic states, they correspond to the minimum energy of these states, ε_1, and ε_2, and thus, they are the VDC states.[3]

Previously, we have shown that for the S_N2 reaction between ammonia and methylammonium ion in the gas phase, the CDC states remain roughly on the covalent potential energy surface as the molecular geometry distorts

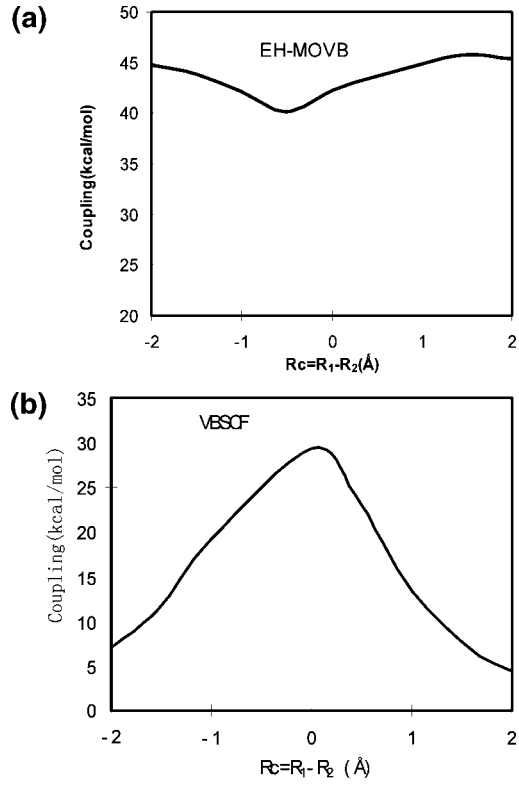

Figure 7. Computed resonance energy (kcal/mol), also called diabatic coupling, along the minimum energy path expressed by the difference between the distance between the breaking and forming bonds, i.e., $R_c = R_1 - R_2$, which is given in angstroms: (a) determined using the CDC-MOVB method and (b) computed using the CDC-VBSCF model.

away from the respective reactant and product state minimum.[3] On the other hand, the VDC states converge largely to the corresponding ionic configurations, which have much lower energies than the covalent states, by the same geometrical variations. These findings are clearly reflected by comparing the CDC diabatic states shown in Figures 4 and 5 with the VDC states shown in Figures 8 and 9. At the VBSCF(6) level of theory, the CDC potential surfaces (Figure 4) have energy variations of more than 200 kcal/mol both for the reactant and product states as the two chemical bonds formed and broken, respectively. On the other hand, the VDC potentials surfaces have smaller energy changes, about 130 kcal/mol within the same structural variations (Figure 8). Similar trends are observed for the EH-MOVB(2) model in Figures 5 and 9, although a small subtle difference between VBSCF(6) and EH-MOVB(2) can be noticed in the CDC states in that the former model seems to generate slightly less steep potential surfaces than the latter. The agreement between the VDC surfaces obtained from the VBSCF(6) and EH-MOVB(2) methods is very good.

We emphasize that there is no unique way of defining the diabatic states in a two-state model to represent an intrinsically multiconfigurational wave function for the reaction system and that we have presented two approaches here to optimize the wave functions of these diabatic states. Thus, it is important to specify the way in which the diabatic states are defined and the procedure by which their wave functions are optimized to interpret the properties and reactivity of a

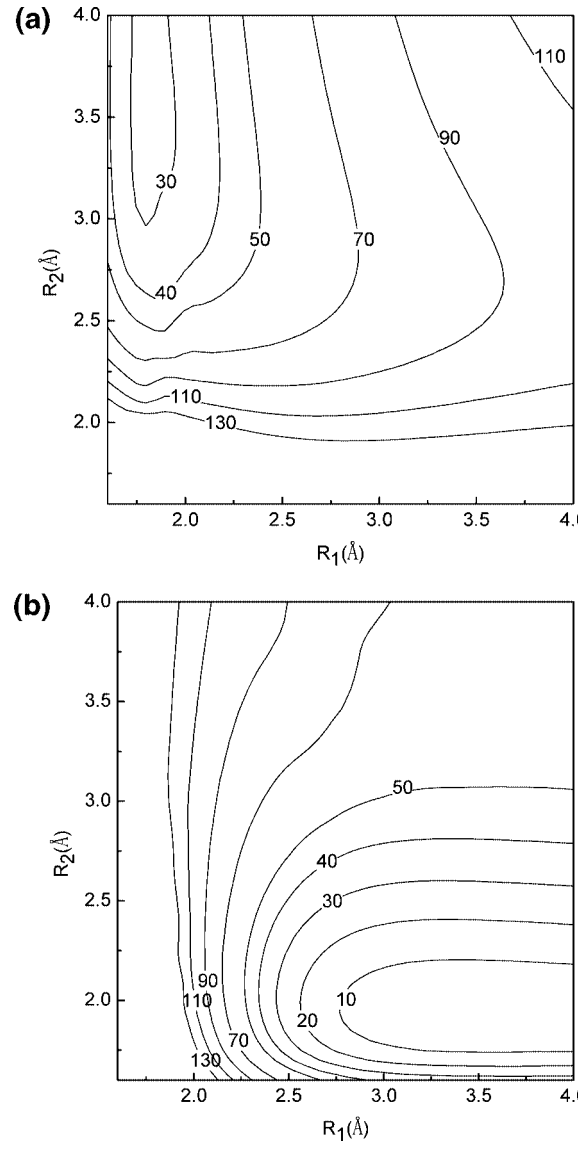

Figure 8. MOVB variational diabatic configurations (VDC) for (a) the reactant state and (b) the product state for the S_N2 reaction between hydrosulfide ion and chloromethane in the gas phase. Relative energies are given in kcal/mol.

chemical system. In addition, the nature of the diabatic states in their covalent and ionic characters will also be altered by solvation. This will significantly affect the quantitative values and the interpretation of solvent reorganization energies since the computational results depend on the charge polarization of the diabatic states. Clearly, a rigorous assessment of the definition of the diabatic states and the method used to estimate the solvent reorganization energy is as critical as the quantitative result itself.

We also note that it is sometimes informative to use a generalized solvent reaction coordinate such as the energy gap between the reactant and product diabatic states,[1,2,19,20] $\Delta E = \varepsilon_2(\mathbf{R}) - \varepsilon_1(\mathbf{R})$. Since the energies of the diabatic states include both the internal energy change as well as the interactions with the solvent and protein media, the change in this energy difference reflects both the progress of the geometries of the reacting molecules and the polarization of the environment. This approach which was originally used in the Marcus theory for electron transfer reactions has been

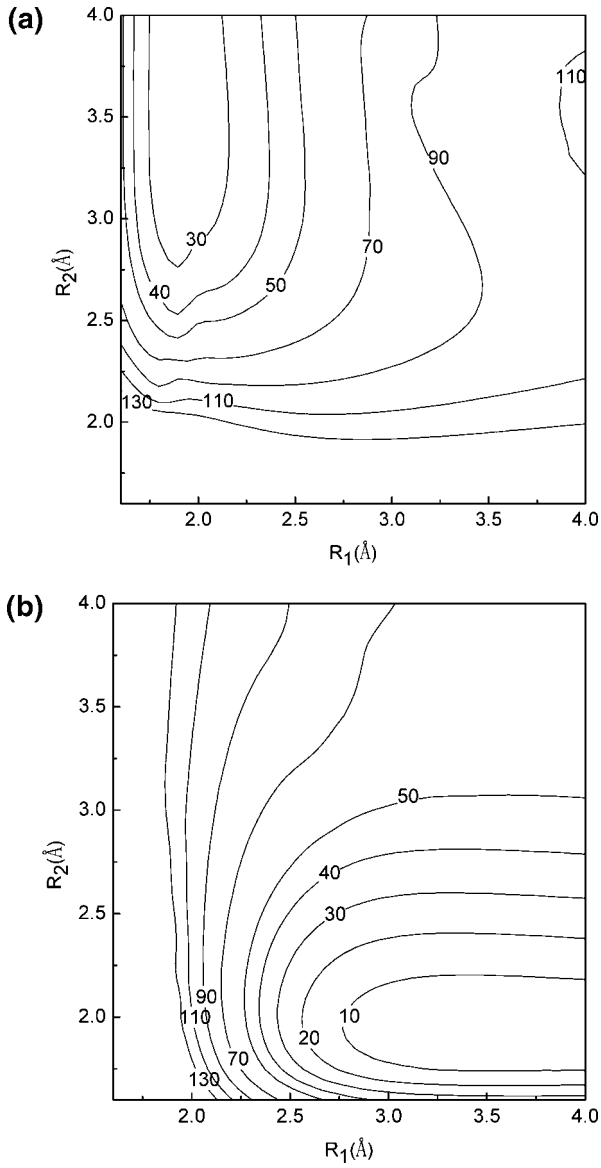

Figure 9. VBSCF variational diabatic configurations (VDC) for (a) the reactant state and (b) the product state for the S_N2 reaction between hydrosulfide ion and chloromethane in the gas phase. Relative energies are given in kcal/mol.

broadly applied, due to Warshel's work, to other chemical reactions in solution and in enzymes.[1,2,19,20,52] In principle, the energy gap reaction coordinate can also be defined either by using the CDC states or by using the VDC states. It is straightforward computationally to employ the VDC energy gap,[1,2,19,20] $\Delta E^{VDC} = \varepsilon_2(\mathbf{R}) - \varepsilon_1(\mathbf{R})$, as the potential energy function to directly carry out molecular dynamics simulations to obtain the potential of mean force as a function of ΔE^{VDC} for a chemical reaction.[52] It is also desirable conceptually to use this representation since the VDC states represent the true energies of the diabatic states.

5. Conclusions

An effective Hamiltonian-mixed molecular orbital and valence bond (EH-MOVB) method has been presented to obtain an accurate potential energy surface for chemical reactions. Building upon previous results on the construction of diabatic and adiabatic potential surfaces using *ab initio* MOVB theory,[3] we introduced a diabatic coupling scaling factor to uniformly scale the *ab initio* off-diagonal matrix element H_{12} such that the computed energy of activation from the EH-MOVB method is adjusted to be in exact agreement with the target value, either directly from experiment or from high-level *ab initio* calculations. In practice, the scaling constant is only a fraction of one percent of the original value of the off-diagonal matrix element, resulting in minimal alteration of the shape of the potential energy surface of the original MOVB model. Furthermore, the relative energy between the reactant and product diabatic states in the EH-MOVB method can be improved by adding a constant value, which is the deviation from the experimental result, to the potential energy surface of the diagonal matrix element. This approach is similar to the calibration procedure used by Warshel and co-workers in the empirical valence bond (EVB) model,[19] but the present EH-MOVB method is based on *ab initio* electronic structure theory in which the off-diagonal matrix elements are functions of all degrees of freedom of the system and the overlap matrix is explicitly evaluated.

We have chosen the nucleophilic substitution reaction between hydrosulfide and chloromethane to illustrate the present effective Hamiltonian approach. We used the results from *ab initio* self-consistent valence bond (VBSCF) calculations as the calibration target, noting that any other high-level methods or experimental data can be used. For the construction of diabatic states, two optimization schemes are considered. In the first approach, called consistent diabatic configurations (CDC), the wave functions for the diabatic states are obtained as a result of the variational minimization of the adiabatic ground state. In the second model, called variational diabatic configurations (VDC), the wave functions of these states are individually minimized to obtain the energy of the diabatic states. The potential energy surface for the adiabatic ground-state has been constructed using the CDC states in the two-state EH-MOVB model, and the resulting energy contours as functions of the breaking and forming bond distances are in excellent accord with those from VBSCF calculations. It was found that the stabilization energy due to diabatic coupling (the off-diagonal matrix element in the generalized secular equation) has small variations along the minimum reaction path coordinate in the EH-MOVB model, whereas it shows a maximum value at the transition state and has nearly zero values in the regions of the ion-dipole complexes from VBSCF calculations. The difference in the diabatic coupling stabilization between the two method is attributed to the large overlap integral in the computationally efficient MOVB method, which has larger contributions from the ionic state due to the use block-localized orbitals in a single determinant representation, whereas in VBSCF the overlap integral is more geometrical dependent. We have also discussed the distinction between VDC and CDC diabatic states, with the former representing the potential energy surface of the diabatic states and the latter specifies purely the diagonal matrix elements of the Hamiltonian. These differences make it necessary to clearly define the diabatic states and validate the energies in discussion of reactivity and reorganization energies.

Acknowledgment. We thank the National Institutes of Health (GM46736) and the Office of Naval Research for support of this work.

References

(1) Mo, Y.; Gao, J. *J. Comput. Chem.* **2000**, *21*, 1458.

(2) Mo, Y.; Gao, J. *J. Phys. Chem. A* **2000**, *104*, 3012.

(3) Song, L.; Gao, J. J. Phys. Chem. A 2008, ASAP.

(4) Mo, Y.; Peyerimhoff, S. D. *J. Chem. Phys.* **1998**, *109*, 1687.

(5) Mo, Y.; Zhang, Y.; Gao, J. *J. Am. Chem. Soc.* **1999**, *121*, 5737.

(6) Mo, Y.; Gao, J.; Peyerimhoff, S. D. *J. Chem. Phys.* **2000**, *112*, 5530.

(7) (a) Gianinetti, E.; Raimondi, M.; Tornaghi, E. *Int. J. Quantum Chem.* **1996**, *60*, 157. (b) Gianinetti, E.; Vandoni, I.; Famulari, A.; Raimondi, M. *Adv. Quantum Chem.* **1998**, *31*, 251.

(8) Raimondi, M.; Famulari, A.; Specchio, R.; Sironi, M.; Moroni, F.; Gianinetti, E. *THEOCHEM* **2001**, *573*, 25.

(9) Khaliullin, R. Z.; Head-Gordon, M.; Bell, A. T. *J. Chem. Phys.* **2006**, *124*, 204105/1.

(10) Khaliullin, R. Z.; Cobar, E. A.; Lochan, R. C.; Bell, A. T.; Head-Gordon, M. *J. Phys. Chem. A* **2007**, *111*, 8753.

(11) Mo, Y.; Song, L.; Lin, Y. *J. Phys. Chem. A* **2007**, *111*, 8291.

(12) *Valence Bond Theory*; Cooper, D. L., Ed.; Elsevier: Amsterdam, 2002.

(13) Cooper, D. L.; Gerratt, J.; Raimondi, M. *Adv. Chem. Phys.* **1987**, *69*, 319.

(14) Hiberty, P. C.; Flament, J. P.; Noizet, E. *Chem. Phys. Lett.* **1992**, *189*, 259.

(15) Wu, W.; Song, L.; Cao, Z.; Zhang, Q.; Shaik, S. *J. Phys. Chem. A* **2002**, *106*, 2721.

(16) Song, L.; Mo, Y.; Zhang, Q.; Wu, W. *J. Comput. Chem.* **2005**, *26*, 514.

(17) Shaik, S.; Shurki, A. *Angew. Chem., Int. Ed.* **1999**, *38*, 587.

(18) Warshel, A.; Weiss, R. M. *J. Am. Chem. Soc.* **1980**, *102*, 6218.

(19) (a) Warshel, A. *Computer Modeling of Chemical Reactions in Enzymes and Solutions*; Wiley: New York, 1991. (b) Aqvist, J.; Warshel, A. *Chem. Rev.* **1993**, *93*, 2523. (c) Villa, J.; Warshel, A. *J. Phys. Chem. B* **2001**, *105*, 7887.

(20) (a) Hong, G.; Rosta, E.; Warshel, A. *J. Phys. Chem. B* **2006**, *110*, 19570–19574. (b) Xiang, Y.; Warshel, A. *J. Phys. Chem. B* **2008**, *112*, 1007–1015.

(21) (a) Wu, Q.; Cheng, C.-L.; Van Voorhis, T. *J. Chem. Phys.* **2007**, *127*, 16419. (b) Sharir-Ivry, A.; Shurki, A. J. Phys. Chem. A **2008**,ASAP.

(22) Schlegel, H. B.; Sonnenberg, J. L. *J. Chem. Theory Comput.* **2006**, *2*, 905.

(23) Chang, Y. T.; Miller, W. H. *J. Phys. Chem.* **1990**, *94*, 5884.

(24) Schmitt, U. W.; Voth, G. A. *J. Phys. Chem. B* **1998**, *102*, 5547.

(25) (a) Day, T. J. F.; Soudackov, A. V.; Cuma, M.; Schmitt, U. W.; Voth, G. A. *J. Chem. Phys.* **2002**, *117*, 5839. (b) Maupin, C. M.; Wong, K. F.; Soudackov, A. V.; Kim, S.; Voth, G. A. *J. Phys. Chem. A* **2006**, *110*, 631.

(26) Vuilleumier, R.; Borgis, D. *J. Phys. Chem. B* **1998**, *102*, 4261.

(27) Sonnenberg, J. L.; Schlegel, H. B. *Mol. Phys.* **2007**, *105*, 2719.

(28) Kim, Y.; Corchado, J. C.; Villa, J.; Xing, J.; Truhlar, D. G. *J. Chem. Phys.* **2000**, *112*, 2718.

(29) Tishchenko, O.; Truhlar, D. G. *J. Phys. Chem. A* **2006**, *110*, 13530.

(30) Lin, H.; Zhao, Y.; Tishchenko, O.; Truhlar, D. G. *J. Chem. Theory Comput.* **2006**, *2*, 1237.

(31) Goddard, W. A., III.; Dunning, T. H., Jr.; Hunt, W. J.; Hay, P. J. *Acc. Chem. Res.* **1973**, *6*, 368.

(32) Mead, C. A.; Truhlar, D. G. *J. Chem. Phys.* **1982**, *77*, 6090.

(33) Pacher, T.; Cederbaum, L. S.; Koppel, H. *J. Chem. Phys.* **1988**, *89*, 7367.

(34) Mo, Y.; Wu, W.; Zhang, Q. *J. Chem. Phys.* **2003**, *119*, 6448.

(35) Mo, Y. *J. Chem. Phys.* **2007**, *126*, 224104.

(36) Sidis, V. *Adv. Chem. Phys.* **1992**, *82*, 73.

(37) Van Lenthe, J. H.; Verbeek, J.; Pulay, P. *Mol. Phys.* **1991**, *73*, 1159.

(38) Van Lenthe, J. H.; Dijkstra, F.; Havenith, R. W. A. *Theor. Comput. Chem.* **2002**, *10*, 79.

(39) Sheppard, M. G.; Freed, K. F. *J. Chem. Phys.* **1981**, *75*, 4507.

(40) Hurtubise, V.; Freed, K. F. *Adv. Chem. Phys.* **1993**, *83*, 465.

(41) Martin, C. H.; Graham, R. L.; Freed, K. F. *J. Phys. Chem.* **1994**, *98*, 3467.

(42) Bernardi, F.; Olivucci, M.; Robb, M. A. *J. Am. Chem. Soc.* **1992**, *114*, 1606.

(43) Bearpark, M. J.; Robb, M. A.; Bernardi, F.; Olivucci, M. *Chem. Phys. Lett.* **1994**, *217*, 513.

(44) Bearpark, M. J.; Bernardi, F.; Olivucci, M.; Robb, M. A. *J. Phys. Chem. A* **1997**, *101*, 8395.

(45) Bearpark, M. J.; Smith, B. R.; Bernardi, F.; Olivucci, M.; Robb, M. A. *ACS Symp. Ser.* **1998**, *712*, 148.

(46) Heitler, W.; London, F. *Z. Phys.* **1927**, *44*, 455.

(47) Mo, Y.; Lin, Z.; Wu, W.; Zhang, Q. *J. Phys. Chem.* **1996**, *100*, 11569.

(48) Thorsteinsson, T.; Cooper, D. L.; Gerratt, J.; Karadakov, P. B.; Raimondi, M. *Theor. Chim. Acta* **1996**, *93*, 343.

(49) Hiberty, P. C.; Humbel, S.; Archirel, P. *J. Phys. Chem.* **1994**, *98*, 11697.

(50) Song, L.; Wu, W.; Hiberty, P. C.; Shaik, S. *Chem.-- Eur. J.* **2006**, *12*, 7458.

(51) Su, P.; Ying, F.; Wu, W.; Hiberty, P. C.; Shaik, S. *ChemPhysChem* **2007**, *8*, 2603.

(52) Gao, J.; Garcia-Viloca, M.; Poulsen, T. D.; Mo, Y. *Adv. Phys. Org. Chem.* **2003**, *38*, 161.

(53) Gao, J.; Mo, Y. *Prog. Theor. Chem. Phys.* **2000**, *5*, 247.

(54) Mo, Y.; Gao, J. *J. Phys. Chem. A* **2001**, *105*, 6530.

(55) Mo, Y.; Subramanian, G.; Gao, J.; Ferguson, D. M. *J. Am. Chem. Soc.* **2002**, *124*, 4832.

(56) Mo, Y.; Wu, W.; Song, L.; Lin, M.; Zhang, Q.; Gao, J. *Angew. Chem., Int. Ed.* **2004**, *43*, 1986.

(57) Mo, Y.; Gao, J. *Acc. Chem. Res.* **2007**, *40*, 113.

(58) Brauer, C. S.; Craddock, M. B.; Kilian, J.; Grumstrup, E. M.; Orilall, M. C.; Mo, Y.; Gao, J.; Leopold, K. R. *J. Phys. Chem. A* **2006**, *110*, 10025.

(59) Mo, Y.; Gao, J. *J. Phys. Chem. B* **2006**, *110*, 2976.

(60) Frisch, M. J. G. W. T.; Schlegel, H. B.; Scuseria, G. E.; Robb, M. A.; Montgomery, J. R. C. J. A., Jr.; Vreven, T.; Kudin, K. N.; Millam, J. C. B. J. M.; Iyengar, S. S.; Tomasi, J.; Barone, V.; Cossi, B. M. M.; Scalmani, G.; Rega, N.; Petersson, G. A.; Hada, H. N. M.; Ehara, M.; Toyota, K.; Fukuda, R.; Ishida, J. H. M.; Nakajima, T.; Honda, Y.; Kitao, O.; Nakai, H.; Knox, M. K. X.; Li, J. E.; Hratchian, H. P.; Cross, J. B.; Bakken, V.; Jaramillo, C. A. J.; Gomperts, R.; Stratmann, R. E.; Yazyev, O.; Cammi, A. J. A. R.; Pomelli, C.; Ochterski, J. W.; Ayala, P. Y.; Voth, K. M. G. A.; Salvador, P.; Dannenberg, J. J.; Zakrzewski, V. G.; Daniels, S. D. A. D.; Strain, M. C.; Farkas, O.; Rabuck, D. K. M. A. D.; Raghavachari, K.; Foresman, J. B.; Cui, J. V. O. Q.; Baboul, A. G.; Clifford, S.; Cioslowski, J.; Liu, B. B. S. G.; Liashenko, A.; Piskorz, P.; Komaromi, I.; Fox, R. L. M. D. J.; Keith, T.; Al-Laham, M. A.; Peng, C. Y.; Challacombe, A. N. M.; Gill, P. M. W.; Johnson, B. W. C.; Wong, M. W.; Gonzalez, C.; Pople, J. A. *Gaussian03, Revision D.01*; Gaussian, Inc.: 2004.

(61) Chirgwin, H. B.; Coulson, C. A. *Proc. R. Soc. London Ser. A* **1950**, *2*, 196.

CT800421Y

JCTC Journal of Chemical Theory and Computation

Location of Two Seams in the Proximity of the C_{2v} $\pi\pi^*$ Minimum Energy Path of Formaldehyde

Luca De Vico* and Roland Lindh

Department of Theoretical Chemistry, Lund University, P.O. Box 124, SE-22100 Lund, Sweden

Received August 22, 2008

Abstract: Photochemical reactions rationalization is a key aspect for the understanding and setup of novel experiment and novel photoinitiated pathways. In this respect, the relationship between minimum energy paths over an excited-state and the intersection to lower potential energy surfaces is fundamental. In order to help the understanding of this relationship, in this study we present a novel kind of constraint for geometry optimizations, namely, an "orthogonality" constraint. Its possible applications are described. A complete example on how to retrieve the direct relationship between a minimum energy path over an excited-state potential energy surface and a conical intersection seam is given for C_{2v} symmetry constrained formaldehyde. The advantages of using the novel constraint when rationalizing a (photo)chemical reaction are presented.

Introduction

Since Teller demonstrated the possibility for the existence of crossings of potential energy surfaces,[1] the interest for such entities increased, with an exponential trend in the latest years.[2] The available computational tools, coupled with the increasing capabilities of computers, turned the search for potential energy surface (PES) degeneracy points into an everyday matter,[3] making it indispensable when one wants to describe any photochemical reaction from the theoretical chemist point of view. Formally, the crossing between two potential energy surfaces of different spin symmetry is called intersystem crossing (ISC), while if the two surfaces share the same spin symmetry, the crossing is referred to as a conical intersection (CI).[4] Nevertheless, when considering molecules with symmetry, the crossing of two surfaces of the same spin belonging to different spatial symmetry can be treated in the same way as an ISC.

The nature of CIs (ISCs) has been extensively studied, by analyzing the PES around them. For example, Atchity and co-workers gave a classification of conical intersections based on the shape of the PES forming the CI.[5] On the base of which class a CI belongs to, they predicted different behaviors for the molecules passing through it and consequently for the photoreaction in general. Another aspect of crossings is their extension in the molecular coordinate space. In fact, there does not exist only one point of degeneracy but an infinite series.[6] This is usually referred to as intersection space[5] or intersection seam.[7] The nature of the points belonging to a seam has been recently studied by Sicilia and co-workers.[8] They analyzed the second-order nature of conical intersections and defined if they were minima or transition states inside the intersection space. Through this analysis, the authors were able to give a description of the CI seam and its main features. Very recently,[9] the same authors suggested an algorithm to connect the stationary points inside the intersection space.

Maybe more relevant for the study of a photochemical reaction is the relationship between the minimum energy paths (MEPs) over an excited-state PES and the seam connecting such a surface to other(s). To our knowledge, not too many studies have been conducted in this sense. Various attempts in this direction have been done, for example by locating the nearest crossing to a given structure, usually the Franck−Condon.[10,11] To name a few other examples related to different classes of molecules where the seam has been studied in more details, ref 12 reports a CI seam involved in the photochemistry of the ring-opening of cyclohexa-1,3-diene. Migani and co-workers analyzed the

* Corresponding author e-mail: luca@kemi.ku.dk. Current address: Department of Chemistry, University of Copenhagen, Universitetsparken 5, DK-2100 Copenhagen, Denmark.

10.1021/ct800348s CCC: $40.75 © 2009 American Chemical Society
Published on Web 12/08/2008

CI seams of various models of the retinal chromophore.[13] Cembran et al. reported an extensive area of degeneracy for azobenzene,[14] while Frutos et al. described the involvement of CI seams in the photochemistry of tricyclo[3.3.0.0^{2,6}]octa-3,7-diene.[15] The knowledge of the relationship between a MEP and a CI seam has been, most interestingly, related also to the possibility of fine controlling the outcome of a photoreaction.[16] In fact, by knowing which internal modes correlate the MEP and the seam, one could define which vibrational levels should be pre-emptively excited in order to populate such modes. In turn, a coherent femtosecond pulsed laser experiment could be devised, in order to obtain the maximum yield of a desired photoproduct.[17]

The previously cited theoretical articles have one feature in common: the seam has been retrieved once the minimum energy crossing point (MECP) has been found or if a point along the MEP is also a crossing point. Starting from this structure, the rest of the seam is conceived. In a second moment, the seam and the MEP are put in energetic relation between each other. In other words, the relationship seam – MEP is partial (only energetic data are considered) and indirect. We devised a way to correlate a minimum energy path computed on an excited-state to the closest crossing that could be reached by vibrations along modes other than those involved in the MEP itself, in other words, along those modes perpendicular to the motion along the MEP. Since the MEP is defined as the steepest descend path, that is by the gradient, the crossing has to be located in the subspace of coordinates orthogonal to the gradient vector. In this way, the relationship seam – MEP is direct and easier to be rationalized. This is achieved because each point of the MEP is directly related to the points of the seam, in a one-to-one manner.

In the next paragraphs, we will give some more details on how this has been achieved, plus an application of the method to C_{2v} symmetry constrained formaldehyde on its evolution along the $\pi\pi^*$ excited state, together with related discussion.

2. Method

The methods section is divided into five parts: in the first we will sketch the theory behind the new kind of constraint we introduced, followed by a general discussion about its possible applications and its implementation. Finally, we will give the computational details of the application of the new kind of constraint to the search of a CI seam close to the C_{2v} $\pi\pi^*$ MEP of formaldehyde.

2.1. A New Type of Constraint: Theory. A new kind of constraint has been introduced and applied, an "orthogonality" constraint. Given a point in the coordinate space of a molecule (structure) and a vector associated to it (typically the energy gradient), the coordinate space available during a geometry optimization is reduced by the constraint to the subspace of coordinates orthogonal to the vector.

The constraint to fulfill can be expressed as

$$\langle \boldsymbol{g} \cdot (\boldsymbol{r_0} - \boldsymbol{r}) \rangle = 0 \qquad (1)$$

where $\boldsymbol{g}$ is the reference vector (gradient), $\boldsymbol{r_0}$ is the reference coordinates, and $\boldsymbol{r}$ is the coordinates of the current structure.

Scheme 1

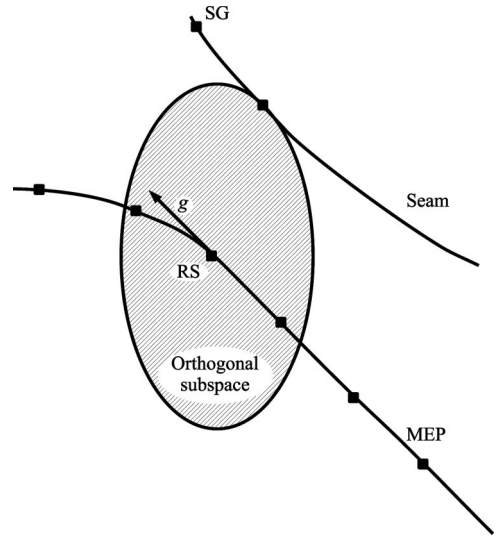

This kind of constraint is nearly useless when applied alone. In fact, in a typical situation, the reference vector is the gradient computed at the reference geometry $\boldsymbol{g} = \boldsymbol{g}(\boldsymbol{r_0})$. Once the orthogonality constraint is applied, the result of a constrained optimization would be the same reference geometry, since it is a minimum in the orthogonal subspace too. In fact, the only possibility to reach a structure with lower energy would be to follow the gradient, which has been cut out by the constraint. Once the geometry reaches the reference structure, the constraint vanishes, since one has $\boldsymbol{r} = \boldsymbol{r_0}$ in eq 1.

In an ideal situation, if the reference structure is a stationary point (minimum or transition state), the orthogonality constraint is noneffective. In fact, the reference gradient would be zero by definition ($\boldsymbol{g}(\boldsymbol{r_{eq}}) = 0$ in eq 1). The other eventual applied constraints would be the only effective.

2.2. Current Application to Photoreactions. The most interesting use, instead, is when the orthogonality constraint is coupled together with some other kind of constraint. This will induce $\boldsymbol{r} \neq \boldsymbol{r_0}$, making eq 1 meaningful. For example, in the present contribution, we coupled the orthogonality constraint together with the energy difference constraint. By doing so, we searched for the lowest energy degeneracy between two given potential energy surfaces inside the subspace orthogonal to the gradient computed at a given geometry. The obtained structure is not the absolute MECP but the lowest in energy and possibly closest crossing to the reference structure or to the starting geometry (*vide infra*). This is depicted in Scheme 1.

As for the hyperspherical constraint,[10] it is possible to specify a starting geometry and a reference structure/vector relative to another structure previously determined. For example, this has been applied in the present contribution to locate an intersection seam in the proximity of a previously computed MEP. In fact, the starting geometry (**SG**) was chosen to be already part of the seam that we wanted to explore. This, in turn, ensured continuity in the obtained seam. The gradient vector ($\boldsymbol{g}$) and the reference structure (**RS**), instead, were those of the MEP structure for which

Scheme 2

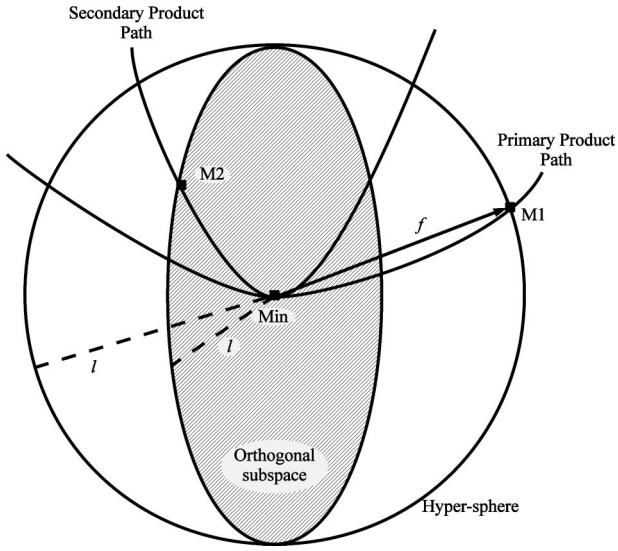

we were looking for the closest crossing point. More details on this procedure will be given in section 3.1.

2.3. Possible Applications to Thermal Reactions. Another possible usage of the orthogonality constraint is to find additional pathways leaving from a minimum. This, in turn, would help in locating secondary paths in, for example, thermal reactions. This usage has not been exploited in the present contribution, so it will be shortly described here. The procedure is depicted in Scheme 2. All minimizations described in this section are supposed to be fully successful.

Once a minimum structure (**Min**) has been optimized, it is possible to locate the first structure of a path (**M1**) leading away from it, by employing a normal hyperspherical constraint. That is, the only applied constraint is that **M1** is at a given distance l from **Min**. In this way, the structure with the lowest energy at the distance l from **Min** is found. In other words, given that the constrained optimization is successful, **M1** is the global minimum with respect to the hypersphere of radius l around **Min**.

One can define the vector between the two structures as the difference between the coordinates: $\boldsymbol{f} = Coord_{M1} - Coord_{Min}$. It is possible to start from **Min** another hyperspherical search with the same radius l and employing the additional constraint of being performed in the subspace orthogonal to $\boldsymbol{f}$. The so-found structure (**M2**) will be at higher energy than **M1**, but still a local minimum on the hyperspere. In other words, the two subsequent optimizations on the same hypersphere of radius l yields two different minima: the lowest in energy **M1** and the second to lowest **M2**.

In our view, **M2** represents the first point along a path that would lead from **Min** to a secondary reaction product. In principle, it is possible to define another vector $\boldsymbol{f}'$ as the difference between the coordinates of **M2** and **Min**. A subsequent hyperspherical search from **Min** in the subspace orthogonal to both $\boldsymbol{f}$ and $\boldsymbol{f}'$ would find a third local minimum, and so on. This procedure could be applied as long as the studied molecule has available degrees of freedom.

2.4. Implementation. The orthogonality constraint has been implemented in the MOLCAS code,[18] to be used in the same way as the other implemented constraints, through the usage of Lagrangian multipliers.[10] Our implementation[10] follows that of Anglada and Bofill[19] for constrained optimizations, in combination with the Rational Function approach[20] and no line-search techniques. In this approach the coordinate space is divided into two parts, one with dimensionality m where the constraint is fulfilled, and one of $3N-6(5)-m$ dimensions where an energy minimization is conducted (N being the number of atoms). In the first subspace the minimization is simply linear, according to eq 8 in ref 10. There is no need for an analytic Hessian evaluation. In the second subspace, the method makes use of the Broyden Fletcher Goldfarb Shanno (BFGS)[21] method for updating the approximate Hessian matrix. All the described optimization procedures require the evaluation of only first derivatives of the energy with respect to the spatial coordinates.

2.5. Computational Details. All calculations were performed in C_{2v} symmetry using a triple-ζ ANO-RCC basis set[22] with contraction scheme [4s3p2d1f] for C and O, [3s2p1d] for H. Energies and analytical gradients were computed at the state average (SA) complete active space multiconfigurational self-consistent field (CASSCF)[23] level of theory. The computed roots were as follows: the first two roots of symmetry $^1A_1$ (S_0 and $\pi\pi^*$) and the first root of symmetry $^1B_1$ ($\sigma\pi^*$). The active space comprised 6 electrons in 5 orbitals (6-in-5). The orbitals were chosen as the C-O π, π^*, σ, and σ^*, plus the O lone pair perpendicular to the π system. All minimum energy path (MEP) and conical intersection (CI) optimizations were performed as constrained optimization, using Lagrangian multipliers, as described in ref 10. All calculations were performed using the MOLCAS[18,24] version 7.1 suite of programs for quantum chemistry.

3. Results and Discussion

3.1. MEP and Seams Construction. The coordinates and CASSCF energies of all the computed geometries are reported in Tables 2 and 3, respectively, in the Supporting Information. The formaldehyde structure was fully optimized on the S_0 state. Such geometry was used as a starting point (Franck−Condon structure, **FC**) for a subsequent MEP search in the $\pi\pi^*$ state. The used step was 0.05 au (in mass-renormalized mass-weighted coordinates).[25] The MEP search was stopped as soon as a minimum was located (**Min** $\boldsymbol{\pi\pi^*}$). The MEP is reported in Figure 1 as a red continuous line. For each MEP point, the S_0 (light blue dot-dashed line in Figure 4 in the Supporting Information) and $\sigma\pi^*$ (dashed green line in Figure 1) energies were computed. A conical intersection between the $\pi\pi^*$ and the $\sigma\pi^*$ potential energy surfaces (PESs) was also located as a minimum energy crossing point. This **MECP** was found to lie close to the MEP structure **MEP6** that lies 0.3 au from **FC**.

Using as reference the **FC** structure and its energy gradient vector as computed on the $\pi\pi^*$ PES, another conical intersection was searched, employing the additional orthogonality constraint. This structure (**SA0**), even if it has nearly the same energy as the $\pi\pi^*$ state energy of **FC**, presents a

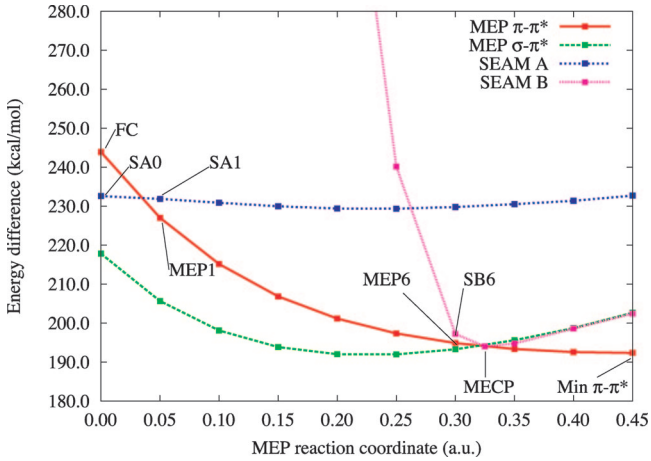

Figure 1. MEP - seam energy relation. For the MEP points, both $\pi\pi^*$ and $\sigma\pi^*$ energies are reported. Along the seams these two potential energy surfaces are degenerate. Energies computed as relative to the S_0 energy of FC, in kcal/mol. Reaction coordinate in mass-renormalized mass-weighted a.u. The complete SEAM B is reported in Figure 4 in the Supporting Information.

Table 1. Geometrical Data (Distances in Ångstroms, Angles in Degrees) for the Notable Structures Discussed in the Text

structure	O-C	C-H	O-C-H
Min S_0 **FC**	1.215	1.082	121.2
Min $\pi\pi^*$	1.631	1.065	118.9
MECP	1.561	1.060	114.9
SA0	1.810	1.059	74.5
SB0	1.337	0.468	144.5

quite distorted geometry. See Table 1. **SA0** is around 0.7 au far from **FC**.

SA0 was used as the starting structure to locate the rest of SEAM A, in an iterative way. In fact, **SA1** was located via a constrained optimization, where the constraints were the $\pi\pi^*$ and $\sigma\pi^*$ energies difference and the condition of orthogonality to **MEP1**, the first MEP point after **FC**, as depicted in Scheme 1. In other words, **MEP1** was used as **RS** and the gradient as ***g*** vector. **SA0** was, instead, the **SG**. The geometry of **SA1** was used as the starting geometry to locate **SA2** in a similar manner and so on for the rest of the SEAM A points. In this way, continuity of the seam was ensured. The results are presented in Figures 1 and 2 as a dotted dark blue line.

As can be seen in Figure 2, SEAM A is never closer than 0.5 au to the computed MEP. On the other hand, **MECP** was found to be quite close to the MEP (less than 0.05 au). We decided to search for an alternative seam, using **MECP** as **SG** and **MEP6** for reference, both structure and gradient vector. In this way we located another crossing point not part of SEAM A. We named this structure **SB6**. Using the geometry of **SB6** as the starting structure, we located the other points of SEAM B iteratively, as before, as relative to the entire MEP structures. These are reported in Figures 1 and 2 as a dotted violet line.

3.2. Seams Comparison. As can be clearly seen from Figures 1 and 2, the two seams are quite different from each other. As previously mentioned, SEAM A is almost always

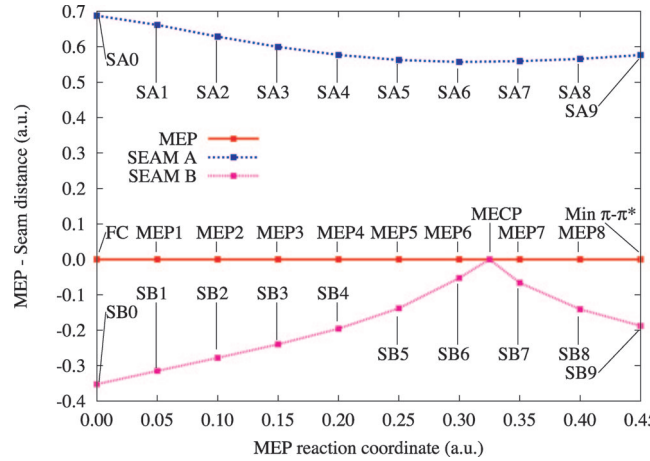

Figure 2. MEP - seam distance relation, in mass-renormalized mass-weighted au.

at the same energy (Figure 1) but is never close to the MEP (Figure 2). The situation is quite the opposite for SEAM B. The seam starts quite high in energy (Figure 4 in the Supporting Information) but gets very close to the MEP (Figure 2) before slowly getting far from it again. Notably, SEAM A is always lower in energy than the $\pi\pi^*$ energy of **FC**, while SEAM B goes under this value only in close proximity to **MECP**. On the other hand, after **FC** SEAM A is always higher in energy than the MEP.

3.3. MEP - Seam Relation. The differences of the two seams make them differently accessible. In fact, by simply following the MEP, SEAM B would be accessed only when the MEP reaches the proximity of **MECP**. This motion requires some stretching of the C═O bond. To access SEAM B otherwise earlier, a certain quantity of extra vibrational energy is needed.

Since it is always far from the MEP, also SEAM A cannot be accessed unless some vibrational energy is spent. Figure 3 shows the different structural changes to access **SA0** or **SB0** from **FC**. If **FC** would possess enough vibrational energy along its CH_2 scissoring mode, the molecule would then access SEAM A. If, instead, it would possess enough vibrational energy along its CH_2 symmetric stretching mode, it will access SEAM B. Since the two modes, CH_2 scissoring and stretching, have different and well separated absorption peaks (ca. 2782 and ca. 1500 cm^{-1} respectively),[26] it should be possible to direct the decay toward one of the seams. If, otherwise, the most populated vibrational mode would be the C═O stretching (ca. 1746 cm^{-1}),[26] then the molecule would follow preferably the MEP and decay at **MECP**.

Obviously, apart from the vibrational mode, also the quantity of vibrational energy is important. As evident from Figure 1, in order to reach SEAM A is necessary less (no) energy than to reach the first part of SEAM B. A higher level computational method taking in consideration full electron correlation like (MS-)CASPT2,[27] would then be needed for a more quantitative evaluation of the amount of vibrational energy needed.

3.4. Photoreaction Rationalization. Through the analysis of the direct relationship between the computed MEP and seams, it is possible to rationalize the photoreaction of formaldehyde.

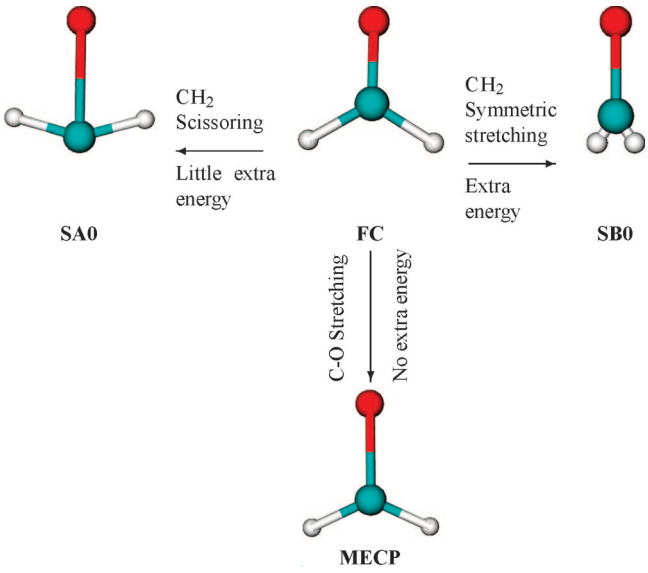

Figure 3. Structures of **FC**, **SA0**, **SB0**, and **MECP**. Indicated the relative vibrational modes, of A_1 symmetry, involved when the molecule exits **FC**. Also, a qualitative indication of the amount of energy needed to reach each structure is reported.

After the photoexcitation, depending on which vibrational mode is active, it is possible to indicate three possible fates for the molecule. For the purposes of this study, this analysis is only qualitative, since the energetic data are based on CASSCF results and not on a more accurate method, as previously mentioned. This is depicted also in Figure 3.

(i) If formaldehyde is vibrationally excited along its C=O stretching mode, it will follow the MEP, and decay on the lower state at **MECP** or in close proximity to it. No vibrational energy is strictly needed to access **MECP**, since it is part of the MEP.

(ii) When the CH_2 scissoring mode is active, the molecule has a high chance of reaching SEAM A, since it is nearly at the same energy as **FC**.

(iii) If the CH_2 symmetric stretching mode is populated with sufficient energy, it is possible for the molecule to decay through SEAM B earlier than MECP.

Obviously, the amount of energy needed to reach **SA0** or **SB0** should take into consideration also the eventual presence of a barrier. However, in the proximity of the MEP it is expected that the potential energy surface, in the direction perpendicular to the MEP, is harmonic, i.e. no energy barrier to reach the seam is expected.

The general methodology we described can be applied to any kind of photoreaction. We would like to stress the importance such an analysis might have with the following example. One could consider the situation reported in Scheme 3, similar to what was reported in Figure 2. Along the MEP of Scheme 3, a MECP has been found. The usual methodologies would use this structure as a starting point to explore and characterize SEAM Y. It is possible, although, that this would not find SEAM X. If SEAM X would be energetically accessible from the MEP, then not including it would cause serious mistakes. For example, by considering only the relationship between the MEP and SEAM Y, one might draw

Scheme 3

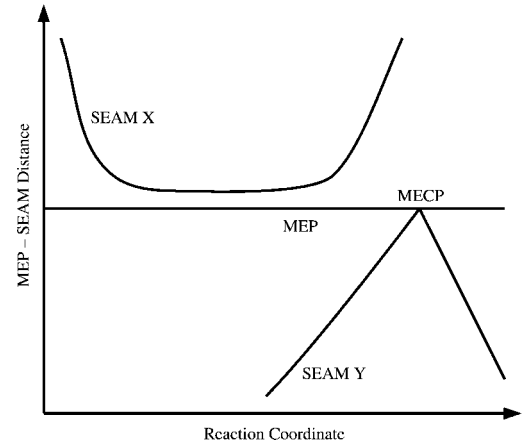

some erroneous conclusions about the decaying rate of the excited molecule. Moreover, if the photoproducts of SEAM X and SEAM Y would be different, the photoproduct of SEAM X would be totally ignored. With our approach, instead, SEAM X would be immediately found, as happened with formaldehyde. Starting then from MECP, also SEAM Y would be located.

If the molecule would possess enough degrees of freedom, additional seams could be searched. Let us consider a point of the MEP, for example the tenth, MEP10. By the previous analysis, the corresponding seam points SX10 and SY10 belonging to SEAM X and Y, respectively, have been found. It is possible to compute the geometry difference vectors $\boldsymbol{f} = Coord_{SX10} - Coord_{MEP10}$ and $\boldsymbol{f}' = Coord_{SY10} - Coord_{MEP10}$. For each of the vectors g (the gradient of MEP10), $\boldsymbol{f}$ and $\boldsymbol{f}'$, one orthogonality constraint is applied. A subsequent optimization of an energy difference structure would locate a point belonging to a third different seam, SEAM Z. This procedure could be carried on for as long as there are available degrees of freedom. In practice, of course, the energy difference between the MEP and the seam should indicate when it is not meaningful anymore to search for additional seams.

4. Conclusions

In this study we presented a novel kind of constraint, namely a orthogonality constraint. We demonstrated how the usage of this constraint in conjunction with the one to minimize the energy difference between two potential energy surfaces can be successfully used to describe conical intersection seams, in relationship to excited-state minimum energy paths. In particular, we showed how to locate two different seams in the proximity of the C_{2v} $\pi\pi^*$ minimum energy path of formaldehyde. The direct relation seam - MEP permitted the easy rationalization of the normal modes possibly involved in the photoreaction.

As previously mentioned, the orthogonality constraint requires only first derivatives of the energy with respect to the spatial coordinates. This fact permitted us to explore a seam without the further need of an analytical Hessian. An approximative Hessian in association with the BFGS update method is, in fact, sufficient.

As an outlook, we are currently studying how to implement an explicit vibrational analysis of the reduced Hessian along the MEP. In other words, for each of the retrieved MEP points, a vibrational analysis should be performed on all molecular modes except the gradient. Coupling this information with the knowledge of where the seam lies should give a complete as possible view of the photochemical event. Today, this can be achieved only through the use of the computationally very expensive molecular dynamics methods.

It is our hope that in the future our procedure will be applied to study how to enhance the quantum yields of desired photoproducts by the rational design of coherent femtosecond pulsed laser experiments. The application of our constraint in order to explore the paths leading to secondary products of thermal reaction is also highly expected. Also in this case, the geometries of the structures along the different paths should be analyzed in relationship with the vibrational modes of the fundamental state minimum. This, in turn, should provide a rational way to direct thermal reaction through excitation by specific infrared frequencies.

Acknowledgment. The authors thank LUNARC computer centre of Lund University and SNAC for granted computational time and the Swedish Scientific Research Council (VR). L.D.V. acknowledges a grant from the Foundation BLANCEFLOR Boncompagni-Ludovisi neé Bildt.

Supporting Information Available: Figure with the complete energetic of Figure 2 (Figure 4) and tables with the coordinates and relative energies of all computed structures (Tables 2 and 3). This material is available free of charge via the Internet at http://pubs.acs.org.

References

(1) Teller, E. *J. Phys. Chem.* **1937**, *41*, 109.

(2) Domke, W.; Yarkony, D. R.; Köppel, H. *Conical Intersections Electronic Structure, Dynamics & Spectroscopy*; World Scientific: Singapore, 2004.

(3) Olivucci, M. *Computational Photochemistry*; Elsevier: Amsterdam, 2005.

(4) Braslavsky, S. E. *Pure Appl. Chem.* **2007**, *79*, 293–465.

(5) Atchity, G. J.; Xantheas, S. S.; Ruedenberg, K. *J. Chem. Phys.* **1991**, *95*, 1862–1876.

(6) (a) Salem, L. *Electrons in Chemical Reactions: First Principles*; Wiley: New York, 1982. (b) Klessinger, M.; Michl, J. *Excited States and Photochemistry of Organic Molecules*; VCH Publishers: New York, 1995.

(7) Yarkony, D. R. *J. Phys. Chem. A* **2001**, *105*, 6277–6293.

(8) (a) Sicilia, F.; Blancafort, L.; Bearpark, M. J.; Robb, M. A. *J. Phys. Chem. A* **2007**, *111*, 2182–2192. (b) Sicilia, F.; Bearpark, M. J.; Blancafort, L.; Robb, M. A. *Theor. Chem. Acc.* **2007**, *118*, 241–251.

(9) Sicilia, F.; Blancafort, L.; Bearpark, M. J.; Robb, M. A. *J. Chem. Theory Comput.* **2008**, *4*, 257–266.

(10) De Vico, L.; Olivucci, M.; Lindh, R. *J. Chem. Theory Comput.* **2005**, *1*, 1029.

(11) Levine, B. G.; Coe, J. D.; Martínez, T. J. *J. Phys. Chem. B* **2008**, *112*, 405–413.

(12) Garavelli, M.; Page, C. S.; Celani, P.; Olivucci, M.; Schmid, W. E.; Trushin, S. A.; Fuss, W. *J. Phys. Chem. A* **2001**, *105*, 4458–4469.

(13) (a) Migani, A.; Robb, M. A.; Olivucci, M. *J. Am. Chem. Soc.* **2003**, *125*, 2804–2808. (b) Migani, A.; Sinicropi, A.; Ferré, N.; Cembran, A.; Garavelli, M.; Olivucci, M. *Faraday Discuss.* **2004**, *127*, 179–191.

(14) Cembran, A.; Bernardi, F.; Garavelli, M.; Gagliardi, L.; Orlandi, G. *J. Am. Chem. Soc.* **2004**, *126*, 3234–3243.

(15) Frutos, L. M.; Sancho, U.; Garavelli, M.; Olivucci, M.; Castano, O. *J. Phys Chem. A* **2007**, *111*, 2830–2838.

(16) Hunt, P. A.; Robb, M. A. *J. Am. Chem. Soc.* **2005**, *127*, 5720–5726.

(17) Dantus, M.; Lozovoy, V. V. *Chem. Rev.* **2004**, *104*, 1813–1859.

(18) Karlström, G.; Lindh, R.; Malmqvist, P.-Å.; Roos, B. O.; Ryde, U.; Veryazov, V.; Widmark, P.-O.; Cossi, M.; Schimmelpfennig, B.; Neogrady, P.; Seijo, L. *Comput. Mater. Sci.* **2003**, *28*, 222.

(19) Anglada, J. M.; Bofill, J. M. *J. Comput. Chem.* **1997**, *18*, 992–1003.

(20) Banerjee, A.; Adams, N.; Simons, J.; Shepard, R. *J. Phys. Chem.* **1985**, *89*, 52–57.

(21) (a) Broyden, C. G. *Math. Comput.* **1970**, *24*, 365–382. (b) Fletcher, R. *Comput. J.* **1970**, *13*, 317–322. (c) Goldfarb, D. *Math. Comput.* **1070**, *24*, 23–26. (d) Shanno, D. F. *Math. Comput.* **1970**, *24*, 647–656.

(22) Roos, B. O.; Lindh, R.; Malmqvist, P.-Å.; Veryazov, V.; Widmark, P.-O. *J. Phys. Chem. A* **2005**, *108*, 2851.

(23) Roos, B. O.; Taylor, P. R. *Chem. Phys.* **1980**, *48*, 157–173.

(24) Veryazov, V.; Widmark, P.-O.; Serrano-Andrés, L.; Lindh, R.; Roos, B. O. *Int. J. Quantum Chem.* **2004**, *100*, 626–635.

(25) The mass-weighted coordinates are divided by the square root of the total molecular mass. Hence, the mass-renormalized mass-weighted coordinates correspond to a length.

(26) Wohar, M. M.; Jagodzinski, P. W. *J. Mol. Spectrosc.* **1991**, *148*, 13–19.

(27) (a) Andersson, K.; Malmqvist, P.-Å.; Roos, B. O.; Sadlej, A. J.; Wolinski, K. *J. Phys. Chem.* **1990**, *94*, 5483. (b) Andersson, K.; Malmqvist, P.-Å.; Roos, B. O. *J. Chem. Phys.* **1992**, *96*, 1218. (c) Roos, B.; Andersson, K.; Fülscher, M.; Malmqvist, P.-Å.; Serrano-Andŕes, L.; Pierloot, K.; Merchán, M. Multiconfigurational perturbation theory: Applications in electronic spectroscopy In *Advances in Chemical Physics: New Methods in Computational Quantum Mechanics*; Prigogine, I.; Rice, S., Eds.; John Wiley & Sons: New York, 1996; pp 219−332.

CT800348S

JCTC Journal of Chemical Theory and Computation

Validation of the B3LYP/N07D and PBE0/N07D Computational Models for the Calculation of Electronic *g*-Tensors

Vincenzo Barone*,† and Paola Cimino‡

Istituto per i Processi Chimico-Fisici del Consiglio Nazionale delle Ricerche, Via G. Moruzzi 1, I-56124 Pisa, Italy, and Dipartimento di Scienze Farmaceutiche, Università di Salerno, via Ponte don Melillo, I-84084 Fisciano (Sa), Italy

Received July 16, 2008

Abstract: Calculations on a large set of free radicals containing atoms of the second and third row show that the computational model defined by the new N07D basis set and hybrid density functionals (B3LYP and PBE0) provides remarkably accurate *g*-tensor values at reasonable computational costs. Since in previous works it has been shown that the same computational model delivers reliable results also for structural parameters and hyperfine couplings, the route seems paved toward full a priori computation of EPR spectra of large free radicals both in vacuo and in condensed phases.

Introduction

The electronic *g*-tensor is one of the most important parameters of electronic paramagnetic resonance spectroscopy (EPR) since it contains a wealth of information about the electronic and geometrical structure of molecules with unpaired electrons. Although, theoretical approaches using density functional theory (DFT) have met considerable success for the calculation of hyperfine coupling constants,[1−8] only a limited number of systematic studies have been performed for *g*-tensors.[9−11] All magnetic tensors are, however, needed for developing an integrated computational approach to EPR spectra taking into account the proper stereoelectronic, environmental, and vibrational averaging effects.[12−14] Validation of effective methods able to compute the different building blocks of such an integrated approach for large systems is currently under way in our laboratories.[14,15]

As recently reported,[7,8] the hyperfine coupling constants calculated with PBE0 and B3LYP functionals and the new N07D basis set are in excellent agreement with experimental data; in particular our results represent significant improvements with respect to those delivered by conventional (e.g., cc-pVXZ) and purposely tailored (e.g., EPR-II and EPR-III) basis sets.[16] So, we decided to extend this investigation to other EPR parameters and, in particular, to the *g*-tensors. In this paper we analyze the performance of the N07D basis set for a large number of radicals (92) for which reliable experimental values[17−76] are available for *g*-tensors. This set is large enough to become, in our opinion, a reference benchmark for new methods and/or basis sets.

In our previous papers[7,8] we have discussed geometrical and energetic data, together with hyperfine coupling constants for a data set including the present one, so that we will analyze in the following only *g*-tensor values.

Our aim is to show that a single model (functional/basis set) provides accurate results for second- and third-row atoms and for a large set of different radicals. In our opinion, the quality of the results and the reasonable computational cost represent a convincing proof of the utility of this basis set (N07D) in the calculation of EPR parameters.

Computational Details

All the calculations were carried out by the Gaussian03 package[77] using the B3LYP[78] and PBE0[79] hybrid density functionals with the N07D[7,8] basis set, which was recently obtained adding to a double-ζ description of valence orbitals single sets of optimized core-valence *s* (on all atoms except H), diffuse *p* (on all atoms except H), polarization (on all atoms), and diffuse *d* (on O, F, Cl atoms) functions. The

* Corresponding author e-mail: baronev@unina.it.

† Istituto per i Processi Chimico-Fisici del Consiglio Nazionale delle Ricerche.

‡ Università di Salerno.

10.1021/ct800279g CCC: $40.75 © 2009 American Chemical Society
Published on Web 12/03/2008

Table 1. Theoretical and Experimental g_{iso}-Tensor (in ppm)

stucture	PBE0/EPR-III[a]	B3LYP/EPR-III[a]	PBE0/N07D	B3LYP/N07D	exp	ref
1	2.0008	2.0008	2.0010	2.0010	2.0007	17
2	2.0005	2.0005	2.0006	2.0006	2.0000	18
3	2.0002	2.0003	2.0004	2.0003	2.0003	19
4	2.0027	2.0027	2.0027	2.0027	2.0027	20
5	2.0040	2.0041	2.0039	2.0039	2.0045	21
6	2.0040	2.0040	2.0038	2.0039	2.0041	21
7	2.0033	2.0034	2.0032	2.0033	2.0031	21
8	2.0028	2.0028	2.0027	2.0028	2.0028	22
9	2.0042	2.0042	2.0041	2.0041	2.0036	23
10	2.0027	2.0027	2.0026	2.0027	2.0027	20
11	2.0028	2.0028	2.0027	2.0028	2.0028	24
12	2.0029	2.0029	2.0028	2.0028	2.0026	25
13	2.0045	2.0047	2.0044	2.0045	2.0049	26
14	2.0046	2.0047	2.0044	2.0045	2.0047	27
15	2.0044	2.0045	2.0043	2.0044	2.0045	28
16	2.0043	2.0044	2.0041	2.0042	2.0043	29
17	2.0046	2.0047	2.0044	2.0045	2.0045	29
18	2.0044	2.0045	2.0042	2.0043	2.0045	30
19	2.0034	2.0035	2.0033	2.0034	2.0032	31
20	2.0036	2.0037	2.0035	2.0036	2.0035	29
21	2.0037	2.0038	2.0036	2.0037	2.0036	32
22	2.0038	2.0039	2.0037	2.0037	2.0035	33
23	2.0039	2.0039	2.0037	2.0038	2.0037	29
24	2.0028	2.0028	2.0028	2.0028	2.0028	34
25	2.0028	2.0029	2.0028	2.0028	2.0029	22
26	2.0038	2.0039	2.0037	2.0037	2.0038	35
27	2.0038	2.0039	2.0037	2.0037	2.0038	35
28	2.0039	2.0039	2.0037	2.0038	2.0038	35
29	2.0038	2.0039	2.0037	2.0037	2.0036	36
30	2.0035	2.0035	2.0034	2.0034	2.0034	37
31	2.0002	2.0002	2.0004	2.0004	2.0024	38
32	2.0036	2.0034	2.0039	2.0039	2.0042	39
33	2.0007	2.0007	2.0008	2.0008	2.0024	38
34	2.0036	2.0035	2.0037	2.0037	2.0042	39
35	2.0036	2.0035	2.0037	2.0037	2.0042	39
36	2.0034	2.0033	2.0035	2.0035	2.0039	40
37	2.0019	2.0018	2.0019	2.0019	2.0020	38
38	2.0056	2.0057	2.0053	2.0055	2.0050	41
39	2.0057	2.0058	2.0054	2.0056	2.0050	41
40	2.0057	2.0058	2.0054	2.0056	2.0049	42
41	2.0041	2.0042	2.0039	2.0041	2.0028	34
42	2.0046	2.0047	2.0045	2.0047	2.0028	43
43	2.0047	2.0048	2.0045	2.0048	2.0057	44
44	2.0050	2.0052	2.0048	2.0052	2.0060	44
45	2.0048	2.0050	2.0047	2.0050	2.0055	45
46	2.0042	2.0043	2.0041	2.0043	2.0062	46
47	2.0050	2.0052	2.0048	2.0052	2.0063	47
48	2.0050	2.0051	2.0048	2.0049	2.0047	48
49	2.0049	2.0051	2.0048	2.0049	2.0047	48
50	2.0068	2.0069	2.0064	2.0066	2.0057	37
51	2.0063	2.0064	2.0060	2.0061	2.0055	49
52	2.0063	2.0063	2.0059	2.0060	2.0054	49
53	2.0062	2.0063	2.0058	2.0060	2.0059	45
54	2.0063	2.0064	2.0060	2.0061	2.0060	50
55	2.0063	2.0064	2.0060	2.0061	2.0059	51
56	2.0010	2.0010	2.0011	2.0011	2.0013	17
57	2.0091	2.0091	2.0085	2.0089	2.0041	52
58	2.0080	2.0084	2.0076	2.0081	2.0093	17
59	1.9993	1.9993	1.9995	1.9994	2.0002	18
60	2.0016	2.0016	2.0017	2.0017	2.0010	53
61			2.0003	2.0002	2.0020	54
62			2.0008	2.0009	2.0036	55
63			2.0043	2.0046	2.0032	56
64			2.0017	2.0020	2.0009	56
65			2.0024	2.0027	2.0017	57
66			2.0037	2.0037	2.0032	58
67			2.0036	2.0036	2.0031	59
68			2.0034	2.0035	2.0032	20
69			2.0016	2.0017	2.0012	60
70			2.0033	2.0033	2.0030	59
71			2.0053	2.0054	2.0050	59

Table 1. Continued

stucture	PBE0/EPR-III[a]	B3LYP/EPR-III[a]	PBE0/N07D	B3LYP/N07D	exp	ref
72			2.0087	2.0089	2.0087	61
73			2.0116	2.0118	2.0130	62
74			2.0166	2.0200	2.0250	56
75			2.0028	2.0028	2.0030	63
76			2.0057	2.0059	2.0050	64
77			2.0065	2.0067	2.0059	65
78			2.0032	2.0031	2.0035	62
79			2.0044	2.0048	2.0030	66
80			2.0119	2.0121	2.0123	67
81			2.0020	2.0074	2.0070	68
82			2.0063	2.0063	2.0055	69
83			2.0044	2.0042	2.0058	68
84			2.0068	2.0070	2.0071	70
85			2.0068	2.0073	2.0045	71
86			2.0088	2.0088	2.0084	72
87			2.0086	2.0086	2.0079	72
88			2.0105	2.0105	2.0094	73
89			2.0066	2.0065	2.0061	74
90			2.0085	2.0084	2.0085	75
91			2.0076	2.0075	2.0071	72
92			2.0086	2.0086	2.0081	76

[a] Single point calculations on geometries optimized at the PBE0/N07D level.

Table 2. Data Analysis for Structures with Second-Row Atoms[a]

	PBE0/EPR-III[b]	B3LYP/EPR-III[b]	PBE0/N07D	B3LYP/N07D	exp
60 molecules					
MAD	0.0006	0.0006	0.0005	0.0005	
max absolute error	0.0050	0.0050	0.0044	0.0048	
R2	0.7303	0.7447	0.7403	0.7505	
intercept	0.1046	0.0440	0.2439	0.1470	
slope	0.9478	0.9781	0.8782	0.9266	
max	2.0091	2.0091	2.0085	2.0089	2.0093
min	1.9993	1.9993	1.9995	1.9994	2.0000

[a] MAD (mean absolute deviation in Gauss) = $\Sigma g_{calc} - g_{exp}$/N. [b] Single point calculations on geometries optimized at the PBE0/N07D level.

inner electrons of second- and third-row atoms are described by the 6G basis set.[80]

Geometry optimizations and evaluations of harmonic frequencies have been performed in the gas-phase using analytical gradients and Hessians.

The gyromagnetic tensor can be written as $\boldsymbol{g} = g_e\mathbf{1}_3 + \Delta\boldsymbol{g}_{RM} + \Delta\boldsymbol{g}_G + \Delta\boldsymbol{g}_{OZ/SOC}$ where g_e is the free-electron value (2.0023193). Computation of the relativistic mass (RM) and gauge (G) corrections is quite straightforward because they are first-order contributions.[81] The last term arises from the coupling of the orbital Zeeman (OZ) and the spin−orbit coupling (SOC) operator. The OZ contribution is computed using the gauge-including atomic orbital (GIAO) approach,[82] whereas for light atoms the two electron SOC operator can be reliably approximated by a one electron operator involving adjusted effective nuclear charges.[83] Although those charges were optimized for MCSCF wave functions, a number of test computations showed that they are nearly optimal for DFT computations too. Upon complete averaging by rotational motions, only the isotropic part of the g tensor survives, which is given by $g_{iso} = {}^1/_3\mathrm{Tr}(g)$. Of course, the corresponding shift from the free electron value is $\Delta g_{iso} = g_{iso} - g_e$. All the results will be given in the following as g-tensor values.

Results and Discussion

The N07D basis set[7,8] has been assessed by comparison with EPR-III[84] basis set for the g-tensors. Our results are collected in Tables 2−4 and compared with experimental results. A variety of molecules containing atoms from the second and third row of the periodic table have been studied. The selected set of 92 radicals (shown in Figure a-b) includes neutral, cationic, anionic, localized, and conjugated species. Before considering detailed results, we recall that the EPR-III[84] basis set is available only for hydrogen and second-row atoms (Tables 1 and 2).

Table 3. Data Analysis for Structures with Second- and Third-Row Atoms[a]

	PBE0/N07D	B3LYP/N07D	exp
92 molecules			
MAD	0.0006	0.0006	
max absolute error	0.0050	0.0048	
R2	0.8159	0.8525	
intercept	0.1369	0.0595	
slope	0.9317	0.9704	
max	2.0120	2.0121	2.0130
min	1.9995	1.9994	2.0000

[a] MAD (mean absolute deviation in Gauss) = $\Sigma g_{calc} - g_{exp}$/N.

A statistical analysis has been performed for the whole data set. In detail, we report the number of data (N), mean absolute deviation (MAD), and data range between calculated and experimental values. Next we give the correlation coefficient (R^2), slope, and intercept of the least-squares line. The MAD is an absolute value, so that all deviations are converted to positive numbers, added, and then averaged.

Table 4. Calculated and Experimental *g*-Tensors (ppm) of Glycine Radical in Aqueous Solution

	exp		PBE0/EPR-III		PBE0/N07D		B3LYP/EPR-III		B3LYP/N07D	
	cis	trans	cis	trans	cis	trans	cis	trans	cis	trans
Δg_{xx}			2503.3	2620.4	2276.2	2388.2	2593.1	2702.6	2362.9	2468.5
Δg_{yy}			1386.3	1994.9	1259.1	1814.9	1437.8	2059.2	1295.9	1857.5
Δg_{zz}			−177.4	−175.7	−171.9	−172.0	−179.4	−177.6	−175.3	−173.2
g_{iso}	2.00340	2.00340	2.00356	2.00380	2.00344	2.00366	2.00360	2.00385	2.00348	2.00370
					with $\Delta_{PCM\text{-}gas}$					
Δg_{xx}			2586.3	2565.7	2359.2	2333.5	2676.1	2647.9	2445.9	2413.8
Δg_{yy}			1413.7	1928.2	1286.5	1748.2	1465.2	1992.5	1323.3	1790.8
Δg_{zz}			−191.8	−187.1	−186.3	−183.4	−193.8	−189.0	−189.7	−184.6
g_{iso}	2.00340	2.00340	2.00360	2.00375	2.00348	2.00361	2.00364	2.00380	2.00352	2.00365
					with $\Delta_{GLOB/ADMP\text{-}gas}$					
g_{iso}	2.00340	2.00340	2.00356	2.00371	2.00344	2.00357	2.00360	2.00376	2.00348	2.00361

Table 5. Calculated and Experimental *g*-Tensors (ppm) of Glycyl Radical in Solution (Water)[a]

	$\Delta g_{298}{}^{\circ}$	Δg_{solv}	Δg_{gas}N07D[b]	Δg_{gas} EPR-III[b]	Δg_{gas} EPR-III[c]
Δg_{xx}	−26.4	320.9	2190.1	2423.5	2363.9
Δg_{yy}	−28.9	−489.4	1402.1	1546.4	1524.9
Δg_{zz}	4.4	−5.4	−164.9	−170.3	−173.3

	Best estimate			exp[d]				
	N07D[b]	EPR-III[b]	EPR-III[c]	RNR	RNR	PFI	BSS	N-acetyl glycyl
Δg_{xx}	2484.6	2718.0	2658.4	1900	2000	2400	2200	2200/1900
Δg_{yy}	883.8	1028.1	1006.6	1000	1000	1600	1300	800/900
Δg_{zz}	−165.9	−171.3	−174.3	0	0	200	−100	−300/400

[a] The experimental data are given with an error of ±400 ppm. [b] Geometry optimized at the PBE0/N07D level. [c] Geometry optimized at the PBE0/6−31+G(d,p) level. [d] From ref 11a.

Moreover, regression analysis represents, in our opinion, the simplest and most useful approach for an unbiased comparison between large sets of computed and experimental values.

We analyze the data in two steps. In the first one, we consider the 60 structures (Table 2) containing second-row atoms (Figure a) and compare the results obtained with the new basis set with both experimental and theoretical (EPR-III) data; next, we compare for all structures, i.e. including those containing also third-row atoms (Table 3), the *g*-tensors values calculated with the N07D basis set to experimental data. In general terms our calculations (Tables 1−3) show that the density functional (PBE0 vs B3LYP) has a marginal effect on the magnitude of the *g*-tensor (Tables 1−3). Thus, the performance of the basis sets has been evaluated using the PBE0 and B3LYP functionals and compared in Tables 2 and 3 (MADs). The N07D results (Table 2) are slightly better (0.0005 vs 0.0006 ppm for both functionals) than the EPR-III results in terms of MADs, and the corresponding computational cost is significantly lower. As a matter of fact, the difference between N07D basis sets for PBE0 and B3LYP functional involves only tight s functions, which have a negligible effect on valence properties like *g*-tensors. In the same vein, 6−31+G(d,p) results should be comparable for *g*-tensors, but this is not the case for structures and hyperfine parameters. The strength of the N07D basis set is the contemporary reproduction of all those properties at a reasonable cost: this is especially significant for second-order properties (like *g*-tensors) whose computation has a scaling with the number of basis functions significantly worse than that of first order properties (like hyperfine properties). For instance, the number of contracted functions for a second-row atom is 19 and 40 for N07D and EPR-III basis sets, respectively. The N07D basis set is thus characterized by an excellent accuracy/time ratio: this is a crucial result for our aim of using a unique functional/basis set model for the calculation of geometric, electronic, and magnetic properties of free radicals.

The performances of the B3LYP/N07D and PBE0/N07D models for a typical problem involving at the same time stereoelectronic, vibrational, and environmental effects can be judged by the results reported in Tables 4 and 5 for the glycine[13c,15a] and glycyl[10b] radicals (Figure 2) in condensed phases. Let us start from the glycine radical. In Table 4 are reported the principal components of the *g*-tensors (δg_{xx}, δg_{yy}, and δg_{zz}) and the g_{iso} values carried out using both functionals (PBE0 and B3LYP) and basis sets (EPR-III and N07D) together with the g_{iso} value measured in aqueous solution (2.00340 ± 0.00005). Since the *g*-tensors computed for the minimum energy structure in vacuum are significantly tuned by both intramolecular vibrations and by solvent librations, the reported results are obtained by averaging over 100 frames extracted at regular time steps from the ab initio dynamics described in ref 15a. As shown, the *g*-tensors are sensitive to the conformation of the radical, e.g. the *g*-tensors of GlyR^{cis} and GlyR^{trans} are significantly different (Table 4). In particular, the results obtained with the N07D basis set for GlyR^{cis} are in remarkable agreement with experiment, confirming the prevalence of this isomer in aqueous solution suggested by direct energetic evaluations.

In Table 5, we compare our results for the glycyl radical with the theoretical ones issuing from PBE0/EPR-III com-

(A)

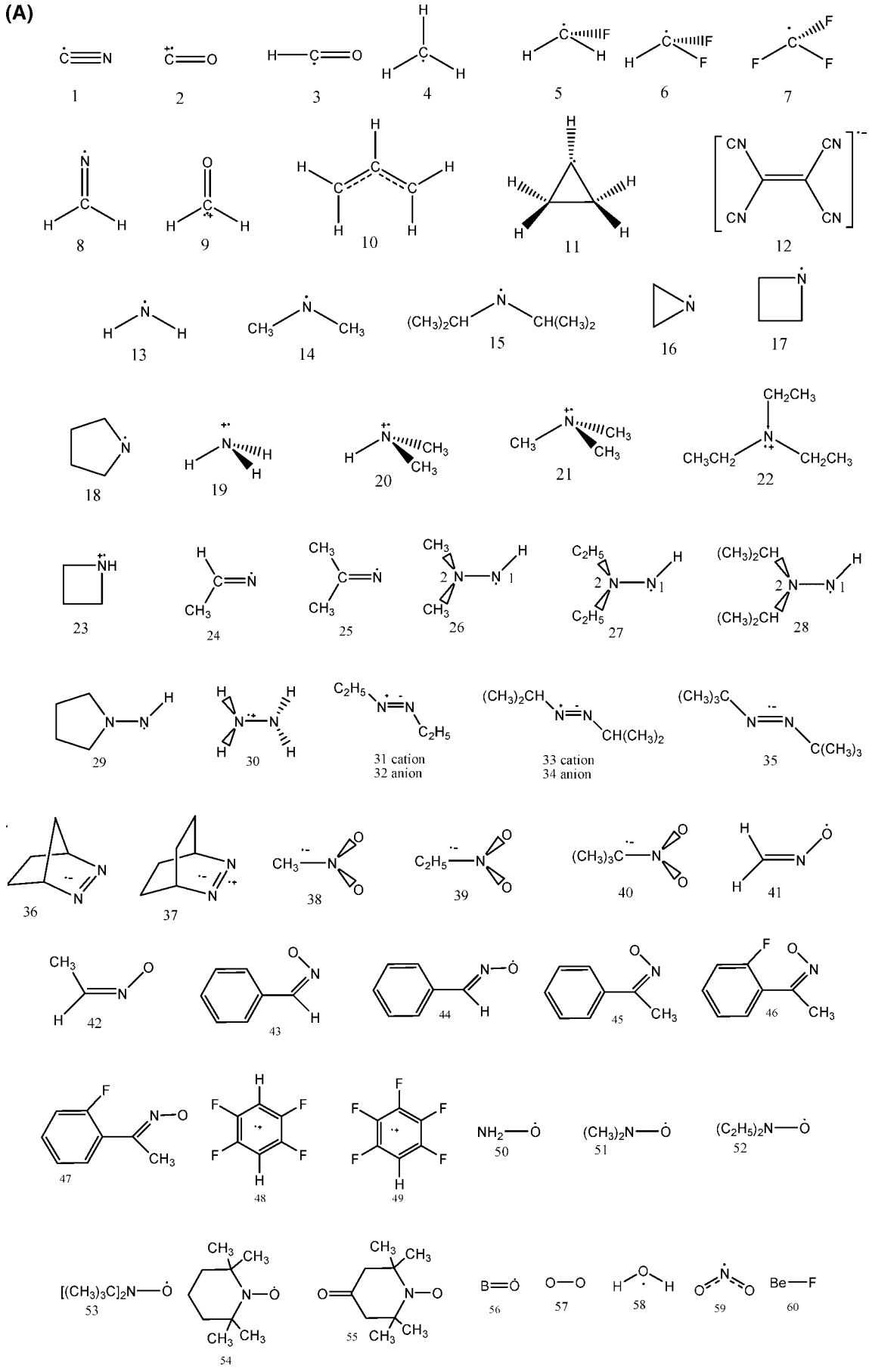
1
2
3
4
5
6
7
8
9
10
11
12
13
14
15
16
17
18
19
20
21
22
23
24
25
26
27
28
29
30
31 cation
32 anion
33 cation
34 anion
35
36
37
38
39
40
41
42
43
44
45
46
47
48
49
50
51
52
53
54
55
56
57
58
59
60

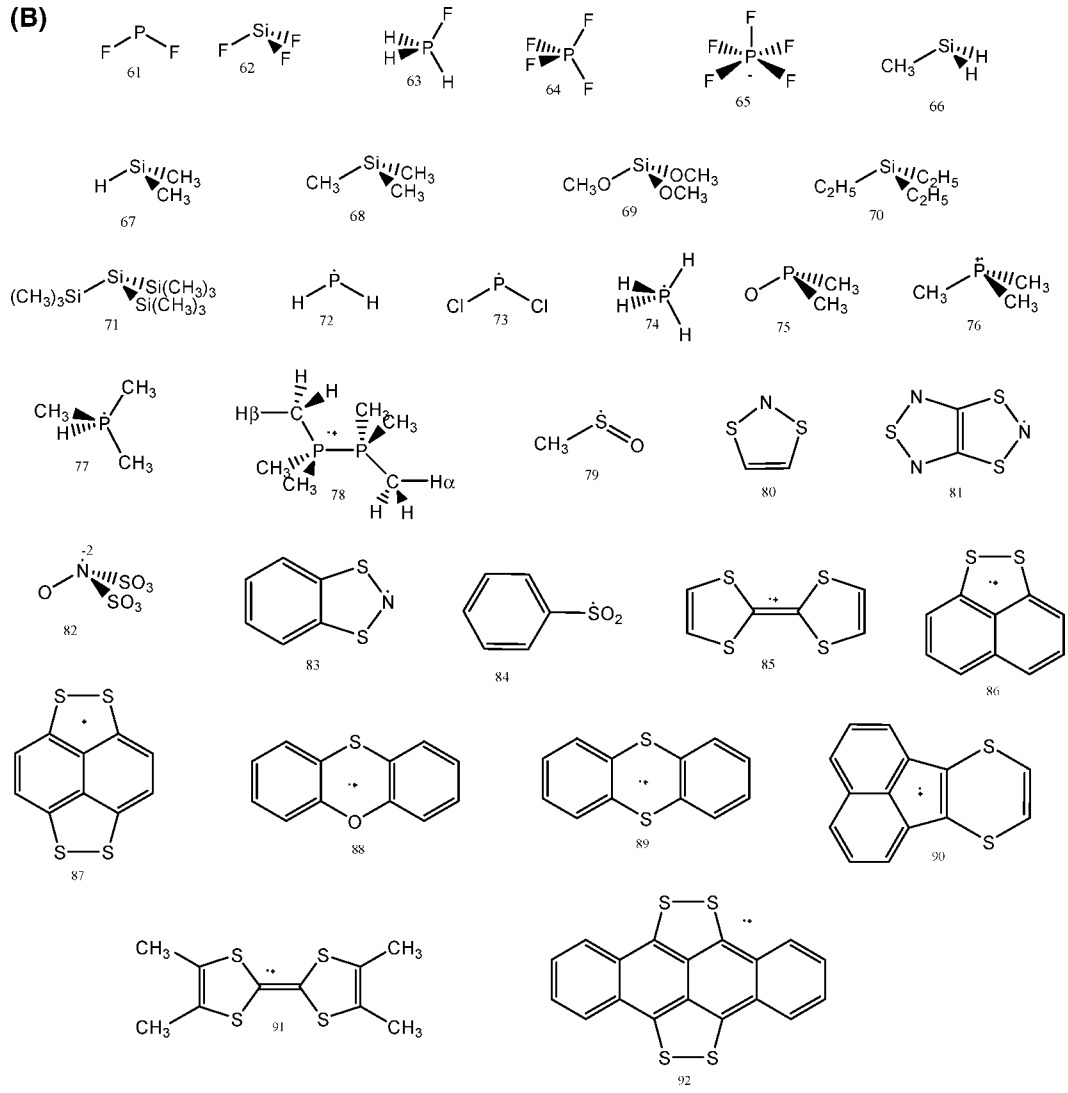

Figure 1. Structures of the radicals studied with (a) second-row atoms and (b) third-row atoms.

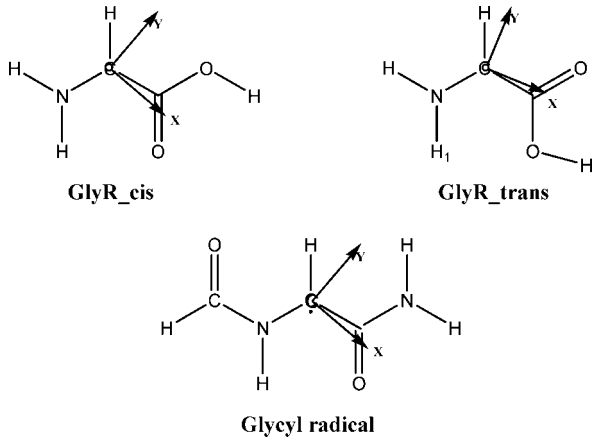

Figure 2. Structures of glycine and glycyl radicals. The orientations of the principal axes of the *g*-tensor are also shown.

putations and with experimental data obtained for different enzymes and for N-acetylglycyl radical. In general, the *g*-tensors calculated with the N07D basis set are slightly smaller than those obtained with EPR-III basis set. Moreover, as reported in previous papers, the *g*-tensors are affected by both direct and indirect solvent effects as well as by intramolecular motions. Comparison with experiment confirms the remarkable performances of B3LYP/N07D and PBE0/N07D computational models when taking into account the proper dynamical and environmental effects.

Concluding Remarks

The present paper reports the results of a systematic computational study devoted to the calculation of *g*-tensor values using the new N07D basis set. The PBE0/N07D and B3LYP/N07D results for a representative set of organic free radicals seem accurate enough to allow for quantitative studies. This finding together with the computational efficiency of the approach suggest that we dispose of a quite powerful tool for the study of free radicals, especially taking into account that the same density functional and basis set can be used for different properties and for second- and third-row atoms. Furthermore, the availability of effective discrete/continuum solvent models and of different dynamical approaches, together with the reduced dimensions of the N07D basis set, allow for performing comprehensive analyses aimed at evaluating the roles of stereoelectronic, vibrational, and environmental effects in determining the overall

properties of large flexible radicals of current biological and/or technological interest.

References

(1) Barone, V.; Adamo, C.; Russo, N. *Chem. Phys. Lett.* **1993**, *212*, 5.

(2) Barone, V. *J. Phys. Chem.* **1995**, *99*, 11659.

(3) Improta, R.; Barone, V. *Chem. Rev.* **2004**, *104*, 1231.

(4) Schoneborn, J. C.; Neese, F.; Thiel, W. *J. Am. Chem. Soc.* **2005**, *127*, 5840.

(5) Mattar, S. M. *J. Phys. Chem. A* **2007**, *111*, 251.

(6) Kaprzac, S.; Reviakine, R.; Kaupp, M. *J. Phys. Chem. B* **2007**, *111*, 811.

(7) Barone, V.; Cimino, P. *Chem. Phys. Lett.* **2008**, *454*, 139.

(8) Barone, V.; Cimino, P.; Stendardo, E. *J. Chem. Theory Comput.* **2008**, *4*, 751.

(9) (a) Malkina, O. L.; Vaara, J.; Schimmelpfenning, B.; Munzarova, M.; Malkin, V. G.; Kaupp, M. *J. Am. Chem. Soc.* **2000**, *122*, 9206. (b) Kaupp, M.; Remenyi, C.; Vaara, J.; Malkina, O. L.; Malkin, V. G. *J. Am. Chem. Soc.* **2002**, *124*, 2709.

(10) (a) Neese, F. *J. Chem. Phys.* **2001**, *115*, 11080. (b) Patchkovskii, S.; Ziegler, T. *J. Phys. Chem. A* **2001**, *105*, 5490.

(11) (a) Ciofini, I.; Barone, V.; Adamo, C. *J. Chem. Phys.* **2004**, *121*, 6710. (b) Barone, V.; Carbonniere, P.; Pouchan, C. *J. Chem. Phys.* **2005**, *122*, 224308.

(12) (a) Barone, V. *J. Chem. Phys.* **1994**, *101*, 10666. (b) Barone, V. *J. Chem. Phys.* **2005**, *122*, 014108.

(13) (a) Crescenzi, O.; Pavone, M.; deAngelis, F.; Barone, V. *J. Phys. Chem. B* **2005**, *109*, 445. (b) Pavone, M.; Cimino, P.; DeAngelis, F.; Barone, V. *J. Am. Chem. Soc.* **2006**, *128*, 4338. (c) Barone, V.; Causà, M. *Chem. Phys. Lett.* **2008**, *452*, 89. (d) Barone, V.; Improta, R.; Rega, N. *Acc. Chem. Res.* **2008**, *41*, 605.

(14) (a) Barone, V.; Polimeno, A. *PCCP* **2006**, *8*, 4609. (b) Barone, V.; Brustolon, M.; Cimino, P.; Polimeno, A.; Zerbetto, M.; Zoleo, A. *J. Am. Chem. Soc.* **2006**, *128*, 15865. (c) Carlotto, S.; Cimino, P.; Zerbetto, M.; Franco, L.; Corvaja, C.; Crisma, M.; Formaggio, F.; Toniolo, C.; Polimeno, A.; Barone, V. *J. Am. Chem. Soc.* **2007**, *129*, 11248.

(15) (a) Brancato, G.; Rega, N.; Barone, V. *J. Am. Chem. Soc.* **2007**, *129*, 15380. (b) Zerbetto, M.; Polimeno, A.; Cimino, P.; Barone, V. *J. Chem. Phys.* **2008**, *128*, 024501.

(16) (a) Hermosilla, L.; Calle, P.; Garcia de la Vega, J. M.; Sieiro, C. *J. Phys. Chem. A* **2005**, *109*, 114. (b) Hermosilla, L.; Calle, P.; Garcia de la Vega, J. M.; Sieiro, C. *J. Phys. Chem. A* **2005**, *109*, 7626. (c) Hermosilla, L.; Calle, P.; Garcia de la Vega, J. M.; Sieiro, C. *J. Phys. Chem. A* **2006**, *110*, 13600.

(17) Brownridge, S.; Grein, F.; Tatchen, J.; Kleinscmidt, M.; Marian, C. M. *J. Chem. Phys.* **2003**, *118*, 9552–9563.

(18) Schreckenbach, G.; Ziegler, T. *J. Phys. Chem. A* **1997**, *101*, 3388.

(19) Holmberg, R. W. *J. Chem. Phys.* **1969**, *51*, 3255.

(20) Cook, M. D.; Roberts, B. P. *J. Chem. Soc.* **1983**, 264.

(21) Chen, K. S.; Krusic, P. J.; Meakin, P.; Kochi, J. K. *J. Phys. Chem.* **1974**, *78*, 2014.

(22) Cooper, J. W.; Roberts, B. P.; Winter, J. N. *J. Chem. Soc., Chem. Commun.* **1977**, 320.

(23) Knight, L. B., Jr.; Steadman, J. *J. Chem. Phys.* **1984**, *80*, 1018.

(24) Chen, K. S.; Edge, D. J.; Kochi, J. K. *J. Am. Chem. Soc.* **1973**, *95*, 7036.

(25) Maity, A. N.; Schwedershi, B.; Kaim, W. *Inorg. Chem. Commun.* **2005**, *8*, 600.

(26) Cochran, E. L.; Adrian, F. J.; Bowers, V. A. *J. Chem. Phys.* **1969**, *51*, 2759.

(27) Elford, P. E.; Roberts, B. P. *J. Chem. Soc., Perkin Trans. II* **1998**, 1413.

(28) Pratt, D. W.; Dillon, J. J.; Lloyd, R. V.; Wood, D. E. *J. Phys. Chem.* **1971**, *75*, 3486.

(29) Qin, X. Z.; Williams, F. *J. Phys. Chem.* **1986**, *90*, 2292.

(30) Butcher, E.; Rhodes, C. J.; Glidewell, C. *J. Chem. Soc., Perkin Trans. II* **1992**, 1461.

(31) Knight, L. B., Jr.; Steadman, J. *J. Chem. Phys.* **1982**, *77*, 1750.

(32) Atalay, H.; Kalkan, M.; Yavuz, I.; Senel, *ARI* **1998**, *51*, 81.

(33) Gilbert, B. C.; Larkin, J. P.; Norman, R. O. C. *J. Chem. Soc., Perkin Trans. II* **1972**, 794.

(34) Roberts, B. P.; Winter, J. N. *J. Chem. Soc., Perkin Trans. II* **1979**, 1353.

(35) Malatesta, V.; Ingold, K. U. *J. Am. Chem. Soc.* **1973**, *95*, 6110.

(36) Wood, D. E.; Wood, C. A.; Lathan, W. A. *J. Am. Chem. Soc.* **1972**, *94*, 9278.

(37) Chawla, O. P.; Fessenden, R. W. *J. Phys. Chem.* **1975**, *79*, 2693.

(38) Rhodes, C. J.; Agirbas, H.; Lindgren, M.; Antzutkin, O. N. *J. Chem. Soc., Perkin Trans. II* **1993**, 2135.

(39) Sustmann, R.; Sauer, R. *J. Chem. Soc., Chem. Commun.* **1985**, 1248.

(40) Gerson, F.; Sahin, C. *J. Chem. Soc., Perkin Trans. II* **1997**, 1127.

(41) Zeldes, H.; Livingston, R. *J. Am. Chem. Soc.* **1968**, *90*, 4540.

(42) Gilbert, B. C.; Larkin, J. P.; Norman, R. O. C. *J. Chem. Soc., Perkin Trans. II* **1972**, 1272.

(43) Cooper, J. W.; Roberts, B. P.; Winter, J. N. *J. Chem. Soc., Chem. Commun.* **1977**, 320.

(44) Lucarini, M.; Pedulli, G. F. *J. Org. Chem.* **1994**, *59*, 1980.

(45) Mackor, A. *J. Org. Chem.* **1978**, *43*, 3241.

(46) Gilbert, B. C.; Norman, R. O. C. *J. Chem. Soc (B)* **1968**, 123.

(47) Lin, T.-S. *J. Chem. Phys.* **1975**, *63*, 384.

(48) Yim, M. B.; Wood, D. E. *J. Am. Chem. Soc.* **1976**, *98*, 2053.

(49) Florin, R. E. *J. Chem. Phys.* **1967**, *47*, 345.

(50) Gottinger, H. A.; Zubarev, V. E.; Brede, O. *J. Chem. Soc., Perkin Trans. II* **1997**, 2167.

(51) Snipes, W.; Cupp, J.; Cohn, G.; Keith, A. *Biophys. J.* **1974**, *14*, 20.

(52) Vahtras, O.; Minaev, B.; Agren, H. *Chem. Phys. Lett.* **1997**, *281*, 186.

(53) Bruna, P. J.; Grein, F. *J. Phys. Chem. A* **2001**, *105*, 3328.

(54) Nelson, W.; Jacket, G.; Gordy, W. *J. Chem. Phys.* **1970**, *52*, 4572.

(55) Merritt, M. V.; Fessenden, R. W. *J. Chem. Phys.* **1972**, *56*, 2353.

(56) Colussi, A. J.; Morton, J. R.; Preston, K. F. *J. Phys. Chem.* **1975**, *79*, 1855.

(57) Mishra, S. P.; Symons, M. C. R. *J. Chem. Soc., Chem. Commun.* **1974**, 279.

(58) Sharp, J. H.; Symons, M. C. R. *J. Chem. Soc. A* **1970**, 3084.

(59) Bennett, S. W.; Eaborn, C.; Hudson, A.; Jackson, R. A.; Root, K. D. J. *J. Chem. Soc. A* **1970**, 348.

(60) Johnson, K. M.; Roberts, B. P. *J. Chem. Soc., Perkin Trans. II* **1989**, 1111.

(61) Jackell, G. S.; Gordy, W. *Phys. Rev.* **1968**, *176*, 443.

(62) Aagaard, O. M.; de Waal, B. F. M.; Cabbolet, J. T. F.; Janssen, R. A. J. *J. Phys. Chem.* **1992**, *96*, 614.

(63) Begum, A.; Symons, M. C. R. *J. Chem. Soc., Faraday Trans.* **1973**, 243.

(64) Hasegawa, A.; McConnache, G. D. G.; Symons, M. C. R. *J. Chem. Soc., Faraday Trans. I* **1984**, *80*, 1005.

(65) Nishikida, K.; Williams, F. *J. Am. Chem. Soc.* **1975**, *97*, 5462.

(66) Nishikida, K.; Williams, F. *J. Am. Chem. Soc.* **1974**, *96*, 4781.

(67) Mattar, S. M. *Chem. Phys. Lett.* **1999**, *300*, 545.

(68) Mattar, S. M. *Chem. Phys. Lett.* **2005**, *405*, 382.

(69) Dalgaard, E.; Linderberg, J. *J. Chem. Phys.* **1976**, *65*, 692.

(70) Chatgilialoglu, C.; Gilbert, B. C.; Norman, R. O. C. *J. Chem. Soc., Perkin Trans. II* **1979**, 770.

(71) Atsushi, T.; Hiroaki, O.-N.; Noboru, H.; Hiroshi, A.; Tokuzo, K.; Shigeo, Y.; Toyonari, S.; Zen-ichi, Y. *Bull. Chem. Soc. Jpn.* **1984**, *57*, 1760.

(72) Bramwell, F. B.; Haddon, R. C.; Wudl, F.; Kaplan, M. L.; Marshall, J. H. *J. Am. Chem. Soc.* **1978**, *100*, 4612.

(73) Baciu, I.; Hillebrand, M.; Sahini, V. E. *J. Chem. Soc., Perkin Trans. II* **1974**, 986.

(74) Depew, M. C.; Zhongli, L.; Wan, J. K. S. *J. Am. Chem. Soc.* **1983**, *105*, 2480.

(75) Bryce, M. R.; Lay, A. K.; Chesney, A.; Batsanov, A. S.; Howard, J. A. K.; Buser, U.; Gerson, F.; Merstetter, P. *J. Chem. Soc., Perkin Trans. II* **1999**, 755.

(76) Griller, D.; Barclay, L. R. C.; Ingold, K. U. *J. Am. Chem. Soc.* **1975**, *97*, 6151.

(77) M. J. Frisch, G. W.; Trucks, H. B.; Schlegel, G. E.; Scuseria, M. A.; Robb, J. R.; Cheeseman, J. A.; Montgomery, Jr., T.; Vreven, K. N.; Kudin, J. C.; Burant, J. M.; Millam, S. S.; Iyengar, J.; Tomasi, V.; Barone, B.; Mennucci, M.; Cossi, G.; Scalmani, N.; Rega, G. A.; Petersson, H.; Nakatsuji, M.; Hada, M.; Ehara, K. ; Toyota, R.; Fukuda, J.; Hasegawa, M.; Ishida, T.; Nakajima, Y.; Honda, O.; Kitao, H.; Nakai, M.; Klene, X.; Li, J. E.; Knox, H. P.; Hratchian, J. B.; Cross, C.; Adamo, J.; Jaramillo, R.; Gomperts, R. E.; Stratmann, O.; Yazyev, A. J.; Austin, R.; Cammi, C.; Pomelli, J. W.; Ochterski, P. Y.; Ayala, K.; Morokuma, G. A.; Voth, P.; Salvador, J. J.; Dannenberg, V. G.; Zakrewski, S.; Dapprich, A. D.; Daniels, M. C.; Strain, O.; Farkas, D. K.; Malick, A. D.; Rabuck, K.; Raghavachari, J. B.; Foresman, J. V.; Ortiz, Q.; Cui, A. G.; Baboul, S.; Clifford, J.; Cioslowski, B. B.; Stefanov, G.; Liu, A.; Liashenko, P.; Piskorz, I.; Komaromi, R. L.; Martin, D. J.; Fox, T.; Keith, M. A.; Al-Laham, C. Y.; Peng, A.; Nanayakkara, M.; Challacombe, P. M. W.; Gill, B.; Johnson, W.; Chen, M. W.; Wong, C.; Gonzalez, J. A.; Pople, *Gaussian 03, Revision D.02*; Gaussian, Inc.: Wallingford, CT, 2004. (b) Stephens, P. J.; Devlin, F. J.; Chabalowski, C. F.; Frisch, M. J. *J. Phys. Chem.* **1994**, *98*, 11623.

(78) Adamo, C.; Barone, V. *J. Chem. Phys.* **1999**, *110*, 6158.

(79) Hariharan, P. C.; Pople, J. A. *Theor. Chim. Acta* **1973**, *28*, 213.

(80) (a) Neese, F. *J. Chem. Phys.* **2001**, *115*, 11080. (b) Neese, F. *J. Chem. Phys.* **2005**, *122*, 034107.

(81) Cheesman, J. R.; Trucks, G. W.; Keith, T. A.; Frisch, M. J. *J. Chem. Phys.* **1998**, *104*, 5497.

(82) Koseki, S.; Schmidt, M. W.; Gordon, M. S. *J. Phys. Chem.* **1992**, *96*, 10768.

(83) Rega, N.; Cossi, M.; Barone, V. *J. Chem. Phys.* **1996**, *105*, 11060.

(84) (a) Rega, N.; Cossi, M.; Barone, V. *J. Am. Chem. Soc.* **1997**, *119*, 12962. (b) Rega, N.; Cossi, M.; Barone, V. *J. Am. Chem. Soc.* **1998**, *120*, 5723.

CT800279G

JCTC Journal of Chemical Theory and Computation

Simulation of Vibrational Spectra of Large Molecules by Arbitrary Time Propagation

Jan Kubelka*,† and Petr Bouř*,‡

Department of Chemistry, University of Wyoming, 1000 East University Avenue, Laramie, Wyoming 82071, and Institute of Organic Chemistry and Biochemistry, Academy of Sciences, Flemingovo nám. 2, 16610, Praha 6, Czech Republic

Received July 25, 2008

Abstract: Modern ab initio and multiscale methods enable the simulation of vibrational properties of very large molecules. Within the harmonic approximation, the traditional generation of the spectra based on the force field diagonalization can become inefficient due to the excessive demands on computer time and memory. The present study proposes to avoid completely the matrix diagonalization with a direct generation of the spectral shapes. For infrared absorption (IR) and vibrational circular dichroism (VCD) electric and magnetic dipole moments are propagated in a fictitious time and spectral intensities are obtained by Fourier transformation. The algorithm scales quasi-linearly, and for model polypeptide molecules the method was found numerically stable and faithfully reproduced exact transition frequencies and relative intensities.

1. Introduction

Modern vibrational spectroscopy provides a powerful means for studying the structure of polymeric materials and biological molecules.[1] In particular, the infrared absorption (IR) and vibrational circular dichroism (VCD) techniques shed light on structure and structural transitions in peptides and proteins,[2,3] nucleic acids,[4,5] biological membranes,[6] and on enzymatic function.[7] Kinetic and nonlinear response enhancements are possible owing to the time-dependent[8] and two-dimensional (two-photon) techniques.[9]

Ultimately, the information about the structure and dynamics of studied systems can be verified by comparison of the measured spectra with simulations. Unfortunately, structural interpretation of the vibrational spectra is often far from being straightforward, especially for large molecules with a plethora of overlapping spectral transitions. Although the molecular size remains the main limitation for quantum mechanical calculations, the exciting possibility of obtaining accurate vibrational force fields for the whole molecules appears realistic owing to the latest advances in quantum chemistry.[10−12] In the meantime, the Cartesian transfer tensor techniques[13] obtained spectroscopically accurate fields for large molecules from quantum-chemical computations on smaller fragments.[3,14] In principle, such fragmentation approaches would enable calculation of the vibrational spectra for arbitrarily large structures. However, for systems with thousands of atoms a new problem arises: the force field matrices become too large for direct diagonalization, which is necessary to obtain the vibrational frequencies and intensities. For such very large matrices special computational procedures have to be applied.[11]

Traditionally, the Householder transformation and the following complete diagonalization routine based on the QL or QR algorithm provide the fastest in-memory procedure for the determination of the eigenvectors and eigenvalues of a real symmetric matrix.[15] Similar routines exist for a partial diagonalization, yielding a given number of the lowest or highest eigenvalues, but these algorithms are less efficient except for cases when the number of the vectors of interest is small.[16] For matrices that cannot be stored in computer memory or elements of which are created on the fly, the power iteration methods appear as a better alternative.[11,17] The eigenvalues and vectors are built from the smallest or the largest value iteratively, using a limited number of trial vectors ("Krylov space").[18] This is very convenient, for example, for the configuration interaction electron computations, when only a limited number of the low energy

* Corresponding author e-mail: jkubelka@uwyo.edu (J.K.), bour@uochb.cas.cz (P.B.).

† University of Wyoming.

‡ Academy of Sciences.

10.1021/ct800298n CCC: $40.75 © 2009 American Chemical Society
Published on Web 12/02/2008

electronic states (often just the ground state) is needed. However, for the vibrational problem it is usually not sufficient to find a few largest or smallest eigenvalues. Rather, a complete spectrum, or at least a broad frequency range, is desired, which is rarely limited to either the high or low frequency side. For such a task the iterative (often called Davidson) methods quickly become impractical. As each new vector has to be normalized to the rest, the process slows down progressively. Additionally, for semidegenerate eigenvalues, the method can become numerically unstable.[11]

Fortunately, in some cases, the force field matrix diagonalization can be completely avoided by Fourier techniques and time propagations of molecular properties. An interesting alternative is offered by the normal mode tracking,[19] where the orthogonality of the harmonic normal modes is used to construct an incomplete Hamiltonian, and, in a final effect, a preselected part of the vibrational spectrum is obtained. The decision as to which mode to follow has to be done already at the ab initio stage of computation of the force field, which somewhat limits possible applications. The Fourier procedures pursued in the presented work were also successfully used in the past, e.g. for generation of the infrared absorption (IR) and optical activity (vibrational circular dichroism, VCD) in connection with empirical[12] or ab initio[20] based force fields. In this work, we investigate a variant of these approaches which differs from the previous schemes in that the time propagation is based directly on the force field matrix instead of the harmonic Hamiltonian. The spectra are not collected in a real frequency (ω) space, but in the space of the force field eigenvalues λ ($\lambda=\omega^2$). This approach brings a tremendous simplification of the process, because it eliminates the problems associated with molecular dynamics, such as the temperature definition, normal mode energy-redistribution,[20] and the need to hold the large force field matrix in memory. For giant molecules this method yields accurate relative absorption and VCD intensities and the exact IR/VCD ratio in a fraction of computer time needed for the direct diagonalization routines. The principal drawback is that the exact relative intensity distribution is somewhat dependent on the initial guess, but this can be circumvented by averaging of more trajectories. While the absolute intensities retain a small amount of error, this does not represent a major problem in the practical applications.

In this report, we briefly review the process of generating the theoretical IR and VCD spectra within the harmonic approximation. Most of the Method section is devoted to the detailed description of the new algorithm. Finally, the numerical stability and convergence tests and comparisons with other diagonalization methods for model polypeptide IR and VCD spectra simulations are presented and discussed.

2. The Method

Vibrational Analysis. In the harmonic approximation[21] the vibrational Hamiltonian can be written in terms of nuclear momenta P_i and displacements from equilibrium positions of N atoms ΔR_i ($i = 1..N$) as

$$H=\frac{1}{2}\left(\sum_{i=1}^{3N}\frac{P_i^2}{M_i}+\sum_{i=1}^{3N}\sum_{j=1}^{3N}F_{ij}\Delta R_i\Delta R_j\right)=\frac{1}{2}(\mathbf{p}^t\cdot\mathbf{p}+\mathbf{q}^t\cdot\mathbf{f}\cdot\mathbf{q}) \tag{1}$$

where M_i are nuclear masses, $p_i = P_i/(M_i)^{1/2}$ $q_i = (M_i)^{1/2}\,\Delta R_i$, and $f_{ij} = F_{ij}/(M_iM_j)^{1/2}$ are the respective mass-weighted momenta, coordinates, and force field. The harmonic force field (referred to also as the Hessian or Cartesian force constant matrix) is formed by the second energy (ε) derivatives

$$F_{ij}=\frac{\partial^2\varepsilon}{\partial R_i\,\partial R_j} \tag{2}$$

The multidimensional problem is solved by a transformation into the normal coordinates, $Q_k = \sum_{j=1}^{3N} s_{kj}^{-1}q_j$, and to corresponding momenta $\Pi_k = \sum_{j=1}^{3N} s_{kj}^{-1}p_j$, so that $\mathbf{s}^t\cdot\mathbf{s} = \mathbf{E}$, where $\mathbf{E}$ is the identity matrix and the transformed force field becomes diagonal

$$s_{ki}f_{k_i}s_{ij}=\omega_i^{\,2}\delta_{ij} \tag{3}$$

where δ_{ij} is the Kronecker symbol ($\delta_{ij} = 1$ for $i = j$, $\delta_{ij} = 0$ for $i \neq j$), and ω_i are the normal mode angular frequencies. The vibrational Hamiltonian then becomes a sum of one-dimensional harmonic oscillator Hamiltonians h_i

$$H=\frac{1}{2}\sum_{i=1}^{3N}(\Pi_i^2+\omega_i^2Q_i^2)=\sum_{i=1}^{3N}h_i(Q_i) \tag{4}$$

Consequently, the equations of motion for the nuclei reduce to a set of *3N* uncoupled one-dimensional Schrödinger equations, energies, and wave functions of which can be obtained analytically.[21] (Equation 4 comprises also the translational and rotational modes not visible in the spectrum.) In particular, frequencies of the fundamental vibrational bands are equal to ω_i. Solving the vibrational problem therefore reduces to the diagonalization of the force field matrix $\mathbf{f}$ (eq 3).

The intensities of the absorption and VCD bands of a fundamental transition $0\rightarrow v$ are proportional, respectively, to the dipolar (D) and rotational (R) strength defined as $D_{0v} = \boldsymbol{\mu}_{0v}\cdot\boldsymbol{\mu}_{v0}$ and $R_{0v} = \mathrm{Im}\,\boldsymbol{\mu}_{0v}\cdot\mathbf{m}_{v0}$, where $\boldsymbol{\mu}_{0v}$ is the electric and the $\mathbf{m}_{0v}$ is the magnetic transition dipole moment, $v = 1..3N$. These are obtained as[22]

$$\boldsymbol{\mu}_{0v}=\left(\frac{\hbar}{2\omega_v}\right)^{1/2}\sum_{i=1}^{3N}\mathbf{p}_iS_{vi} \tag{5a}$$

$$\mathbf{m}_{v0}=-\sqrt{2\hbar^3\omega_v}\sum_{i=1}^{3N}\mathbf{a}_iS_{vi} \tag{5b}$$

where $\mathbf{p}_i$ is the atomic polar tensor (APT), and $\mathbf{a}_i$ is the atomic axial tensor (AAT) with Cartesian ($\beta=x,y,z$) components

$$p_{i\beta}=\frac{\partial\mu_\beta}{\partial R_i} \tag{6a}$$

$$a_{i\beta}=\frac{\sqrt{-1}M_i}{2\hbar}\frac{\partial m_\beta}{\partial P_i} \tag{6b}$$

$S_{vi} = \partial R_i/\partial Q_v = s_{vi}/\sqrt{M_i}$ is the direct (not mass-weighed) Cartesian-normal mode transformation matrix, and $\hbar$ is the

Planck constant.[23] For calculation of the infrared absorption and VCD intensities it is therefore necessary to compute the derivatives of the molecular electric ($\boldsymbol{\mu}$) and magnetic ($\mathbf{m}$) dipole moments.

The Algorithm. As stated in the Introduction, for very large molecules the direct or iterative procedures for finding the eigenvalues and eigenfunctions of the force field matrix $\mathbf{f}$ (eq 3) become impractical. An alternative means is to use the force field matrix to propagate an arbitrary test vector in time. The process is started by a generation of a random set of M unit vectors $\boldsymbol{\sigma_1}...\boldsymbol{\sigma_M}$ at the Cartesian coordinate $3N$-dimensional space. These can be thought of as linear combinations of the eigenvectors of the force field matrix, $\boldsymbol{\sigma}_i = \sum_{j=1}^{3N} c_{ij}\mathbf{s}_j$. Then we introduce time-dependent vectors $\boldsymbol{\sigma}_i(t) = \sum_j c_{ij}\mathbf{s}_j e^{i\lambda_j t}$. Note that t referred to as the fictitious "time" has units of second^2 (in this work corresponding atomic units are used) since λ_j is not a frequency, but $\lambda_j = \Lambda_{jj} = \omega_j^2$. Using eq 3 we get $f_{\beta\alpha}s_{j\alpha} = \lambda_j s_{j\beta}$, and the propagation of $\boldsymbol{\sigma}_i$ can be approximated for small time intervals dt as

$$\boldsymbol{\sigma}_i(t+dt) \cong \boldsymbol{\sigma}_i(t) + \frac{d\boldsymbol{\sigma}_i(t)}{dt}dt + \frac{1}{2}\frac{d^2\boldsymbol{\sigma}_i(t)}{dt^2}dt^2 = \boldsymbol{\sigma}_i(t) + \sum_j ic_{ij}\lambda_j\mathbf{s}_j e^{i\lambda_j t}dt + \boldsymbol{\sigma}_i^{(2)} = \boldsymbol{\sigma}_i(t) + i\mathbf{f}.\boldsymbol{\sigma}_i(t)dt + \boldsymbol{\sigma}_i^{(2)} \quad (7)$$

In the current implementation the second-derivative correction $\boldsymbol{\sigma}_i^{(2)}$ is not calculated directly, as this would involve a computationally impractical formation of the square matrix $\mathbf{f}^2$. Instead, we use an approximate formula, $\boldsymbol{\sigma}_i^{(2)}(t) \cong 0.5(\bar{\boldsymbol{\sigma}}_i(t-2dt) + \bar{\boldsymbol{\sigma}}_i(t) - 2\bar{\boldsymbol{\sigma}}_i(t-dt))$, where $\bar{\boldsymbol{\sigma}}_i$ are the vectors propagated according to eq 7 with finite time steps dt and normalized afterward. The involvement of $\boldsymbol{\sigma}^{(2)}$ appeared very beneficial for the quality of the results by allowing for a significant increase of dt. Only a minor influence of a third-derivative correction introduced in a similar manner was observed; therefore, the third derivative was not used by default.

In principle, we can construct autocorrelation functions

$$C_i(t) = \boldsymbol{\sigma}_i(t)\cdot\boldsymbol{\sigma}_i = \sum_j c_{ij}^2 e^{i\lambda_j t} \quad (8)$$

and obtain the eigenvalues as peak positions of its Fourier transform $I_i(\lambda)$

$$I_i(\lambda) = \int C_i(t)e^{-i\lambda t}dt = 2\pi\sum_j c_{ij}^2\delta(\lambda_j - \lambda) = \sum_j I_{ij}(\lambda) \quad (9)$$

In a similar way, we can define M time-dependent electric and magnetic dipole moments as

$$\mu_{i\beta}(t) = \sum_{j=1}^{3N} p_{j\beta}\sigma_{ij}(t) \text{ and } m_{i\beta}(t) = \sum_{j=1}^{3N} a_{j\beta}\sigma_{ij}(t) \quad (10)$$

with corresponding Fourier transforms

$$\boldsymbol{\mu}_i(\lambda) = \int \boldsymbol{\mu}_i(t)e^{-i\lambda t}dt \text{ and } \mathbf{m}_i(\lambda) = \int \mathbf{m}_i(t)e^{-i\lambda t}dt \quad (11)$$

For a finite-time propagation the δ-functions in (9) can be thought of as finite-width peaks. In fact, in the actual simulations the transforms (eq 11) were calculated for a discrete set of vibrational frequencies ω_i ($\omega_i = \lambda_i^2$), typically spaced by 1 cm^{-1} from 100 to 4000 cm^{-1}. Instead of the usual fast Fourier transformation the Fourier sums (9. 11) were incremented at each step, which did not significantly increase the total time but enabled to avoid storage of the entire trajectory in computer memory. To avoid too narrow peaks, at each time step the transforms were additionally convoluted with a dispersion function in the form of either Lorentzian, $(2/\pi\Delta)/\{1+[2(\omega-\omega_0)/\Delta]^2\}$, or Gaussian, $2(\ln(2))^{1/2}\exp\{-[2(\ln(2))^{1/2}(\omega-\omega_0)/\Delta]^2\}/(\Delta\sqrt{\pi})$, peaks; Δ is the full width at half-maximum.

Performing the integration (11), from (8) and (10) we obtain for the electric dipole $\boldsymbol{\mu}_i(\lambda) = 2\pi\sum_v c_{iv}\sum_k \mathbf{p}_k s_{vk}\delta(\lambda_v - \lambda)$. Thus for each resolved transition v the integration of $\boldsymbol{\mu}_i(\lambda)$ would yield a spectral intensity proportional to the sum $\sum_k \mathbf{p}_k s_{vk}$ (cf. eq 5a). But the expansion coefficients c_{iv} are unknown. They can in principle be obtained from eq 9, but this is impractical as unrealistically long accumulation times are required to resolve modes that are very close in frequency. Instead, we use a numerically more stable procedure and directly calculate the dipolar strengths averaged over the M $\boldsymbol{\sigma}$-vectors as

$$\langle D(\lambda)\rangle = M^{-1}\sum_{i=1,M}\mathrm{Re}\boldsymbol{\mu}_i(\lambda)\cdot\mathrm{Re}\boldsymbol{\mu}_i(\lambda)$$

$$= (2\pi)^2 M^{-1}\sum_{i=1,M}\sum_{v,v'}\langle c_{iv}c_{iv'}\rangle\sum_{k,k'}\mathbf{p}_k\cdot\mathbf{p}_{k'}s_{v',k'}s_{vk}\delta(\lambda_v-\lambda)\delta(\lambda_{v'}-\lambda)$$

$$\cong (3N)^{-1}K(2\pi)^2 M^{-1}\sum_{i=1,M}\sum_v\sum_{k,k'}\mathbf{p}_k\cdot\mathbf{p}_{k'}s_{vk}s_{vk}\delta(\lambda_v-\lambda) \quad (12a)$$

where we multiplied the finite-width "δ-functions" as $\delta(\lambda_v-\lambda)*\delta(\lambda_{v'}-\lambda) = K\delta_{vv'}\delta(\lambda_v-\lambda)$, where K is a constant dependent on the actual shape of δ. For the Gaussian shapes, for example, $K = 1/(\Delta\sqrt{2\pi})$, $\Delta = 2\omega d$, where d is the bandwidth. For a random initial distribution of the coefficients $\langle c_{iv}^2\rangle = (3N)^{-1}$, where N is the number of atoms. Analogously, we get for the rotational strength

$$\langle R(\lambda)\rangle = M^{-1}\sum_{i=1,M}\mathrm{Re}\,\boldsymbol{\mu}_i(\lambda)\cdot\mathrm{Re}\,\mathbf{m}_i(\lambda) \cong (3N)^{-1}K(2\pi)^2M^{-1}\times\sum_{i=1,M}\sum_v\sum_{k,k'}\mathbf{p}_k\cdot\mathbf{a}_{k'}s_{vk'}s_{vk}\delta(\lambda_v-\lambda) \quad (12b)$$

Thus, if we allow for a small inaccuracy of the absolute intensity scale given by the variance of the peak shapes ("δ-functions", which may deviate from the Gaussian peaks), we obtain precise relative absorption and circular dichroism peak intensities with correct ABS/CD ratios from eqs 12a-b.

Matrix Storage. The storage of the Hessian matrix $\mathbf{F}$ requires $(3N)^2$ words of memory. Although this is usually a minor problem for modern computers, the handling of the matrix may still become impractical for systems with several thousands of atoms. Moreover, because of the locality of vibrational interactions,[24] an overwhelming majority of the matrix elements is negligible. Particularly if the force field of a "big" molecule is constructed from smaller fragments, as in the Cartesian tensor transfer (CCT) method,[13] for linear biopolymers (nucleic acids, peptides) only a diagonal-like band of the matrix is formed, and the required amount of memory scales linearly with N. Therefore, in the current implementation, for each line l of the matrix we store only

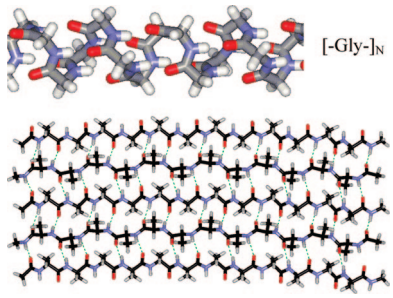

Figure 1. The model systems, variable-length polyglycine in the α-helical conformation (top) and the 5-strand antiparallel β-sheet with Ac-$(Ala)_{12}$-Me strands (Ac=acetyl, Ala=alanine, Me=methyl, bottom).

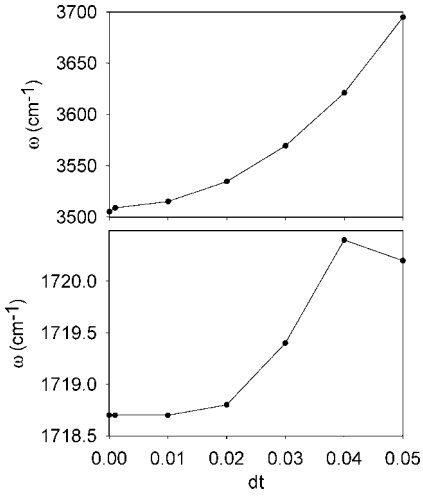

Figure 2. The dependence of the frequency on the integration time step (fictitious time in atomic units, see text), for a N−H stretching (high frequency - top) and C=O stretching (low frequency -bottom) vibrational bands of Gly_{130}.

n_l nonzero nonredundant elements F_{lk}, $k = r_1...r_{nl}$ (using $F_{ij}=F_{ji}$) and the corresponding row-indices r_i. For convenience, diagonal elements F_{ii} are divided by two; then multiplication of a vector **A** by **F, B = F.A,** can be realized by a simple algorithm when only one line of **F** at a time is read from the disk and stored in computer memory:

1. Zero-out **B**, $l = 1$.
2. Read-in l-line of **F**.
3. For all $j \in (r_1...r_{nl})$, update $B_j = B_j + F_{lj}A_l$ and $B_l = B_l + F_{lj}A_j$.
4. Increment $l = l + 1$, if $l < 3N$ go to 2.

The storage required for the atomic axial and polar tensors cannot be reduced; however, this scales linearly with N and thus does not limit computations of even considerably large molecules.

Model Systems. The method was tested on model periodic systems, the polyglycine peptide in an α-helical conformation, and a five-strand antiparallel β-sheet 5 × Ac-$(Ala)_{12}$-Me, shown in Figure 1. The periodicity facilitated the construction of a reasonably accurate force field based on ab initio computation of smaller fragments. For the α-helix a peptide heptamer (containing 7 peptide bonds), Ac-$[Gly]_6$-Me, in the same conformation was subjected to the normal mode optimization routine[25] with modes within −300.300 cm^{-1} fixed. Thus the higher-frequency mode visible in the spectra could be relaxed under a minimal change of the geometry. Similarly for the β-sheet, a smaller 3 × Ac-$(Ala)_2$-Me fragment[26] was used as a source of the force field and the intensity tensors, the geometry of which was optimized with fixed main chain torsion angles. The BPW91 level of approximation[27] and 6−31+G** (α-helix) and 6−31G** (β-sheet) bases were used for the calculation with the aid of the Gaussian program package.[28] For the optimized geometries, the harmonic force field and intensity tensors were computed at the same level by Gaussian and transferred on the polymer by the Cartesian tensor transfer techniques.[13]

3. Results and Discussion

Time Step Dependence. First we have investigated the sensitivity of the method to the size of the integration time step. Previous simulation of the vibrational spectra using classical molecular dynamics trajectories revealed a significant dependence of the Fourier-transformed frequencies on the integration steps.[20] This is true also for the current method, as can be seen in Figure 2 where the dependence is plotted for a low (carbonyl stretching) and high (N−H stretching) frequency band of the $(Gly)_{130}$ system. The "time" variable, the force field, and the eigenvalues Λ_{ii} are given in atomic units; then we can obtain the angular frequency ω (wavenumber) in cm^{-1} as $\omega = 1302.8\sqrt{\Lambda_{ii}}$. We can see that the dependence is much sharper for the N−H stretching band, where the time step dt of 0.05 (au) introduces a huge error of ∼200 cm^{-1}. However, this can be easily fixed by keeping the step small as with dt ∼0.01 an acceptable error is obtained even for the higher-frequency band, while the propagation gives virtually the exact value for the carbonyl stretch. Note that harmonic frequencies of the higher-frequency hydrogen stretching transitions computed by quantum chemical methods are regularly by up to 10% larger than the experimental transitions,[29] which makes a 1% inaccuracy (∼10−30 cm^{-1}) in the vibrational frequencies acceptable. Shorter steps are not desirable as they make the computation unnecessarily longer.

Band Width Convergence. As pointed out in the Method section, the consequence of the finite interval of time propagation is that spectral peaks are not infinitely sharp but have finite widths. Therefore, it is necessary to establish the number of the time propagation steps needed to obtain sufficiently narrow bands. The dependence of the absorption and VCD spectra on the number of the propagation steps plotted in Figure 3 reflects the obvious behavior of the Fourier transformation where the peak width is inversely proportional to the evolution time. However, as the square of the frequency is transformed, we can observe that the higher-frequency bands become narrower than the lower-frequency ones. This is shown quantitatively in Figure 4, where the spectral line widths for the C=O (1718 cm^{-1}) and N−H (3505 cm^{-1}) stretching bands are plotted as functions of the number of propagation steps. Needless to say, for any given region of the spectrum, an arbitrarily narrow width can be obtained by a sufficiently long simulation time. Overall, already at the early stages of the propagation correct relative absorption intensities are obtained. The converged

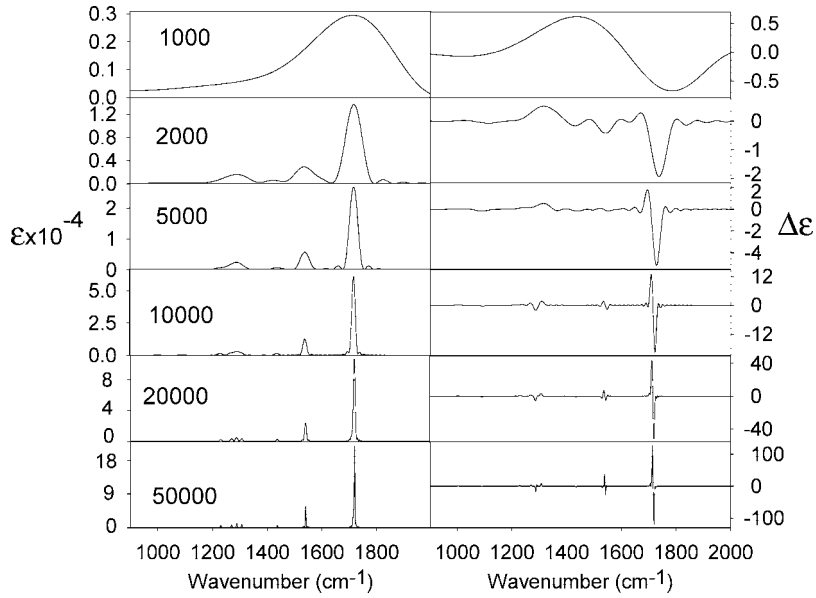

Figure 3. The dependence of the absorption (left) and VCD (right) spectra of Gly_{130} on the number of the propagation steps (indicated in the left panel, for 50 average spectra).

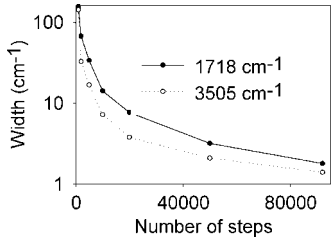

Figure 4. The dependence of the full widths at half-maximum of the two selected peaks, the N−H stretch (3505 cm^{-1}) and C═O stretch (1718 cm^{-1}) in Gly_{130} on the number of the propagation steps. Note, that the y-scale is logarithmic.

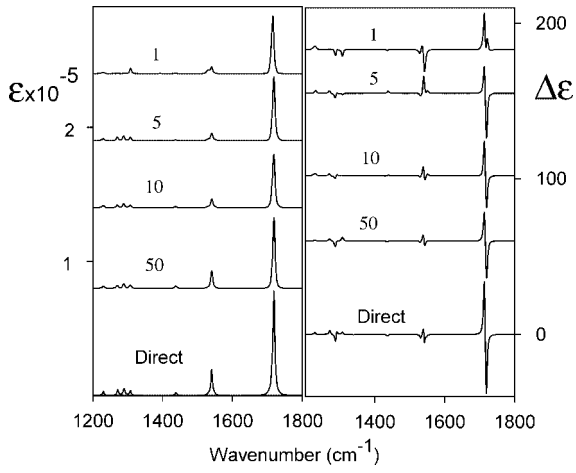

Figure 5. Absorption (left) and VCD (right) spectra simulated (from top, for 2000 propagation points) for 1, 5, 10, and 50 random vector averages as compared to the exact results obtained by the direct diagonalization (bottom traces), for Gly_{130}.

VCD shapes require a longer time; for example, the conservative carbonyl stretching split-band at ∼1718 cm^{-1} stabilizes at ∼20000 steps. For a typical IR or VCD experiment where the inhomogeneous band widths seldom become smaller than ∼10 cm^{-1} a propagation with ∼20000 steps thus already provides the desired spectral shape in the C═O stretching region.

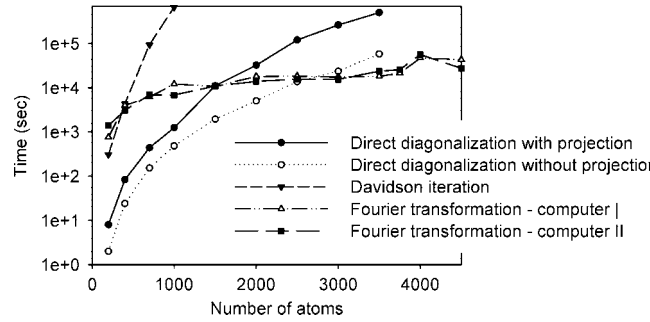

Figure 6. The dependence of the time (in seconds, on a logarithmic scale) needed to diagonalize the force field matrix on the number of atoms in the $(Gly)_N$ polymer. (Detailed description of each method is given in the text.)

Trial Vector Averaging. With a sufficiently small integration step the procedure yields the correct vibrational frequencies. However, the spectral intensities resulting from a particular propagation run differ as a consequence of the randomly chosen initial vectors $\boldsymbol{\sigma}_i$. To obtain a stable solution, independent of the choice of the initial conditions, it is necessary to average several such runs. The convergence of the relative IR and VCD band intensities on the number of the initial vectors $\boldsymbol{\sigma}_i$ is explored in Figure 5. An instantaneous convolution with the Lorentzian bands was performed during the simulation in order to achieve a constant bandwidth of 10 cm^{-1}. The resultant spectra of $(Gly)_{130}$ for $M = 1$, 5, 10, and 50 are compared with the exact result based on the direct Householder diagonalization. While a randomly selected vector ($M = 1$) provides unrealistic relative intensities, even with some wrongly predicted VCD signs, the spectral profile quickly stabilizes, and for $M = 50$ the spectra are practically indistinguishable from the exact intensities. As explained above, the minor underestimation of the absolute intensities can be explained

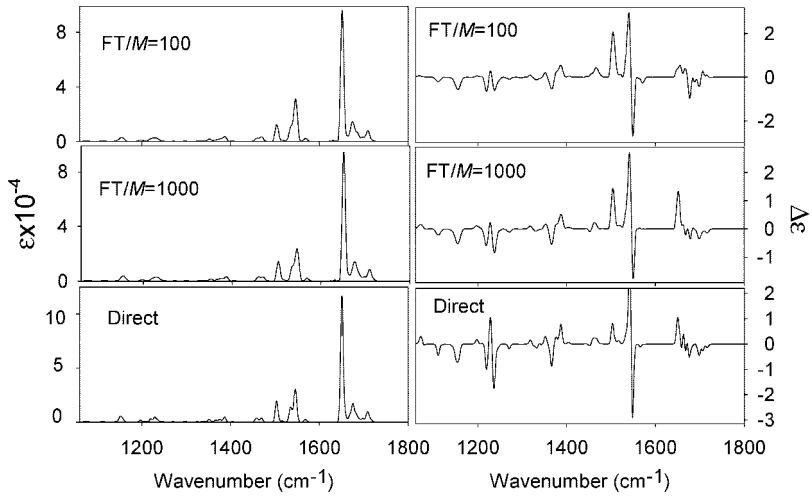

Figure 7. Absorption (left) and VCD (right) spectra of the 660 atom β-sheet simulated by the time propagation (FT, for $M = 100$ and 1000 trial vectors) as compared to the exact results obtained by the direct diagonalization (bottom trace); the 5 cm^{-1} bandwidth was used in the simulations.

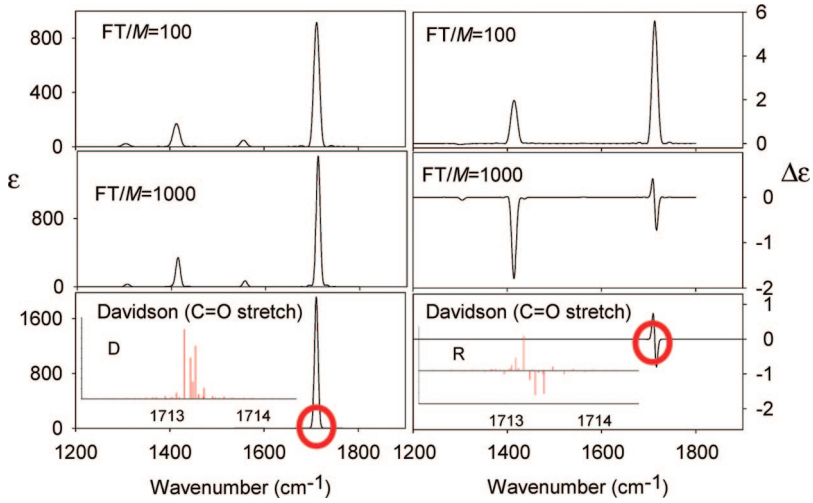

Figure 8. Absorption (left) and VCD (right) spectra of the 14000 atom poly glycine α-helix simulated by the time propagation (for $M = 100$ and 1000 trial vectors, 8 h and 3.5 days of the computer time was needed, respectively) as compared to the exact result obtained by the Davidson method (finished in 9 days and 15 h, only the C=O stretching was included). The spectra were normalized to one amide, and 5 cm^{-1} bandwidth was used. For the Davidson method, positions of the dipolar and rotatory strengths of individual C=O stretching transitions are indicated in the inset graphs.

by the approximation for the averaging and the δ-function multiplication.

CPU Time Scaling. As the number of nonzero matrix elements is approximately proportional to the number of atoms N, and the matrix-vector multiplication in eq 7 required for the propagation $\boldsymbol{\sigma}_i$ involves a number of multiplications proportional to N^2, we can expect practical scaling between N^1 and N^2. This is confirmed by the time dependence on the number of atoms for $(\mathrm{Gly})_K$, $K = 28...0.642$ plotted in Figure 6. The detailed scaling of the disk-based time-propagation procedure is dependent on the disk fragmentation and detailed memory management; therefore, two computers with the same processors ("computer I and II" in the Figure 6, AMD64 1 GHz) provided slightly different dependencies. Curiously, a larger force field matrix can occasionally even yield a shorter simulation time. We can see that the Fourier method scales much more favorably than the other procedures. For the comparison we used our own implementation of the iteration (Davidson) method based on the Mitin's modification of the algorithm,[26] while a standard code was used for the direct (Householder) diagonalization, expanded by the possibility of correcting the ab intio force fields for the translational and rotational invariance.[15] In Figure 6 we can see that the complete Davidson diagonalization is faster than the time propagation up to $N\sim500$, and then the time quickly grows to immeasurable values. The direct Householder diagonalization is more efficient up to $N\sim1500$, which can be somewhat improved by skipping the projection of the zero-vibrational modes (rotations and translations) from the force field. However, because of the intrinsic N^3 dependence and huge memory requirements of the direct method, the propagation in the fictitious time becomes the only method usable for $N > 3000$.

Large Peptide Systems. We have applied the Hessian propagation to simulations of the IR and VCD spectra for the β-sheet poly alanine segment (660 atoms) and the poly

glycine α-helix containing 14000 atoms (Figure 1). The absorption and VCD spectra for these two protein models simulated for 20000 time steps are plotted in Figures 7 and 8. The β-sheet spectrum could be compared to that obtained by the Householder diagonalization, while the reference α-helical spectrum was calculated using a limited Davidson diagonalization. The Davidson method provided 2000 vibrational C═O stretching mode frequencies, starting from the highest value, when hydrogen masses were arbitrarily increased to 10 g/mol, not to interfere with the carbonyl vibrations. For both systems, we can see that the time propagation method faithfully reproduces the relative IR intensity and VCD sign patterns, although a relatively large number of the trial vectors is needed for accurate results. Particularly, for the α-helix, the 100-vector average (Figure 8, top) is not sufficient for the VCD simulation as it provides a net positive signal instead of the split carbonyl band. The results nicely confirm the ability of the IR and VCD spectroscopies to distinguish various peptide and protein secondary structures: the high-frequency IR carbonyl stretch components (1660−1740 cm^{-1}, Figure 8) and the associated weak VCD signal are characteristic for the β-sheet forms,[30] while a single IR carbonyl band and an intense, positive VCD couplet (i.e., positive to negative, from low to high frequency) correspond well to the experimental data from helix-rich proteins.[3]

The absorption and VCD spectra of regular structures, particularly the poly glycine α-helix, originate in a few semidegenerate transitions. The positions of the most intense peaks are shown in the insets in the bottom panels of Figure 8. Most of the intensities come from a frequency interval about 0.5 cm^{-1} wide. As discussed previously, this accumulation of spectral intensities reflects the translational symmetry of the structure and phonon-like delocalized normal modes.[5] Therefore, the propagation method is capable of correctly reproducing the overall spectral shape arising from the specific intensity distribution also among nearly degenerate modes. However, the degeneracy of the C═O stretching transitions requires a relatively large number of the trial vectors (∼1000) to be averaged, which leads to longer computational time.

Another limitation of the present approach is the restriction to the harmonic force field, although diagonal anharmonic effects and Fermi resonances might be important for many spectroscopic phenomena.[21,31] In general, the wave function propagation and Fourier transformation of an autocorrelation function is suitable for obtaining transition energies of any Hamiltonian;[32] the implementation for large molecules, however, exceeds the scope of the present work.

4. Summary

The force-field mediated time propagation of trial vectors proved to be a stable algorithm for the generation of vibrational spectra. It can offer important computational advantages over standard matrix diagonalization methods for very large systems. The method yielded accurate IR and VCD intensities for model systems, provided that the time propagation was averaged over a sufficient number of the trial initial vectors. As a drawback, the procedure provides only approximate absolute spectral intensities. However, this is seldom a problem in most applications, since the absolute IR and VCD intensities are difficult to measure, and the structural properties are deduced mostly from the spectral shapes. Because of the modest computer time and memory requirements the time propagation thus represents a convenient means for modeling of vibrational properties of large molecular systems.

Acknowledgment. The work was supported by Faculty Grant-in-Aid and Basic Research Grant programs of the University of Wyoming, by the Grant Agency of the Czech Republic (grants 203/06/0420, 202/07/0732), and the Grant Agency of the Academy of Sciences (A400550702).

References

(1) (a) Gregoriou, V. G.; Braiman, M. S. *Vibrational spectrosopy of biological and polymeric materials*; CRC: Boca Raton, FL, 2005. (b) Gremlich, H. U.; Yan, B. *Infrared and Raman Spectroscopy of Biological Materials*; CRC: Boca Raton, FL, 2005.

(2) (a) Barth, A.; Zscherp, C. *Q. Rev. Biophys.* **2002**, *35*, 369–430. (b) Haris, P. I. Fourier Transform Infrared Spectroscopic Studies of Peptides: Potentials and Pitfalls. In *Infrared Analysis of Peptides and Proteins: Principles and Applications. ACS Symposium Series*; Ram Singh, B., Ed.; ACS: Washington, DC, 2000; pp 54−95. (c) Braiman, M. S.; Rothschild, K. J. *Annu. Rev. Biophys. Biophys. Chem.* **1988**, *17*, 541–570.

(3) Keiderling, T. A.; Kubelka, J.; Hilario, J., Vibrational circular dichroism of biopolymers. Summary of methods and applications. In *Vibrational spectroscopy of polymers and biological systems*; Braiman, M., Gregoriou, V., Eds.; CRC Press: Boca Raton, 2006; pp 253−324.

(4) Andrushchenko, V.; Bouř, P. *J. Phys. Chem. A* **2007**, *111*, 9714–9723.

(5) Andrushchenko, V.; Bouř, P. *J. Comput. Chem.* **2008**, *29*, 2693–2703.

(6) (a) Dluhy, R. A.; Stephens, S. M.; Widayati, S.; Williams, A. D. *Spectrochim. Acta, Part A* **1995**, *51*, 1413–1447. (b) Goormaghtigh, E.; Raussens, V.; Ruysschaert, J. M. *Biochim. Biophys. Acta* **1999**, *1422*, 105–185.

(7) (a) Barth, A.; Zscherp, C. *FEBS Lett.* **2000**, *477*, 151–156. (b) Pandyra, A. A.; Yamniuk, A. P.; Andrushchenko, V.; Wieser, H.; Vogel, H. *Biopolymers* **2005**, *79*, 231–237.

(8) (a) Callender, R.; Dyer, R. B. *Chem. Rev.* **2006**, *106*, 3031–3042. (b) Callender, R. H.; Dyer, B. R.; Gilmanshin, R.; Woodruff, W. H. *Annu. Rev. Phys. Chem.* **1998**, *49*, 173–202.

(9) (a) Hamm, P.; Lim, M.; Hochstrasser, R. M. *J. Phys. Chem. B* **1998**, *102*, 6123–6138. (b) Zanni, M. T.; Hochstrasser, R. M. *Curr. Opin. Struct. Biol.* **2001**, *11*, 516–522. (c) Ganim, Z.; Chung, H. S.; Smith, A. W.; Deflores, L. P.; Jones, K. C.; Tokmakoff, A. *Acc. Chem. Res.* **2008**, *41*, 432–441.

(10) Besley, N. A. *Philos. Trans. R. Soc., A* **2007**, *365*, 2799–2812.

(11) Kaledin, A. L.; Kaledin, M.; Bowman, J. M. *J. Chem. Theory Comput.* **2006**, *2*, 166–174.

(12) Choi, J. H.; Lee, H.; Lee, K. K.; Hahn, S.; Cho, M. *J. Chem. Phys.* **2007**, *126*, 045102.

(13) Bouř, P.; Sopková, J.; Bednárová, L.; Maloň, P.; Keiderling, T. A. *J. Comput. Chem.* **1997**, *18*, 646–659.

(14) Silva, R. A. G. D.; Kubelka, J.; Decatur, S. M.; Bouř, P.; Keiderling, T. A. *Proc. Natl. Acad. Sci. U.S.A.* **2000**, *97*, 8318–8323.

(15) Press, W. H.; Teukolsky, S. A.; Vetteling, W. T.; Flannery, B. P. *Numerical Recipes in Fortran*, 2nd ed.; Cambridge University Press: New York, 1992.

(16) Grotendorst, J. *Modern methods and algorithms of quantum chemistry*; John von Neumann Institute for Computing: Jülich, 2000; Vol. 1.

(17) (a) Davidson, E. R. *J. Comput. Phys.* **1975**, *17*, 87–94. (b) Mitin, A. V. *J. Comput. Chem.* **1994**, *15*, 747–751. (c) Martins, J. L.; Cohen, M. L. *Phys. Rev. B* **1988**, *37*, 6134–6138.

(18) vanderVorst, H. A. *Iterative Krylov Methods for Large Linear Systems*; Cambridge University Press: Cambridge, 2003.

(19) (a) Reiher, M.; Neugebauer, J. *J. Chem. Phys.* **2003**, *118*, 1634–1641. (b) Neugebauer, J.; Reiher, M. *J. Phys. Chem. A* **2004**, *108*, 2053–2061.

(20) Horníček, J.; Kaprálová, P.; Bouř, P. *J. Chem. Phys.* **2007**, *127*, 084502.

(21) Papoušek, D.; Aliev, M. R. *Molecular Vibrational/Rotational Spectra*; Academia: Prague, 1982.

(22) Stephens, P. J.; Devlin, F. J.; Ashvar, C. S.; Chabalowski, C. F.; Frisch, M. J. *Faraday Discuss.* **1994**, *99*, 103–119.

(23) (a) Stephens, P. J. *J. Phys. Chem.* **1985**, *89*, 748–752. (b) Stephens, P. J.; Devlin, F. J.; Chabalowski, C. F.; Frisch, M. J. *J. Phys. Chem.* **1994**, *98*, 11623–11627. (c) Polavarapu, P. L. *Vibrational spectra: principles and applications with emphasis on optical activity*; Elsevier: Amsterdam, 1998; Vol. 85. (d) Nafie, L. A.; Freedman, T. B. Vibrational optical activity theory. In *Circular Dichroism. Principles and Applications*, 2nd ed.; Berova, N., Nakanishi, K., Woody, R. W., Eds.; Wiley-VCH: New York, 2000; pp 97−131.

(24) (a) Andrushchenko, V.; Wieser, H.; Bouř, P. *J. Phys. Chem. B* **2003**, *91*, 12623–12634. (b) Bouř, P.; Keiderling, T. A. *J. Phys. Chem. B* **2005**, *109*, 23687–23697. (c) Bouř, P.; Kubelka, J.; Keiderling, T. A. *Biopolymers* **2002**, *65*, 45–69.

(25) (a) Bouř, P.; Keiderling, T. A. *J. Chem. Phys.* **2002**, *117*, 4126–4132. (b) Bouř, P. *Collect. Czech. Chem. Commun.* **2005**, *70*, 1315–1340.

(26) Kubelka, J.; Keiderling, T. A. *J. Am. Chem. Soc.* **2001**, *123*, 6142–6150.

(27) Becke, A. *Phys. Rev. A* **1988**, *38*, 3098–3100.

(28) Frisch, M. J.; Trucks, G. W.; Schlegel, H. B.; Scuseria, G. E.; Robb, M. A.; Cheeseman, J. R.; Montgomery, J. A., Jr.; Vreven, T.; Kudin, K. N.; Burant, J. C.; Millam, J. M.; Iyengar, S. S.; Tomasi, J.; Barone, V.; Mennucci, B.; Cossi, M.; Scalmani, G.; Rega, N.; Petersson, G. A.; Nakatsuji, H.; Hada, M.; Ehara, M.; Toyota, K.; Fukuda, R.; Hasegawa, J.; Ishida, M.; Nakajima, T.; Honda, Y.; Kitao, O.; Nakai, H.; Klene, M.; Li, X.; Knox, J. E.; Hratchian, H. P.; Cross, J. B.; Bakken, V.; Adamo, C.; Jaramillo, J.; Gomperts, R.; Stratmann, R. E.; Yazyev, O.; Austin, A. J.; Cammi, R.; Pomelli, C.; Ochterski, J. W.; Ayala, P. Y.; Morokuma, K.; Voth, G. A.; Salvador, P.; Dannenberg, J. J.; Zakrzewski, V. G.; Dapprich, S.; Daniels, A. D.; Strain, M. C.; Farkas, O.; Malick, D. K.; Rabuck, A. D.; Raghavachari, K.; Foresman, J. B.; Ortiz, J. V.; Cui, Q.; Baboul, A. G.; Clifford, S.; Cioslowski, J.; Stefanov, B. B.; Liu, G.; Liashenko, A.; Piskorz, P.; Komaromi, I.; Martin, R. L.; Fox, D. J.; Keith, T.; Al-Laham, M. A.; Peng, C. Y.; Nanayakkara, A.; Challacombe, M.; Gill, P. M. W.; Johnson, B.; Chen, W.; Wong, M. W.; Gonzalez, C.; Pople, J. A. *Gaussian 03, Revision C.02*; Gaussian, Inc.: Wallingford, CT, 2004.

(29) Pulay, P. *J. Phys. Chem.* **1995**, *99*, 3093–3100.

(30) (a) Setnička, V.; Huang, R.; Thomas, C. L.; Etienne, M. A.; Kubelka, J.; Hammer, R. P.; Keiderling, T. A. *J. Am. Chem. Soc.* **2005**, *127*, 4992–4993. (b) Torii, H. *J. Phys. Chem. B* **2008**, *112*, 8737–8743.

(31) Palmer, R. A. 2-D Infrared-Spectroscopy Chem. Eng. News 1990; Mar 26, pp 6175−6185.

(32) Žd'ánská, P.; Moiseyev, N. *J. Chem. Phys.* **2004**, *121*, 6175–6185.

CT800298N

JCTC Journal of Chemical Theory and Computation

Systematic Comparison of Second-Order Polarization Propagator Approximation (SOPPA) and Equation-of-Motion Coupled Cluster Singles and Doubles (EOM-CCSD) Spin−Spin Coupling Constants for Molecules with C, N, and O Double and Triple Bonds and Selected F-Substituted Derivatives

Janet E. Del Bene,*,† Ibon Alkorta,‡ and José Elguero‡

Department of Chemistry, Youngstown State University, Youngstown, Ohio 44555, and Instituto de Química Médica, CSIC, Juan de la Cierva, 3, E-28006 Madrid, Spain

Received August 6, 2008

Abstract: Ab initio EOM-CCSD and SOPPA calculations with the Ahlrichs (qzp,qz2p) basis set have been carried out to evaluate one-, two-, and three-bond spin−spin coupling constants for molecules $H_mX{=}YH_n$ and $H_mX{\equiv}YH_n$ for X, Y = ^{13}C, ^{15}N, and ^{17}O, and selected ^{19}F-substituted derivatives. In the great majority of cases, EOM-CCSD one-bond C−C, C−N, C−O, C−F, N−N, N−O, and N−F coupling constants and three-bond F−F coupling constants are smaller in absolute value than the corresponding SOPPA coupling constants, with the EOM-CCSD values in better agreement with experimental data. SOPPA tends to significantly overestimate the absolute values of large one- and three-bond couplings involving fluorine. The majority of two-bond SOPPA coupling constants are in better agreement with experiment than EOM-CCSD, although differences between EOM-CCSD and experimental values are not dramatic. A statistical analysis of thirty EOM-CCSD and SOPPA coupling constants versus experimental coupling constants demonstrates that better agreement with experiment is found when EOM-CCSD is the computational method.

Introduction

In a previous paper,[1] we reported a comparison between computed spin−spin coupling constants obtained by two different theoretical methods: the second-order polarization propagator approximation (SOPPA) and the equation-of-motion coupled cluster singles and doubles method (EOM-CCSD). That study was carried out with the Ahlrichs (qzp,qz2p) basis set on a series of molecules $H_mX{-}YH_n$, for X−Y a single bond involving C, N, O, and F, as well as a set of fluorine derivatives of these molecules for which experimental spin−spin coupling constants were available. Also included were the neutral hydrides NH_3, H_2O, and HF and their protonated and deprotonated ions, as well as the hydrogen-bonded complexes which could be formed from these species. The methods chosen for investigation, EOM-CCSD and SOPPA, explicitly treat electron correlation effects, with EOM-CCSD providing a higher level of treatment. However, the higher level treatment of correlation effects makes EOM-CCSD significantly more expensive computationally and limits it application to relatively small systems and/or those with high computational symmetry. On the other hand, SOPPA is much more tractable computationally. The question then is how well does SOPPA perform.

It was not surprising to find in ref 1 that for the neutral molecules $H_mX{-}YH_n$ and their F-substituted derivatives, EOM-CCSD coupling constants were in better agreement with experimental coupling constants than SOPPA, particular for couplings involving fluorine, in which cases the SOPPA data were significantly in error. However, SOPPA coupling constants were consistent with EOM-CCSD coupling con-

* Corresponding author e-mail: jedelbene@ysu.edu.
† Youngstown State University.
‡ Instituto de Química Médica.

10.1021/ct800321b CCC: $40.75 © 2009 American Chemical Society
Published on Web 12/02/2008

stants for some of the one-bond couplings and for the hydrogen-bonded complexes. In the present paper, we report an extension of our previous study to molecules H_mXYH_n in which X and Y are doubly- (X=Y) and triply bonded (X≡Y) and selected F-substituted derivatives. These derivatives have been included because of the availability of experimental coupling constants and the discrepancies observed in ref 1 between experimental and computed SOPPA coupling constants involving F. In this paper we compare computed EOM-CCSD and SOPPA coupling constants with each other and with experimental data.

Methods

Molecular structures have been optimized at second-order Møller−Plesset perturbation theory (MP2)[2−5] with the 6−31+G(d,p) basis set.[6−9] Vibrational frequencies have been computed to establish that each structure is a local minimum on its potential surface. These optimized geometries were used for the calculation of coupling constants for the majority of molecules. However, for molecules with experimentally determined ground-state geometries[10−15] and experimentally measured coupling constants,[16−21] the experimental ground-state geometry was used in an effort to minimize the effect of neglecting zero-point vibrational corrections.[22] Although the importance of zero-point vibrational corrections has been demonstrated previously by others, imposing such corrections does not always lead to better agreement with experiment. For example, in a previous study of FCCF,[18] we demonstrated that the three-bond F−F coupling constant was extremely sensitive to geometry. Optimized geometries even at CCSD(T)/aug-cc-pVTZ had C−C and C−F distances that were too long and absolute values of ^{3}J(F−F) which were significantly greater than the experimental value of this coupling constant. Imposing zero-point corrections increased these distances and led to even larger discrepancies. It was only when the experimental geometry of FCCF was used that computed values of ^{3}J(F−F) at both levels of theory approached the experimental value, with the absolute value of the EOM-CCSD coupling constant in very good agreement with experiment.

Spin−spin coupling constants involving ^{13}C, ^{15}N, ^{17}O, and ^{19}F were computed using the second-order polarization propagator approximation (SOPPA)[23−27] and the equation-of-motion coupled cluster singles and doubles (EOM-CCSD) method in the CI(configuration interaction)-like approximation,[28,29] with all electrons correlated. Both of these methods explicitly include electron correlation effects. For these calculations, only one basis set has been employed, namely, the Ahlrichs[30] qzp basis set for ^{13}C, ^{15}N, ^{17}O, and ^{19}F atoms and the qz2p basis set for ^{1}H atoms. Thus, the levels of theory may be represented as EOM-CCSD/(qzp,qz2p) and SOPPA/(qzp,qz2p). Coupling constants have not been evaluated at SOPPA(CCSD),[23,31] a method in which the MP2 amplitudes are replaced by CCSD amplitudes. In ref 1 it was observed that SOPPA significantly overestimates the absolute values of ^{1}J(O−F) for FOF and FOOF. These coupling constants increase in absolute value at SOPPA(CCSD) and are further removed from the EOM-CCSD and experimental values.

In the Ramsey approximation, the total coupling constant (J) is a sum of four contributions: the paramagnetic spin−orbit (PSO), diamagnetic spin−orbit (DSO), Fermi-contact (FC), and spin-dipole (SD). All terms have been computed for all molecules. Geometry optimizations were carried out with the Gaussian 03 suite of programs.[32] SOPPA calculations were performed using Dalton-2[33] on the IQM computers, and the EOM-CCSD calculations were done with ACES II[34] on the Itanium Cluster at the Ohio Supercomputer Center.

Results and Discussion

Table 1 presents computed SOPPA and EOM-CCSD spin−spin coupling constants, along with the available experimental data. The components of J can be found in Tables S1 and S2 of the Supporting Information. Listed first in Table 1 are molecules with triple bonds, beginning with HC≡CH and its F-substituted derivatives, followed by molecules with C≡N bonds, and then C≡O and N≡N. Molecules with double bonds are arranged starting with H_2C=CH_2 and its derivatives, followed by molecules with C=N, C=O, N=N, and N=O double bonds. Three molecules originally included in this list (HN=O and *cis* and *trans* HN=NH) have been removed because of large t_2 amplitudes of 0.15, which are indicative of the inadequacy of a single-reference treatment. The last three entries in Table 1 are the cumulenes, H_2C=C=CH_2, H_2C=C=NH, and H_2C=C=O.

One-Bond Coupling Constants. Table 1 shows that the computed SOPPA and EOM-CCSD 1-bond C−C coupling constants are always positive and usually similar, with the SOPPA coupling constants greater than EOM-CCSD. ^{1}J(C−C) has been determined experimentally for only 3 molecules included in this study, HCCH, H_2CCH_2, and H_2CCCH_2. For each of these, the computed values overestimate the experimental, although the EOM-CCSD coupling constants are closer to experiment. Both EOM-CCSD and SOPPA overestimate ^{1}J(C−C) for coupling across the C−C triple bond, with computed values of 198.6 and 194.9 Hz, respectively, compared to the experimental gas-phase value of 174.8 Hz.[21] Unfortunately, experimental ^{1}J(C−C) values for FCCH and FCCF are not available. However, both methods predict that F-substitution would significantly increase ^{1}J(C−C) for FCCH (288.5 and 281.0 at SOPPA and EOM-CCSD, respectively) and for FCCF (430.2 and 417.5 Hz, respectively).

SOPPA and EOM-CCSD values of ^{1}J(C−N) are similar, relatively small, and may be positive or negative. ^{1}J(C−O) is always positive, while ^{1}J(N−N) and ^{1}J(N−O) are negative. The absolute values of the SOPPA coupling constants are greater than the corresponding EOM-CCSD coupling constants, with the EOM-CCSD values in better agreement with available experimental data. Since the magnetogyric ratios of ^{13}C and ^{19}F are positive while those of ^{15}N and ^{17}O are negative, the reduced one-bond coupling constants ^{1}K(C−O), ^{1}K (N−N), and ^{1}K(N−O) are negative and thus in violation of the Dirac Vector Model.[35]

What makes ^{1}K(C−O), ^{1}K(N−N), and ^{1}K(N−O) negative? From Tables S1 and S2 it can be seen that all ^{1}J(C−O) are positive because both the PSO and FC terms are positive.

Table 1. SOPPA, EOM-CCSD, and Experimental Spin-Spin Coupling Constants J (Hz)[a]

molecule	^{n}J(X−Y)	SOPPA	EOM-CCSD	exptl
	Molecules with Triple Bonds			
1 HC≡CH[b]	^{1}J(C−C)	198.6	194.9	174.8[c]
2 FC≡CH	^{1}J(C−C)	288.5	281.0	
	^{1}J(C−F)	−363.2	−323.2	
3 FC≡CF[d]	^{1}J(C−C)	430.2	417.5	
	^{1}J(C−F)	−318.3	−277.7	−287.3[e]
	^{2}J(C−F)	37.9	40.2	28.7[f]
	^{3}J(F−F)	−9.5	1.4	2.1[e]
4 HC≡N	^{1}J(C−N)	−9.7	−12.6	
5 H_3CC≡N[g]	^{1}J(C−N)	−13.5	−16.6	−17.5[h]
6 FC≡N	^{1}J(C−N)	13.3	5.9	
	^{1}J(C−F)	−515.8	−465.9	
7 C≡O[b]	^{1}J(C−O)	23.1	18.6	16.4[i]
8 N≡N[b]	^{1}J(N−N)	−4.8	−3.1	−1.8[j]
	Molecules with Double Bonds			
9 H_2C=CH_2[g]	^{1}J(C−C)	75.0	71.1	67.2[k]
10 F_2C=CH_2[l]	^{1}J(C−C)	123.7	119.7	
	^{1}J(C−F)	−319.0	−290.2	−287[m]
	^{2}J(F−F)	24.1	45.3	32.7[n]
11 FHC=CHF *cis*[o]	^{1}J(C−C)	109.7	105.0	
	^{1}J(C−F)	−283.1	−259.4	
	^{2}J(C−F)	14.1	8.4	5.9[p]
	^{3}J(F−F)	−8.4	−15.1	−18.7[q]
12 FHC=CHF *trans*	^{1}J(C−C)	123.1	117.2	
	^{1}J(C−F)	−271.6	−246.5	
	^{2}J(C−F)	54.8	48.0	
	^{3}J(F−F)	−150.2	−137.6	−132.7[q]
13 F_2C=CF_2[o]	^{1}J(C−C)	210.5	204.3	
	^{1}J(C−F)	−302.1	−270.1	
	^{2}J(C−F)	52.1	46.8	
	^{2}J(F−F)	122.0	134.1	124[q]
	^{3}J(F−F) *cis*	86.7	67.6	73.3[q]
	^{3}J(F−F) *trans*	−124.1	−115.2	−114[q]
14 H_2C=NH	^{1}J(C−N)	−1.5	−1.9	
15 F_2C=NH	^{1}J(C−N)	−9.7	−11.6	
	^{1}J(C−F) *cis to H*	−398.1	−360.7	
	^{1}J(C−F) *trans to H*	−308.8	−278.3	
	^{2}J(F−F)	−88.7	−61.8	−54.6[q]
16 FHC=NF *cis*	^{1}J(C−N)	2.3	3.9	
	^{1}J(C−F)	−382.7	−347.5	
	^{1}J(N−F)	131.2	116.1	
	^{3}J(F−F)	−60.3	−49.3	
17 FHC=NF *trans*	^{1}J(C−N)	2.6	1.3	
	^{1}J(C−F)	−308.4	−277.7	
	^{1}J(N−F)	114.0	99.6	
	^{3}J(F−F)	−247.6	−213.4	
18 H_2C=O	^{1}J(C−O)	38.0	32.8	
19 F_2C=O	^{1}J(C−O)	30.5	22.9	
	^{1}J(C−F)	−375.4	−337.1	
	^{2}J(F−F)	−165.2	−141.7	
20 FN=NF *cis*[o]	^{1}J(N−N)	0.93	−0.59	
	^{1}J(N−F)	240.9	211.8	211.0[r]
	^{2}J(N−F)	−19.3	−17.9	−25.4[r]
	^{3}J(F−F)	−190.1	−128.8	
21 FN=NF *trans*[s]	^{1}J(N−N)	−20.7	−19.1	
	^{1}J(N−F)	194.6	171.8	172.8[r]
	^{2}J(N−F)	−58.7	−53.8	−62.8[r]
	^{3}J(F−F)	−381.9	−307.1	
22 FN=O	^{1}J(N−O)	−47.9	−38.5	
	^{1}J(N−F)	131.7	84.2	
	Cumulenes			
23 H_2C=C=CH_2[g]	1J(C−C)	111.6	105.4	98.7[t]
24 H_2C=C=NH	^{1}J(C−C)	112.5	109.0	
	^{1}J(C−N)	−12.4	−14.5	
25 H_2C=C=O	^{1}J(C−C)	110.7	110.3	
	^{1}J(C−O)	30.3	23.2	

[a] J for molecules with experimentally determined coupling constants were computed at experimental geometries, except for molecules **12** (HFC=CFH trans) and **15** (F_2C=NH). [b] Reference 10. [c] Reference 21. [d] Reference 11. [e] Reference 17. [f] Reference 18. [g] Reference 12. [h] Reference 16, p 375. [i] Reference 19, p 386. [j] Reference 19, p 274. [k] Reference 16, p 370. [l] Reference 13. [m] Reference 20, p 579. [n] Reference 19, p 636. [o] Reference 14. [p] Reference 20, p 581. [q] Reference 19, p 646. [r] Reference 19, p 277. [s] Reference 15. [t] Reference 20, p 550.

Similarly, ^{1}J(N−N) for N_2 and *trans* FNNF and ^{1}J(N−O) for FNO are negative because both PSO and FC terms are negative. The only molecule that does not fit this pattern is *cis* FNNF, in which case the PSO term is relatively small and negative, and the FC and SD terms are small but positive. ^{1}J(N−N) for *cis* FNNF has opposite signs at SOPPA and EOM-CCSD, but its absolute value is less than 1 Hz.

In the set of molecules included in this study, there are 12 one-bond C−F coupling constants and 5 one-bond N−F coupling constants. All one-bond C−F coupling constants

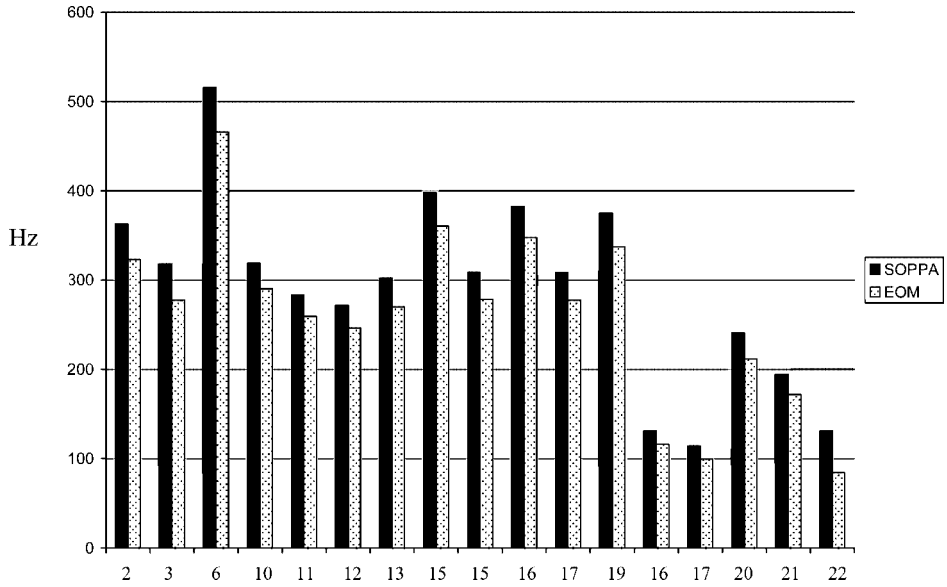

Figure 1. SOPPA and EOM-CCSD one-bond coupling constants. The numbers on the *x*-axis correspond to the molecule numbers in Table 1. The first 12 pairs of bars are the absolute values of ^{1}J(C−F); the remaining 5 pairs are ^{1}J(N−F).

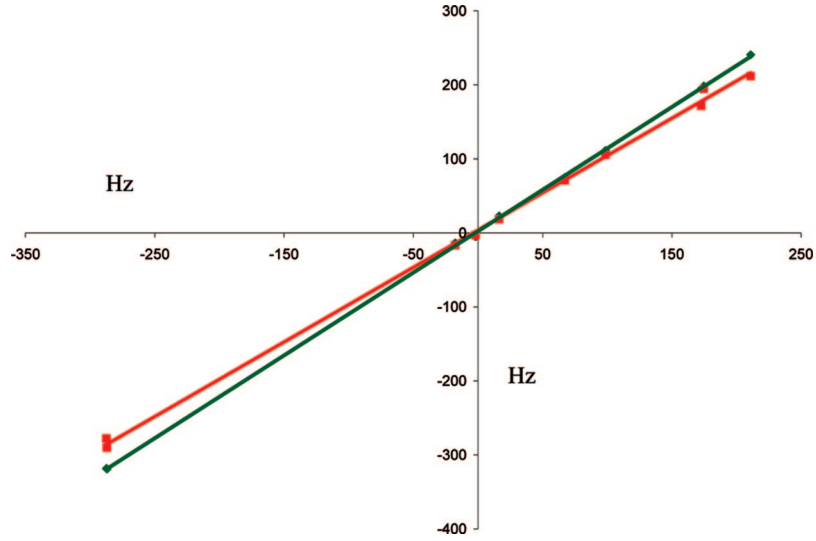

Figure 2. EOM-CCSD (■) and SOPPA (♦) one-bond coupling constants ^{1}J(X−Y) plotted against the experimental values.

are negative, and all one-bond N−F coupling constants are positive, which means that the reduced one-bond coupling constants ^{1}K(C−F) and ^{1}K(N−F) are also negative and in violation of the Dirac Vector Model. This is most likely a consequence of the presence of lone pairs of electrons on the coupled atoms.[36] The bar graph of Figure 1 shows the absolute values of SOPPA and EOM-CCSD ^{1}J(C−F) (pairs **1**−**12**) and the values of ^{1}J(N−F) (pairs **13**−**17**). The numbers on the horizontal axis correspond to the molecule numbers in Table 1. It is evident that there can be a significant difference between coupling constants computed at these two levels of theory, with the absolute values of the SOPPA couplings always greater than EOM-CCSD. This difference arises from the difference in the absolute values of the FC terms, which are 20 to 50 Hz greater at SOPPA compared to EOM-CCSD. One-bond C−F coupling constants for molecules **3** (FCCF) and **10** (F_2CCH_2) and one-bond N−F couplings for molecules **20** and **21** ("*cis*" and "*trans*" FNNF) have been measured experimentally. The EOM-CCSD values are in much better agreement with experiment than the SOPPA values, which overestimate ^{1}J(C−F) and ^{1}J(N−F) in these molecules by 31, 22, 30, and 22 Hz, respectively. Figure 2 shows a plot of the SOPPA and EOM-CCSD one-bond coupling constants versus the experimental values. If the correlation between theory and experiment were perfect, the trendline would have a slope of 1.00, an intercept of 0.00 Hz, and a correlation coefficient of 1.00. The equations of the trendlines in Figure 2 are

$$^1\text{J(SOPPA)} = 1.12\ ^*{}^1\text{J(exptl)} + 2.34 \quad n = 10;\ R^2 = 1.000$$

$$^1\text{J(EOM-CCSD)} = 1.01\ ^*{}^1\text{J(exptl)} + 3.76 \quad n = 10;\ R^2 = 0.999$$

Both SOPPA and EOM-CCSD coupling constants correlate linearly with experimental data. Although the intercept of the SOPPA trendline is closer to 0.00 Hz, its greater slope can be traced to the tendency of SOPPA to overestimate the absolute values of the large one-bond C−F and N−F

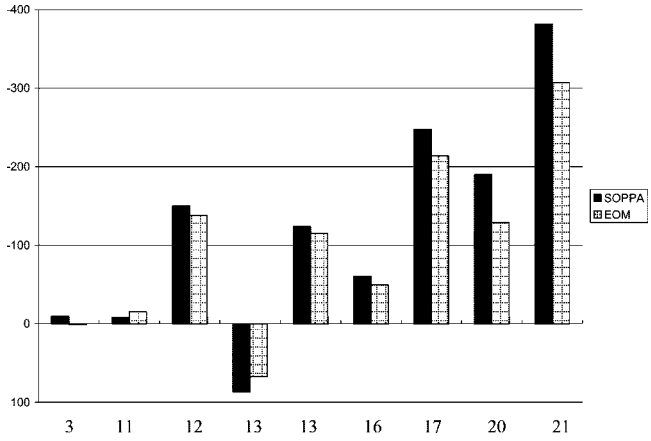

Figure 3. SOPPA and EOM-CCSD three-bond F−F coupling constants ^{3}J(F−F).

coupling constants. The slope of the EOM-CCSD trendline is very close to 1.00, which means that EOM-CCSD gives better agreement with experiment over the entire range of coupling constant values.

Three-Bond F−F Coupling Constants. The only three-bond couplings included in this study are F−F couplings. Figure 3 presents a bar graph showing the nine three-bond SOPPA and EOM-CCSD F−F coupling constants. ^{3}J(F−F) for **3** (FCCF) and **11** (*cis* HFC═CFH) are relatively small, with the absolute value of the SOPPA F−F coupling for **11** less than the EOM-CCSD value, but the EOM-CCSD coupling constants for both **3** and **11** are in better agreement with experiment. These small couplings result from competing contributions from negative PSO terms and positive FC and SD terms, as can be seen in Table S1. In a previous study,[18] it was shown that ^{3}J(F−F) for FCCF (**3**) is extremely sensitive to both C−C and C−F distances, and only at the experimental geometry do the computed EOM-CCSD and SOPPA coupling constants approach the experimental value.

Only ^{3}J(F−F) for *cis* F−F coupling in molecule **13** (F_2CCF_2) is positive, in which case the PSO and SD terms are both positive and the major contributors to J. The remaining six couplings are negative and dominated by large negative PSO terms. The absolute values of the SOPPA coupling constants are greater than the corresponding EOM-CCSD coupling constants, a reflection of the larger PSO terms. This difference is dramatic for F−F coupling in *cis* and *trans* FNNF (**20** and **21**). Experimental coupling constants are available for three of these seven molecules, and, in each case, the EOM-CCSD value is in better agreement with experiment, with SOPPA overestimating the experimental values by 18, 13, and 10 Hz, respectively, for **12** ("*trans*" FHC═CHF) and for "*cis*" and "*trans*" F−F couplings in **13** (F_2CCF_2).

Figure 4 presents plots of SOPPA and EOM-CCSD three-bond coupling constants ^{3}J(F−F) versus the experimental coupling constants. The equations of the trendlines are

$$^3\text{J(SOPPA)} = 1.13\ *{}^3\text{J(exptl)} + 1.66 \quad n = 5;\ R^2 = 0.991$$

$$^3\text{J(EOM-CCSD)} = 1.00\ *{}^3\text{J(exptl)} - 1.83 \quad n = 5;\ R^2 = 0.998$$

Once again, the slope of the EOM-CCSD trendline is significantly better than that of the SOPPA trendline.

Two-Bond X−F Coupling Constants. From the above analysis and ref 1, it is apparent that one- and three-bond SOPPA coupling constants in molecules with single, double, and triple bonds tend to have greater absolute values than EOM-CCSD coupling constants, with the latter in overall better agreement with experiment data, particularly for couplings involving F. However, the two-bond coupling constants do not fit this pattern. Figure 5 presents bar graphs comparing the EOM-CCSD and SOPPA values. The first 4 pairs are ^{2}J(C−F); pairs 5−8 are ^{2}J(F−F); and the remaining two are ^{2}J(N−F). It is apparent from Figure 5 that SOPPA and EOM-CCSD ^{2}J(C−F) and ^{2}J(N−F) values are quite similar. Nevertheless, the SOPPA values for molecules **3**, **20**, and **21** are closer to experiment than the EOM-CCSD values. Both SOPPA and EOM-CCSD overestimate ^{2}J(C−F) for FCCF by 9 and 12 Hz, respectively. Both underestimate the absolute values of ^{2}J(N−F) for "*cis*" FNNF by 6 and 8 Hz and for "*trans*" FNNF by 4 and 9 Hz, respectively. In contrast, EOM-CCSD overestimates ^{2}J(C−F) for "*cis*" FHC═CHF by only 3 Hz, while SOPPA overestimates it by 8 Hz.

The data for ^{2}J(F−F) do not fit a simple pattern. It is interesting to note that both levels of theory predict that ^{2}J(F−F) is positive for $F_2C{=}CH_2$ and $F_2C{=}CF_2$ but negative for $F_2C{=}NH$ and $F_2C{=}O$. This suggests that the sign of this two-bond coupling constant is influenced by whether or not the double bond is homonuclear or heteronuclear. That is, the presence of lone pairs of electrons on the remote atom of the double bond strongly influences the two-bond F−F coupling of the fluorines bonded to C. When ^{2}J(F−F) is positive, either PSO, FC, and SD terms are all positive ($F_2C{=}CF_2$), or positive FC and SD terms dominate the negative PSO term ($F_2C{=}CH_2$). For these two couplings, the EOM-CCSD values are greater than the SOPPA values, with the SOPPA values closer to experiment. SOPPA underestimates ^{2}J(F−F) for $F_2C{=}CH_2$ and $F_2C{=}CF_2$ by 9 and 2 Hz, respectively, while EOM-CCSD overestimates the experimental values by 13 and 10 Hz, respectively. In contrast, ^{2}J(F−F) values are negative for $F_2C{=}NH$ and $F_2C{=}O$ and are dominated by very large and negative PSO terms. The absolute values of the SOPPA coupling constants are greater than the EOM-CCSD. Only ^{2}J(F−F) for $F_2C{=}NH$ has been measured experimentally, and while EOM-CCSD overestimates its absolute value by 7 Hz, SOPPA overestimates it significantly by 34 Hz. Thus, while 5 of 7 SOPPA two-bond X−F coupling constants are in better agreement with experiment than EOM-CCSD, the differences between these two methods are relatively small except for $F_2C{=}NH$. This exception has a dramatic effect on the relationship between computed and experimental two-bond coupling constants, as illustrated in Figure 6. The equations of the trendlines are

$$^2\text{J(SOPPA)} = 1.055\ *{}^2\text{J(exptl)} - 2.82 \quad n = 7;\ R^2 = 0.954$$

$$^2\text{J(EOM-CCSD)} = 1.054\ *{}^2\text{J(exptl)} + 6.20 \quad n = 7;\ R^2 = 0.992$$

Thus, the two trendlines are parallel, and the intercept for the SOPPA data is closer to 0.0 Hz. However, as evident from Figure 6, the SOPPA point for $F_2C{=}NH$ lies far from

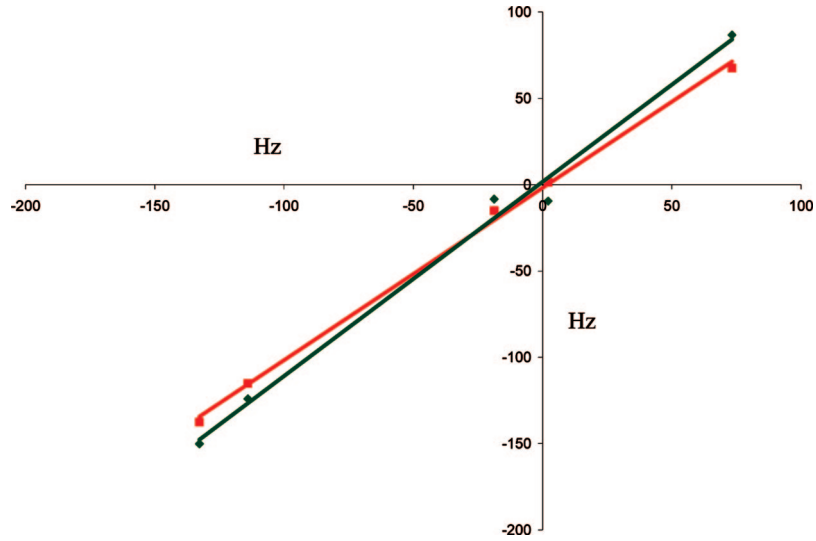

Figure 4. EOM-CCSD (■) and SOPPA (♦) three-bond coupling constants ^{3}J(F−F) plotted against the experimental values.

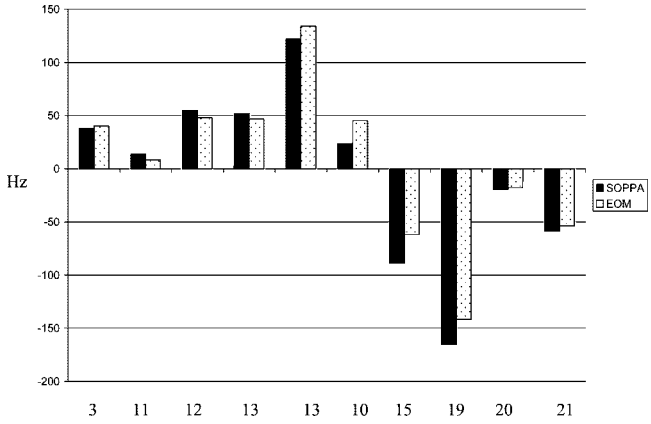

Figure 5. SOPPA and EOM-CCSD two-bond coupling constants. The first 4 pairs are ^{2}J(C−F); the next 4 are ^{2}J(F−F); and the final 2 pairs are ^{2}J(N−F).

the trendline and is responsible for the decrease in the correlation coefficient. Can this difference be attributed at least in part to the use of an optimized rather than an experimental geometry for this molecule? Why these two-bond coupling constants behave so differently is a subject for future study.

Statistical Analysis of One-, Two-, and Three-Bond Couplings. Figure 7shows a plot of SOPPA and EOM-CCSD coupling constants versus all of the experimental coupling constants reported in Table 1 and also includes the one-bond X−Y and X−F coupling constants from ref 1. It is obvious from the trendlines shown in Figure 7 that both SOPPA and EOM-CCSD coupling constants correlate linearly with the experimental coupling constants. The equations of the trendlines are

$$J(\text{SOPPA}) = (1.25 \pm 0.04)^* J(\text{exptl}) - (6.72 \pm 6.59)$$
$$n = 30;\ R^2 = 0.970;\ \text{RMS} = 35.8\ \text{Hz}$$

$$J(\text{EOM-CCSD}) = (1.02 \pm 0.01)^* J(\text{exptl}) + (2.41 \pm 1.84)$$
$$n = 30;\ R^2 = 0.996;\ \text{RMS} = 10.0\ \text{Hz}$$

As judged by the slope, intercept, and correlation coefficient, the agreement between theory and experiment is better at EOM-CCSD/(qzp,qz2p) than at SOPPA/(qzp,qz2p). The SOPPA coupling constant which lies farthest from the trendline is ^{1}J(F−O) for FOOF, which has a value of −690 Hz

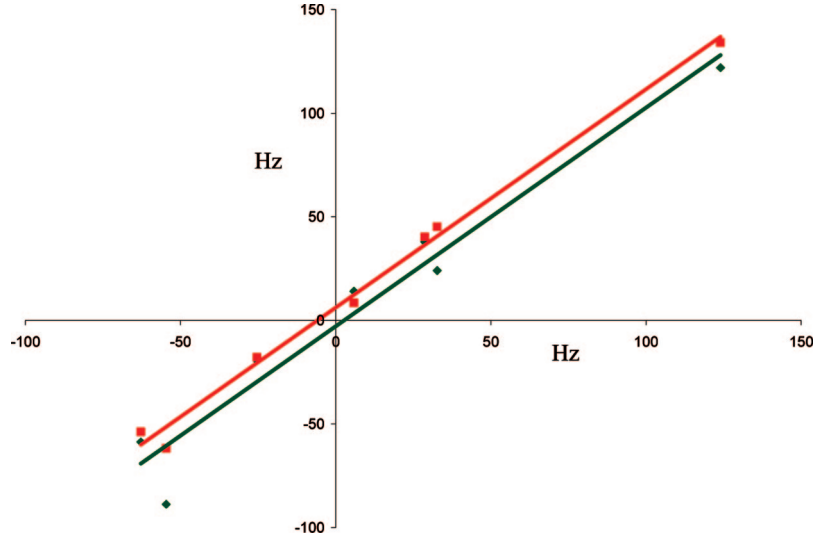

Figure 6. EOM-CCSD (■) and SOPPA (♦) two-bond coupling constants ^{2}J(X−F) plotted against the experimental values.

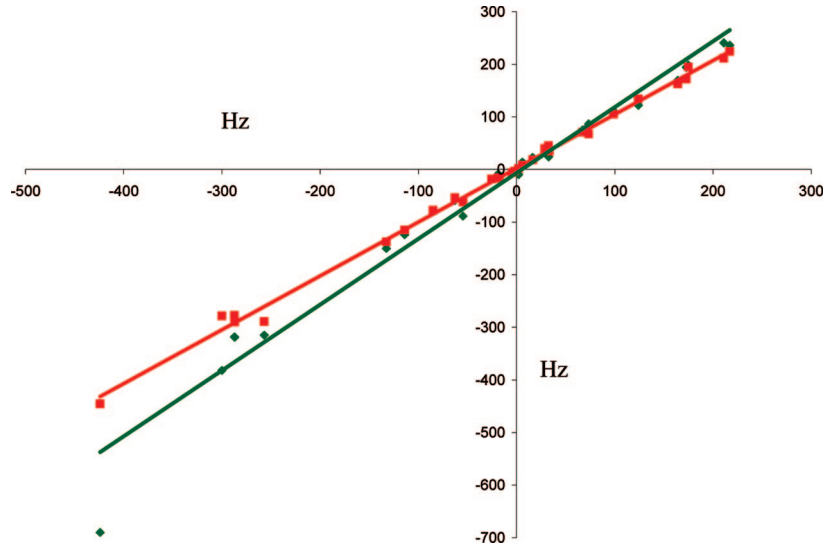

Figure 7. EOM-CCSD (■) and SOPPA (♦) one-, two-, and three-bond X−Y coupling constants plotted against the experimental values.

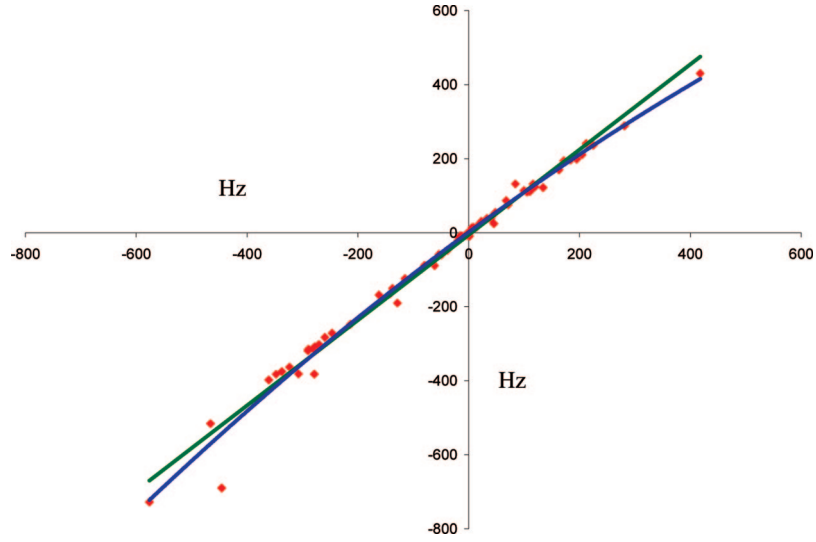

Figure 8. SOPPA vs EOM-CCSD one-, two-, and three-bond coupling constants showing first-order (green) and second-order (blue) trendlines.

and significantly overestimates the absolute value of the experimental coupling constant, −424 Hz. The EOM-CCSD value is −446 Hz. Removing this point significantly improves the SOPPA statistics, but the slope of the trendline still remains too high at 1.14. Once again, the greater slope for the SOPPA trendline results from the tendency of SOPPA to overestimate the absolute values of large one- and three-bond coupling constants which involve fluorine. Although it would be possible to present further statistics including percent errors and deviations, these are not very useful given the large range of values of coupling constants. For example, the percent error for ^{3}J(F−F) for FCCF is 33 and 352% at EOM-CCSD and SOPPA, respectively, but the differences between computed and experimental coupling constants are 0.7 and 7.4 Hz. On the other hand, SOPPA overestimates ^{1}J(C−F) for $F_2C{=}CH_2$ by 32 Hz, but the percent error is only 11%.

In our comparison between theory with experiment, there are some limitations in our treatment of the experimental data which should be noted. For some molecules more than one experimental value of a particular coupling constant has been reported, and we have used that one judged to be the most reliable. We have made no adjustments for uncertainties in the experimental assignments or for reported error bars. Finally, we have not taken into account the fact that the experimental coupling constants have been measured under different conditions, some in the gas phase and others in solution, and no adjustments have been made to account for possible interactions between the solute and the solvent.

Figure 8 presents a plot of SOPPA vs EOM-CCSD coupling constants for all one-, two-, and three-bond X−Y, X−F, and F−F couplings reported in this work and in ref 1. The equations of the first- and second-order trendlines are

$$\text{SOPPA} = 1.15 * \text{EOM} - 5.73 \quad n = 80;\ R^2 = 0.985$$

$$\text{SOPPA} = -0.0003 * \text{EOM}^2 + 1.10 * \text{EOM} + 1.60 \quad n = 80;\ R^2 = 0.989$$

Although the quadratic term has only a very small coefficient, this term becomes significant for large coupling constants and introduces curvature into the relationship between computed SOPPA and EOM-CCSD coupling constants. It

reflects primarily the tendency of SOPPA to overestimate large coupling constants involving F.

Conclusions

Ab initio EOM-CCSD/(qzp,qz2p) and SOPPA/(qzp/qz2p) calculations have been carried out to evaluate one-, two-, and three-bond coupling constants for molecules $H_mX{=}YH_n$ and $H_mX{\equiv}YH_n$ for X, Y = ^{13}C, ^{15}N, and ^{17}O and selected ^{19}F-substituted derivatives. The results of these calculations support the following statements.

1. ^{1}J(C−C) are always positive at the two levels of theory, whereas ^{1}J(C−N) are relatively small and either positive or negative. SOPPA and EOM-CCSD coupling constants are similar. One-bond coupling constants ^{1}J(C−O) are always positive, whereas ^{1}J(N−N) and ^{1}J(N−O) are negative, in violation of the Dirac Vector Model which states that reduced one-bond coupling constants are positive. The EOM-CCSD coupling constants are usually in better agreement with experiment.

2. All one-bond C−F coupling constants are negative, and all one-bond N−F coupling constants are positive, once again violating the Dirac Vector Model. The absolute values of the SOPPA coupling constants are greater than the EOM-CCSD values, with the latter in better agreement with experimental data. As observed previously, SOPPA tends to overestimate the absolute values of large one-bond couplings involving ^{19}F.

3. Three-bond coupling constants ^{3}J(F−F) are usually larger in absolute value when evaluated at SOPPA compared to EOM-CCSD, a result of larger contributions from the PSO terms. In all cases, the three-bond EOM-CCSD coupling constants are in better agreement with experimental data.

4. There is no simple identifiable pattern for the relationship between SOPPA and EOM-CCSD two-bond coupling constants. For the majority of these, SOPPA is in better agreement with experiment, although the differences between the computed EOM-CCSD values and experimental values are not dramatic. However, SOPPA significantly overestimates the absolute value of ^{2}J(F−F) for $F_2C{=}NH$.

5. A statistical analysis of 30 EOM-CCSD/(qzp/qz2p) and SOPPA/(qzp,qz2p) coupling constants versus experimental one-, two-, and three-bond coupling constants demonstrates that better agreement with experiment is found when EOM-CCSD is used as the computational method.

It is well-known that the performance of any given method for the calculation of coupling constants depends on the quality of the method, the geometry, and the basis set used for the calculations. Since SOPPA does give reasonable values for many coupling constants, a question for future study is whether the performance of SOPPA can be systematically improved, particularly for couplings involving fluorine, if a different basis set were used for the calculations. Some studies of the basis sets used for SOPPA calculations have been reported.[23,36a,37] A systematic basis-set dependence investigation of the SOPPA coupling constants presented in this paper which identified an optimal basis set would be of immense value, allowing this method to be applied with confidence to much larger molecules of interest to both theorists and experimentalists.

Acknowledgment. Thanks are given to the Ohio Supercomputer Center for continuing computational support and to CTI (CSIC) for an allocation of computer time. This work was carried out with financial support from the Ministerio de Educacion y Ciencia (Project No. CTQ2007-61901/BQU) and Comunidad Autónoma de Madrid (Project MADRISOLAR, ref S-0505/PPQ/0225).

Supporting Information Available: SOPPA and EOM-CCSD PSO, DSO, FC, and SD components of J for all molecules investigated in this study and full references for refs 32, 33, and 34. This material is available free of charge via the Internet at http://pubs.acs.org.

References

(1) Del Bene, J. E.; Alkorta, I.; Elguero, J. A systematic comparison of second-order polarization propagator approximation (SOPPA) and equation-of-motion coupled cluster singles and doubles (EOM-CCSD) spin-spin coupling constants for selected singly-bonded molecules, and the hydrides NH_3, H_2O, and HF and their protonated and deprotonated ions and hydrogen-bonded complexes. *J. Chem. Theory Comput.* **2008**, *4*, 967.

(2) Pople, J. A.; Binkley, J. S.; Seeger, R. Theoretical models incorporating electron correlation. *Int. J. Quantum Chem. Quantum Chem. Symp.* **1976**, *10*, 1.

(3) Krishnan, R.; Pople, J. A. Approximate fourth-order perturbation theory of the electron correlation energy. *Int. J. Quantum Chem.* **1978**, *14*, 91.

(4) Bartlett, R. J.; Silver, D. M. Many-body perturbation theory applied to electron pair correlation energies. I. Closed-shell first-row diatomic hydrides. *J. Chem. Phys.* **1975**, *62*, 3258.

(5) Bartlett, R. J.; Purvis, G. D. Many-body perturbation theory, coupled-pair many-electron theory, and the importance of quadruple excitations for the correlation problem. *Int. J. Quantum Chem.* **1978**, *14*, 561.

(6) Hehre, W. J.; Ditchfield, R.; Pople, J. A. Self-consistent molecular orbital methods. XII. Further extensions of Gaussian-type basis sets for use in molecular orbital studies of organic molecules. *J. Chem. Phys.* **1982**, *56*, 2257.

(7) Hariharan, P. C.; Pople, J. A. The influence of polarization functions on molecular orbital hydrogenation energies. *Theor. Chim. Acta* **1973**, *28*, 213.

(8) Spitznagel, G. W.; Clark, T.; Chandrasekhar, J.; Schleyer, P. v. R. Stabilization of methyl anions by first-row substituents. The superiority of diffuse function-augmented basis sets for anion calculations. *J. Comput. Chem.* **1982**, *3*, 363.

(9) Clark, T.; Chandrasekhar, J.; Spitznagel, G. W.; Schleyer, P. v. R. Efficient diffuse function-augmented basis sets for anion calculations. III. The 3−21+G basis set for first-row elements, Li-F. *J. Comput. Chem.* **1983**, *4*, 294.

(10) Harmony, M. D.; Laurie, V. W.; Kuczkowski, R. L.; Schwendeman, R. H.; Ramsay, D. A.; Lovas, F. J.; Lafferty, W. J.; Maki, A. G. Molecular structures of gas-phase polyatomic molecules determined by spectroscopic methods. *J. Phys. Chem. Ref. Data* **1979**, *8*, 619.

(11) Bürger, H.; Schneider, W.; Sommer, S.; Thiel, W.; Willner, H. The vibrational spectrum and rotational constants of difluoroethyne FCCF. Matrix and high resolution infrared studies and *ab initio* calculations. *J. Chem. Phys.* **1991**, *95*, 5660.

(12) Herzberg, G. *Electronic spectra and electronic structure of polyatomic molecules*; Van Nostrand: New York, 1966; pp 629, 631, 640.

(13) Sverdlov, L. M.; Kovner, M. A.; Krainov, E. P. *Vibrational spectra of polyatomic molecules*; Wiley: New York, 1974; p 427.

(14) Laurie, V. W.; Pence, D. T. *J. Chem. Phys.* **1963**, *38*, 2693.

(15) Bohn, R. K.; Bauer, S. H. An electron diffraction study of the structures of *cis*-and *trans*-N_2F_2. *Inorg. Chem.* **1967**, *6*, 309.

(16) Stothers, J. B. *Carbon-13 NMR Spectroscopy*; Academic Press: New York, 1972; pp 370, 375.

(17) Bürger, H.; Sommer, S. Isolation, characterization and some properties of free difluoroethyne, FC≡CF. *J. Chem. Soc., Chem. Commun.* **1991**, 456.

(18) Del Bene, J. E.; Provasi, P.; Alkorta, I.; Elguero, J. Resolving an apparent discrepancy between theory and experiment: Spin-spin coupling constants for FCCF. *Magn. Reson. Chem.* **2008**, *46*, 1003.

(19) Berger, S.; Braun, S. Kalinowski, H.-O. *NMR Spectroscopy of the Non-Metallic Elements*; John Wiley & Sons: Chichester, 1997; pp 274, 277, 386, 636, 646.

(20) Kalinowski, H.-O.; Berger, S.; Braun, S. *Carbon-13 NMR Spectroscopy*; John Wiley & Sons: Chichester, 1988; pp 550, 579.

(21) Jackowski, K.; Wilczek, M.; Pecul, M.; Sadlej, J. Nuclear magnetic shielding and spin-spin coupling of 1,2-^{13}C-enriched acetylene in gaseous mixtures with xenon and carbon dioxide. *J. Phys. Chem. A* **2000**, *104*, 5955.

(22) (a) Ruden, T. A.; Lutnæs, O. B.; Helgaker, T.; Ruud, K. Vibrational corrections to indirect nuclear spin-spin coupling constants calculated by density-functional theory. *J. Chem. Phys.* **2003**, *118*, 9572. (b) Ruden, T. A.; Helgaker, T.; Jaszunski, M. The NMR indirect nuclear spin-spin coupling constants for some small rigid hydrocarbons: molecular equilibrium values and vibrational corrections. *Chem. Phys.* **2004**, *296*, 53. (c) Ruden, T. A.; Ruud, K. Ro-vibrational corrections to NMR parameters. In *Calculation of NMR and EPR Parameters*; Kaupp, M., Bühl, M., Malkin, V. G., Eds.; Wiley-VCH: Weinheim, 2004; p 153. (d) Helgaker, T.; Jaszuński, M.; Pecul, M. The quantum-chemical calculation of NMR indirect spin-spin coupling constants. *Prog. Nucl. Magn. Reson. Spectrosc.* **2008**, *53*, 249.

(23) Enevoldsen, T.; Oddershede, J.; Sauer, S. P. A. Correlated calculations of indirect nuclear spin-spin coupling constants using second-order polarization propagator approximations: SOPPA and SOPPA(CCSD). *Theor. Chem. Acc.* **1998**, *100*, 275.

(24) (a) Geertsen, J.; Oddershede, J.; Scuseria, G. E. Spin-spin coupling constants of CO and N_2. *J. Chem. Phys.* **1987**, *87*, 2138. (b) Oddershede, J.; Geertsen, J.; Scuseria, G. E. Nuclear spin-spin coupling constant of HD. *J. Phys. Chem.* **1988**, *92*, 3056.

(25) (a) Nielsen, E. S.; Jørgensen, P.; Oddershede, J. Transition moments and dynamic polarizabilities in a second order polarization propagator approach. *J. Chem. Phys.* **1980**, *73*, 6238. (b) Oddershede, J.; Jørgensen, P.; Yeager, D. L. Polarization Propagator Methods in Atomic and Molecular Calculations. *Comp. Phys. Rep.* **1984**, *2*, 33.

(26) Packer, M. J.; Dalskov, E. K.; Enevoldsen, T.; Jensen, H. J. Aa.; Oddershede, J. A new implementation of the second-order polarization propagator approximation (SOPPA): The excitation spectra of benzene and naphthalene. *J. Chem. Phys.* **1996**, *105*, 5886.

(27) Dalskov, E. K.; Sauer, S. P. A. Correlated, static and dynamic polarizabilities of small molecules. Comparison of four "Black Box" methods. *J. Phys. Chem. A* **1998**, *102*, 5269.

(28) Perera, S. A.; Sekino, H.; Bartlett, R. J. Coupled-cluster calculations of indirect nuclear coupling constants: The importance of non-Fermi contact contributions. *J. Chem. Phys.* **1994**, *101*, 2186.

(29) Perera, S. A.; Nooijen, M.; Bartlett, R. J. Electron correlation effects on the theoretical calculation of nuclear magnetic resonance spin-spin coupling constants. *J. Chem. Phys.* **1996**, *104*, 3290.

(30) Schäfer, A.; Horn, H.; Ahlrichs, R. Fully optimized contracted Gaussian basis sets for atoms Li to Kr. *J. Chem. Phys.* **1992**, *97*, 2571.

(31) (a) Gauss, J.; Stanton, J. F. Electron-correlated methods for the calculation of NMR chemical shifts. In *Calculation of NMR and EPR Parameters*; Kaupp, M., Bühl, M., Malkin, V. G., Eds.; Wiley-VCH: Weinheim, 2004; p 153. (b) Sauer, S. P. A.; Paidarová, I. Correlated linear response calculations of the C6 dispersion coefficients of hydrogen halides. *Comput. Lett.* **2007**, *3*, 399.

(32) Frisch, M. J.; et al. *Gaussian 03*; Gaussian, Inc.: Wallingford, CT, 2004.

(33) Angeli, C. et al. *DALTON, a molecular electronic structural program, Release 2.0*; 2005. http://www.kjemi.uio.no/software/dalton/dalton.html (accessed Oct 16, 2006).

(34) Stanton, J. F.; et al. *ACES II, a program product of the Quantum Theory Project*; University of Florida: Gainesville, FL.

(35) Lynden-Bell, R. M.; Harris, R. K. *Nuclear Magnetic Resonance Spectroscopy*. Appleton Century Crofts: New York, 1969.

(36) (a) Provasi, P. F.; Aucar, G. A.; Sauer, S. P. A. The effect of lone pairs and electronegativity on the indirect nuclear spin-spin coupling constants in CH_2X (X = CH_2, NH, O, S): Ab initio calculations using optimized contracted basis sets. *J. Chem. Phys.* **2001**, *115*, 1324. (b) Barone, V.; Peralta, J. E.; Contreras, R. H.; Sosnin, A. V.; Krivdin, L. B. Natural J coupling (NJC) analysis of the electron lone pair effect on NMR couplings: Part 1. The lone pair orientation effect. *Magn. Reson. Chem.* **2001**, *39*, 600. (c) Wu, A.; Cremer, D. Analysis of multipath transmission of spin-spin coupling constants in cyclic compounds with the help of partially spin-polarized orbital contributions. *Phys. Chem. Chem. Phys.* **2003**, *5*, 4541. (d) Pecul, M.; Helgaker, T. The spin-spin coupling constants in ethane, methanol and methylamine: A comparison of DFT, MCSCF and CCSD results. *Int. J. Mol. Sci.* **2003**, *4*, 143. (e) Rusakov, Y. Y.; Krivdin, L. B.; Schmidt, E. Y.; Mikhaleva, A. I.; Trofimov, B. A. Nonempirical calculations of NMR indirect spin-spin coupling constants. Part 15: Pyrrolylpyridines. *Magn. Reson. Chem.* **2006**, *44*, 692.

(37) (a) Christiansen, O.; Koch, H.; Jørgensen, P.; Helgaker, T. Integral direct calculation of CC2 excitation energies: singlet excited states of benzene. *Chem. Phys. Lett.* **1996**, *263*, 530. (b) Cybulski, H.; Pecul, M.; Sadlej, J. On the calculation of nuclear spin-spin coupling constants in small water clusters. *Chem. Phys.* **2006**, *326*, 431.

CT800321B

JCTC Journal of Chemical Theory and Computation

Dissociative Electron Attachment to Formamide: Direct and Indirect Pathways from Resonant Intermediates

T. P. M. Goumans,[†] F. A. Gianturco,*[,‡] F. Sebastianelli,[‡] I. Baccarelli,[§] and J. L. Rivail[||]

Department of Chemistry, University College London, 20 Gordon Street, London WC1H 0AJ, United Kingdom, Department of Chemistry and CNISM, University of Rome La Sapienza, Piazzale A. Moro 5, 00185 Rome, Italy SuperComputing Center CASPUR, via dei Tizii 6, 00185 Rome, Italy, and Laboratoire de Chimie Theorique, Université Henri Poincare, F54506 Vandoeuvre-les-Nancy, France

Received September 9, 2008

Abstract: Dissociative electron attachment (DEA) to formamide ($HCONH_2$), the smallest molecule with a peptide bond, is investigated with electron-molecule scattering calculations. At the equilibrium geometry we identify two resonances of A″ and A′ symmetry at 3.77 and 14.90 eV, respectively. To further assess potential bond-breaking pathways for the transient negative ions (TNIs), the behavior of the resonances upon bond stretching of the C−H and C−N bond is investigated. While along the C−H dissociation coordinate neither resonance changes significantly, we find instead that both resonances are stabilized upon stretching the peptide C−N bond, with their resonance energy and width coming down rapidly, most strongly so for the A′ resonance. The A′ resonance is thus seen to disappear when the C−N bond is stretched for more than 1 Å, where it presumably smoothly connects to a bound anion state, a direct DEA pathway for the A′ TNI to yield NH_2^- and HCO. The A″ resonance is found instead not to be purely dissociative along the C−N coordinate but to evolve into forming a low-lying resonance on the NH_2 fragment. Furthermore, symmetry considerations dictate here that the incoming electron attaches itself to an orbital of A′ symmetry of the NH_2^- and HCO asymptotic fragments. Therefore, DEA from the A″ TNI has to occur via a symmetry-breaking, nonadiabatic curve crossing which connects to the purely dissociative A′ metastable anionic state that is coming down in energy as the bond stretching occurs.

1. Introduction

The chemistry of low-energy electrons (LEEs) is currently actively investigated in view of its important role in radiation-induced damage to biomolecules[1−14] and in the processing of interstellar ices by cosmic rays.[15−23] The primary ionizing events are known to generate large amount of secondary electrons in the range of 0−20 eV[24] which can then resonantly attach themselves to molecular targets and yield formation of transient negative ions (TNIs). The energized TNI, in turn, could either evolve by autodetaching the extra electron or could dispose of the excess energy within its molecular framework, a path which may ultimately lead to rupture of a chemical bond within the target: this process, yielding a stable anion and a radical fragment, is known as dissociative electron attachment (DEA). Here we study the resonances of formamide and its potential DEA pathways by using electron-molecule quantum scattering calculations. With similar methods, DEA processes in glycine,[11] uracil,[3] and formic acid[4] have been studied, while quantum dynamics coupled to quantum chemistry calculations have been used to study DEA in the sugar-DNA backbone.[5]

* Corresponding author e-mail: fa.gianturco@caspur.it.
[†] University College London.
[‡] University of Rome La Sapienza.
[§] SuperComputing Center CASPUR.
[||] Université Henri Poincare.

10.1021/ct800379h CCC: $40.75 © 2009 American Chemical Society
Published on Web 12/05/2008

Formamide is the smallest molecule with a peptide bond and has two resonance structures that give the C−N bond partial double bond character with a planarized nitrogen atom.[25,26] Formamide is observed in the interstellar medium, in star-forming regions[27−31] and in the comet Hale-Bopp[32] and has been suggested as a potential biological precursor because it forms nucleobases in the present of oxides when UV-irradiated[33] or heated.[34] The processing of pure thin-film formamide ices has also been studied with low-energy electrons[35] and keV protons.[36] From anion-desorption studies of thin films of 1d-formamide on platinum Cloutier et al. conclude that H^- dissociates from the NH_2-group from a core-excited resonance (two-particle one-hole state) at ∼8 eV[35] but have not studied how the ice itself is processed. Brucato et al. report the formation of CO, CO_2, N_2O, HNCO, and $NH_4^+OCN^-$ from irradiation of thin films of formamide on a silicon substrate with 200 keV protons,[36] which presumably results from the interaction of secondary low-energy electrons with the solid formamide.

Here we study the behavior of shape-resonances in gaseous formamide upon the stretching of the H−N, C−H, and C−N bonds to identify potential dissociative electron attachment pathways in the title molecule and to unravel possible energy deposition mechanisms.

2. The Computational Approach

The molecular quantum dynamical method we use in this study has been described in much detail previously;[37−39] therefore we give here only a short outline of it. The elastic electron-molecule scattering process is described within the fixed-nuclei approximation,[38] and the antisymmetrized scattering (electron + molecule) wave function is expanded from the Hartree−Fock (HF) orbitals of the neutral ground-state species, where the N electrons of the molecule target maintain their ground-state configuration during the scattering process, i.e. no core-excited resonances are considered. The scattering equations, orbitals, and potentials are expanded in a set of symmetry-adapted angular functions around the center of mass[38,39] and over a numerical radial grid out to the asymptotic region. The electron-molecule interaction potential is modeled by replacing the exact nonlocal exchange potential by an energy-dependent local potential, the Hara free-electron gas exchange,[40] and the correlation potential by the Perdew−Zunger potential.[41] Inclusion of a long-range polarization term changed very little the resonance results at the equilibrium geometry of formamide (see section 3.1). This is an expected behavior[11] since such transient state formations are clearly dominated by short-range correlation effects, and even more so when molecules with permanent dipole moments are considered. We can thus simplify the modeling of the interaction potential by neglecting the long-range polarization term.

Geometry optimizations and the potential energies of the neutral species along the bond-stretching coordinates have been calculated at the B3LYP/6−311+G** level with Gaussian03,[42] while the HF/6−311+G** orbitals are used for the scattering calculations. Elastic cross-sections and poles of the S-matrix have been calculated within A′ and A″ symmetry with the ePolyScat program,[43] at the equilibrium geometry and at geometries where one of the bonds was stretched while all other bond lengths and angles have been held fixed, thus providing a pseudo-one-dimensional picture of the multidimensional Intramolecular Vibrational Redistribution (IVR) process as triggered by the resonant electron dynamics. For the S-matrix calculations we expanded the wave function with a maximum angular momentum value of 50, and a maximum of 14 partial waves was used for the scattering electron expansion within the piecewise diabatic representation. Increasing either values of the maximum angular momentum had no significant effect on the final results.

3. Scattering Results

3.1. Equilibrium Geometry. By searching for poles of the S-matrix in the complex plane, we find that, at the equilibrium geometry, two shape-resonances are deemed to be physically realistic, one for each symmetry. The A′ resonance is at 14.90 eV and is very broad (with a hwhm of 2.08 eV), while the lower-lying A″ resonance (3.77 eV) is much narrower (hwhm 0.52 eV). As in ref 11, also in the present case we checked the validity of our assumption concerning the negligibility of the long-range polarizability effects on the resonances' parameters. Hence, we repeated the calculations for the A″ resonance at the equilibrium geometry by including the long-range part of the electron-molecule interaction. The spherical polarizability of the formamide employed in our calculations (25.30 $Bohr^3$) was calculated at the same level of theory used to describe the ground-state of the neutral target (i.e., B3LYP/6311+G**) and produced a value for the position of the π^* resonance shifted to higher energies by 0.008 eV. Such negligible shift confirms, once again, the validity of our assumption regarding the nature of the scattering potential which is responsible of the formation of transient anions. Hence, all the calculations at different nuclear geometries, discussed in the following section, do not include the long-range polarization interaction.

Our calculated A″ resonance is almost 2 eV higher in energy than the one resonant feature determined by electron transmission spectroscopy (2.05 eV, fwhm 0.82 eV).[44] This discrepancy is most likely due to uncertainties in the measurements as well as inaccuracies in our calculations (fixed-nuclei approximation, model exchange interaction, localized correlation effects). Analysis of the piecewise adiabatic potential shows that the incoming electron is trapped by an $l = 2$ centrifugal barrier in the A″ resonance and is therefore classified as a d π-resonance. The resonant wave function (depicted in Figure 1) has a nodal plane between the C−N and C−H bonds, which suggest possible cleavage of these bonds as a potential dissociative electron attachment pathway.[37] Because Cloutier et al. observe H^- fragments from the NH_2 group upon low-energy electron impact, we also consider N−H rupture, even though this process was there surmised to stem from a core-excited resonance without any further support for its occurrence and could also be heavily influenced by the metal substrate as well as other solid-state effects.[35] The corresponding spatial depiction of the broader

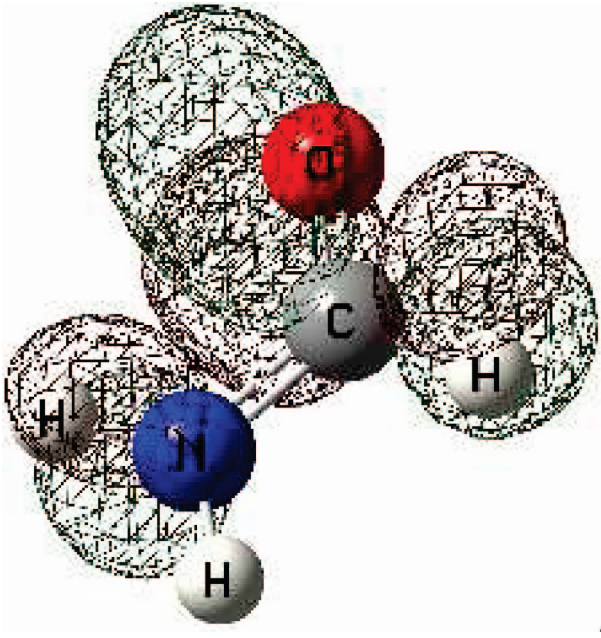

Figure 1. Mesh representation of A″ resonant wave function at the formamide equilibrium geometry.

Figure 2. Mesh representation of A′ resonant wave function at the formamide equilibrium geometry.

A′ resonance at higher energies (around 14 eV) is reported in Figure 2. We see there again the presence of an antibonding plane across the C−N bond and the additional presence of extra-electron densities above and below the C and the N atoms.

3.2. Stretching of the C−H and N−H Bonds. We carried out additional calculations, not reported here for the sake of brevity, which clearly showed that neither of the shape resonances changes much its location and width when either of the N−H bonds is stretched. More precisely, both resonances move slightly higher in energy, which excludes N−H bond stretching as a favorable pathway for transferring the excess energy of the TNI into the nuclear network. These results are in agreement with the proposal that the resonance at 8 eV giving rise to DEA by N−H bond rupture is not originating from a shape resonance but probably from some other mechanism.[35] On the other hand, upon stretching of the C−H bond both the A′ and A″ resonances decrease very gradually in energy (∼0.1 eV per 0.1 Å) when the bond is stretched beyond 0.1 Å. The energy is here with respect to the neutral species electronic energy taken to be the reference value. However, since the potential energy curve for the neutral species (see Figure 3) increases much more steeply than the actual resonance energy component decreases, C−H bond breaking is also surmised to be an unfavorable pathway for DEA processes which originate from the present shape resonances as intermediate anionic states: the overall anion electronic energy, in fact, increases as that bond is stretched.

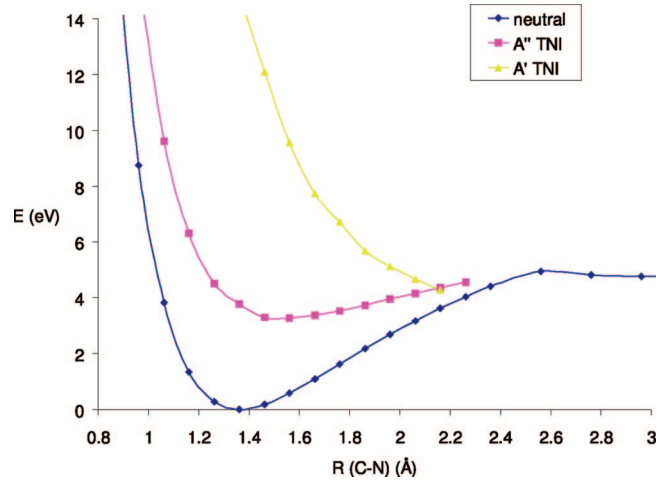

Figure 3. Electronic energy changes of formamide for the neutral and the two TNIs resonant states along the C−N stretching coordinate.

3.3. Stretching of the C−N Bonds. Our further calculations clearly show, however, that both A′ and A″ resonances are stabilized by the stretching of the central peptide bond. They quickly, and consistently, become lower in energy and more sharp (i.e., longer-lived) when the C−N bond is stretched from the equilibrium value of 1.306 Å, while compressing the C−N bond renders the resonances higher in energy and less stable, thereby making the electron-detachment path more likely to occur before energy redistribution within the nuclear network. To investigate the plausibility of C−N bond breaking as a potential pathway for DEA evolution of the TNIs, we followed the poles of the resonances until they disappeared, indicating formation of a stable anion. In Figure 3, we plot the energies of the neutral species and the A′ and A″ TNIs along the C−N stretching coordinate. The energies of the TNIs at every geometry are calculated as the sum of the neutral species (at the B3LYP/6−311+G** level) and the resonance energy:

$$E_{TNI}(R) = E_{res}(R) + E_{neutral}(R) - E(R_{eq}) \qquad (1)$$

We see in the figure that the higher-energy A′ resonance gets stabilized much more markedly as we stretch the bond than does the A″ resonance, a finding which makes the C−N stretching deformation a very efficient process for the transfer of the excess energy of the resonantly attached A′ electron (14.9 eV) into the resulting fragments, although the short-lived TNI still has to compete with flux-losses into the electron autodetachment channel. When the C−N bond is

stretched by 0.8 Åout to 2.106 Å, the A′ resonance (0.64 eV, hwhm 0.27 eV) has even become lower in energy than the A″ resonance (0.74 eV, hwhm 0.02 eV). Further stretching leads to a disappearance of the A′ resonance which indicates the formation of a stable anion. This feature is indicated in our calculations by the fact that the pole of the Scattering Matrix (S-matrix) locating the resonance now moves on the negative branch of the real energy axis and very close to it. Indeed we see in the figure that, when looking at the B3LYP/6−311+G** level of calculations for the neutral species reported by diamonds in the figure, the anion of A′ symmetry would proceed to become more stable than the neutral species when the C−N bond is stretched beyond 2.2 Å. We also find that the excess electron gets localized on the NH_2 fragment, indicating HCO + NH_2^- as the likely DEA pathway of fragmentation. To obtain the actual crossing in Figure 3, however, we would need additional, separate calculations of the new bound (N+1) electron system within that range of geometries using conventional quantum chemistry codes, a test which is outside the scope of the present work and would not add to our analysis of the DEA processes as stabilizing mechanisms for resonant states.

One should further note here that, while the A″ resonance gets also stabilized by C−N bond stretching, it does not disappear now into a bound state of the (N+1) electrons system for large C−N distances but rather evolves into a low-energy resonant state that localizes the excess electron onto the NH_2 fragment. Because the excess electron has to attach itself to an orbital of A′ symmetry in the asymptotic HCO + NH_2^- channel, we see that the A″ TNI does not give rise to a direct DEA process: instead the existing TNI has to couple to the now nearby, fully dissociative A′ potential curve by symmetry-breaking (e.g., pyramidalization of the NH_2 group) in order to further proceed along a dissociative pathway. Our present calculations show that the two TNI curves are now crossing each other around 2.15 Å (Figure 3) at an energy of ∼4.3 eV above the ground-state energy of the neutral formamide. Therefore our dynamical modeling suggests here that for the 3.77 eV A″ resonance to yield HCO + NH_2^- via an indirect DEA pathway it must cross the A′ curve at a C−N distance of 2.15 Å, where the crossing will occur with an energy of ∼0.5 eV in excess of the resonance energy. Thus, the complex anion must therefore undergo a multidimensional IVR rearrangement before reaching the symmetry-breaking conical intersection that will yield the NH_2^- fragment.

4. Discussion

Using realistic quantum scattering calculations, we have identified a direct (14.90 eV) and an indirect (3.77 eV) DEA pathways which could be followed by the fragmentation of gas phase formamide to yield HCO + NH_2^-. Our calculations also show that a dissociation of the H−C or the N−H bonds constitutes an unfavorable process for both TNIs observed in this system. The 3.77 eV shape resonance identified in our scattering calculations turns out to be located at a higher energy than the experimentally determined value of 2.05 eV (electron transmission spectroscopy),[44] which is an indication that the true resonance is probably somewhere in between and that the indirect DEA pathway is also likely to be unfavored because of the sizable amount of excess energy needed to reach the seam where the A′ and A″ anion curves cross and can therefore optimally undergo nonadiabatic coupling.

Low-energy electron irradiation of thin films of solid 1d-formamide has established that mainly H^- anions desorb into the gas phase, resulting from N−H bond dissociation from a core-excited resonance around 8 eV.[35] However, that experiment would not detect any NH_2^- fragments that would have been formed by the shape-resonances around 3.8 and 15 eV and get trapped in the bulk since none of the products in the processed ice is experimentally determined. Likewise, our technique cannot be applied to identify possible core-excited resonances so we cannot uniquely establish whether or not the N−H formation is a plausible pathway for DEA processes originating from 8 eV low-energy electrons. Furthermore, since the solid matrix could considerably affect the position of the resonances by altering the permittivity and the geometries of the physisorbed species, and we have shown here that a small stretching of the C−N bond could already have a large effect on the position of the A′ resonance (Figure 3), it is not at all clear that the feature around 8 eV seen experimentally actually occurs from molecules in their ground vibrational states and not from a lowering of the A′ resonance due to some vibrational excitation effect.

Brucato et al. have identified several new molecules upon 200 keV proton irradiation of frozen formamide.[36] Since both products that appear to stem from C−N rupture (CO, CO_2) and from N−H rupture (HNCO, OCN^-) are observed, it could be argued that the secondary low-energy electrons generated in that process are actually producing both DEA processes. A detailed gas phase scattering study of formamide could shed more light on whether indeed fragmentation paths to NH_2^- + HCO take place from the high-energy (15 eV) and low-energy (3.7 eV) shape-resonances via the direct and indirect mechanisms which our calculations suggest. It is, in any event, of interest to have been able to argue purely from quantum calculations the likely presence of two possible, and distinct, molecular mechanisms that can lead to electron-induced fragmentation processes in gas phase formamide.

Acknowledgment. The work has been performed under the Project HPC-EUROPA++ project (project number: 211437), with the support of the European Community - Research Infrastructure Action of the FP7 "Coordination and support action" Programme. We also thank the CASPUR Supercomputing Consortium for computational support. The EPSRC is acknowledged for a postdoctoral fellowship for T.P.M.G. (EP/D500524), while the financial support of the University of Rome Research Committee is also acknowledged for the present research.

References

(1) Boudaiffa, B.; Cloutier, P.; Hunting, D.; Huels, M. A.; Sanche, L. *Science* **2000**, *287*, 1658–1660.

(2) Sabin, J. R. Theoretical studies of the Interaction of Radiation with Biomolecules In *Advances in Quantum Chemistry*; Brändas, E., Sabin, J. R., Eds.; Elsevier: Amsterdam, 2007; Vol. 52, pp 1−3.

(3) Gianturco, F. A.; Sebastianelli, F.; Lucchese, R. R.; Baccarelli, I.; Sanna, N. *J. Chem. Phys.* **2008**, *128*, 174302.

(4) Rescigno, T. N.; Trevisan, C. S.; Orel, A. E. *Phys. Rev. Lett.* **2006**, *96*, 213201.

(5) Simons, J. *Acc. Chem. Res.* **2006**, *39*, 772–779.

(6) Balog, R.; Langer, J.; Gohlke, S.; Stano, M.; Abdoul-Carime, H.; Illenberger, E. *Int. J. Mass Spectrom.* **2004**, *233*, 267–291.

(7) Sanche, L. *Mass Spectrom. Rev.* **2002**, *21*, 349–369.

(8) Ingolfsson, O.; Weik, F.; Illenberger, E. *Int. J. Mass Spectrom. Ion Processes* **1996**, *155*, 1–68.

(9) Sanche, L. *Eur. Phys. J. D* **2005**, *35*, 367–390.

(10) Baccarelli, I.; Gianturco, F. A.; Grandi, A.; Sanna, N.; Lucchese, R. R.; Bald, I.; Kopyra, J.; Illenberger, E. *J. Am. Chem. Soc.* **2007**, *129*, 6269–6277.

(11) Baccarelli, I.; Grandi, A.; Gianturco, F. A.; Lucchese, R. R.; Sanna, N. *J. Phys. Chem. B* **2006**, *110*, 26240–26247.

(12) Gianturco, F. A.; Lucchese, R. R. *J. Chem. Phys.* **2004**, *120*, 7446–7455.

(13) Anusiewicz, I.; Sobczyk, M.; Berdys-Kochanska, J.; Skurski, P.; Simons, J. *J. Phys. Chem. A* **2005**, *109*, 484–492.

(14) Chipman, D. M. *J. Chem. Phys.* **2007**, *127*, 194309.

(15) Lafosse, A.; Bertin, M.; Domaracka, A.; Pliszka, D.; Illenberger, E.; Azria, R. *Phys. Chem. Chem. Phys.* **2006**, *8*, 5564–5568.

(16) Sedlacko, T.; Balog, R.; Lafosse, A.; Stano, M.; Matejcik, S.; Azria, R.; Illenberger, E. *Phys. Chem. Chem. Phys.* **2005**, *7*, 1277–1282.

(17) Bennett, C. J.; Kaiser, R. I. *Astrophys. J.* **2007**, *661*, 899–909.

(18) Bennett, C. J.; Kaiser, R. I. *Astrophys. J.* **2007**, *660*, 1289–1295.

(19) Bennett, C. J.; Chen, S. H.; Sun, B. J.; Chang, A. H. H.; Kaiser, R. I. *Astrophys. J.* **2007**, *660*, 1588–1608.

(20) Bennett, C. J.; Jamieson, C. S.; Osamura, Y.; Kaiser, R. I. *Astrophys. J.* **2006**, *653*, 792–811.

(21) Bennett, C. J.; Kaiser, R. I. *Astrophys. J.* **2005**, *635*, 1362–1369.

(22) Holtom, P. D.; Bennett, C. J.; Osamura, Y.; Mason, N. J.; Kaiser, R. I. *Astrophys. J.* **2005**, *626*, 940–952.

(23) Wada, A.; Mochizuki, N.; Hiraoka, K. *Astrophys. J.* **2006**, *644*, 300–306.

(24) Cobut, V.; Frongillo, Y.; Patau, J. P.; Goulet, T.; Fraser, M. J.; Jay-Gerin, J. P. *Radiat. Phys. Chem.* **1998**, *51*, 229–243.

(25) Basch, H.; Hoz, S. *Chem. Phys. Lett.* **1998**, *294*, 117–125.

(26) Kemnitz, C. R.; Loewen, M. J. *J. Am. Chem. Soc.* **2007**, *129*, 2521–2528.

(27) Rubin, R. H.; Swenson, G. W.; Benson, R. C.; Tigelaar, H. L.; Flygare, W. H. *Astrophys. J.* **1971**, *169*, L39−L44.

(28) Hollis, J. M.; Lovas, F. J.; Remijan, A. J.; Jewell, P. R.; Ilyushin, V. V.; Kleiner, I. *Astrophys. J.* **2006**, *643*, L25−L28.

(29) Nummelin, A.; Bergman, P.; Hjalmarson, A.; Friberg, P.; Irvine, W. M.; Millar, T. J.; Ohishi, M.; Saito, S. *Astrophys. J. Suppl. Ser.* **2000**, *128*, 213–243.

(30) Schilke, P.; Groesbeck, T. D.; Blake, G. A.; Phillips, T. G. *Astrophys. J., Suppl. Ser.* **1997**, *108*, 301–337.

(31) Raunier, S.; Chiavassa, T.; Duvernay, F.; Borget, F.; Aycard, J. P.; Dartois, E.; d'Hendecourt, L. *Astron. Astrophys.* **2004**, *416*, 165–169.

(32) Bockelee-Morvan, D.; et al. *Astron. Astrophys.* **2000**, *353*, 1101–1114.

(33) Senanayake, S. D.; Idriss, H. *Proc. Natl. Acad. Sci. U.S.A.* **2006**, *103*, 1194–1198.

(34) Costanzo, G.; Saladino, R.; Crestini, C.; Ciciriello, F.; Di Mauro, E. *BMC Evol. Biol.* **2007**, *7*, S1.

(35) Cloutier, P.; Sicard-Roselli, C.; Escher, E.; Sanche, L. *J. Phys. Chem. B* **2007**, *111*, 1620–1624.

(36) Brucato, J. R.; Baratta, G. A.; Strazzulla, G. *Astron. Astrophys.* **2006**, *455*, 395–399.

(37) Baccarelli, I.; Gianturco, F. A.; Grandi, A.; Lucchese, R. R.; Sanna, N. Electron-driven molecular processes induced in biological systems by electromagnetic and other ionizing sources. In *Advances in Quantum Chemistry*; Elsevier: 2007; Vol. 52, pp 189−230.

(38) Gianturco, F. A.; Jain, A. *Phys. Rep.* **1986**, *143*, 347–425.

(39) Lucchese, R. R.; Gianturco, F. A. *Int. Rev. Phys. Chem.* **1996**, *15*, 429–466.

(40) Hara, S. *J. Phys. Soc. Jpn.* **1967**, *22*, 710–&.

(41) Perdew, J. P.; Zunger, A. *Phys. Rev. B* **1981**, *23*, 5048–5079.

(42) Frisch, M. J. et al. *Gaussian 03, Revision C.02*; Gaussian, Inc.: Wallingford, CT, 2004.

(43) Lucchese, R. R.; Sanna, N.; Natalense, A. P. P.; Gianturco, F. A. ePolyScat (Version E2).www.chem.tamu.edu/rgroup/lucchese/ePolyScat.E2.manual/manual.html (accessed May 1, 2008).

(44) Seydou, M.; Modelli, A.; Lucas, B.; Konate, K.; Desfrancois, C.; Schermann, J. P. *Eur. Phys. J. D* **2005**, *35*, 199–205.

CT800379H

JCTC Journal of Chemical Theory and Computation

Transition States in a Protein Environment − ONIOM QM:MM Modeling of Isopenicillin N Synthesis

Marcus Lundberg,[†] Tsutomu Kawatsu,[†] Thom Vreven,[‡] Michael J. Frisch,[‡] and Keiji Morokuma*,[†]

Fukui Institute for Fundamental Chemistry, Kyoto University, 34-4 Takano Nishihiraki-cho, Sakyo-ku, Kyoto 606-8103, Japan, and Gaussian, Inc., 340 Quinnipiac Street, Building 40, Wallingford, Connecticut 06492

Received November 4, 2008

Abstract: To highlight the role of the protein in metal enzyme catalysis, we optimize ONIOM QM:MM transition states and intermediates for the full reaction of the nonheme iron enzyme isopenicillin N synthase (IPNS). Optimizations of transition states in large protein systems are possible using our new geometry optimizer with quadratic coupling between the QM and MM regions [Vreven, T. et al. *Mol. Phys.* **2006**, *104*, 701−704]. To highlight the effect of the metal center, results from the protein model are compared to results from an active site model containing only the metal center and coordinating residues [Lundberg, M. et al. *Biochemistry* **2008**, *47*, 1031−1042]. The analysis suggests that the main catalytic effect comes from the metal center, while the protein controls the reactivity to achieve high product specificity. As an example, hydrophobic residues align the valine substrate radical in a favorable conformation for thiazolidine ring closure and contribute to product selectivity and high stereospecificity. A low-barrier pathway for β-lactam formation is found where the proton required for heterolytic O−O bond cleavage comes directly from the valine N−H group of the substrate. The alternative mechanism, where the proton in O−O bond cleavage initially comes from an iron water ligand, can be disfavored by the electrostatic interactions with the surrounding protein. Explicit protein effects on transition states are typically 1−6 kcal/mol in the present enzyme and can be understood by considering whether the transition state involves large movements of the substrate as well as whether it involves electron transfer.

1. Introduction

Transition-metal enzymes catalyze some of the most fundamental biochemical processes and can serve as inspiration for novel biomimetic catalysts. From the latter perspective, it is important to understand how the metal center and the protein matrix separately contribute to the catalytic activity of the enzyme system. A well-established approach to clarify the catalytic power of enzymes is to compare rates for the same reaction in enzyme and solution.[1,2] This is not possible for most transition-metal enzymes because their activity is critically linked to the redox activity of the metal. An alternative approach, employed in this investigation, is to calculate reaction barriers in the protein environment and directly compare these to barriers obtained without protein environment and to experimental reaction rates.

In the present investigation, the catalytic mechanism of the nonheme iron enzyme isopenicillin N synthase (IPNS)[3,4] is analyzed using ONIOM(QM:MM), an integrated quantum mechanics:molecular mechanics (QM:MM) method.[5−8] In the present QM:MM model, the metal center, i.e., iron, iron ligands, and substrate, is treated by density-functional theory (DFT), while the rest of the enzyme is treated by a classical force field. The two-layer approach not only is computationally efficient but also makes it easier to separate effects from the metal center from those of the surrounding protein

* Corresponding author phone:+81-75-711-7843; e-mail: morokuma@fukui.kyoto-u.ac.jp.

[†] Kyoto University.

[‡] Gaussian, Inc.

10.1021/ct800457g CCC: $40.75 © 2009 American Chemical Society
Published on Web 12/03/2008

Scheme 1. General Reaction for Isopenicillin N Synthase Including the Proposed [Fe(IV)=O] Intermediate[a]

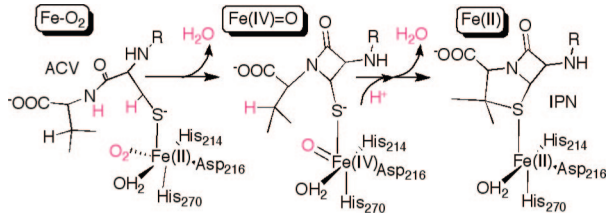

[a] R = L-α-amino-δ-adipoyl.

because they are described at different computational levels. To further highlight the effects of the protein, the ONIOM results are compared to results from a study where the protein was treated as a homogeneous dielectric medium (active-site QM-only approach).[9] QM/MM methods can be considered as extensions of the active-site approach as they explicitly include the effects of the protein on geometry, electronic structure, and energies.[10]

The most important feature of the investigation is the large number of fully optimized transition states in QM:MM models with several thousands of atoms. This is possible by the use of an advanced optimization algorithm, the "fully coupled macro/microiterative" optimization scheme.[11] In this method, the macroiteration of the "macro/microiteration" scheme[12] is modified by explicitly including the quadratic coupling of the QM region with the MM region, which significantly improves the geometry convergence for optimization of transition states and avoids restrictions common in standard schemes. The MM contributions to the Hessian are described using analytical second derivatives of the MM potentials. To avoid cubic scaling with system size, direct and linear scaling (FMM) methods for the MM contributions are used to make this step feasible. The same optimization algorithm has previously been used to identify two transition states in mammalian glutathione peroxidase (GPx)[13] and a transition state for homolysis of the Co−C bond in methylmalonyl-CoA mutase.[14]

The ability to locate transition states makes it possible to see how the protein matrix affects the reaction coordinate and to quantify the effects on reaction rates. Optimization approaches are appropriate when there are no major changes in protein structure but cannot describe major changes in protein conformation. Still, optimized transition states give the best estimate of the reaction coordinate and are ideal starting points for calculations of enzymatic free energies, using e.g., quantum mechanical thermodynamic cycle perturbation (QTCP)[15] or QM/MM free-energy perturbation.[16]

Isopenicillin N synthase is a member of a family of mononuclear nonheme iron enzymes with a 2-His-1-carboxylate iron-binding motif.[17−19] It uses the four-electron oxidative power of O_2 to transform the tripeptide substrate δ-(L-α-aminoadipoyl)-L-cysteinyl-D-valine (ACV) to isopenicillin N (IPN). The proposed mechanism[20] fits into a general scheme for the oxygen-activated nonheme iron enzymes, with initial formation of a ferryl-oxo [Fe(IV)=O] intermediate that then acts as a powerful oxidant, see Scheme 1. The reaction starts when dioxygen binds to the high-spin[21] ferrous iron, which gives a ferric superoxo species[22] that activates the cysteine β-C-H bond leading to formation of an iron-bound peroxide.[23] According to the proposal in ref 20, the peroxide abstracts the valine N−H proton to generate the ferryl-oxo and a water molecule. At the same time, the nitrogen performs a nucleophilic attack on the cysteine β-carbon, which leads to formation of the four-membered β-lactam ring, see Scheme 2. This pathway, in the present paper called the "substrate donor" mechanism, could not be found in previous active-site modeling.[9,24] In the alternative "ligand donor" mechanism a water ligand provides the proton required for O−O bond cleavage, and the ferryl-oxo is formed before the β-lactam ring can close, see Scheme 2.[9] In the ligand donor mechanism, β-lactam ring closure is coupled to a separate proton transfer reaction from the substrate to the iron water ligand. In total, this leads to the same ferryl-oxo intermediate as in the substrate donor mechanism, see Scheme 2. From this intermediate, the high-valent iron species further oxidizes the substrate by activation of the strong valine β-C-H bond. This reaction produces a reactive substrate radical that attacks the thiolate, leading to formation of the five-membered thiazolidine ring and the completed IPN product, see Scheme 1. There are fully synthetic routes to generate IPN,[25] but the enzymatic reaction is still used in large-scale production of antibiotics.[26] A detailed understanding of the enzyme−substrate interactions can help to design biosynthetic routes for β-lactam antibiotics of clinical importance.

Isopenicillin N synthase is a suitable target for QM/MM investigations because X-ray structures have been collected at different stages of the reaction, including the IPN product and an analogue of the β-lactam intermediate.[20,27] Independent deuterium kinetic isotope effects for both the cysteine β-carbon and the valine β-carbon suggest that both C−H bond activation steps are at least partially rate-limiting,[28] which gives two steps where the calculated barrier can be compared to experiment.

2. Computational Details

Methods. In a two-layer ONIOM calculation[5−8] the system is divided into two parts, a selected model system treated by a high-level (QM) method and the remainder treated by a low-level method, often molecular mechanics (MM). In this study the high-level method was the density functional B3LYP,[29,30] and the low-level method was the Amber96 force field.[31] The applicability of the ONIOM (B3LYP:Amber) method has previously been illustrated for several enzymatic systems.[32−36] Geometries were optimized at the 6−31G(d) level, and final energies were evaluated with the 6−311+G(d,p) basis set.[9] Differences between active-site and ONIOM models come not only from the potential energy but also from the dielectric continuum that was used to approximate the protein in the active-site model but that was not included in the ONIOM models. Zero-point and thermal corrections were assumed to be similar between the two approaches and were taken from fully optimized active-site models.

Scheme 2. Ligand Donor and Substrate Donor Mechanisms for Heterolytic O−O Bond Cleavage and β-Lactam Formation

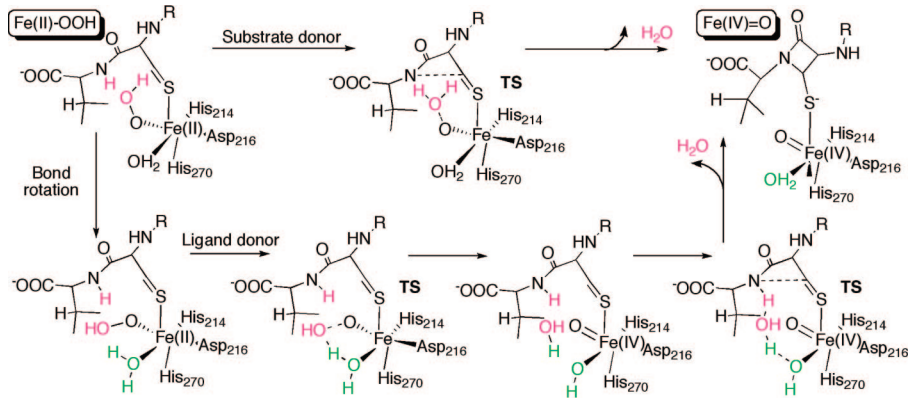

Calculations have been performed using a private development version of Gaussian[37] that includes the "fully coupled macro/microiterative" optimization scheme described previously. The algorithm was initially implemented for the mechanical embedding (ME) scheme, and all optimizations have been performed with ONIOM-ME. Stationary points, including transition states, are fully optimized using the default convergence criteria, while transition state ^{5}**7S** has all but the maximum displacement converged (details in the Supporting Information). Transition states are characterized by a single negative eigenvalue in the Hessian matrix.

In mechanical embedding, the electrostatic interactions between the reactive region and the surrounding protein are calculated classically. In the standard implementation the point charges assigned to the reactive region are not automatically updated. The present models use charges from ESP (Merz−Kollman) calculations. Charges are calculated for the first stationary point of each model, and the same charges are then used in all optimizations with that model. Details are given in the description of the model setup below. Standard ONIOM-ME only includes electrostatic effects due to geometrical changes but neglect the changes in the electronic structure of the model system, e.g., on charge transfer. A common alternative approach is to calculate the electrostatic interactions semiclassically, i.e., to incorporate the MM charges into the QM Hamiltonian (electronic embedding or EE).[8,38] The main advantage is that QM/MM-EE includes the exact electrostatic interaction between the electron density and the point charges in the protein environment. In addition, QM/MM-EE self-consistently updates the response of the electron density to the external charges. However, QM/MM methods typically neglect electronic polarization of the MM part, which should lead to an overestimation of the effect of the MM charges. Optimization schemes also underestimate effects of geometric polarization as the geometry stays in the same local minima.

If a dielectric constant of four, as commonly used in protein modeling, is introduced into the Coulomb expression for electrostatic interactions, these effects decreases to $^1/_4$. ONIOM-EE should correctly indicate the presence and the direction of protein electrostatic effects, but the effects are likely to be overestimated, especially for distant residues. ONIOM-ME neglects some effects while it may overestimate others and only gives the correct energy if the total effect is small or if there is a favorable cancelation of errors. In this report results are given at the ONIOM-ME level, because this is the level where all structures have been optimized. Reaction steps where ONIOM-EE (still using ONIOM-ME geometries) gives a significantly different description of the relative energy are discussed separately in the text.

Models. The original design of the ONIOM system was made to facilitate a comparison between previously published active-site (B3LYP) and QM:MM (B3LYP:Amber) approaches. In the first series of ONIOM models (A-C), the model system is identical to the corresponding active-site model.[9] Initially the model system includes Fe, a water ligand, selected parts of the three amino acids His214, Asp216, and His270 (*Aspergillus nidulans* numbering), and the substrate (model A), see Figure 1. Model A contains 65 atoms including the link hydrogens. In the active-site study, the water formed after O−O bond cleavage was removed from the model because its mobility led to problems with artificial hydrogen bonds. In the ONIOM setup the same water was moved to the MM part in model B. For similar reasons the substrate carboxylate was moved to the MM part after β-lactam ring formation (model C). The changes in ONIOM setup were made to enable a direct comparison between the QM contribution in the active-site and the ONIOM models and would not have been required in regular ONIOM modeling. Model A is applied to stationary points 1−9 and uses QM charges calculated at point 1. Models B (points 9−13) and C (points 13−18) use charges from stationary points 9 and 13, respectively.

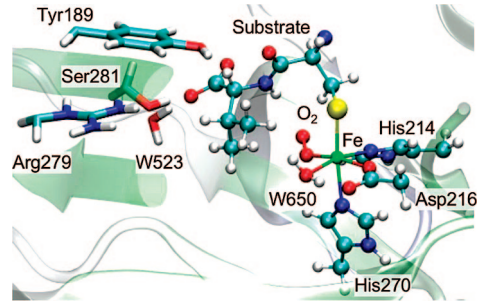

Figure 1. ONIOM QM:MM models A and D. The high-level part of model A includes all atoms in ball-and-stick representation, while the high-level part of model D additionally includes residues in stick representation. Water molecules are numbered according to the PDB structure 1BLZ.

In ONIOM model D, an extension of the QM part is made by including selected parts of the side chains of Tyr189, Arg279, and Ser281 and a water molecule interacting with the substrate carboxylate, see Figure 1. The extension is made in order to improve the description of the substrate donor mechanism. The QM part of model D contains 103 atoms. The QM charges are taken from the parametrization of model A, and Amber charges are used for the newly added residues. The procedure facilitates the comparisons between model D and model A.

The setup of the real system of models A-D largely follows the procedure used to study O_2-binding in IPNS.[39] A detailed description is available in the Supporting Information. The real system includes all protein atoms in the X-ray structure and crystallographic water within 20 Å from iron. No solvent water molecules were included, similar to a previous QM/MM study of camphor hydroxylation in which no major effect of solvent water could be observed.[40] The real system includes 5368 atoms, including hydrogens.

Investigations of the reaction mechanism were made with a protein structure obtained by optimization of the X-ray structure. During optimization of large systems, structural changes may occur that are not directly related to the reaction coordinate. To approximately handle these artificial changes, iterations between reactant and product states were performed until both had the same conformation of the protein environment. Transition states are also relaxed both in the forward and backward direction. This does not prove that there is a connection between reactant, transition state, and product, but at least it gives an indication about the shape of the potential energy surface. The improved ONIOM optimization algorithm minimizes the number of bad steps and helps the MM part to stay in the same local minimum during the reaction.[11]

The static optimization procedure does not take into consideration the possibility of changes in the protein configuration or large movement of water molecules. In the ligand donor mechanism, one of the reaction steps involves a proton transfer from the substrate to an iron ligand through a bridging water molecule. In the structure obtained by a static QM:MM optimization, this reaction is highly unfavorable because there is no water molecule bridging the donor and acceptor sites. To probe the possibility of other more favorable water configurations, an alternative model setup, based on a classical molecular dynamics simulation, was used for the proton transfer step in the ligand donor mechanism (model E).

Here an ensemble of starting geometries was obtained from an MD simulation with the geometry of the QM part frozen (details of the simulations are provided in the Supporting Information). Calculations were performed using the program NAMD2.[41] After 2.5 ns of equilibration, a snapshot was obtained each 50 ps for 500 ps, with one additional structure selected after visual inspection of the trajectory. This gave a total of 12 different starting structures with different alignment of water molecules around the active site. Model E uses the same high-level part as model B, but the real system includes all protein atoms and all water molecules with at least one atom within 15 Å from any high-level atom. Atoms more than 12 Å from any high-level atom were kept frozen to eliminate movement at the model surface.

Additional models have been used to analyze specific reaction steps, but they only include minor modifications and will therefore be introduced in the Results section.

3. Results

The effects of the protein will be described by following the reaction from the iron-bound dioxygen species until the formation of the thiazolidine ring. The term "protein effect" is used for changes in relative energy when going from the active-site model (without explicit treatment of the protein matrix) to the QM:MM protein model. It is not a stringent definition because it depends on the choice of model system. In the present comparison, the active-site model only includes a minimum amount of residues, and this should give large protein effects.

Whether the protein effect is considered significant depends on the properties of interest. If the purpose is to propose a general reaction mechanism, a protein effect of a few kcal/mol does not change the conclusions because the high-level hybrid DFT method has an error of ~5 kcal/mol,[42] and the window for accepting mechanisms based on the barrier height is therefore rather wide. However, when discussing rates of competing reactions, a protein effect of 3 kcal/mol can determine the relative product distribution.

The biosynthesis of isopenicillin N involves a large number of stationary points, and to facilitate the discussion each point is assigned a number (appearing in bold face) according to the order in which it appears along the reaction coordinate. The nature of the stationary point is indicated with TS for a transition state and INT for reaction intermediate. A left superscript shows the spin multiplicity of the state. For example, the label ^{5}**3** TS is assigned to the third stationary point on the quintet spin surface, which is a transition state. Transition states have not been optimized for some minor steps, e.g., bond rotation, and two intermediates may therefore appear next to each other in the reaction energy diagram.

3.1. Transition State for Cys-*β*-C-H Bond Activation. The reaction is initiated by binding of dioxygen to the metal center. Our previous ONIOM QM:MM study showed that explicit inclusion of the protein stabilized the O_2-bound state by 8−10 kcal/mol by improving the description of the metal coordination geometry and the van der Waals interactions.[39] In the ONIOM model, binding of dioxygen was close to thermoneutral (+1.0 for O_2 bound end-on and +2.5 kcal/mol for side-on binding). For completeness, the initial [Fe(II) + O_2] state is included in the energy diagram, but to be consistent with ref 9, the structure with O_2 bound side-on (^{7}**1** Reactant) is taken as the zero-energy level in the energy diagram below.

Oxygen binding gives a ferric superoxide where an electron from iron has been transferred to an antibonding π^*-orbital on oxygen. Spectroscopic studies highlight the role of charge donation from the ACV thiolate ligand that renders the formation of the ferric superoxo complex energetically more favorable.[22] The six unpaired electrons required to form the septet come from the parallel alignment of the unpaired

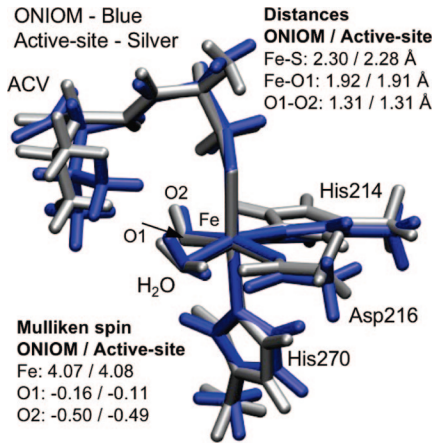

Figure 2. Geometries and spin populations for the intermediate with end-on bound dioxygen in the quintet state (^{5}**2** INT) optimized using the active-site model (silver) and the ONIOM QM:MM model (blue).

spin on the superoxide with the spins from the five d-electrons of Fe(III). As the quintet state is the most reactive in C−H bond activation,[9] the unpaired electron on the superoxo must first flip, but this spin transition does not affect the rate of the reaction.[43] In the quintet spin state, the end-on structure (^{5}**2** INT) is the most stable, and this structure is in good alignment to abstract hydrogen from the Cys β-carbon.[22] Compared to the active-site model, explicit inclusion of the protein mainly affects the position of the hydrophobic side chain of the valine and the orientation of the amino acid ligands but has only small effects on the alignment of the reactive superoxide or the cysteine part of the substrate, see Figure 2.

After probing the reaction coordinate using the C1−H1 and the O2−H1 distances (see Figure 3 for labels), a transition state for C−H bond activation (^{5}**3** TS) could be fully optimized in the "fully coupled macro/microiterative" optimization scheme. The same method, i.e., initial mapping of the reactive space using one or two reaction coordinates followed by full optimization, has been used for all transition states.

Compared to the end-on quintet state (^{5}**2** INT), the relative energy of the transition state ^{5}**3** is 10.2 kcal/mol in the ONIOM model compared to 11.7 kcal/mol in the active-site model, see Figure 4. Using ONIOM-EE instead of ONIOM-ME has a limited effect (+0.2 kcal/mol). The relatively small effect of the protein environment on the C−H bond activation step can be rationalized from the nature of the reaction. The Mulliken spin populations, see Figure 3, show significant spin (−0.39) building up on the Cys β-carbon, indicative of a hydrogen atom transfer for which no large electrostatic effects should be expected. Further, the reaction does not require any major geometrical changes, and potential steric effects of protein are limited. The structural differences in the alignment of the valine side chain and the histidine ligands are seen already in the reactant structure (compare Figures 2 and 3) and should not affect the relative energy between ^{5}**2** INT and ^{5}**3** TS.

Based on these considerations, the origin of the 1.5-kcal/mol effect is not easy to pinpoint. The most significant geometric effect is a decrease in the C−H bond distance from 1.41 Å in the active-site structure to 1.36 Å with QM:MM, leading to a shorter donor−acceptor distance that may facilitate the reaction. In summary, the barrier of the C−H bond activation step from ^{5}**2** INT to ^{5}**3** TS is mainly determined by the electronic properties of the iron center with only minor effects of the surrounding protein.

However, the total reaction barrier must be calculated from the lowest preceding intermediate, which in both models still is the state before oxygen binding, see Figure 4. As the QM:MM model stabilizes the end-on quintet state by >10 kcal/mol, the total C−H bond activation barrier in the QM:MM model is only 11.8 kcal/mol. This step is proposed to be partially rate limiting, and the barrier, as calculated by transition state theory, should be close to 16.8 kcal/mol.[44] The modeled reaction barrier is thus underestimated by 5 kcal/mol.

After passing the transition state, the system reaches a ferrous peroxide [Fe(II)-OOH] intermediate (^{5}**4** INT). Formation of this product requires that one proton and *two* electrons are transferred from the substrate. This does not contradict the observation that the transition state describes hydrogen atom transfer, because intrinsic reaction coordinate (IRC) calculations showed that the second electron is transferred only after passing the transition state.[9] The relative energy of the ferrous peroxide intermediate is similar in active-site and ONIOM-ME models when the preceding intermediate ^{5}**2** is used as reference, see Figure 4. However, the protein effect of the "electron transfer" from substrate to iron that occurs after ^{5}**3** TS is not properly included in any of these models. The effect on the relative energy of ^{5}**4** INT of applying ONIOM-EE instead of ONIOM-ME is large, approximately +8 kcal/mol, even after geometry relaxation at the ONIOM-EE level.

3.2. Transition States for O−O Bond Cleavage - Ligand Donor Mechanism. The next step in the reaction is closing of the β-lactam ring together with formation of [Fe(IV)═oxo]. In the active-site study,[9] a new mechanism for O−O bond cleavage was proposed in which the water ligand acts as a proton donor. The first step in this mechanism is rotation of the peroxide (^{5}**4** → ^{5}**5**) to align the outer oxygen in a position where it can accept a proton from the water ligand. This bond rotation is slightly less exothermal (by 2.4 kcal/mol) than in the active-site model, because the QM:MM model includes the original protein-carboxylate interactions at the MM level, which prevents formation of artificial hydrogen bonds between peroxide and substrate carboxylate, see Figure 5. The same effect was seen in a larger active-site model that included residues interacting with the carboxylate (Tyr189, Arg279, and Ser281),[9] but if the purpose is simply to keep the hydrogen bond network intact a QM:MM model is significantly cheaper than a large QM model. The reason the energetic effect is still relatively small is that a large part of the error in the active-site model disappears when the solvent correction is included.

O−O bond cleavage in the ligand donor mechanism proceeds by initial electron transfer from iron to an anti-bonding O−O σ^* orbital (^{5}**6** TS). This process leads to a shallow minimum with a long O−O bond (^{5}**7** INT) that

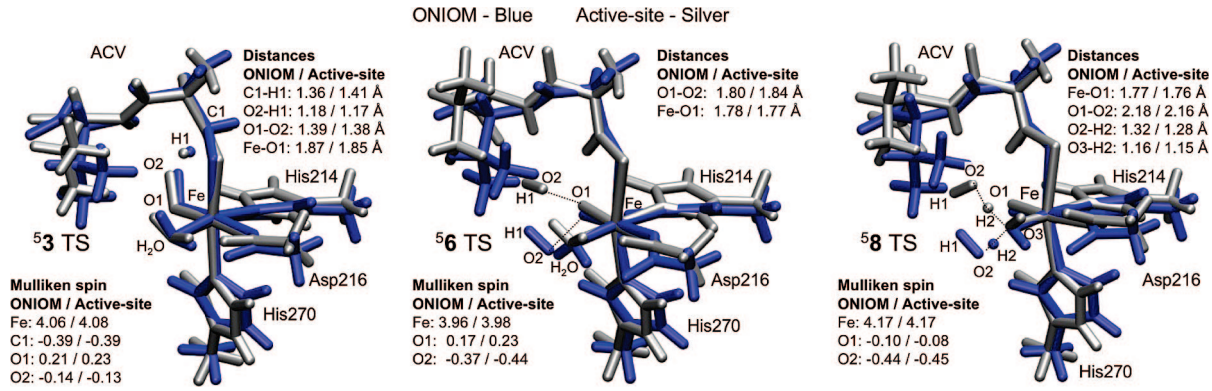

Figure 3. Geometries and spin populations of the transition states for Cys-β-C-H bond activation ^{5}**3** TS (left), initial O−O bond cleavage in the ligand donor mechanism ^{5}**6** TS (middle), and water formation ^{5}**8** TS (right). The active-site model is shown in silver, and the high-level part of the ONIOM QM:MM model is shown in blue.

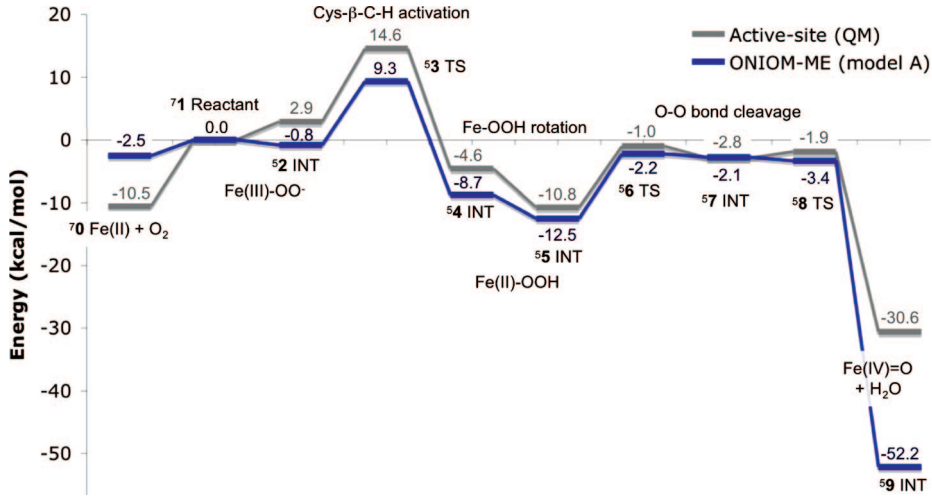

Figure 4. Energy diagrams for formation of [Fe(IV)═oxo] in the ligand donor mechanism. Energies calculated with the active-site model are shown in gray, while energies from the ONIOM-ME QM:MM system are shown in blue.

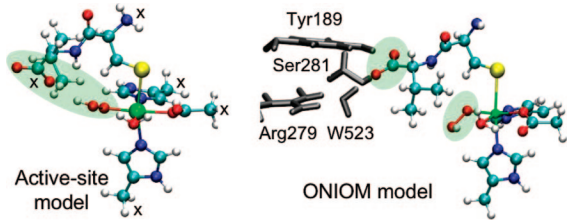

Figure 5. The QM:MM model (right) avoids artificial hydrogen bonds between peroxide and the valine carboxylate group in the Fe(II)-OOH intermediate ^{5}**5**. The active-site model (left) is optimized with atoms frozen in the position from the X-ray structure (marked with X). The QM:MM model has the same size of the QM region but includes MM residues hydrogen bonding to the carboxylate in the QM:MM description (shown in gray) as well as all other protein residues.

quickly abstracts a proton from the water ligand and a second electron from iron to form water, see ref 9 for details. O−O bond cleavage is similarly described in the active-site and the ONIOM models, but the orientation of the donating water and the peroxide changes due to the difference in the initial position of the peroxide, see Figure 3. The effect on the relative energies is small with the barrier for ^{5}**6** TS going from 9.8 kcal/mol in the active-site model to 10.3 kcal/mol in the ONIOM model, see Figure 4. The second transition state (^{5}**8** TS) disappears after adding corrections for thermal effects and large basis, but whether the intermediate ^{5}**7** appears on the calculated potential energy surface seems to be determined by minor details, and for all practical purposes, O−O bond heterolysis can be considered as a concerted reaction.

The first step, from ^{5}**5** INT to ^{5}**6** TS, is an electron transfer from iron to oxygen, and there is a non-negligible effect when going to ONIOM-EE (+5.9 kcal/mol at the ONIOM-ME geometry). Such a large effect would make this step potentially rate limiting, but, as argued before, it is likely to be overestimated.

The total O−O bond cleavage reaction is heterolytic and leads to formation of a water molecule and an [HO-Fe(IV)═O] intermediate (^{5}**9**). Unlike the previous reaction steps, the protein effect is very large, −20.1 kcal/mol, see Figure 4. The effect comes from interactions between the released water and atoms outside the QM model. In the active-site model the newly formed water bridged the valine N−H group and the iron hydroxo ligand. In the ONIOM model the same water makes hydrogen bonds with explicit MM waters instead of the substrate, see Figure 6, which leads to large effects on the reaction energy for this step. As a general observation, release of a product shows large protein

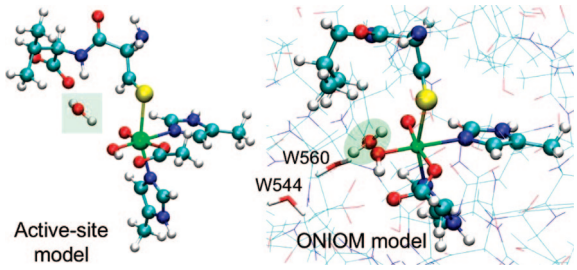

Figure 6. Different alignment of the water formed after O−O bond heterolysis, highlighted in green, in active-site and ONIOM models. Selected water residues in the MM description are shown in stick representation.

effects due to explicit interactions with residues not included in the active-site model. These effects are also sensitive to the choice of mechanical or electronic embedding.

3.3. Transition State for *β*-Lactam Ring Formation - Ligand Donor Mechanism. To conclude the formation of the *β*-lactam ring, the valine N−H proton should be transferred to the hydroxyl ligand at the same time as the C−N bond of the four-membered *β*-lactam ring is formed, see Scheme 2. However, the barrier for the first step in this mechanism (^{5}**10** TS) becomes unreasonably high (>45 kcal/mol) in the original ONIOM model. The corresponding barrier was ∼11 kcal/mol in the active-site model, so the protein effect is >30 kcal/mol. The large effect is different from what was observed for C−H bond activation (^{5}**3** TS) and O−O bond cleavage (^{5}**6** and ^{5}**8** TS) but similar to the effect on the preceding water formation step. The reason is that to function as a proton relay in ^{5}**10** TS the QM water must return to the position where it bridges the valine N−H group and the hydroxo ligand. The QM:MM interactions that stabilized water release are lost in the transition state, which leads to an exceedingly high barrier.

A deficiency in the optimization approach is the relatively static description of the protein that usually leads to small changes in the position of different groups. This is problematic when handling potentially mobile water molecules. In the ligand donor mechanism, the barrier for *β*-lactam ring formation is sensitive to the position of a single water molecule, exactly the kind of situation that the optimization approach has problems to handle. It is possible that the required bridging position is empty because water molecules inside the protein simply cannot move to the desired position during an optimization.

To find configurations where water is bridging the substrate and the iron ligand, twelve snapshots were taken from a molecular dynamics (MD) equilibration with the QM coordinates frozen from ^{5}**10** TS as described in the Computational details (model E). Proton transfer barriers were calculated by separately optimizing the reactant and a transition state guess with frozen proton-transfer coordinates from the MD snapshot.

This approach gave barriers ranging from 20.8 to 43.3 kcal/mol, and the major difference comes from the low-level MM contribution, see Figure 7. The large variability in the barrier height reflects the number of conformations available for water molecules around the active site, see Figure S1. Taking the lowest barrier (snapshot at 2.75 ns) and performing a

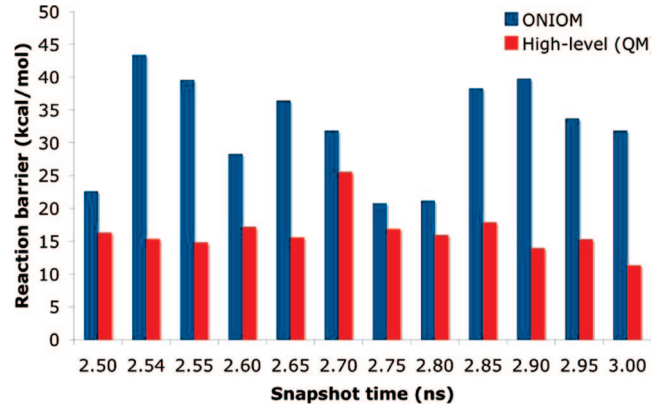

Figure 7. Proton transfer barriers (^{5}**10** TS) for different snapshots from a molecular dynamics trajectory. In the snapshot at 2.7 ps, the QM barrier is high because the accepting hydroxo ligand has lost its hydrogen bond to Asp216.

full transition state optimization of the QM:MM model gives a barrier of 20.7 kcal/mol. As an alternative, taking the structure with the highest barrier for a single water bridge (2.54 ns snapshot) and transferring the proton using one additional QM water (model F) leads to an optimized barrier of 21.0 kcal/mol, see Figure S2.

The calculated barrier of ∼21 kcal/mol is high compared to the experimental limit of 17 kcal/mol, despite the fact that performing the MD simulation with the QM geometry frozen at the transition state could overestimate the stability of that state and underestimate the barrier height. However, the modeled reaction is restricted to residues in the QM system, and alternative pathways may be available in the real protein. The ligand donor mechanism can therefore not be excluded. Instead, the most important conclusion is that barriers for reactions involving mobile water molecules cannot be consistently modeled with pure optimization schemes.

3.4. Transition States for O−O Bond Cleavage and *β*-Lactam Formation - Substrate Donor Mechanism. The most direct way to close the *β*-lactam ring is to use the valine N−H proton during O−O bond cleavage, see Scheme 2. Previous active-site investigations[9,24] could not find a low-energy path for the substrate donor mechanism. With ONIOM model A the search for the substrate donor pathway eventually led to the electron transfer required to weaken the O−O bond, but the electron came from the substrate carboxylate, not from iron. The observed reaction was therefore decarboxylation rather than *β*-lactam formation. From this observation it is clear that the problem with model A (in active-site and ONIOM-ME) is that the ionization potential of the carboxylate is underestimated unless its hydrogen-bonding residues are included. To handle this deficiency, the QM system is extended by including residues closest to the valine carboxylate (Tyr189, Arg279, Ser281, and W523), see model D in Figure 1. The same extension of the active-site model in ref 9 would also have been sufficient. This illustrates the importance of including a large QM part in active-site and QM:MM-ME calculations. The advantage of the QM:MM model is that it allows the additional QM residues to move with the substrate without the risk of creating new artificial hydrogen bonds.

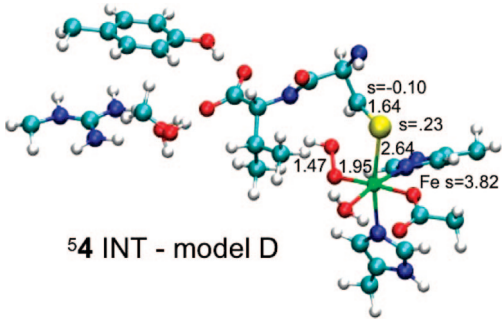

Figure 8. Geometry and spin population of the [Fe(II)-OOH] intermediate ^{5}**4** optimized with ONIOM model D.

Starting from the [Fe(II)-OOH] intermediate ^{5}**4**, see Figure 8, the reaction proceeds through three separate transition states, although no long-lived intermediate is expected to appear along the pathway. The initial reaction coordinate is elongation of the O−O bond, coupled to electron transfer from iron. Passing ^{5}**5S** TS at an O−O bond distance of 1.73 Å, see Figure 9, has a barrier of 7.8 kcal/mol and leads to an intermediate with a long (2.17 Å) O−O bond (^{5}**6S** INT). The additional label **S** refers to intermediates appearing only along the substrate donor pathway. Further O−O bond elongation leads to a second electron transfer from iron to the leaving hydroxyl, and the valine N−H proton is transferred from the substrate to complete the formation of water (^{5}**7S** TS). This leads to a high-energy ferryl-oxo structure (^{5}**8S** INT) with a linear substrate that quickly undergoes cyclization (^{5}**9S** TS) to form the β-lactam ring (^{5}**10S** INT). All transition states along the pathway are shown in Figure 9. The highest barrier, 9.3 kcal/mol, is observed for proton transfer from the substrate (^{5}**7S** TS), while cyclization, i.e., C−N bond formation (^{5}**9S** TS), has a barrier of only 2.8 kcal/mol compared to the peroxide intermediate ^{5}**4** INT, see Figure 10.

After formation of water and the β-lactam ring, the relative energy of ^{5}**10S** INT is much higher than the energy of the corresponding [Fe(IV)═oxo] intermediate ^{5}**13** INT along the ligand donor pathway. In ^{5}**10S** the water formed during O−O bond heterolysis remains in the hydrophobic pocket trans to Asp216, but it is assumed that it can rearrange to reach the low-energy structure observed in the ligand donor pathway.

To be able to directly compare the ligand and substrate donor mechanisms, the former mechanism was reoptimized using model D, see Figure 10. Compared to model A with its smaller model system, the changes in transition state barriers are relatively small (−0.3 kcal/mol for ^{5}**6** TS and −0.6 kcal/mol for ^{5}**8** TS).

The barrier for O−O bond cleavage in the substrate donor mechanism, 9.3 kcal/mol, is slightly lower than the highest barrier in the ligand donor mechanism, 10.0 kcal/mol, see Figure 10. Single point calculations using ONIOM-EE gives a much larger difference in barrier height (8.5 kcal/mol), mainly due to the electrostatic effects on O−O bond cleavage in the ligand donor mechanism. Even if the effect is overestimated, it is still likely that electrostatic interactions favor the substrate donor pathway by a few kcal/mol.

3.5. Transition State for Val-β-C-H Bond Activation. After formation of the [Fe(IV)═oxo] intermediate, the reaction proceeds by C−H bond activation at the valine β-carbon. Using the optimized structure obtained from previous modeling (^{5}**13** INT), the valine side chain must rotate almost 180° to align the C−H bond toward the iron center (^{5}**14** INT). This is a difficult reaction to model, because it could be accompanied by changes in the conformation of the hydrophobic residues surrounding the side chain. In ONIOM model C, which is similar to model A, the rotation leads to movement of the newly formed water, but the reaction energy for bond rotation is the same in the active-site and ONIOM models (+0.9 kcal/mol).

Activation of the Val-β-C-H bond (^{5}**15** TS) is a hydrogen atom transfer, and the effect of the protein is expected to be small, as it was for the activation of the corresponding Cys-β-C-H bond. On the contrary, in ONIOM model C the reaction barrier becomes 22.0 kcal/mol compared to 15.3 kcal/mol in the active-site model, see Figure 11. This is a significant effect, but it makes the barrier much higher than the experimental value of ∼17 kcal/mol for this partly rate-limiting step.

What distinguishes this reaction from the previous C−H bond activation (^{5}**3** TS) is that it requires a large movement of the substrate, because the valine side chain must approach the oxo group. All comparisons of the optimized structures from active-site and ONIOM models show large differences in the alignment of the valine side chain, see e.g., Figure 2. This is true also in the transition state ^{5}**15** TS, although the effect on the reaction coordinate is less obvious. The ONIOM model has a longer C2−H3 distance and a slightly shorter O1−H3 distance, see Figure 12.

In the active-site model the transition state was favored by 3.5 kcal/mol by the IEFPCM solvent description because the movement of the side chain leads to a more compact QM region and therefore a decrease in the cavitation energy. Explicit inclusion of the protein in model C instead disfavors the transition state by 3.2 kcal/mol (+2.9 at the high level and +0.3 kcal/mol from the low level). The sum of these two effects leads to the large difference between the ONIOM and the active-site model.

As the barrier in the ONIOM model is too high compared to experiment, several attempts were made to find a lower barrier. Applying model D with its larger QM part did not change the total barrier from ^{5}**13** INT, and the barrier was not stabilized with ONIOM-EE (effect of +0.8 kcal/mol). The reaction pathway was also optimized on the septet and the triplet surfaces, but the barriers were higher in energy (by 3.6 kcal/mol for ^{7}**15** TS and by 3.7 kcal/mol for ^{3}**15** TS).

In order to check for major errors in the structure, the optimized structure of ^{5}**13** INT was compared with an X-ray structure of ACmC that forms an analogue of the monocyclic β-lactam intermediate.[27] The major structural differences are in the arrangement of the water molecules. In the ONIOM structure the newly formed water molecule is located close to the oxo ligand trans to Asp216, but there is no water in that position in the X-ray structure of the ACmC substrate. Furthermore, there is no water in the corresponding pocket

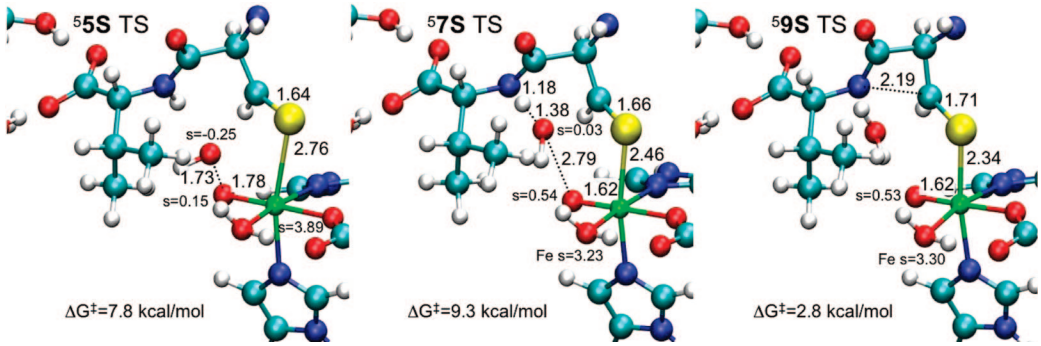

Figure 9. Close-ups of the transition states for heterolytic O−O bond cleavage and β-lactam formation in the "substrate donor" mechanism. Labels show important bond distances in Å and Mulliken spin populations.

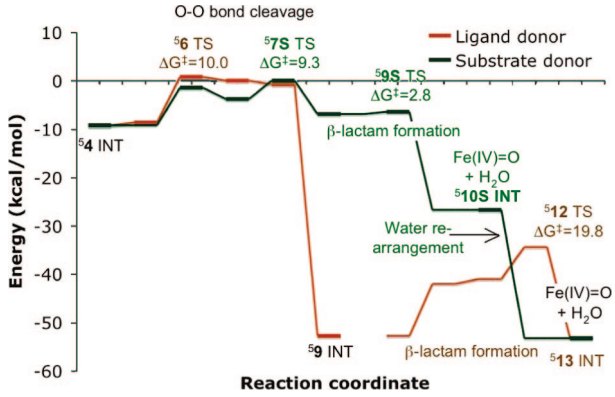

Figure 10. Energy diagram for formation of the β-lactam + [Fe(IV)═oxo] intermediate from [Fe(II)-OOH] in substrate and ligand donor mechanisms using model D. The energies for β-lactam ring closure in the ligand donor mechanism (thin brown line) are taken from the active-site model.

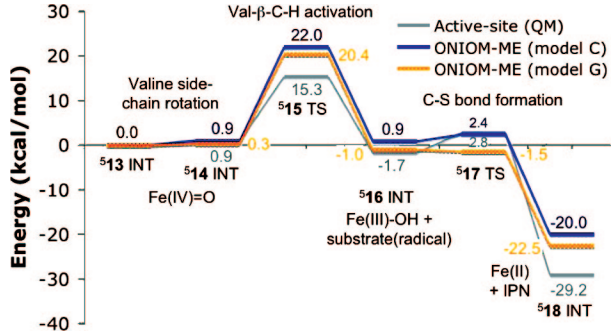

Figure 11. Energy diagrams for Val-β-C-H bond activation and thiazolidine ring closure with the active-site model and ONIOM models C and G. Values of relative energies are placed below the line for the active-site model, above the line for ONIOM model C, and on the side for ONIOM model G.

in the X-ray structure with ACV and NO[20] or in the structure of the IPN product, see Figures S3 and S4.[27] The presence of a water molecule in that position was investigated by classical MD simulations. In these simulations, the QM region was kept frozen (except the water molecule and the hydrophobic valine side chain). After a few picoseconds water leaves its position close to the oxo group and does not return. Details of the MD simulations are given in the Supporting Information.

Consequently, it was assumed that the water molecule leaves the active site through the channel occupied by

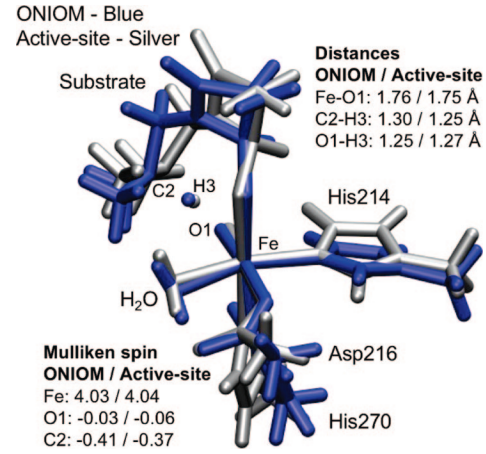

Figure 12. Geometries and spin populations for the transition state for Val-β-C-H bond activation (^{5}**15** TS) optimized using the active-site model (silver) and the ONIOM QM:MM model C (blue).

WAT544 and WAT560 in the X-ray structure, see Figure 6. This process is difficult to model, and the water molecule was simply removed from model D to form the new ONIOM model G. Optimization of the C−H activation transition state with the new model gave a total barrier of 20.4 kcal/mol, 1.6 kcal/mol lower than models with a water in close to the oxo group, see Figure 11.

The product of the C−H bond activation is a ferric hydroxo species and a substrate radical located on the valine-β-carbon (^{7}**16** INT). The relative energy of this intermediate is rather similar in all different models.

3.6. Transition State for Thiazolidine Ring Formation. From the substrate radical state (^{5}**16** INT) the five-membered thiazolidine ring can be formed by an attack of the carbon radical on sulfur. Compared to the QM model, the ONIOM transition state for C−S bond formation (^{5}**17** TS) does not change much (from 2.73 Å in the active-site model to by 2.71 Å), but the barrier drops from 4.5 to 1.5 kcal/mol compared to the preceding intermediate ^{5}**16** INT. A tentative explanation for the decrease in barrier is that the protein favorably aligns the valine-β-carbon radical for a reaction with the thiolate, see Figure 13. A geometric indication is that the C−S distance in the reactant is 3.6 Å in the protein and slightly longer in the active-site structure (3.79 Å). The barrier height is sensitive to the choice of QM model because in both models with larger QM part (D and

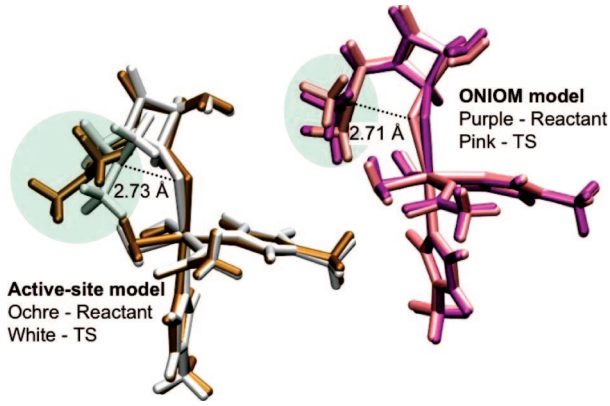

Figure 13. Reactant and transition state for thiazolidine ring formation in the active-site model (left) and ONIOM model C (right). The improved alignment of the substrate side chain in the ONIOM model is highlighted in blue.

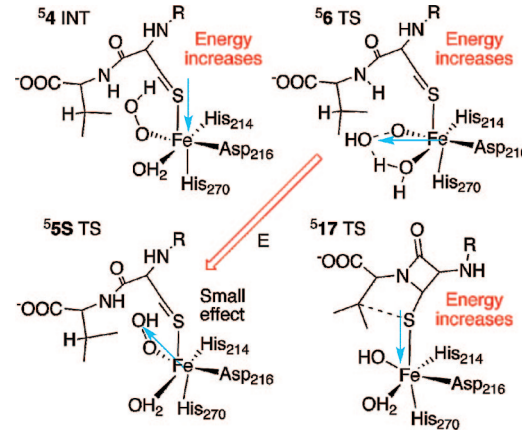

Figure 14. Cartoon to rationalize electrostatic effects on electron transfer in the ONIOM-EE description. The red arrow shows the rough direction of the electric field, while blue arrows show the estimated "direction" of electron transfer.

G), the barrier disappears after the basis set correction has been applied, see Figure 11.

Formation of the thiazolidine ring includes a final electron transfer from the thiolate to iron to regenerate Fe(II), and again there is a significant difference between ONIOM-ME and ONIOM-EE (+3−4 kcal/mol at the ONIOM-ME geometry for different models).

Formation of the C−S bond creates the thiazolidine ring and completes the formation of the bicyclic IPN product (^{5}**18** INT). The reaction decreases the strength of the substrate-metal coordination, and in all models the substrate loses its coordination to iron. The energy of product formation is rather different in the active-site and the ONIOM models, see Figure 11. The ONIOM models give much shorter Fe−S bond distances (3.2−3.5 Å) compared to the active-site model (Fe−S distance of 4.2 Å).

However, the Fe−S distance is still much longer than in the X-ray structure of the IPN product (Fe−S distance of 2.87 Å, see Figure S3). In the X-ray structure, the water formed during the second part of the reaction has already left the active site and iron is five-coordinated.[27] This is different from the final optimized structure ^{5}**18** INT that still has a hydroxyl ligand trans to Asp216. To complete the enzymatic reaction the hydroxyl group should receive a proton and form water. This proton is equivalent to the proton lost from the thiol during the initial binding of ACV, but these processes are not modeled because no proton acceptor/donor was included in the QM part. Attempts to reproduce the Fe−S distance in the product X-ray structure using a model with a water ligand (model H) or a model with five-coordinate iron (model I) did not succeed (Fe−S distances >3.2 Å). The QM:MM models still has problems to describe structures with very weak metal ligand interactions that are balanced by large changes in the MM interactions during substrate release.

4. Discussion

4.1. Transition State Effects. The reaction barrier is the most common computational criterion when discriminating between different reaction mechanisms. In the present study, the ease in which transition states can be optimized allows for a broad comparison of protein effects on different types of transition states.

The effects of the protein in the current study are either steric or electrostatic and can be rationalized by considering whether the transition state involves large movements of the substrate, or whether it involves electron transfer. In the ONIOM-ME description, the protein effect is small (∼1−2 kcal/mol) for transition states, ^{5}**3** (Cys-β-C-H bond activation), ^{5}**6**, and ^{5}**8** (O−O bond cleavage), because they lead to relatively small changes in the active site structure, see Figure 3. Although not compared to an active-site model, transition states ^{5}**5S** and ^{5}**7S** (O−O bond cleavage) in Figure 9 also belong to this category. Protein effects are larger (3−6 kcal/mol) for transition states that involve movement of the hydrophobic side chain, i.e., ^{5}**15** (Val-β-C-H bond activation) and ^{5}**17** (thiazolidine ring formation), see Figures 12 and 13. The transition state for β-lactam ring closure, ^{5}**9S** in Figure 9, is likely to belong to this category. The absolutely largest protein effect is observed for the transition state ^{5}**10** (proton transfer) that requires rearrangement of a mobile water molecule, a situation that is not handled well with the present approach.

In the single-point ONIOM-EE description, electrostatic effects become significant (>4 kcal/mol) for the transition states ^{5}**6** (O−O bond cleavage) and ^{5}**17** (thiazolidine ring formation) that include electron transfer between substrate and iron. In both cases the effect leads to an increase in the barrier. The transition states for O−O bond cleavage in the substrate donor mechanism (^{5}**5S** and ^{5}**7S**) also involve electron transfer, but the effects of applying ONIOM-EE are small. A rough rationalization of the electrostatic effects can be made by considering the "direction" of electron transfer relative to the electric field of the protein, see Figure 14. The electrostatic interactions favor the substrate donor pathway because the critical electron transfer from iron to the antibonding O−O π^* orbital proceeds perpendicular to the electric field, while in the ligand donor mechanism it proceeds partly in the direction of the electric field. Although the electrostatic effects are difficult to calculate correctly, control of the reactivity in IPNS by a directional electric

field is an interesting concept that requires a more careful investigation.

In principle, both ligand and substrate donor routes could be active as they lead to the same [Fe(IV)═oxo] state (^{5}**13** INT), assuming that there really is a proton transfer pathway from substrate to the iron ligand W650. The difference between the two mechanisms could become clearer by studying the enzymatic reaction with the alternative ACOV substrate. The major difference between the normal substrate (ACV) and ACOV is that the latter lacks a valine N−H proton. The substrate donor mechanism is therefore not viable. Experimentally, reactions with ACOV lead to hydroxylation of the Cys-β-carbon, presumably by the iron bound peroxide (^{5}**4** INT).[45] In the ligand donor mechanism, the [Fe(IV)═oxo] species (^{5}**9** INT) can still be generated without the substrate proton. If it can be shown that the ferryl-oxo intermediate does not lead to hydroxylation of the Cys-β-carbon, the ligand donor mechanism can be ruled out.

4.2. Other Significant Protein Effects. As the real transition state barrier should be calculated against the lowest preceding intermediate, relative energies of intermediates can affect the rate of a reaction step. As an example, the barrier for the first C−H bond activation step, ^{5}**3** TS in Figure 4, decreases significantly when the protein is included, mainly due to the failures of the active-site model to describe O_2 binding.[39] In the present study, large effects on relative energies are found for reactions involving formation of water and the IPN product. These effects are handled mainly at the MM level and are difficult to describe accurately. Fortunately, the effects are not critical when determining the reaction mechanisms because product formation is often exothermal and the degree of exothermicity has no effect on the barrier of the next step. As an example, the barrier for Cys-β-C-H bond activation is not affected by the calculated exothermicity of β-lactam formation.

Formation of the [Fe(II)-OOH] species (^{5}**4** INT) shows large electrostatic effects with ONIOM-EE because it involves electron transfer from substrate to iron. As long as peroxide formation is still an exothermal reaction, this should not affect the rate of O−O bond cleavage.

4.3. Modeling Accuracy. Assuming that the two C−H bond activation transition states both are partially rate-limiting with barriers of ∼17 kcal/mol, the discrepancy between experiment and calculation is 5 and 3 kcal/mol, respectively. This is not considered a reason to re-evaluate the mechanism, because 3−5 kcal/mol is within the expected accuracy for density functional calculations of transition-metal systems. The first C−H bond activation (^{5}**3** TS) is a simple hydrogen atom transfer from the substrate to the superoxo radical, a reaction type for which DFT might underestimate the barrier. The second C−H bond activation (^{5}**15** TS) is also a hydrogen atom transfer, but here the reaction barrier is overestimated. A significant difference is that this C−H bond activation requires a change in the electronic configuration of the iron-oxo bond, a situation where trends from simple organic reactions may no longer hold. A possible reason for the too high barrier for ^{5}**15** TS is that the optimization to the *closest* local minimum may not allow the protein model to relax properly. This could overestimate the energy required to move the substrate toward the oxo group.

There are also shortcomings in the description of the protein interactions. As discussed in the Computational details, mechanical embedding largely neglects protein effects on electron transfer, while electronic embedding qualitatively gives a better description of the direction of the electrostatic effects but is likely to overestimate the effects due to lack of polarization of the MM part. We are at present testing improved optimization algorithms for electronic embedding as well as two-layer DFT:DFTB[46,47] and three-layer DFT:DFTB:MM models that naturally include electronic polarization and charge transfer effects through an inexpensive QM layer.

Another issue concerns the setup of the model, especially water molecules whose positions are not well determined, but still can have large effects in QM:MM calculations.[48,49] This is illustrated by the large differences in barrier for water-mediated proton transfer (^{5}**10** TS, see Figure 7). A related problem is the uncertainty in the position of the water molecule formed after O−O bond heterolysis. In the present static study, two alternatives have been accounted for, one where the water is located close to the oxo group, and one where it has been removed from the system. The latter choice is supported by a separate molecular dynamics simulation. It also leads to a lower barrier for C−H bond activation by ∼2 kcal/mol.

4.4. Catalytic Efficiency of the Metal Center. The low barriers achieved with an active-site model indicated that the main catalytic effect of IPNS comes from the metal center. In principle agreement with experiment can be achieved with a method that consequently underestimates barriers together with a neglect of the "real" protein effects. A QM/MM model that includes an explicit description of the protein is therefore a better argument for the catalytic proficiency of the nonheme iron center. The competence of the metal center is also shown by the reactivity of biomimetic complexes,[17,50,51] although they do not show the same efficiency and specificity as the enzymatic reactions.

4.5. Protein Control of IPNS Reactivity. Apart from the initial O_2-binding step, the suggested role of the protein in IPNS is to control the reactivity of the metal center. One example is the effect of the hydrophobic side chains that orient the valine side chain in an orientation that is favorable for thiazolidine ring formation. Although not important for the total reaction rate, this protein effect may prevent side reactions of the substrate radical. It has previously been observed that mutations of the hydrophobic residue Leu223 lining the valine side chain leads to changes in the product ratio for an alternative substrate.[52] The conclusion was that the bulky side chain hinders the rotation of the substrate in the native enzyme. These two mechanisms may work in concert to achieve high product and stereospecificity in IPNS.[53]

An important result of the ONIOM calculations is the detailed description of the substrate donor mechanism for β-lactam formation. However, the reason this pathway could be found was not the long-range protein effects but that the QM:MM model made it easier to include residues close to

the substrate while still keeping the hydrogen bonds intact during β-lactam ring formation. The residues (Tyr189, Arg279, Ser281, and W523) can have a role in preventing side reactions, e.g., decarboxylation or cleavage of the C−C bond between the carbonyl and the carboxylate.

5. Conclusions

With the new quadratically coupled QM/MM geometry optimization algorithm it is feasible to locate transition states in protein systems, similar as in single-layer QM calculations. The optimization procedure allows for a direct evaluation of protein effects on all the transition states appearing along the reaction pathway of isopenicillin N synthase. The effects are typically smaller than 4 kcal/mol and can be understood by considering whether the transition state involves large movements of the substrate and whether it involves electron transfer.

The lack of major stabilizing protein effects on the rate-limiting transition states of IPNS suggest that a large part of the catalytic effect comes from the metal center. The suggested role of the protein is to control the reaction and achieve high product specificity. Hydrophobic residues align the valine substrate radical in a favorable conformation for thiazolidine ring closure and contribute to the product selectivity and high stereospecificity of the reaction. An interesting possibility that merits further investigation is that the mechanism for heterolytic O−O bond cleavage is determined by the direction of the electric field at the active site.

A detailed comparison of the polarization/charge transfer effects in the ONIOM QM:MM-EE, QM:QM, and QM:QM:MM models will be presented in a separate paper. Another extension is to include statistical averaging of the protein effects over an ensemble of MM configurations. Detailed studies on this aspect using free-energy perturbation and other methods will also be discussed separately.

Acknowledgment. One of the authors (M.L.) acknowledges a Fukui Institute for Fundamental Chemistry Fellowship. The work was in part supported by a CREST (Core Research for Evolutional Science and Technology) grant in the Area of High Performance Computing for Multiscale and Multiphysics Phenomena from the Japan Science and Technology Agency (JST). The use of computational resources at the Fukui Institute for Fundamental Chemistry and at the Research Center of Computer Science (RCCS) at the Institute for Molecular Science (IMS) is acknowledged.

Supporting Information Available: Summary of models used to investigate the IPNS reaction, detailed description of the computational setup and the molecular dynamics simulations, comments on the optimization of ^{5}**7S** TS, details of the mechanism for proton transfer in the ligand donor mechanism ^{5}**10** TS, comparison of optimized and X-ray structures of the β-lactam intermediate and the IPN product, and structures of stationary points along the reaction pathways (in PDB format). This material is available free of charge via the Internet at http://pubs.acs.org.

References

(1) Miller, B.; Wolfenden, R. *Annu. Rev. Biochem.* **2002**, *71*, 847–885.

(2) Warshel, A.; Sharma, P. K.; Kato, M.; Xiang, Y.; Liu, H.; Olsson, M. H. M. *Chem. Rev.* **2006**, *106*, 3210–3235.

(3) Baldwin, J. E.; Bradley, M. *Chem. Rev.* **1990**, *90*, 1079–1088.

(4) Schenk, W. A. *Angew. Chem., Int. Ed.* **2000**, *39*, 3409–3411.

(5) Maseras, F.; Morokuma, K. *J. Comput. Chem.* **1995**, *16*, 1170–1179.

(6) Svensson, M.; Humbel, S.; Froese, R. D. J.; Matsubara, T.; Sieber, S.; Morokuma, K. *J. Phys. Chem.* **1996**, *100*, 19357–19363.

(7) Dapprich, S.; Komáromi, I.; Byun, K. S.; Morokuma, K.; Frisch, M. J. *J. Mol. Struct. (THEOCHEM)* **1999**, *461*, 1–23.

(8) Vreven, T.; Byun, K. S.; Komáromi, I.; Dapprich, S.; Montgomery, J. A., Jr.; Morokuma, K.; Frisch, M. J. *J. Chem. Theory Comput.* **2006**, *2*, 815–826.

(9) Lundberg, M.; Siegbahn, P. E. M.; Morokuma, K. *Biochemistry* **2008**, *47*, 1031–1042.

(10) Senn, H. M.; Thiel, W. *Top. Curr. Chem.* **2007**, *268*, 173–290.

(11) Vreven, T.; Frisch, M. J.; Kudin, K. N.; Schlegel, H. B.; Morokuma, K. *Mol. Phys.* **2006**, *104*, 701–704.

(12) Vreven, T.; Morokuma, K.; Farkas, Ö.; Schlegel, H. B.; Frisch, M. J. *J. Comput. Chem.* **2003**, *24*, 760–769.

(13) Prabhakar, R.; Vreven, T.; Frisch, M. J.; Morokuma, K.; Musaev, D. G. *J. Phys. Chem. B* **2006**, *110*, 13608–13613.

(14) Kwiecien, R. A.; Khavrutskii, I. V.; Musaev, D. G.; Morokuma, K.; Banerjee, R.; Paneth, P. *J. Am. Chem. Soc.* **2006**, *128*, 1287–1292.

(15) Rod, T. H.; Ryde, U. *Phys. Rev. Lett.* **2005**, *94*, 138302−(1−4)

(16) Hu, H.; Yang, W. *Annu. Rev. Phys. Chem.* **2008**, *59*, 573–601.

(17) Costas, M.; Mehn, M. P.; Jensen, M. P.; Que, L., Jr. *Chem. Rev.* **2004**, *104*, 939–986.

(18) Koehntop, K. D.; Emerson, J. P.; Que, L. *J. Biol. Inorg. Chem.* **2005**, *10*, 87–93.

(19) Bassan, A.; Blomberg, M. R. A.; Borowski, T.; Siegbahn, P. E. M. *J. Inorg. Biochem.* **2006**, *100*, 727–743.

(20) Roach, P. L.; Clifton, I. J.; Hensgens, C. M. H.; Shibata, N.; Schofield, C. J.; Baldwin, J. E. *Nature* **1997**, *387*, 827–830.

(21) Chen, V. J.; Orville, A. M.; Harpe, M. R.; Frolik, C. A.; Surerus, K. K.; Münck, E.; Lipscomb, J. D. *J. Biol. Chem.* **1989**, *264*, 21677–21681.

(22) Brown, C. D.; Neidig, M. L.; Neibergall, M. B.; Lipscomb, J. B.; Solomon, E. I. *J. Am. Chem. Soc.* **2007**, *129*, 7427–7438.

(23) Baldwin, J. E.; Bradley, M. *Chem. Rev.* **1990**, *90*, 1079–1088.

(24) Wirstam, M.; Siegbahn, P. E. M. *J. Am. Chem. Soc.* **2000**, *122*, 8539–8547.

(25) Lau, R. L.; van Eupen, J. T. H.; Schipper, D.; Tesser, G. I.; Verweij, J.; de Vroom, E. *Tetrahedron* **2000**, *56*, 7601–7606.

(26) Andersson, I.; Terwisscha van Scheltinga, A. C.; Valegård, K. *Cell. Mol. Life Sci.* **2001**, *58*, 1897–1906.

(27) Burzlaff, N. I.; Rutledge, P. J.; Clifton, I. J.; Hensgens, C. M. H.; Pickford, M.; Adlington, R. M.; Roach, P. L.; Baldwin, J. E. *Nature* **1999**, *401*, 721–724.

(28) Baldwin, J. E.; Abraham, E. *Nat. Prod. Rep.* **1988**, *5*, 129–145.

(29) Becke, A. D. *J. Chem. Phys.* **1993**, *98*, 5648–5652.

(30) Lee, C.; Yang, W.; Parr, R. G. *Phys. Rev. B* **1988**, *37*, 785–789.

(31) Cornell, W. D.; Cieplak, P.; Bayly, C. I.; Gould, I. R.; Merz, K. M., Jr.; Ferguson, D. M.; Spellmeyer, D. C.; Fox, T.; Caldwell, J. W.; Kollman, P. *J. Am. Chem. Soc.* **1995**, *117*, 5179–5197.

(32) Torrent, M.; Vreven, T.; Musaev, D. G.; Morokuma, K.; Farkas, Ö.; Schlegel, H. B. *J. Am. Chem. Soc.* **2002**, *124*, 192–193.

(33) Vreven, T.; Morokuma, K. *Theo. Chem. Acc.* **2003**, *109*, 125–132.

(34) Li, J.; Cross, J. B.; Vreven, T.; Meroueh, S. O.; Mobashery, S.; Schlegel, H. B. *Proteins* **2005**, *61*, 246–257.

(35) Yoshizawa, K.; Shiota, Y. *J. Am. Chem. Soc.* **2006**, *128*, 9873–9881.

(36) Godfrey, E.; Porro, C. S.; de Visser, S. P. *J. Phys. Chem. A* **2008**, *112*, 2464–2468.

(37) Frisch, M. J. ; Trucks, G. W.; Schlegel, H. B.; Scuseria, G. E.; Robb, M. A.; Cheeseman, J. R.; Montgomery, J. A., Jr.; Vreven, T.; Kudin, K. N.; Burant, J. C.; Millam, J. M.; Iyengar, S. S.; Tomasi, J.; Barone, V.; Mennucci, B.; Cossi, M.; Scalmani, G.; Rega, N.; Petersson, G. A.; Nakatsuji, H.; Hada, M.; Ehara, M.; Toyota, K.; Fukuda, R.; Hasegawa, J.; Ishida, M.; Nakajima, T.; Honda, Y.; Kitao, O.; Nakai, H.; Klene, M.; Li, X.; Knox, J. E.; Hratchian, H. P.; Cross, J. B.; Bakken, V.; Adamo, C.; Jaramillo, J.; Gomperts, R.; Stratmann, R. E.; Yazyev, O.; Austin, A. J.; Cammi, R.; Pomelli, C.; Ochterski, J. W.; Ayala, P. Y.; Morokuma, K.; Voth, G. A.; Salvador, P.; Dannenberg, J. J.; Zakrzewski, V. G.; Dapprich, S.; Daniels, A. D.; Strain, M. C.; Farkas, O.; Malick, D. K.; Rabuck, A. D.; Raghavachari, K.; Foresman, J. B.; Ortiz, J. V.; Cui, Q.; Baboul, A. G.; Clifford, S.; Cioslowski, J.; Stefanov, B. B.; Liu, G.; Liashenko, A.; Piskorz, P.; Komaromi, I.; Martin, R. L.; Fox, D. J.; Keith, T.; Al-Laham, M. A.; Peng, C. Y.; Nanayakkara, A.; Challacombe, M.; Gill, P. M. W.; Johnson, B.; Chen, W.; Wong, M. W.; Gonzalez, C.; Pople, J. A. *Gaussian Development Version*; Gaussian, Inc.: Wallingford, CT, 2008.

(38) Bakowies, D.; Thiel, W. *J. Phys. Chem.* **1996**, *100*, 10580–10594.

(39) Lundberg, M.; Morokuma, K. *J. Phys. Chem. B* **2007**, *111*, 9380–9389.

(40) Altun, A.; Shaik, S.; Thiel, W. *J. Comput. Chem.* **2006**, *27*, 1324–1337.

(41) Phillips, J. C.; Braun, R.; Wang, W.; Gumbart, J.; Tajkhorshid, E.; Villa, E.; Chipot, C.; Skeel, R. D.; Kale, L.; Schulten, K. *J. Comput. Chem.* **2005**, *26*, 1781–1802.

(42) Siegbahn, P. E. M. *J. Biol. Inorg. Chem.* **2006**, *11*, 695–701.

(43) Bassan, A.; Borowski, T.; Siegbahn, P. E. M. *Dalton Trans.* **2004**, *20*, 3153–3162.

(44) Kriauciunas, A.; Frolik, C. A.; Hassell, T. C.; Skatrud, P. L.; Johnson, M. G.; Holbrok, N. I.; Chen, V. J. *J. Biol. Chem.* **1991**, *266*, 11779–11788.

(45) Ogle, J. M.; Clifton, I. J.; Rutledge, P. J.; Elkins, J. M.; Burzlaff, N. I.; Adlington, R. M.; Roach, P. L.; Baldwin, J. E. *Chem. Biol.* **2001**, *8*, 1231–1237.

(46) Zheng, G.; Witek, H.; Bobadova-Parvanova, P.; Irle, S.; Musaev, D. G.; Prabhakar, R.; Morokuma, K.; Lundberg, M.; Elstner, M.; Köhler, C.; Frauenheim, T. *J. Chem. Theory Comput.* **2007**, *3*, 1349–1367.

(47) Iordanov, T. D. *J. Mol. Struct. (THEOCHEM)* **2007**, *850*, 152–159.

(48) Zheng, J. J.; Altun, A.; Thiel, W. *J. Comput. Chem.* **2007**, *28*, 2147–2158.

(49) Lundberg, M.; Blomberg, M. R. A.; Siegbahn, P. E. M. *Top. Curr. Chem.* **2004**, *238*, 79–112.

(50) Bautz, J.; Comba, P.; Lopez de Laorden, C.; Menzel, M.; Rajaraman, G. *Angew. Chem., Int. Ed.* **2007**, *46*, 8067–807.

(51) Borowski, T.; Bassan, A.; Siegbahn, P. E. M. *Inorg. Chem.* **2004**, *43*, 3277–3291.

(52) Rowe, C. J.; Shorrock, C. P.; Claridge, T. D. W.; Sutherland, J. D. *Chem. Biol.* **1998**, *5*, 229–239.

(53) Baldwin, J. E.; Adlington, R. M.; Domayne-Hayman, B. P.; Ting, H.-H.; Turner, N. J. *J. Chem. Soc., Chem. Commun.* **1986**, 110–113.

CT800457G